

**INTEGRATED SEISMIC LITHOLOGIC INTERPRETATION:
THE PETROPHYSICAL BASIS**

**A DISSERTATION
SUBMITTED TO THE DEPARTMENT OF GEOPHYSICS
AND THE COMMITTEE ON GRADUATE STUDIES
OF STANFORD UNIVERSITY
IN PARTIAL FULFILLMENT OF THE REQUIREMENTS
FOR THE DEGREE OF
DOCTOR OF PHILOSOPHY**

By

Jean-Pierre ("J.P.") Dominique BLANGY

July 1992


Disclosure statement:

The methodologies and interpretations presented in this thesis are solely those of the author and do not necessarily reflect the opinion of Norsk Hydro S.A. or of the Troll Licensing group.

©Copyright by J.P. Blangy, 1992

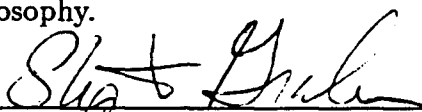
All Rights Reserved

I certify that I have read this dissertation and that in my opinion it is fully adequate, in scope and quality, as a dissertation for the degree of Doctor of Philosophy.



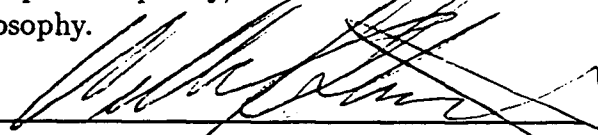
 Amos Nur (Geophysics): Principal Advisor

I certify that I have read this dissertation and that in my opinion it is fully adequate, in scope and quality, as a dissertation for the degree of Doctor of Philosophy.




 Steve Graham (Geology)

I certify that I have read this dissertation and that in my opinion it is fully adequate, in scope and quality, as a dissertation for the degree of Doctor of Philosophy.



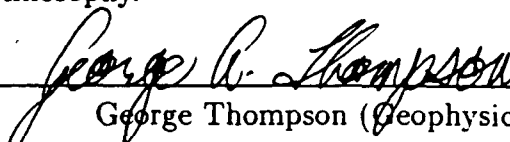
 Bill Ostrander (Geophysics)

I certify that I have read this dissertation and that in my opinion it is fully adequate, in scope and quality, as a dissertation for the degree of Doctor of Philosophy.



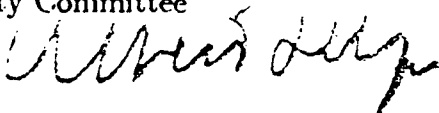
 John Harbaugh (Applied Earth Sciences)

I certify that I have read this dissertation and that in my opinion it is fully adequate, in scope and quality, as a dissertation for the degree of Doctor of Philosophy.

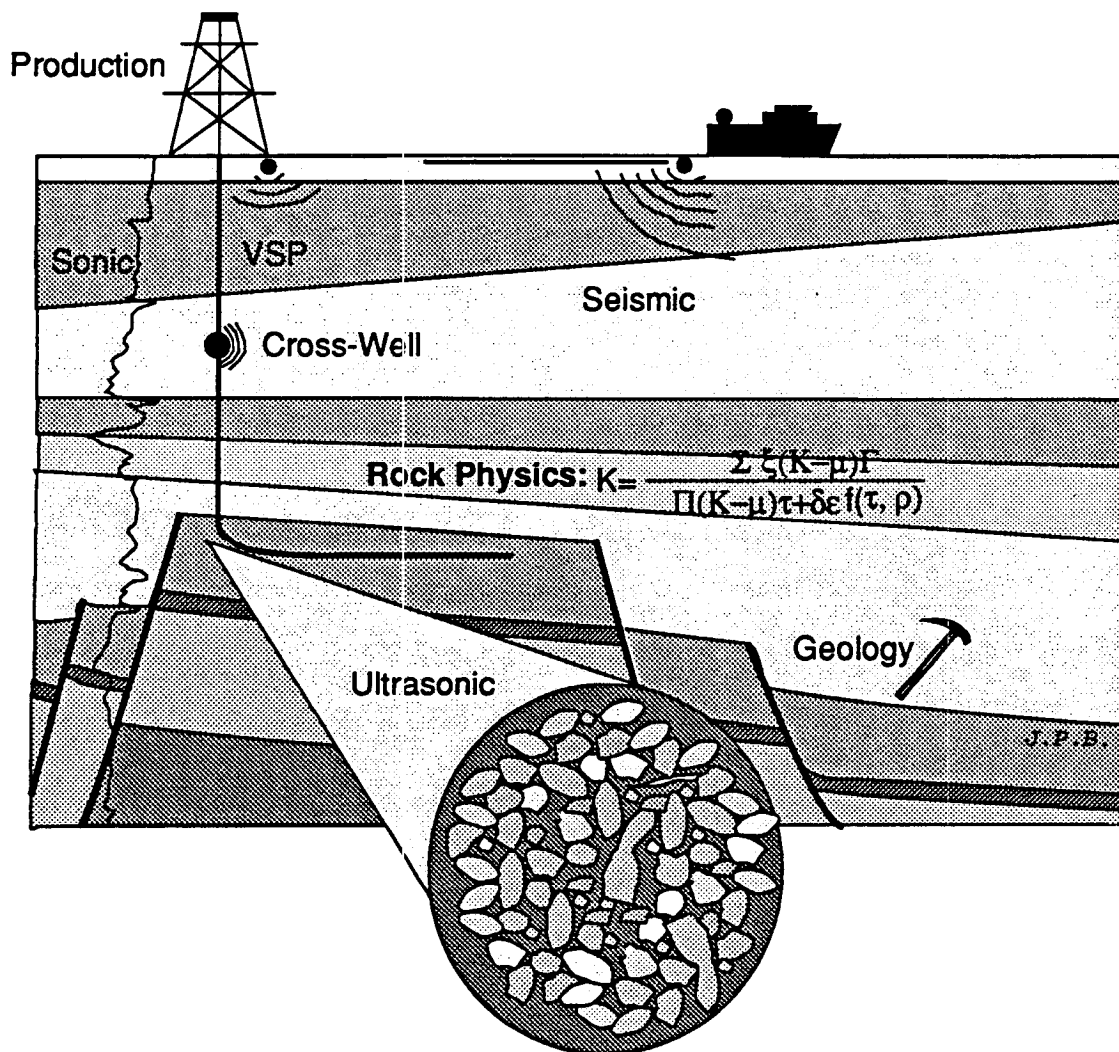


 George Thompson (Geophysics)

Approved for the University Committee
 on Graduate Studies:



Integrated Seismic Lithologic Interpretation: The Petrophysical Basis



Abstract

Reflection seismic methods are, and will continue to be, the key geophysical tool for imaging heterogeneities in the subsurface of the earth. Surprisingly, the amount of financial effort spent on quantitative lithologic interpretation is much less than that spent on acquisition and processing of the data. In spite of great advances in acquisition and processing, the primary product of conventional seismic work is still only the spatial pattern of reflectivity, which is essentially a measure of velocity variations. The seismic amplitude information is rich yet goes mostly unused. I attribute this to a general lack of understanding or knowledge of petrophysics, and I believe that **petrophysics** appears to have been the "weak link in quantitative seismic lithologic interpretation".

The above statement is the more surprising, when considering the following:

- the pressing need for lithologic inversion as opposed to elastic velocity inversion, since explorationists and "exploitationists-productionists" are ultimately interested in rock properties, and not in velocities or impedance contrasts.
- the necessity for a quantitative methodology to integrate different data types and scales, and to use them for the best parameterization possible in theoretical models of wave propagation.

The complexity of interaction between the numerous parameters affecting seismic waves dictates that any quantitative extraction of rock properties from seismic be **model-based**. Having recognized this fact, I first concentrate on understanding the wave equation and on details of wave propagation through complex media. This leads to the identification of the key parameters affecting seismic reflection signatures: elastic velocities, density, anisotropy, and anelasticity.

Second, I devise a state-of-the-art methodology to estimate these crucial parameters from diverse sets of different rock properties. An integrated deterministic modeling scheme is proposed, whereby detailed petrophysical properties from the microscale are used in the determination of smoothed long wavelength equivalent transverse isotropic media at the seismic macroscale. This is **integration of scales**. Integration reduces the non-uniqueness problem and allows for the combined benefits of borehole information which is very accurate in the vertical direction and of seismic which has a large scale lateral resolution. This is **integration of techniques and disciplines**.

The two previous theoretical efforts are then put to the test in the study of a loosely consolidated reservoir from the North sea. Using both seismic amplitudes and velocities with emphasis on AVO analysis, I show that petrophysics can serve as the linking bridge between **integrated reservoir characterization** and the **actual geology** of the subsurface. I then show that the use of model-based seismic interpretation combined with sound petrophysical principles can lead to better reservoir management.

Acknowledgements

The work presented in this thesis is the product of a great many discussions with a lot of geoscientists over the last ten years. Amos Nur provided financial support throughout this study, and made it all possible.

Keith Wrolstad of Unocal was the first to introduce me to AVO analysis. Working with Keith for two years was a great privilege and his advice and understanding of the industry's needs shaped my initial work on AVO. Leon Thomsen and Richard Lindsay of Amoco, Tai Ng of Canadian Hunter, and Jack Ward of Simon-Geolithic provided sound advice on petrophysical modeling.

Steve Grahams' enthusiasm about seismic interpretation and his devotion to students was of great value in the final version of this work. Bill Ostrand's insight and practical view on seismic processing and analysis, and especially on AVO issues, were greatly appreciated. Special thanks to John Harbaugh and George Thompson for reviewing the final draft.

Sverre Strandenes made the analysis of the field data possible, and insured its release from Norsk Hydro. Working with Sverre at Stanford was a relatively short but enjoyable experience. He not only contributed toward this thesis, but also passed on his permanent positive outlook on life, and became a very good friend.

Discussions with Jerry Harris, Mark Zoback, Gary Mavko, Lev Vernik, Jack Dvorkin, Dan Moos, and Colleen Barton were all very fruitful. I thank Pierre Samec for sharing his understanding of wave propagation, Marc Van Schaack for his pointers on how to get around computers, Jaime Rector for his help in borehole geophysics and his epicurian outlook, Alan Carroll for his understanding of organic rocks, Roger Bloch for communicating his enthusiasm on seismic stratigraphy, and all of the S.R.B. members for helpful discussions.

Ron Lyon and the Stanford remote sensing group provided software for the clustering and pattern recognition of seismic attributes; special thanks go to Kai Lanz. The data for the Troll work was provided courtesy of Norsk Hydro; I made the ultrasonic laboratory measurements and thin-section analyses at the S.R.B. facilities, the 3-D seismic interpretation on an IBM RT based system provided by Landmark Graphics, the log analysis on a terrastation provided by Terrasciences, and the processing of seismic data with Advance's ProMAX.

Finally, I want to thank Margaret Muir for always being there, and my parents, Bernard and Annick, together with my sister, Florence for their infinite patience and support throughout this work. My stay at Stanford was made possible by the financial support of the Stanford Rock and Borehole project (S.R.B.), the Gas Research Institute (G.R.I.), the Office of Naval Research (O.N.R.) and the Department of Energy (D.O.E.). Some of this work was also supported by a Chevron Scholarship. The Triple Society is acknowledged for moral support.

Table of Contents

<u>ABSTRACT</u>	v
Acknowledgements	vi
<u>INTRODUCTION</u>	1
1-Global perspectives	1
2-Natural gas	1
3-Motivation for <u>new</u> research	2
4-Need for <u>quantitative integrated</u> modeling techniques	3
5-Overview of the work: Message of the thesis	3
"Mission statement"	4
6-Organization of the thesis	5
6.a Part I: Theory: Chapters 1, 2, and 3	5
6.b Parts II and III: Applications: Chapters 4 and 5	7
<u>PART I</u>	
Introduction to part I: THEORY	11
1) Chapter 1: A.A.A.: Attenuation, Anisotropy, and AVO	11
Abstract	12
I) Introduction	13
II) Review of current AVO techniques	14
II.1 AVO studies in isotropic media	14
II.2 A simple example	18
II.3 Sensitivity to changes in elastic parameters	25
III) Attenuation, Anisotropy, and AVO	25

III.1 The Importance of viscoelastic attenuation and anisotropy	25
III.2 Previous theoretical studies in anisotropic media	27
III.3 The response of two media with anisotropic and anelastic properties	32
III.3.a Time domain modeling algorithm for anisotropic viscoelastic solids	32
III.3.b Implementation of the modeling algorithm for the study of seismic reflections	35
III.3.c Modeling benchmarks and calibration of reflections	37
III.3.d Effect of viscoelastic attenuation on AVO measurements ..	42
III.3.e Effect of elastic anisotropy and attenuation anisotropy on AVO measurements	51
III.3.f Results	56
III.3.g Future work	59
IV) Simplified Zoeppritz equations for T.I. media	60
V) Conclusions	64
2) Chapter 2: Deterministic Modeling for AVO studies: The calculation of "missing" properties	69
Abstract	69
I) Introduction	70
II) Relevance of Rock Physics to AVO modeling	71
II.1 Emphasis placed on Integration	71
II.2 Rock Physics	72
II.2.a Traditional Rock Physics	72
II.2.b Current directions in Petrophysical studies	79
Review of bounding methods	80
Self-Consistent approaches	83

II.3 Rock Physics to approximate anisotropy: Bakken shale example .	84
Review of anisotropy	84
Elliptical anisotropy	85
Transverse isotropy	92
Phase and group velocities	95
II.4 Reservoir heterogeneities	97
III) Deterministic modeling of Shear Velocities	98
III.1 The Gregory-Pickett method	99
The Castagna method	101
III.2 The Biot-Consistent method	102
III.3 The Krief method	105
III.4 The Calibrated Empirical Method (CEM)	107
a) Observations	107
b) Empirical model	108
c) Comparison with other models	114
d) Implications of the model	119
e) Applications of the model	122
IV) Deterministic modeling of Viscoelastic Attenuation	125
V) Conclusions	133
3) Chapter 3: Deterministic modeling for AVO studies: An Integrated approach	141
Abstract	141
I) Introduction	143
The need for integration	143
The need for a systematic procedure for integration	143
II) In-situ properties from logs and cores: Lithologic "zoning"	144
Environmental corrections (P_e , T)	148

III) Classification of sedimentary rocks for establishing parameter variations	150
IV) Up-scaling and equivalent transversely isotropic media	151
IV.1 For a series of isotropic homogeneous microlayers	154
IV.2 For a series of transversely isotropic homogeneous microlayers	156
IV.3 Convenient notation for transverse isotropy	157
V) Dispersion corrections of moduli	159
VI) Potential applications	160
VI.1 Calculation of average bulk properties at a well	160
VI.2 Extrapolation of average bulk properties away from a well	160
VII) Conclusions	161
Introduction to parts II and III: APPLICATIONS	167

PART II

Introduction to part II: APPLICATIONS-1	170
4) Chapter 4: An integrated 3-D seismic stacked Interpretation of the Troll West Oil Province	172
Abstract	172
I) Introduction	173
Troll field description	173
II) Global setting and regional structural control	176
II.1 The North Sea	176
II.2 Structural and depositional controls at Troll	177
II.3 Key parameters in the evolution of hydrocarbon traps at Troll	181
II.4 Discovery of the Troll field and future plans	182
III) Reservoir description	183
III.1 General description	183

III.2 Subdivisions within the reservoir	185
III.3 Mineralogy and diagenesis	188
IV) Major structural controls	190
V) 3-D Interpretation of Troll West	190
V.1 Classical 3-D Interpretation of stacked data	190
V.1.a Survey layout	190
V.1.b Procedure	192
V.1.c Horizon interpretation	196
V.1.d Fault interpretation	199
V.1.e Correlation of depositional cycles identified on	
logs with seismic	203
Calcite stringers	207
Depositional cycles and intra-formational reflectors	207
Limit of seismic resolution	214
V.1.f Results	215
V.2 Exotic 3-D Interpretation of stacked data	217
V.2.a Interpretation of complex trace attributes	217
Time horizon slices	222
V.2.b Pattern recognition of clusters of complex trace	
attributes	224
Methodology	224
Data analysis	225
Unsupervised clustering	225
Supervised clustering	225

VI) Conclusions 229

PART III

Introduction to part III: **APPLICATIONS-2**233

5) Chapter 5: A detailed integrated seismic reservoir study of the Troll West Oil Province **238**

 Abstract 238

 Introduction 232

 I) Core analysis and Interpretation 240

 I.1 Motivation for laboratory work 242

 I.2 Origin of the core samples 243

 I.3 Sample preparation and measurement set-up 243

 I.4 Overview of the core measurement program 245

 I.5 Data corrections 247

 I.6 Measurement accuracy and repeatability 249

 I.7 Thin-section analysis 249

 I.8 Velocity variations with porosity and mineralogy 266

 I.9 Velocity variations with pressure 272

 I.10 V_p/V_s relationships 276

 I.11 Measurements in oil saturated samples 277

 I.12 Effect of temperature 279

 I.13 Other measurements 281

 I.14 Dispersion 281

 I.15 Comparison with other data 283

 I.16 Defining rock parameters for Dognefjord sands 289

 I.17 Summary of the core measurement program 290

 II) Log analysis and interpretation at well 31/5-4S 292

II.1 Litho-density log: Comparison of core and log porosities	292
II.2 Sonic log: Comparison of core and log velocities	292
II.3 Mapping of lithologic changes with logs	297
a- The NGS: Correlation to muscovite content	297
b- Litho-density and sonic: Correlation to calcite	301
II.4 Calculation of "missing" properties	302
Use of calibrated logs at other wells	303
III) Controlled True Amplitude Processing	303
Why reprocess the pre-stack data?	304
Model assisted processing	304
IV) Petrophysics and AVO for Reservoir Characterization	307
IV.1 Preliminary model	310
Considerations of anisotropy	312
Anisotropy in the reservoir	315
IV.2 Building a detailed geological/petrophysical reservoir model ...	319
Single interface reflection coefficients	322
Effective reflection coefficients, synthetic seismograms, and	
model-based interpretation	324
Conclusions on AVO modeling	337
V) Petrophysics and AVO for Reservoir Management	338
V.1 Environmental management	338
V.2 Difficult production conditions at Troll	338
V.3 Production parameters	339
a- Permeability-porosity and permeability-mica content	
relationships	339
b- Elastic properties and fluid content	340
c- Fluid contacts, in-situ conditions and hydrocarbon	

properties	344
d- Model results of fluid flow	344
Summary and conclusions	346
6) General conclusions	352
1- Model-based Integrated Seismic Lithologic Interpretation	352
2- An Inter-disciplinary effort	352
3- An exciting time to be involved in Geosciences	354
4- Looking ahead	355

APPENDICES

APPENDIX A: Phase and Group velocities	358
APPENDIX B: Key lithology and well log responses at Troll West	361
APPENDIX C: Ultrasonic measurements of Troll sands	372
APPENDIX D: Table of common mineral elastic constants and velocities ..	380
APPENDIX E: Other related publications and reports by the author	383

List of Figures

Figure 1.1: Ray configuration and energy conversion considerations for Zoeppritz equations	15
Figure 1.2: Conversion from V_p/V_s ratio to Poisson's ratio and to K/μ	19
Figure 1.3: Single interface AVO response for a shale overlying a water sand and a gas sand	20
Figure 1.4a: Synthetic seismogram using the full elastic response of the water sand in figure 1.3	21
Figure 1.4b: Viscoelastic synthetic seismogram using the full viscoelastic response of the water sand in figure 1.3	22
Figure 1.5a: Synthetic seismogram using the full elastic response of the gas sand in figure 1.3	23
Figure 1.5b: Viscoelastic synthetic seismogram using the full viscoelastic response of the gas sand in figure 1.3	24
Figure 1.6: Changes in AVO response for small variations in normalized velocity and density	26
Figure 1.7: AVO response of transversely isotropic shale over an isotropic sand saturated with either water or gas	28
Figure 1.8: Special case of reversal in (expected) isotropic AVO response, caused by transverse isotropy	30
Figure 1.9: Schematic representation of the effects of viscoelasticity and anisotropy on AVO trends	31
Figure 1.10: Modeling viscoelastic attenuation	34
Figure 1.11: Model set-up, anisotropic parameters used in the modeling, and experimental evidence for attenuation anisotropy	38
Figure 1.12: A typical synthetic gather, and comparison between numerical and theoretical amplitudes for the isotropic case	41
Figure 1.13: Imaginary set-up of receivers placed along different ray paths, and the calculation of reflection coefficients as a function of the angle of incidence	43
Figure 1.14: Comparison between theoretical and numerical reflection coefficients	

(computed using the method summarized in figure 1.13), for the isotropic case .	44
Figure 1.15: Imaginary set-up of receivers placed along different wavefronts, and computation of the signal propagated through a receiver array placed along the wavefront	45
Figure 1.16: Description of an isotropic viscoelastic solid, and of an anisotropic viscoelastic solid	48
Figure 1.17: Comparison between reflected amplitudes, from an elastic and a viscoelastic, isotropic and anisotropic, bottom layer	49
Figure 1.18: Comparison between reflected amplitudes, with a viscoelastic isotropic, and a viscoelastic anisotropic top layer	50
Figure 1.19: Elastic properties of the anisotropic material used for the modeling	52
Figure 1.20: Effect of anisotropy on the reflection coefficient and on AVO measurements	53
Figure 1.21: Effect of an anisotropic upper layer on the AVO response	55
Figure 1.22: Energy distribution along the wavefront in an isotropic solid and an anisotropic solid	57
Figure 2.1: Rock physics as a bridge between seismic and lithology	73
Figure 2.2: Compressional velocities as a double-valued function of clay content (modified after Marion, 1990)	74
Figure 2.3: Example of the effects of clay location on shear wave velocities	78
Figure 2.4: Bounds on bulk moduli for spherical and platey geometries, and comparison to Hashin-Shtrikman bounds	82
Figure 2.5: Isostress and isostrain concepts used to define theoretical velocities in directions perpendicular and parallel to bedding	86
Figure 2.6: Relation between direction in which core samples are taken and isostress and isostrain cases in a finely layered medium to be elliptically isotropic	87
Figure 2.7: Decomposition of the total stress into its normal and tangential components	88
Figure 2.8: Elliptical isotropy as a first order approximation of velocities in Bakken	

shales	90
Figure 2.9: Elliptical isotropy and kerogen content in the Bakken shale	90
Figure 2.10: Model of a finely layered rock with two isotropic and homogeneous components	94
Figure 2.11: Summary of the Biot-Consistent method: Flow chart and example calculation	104
Figure 2.12: Dry and saturated dynamic shear moduli as a function of porosity for consolidated and lesser consolidated rocks	109
Figure 2.13: Dry dynamic bulk moduli as a function of porosity for consolidated and lesser consolidated rocks	110
Figure 2.14: Concepts of the Calibrated Empirical Model (C.E.M.)	112
Figure 2.15: C.E.M. and data comparison	113
Figure 2.16: Comparison of C.E.M. with other models for shear moduli	116
Figure 2.17: Comparison of C.E.M. with Gregory-Pickett method for shear velocities	117
Figure 2.18: Dry V_p/V_s ratios and dry bulk modulus to shear modulus ratios as a function of porosity	120
Figure 2.19: Comparison of velocity-porosity relationships for 100 % saturated samples	121
Figure 2.20: Agreement between synthetic (C.E.M.) shear modulus and measured shear modulus from dipole sonic tool	124
Figure 2.21: Standard linear solid used to quantify intrinsic attenuation (modified after Jones, 1986)	126
Figure 3.1: The deterministic approach	145
Figure 3.2: Lithologic "zoning"	149
Figure 3.3: Lithologic classification of sedimentary rocks	152
Figure 3.4: Petrophysical classification of sedimentary rocks	153
Figure 3.5: The Smooth Transverse Isotropic Long Wavelength equivalent	

(STILWE) concept	155
Figure 3.6: Sensitivity analysis: implementing parameter variations	162
Introduction figure: Troll comparison	171
Figure 4.1: The Troll field: North sea context	175
Figure 4.2: The Troll field: Oil and Gas distribution	178
Figure 4.3: The Troll West Oil Province: 1989 3-D seismic coverage	179
Figure 4.4: Ternary diagram showing the global composition of the Sognefjord reservoir sands	184
Figure 4.5: Stratigraphic column at the "type" well 31/2-5	186
Figure 4.6: Reference line 328 shot through well 31/2-5 with interpreted horizons and faults	198
Figure 4.7: Phases of structural development of the Troll field as seen through the analysis of line 330	201
Figure 4.7 (continued): Phases of structural development of the Troll field .	202
Figure 4.8: Stratigraphic summary at Troll and correlation of allostratigraphic units within the Sognefjord Formation with eustatic sea level curves	205
Figure 4.9: Well to seismic ties at wells 31/5-3 and 31/2-16S	209
Figure 4.10: Well to seismic ties at wells 31/2-5 and 31/2-10	211
Figure 4.11: Well to seismic ties at wells 31/2-13 and 31/2-12	213
Figure 4.12: Distribution of instantaneous frequencies in a time window centered around the Sognefjord	215
Figure 4.13: Tie-loop through line 190 and line 328	216
Figure 4.14: Contour (structure) maps of the top of the Sognefjord and the top of the Fensfjord	218
Figure 4.15: Contour (structure) map of the top of the Brent and isopach map of the Sognefjord	219
Figure 4.16: Direct Hydrocarbon Detection: Flattened time-horizons slices showing stacked amplitudes, instantaneous phase and instantaneous frequency at the top of	

the Sognefjord	223
Figure 4.17: Principles of statistical clustering and factor analysis	226
Figure 4.18:	
a) Superposition of three seismic attributes at the top of the Sognefjord	
b) Supervised clustering of seismic attributes from the top of the Sognefjord ...	228
Figure 5.1: Hydrographical boundaries, average water depths, and average currents in the North sea	241
Figure 5.2: Comparison of Troll porosities (from well 31/5-4S) measured at S.R.B. with those measured by Geco Corelabs	244
Figure 5.3: Measured apparent porosities at Troll, after 1st and 2nd oil cleaning attempts	246
Figure 5.4: Measured volumetric strains at 30 MPa effective pressure	248
Figure 5.5: Dry compressional velocities (at all effective pressures) before and after porosity and length corrections	250
Figure 5.6: Mineral compositions of the Sognefjord sands at well 31/5-4S as obtained from thin section point counting	252
Figure 5.7: Grain density versus mineralogy of the Sognefjord sands	253
Figure 5.8: Mineralogy versus porosity of the Sognefjord sands	253
Figure 5.9: Mineralogy versus grain size of the Sognefjord sands	255
Figure 5.10: Micro photograph of thin sections of typical coarse grained clean Sognefjord sands at well 31/5-4S	257
Figure 5.11: Micro photographs of thin sections of typical medium grained clean and micaceous Sognefjord sands at well 31/5-4S	258
Figure 5.12: Photos of thin sections of highly micaceous fine grained Sognefjord sands at well 31/5-4S	260
Figure 5.13: Micro photographs of thin sections displaying high amounts of altered feldspar and/or mica at well 31/5-4S	261
Figure 5.14: Micro photographs of blue epoxy thin sections showing pore geometries of coarse grained clean sands at well 31/5-4S	263
Figure 5.15: Micro photographs of blue epoxy thin sections showing pore geometries of medium grained clean sands and fine grained highly micaceous sands	

at well 31/5-4S	264
Figure 5.16: Additional features observed in Sognefjord sands	265
Figure 5.17: Dry compressional and shear velocities at 30 MPa effective pressure	266
Figure 5.18: Fully water saturated compressional and shear velocities at 30 MPa effective pressure	267
Figure 5.19: Compressional versus shear velocity at 30 MPa effective pressure for the Sognefjord sands	268
Figure 5.20: Velocity-porosity versus mica content; dry samples.	269
Figure 5.21: Velocity-porosity versus feldspar content; dry samples.	270
Figure 5.22: Velocity-porosity versus feldspar content; saturated samples. ...	271
Figure 5.23: Dry and water saturated compressional and shear velocities versus mica content	273
Figure 5.24: Dry compressional velocities at 30, 25, 20, 15, 10 and 5 MPa effective pressures	274
Figure 5.25: Dry shear velocities at 30, 25, 20, 15, 10 and 5 MPa effective pressures	275
Figure 5.26: Fully saturated compressional velocities at 30, 25, 20, 15, 10 and 5 MPa effective pressures	276
Figure 5.27: Fully saturated shear velocities at 30, 25, 20, 15, 10 and 5 MPa effective pressures	277
Figure 5.28: Dry v_p/v_s ratios at 30, 25, 20, 15, 10, and 5 MPa effective pressures	278
Figure 5.29: Water saturated v_p/v_s ratios at 30, 25, 20, 15, 10 and 5 MPa effective pressures	278
Figure 5.30: Oil and water saturated compressional and shear velocities at 30 MPa effective pressure	280
Figure 5.31: Compressional and shear velocities in oil saturated samples as a function of temperature at 30 MPa effective pressure	281
Figure 5.32: Velocities under full saturation for water, cognac, and champagne at	

room temperature	282
Figure 5.33: Measured water saturated compressional and shear velocities at 30 MPa effective pressure compared to velocities computed from Biot low frequency expressions	284
Figure 5.34: Comparison of different measurements of water saturated compressional velocities in various sandstones at 30 MPa effective pressure	286
Figure 5.35: Comparison of different measurements of water saturated shear velocities in various sandstones at 30 MPa effective pressure	287
Figure 5.36: Comparison of v_p/v_s ratios in various water saturated sandstones at 30 MPa effective pressure	288
Figure 5.37: Water saturated bulk and shear moduli as a function of porosity for Sognefjord sands at 30 MPa effective pressure	290
Figure 5.38: Comparison between core measured (helium) porosities, and log-derived porosities at well 31/5-4S	293
Figure 5.39: Comparison between core measured and log-derived compressional velocities versus depth at well 31/5-4S	294
Figure 5.40: Comparison between core measured and log-derived compressional velocities versus porosity at Troll	296
Figure 5.41: Correlation between potassium content, gamma ray, and mica content as identified from thin-sections	299
Figure 5.42: Indirect velocity-mica relationship for sands from well 31/2-5 ...	300
Figure 5.43: Models of "Primary only" and "Primary and multiples" at well 31/2-5	305
Figure 5.44: Full waveform model and CDP supergather at well 31/2-5	306
Figure 5.45: CDP gathers in the vicinity of well 31/2-5	308
Figure 5.46: CDP supergather in the vicinity of well 31/2-5	309
Figure 5.47: Geological model of the overburden used in the preliminary AVO modeling	311
Figure 5.48: Variations in reflection angle with depth and surface offset, based on	

the preliminary model	313
Figure 5.49: AVO responses from the top of the reservoir and from the GOC	314
Figure 5.50: Reduced travel time CDP gather at well 31/2-5	316
Figure 5.51: Preliminary model of the reservoir zone, based on well 31/2-5 ...	318
Figure 5.52: Phase velocities in the transversely isotropic gas zone, produced by layer induced anisotropy	319
Figure 5.53: AVO responses from the top of the reservoir and from the GOC; effect of anisotropy	320
Figure 5.54: AVO response from the GOC; effect of mica content	321
Figure 5.55: Detailed reservoir model at well 31/2-5	323
Figure 5.56: Brute stack (after sort, supergather binning, spherical divergence statics and F-K "demultiple" filtering)	326
Figure 5.57: Full waveform model at well 31/2-5	327
Figure 5.58: CDP supergather within the vicinity of well 31/2-5 (approximately CDP 355)	328
Figure 5.59: Full waveform model with no mica sands at well 31/2-5	330
Figure 5.60: Full waveform model with no clean sands at well 31/2-5	331
Figure 5.61: Full waveform model with no calcite layers present at well 31/2-5	332
Figure 5.62: Full waveform model with no gas present at well 31/2-5	333
Figure 5.63: CDP supergather in the westernmost part of the Troll West Gas province	335
Figure 5.64: Full waveform model the westernmost part of the Troll West Gas province	336
Figure 5.65: Permeability versus porosity data as measured on cores by Geco for all of the samples at well 31/5-4S	341
Figure 5.66: Permeability versus porosity and permeability versus muscovite content as measured on cores and as predicted at well 31/5-4S	342
Figure 5.67: Permeability versus porosity and permeability versus muscovite	

List of Figures

xxiii

content as inferred from logs at well 31/2-5	343
Figure 5.68: Full waveform model simulating gas coning at well 31/2-5	345
Figure 6.1: Rock Physics as a quantitative tool for Integration	353
Figure 6.2: Evolution of surface seismic methods	356

List of Tables

Table 1.1: AVO response table for a single interface response between two elastic isotropic media	18
Table 1.2 : AVO response table for a single interface response between two weakly anisotropic media	29
Table 2.1 : Calculated lower bounds on δ for several "type" lithologies	96
Table 4.1: Processing sequence used by CGG for the 1989 3-D seismic survey over the Troll West Oil Province	191
Table 4.2: Well coordinates and fluid contacts in ms (two way travel travel time) at the seven major control wells within the 3-D surveyed area	192
Table 4.3: The standard interpretation approach for 3-D seismic data	193
Table 4.4: Formation picks in m (below sea floor) and in ms (two way travel time) at the five major control wells within the 3-D surveyed area	194
Table 4.5: Fluid contacts in m (below sea floor) at the five major control wells within the 3-D surveyed area	195
Table 4.6: Seismic trace attribute properties and characteristics	220
Table 5.1: Main potassium bearing minerals	298

List of Appendices

APPENDIX A: Phase and Group velocities	358
APPENDIX B: Key lithology and well log responses at Troll West	361
APPENDIX C: Ultrasonic measurements of Troll sands	372
APPENDIX D: Table of common mineral elastic constants and velocities ..	380
APPENDIX E: Other related publications and reports by the author	383

For all of you who suffer from writer's cramp, here are some key phrases that you may find useful:

The text

- It has long been known that...
- ...of great theoretical and practical importance...
- While it has not been possible to provide definite answers to these questions...
- To present a comprehensive overview...
- A vital question is the extent of penetration of surficial waters into the crust.
- Our sampling concentrated in areas adjacent to carbonate-rich exposures near the Tuamotu Archipelago.
- Our study was restricted to well-sorted sediments.
- A fiducial reference line...
- Three of the samples were selected for detailed study...
- Typical results are shown...
- Although some detail has been lost in reproduction, it is obvious from the photomicrograph that...
- The age of extension is well constrained in the early M.ocene...
- The timing of the last interglacial period and its relation to orbital forcing is disputed.
- The observed peak and its temperature dependence appear not to be consistent with predicted results.
- The temperature measurements of natural lava flows are in good agreement with experimental melting-temperature measurements.
- Historical data suggest that the region south of the 1972 rupture zone should be considered a gap of high seismic potential.
- Presumably the results that would be obtained from studies over a longer time interval would show...
- Correlation with the predicted curve is excellent.
- ...good.
- ...satisfactory.
- ...fair.
- ...as good as could be expected.
- These results will be reported in a subsequent report.
- It is suggested that...
- It is believed that...
- The most current understanding is that...
- It may be that...
- It is generally believed that...
- It is assumed that...
- Additional studies are currently in the planning stage.
- These results are clearly applicable to other planetary bodies as well.
- It is clear that much more work will be required before a complete understanding...
- The proposed scenario may or may not be viable, depending on which set of age estimates is confirmed.
- Speculative origins for the deposit include...
- Unfortunately, a quantitative theory to account for these effects has not been formulated.
- These results are in substantial agreement with previous work.
- Correct within an order of magnitude.
- The many diverse possibilities seem indistinguishable at present.
- Thanks are due to Peg MTite for assistance with the experiments...
- ...and to Gran O. Diorite for valuable discussions.

The meaning

- I think I read this somewhere...
- I find this interesting.
- This research didn't turn out the way I expected it to, but I figure I can get publication out of it.
- Let's ignore the details.
- I have spent five years working on this already.
- We had to justify going to Tahiti somehow.
- We already had some well-sorted samples from a previous study.
- A scratch...
- I couldn't figure out the other samples so I decided to ignore them.
- The best results are shown...
- It is impossible to tell from this picture...
- We have two age dates.
- I'm not sure what I think, either.
- But I needed something to report in this paper.
- It worked!
- You heard it here first, folks.
- I didn't have time to study this.
- ...fair.
- ...poor.
- ...doubtful.
- ...imaginary.
- ...non-existent.
- I might get around to this sometime.
- I think...
- I think...
- I think...
- I think...
- I can refute this, so I'll mention it now.
- I had to guess.
- I haven't heard from NSF yet.
- I'm planning on sending a proposal to NASA, too.
- Beats me.
- I'm looking for a grad student to work on this.
- We're guessing.
- No one else understands it yet either.
- Any differences with previous work are because they were wrong and I'm probably wrong.
- We're still guessing.
- She did the lab work.
- ...and he explained the results to me.

Fill-in page

This page was inserted for esthetic purposes only, and does not necessarily reflect the author's opinion or his state of mind. It is **NOT** an integral part of the thesis at Stanford University, and was obtained from a series of "reliable" sources out there.

INTRODUCTION

1) Global perspectives

Probably the most difficult decision that Ph. D. students have to make, is that of choosing a dissertation topic. All are faced with the problem of finding a subject that is preferably of direct interest to many, that is both practical and innovative, and that may help in the advancement of human kind; this is true, regardless of the field of research. Currently, there is an explosion of information which is flooding the field of Earth Sciences, and there are literally hundreds of possible flow paths. One strong current is carrying students towards computer related careers, another towards environmental sciences, while yet another, nowadays weaker current, orients them towards the Oil and Gas industry.

In the middle of this apparent chaos of information about our planet, one of the recurring themes seems to be that sooner or later people will have to concentrate on alternative sources of energy than oil, be it for economic or environmental reasons. In general, energy analysts distinguish between two broad categories of energy usage: "Hard" energies, which include oil, natural gas, synthetic fuels, coal and uranium, and "soft" energies, which include solar, hydro, wind, biomass, geothermal, and alternative fuels (Jackson, 1991).

2) Natural gas

Natural gas burns more cleanly than oil, and is also much more energy-efficient than oil. In the past, it has been neglected as an alternative fossil fuel, because of an abundance of cheap crude. However, with rising crude oil prices and increasing environmental pressure, U.S. opinion is starting to change slowly. The U.S. has large natural gas reserves that can be developed at moderate costs. Reserve estimates at \$3/Mcf under current technology fall at approximately 500 Tcf for the lower 48 states (452 Tcf as estimated by Enron, 604 Tcf as estimated by NRC/ICF, and 540 Tcf, as estimated by Clements, 1991). Because 1990 consumption was estimated at 18.3 tcf of natural gas (AAPG), the reserves are equivalent to a 30 year supply under today's production rates.

Federal policies currently clearly encourage exploration for natural gas around the world and especially promote domestic exploration. The goal is clear: to reduce the U.S. dependency on foreign oil. In fact congress recently revised the Natural Gas Policy Act of 1978 and passed legislation that should lead to the complete deregulation of natural gas at the wellhead (Clements, W., 1991).

Concurrently, the technology for direct detection of natural gas reservoirs has improved substantially in the last fifteen years, benefitting from modern state-of-the-art acquisition techniques (Harris, 1988, Kennedy et al., 1988, Rector, 1990),

improved seismic processing methods, increased computer power, and more thorough interpretation procedures (Gassman, 1951, Koefoed, 1955, Backus and Chen, 1975, Domenico, 1976, Gregory, 1976, Kjartanson, 1979, Aki and Richards, 1980, Bourbie, 1982, Ostrander, 1984, Jones, 1986, Robertson, 1989, among others).

In summary, it appears that natural gas is slowly emerging as a viable alternative source of energy from an *politico-economic* standpoint and from an *environmental* perspective. Consequently, it seems both appropriate and beneficial to research existing techniques for the detection of natural gas, and to search for *improved* methods of characterization of *gas* reservoirs. Unfortunately, because of an oversupply of natural gas, its price has remained low, and it is currently difficult for most companies to produce gas at a significant profit.

3) Motivation for new research

The general purpose of this work is three fold:

- First, when placed within the overall context of a slowly deflating "gas bubble", it will eventually become economical for oil companies to seek alternative sources of energy than oil, and *natural gas* will most probably emerge as a viable alternative. Unfortunately, this may take some time.
- Second, with increasing *environmental pressure* from the government and from the general public, oil companies will naturally seek to produce more natural gas, which burns both more cleanly and more efficiently than liquid hydrocarbons.
- Third, with recent new developments in the field of reflection seismology (Amplitude versus offset or AVO, Direct Hydrocarbon Indicators, or DHI) it has become *feasible* in some cases to map gas accumulations directly from seismic. Additionally, since oil accumulations are commonly associated with natural gas, it makes sense to use direct seismic detection of natural gas, in conjunction with geochemistry, as an indicator of the possible presence of oil.

Newly unveiled complexities in AVO modeling and interpretation, due to problems of scale, anisotropy, and attenuation, to state only a few, justify an in-depth research effort to help understand and delineate seismic amplitude anomalies. This endeavour requires a good balance between the implementation of conceptual modeling procedures and the thorough analysis of a selected set of "key" datasets, using a multi-disciplinary approach. I establish a constructive feedback, by which data-specific problems are addressed and solved. My ultimate goal is to integrate the modeling/interpretation of seismic amplitude (including AVO) anomalies within the geological framework of basin deposition and evolution for each dataset.

4) Need for quantitative integrated modeling techniques

As encouraging as future prospects for natural gas may be, it also has become increasingly obvious that the full amount of information obtainable from seismic is not always adequately retrieved. In fact, most seismic work still focuses on purely structural traps, when combination structural-stratigraphic styles have been long recognized as having large reserve potentials. I therefore propose to integrate the principles of rock physics into a quantitative interpretation scheme in order to extract *lithologic* and *fluid properties* from seismically derived information. In summary, I propose to devise a state-of-the-art *methodology* for the detection and the characterization of gas fields and to apply this methodology to a dataset from industry.

The work is intended to concentrate on the integration of various disciplines and concepts. In particular, it relies on complete geological characterizations, on accurate petrophysical descriptions, and on detailed lithologic models of reservoir rocks. The key is to use laboratory-derived properties of seals and reservoir rocks in the calibration of log-derived petrophysical properties and to combine them with properties extracted from seismic data. In particular, the use of the information contained in seismic amplitudes is stressed through detailed and systematic modeling studies.

Timing of the research effort

As a final remark, I believe that the timing of this research effort is excellent, since most practicing geophysicists are becoming increasingly aware of pitfalls in the interpretation of AVO anomalies, yet are left without answers as to the discrepancy between their often relatively simple elastic isotropic reservoir models and the results of drilling in stratigraphically complex areas.

5) Overview of the work - message of the thesis

Because of the growing concern that most "elephants" have already been discovered, seismic investigations have sought new frontiers, by either sounding for deeper and faster structural traps, or by targeting stratigraphic plays. Recent improvements in field acquisition techniques for high resolution seismic surveys, the advent of 3-D seismic, formidable progress in signal processing, and new valuable interpretation techniques combine to offer better pictures of the subsurface than ever before. This has led to a relatively new discipline, **Production or Reservoir geophysics**, which can be aimed at characterizing new reservoirs before production, or at reinvestigating older plays which are now partially depleted. Mature basins are now being re-explored with the emphasis on searching for "subtle traps" and on identifying bypassed reserves.

In short, this thesis shows how petrophysical information can be used to quantitatively interpret **seismic amplitudes** of target reservoirs. Consequently, a large part

of the thesis is devoted to **quantitatively relating**, associating, and integrating **Geology** and **Seismic Stratigraphy** through the systematic use of **Rock Physics**. As it will become clear to the reader, the step of crossing-over from observations in the laboratory to seismic interpretations in the field is not as straightforward as one may assume at first. The thesis contains some short geological reviews that serve as brief summaries and may seem trivial to experts, but will appeal to non-geologists, and that will, above all, establish a clear justification for using petrophysics as the natural link between seismic and geology.

Mission statement

The objective is to test the Feasibility of using Variations in Seismic Amplitudes for the Quantification of Reservoir Properties at and below wavelength Scales.

This work is a function of several critical steps, and in particular: the identification of changes in the character of seismic waveforms through careful processing, the quantitative modeling of those changes, and the interpretation of the changes within a reservoir characterization framework. The simultaneous use of a variety of data types provides a means to bridge properties at a variety of scales, and leads to a geologically consistent depositional model that can be used for prediction of variations in facies.

I focus on quantitative and integrated seismic interpretation for detailed reservoir characterizations. The work can be sub-divided into three broad categories:

- Theory: where AVO interpretation is reviewed and re-examined, within the context of anisotropy and attenuation, and where a general methodology is designed for the quantitative integration of petrophysical properties at all scales.
- Reservoir Characterization: where a comprehensive study of the Troll field provides insight into inferred rock properties for an accurate estimation of total reserves in place.
- Reservoir Management where an attempt is made at monitoring of fluid flow: more specifically, relationships between lithology, porosity, and permeability are developed to assist in determining production parameters for optimal recovery, and a synthetic study simulating production tests within the Troll West Oil province sheds light onto the possibility of monitoring production seismically.

Rock physics provides the natural link between these three broad topics. It is an essential ingredient to the **quantitative integration** of seismic, well logs and core information. Unfortunately, rock physics being a relatively new science has been under-utilized and I regard it as "the missing link" in quantitative seismic lithologic interpretation.

6) Organization of the thesis

Throughout this work, I tried to place the emphasis on practical issues facing the interpreter. This is reflected by the extensive amount of quantitative interpretation case studies, where theory is blended-in with data analysis. True amplitude seismic processing and model-based interpretation of seismic amplitudes are used to obtain a clearer image of reservoirs. The order of investigations reflects the idea that petrophysics serves as the "glue" holding together the three broad categories mentioned previously; investigations are arranged logically as follows:

- **Part I: THEORY** reviews modern AVO concepts and treats of Attenuation, Anisotropy, and AVO. This is followed by a review of rock physics and the development of deterministic modeling technique for the calculation of missing properties and for the integration of data at all scales.
- **Part II: APPLICATIONS-1** presents the results of an integrated interpretation of a modern 3-D seismic survey. Core data, well log data, 3-D stacked data and several complex seismic attributes are combined with petrophysical interpretation and geostatistics, to yield a global structural and stratigraphic picture of the Troll West reservoir.
- **Part III: APPLICATIONS-2** describes Petrophysics for *Reservoir Characterization* and illustrates the applications of Petrophysics to *Reservoir Management*. In particular, changes in lithology, porosity, and fluid content are simulated.

These topics are combined into 5 chapters. The first chapter is dedicated to the THEORY of wave propagation and to complex reflection phenomena; additionally, Zoeppritz theory is applied to anisotropic media. The second chapter emphasizes the role of rock physics in calculating "missing" or auxiliary rock properties and in seismic interpretation. The third chapter describes an integrated approach to modeling the petrophysical properties of rocks at all scales. The remaining two chapters are meant to be practical and concentrate on the APPLICATION of the concepts to detailed field studies. The objective is to use petrophysics as the tie and bridge between geology, geophysics, and reservoir engineering.

6.a) PART I: THEORY

Chapter 1: A.A.A. - Attenuation, Anisotropy, and AVO

This chapter provides the theoretical basis for complex pre-stack seismic responses. The pseudo-spectral method is used to investigate systematically the effects of anisotropy and/or anelastic attenuation on Amplitude Versus Offset (AVO) responses. A series of sensitivity analyses of AVO to anisotropy, attenuation, and attenuation anisotropy

is run and analyzed from an interpreter's viewpoint for a simple model. The method is extremely accurate, but one major drawback is that it is computationally intensive, and this prohibits its application to complicated earth models.

Anisotropy and attenuation can be considered as a *new technological frontier for seismic interpretation*. Both of them strongly condition wave propagation in rocks, and therefore affect seismic reflections. They have commonly been recognized as important rock properties in the past: studies by Kjartanson (1979), Bourbie (1982), Nur and Simmons (1969), and Jones (1986), among others, indicated that attenuation is a key seismic parameter which influences seismic wave propagation and reflections. Additionally, Nur and Simmons (1969) and Crampin (1984) showed the importance of anisotropy in rocks, and Banik (1987) and Thomsen (1987) stressed the influence of anisotropy on seismic reflections.

The pseudo-spectral numerical method is very accurate, but unfortunately, it is too slow for interactive interpretation. Therefore, a faster method based on the Zoeppritz equations is implemented. Thomsen's (1986) model for weak elastic anisotropy and for AVO reflections is applied, including PS, SP, and SS reflection coefficients. This yields a generalized Zoeppritz-type formulation for reflections that can be used to yield model parameters quickly. A more precise modeling approach, based on a full-waveform algorithm such as the pseudo-spectral method, or a faster wave equation method, can then be used to refine those parameters, specially in the presence of thin layers, and to incorporate the effects of intrinsic attenuation.

Chapter 2: Relevance of rock physics to AVO interpretation and Calculation of "missing" rock properties

One of the key issues in seismic modeling is the quantitative determination of rock parameters to be input into the algorithms in order to accurately represent a particular reservoir. More often than not, certain properties are not available from existing well data. This can be due to either the prohibitive cost of acquiring such data, or to the difficulty in measuring such data. Shear wave velocities and intrinsic attenuations are good examples. In this chapter, existing rock models are reviewed and techniques are developed to determine missing rock properties such as shear velocities and intrinsic attenuation. The construction of rock properties, whether they have been measured in-situ or not, is an important step, because it allows the interpreter to not only understand rock properties at a well. It also enables the interpreter to test changes in properties as may be seen away from the control well, through sensitivity analyses.

Chapter 3: An integrated modeling approach for AVO studies

The problem of determining elastic properties from mineral composition, in-situ conditions, state of compaction, degree of diagenesis, and fluid content was ap-

proached by using a series of deterministic models which are tested and calibrated against empirical relations (as in chapter 2). Since different types of rock properties are often measured at different scales of investigation (ie, thin-section scale, core scale, log scale, cross-well tomography scale, VSP scale, seismic scale), they need to be integrated and up-scaled to seismic wavelengths. Hence, a method is developed to integrate and up-scale rock properties to seismic wavelengths. This method yields a Rock Property/Seismic Property transform. It is non-linear and is best suited for detailed forward modeling applications. To facilitate exchanges between different disciplines (geology, geophysics, and petroleum engineering), a common basis and terminology is adopted for the classification of rock types. This classification is also ideal for the establishment of "reasonable" parameter variations to be used in sensitivity analyses within those pre-determined rock types.

6.b) PARTS II AND III: APPLICATIONS

In concentrating on select case histories, the objective is to put together a set of geological knowledge and to demonstrate the feasibility of detailed petrophysical interpretations for the enhanced understanding of reservoirs. In general, geoscientists distinguish between four types of wells, the boundary of which may be more or less "fuzzy":

- 1) **Exploration or Recon wildcats**, which confirm or deny facies models and bring paleontological, mineralogical, sedimentological, geochemical, geophysical and hydrogeological information, as well as structural data.
- 2) **Evaluation wells**, which give additional information on reservoir extensions and allow the refinement of lateral changes within the facies model adopted
- 3) **Development or Exploitation wells**, whose traditional role was to allow for the extraction of hydrocarbons, but whose more recent role has been recognized as important for production, because of valuable geological and geophysical input to reservoir characterizations. Today, these wells are mostly used to allow for a refinement of reservoir heterogeneities and for recalibrations of reservoir models. They also allow for the monitoring of changes in reservoir conditions, such as saturation or temperature. These wells are the basis for reservoir management, ie, decisions pertaining to step-out wells, whether to change the recovery method, and whether to perforate additional horizons.
- 4) **Production wells**, which include injection wells and monitor wells.

Chapter 4 concentrates on wells of type 1 and 2 that are used with 3-D stacked data, while chapter 5 relates to type 3 and 4 wells that are used to calibrate pre-stack data.

PART II: APPLICATIONS-1

Chapter 4: 3-D Integrated Interpretation of the Troll West Oil Province

This chapter summarizes the general geological framework and depositional environment of the Troll field. The analysis of 3-D stacked data yields detailed structural and stratigraphic pictures of the field, and naturally leads to the definition of a subset of the area for a thorough pre-stack analysis.

The interpretation is carried-out one step further, in a more creative manner, by way of analyzing complex seismic attributes that are used as post-stack stratigraphic indicators. Certain seismic attributes, and in particular, the stacked seismic amplitude, are shown to lead to **direct detection** of gas in 3-D at Troll West. This is followed by statistical analyses: the seismic attributes are clustered using principal component analysis and are used for automatic field-wide pattern recognition of hydrocarbons across the field.

PART III: APPLICATIONS-2

Chapter 5: Integrated Reservoir Characterization at Troll West

A complete petrophysical analysis of core and log measurements, and a review of possible rock models assist in establishing the best plausible working seismic models for the Troll West Oil province. The results are then combined with the concepts developed in chapters 2 and 3 to yield a better, more quantitative reservoir description from pre-stack seismic responses.

- **Petrophysics and AVO for Reservoir Characterization:** Models of pre-stack (AVO) responses are compared to seismic CDP gathers in order to better characterize the lithology in terms of mica content, calcite content, and porosity of the sedimentary cycles within the Sognefjord sands.
- **Petrophysics and AVO for fluid monitoring and Reservoir Management:** Fluid properties (compressibility and viscosity) are incorporated into petrophysical models to facilitate the correlation of seismic signatures to the direct detection of fluid movement. In particular, the effects of gas coning are simulated at a production well.

GENERAL CONCLUSIONS

Detailed model-based seismic lithologic interpretations have become feasible with today's understanding of seismic wave propagation. However, these interpretations require the systematic application of **quantitative** principles in order to parameterize earth models realistically. The work presented here is based on petrophysics and represents one possible approach to the quantitative parameterization of seismic lithologies.

REFERENCES

- Aki, K., and Richards, P., G., 1980, Quantitative seismology: W. H. Freeman and Co.
- Backus, M., and Chen, R., 1975, Flat spot exploration: *Geophysical Prospecting*, **23**, 533,577.
- Banik, N., C., 1987, An effective anisotropy parameter in transversely isotropic media: *Geophysics*, **52**, 1654,1664.
- Bourbie, T., 1982, Effect of attenuation on seismic reflections: *S.R.B.* **14** .
- Clements, W., 1991, Policies to assure America's energy future: office of the governor, Austin, Texas, January publication.
- Crampin S., 1984, Effective anisotropic elastic constants for Wave propagation through cracked solids: *Geophys. J. R. Astr. Soc.* , **76**, 135,145.
- Domenico, S. N., 1976, Effect of brine-gas mixture on velocity in an unconsolidated reservoir: *Geophysics*, **41**, 882,894.
- Domenico, S. N., 1977, Elastic properties of unconsolidated porous sand reservoirs: *Geophysics*, **42**, 1339,1368.
- Gassmann, F., 1951: Elasticity of porous media: *Vier. der Natur. Gesellschaft in Zurich*, Heft **I**.
- Gregory, A. R., 1976, Fluid saturation effects on dynamic elastic properties of sedimentary rocks: *Geophysics*, **41**, 895,921.
- Harris, J. 1988, Cross-well seismic measurements in sedimentary rocks, *S.E.G. expanded abstracts*,**1**, 147, 150.
- Jackson, D., 1991, Environment: *Civil Engineering News*, **1**, 24-25.
- Jones, T., 1986, Pore fluids and frequency-dependent wave propagation in rocks: *Geophysics*, **51**, 1939,1953.

- Kennedy W., Wiggins W., Aronstam P., 1988 Swept-frequency borehole source for inverse VSP and cross-borehole surveying, S.E.G. expanded abstracts, **1**, 158, 160.
- Kjartanson, E., 1979, Constant Q-Wave Propagation and Attenuation: J.G.R., **84**, 4737,4748.
- Koefoed, O, 1955, On the effect of Poisson's ratio of rock strata on the reflection coefficients of plane waves: Geophysical Prospecting, **3**, 381,387.
- Nur A. and Simmons, G., 1969, Stress induced velocity anisotropy in rock; an experimental study: J. G. R., **74**, 6667,6674.
- Ostrander, W., J., 1984, Plane-wave reflection coefficients for gas sands at nonnormal angles of incidence: Geophysics, **49**, 1637,1648.
- Rector, J., W., 1990, Utilization of Drill-bit vibrations as a downhole seismic source: Phd Thesis, Stanford University, S.R.B., **44**.
- Robertson, J. D., 1989, Reservoir management using 3-D seismic data: J.P.T., **7**, 663,667.
- Thomsen, L., 1986, Weak elastic anisotropy : Geophysics, **51**, 1954,1966.

INTRODUCTION TO PART I: THEORY

Reflection seismic is increasingly being recognized as the tool of choice for identifying and characterizing reservoir heterogeneities away from existing wells. As a result, more sophisticated processing methods have been, and will continue to be developed in the O&G industry, and a number of seismic modeling algorithms are quickly finding their way on the market. In view of these new developments, it was appropriate to re-examine some fundamental assumptions made in the past about wave propagation, and to evaluate the potential of detailed model-based seismic lithologic interpretation techniques in the future:

- On one hand, most modeling packages assume an isotropic-elastic earth, and it was necessary to investigate and summarize the effects of anisotropy and anelasticity on theoretical seismic pre-stack responses. This is the work of chapter 1.
- On the other hand, the quantitative determination of parameters to be used for model-based seismic lithologic interpretations requires a systematic approach: crucial properties, such as velocities, densities, anisotropy and attenuation must either be measured in-situ or "fabricated" as accurately as possible (chapter 2). This often involves the integration of different techniques and must necessarily incorporate upscaling of the seismic properties of reservoirs (chapter 3).
- Last but not least, the systematic integration of different disciplines involves the classification of rock types and the establishment of "reasonable" parameter variations within those rock groups. It allows for a common set of rules and terminology based on rock characteristics at the microscale, from which upscaling of rock properties can be achieved. This is most useful in reducing uncertainties due to the non-uniqueness of the seismic lithologic inversion process. This work is presented in chapter 3.

CHAPTER 1

A.A.A.: ATTENUATION, ANISOTROPY, AND AVO

"In a more remote future, it may become possible to draw conclusions concerning the lithologic nature of rock strata from the shapes of the reflection coefficient curves of the interfaces by which they are bounded", Koefoed, 1955.

ABSTRACT

In isotropic elastic media, the expected AVO response generally obeys the simple rule: if the sign of the change in compressional velocities between two media is the same as the sign of the change in Poisson's ratio across the interface, an increase in amplitude versus offset will result; a decrease in AVO will result if the signs are opposite. In general, reflected P-wave amplitudes are more sensitive to contrasts in shear wave velocities than to contrasts in compressional wave velocities or contrasts in densities.

In anelastic or anisotropic media however, both *elastic energy focusing* and *viscoelastic attenuation* have to be investigated. They continually alter the signal during wave propagation, through amplitude and phase distortions.

Both isotropic and viscoelastic solids have been investigated in the past by geophysicists. Viscoelastic anisotropic solids have not. Such materials can be fully described accurately using Pseudo-Spectral methods (Kosloff and Baysal, 1982). A similar Fourier Pseudo-Spectral algorithm was adapted by Samec (1991), and used in sensitivity studies (Samec and Blangy, 1992). Results show that body waves propagating in homogeneous viscoelastic anisotropic solids display intrinsic attenuation anisotropy and velocity anisotropy effects, which are decoupled to first order. As a consequence, viscoelastic anisotropic solids can be shown to have two independent energy focusing mechanisms: attenuation anisotropy, and elastic anisotropy. Using

the notations of Thomsen (1986), the reflection coefficients at the boundary between two viscoelastic weakly anisotropic solids are then computed: in short, modeling results show that the impact of attenuation anisotropy on the reflection coefficients can be of the same order as the impact of elastic anisotropy.

Because viscoelastic attenuation and anisotropy both affect AVO responses, they should be accounted for whenever possible and as accurately as possible on pre-stack data prior to interpretation. This is not an easy task in the real world, because of the difficulty in prescribing appropriate physical parameters.

I)- INTRODUCTION

Exploration for hydrocarbon reservoirs strongly depends on the acquisition, processing and interpretation of seismic data. Surprisingly, the overall financial effort spent in the acquisition phase exceeds by far that spent toward the analysis and interpretation of the data. Complex phenomena continuously affect the amplitude and phase of the seismic wavelet as it propagates down into the earth. If we, as petroleum geoscientists, are to attempt to obtain quantitative information from pre-stack data, we need to understand these phenomena and quantify them. The following chapter reviews the modern understanding of elastic and isotropic AVO responses, and applies numerical methods to model complex wave phenomena and their effect on seismic amplitudes from pre-stack gathers. Throughout this thesis, AVO analysis will refer to studies of Amplitude Versus Offset, and AVA will refer to studies of Amplitude Versus Angle of incidence. The two techniques are interchangeable, provided that the velocity structure is known with some certainty.

II)- REVIEW OF CURRENT AVO ANALYSIS TECHNIQUES

1) AVO studies in isotropic media

A.G.C. (Automatic Gain Control) can be viewed as a practical tool to enhance seismic records in difficult areas in order to highlight the structural component of petroleum traps; however, it also destroys much of the "true" seismic amplitude information, because it applies a time varying amplitude adjustment across the traces. This realization, coupled with extra care in using AGC, led to numerous works on the analysis of bright spots (Koefoed, 1955, Tatham and Stoffa, 1976, Backus and Chen, 1975). Without AGC, proper amplitude balancing of seismic sections becomes essential for comparing reflections at deep and shallow times. Wavelet processing is also a crucial issue in AVO studies, as evidenced by the following argument: Gas sands are usually slower and less dense than surrounding material; therefore, reflection coefficients are expected to be negative at the top of the gas zone and positive at its base. It should then be possible to characterize gas sands after deconvolution; from a resolution point of view, this works best when the data is zero-phase.

The theory behind AVO analyses in isotropic media is simple. It relies on the fact that the energy of non-normally incident P-waves is converted into 4 different waves at each interface, as shown in figure 1.1. Zoeppritz (1919) was among the first to derive a set of equations relating the various displacement amplitudes present at an interface; these were derived from basic physical principles, by using Snells' law, the continuity of displacement, and the continuity of stress across each layer. His relations are best expressed in matrix form (after Waters, 1987) as:

$$\begin{pmatrix} \sin(\theta_1) & \cos(\phi_1) & -\sin(\theta_2) & \cos(\phi_2) \\ -\cos(\theta_1) & \sin(\phi_1) & -\cos(\theta_2) & -\sin(\phi_2) \\ \sin(2\theta_1) & \frac{V_1}{S_1} \cos(2\phi_1) & \frac{\rho_2 S_2^2 V_1}{\rho_1 S_1^2 V_2} \sin(2\theta_2) & -\frac{\rho_2 S_2 V_1}{\rho_1 S_1^2} \cos(2\phi_2) \\ \cos(2\phi_1) & -\frac{S_1}{V_1} \sin(2\phi_1) & -\frac{\rho_2 V_2}{\rho_1 V_1} \cos(2\phi_2) & -\frac{\rho_2 S_2}{\rho_1 V_1} \sin(2\phi_2) \end{pmatrix} \begin{pmatrix} A_{RP} \\ A_{RS} \\ A_{TP} \\ A_{TS} \end{pmatrix} = \begin{pmatrix} -\sin(\theta_1) \\ -\cos(\theta_1) \\ \sin(2\theta_1) \\ -\cos(2\phi_1) \end{pmatrix}$$

Using these relations, Koefoed (1955) computed amplitudes as functions of changes in the Poisson's ratios σ_1 and σ_2 of the two media. His work showed that it is the

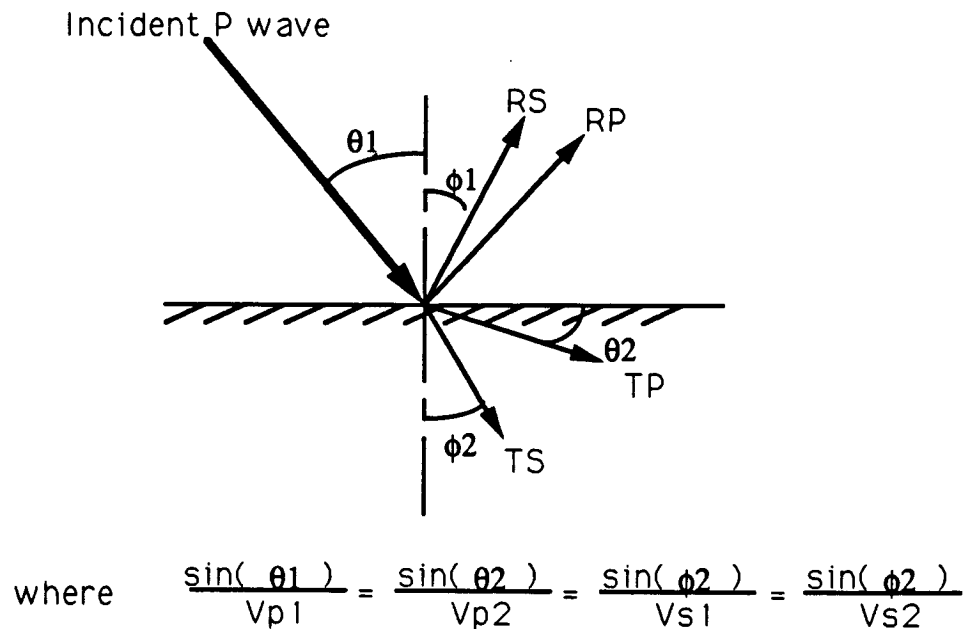


Figure 1.1: Ray configuration and energy conversion considerations for Zoeppritz equations; θ_1 and θ_2 are the P wave incident and refracted angles, and ϕ_1 and ϕ_2 are the S wave reflected and refracted angles.

contrasts in Poisson's ratio across an interface that control the variations in amplitude with offset; he then predicted in his last sentence, that:

"In a more remote future, it may become possible to draw conclusions concerning the lithologic nature of rock strata from the shapes of the reflection coefficient curves of the interfaces by which they are bounded".

In 1982, Ostrander showed that the "remote future" had indeed arrived. Through the use of several case histories, he demonstrated that Poisson's ratio had a strong influence on changes in reflection coefficient versus angle of incidence, and that AVO analysis can often distinguish between gas-related amplitude anomalies from other types of amplitude anomalies. His work was published in 1984. Ostrander (course notes, 1985) also stated that the Poisson's ratios of unconsolidated sediments are on the order of 0.4 or higher, that those of high porosity brine saturated sands are on the order of 0.3 to 0.4, that those of high porosity gas sands are on the order of 0.1, and that they generally decrease as porosity increase.

P-wave reflected amplitudes were approximated by Bortfeld (1961) and Aki and Richards (1980), given small percentage changes in density, compressional velocity, and shear velocity. In particular, the P-P reflection can be expressed as:

$$A_{RP} = \frac{1}{2} \left(1 - 4 \left[\frac{V_s}{V_p} \right]^2 \sin^2 \theta \right) \frac{\Delta \rho}{\rho} + \frac{1}{2 \cos^2 \theta} \frac{\Delta V_p}{V_p} - 4 \left[\frac{V_s}{V_p} \right]^2 \sin^2 \theta \frac{\Delta V_s}{V_s} \quad (1)$$

where V_p , V_s , and ρ are the averages of compressional velocity, shear velocity and density respectively, and where ΔV_p , ΔV_s , and $\Delta \rho$ are the contrasts in compressional velocity, shear velocity and density respectively. This equation has the form $A_{RP} = A \frac{\Delta \rho}{\rho} + B \frac{\Delta V_p}{V_p} + C \frac{\Delta V_s}{V_s}$ where A and C are functions of $\frac{V_p}{V_s}$ and θ and B is a function of θ ; this equation gives great analytical insight in terms of elastic properties from trends in AVO.

As can be seen, it can be difficult to predict the influence of changes in Poissons' ratio on reflection coefficients from the Zoeppritz equations directly. However, in general, it can be said that a larger amount of energy is converted into S-wave energy, as the angle of incidence is increased. In 1961, Bortfeld published another set of equations which approximate the Zoeppritz equations, and which also enhance the importance of the influence of rock properties on reflection amplitudes. In particular, the reflection coefficient for an incident P-wave is listed below:

$$A_{RP} = \left[\frac{1}{2} \text{Ln} \left(\frac{V_2 \rho_2 \cos \theta_1}{V_1 \rho_1 \cos \theta_2} \right) \right] + \frac{\sin^2 \theta_1}{V_1^2} [V_{s1}^2 - V_{s2}^2] \left[2 + \frac{\text{Ln} \frac{\rho_2}{\rho_1}}{\text{Ln} \left(\frac{V_2}{V_1} - \text{Ln} \left(\frac{V_2 V_{s1}}{V_1 V_{s2}} \right) \right)} \right] \quad (2)$$

where the first term has been called the **fluid factor** and has a large contribution for small offsets, and where the second term (called the **rigidity or shear factor**) dominates for large offsets.

As pointed-out by Shuey (1985), the Bortfeld approximations remain difficult to interpret in terms of the inverse problem, ie in terms of an analytical determination of elastic properties from trends in AVO. A further simplification of equation (1) -

known as Shueys approximation - yields the following expressions for the reflection coefficients as a function of the angle of incidence:

$$R(\theta) = R_0 + [A_0 R_0 + \frac{\Delta\sigma}{(1-\sigma)^2}] \sin^2(\theta) + 1/2 \frac{\Delta V_p}{V_p} [\tan^2(\theta) - \sin^2(\theta)] \quad (3)$$

where the reflection coefficient has been decomposed into three terms. A near offset term (R_0), a mid offset term (second term), and a far offset term (third term). However, the expressions of Aki and Richards were derived under the assumptions of small variations in $\frac{\Delta V_p}{V_p}$, $\frac{\Delta V_s}{V_s}$, and $\frac{\Delta\rho}{\rho}$, and the approximations of Shuey are only valid for small ranges of angles of incidence up to approximately 25 degrees. This fact diminishes the statistical reliability of estimates of Poisson's ratio σ , specially for low fold CMP data. The process is nevertheless run routinely by contractors (Western Geophysical's "SLIM" process, Simon's Reconnaissance AVO analysis, among others). It also renders higher order approximations of the Zoeppritz equations inadequate under large variations in $\frac{\Delta V_s}{V_s}$ (Gelfand et al, 1988):

Based on the general relationships between lithology, Poisson's ratio, and effective pressure established by Gregory (1976) and Domenico (1976, 1977), gas sands have a significantly lower Poisson's ratio than water or oil sands at shallow depths; this fact can also be verified using Gassmann's relations (1951), so that it can be concluded that it is the pore fluid type that controls Poisson's ratio for a given isotropic lithology under the same in-situ conditions. However, the contrast in Poisson's ratio is reduced as depth is increased. In conclusion, for relatively shallow depths, it should be possible to "see" direct hydrocarbons from seismic data. The following table (table 1.1) is derived from the Shuey approximation to the Zoeppritz equations and summarizes the expected AVO responses of the reflection at the interface between two isotropic elastic solids: the overburden and the reservoir. It defines the following general rule of thumb: whenever, the change in velocity between the two has the same sign as the change in Poisson's ratio, the AVO response shows an increase with offset. A decrease in AVO occurs whenever the contrast in velocity has the opposite sign to

the contrast in Poisson's ratio. I find this table to be a useful and simple summary of the possible AVO responses at an interface between two isotropic elastic solids, but keep in mind that there are exceptions, because it is derived from an approximation of the reflection coefficient.

Table 1.1:

AVO Response Table			
Case	P-Velocity contrast	Poisson ratio contrast	AVO response
1	negative	negative	increase
2	negative	positive	decrease
3	positive	negative	decrease
4	positive	positive	increase

Because Poisson's ratio seems to be a convenient parameter to yield some physical insight into AVO effects at boundaries between isotropic solids, and since some people prefer to use V_p/V_s ratios, the graph on figure 1.2 provides a convenient and useful way to convert from one to the other. The graph is especially useful, because it also allows a conversion to the ratio of bulk modulus to shear modulus. The "typical" value for a Poisson's ratio of 0.25 corresponds to a V_p/V_s of 1.67 and a K/μ of 1.67.

2) A simple example

To illustrate the previous AVO rule of thumb, I adapted a reflectivity program for isotropic and anelastic media, and ported it onto the Ardent computer. I then generated several elastic synthetic gathers. Let us first examine the single interface reflection coefficients, using the formulation of Aki and Richards (equation (1)). I chose an example of a shale (with properties $V_p = 3.1$ Km/s, $V_s = 1.45$ Km/s, density $\rho = 2.40$ g/cc, and Poisson's ratio $\sigma = .36$), overlying a sand (which when wet has $V_p = 3.0$ Km/s, $V_s = 1.50$ Km/s, density $\rho = 2.30$ g/cc, and Poisson's ratio $\sigma = 0.33$, and when dry has $V_p = 2.5$ Km/s, $V_s = 1.65$ Km/s, density $\rho = 2.15$ g/cc, and Poisson's ratio $\sigma = 0.11$); the parameters of the sand were calculated using Gassman's equations, assuming that the sand had a saturated velocity of 3.0 Km/s

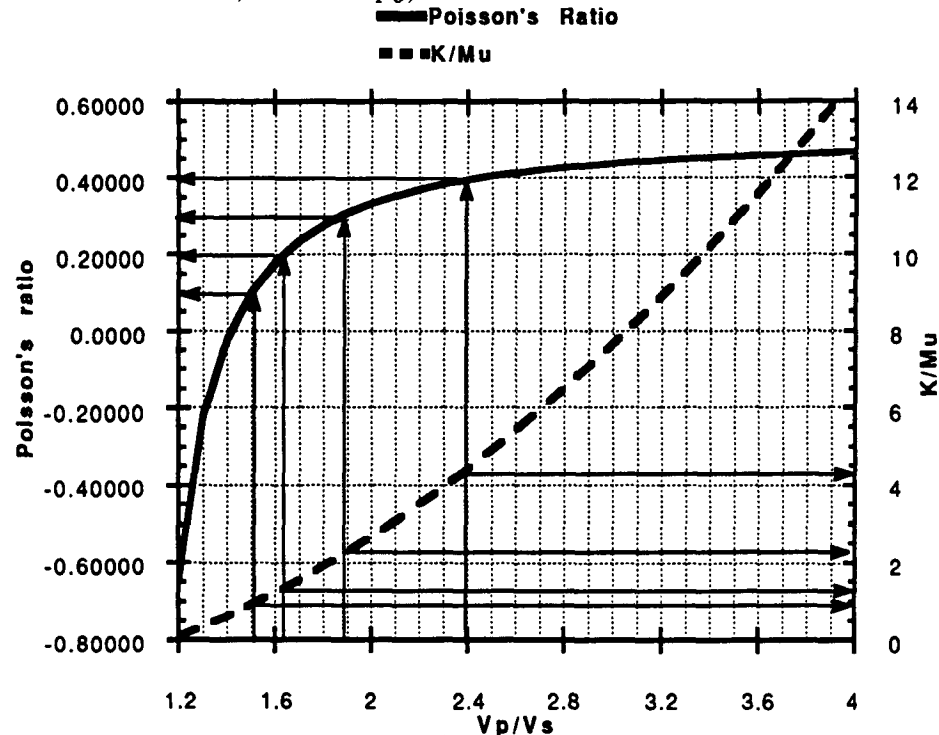


Figure 1.2: Conversion graph from V_p/V_s ratio to Poisson's ratio and to the ratio of Bulk modulus to Shear modulus (K/μ). Note that for most rocks, Poisson's ratio is positive; however, some (rare) rocks can exhibit negative Poisson's ratios. These correspond to rocks with V_p/V_s ratios less than $\frac{\sqrt{2}}{2}$ or with $\frac{K}{\mu}$ ratios less than $\frac{2}{3}$.

at a porosity of 30%. The results are shown in figure 1.3.

Note that the reflection coefficients are clearly seen to increase (in absolute value) with offset for the case of the gas sand; in the case of the wet sand, they decrease or remain constant with offset.

The models and their full isotropic response (including transmission and intrinsic attenuation effects, and multiples and conversions) are shown in figures 1.4 and 1.5; seismic (peak) amplitudes were picked automatically and are displayed at the bottom of each figure, after normalization to the near trace amplitude. Figure 1.4 correspond to a water saturated sand (1.4a is the elastic case and 1.4b is the viscoelastic case), and figure 1.5 simulates the same sand under full gas saturation (1.5a is the elastic case and 1.5b is the viscoelastic case). The acquisition geometry corresponds to that of a shot gather with 50 traces evenly spaced at 20m separation (group interval), starting from 10m (near offset) to 990m (far offset). The acquisition geometry

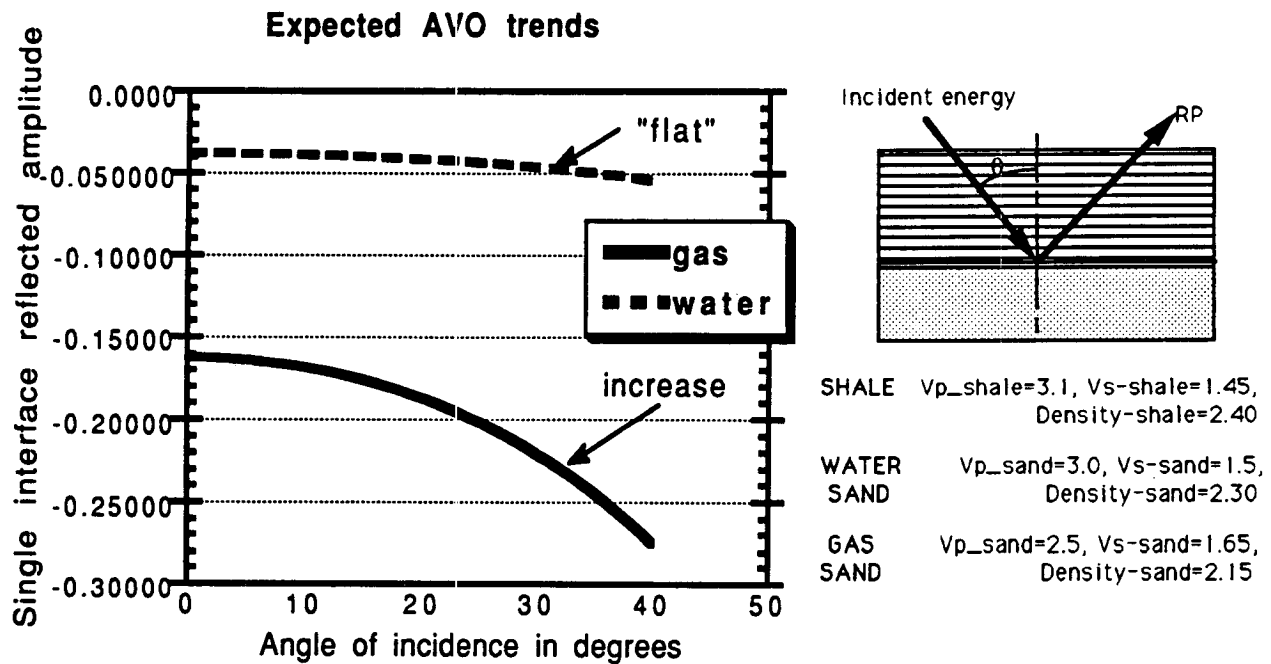


Figure 1.3: Reflection coefficients calculated using the equations of Aki and Richards for a shale overlying a water sand and a gas sand.

consisted of a 3-D explosive source buried at 10 m depth, while the geophones were placed at the surface. The source is a zero-phase Ricker wavelet, with 40 Hz dominant frequency; the intrinsic attenuations are assumed to be constant with frequency (constant Q). The reflection coefficients clearly indicate an increase in amplitude with offset for the elastic gas sand, and a decrease in amplitude with offset for the elastic water sand. The effects of intrinsic attenuation (Q) will be investigated in more detail in section 3. As can be seen in the figures, Q tends to attenuate higher frequencies (it broadens the pulse - specially visible at higher offsets -), tends to change the phase of the wavelet, and also tends to reduce the AVO effect, because longer offsets also have longer travel paths and therefore undergo more attenuation than shorter offsets. While generating these figures, I noted that for this choice of elastic parameters and for Q 's greater than 40 or so, the effects of Q were overwhelmed by the AVO response of the gas sand; this goes to say that **AVO anomalies** associated with gas sands can be very **robust**.

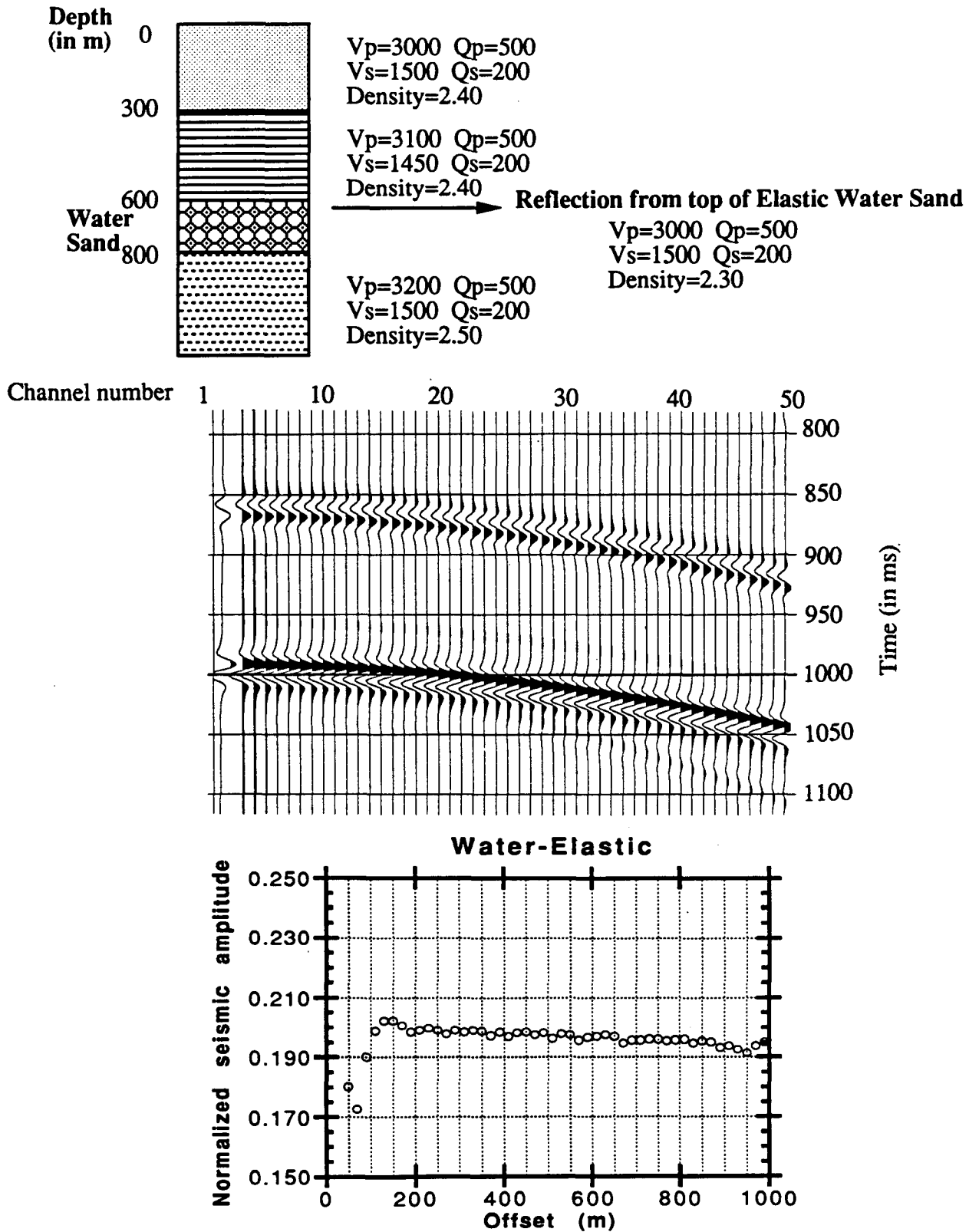


Figure 1.4: a) Elastic synthetic seismogram calculated using the full elastic response of the water sand in figure 1.3. Model parameters consist of four layers and are given at top; acquisition parameters are given in the text. Picked amplitudes are displayed in the bottom graph, after normalization to the near trace amplitude.

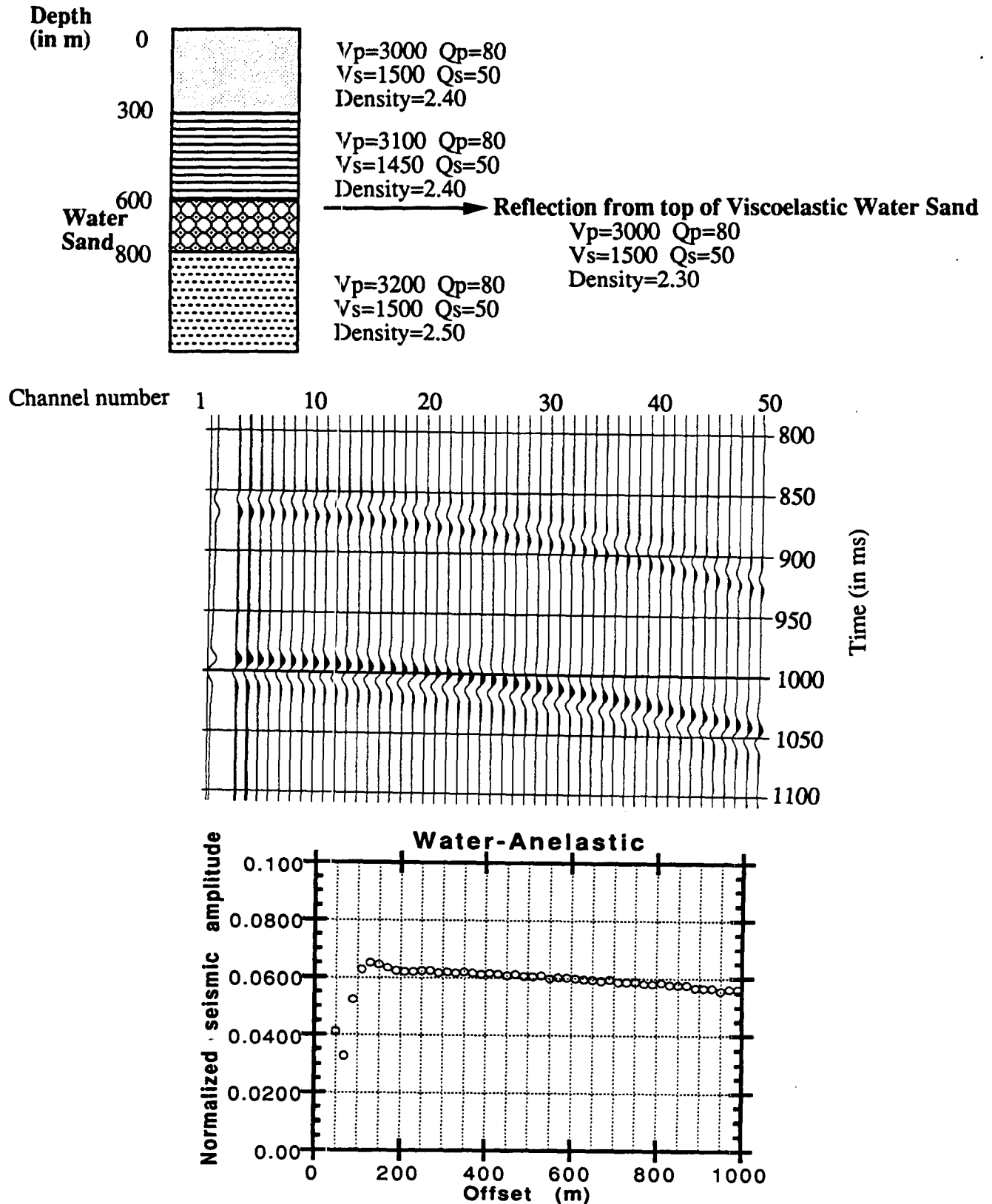


Figure 1.4: b) Viscoelastic synthetic seismogram calculated using the full viscoelastic response of the water sand in figure 1.3. Model parameters consist of four layers and are given at top; acquisition parameters are given in the text. Picked amplitudes are displayed in the bottom graph, after normalization to the near trace amplitude.

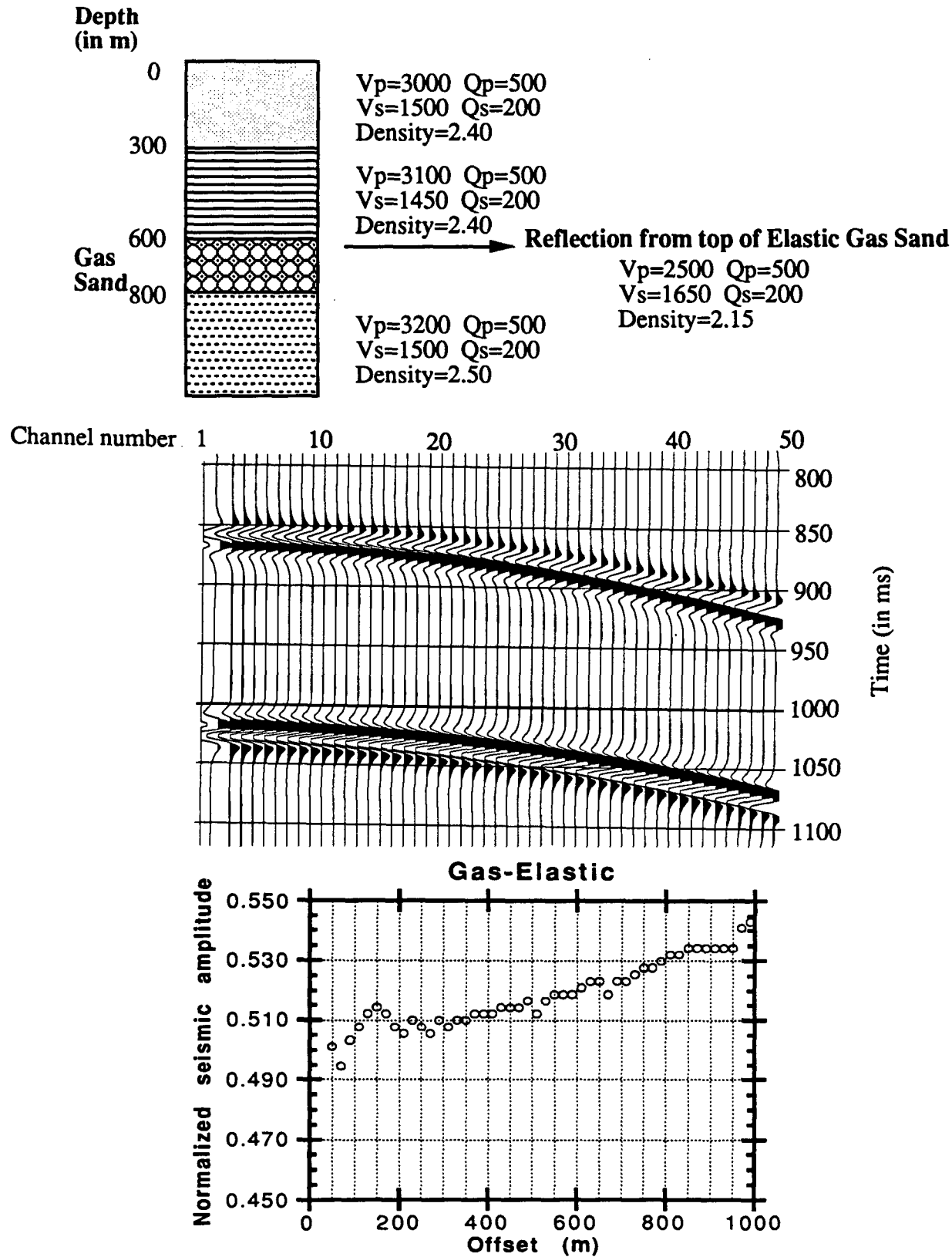


Figure 1.5: a) Elastic synthetic seismogram calculated using the full elastic response of the sand in figure 1.3, saturated with gas. Model parameters consist of four layers and are given at top; acquisition parameters are given in the text. Picked amplitudes are displayed in the bottom graph, after normalization to the near trace amplitude.

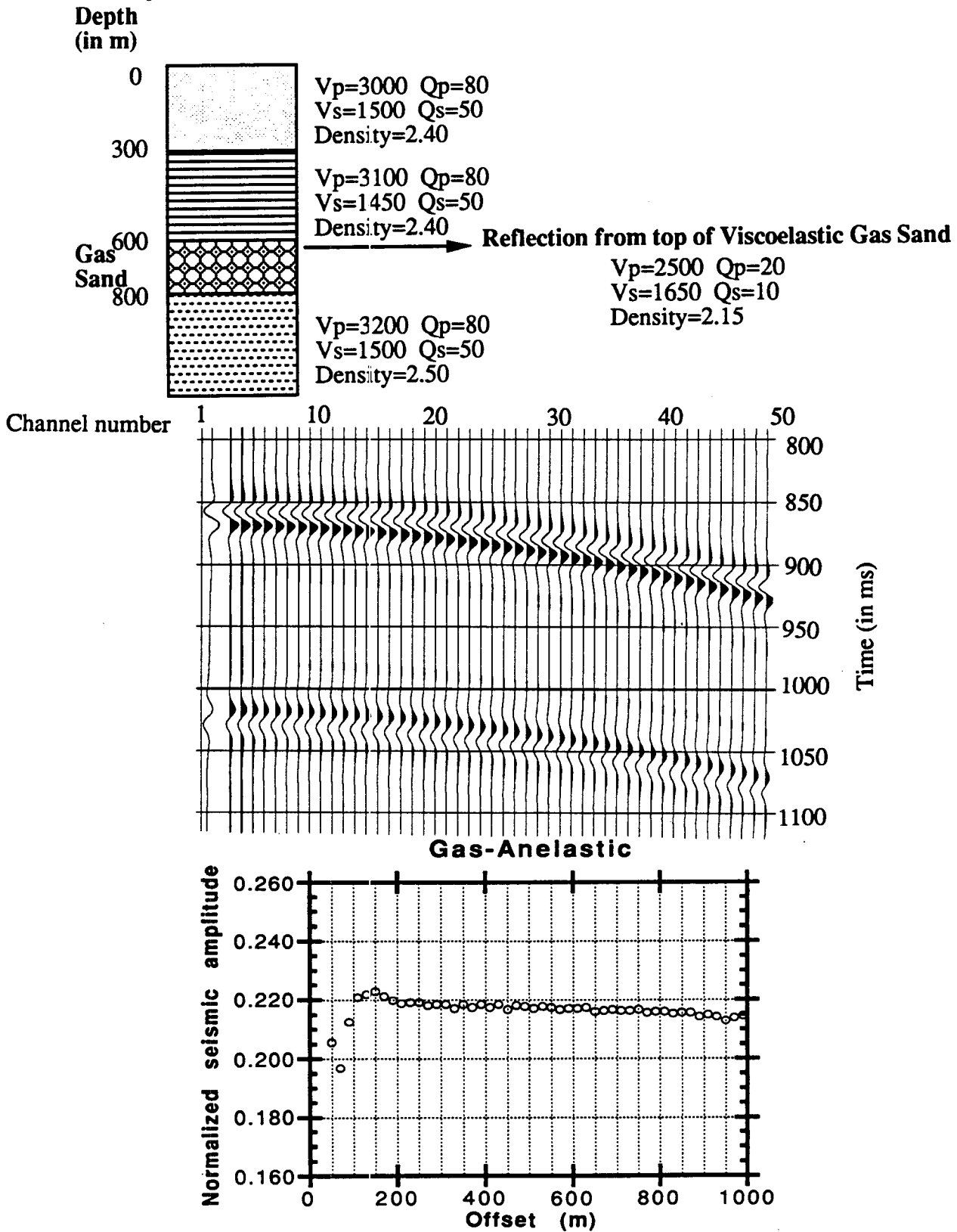


Figure 1.5: b) Viscoelastic synthetic seismogram calculated using the full viscoelastic response of the sand in figure 1.3, saturated with gas. Model parameters consist of four layers and are given at top; acquisition parameters are given in the text. Picked amplitudes are displayed in the bottom graph, after normalization to the near trace amplitude.

3) Sensitivity to changes in elastic parameters

The sensitivity of the AVO method to changes in elastic parameters is a crucial issue. Following Sengupta (1989), I calculated changes in reflection coefficients for small variations in normalized velocity and density, under the assumption that V_p , V_s , and ρ are independent variables (note that this assumption does not always hold):

$$\frac{\delta \{A_{RP}\}}{\delta \left\{ \frac{\Delta V_p}{V_p} \right\}} = \frac{1}{2 \cos^2 \theta} \frac{\Delta V_p}{V_p}; \quad \frac{\delta \{A_{RP}\}}{\delta \left\{ \frac{\Delta V_s}{V_s} \right\}} = -4 \left[\frac{V_s}{V_p} \right]^2 \sin^2 \theta \frac{\Delta V_s}{V_s}; \quad (4)$$

$$\frac{\delta \{A_{RP}\}}{\delta \left\{ \frac{\Delta \rho}{\rho} \right\}} = \frac{1}{2} \left(1 - 4 \left[\frac{V_s}{V_p} \right]^2 \sin^2 \theta \right) \frac{\Delta \rho}{\rho} \quad (5)$$

When the assumption holds, figure 1.6 shows the changes in reflection coefficient as a function of angle of incidence, and as a function of changes in normalized velocity and density. Note that ΔV_p and $\Delta \rho$ have similar effect at near offsets, but that the changes in the reflection coefficient increases with offset for ΔV_p and decreases with offset for $\Delta \rho$ at far offsets. Changes in shear velocity, ΔV_s , have no effect at zero offset, but increase with increasing offset.

Clearly, when interpreting AVO trends, care must be taken to include approximations of uncertainties in V_p , V_s , and ρ , in order to establish confidence limits. Also note that the **effects of changes (or errors) in shear velocity on the AVO response are larger than those in P-wave velocities or in density.** Therefore, understanding the factors that control shear velocities and narrowing bounds on shear moduli is a crucial issue in any AVO analysis. I will analyze this point in more detail in chapter 2.

III)- ATTENUATION, ANISOTROPY, AND AVO

1) The importance of viscoelastic attenuation and anisotropy

Recent studies such as those of Crampin (1984), Banik (1987), and Thomsen (1986), have shown that the elastic properties of shales, chalks and other materials

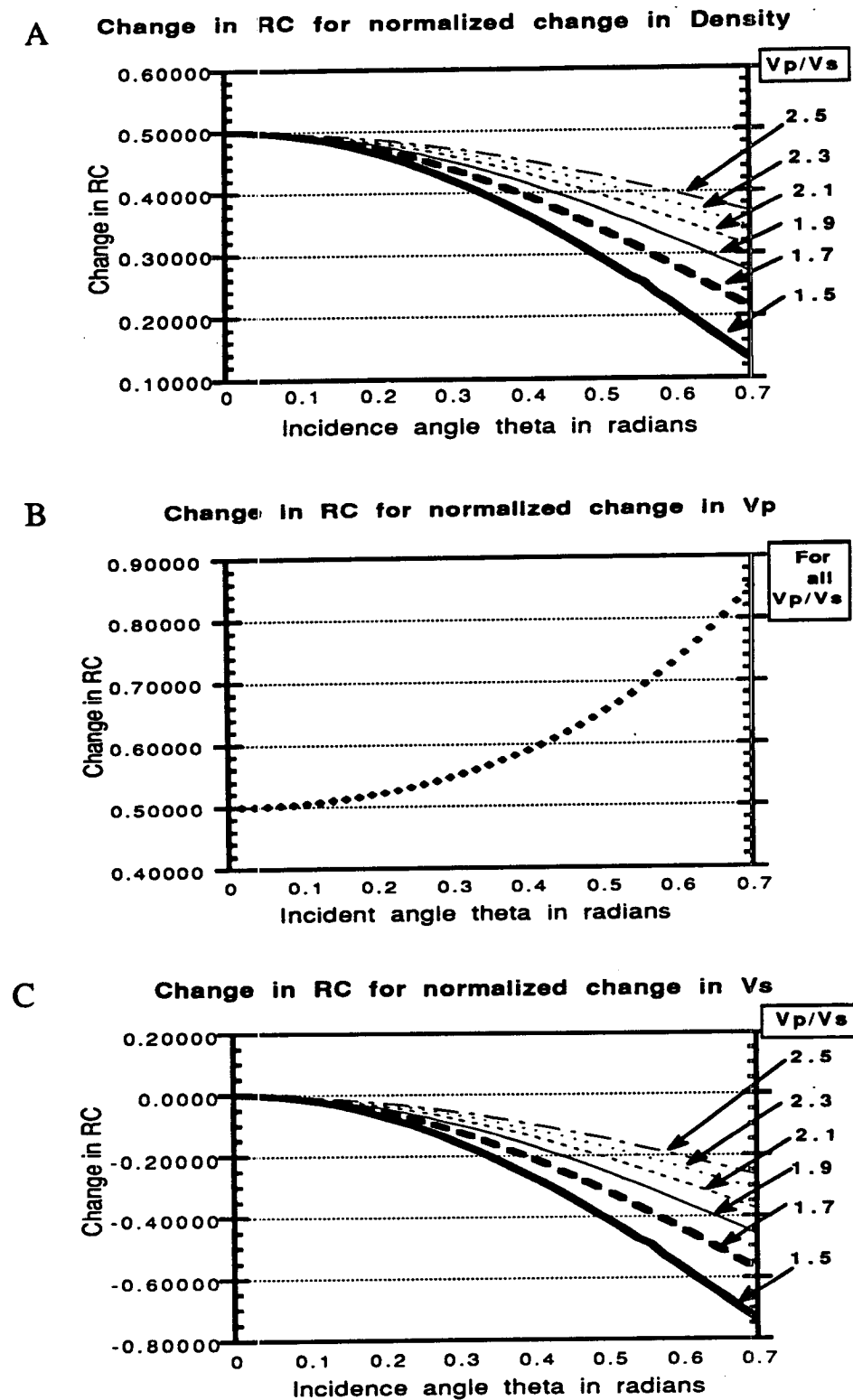


Figure 1.6: Changes in reflection coefficients for small variations in normalized velocity and density; these are the A, B, and C coefficients of equation (1). Note that ΔV_p and $\Delta \rho$ have similar effects at near offsets, but that the changes in the reflection coefficient increases with offset for ΔV_p and decreases with offset for $\Delta \rho$ at far offsets. Changes in shear velocity, ΔV_s , have no effect at zero offset, but increase with increasing offset.

can be highly anisotropic. In fact, much work (Wright, 1987, Thomsen, 1986, Banik, 1987) has been devoted to characterizing transverse isotropy in an attempt to describe more accurately the properties of shales and their effects on reflection coefficients.

On the other hand, numerous investigations (Kjartansson (1979), Bourbie (1982), Jones (1986), Winkler and Nur (1986), Nur and Simmons (1969) among others) have concentrated on the effects of intrinsic attenuation on wave propagation. The results of Hudson (1981), and Hosten et al. (1987), suggest that dissipation itself is an anisotropic phenomenon, and that media with anisotropic elastic properties also display quality factor, or attenuation anisotropy. In fact, Hudson (1981) showed that one could introduce the imaginary part of the elastic tensor to model the effect of cracks on rock anisotropy - this is similar to Fung's correspondance principle, where all relations involving real moduli are replaced with relations involving complex moduli (Fung, 1965) - ; the Q that is obtained in this manner is direction dependent. Hosten (1987) showed that for a composite fine laminated medium, the difference between Q (or attenuation quality factor) measured in a direction parallel to layers, and Q measured perpendicularly to layers, can be as large as an order of magnitude.

Thus, for quantitative studies, it makes sense to consider fully anisotropic media, where both velocity anisotropy *and* attenuation anisotropy are considered.

2) Previous theoretical studies in anisotropic media

The following work is based on the single interface response between media with anisotropic properties.

Wright (1987) and Banik (1987) showed that the effects of elastic anisotropy (or anisotropy in velocities) were important in characterizing AVO amplitude anomalies. Based on the hypothesis that most seals in sand-shale sequences are made-up of transversely isotropic shales, it can be said that AVO anomalies in the Gulf Coast cannot be properly modeled by simple elastic isotropic theory. Figure 1.7 shows the effects of including/neglecting anisotropy on the single interface reflection coefficient

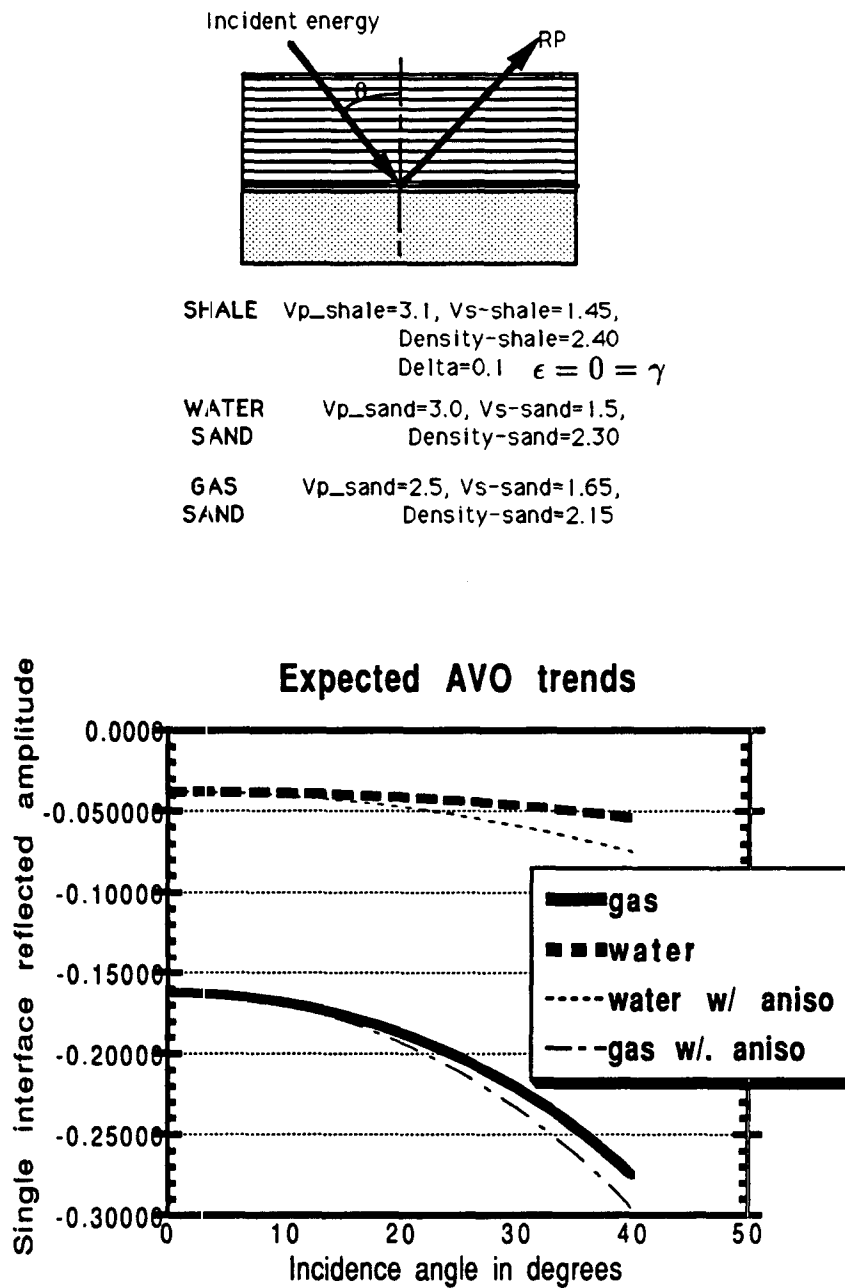


Figure 1.7: Anisotropic elastic reflection coefficient between transversely isotropic shale and isotropic sand fully saturated with either gas or water. The parameters used are similar to those of figure 1.3. The model parameters are listed to the right of the figure, with the shale's anisotropy in Thomsens' notation (1986).

between a shale and a gas-saturated sand. The response is compared to the curves obtained in figure 1.3, which was generated using the same parameters, but for the elastic isotropic case. In certain extreme cases, the AVO trend can even be reversed if anisotropy is included, and if the velocity of the seal is less than that of the reservoir; this can be the case for a water sand, and is shown in (figure 1.8). Table 1.2 summarizes the effects of anisotropy on AVO behavior; it is compiled from equation (19, chapter 1, section IV), where the reader can see that anisotropy has a first order effect in the reflection coefficient at non-normal incidence; as for the case of table 1, table 2 is derived from an approximation, and there will be exceptions. In general, the contributions of anisotropy simply add-on to the overall elastic isotropic contributions. The anisotropy notations used here are those of Thomsen (1986), and are reviewed in section III, 3-b.1, equations (10) in this chapter, and in chapter 3, section IV-3. Anisotropic effects are most important when the isotropic term (the leading term) is weak; in that case, note that it is the **contrasts** in δ that are most important (and that for larger angles, **contrasts** in ϵ contribute through the term $(\frac{1}{2}\Delta\epsilon - \frac{1}{6}\Delta\delta)$).

Table 1.2:

Effects of Anisotropy on AVO Response				
Terms in equation	Isotropic --	Mid Offset Anisotropic: $\Delta\delta$	Far offset Anisotropic $(\frac{1}{2}\Delta\epsilon - \frac{1}{6}\Delta\delta)$	Change in AVO (From isotropy)
case 1	positive	positive	positive	increase
case 2	positive	positive	negative	case dependent
case 3	positive	negative	positive	case dependent
case 4	positive	negative	negative	decrease
case 5	negative	positive	positive	increase
case 6	negative	positive	negative	case dependent
case 7	negative	negative	positive	case dependent
case 8	negative	negative	negative	decrease

The examples studied so far were only concerned with the effects of simple elastic anisotropy or of simple viscoelasticity (constant Q with direction), and the more general case of a fully anisotropic anelastic solid presenting varying degrees of Q-anisotropy as well, will be treated in the following section.

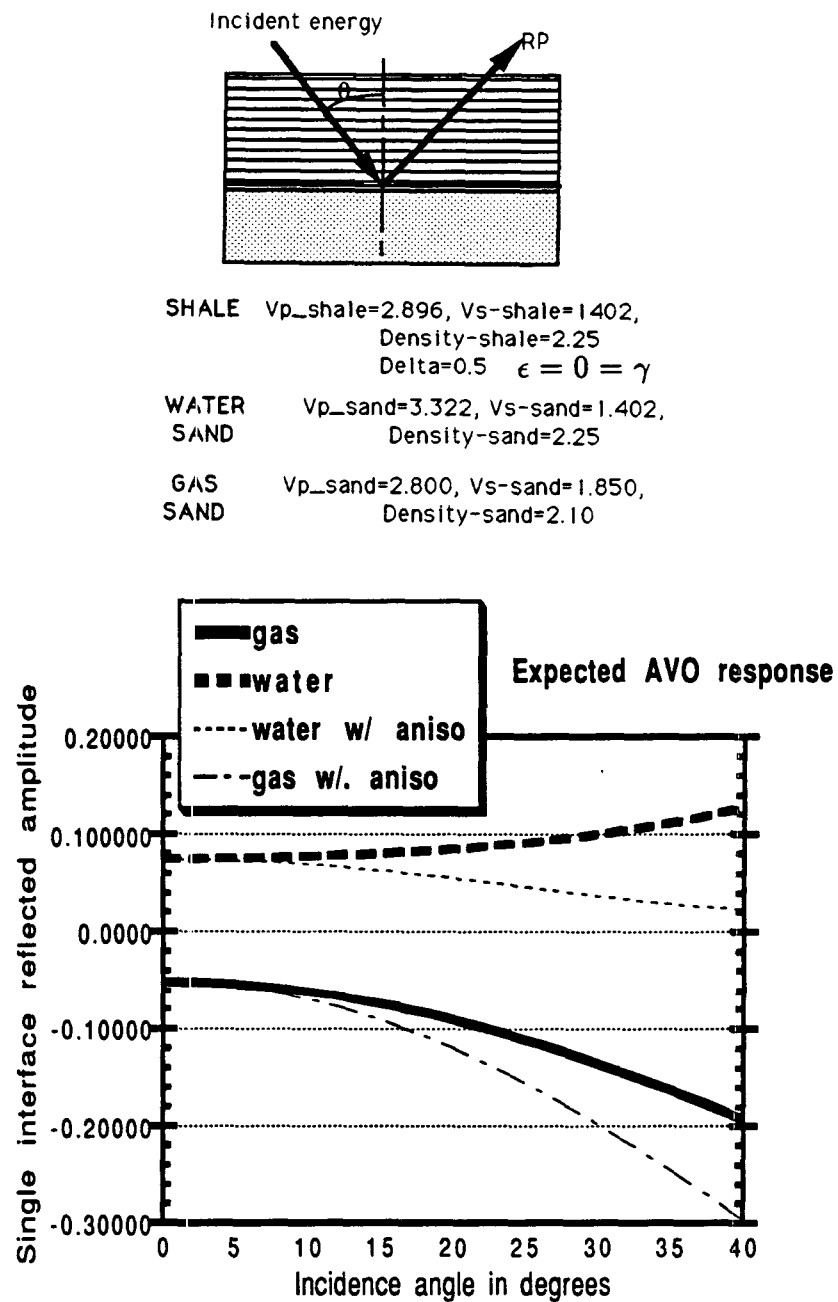


Figure 1.8: Transverse isotropy can reverse the theoretical (expected) isotropic reflection coefficients quite drastically as is shown here; model parameters used are listed to the right of the figure. This model was also used by Wright (1987) and Banik (1987), and constitutes an extreme case.

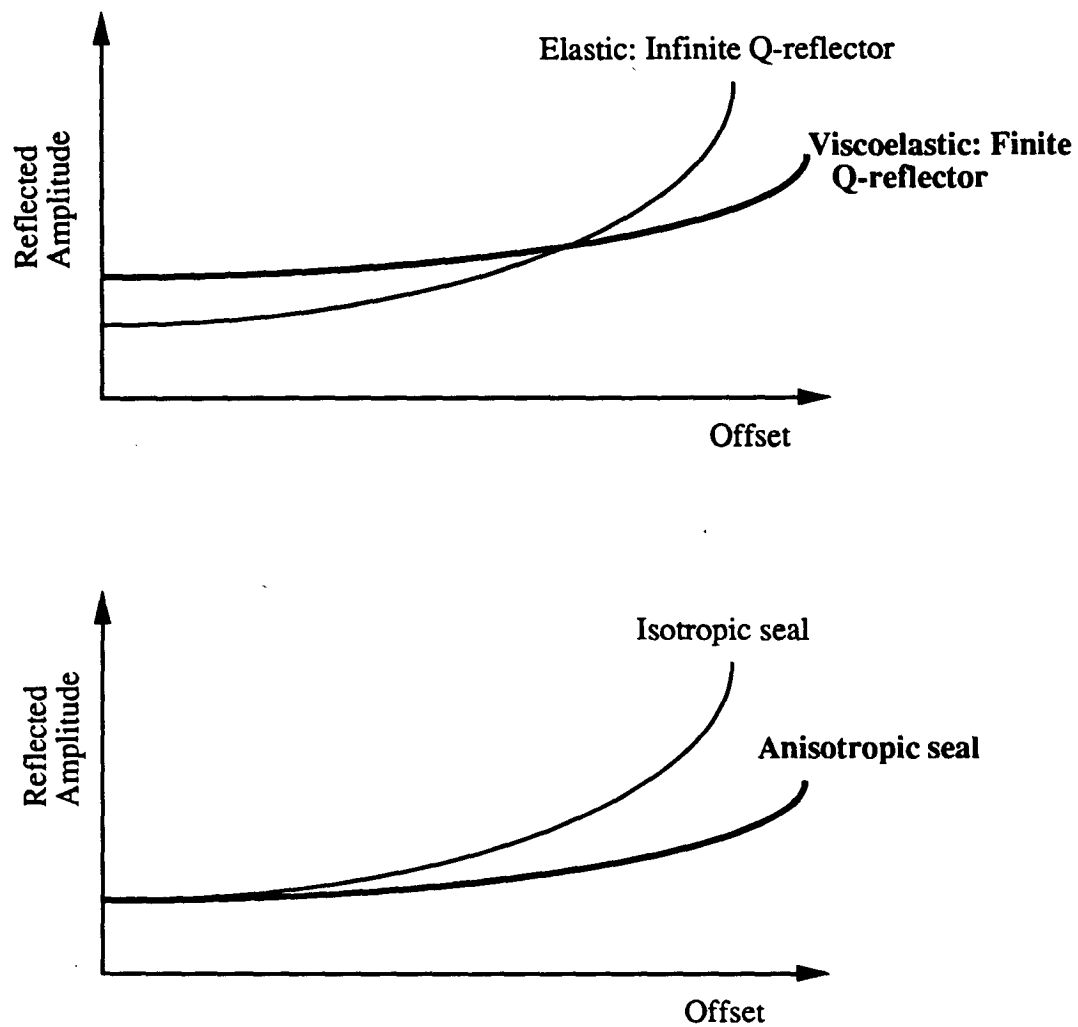


Figure 1.9: Schematic representation of the effects of viscoelasticity and anisotropy on AVO trends: the Q-factor attenuates the far offset traces more than the near traces and can affect the zero-offset amplitude, while anisotropy can lead to differential focusing along the wavefront and can induce radiation patterns. These effects (taken independently or jointly) may lead to a reversal of the AVO trend or to a different behavior than expected for an isotropic case; figures 1.10-1.22 study these effects in greater detail.

3) The response of two media with anisotropic and anelastic properties

In this section, it is shown that anisotropy and anelasticity lead to continuous changes in the phase of the wavelet as it is propagated, and to preferential focusing of the seismic energy along the wavefront (figure 1.9).

In studying the effects of wave propagation in fully anisotropic media, it was found (Samec and Blangy, 1992) that large anisotropic or anelastic effects must be incorporated for accurate modeling of pre-stack data. In fact, it was shown that the expected trend in reflection coefficient amplitude versus angle of incidence may be reversed from the elastic isotropic case if no special care is taken to compensate for:

- First : Source radiation pattern,
- Second : Anelastic or anisotropic focusing of Energy,
- Third : Phase distortions.

which are due to wave propagation in strongly anelastic anisotropic media.

A brief review of the fundamental theory of wave propagation in anisotropic and anelastic media follows; for more details, refer to Samec (1991) or Carcione et al. (1988).

a) Time domain modeling algorithm for anisotropic viscoelastic solids

a.1) Time domain governing equations for anisotropic viscoelastic solids

A linear viscoelastic continuum is defined as a medium for which a set of relaxation functions relating the stress and strain tensor exists, and can be expressed as:

$$\sigma_{ij}(x, t) = c_{ijkl}(x, t) * \epsilon_{kl}(x, t) \quad (6)$$

$$\rho \frac{\partial^2 u_i}{\partial t^2} = \nabla_j(\sigma_{ij}) + f_i \quad (7)$$

Where $\sigma_{ij}(x, t)$ is the stress tensor, $\epsilon_{kl}(x, t)$ is the strain tensor, $c_{ijkl}(x, t)$ is the time dependent elastic tensor, u_i is the i^{th} component of the displacement field, ∇ is the divergence operator, ρ is density, f_i is the distribution of external forces acting on the medium, and $*$ denotes the temporal convolution operator; the equation of motion is a second order partial differential equation in displacement and relates the acceleration vector to the divergence of the stress and the sum of the external forces.

Assuming that the viscoelastic solid behaves as a macroscopic assemblage of springs and dashpots (similar to a Standard Linear Solid model), the time dependent anisotropic elastic tensor can be written as:

$$c_{ijkl}(x, t) = c_{ijkl}(x) \left[1 - \sum_{m=1}^{L_{ijkl}} \left[1 - \frac{\tau_{\epsilon_m}^{ijkl}}{\tau_{\sigma_m}^{ijkl}} \right] e^{-\frac{t}{\tau_{\sigma_m}^{ijkl}}} \right] \quad (8)$$

This is a generalization of the model provided by Tal-Ezer (1986), Liu (1987), and Carcione (1987), and Tal-Ezer et al. (1990). In the previous expression one can recognize the characteristic times $\tau_{\epsilon_m}^{ijkl}$ for the strain relaxation, and $\tau_{\sigma_m}^{ijkl}$ for the stress relaxation of a Standard Linear Solid model, each of the elastic tensor components being modeled by a series assemblage of L_{ijkl} relaxation mechanisms. In order to achieve a frequency independent attenuation, we need, in theory, an infinite sum of relaxation functions. However, in practice, to obtain a quasi-constant quality factor over the seismic band, it is sufficient to take into account only two of these relaxation mechanisms; this is shown in figure 1.10.

a.2) Time domain integration of the governing equations

A detailed description of the solution algorithms is provided in Tal-Ezer et al. (1987) and Carcione (1987). In summary, equation (7) can be transformed into a first order partial differential equation. Then equations (6),(7), and (8) are integrated in the time domain providing the following solution (Carcione et al., 1988):

$$U_n = \int_0^t e^{M_n \tau} F_n(t - \tau) d\tau \quad (9)$$

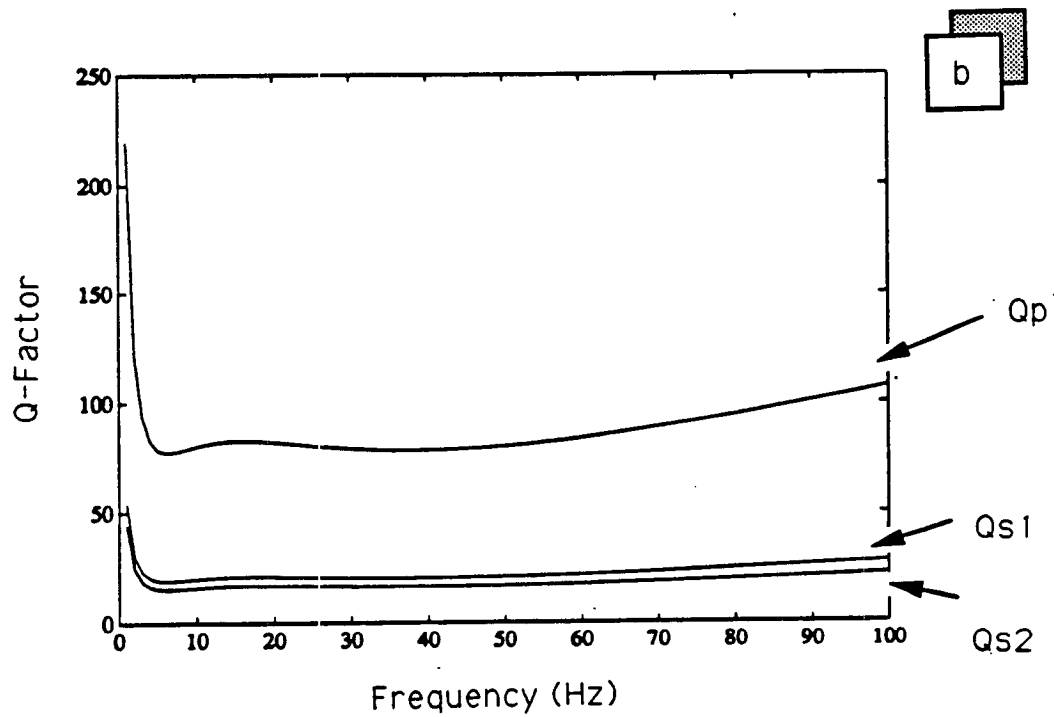
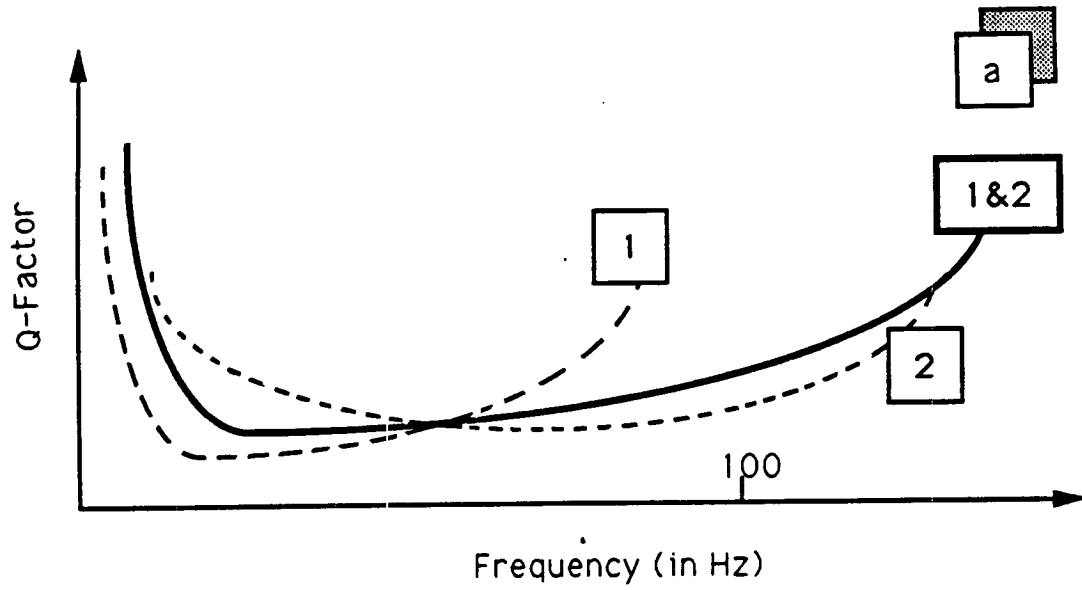


Figure 1.10: Modeling attenuation: a) Attenuation is modeled by assuming that the energy absorption can be represented by two relaxation functions. b) This numerical approach yields a quasi-constant causal Q model over the frequency range investigated by seismic methods (from 5 Hz to 100 Hz).

Here U_n is the displacement field, M_n is the spatial operator, and F_n is the source space-time distribution. The index n denotes the spatial discretization. The spatial derivatives involved in the partial differential operator M are computed in the wavenumber domain after forward Fourier transform, and are transformed back into the space domain using the algorithm initially developed by Kosloff (1982). The time integration step consists of the partial convolution of the source time history with the exponential function $e^{M_n\tau}$, where $e^{M_n\tau}$ is evaluated by a Chebichev expansion. When combined, these two extremely accurate algorithms for the computation of the time integral and the spatial operator yield minimum numerical dispersion and allow for detailed studies of seismic propagation in dispersive viscoelastic media.

b) Implementation of the modeling algorithm for the study of seismic reflections

b.1) Implementation and parameter description

As discussed in the previous section, once generalized to viscoelastic anisotropic media, the Fourier Pseudo-Spectral method (Tal-Ezer et al., 1990) yields an adequate level of modeling accuracy for sensitivity analyses of wave phenomena associated with attenuation and anisotropy. To prevent spurious reflections, the models are padded along their edges with absorbing buffers, using the method of Kosloff and Baysal (1982). These buffers absorb over 99 % of the energy, but a small amount of energy can nevertheless be reflected off the boundaries. After modeling, the P and S wave arrivals are separated, the P waves are calculated from the divergence of the displacement field, and the S waves from the curl of the displacement field. The following parameters are common to the various modeling cases:

- The standard acquisition geometry is described in Figure 1.11a. It consists of a grid of 128×128 samples, with a grid spacing of $10m$. The interface studied is located $450m$ below the receiver line. The receiver line itself is built of 100 receivers with $10m$ spacing between the receivers.

- The seismic source is modeled as a buried isotropic source, having a Ricker wavelet time history, and 35 Hz dominant frequency. Since the modeling is two dimensional, the point source used is actually a line source in three dimensions.
- To describe transverse isotropy, I use once again use the parameterization of Thomsen (1986) for all of the examples that follow. As a reminder, the parameters are defined as:

$$\epsilon = \frac{C_{11} - C_{33}}{2C_{33}}; \gamma = \frac{C_{66} - C_{44}}{2C_{44}}; \delta = \frac{(C_{13} + C_{44})^2 - (C_{33} - C_{44})^2}{2C_{33}(C_{33} - C_{44})} \quad (10)$$

This notation is especially attractive, since vertical compressional and shear velocities are held constant for all of the examples. The parameters ϵ and γ are kept constant and null for all of the modeling cases, and only the parameter δ was adjusted to modify the amount of anisotropy. The compressional velocity is $V_{P_1} = 2896m/s$ for the upper layer, and $V_{P_2} = 3322m/s$ for the lower medium. The shear velocities are respectively $V_{S_1} = 1402m/s$ and $V_{S_2} = 1402m/s$. The densities are the same for both layers, i.e. $\rho = 2.25g/cc$. These elastic parameters have already been published in the literature for a sand/shale configuration (Wright, 1987, Banik, 1987). For the modeling of elastic transversely isotropic solids, δ is set to 0.1.

- In modeling viscoelastic attenuation, two relaxation functions were used and they allow for a quasi-constant causal Q factor over the frequency range of investigation as shown in Figure 1.10b.

As shown in Figure 1.11b, $\delta = 0.1$ is not an uncommon value of anisotropy as measured on core samples, and thus can be taken as a lower bound estimate for some strongly anisotropic shales. Attenuation anisotropy has been experimentally measured on synthetic materials (Hosten et al., 1987), and was theoretically predicted by Hudson (1981). Hosten's experimental results are shown in Figure 11c, and report

a level of attenuation anisotropy for a synthetic layered medium of approximately two and a half. A significantly greater ratio of approximately thirty between high and low attenuation was also predicted theoretically by Hudson (1981). Waters (1987) showed from empirical observations that Q is approximately proportional to the square of velocity for compressional waves. Similarly, Meister et al. (1985) showed analytically that, given the 4 definitions:

$$Q_P = \frac{K_R + \frac{4}{3}\mu_R}{K_I + \frac{4}{3}\mu_I}; \quad Q_S = \frac{\mu_R}{\mu_I}; \quad V_P^2 = \frac{K + \frac{4}{3}\mu}{\rho}; \quad V_S^2 = \frac{\mu}{\rho} \text{ with } \mu = \mu_R \text{ and } K = K_R$$

we have

$$\frac{Q_P}{Q_S} = \left(\frac{\mu_I}{\kappa_I + \frac{4}{3}\mu_I} \right) \frac{V_P^2}{V_S^2}$$

Then for anisotropic velocities with $\frac{V_{horizontal}}{V_{vertical}} = 2$, we would expect a ratio $\frac{Q_{horizontal}}{Q_{vertical}} = 4$ in highly anisotropic formations. The present modeling of anisotropic Q is based on a ratio of approximately five, ie a variation in Q from approximately 15 (a relatively low value of Q) to about 80.

c) Modeling benchmarks and calibration of reflections

I proceed with some numerical tests to investigate the accuracy of the generalized algorithm in evaluating reflected amplitudes and reflection coefficients. Two different methods were implemented; they yield consistent results, and thus satisfy the requirements for the calculation of reflected amplitudes and reflection coefficients.

c.1) Direct measurement of reflected amplitudes

Let us consider the two layer model of figure 1.11a. For cases in which the upper layer is isotropic and purely elastic, recording amplitude variations with offset after geometrical spreading and emergence angle corrections is equivalent to recording the reflection coefficient directly. Since the modeling is two dimensional, the amplitude decay is proportional to $\frac{1}{\sqrt{r}}$ where r is the ray path distance from the source (Aki and Richards, 1980). If the modeling were truly three dimensional, the decay would be proportional to $\frac{1}{r}$.

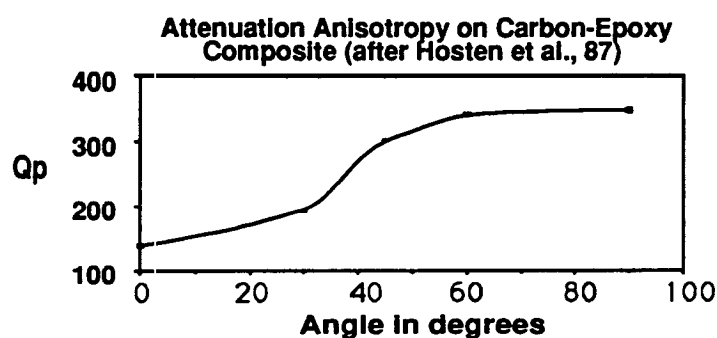
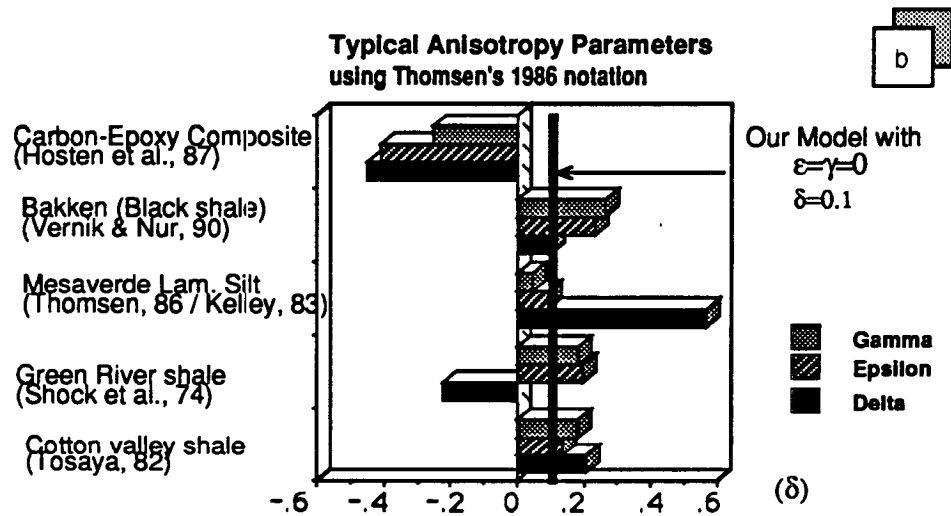
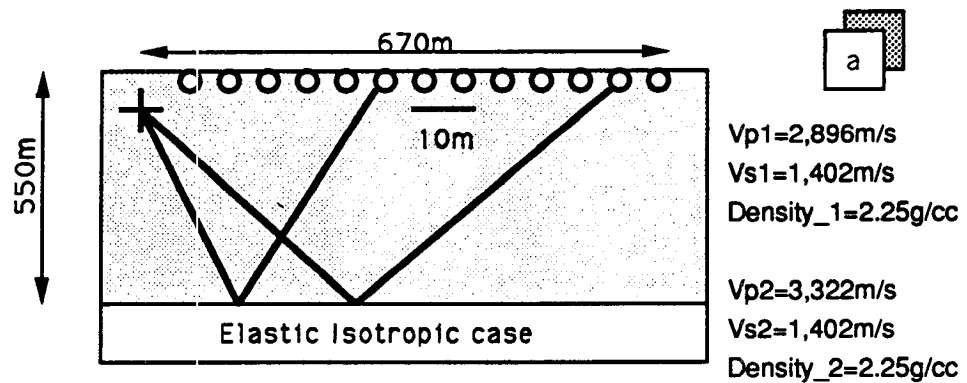


Figure 1.11: a) Set-up for the reflection acquisition. The explosive isotropic point source (+) is placed in the upper left corner of the model. The receiver (o) spacing is 10m. b) The anisotropic properties used in modeling in relation to known measured anisotropic properties. c) Experimental measurement of attenuation anisotropy in a composite material (after Hosten, 1987).

The previous use of the word amplitude is very imprecise; amplitudes can be evaluated in different ways, with different implications for each measurement type. Among other methods, the following were considered:

- Maximum peak amplitude for the reflected event.
- Root mean square average of the reflected arrival amplitude within a window.
- Spectral amplitude for a frequency component of the reflected event.

Each of these methods should yield the same results, provided that the transmission path from source to receivers does not introduce any signal dispersion. Such a requirement can only be met if both the upper and lower layers of the model are purely elastic and isotropic (and if there is no numerical dispersion). When introducing attenuation or anisotropy in either layer, the three methods yield different results:

- Peak amplitudes tend to over-emphasize the effects of phase shifts - because the maximum amplitude of the wave train constantly shifts with the phase -. Overall, picked results were found to be unstable and difficult to interpret, when anisotropy or viscoelasticity were modeled.
- The root mean square average provides a measure of the reflected energy within a given window (Aki and Richards, 1980). This type of measurement eliminates the undesirable phase effects observed when picking amplitudes directly. However, this method merges phase effects and energy focusing effects into one single response, and does not provide the level of discrimination that is needed for systematic sensitivity analyses of numerical results.
- The spectral amplitude method provides a perfectly calibrated measurement of reflected amplitudes for a given frequency, and enables a good level of discrimination between phase distortion effects, and energy focusing mechanisms in a high S/N dataset.

Consequently, when picking the synthetic data shown in later examples, the spectral amplitude method was used.

Figure 1.12 displays the results obtained with the spectral method when top and bottom layers are purely elastic and isotropic. The spectral amplitude data was measured at 35Hz , and corrected for two dimensional geometrical spreading ($\frac{1}{\sqrt{r}}$). Quantitatively, the data is in good agreement with values of the reflection coefficient data, multiplied by the source amplitude at 35Hz ; this confirms that for elastic isotropic media, the measurement of amplitude variations with offset after geometrical spreading correction is directly related to the measure of the reflection coefficient as a function of the incidence angle. Should the upper layer be isotropic and elastic, the spectral measurement previously described, provides a good estimate of the reflection coefficients, since the signal is not distorted while propagating in the upper layer.

c.2) Direct measurement of the reflection coefficient

I have shown that in cases where the upper layer of the model is purely elastic and isotropic, the spectral method allows for a direct computation of the reflection coefficient as a function of the angle of incidence. Should the upper medium be viscoelastic or anisotropic, the transmission effects would dramatically alter the quality of both the incident and reflected waves. In this case, numerical modeling can still yield good estimates of the reflection coefficients. Receivers can be placed along both down-going and up-going ray paths, as shown in Figure 1.13a. This geometry can be used to extract group velocities. The amplitudes picked along these receivers are displayed in Figure 1.13b. The amplitude along the ray path decays due to the effects of both geometrical spreading and attenuation, until the ray reaches the interface. The sudden drop in amplitude provides a direct measurement of the reflection coefficient for each ray path selected. This method yields a direct numerical estimation of the reflection coefficient. By repeating this method for several rays, a family of incidence angles can be defined, and reflection coefficients can be measured *at the reflector* as

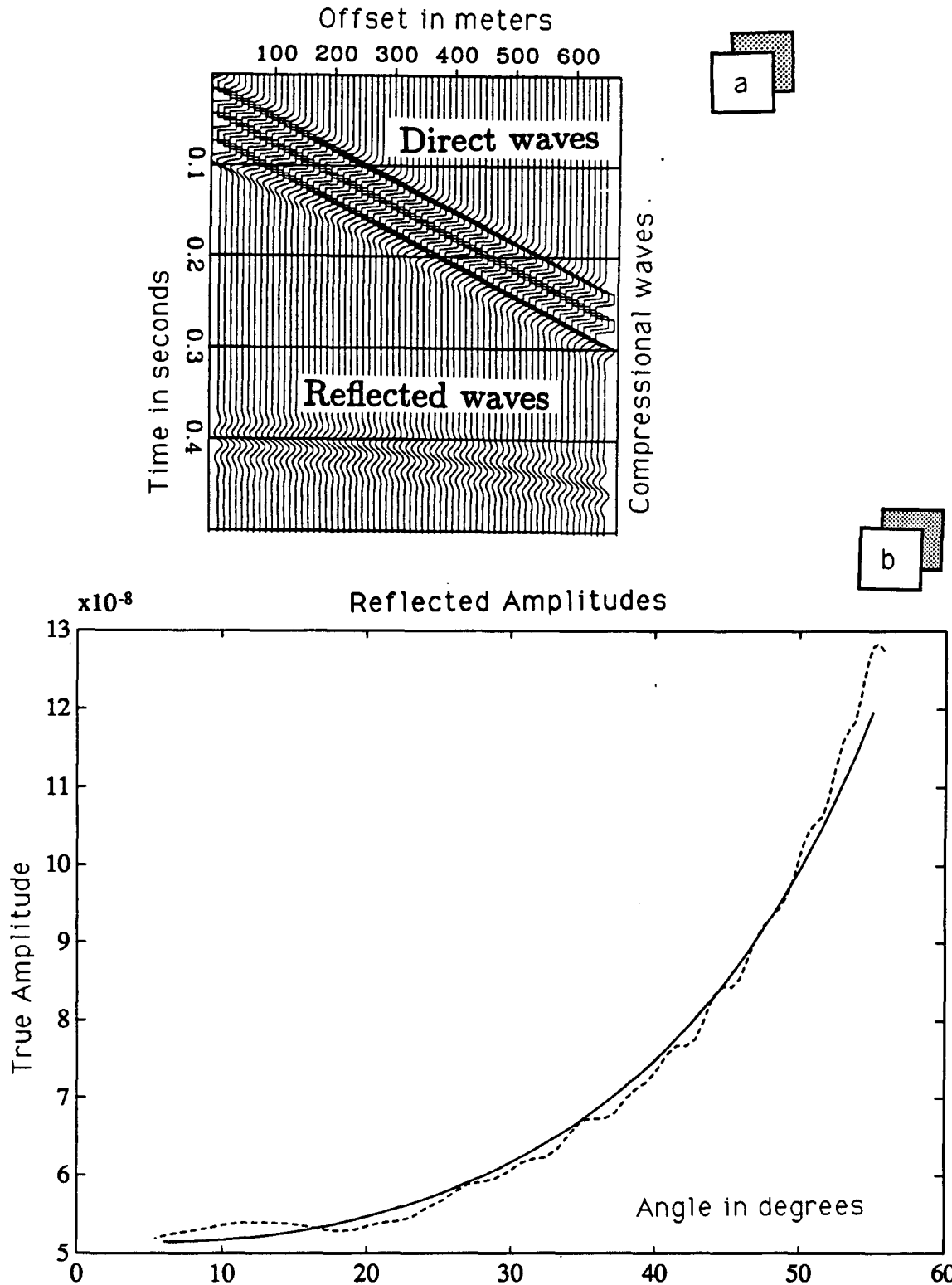


Figure 1.12: a) A typical record for the receiver geometry shown in figure 1.11a. Only compressional waves are displayed in this graph, and two modes can be identified: direct waves and reflected compressional waves. b) Comparison between numerical and theoretical computations of the amplitudes of reflected compressional waves. The theoretical prediction (solid line) is obtained after multiplying the reflection coefficient by the source amplitude. The picked amplitude (dashed line) was corrected for two dimensional geometrical spreading. Differences in amplitudes between figures a) and b) are due to source/receiver directivity; these effects are sometimes also called emergence angle effects.

a function of the angle of incidence. As shown in Figure 1.14, for the elastic isotropic case, there is good agreement between the analytical reflection coefficient (Daley and Hron, 1977), and the numerical computation.

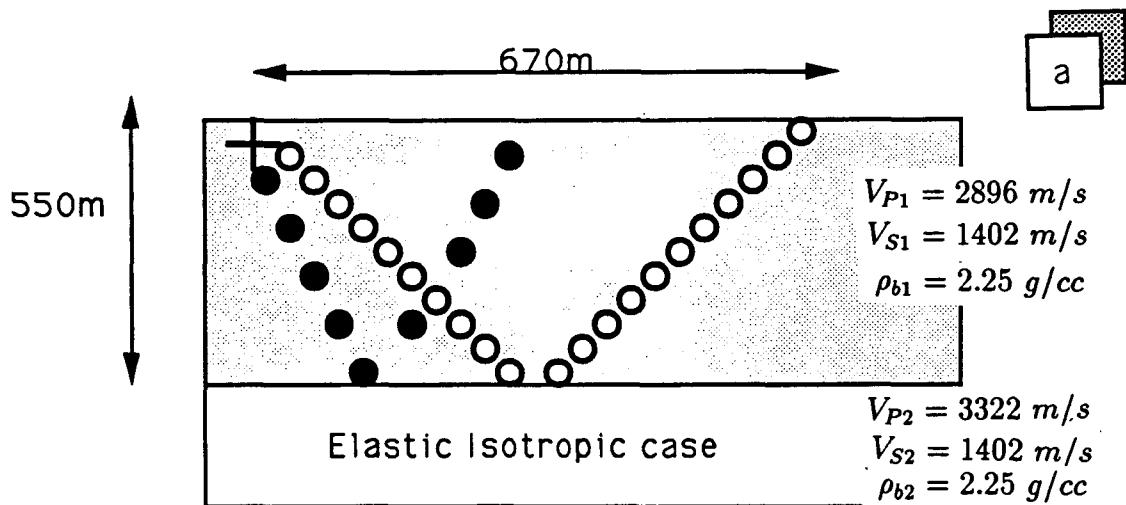
c.3) Monitoring of the wave fronts

To understand the effects of wave propagation phenomena on reflection trends, we must first understand the effects of energy focusing and defocusing along the wave front, due to velocity anisotropy and to attenuation anisotropy. To that end, I introduce yet another receiver geometry. As shown in Figure 1.15a, the receivers are placed around the source, along iso-phase curves. Figure 1.15b shows the signal recorded for one of these receiver arrays, when the upper layer is viscoelastic isotropic, and the lower layer is elastic and isotropic; it clearly displays both the down-going compressional wave and the reflected compressional wave. Since the down-going arrival is stronger than the reflected arrival, it is apparent that the direct arrival in this type of plot can be used as a diagnostic tool to measure both phase distortion effects and energy focusing effects, which are common wave propagation phenomena in anisotropic viscoelastic media.

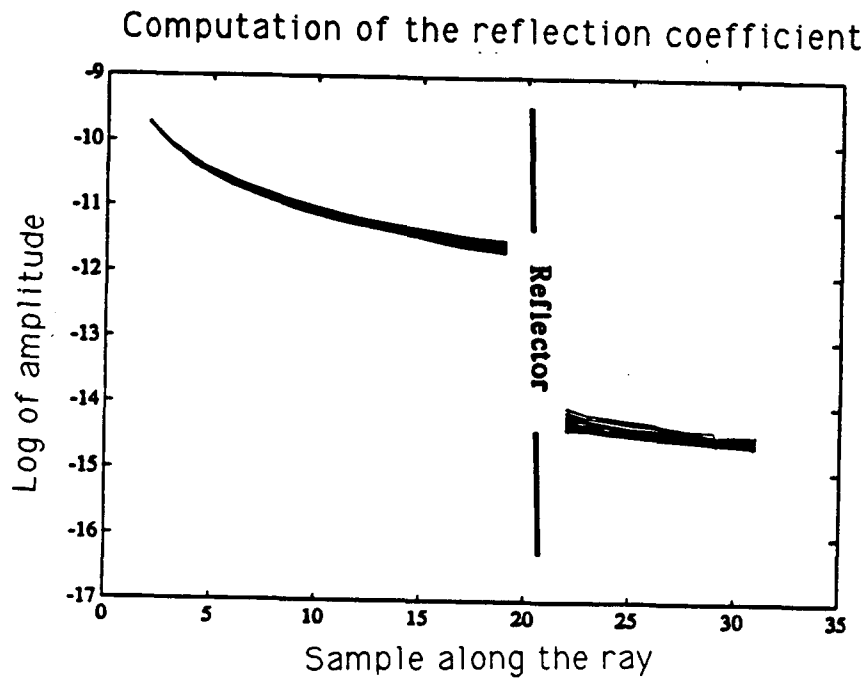
So far, I presented various tools to allow for accurate numerical modeling of wave phenomena in viscoelastic anisotropic media. I will now study the effects of both attenuation and anisotropy on synthetic AVO trends, through several sensitivity analyses. Note that I use the term AVO analysis to refer to either studies of Amplitude Versus Offset or to studies of Amplitude Versus Angle of incidence (AVA). The two techniques are interchangeable, provided that the velocity structure is known with some certainty.

d) Effect of viscoelastic attenuation on AVO measurements

Attenuation has two separate effects on AVO measurements. First, it influences the reflection coefficients at the boundary between two layers, and second, it affects the wave propagation from the seismic source to the reflector and back to the receiver



a



b

Figure 1.13: a) Second acquisition geometry to directly compute the reflection coefficients from receivers placed along ray paths. b) Actual amplitudes picked along the ray paths for the compressional waves as a function of the ray parametrization. The abrupt amplitude drop is due to the reflection coefficient. Each of these curves is plotted for a different incident ray, over an incidence range of approximately 30 degrees, and this allows for the computation of the reflection coefficient as a function of the angle of incidence.

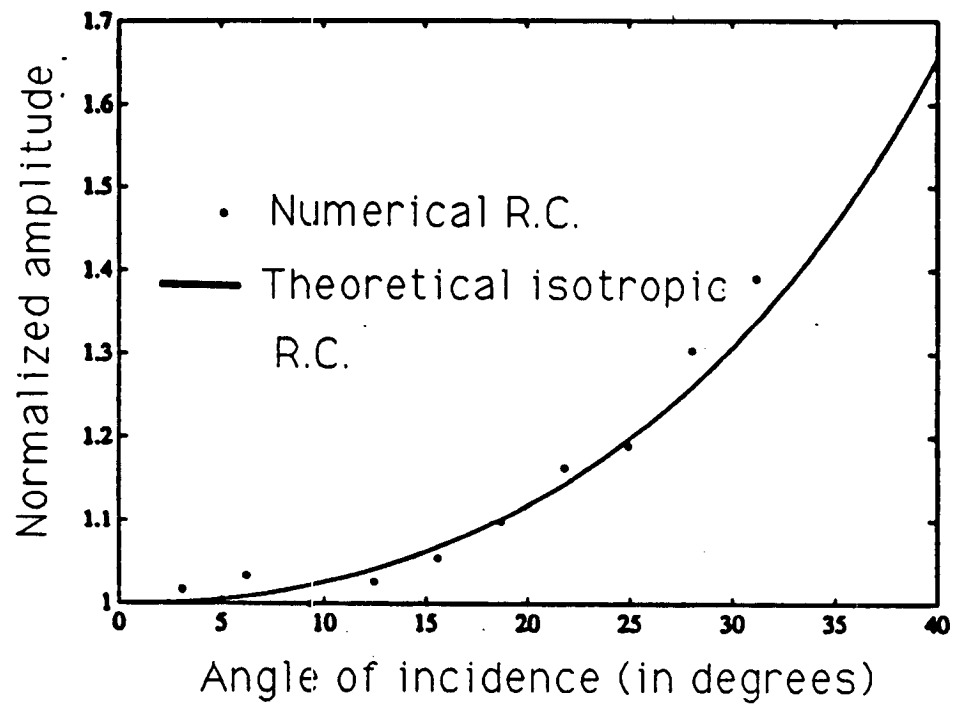


Figure 1.14: Comparison between the theoretical (Daley and Hron, 1977) and numerical reflection coefficients, computed with the method presented in Fig. 1.13b.

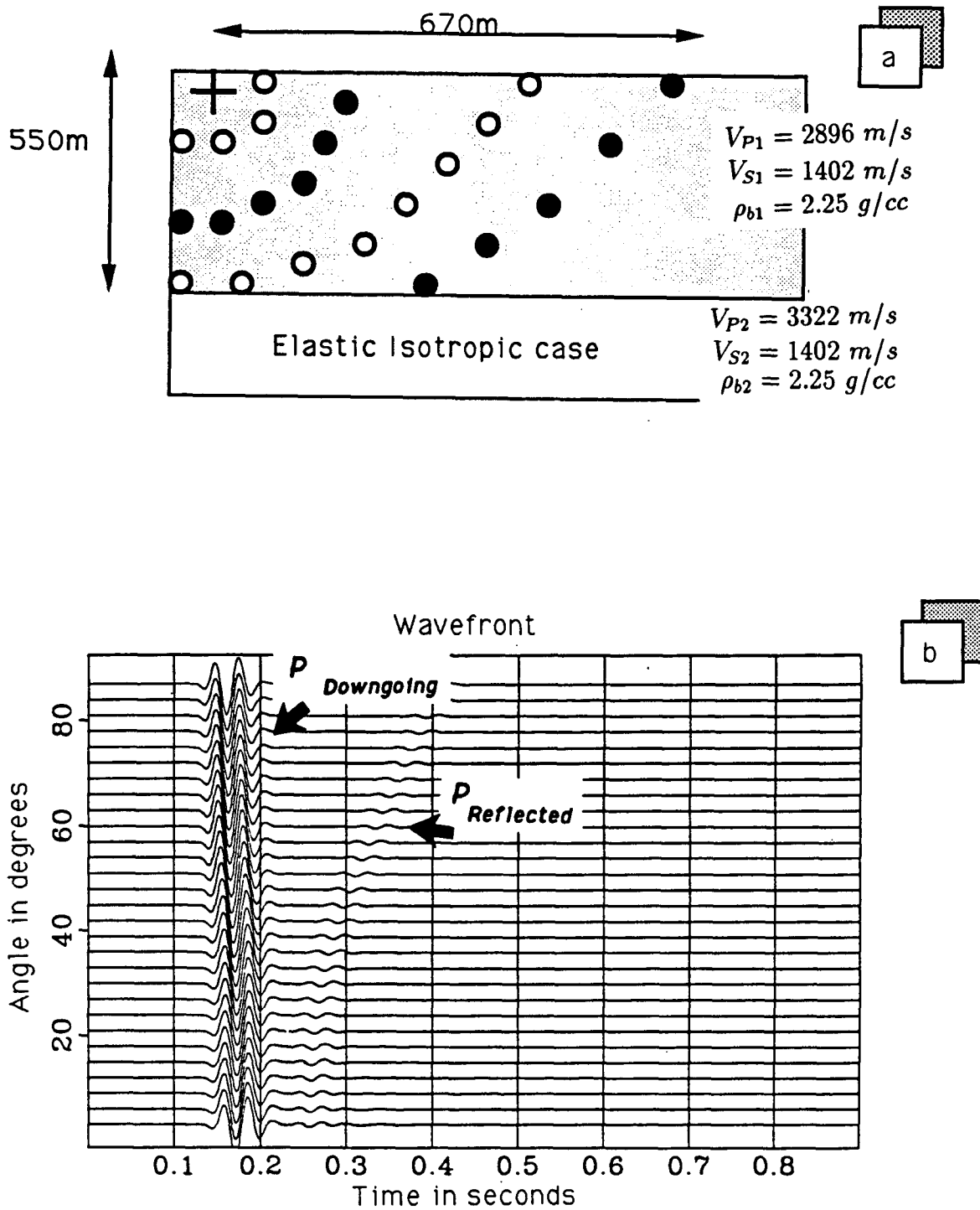


Figure 1.15: a) The distribution of receivers used to monitor the wavefront energy distribution. b) Numerical computation of the signal propagated through a receiver array placed along the wavefront in a viscoelastic medium; layer properties correspond to those of figure 1.16.

array. In this section, I will assume that "wave amplitude" refers to the spectral amplitude of an isolated mode, measured at 35Hz. This corresponds to the central frequency of the synthetic signal. All amplitude displays will be in true "amplitude", and theoretical measurements will be displayed, after normalization by the source amplitude. The examples analyzed in section d.1 will reflect the dependence of AVO trends on viscoelasticity and viscoelastic anisotropy *in the lower layer only*. The upper layer is kept isotropic and elastic for all cases; effectively, this eliminates propagation effects.

d.1) Effect of attenuation on reflection coefficients

Let us consider a **lower layer** which is **viscoelastic**, with both elastic and attenuation parameters being **isotropic**. The parameters are shown in Figure 1.16a. The effect of attenuation on the reflection coefficients is clearly displayed by comparing picked amplitudes at surface receivers (Figure 1.17a) for both an elastic bottom layer (solid line), and a viscoelastic bottom layer (dashed line); the upper layer is kept elastic and isotropic. An overall increase in amplitudes occurs, and no appreciable change in the AVO trend can be observed. The *amplitude jump* is due to an *increase in the apparent impedance contrast* between the two layers; the impedance change is caused by the viscoelasticity of the bottom layer. These numerical results are both qualitatively and quantitatively consistent with those of Bourbie (1982), who showed that for zero incidence angle, the reflection coefficient for compressional waves can be expressed as:

$$RP = \frac{\rho_2 V_{p2} - \rho_1 V_{p1}}{\rho_2 V_{p2} + \rho_1 V_{p1}} + \frac{1}{2\pi} \left(\frac{1}{Q_2} - \frac{1}{Q_1} \right) \text{Log} \left| \frac{\omega}{\omega_0} \right| + \frac{i}{4} \left(\frac{1}{Q_2} - \frac{1}{Q_1} \right)$$

where the Q_i and V_i are taken at the reference frequency ω_0 ; this equation is a valid approximation for Q values greater than 5 or so. This formula confirms that the attenuation contrast is only a secondary effect. The effect of attenuation contrasts will only be observable in cases where large Q contrasts exist, with respect to changes in impedance. The additional information implied by figure 1.17a is that the AVO trend itself should not be affected much by the Q contrasts between two viscoelastic

isotropic layers.

Figure 1.17b shows the amplitudes corresponding to a **bottom layer** which has **anisotropic attenuation**, with the characteristics shown in Figure 1.16b; the upper layer is again isotropic and elastic. Note that the reflection coefficient curve is different from that of an isotropically attenuating bottom layer and from that of an elastic bottom layer considered previously. Comparing the isotropic-Q and the anisotropic-Q cases, I conclude for the following for given set of parameters (Figure 1.17b): at *normal incidence*, the attenuation is *identical* for the isotropic and anisotropic Q models. As the angle of incidence angle is gradually increased, the attenuation decreases, and therefore, the impedance contrast between the upper and lower layer is lowered. This causes a *decrease of the reflection coefficients* beyond 10 degrees for the anisotropic attenuation case in relation to the isotropic-Q case.

d.2) Effect of attenuation on wave propagation

Let us now consider the **upper layer** to be viscoelastic-isotropic on one hand, and viscoelastic-anisotropic on the other, as shown in figure 1.18; the lower layer is kept elastic and isotropic.

For the **isotropic viscoelastic** case (solid line, figure 1.18), the AVO trend is flat instead of being strongly positive, as in the isotropic elastic case. This phenomenon is explained by the fact that longer travel paths are attenuated more, because attenuation is proportional to the distance travelled. The longer the ray paths, the higher the attenuation, and the more the AVO trend created by the reflection coefficient will be masked.

This explanation is reinforced further, when considering the **anisotropic attenuation** case. As offset increases, the propagation or incidence angle also increases, and the amount of attenuation due to propagation becomes smaller. This increases the original AVO trend. In the case of a viscoelastic-anisotropic upper layer (dashed line, figure 18), it is important to note that amplitudes picked directly, and ampli-

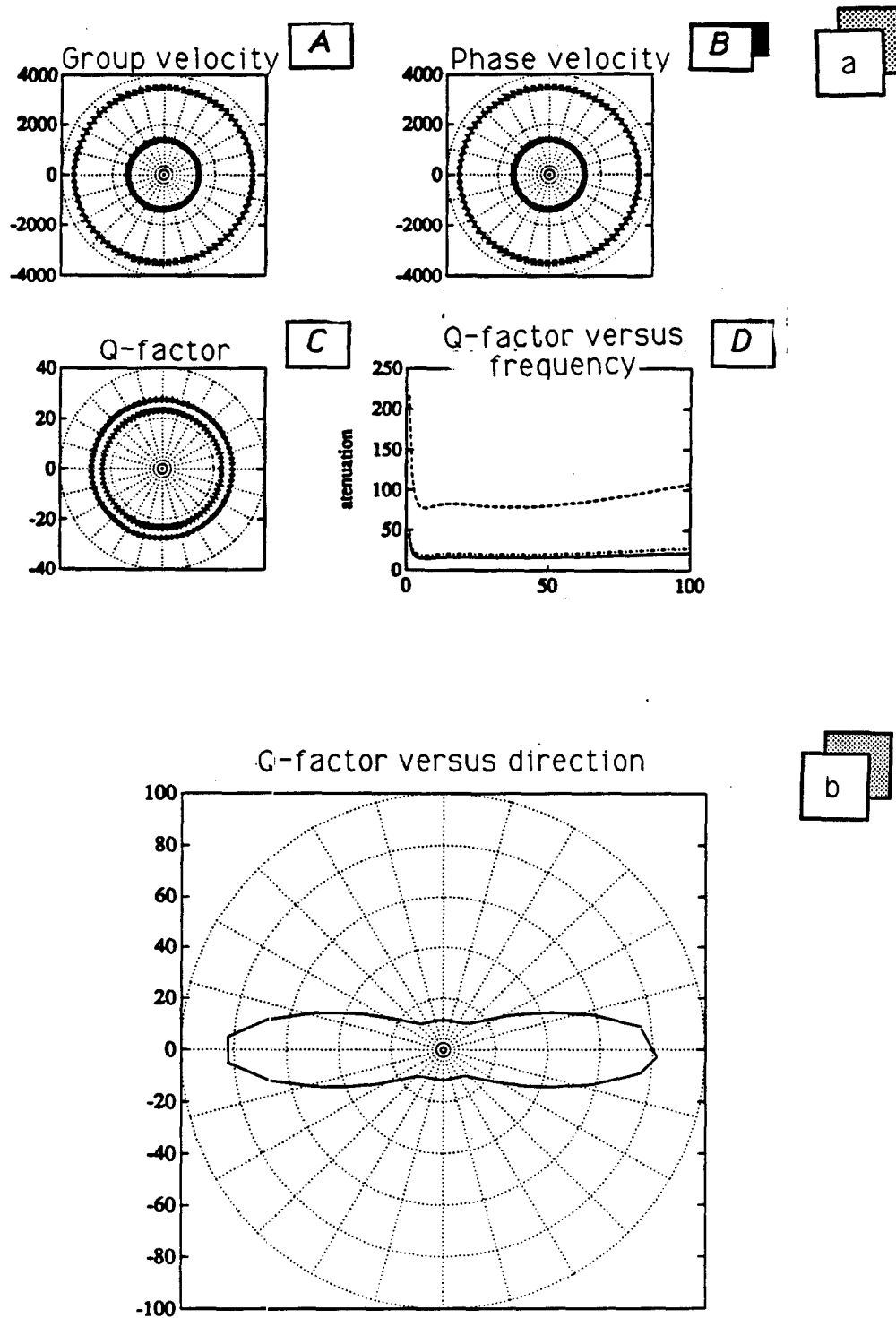


Figure 1.16: a) Description of an isotropic viscoelastic solid. Such a solid can be described by (A) the group velocity, (B) the phase velocity, and (C) the Quality factor for both compressional (outer circles) and shear waves (inner circles). (D) The dependency of the various attenuation parameters on frequency. b) Attenuation anisotropy properties of the material modeled.

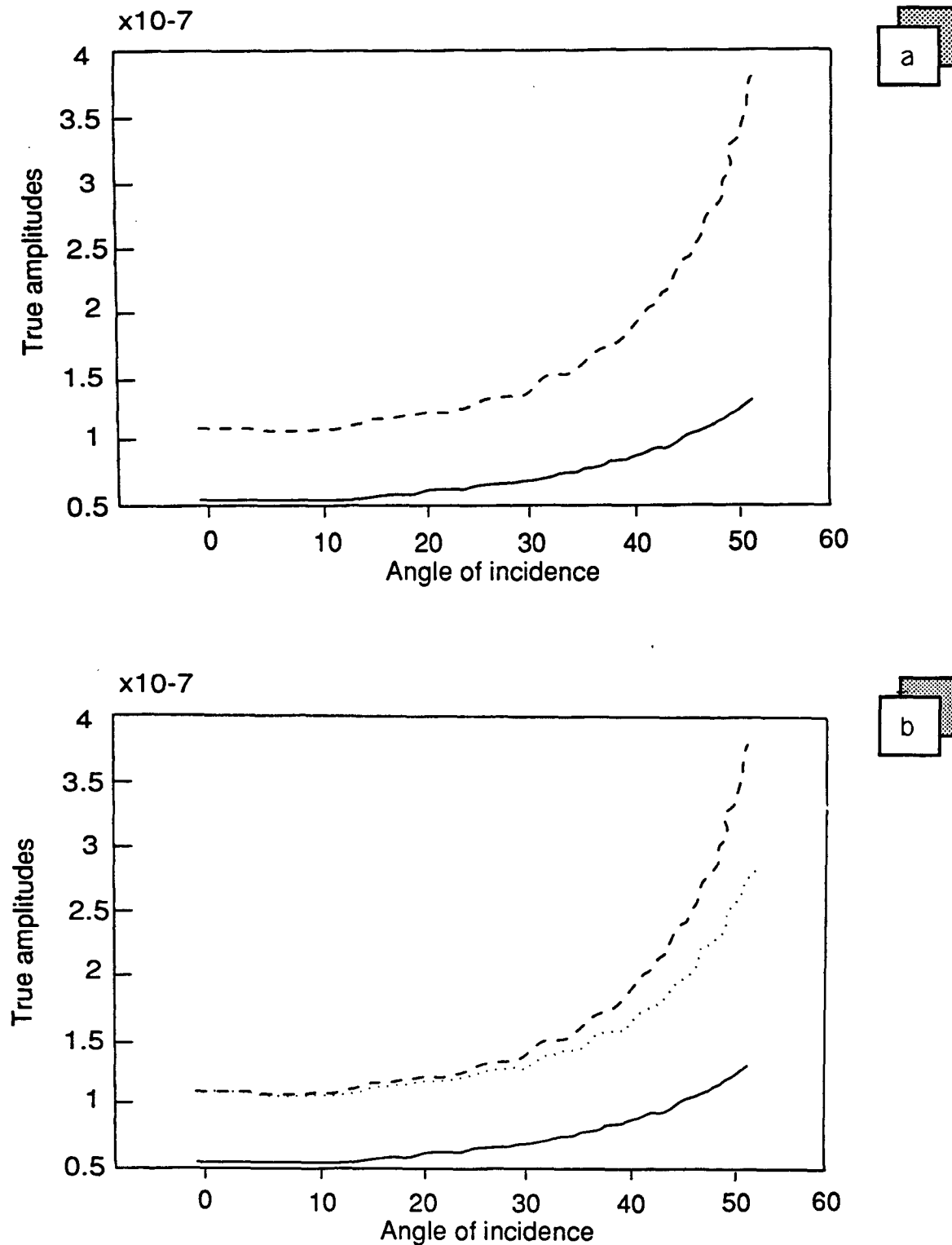


Figure 1.17: a) Comparison between the reflected compressional wave amplitudes where the bottom layer is purely elastic (solid line), and viscoelastic (dashed line). b) Same as figure 1.17a, but the dotted line shows reflected amplitudes, in the case where the bottom layer has anisotropic viscoelastic properties.

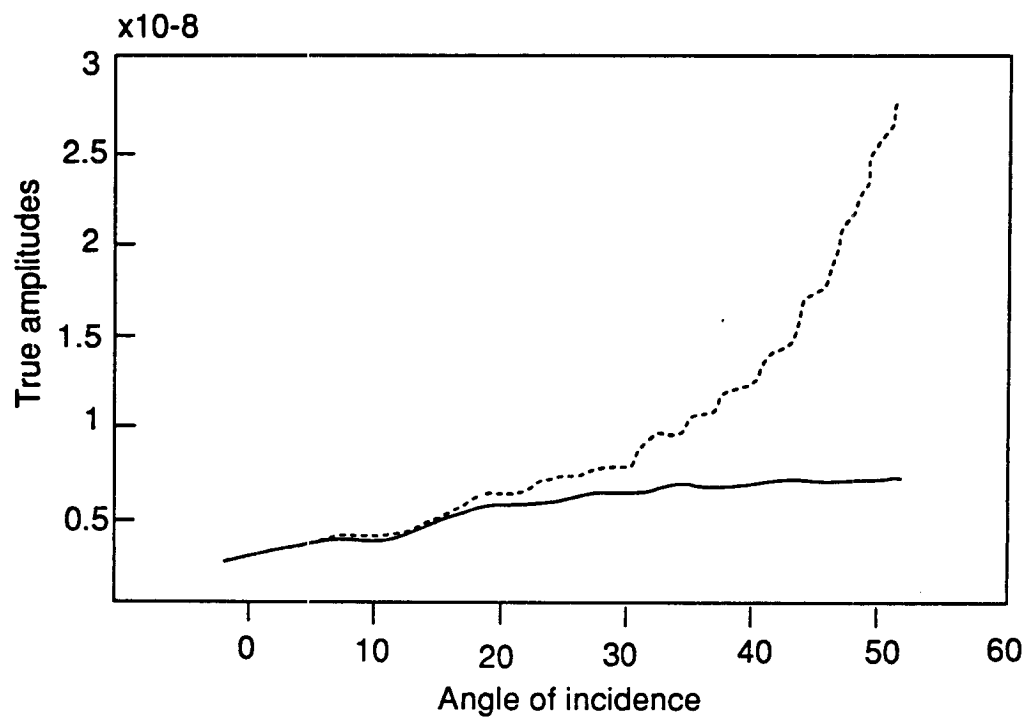


Figure 1.18: Reflected amplitude measurement of compressional waves. In the first case, the top layer is viscoelastic isotropic (solid line). In the second case, the top layer attenuation properties are anisotropic (dashed line).

tudes found with the spectral method do not agree, because of changes in the phase of the reflected event. In an anisotropic attenuating medium, dispersion is due to the difference between phase and group velocity, and is not uniformly spread along the wave front. These changes in the phase of the wavelet create large discrepancies in the picked measurements for the two methods.

e) Effect of elastic **anisotropy** and attenuation **anisotropy** on AVO measurements

Let us consider the anisotropic material depicted in Figure 1.19. It has the same velocities as described previously, and has a $\delta = 0.1$. When considering anelastic anisotropy, I use similar parameters to the ones presented above. As in the previous section, I try to decouple propagation effects from reflection coefficient effects as much as possible, to provide a systematic analysis of the two phenomena. Note that anisotropy due to thin layering, and reflector or wavefront curvature can cause focusing/defocusing effects (Banik et al., 1989); however, these effects were not considered here, because I concentrated on a single interface response in the far field.

e.1) Effect of anisotropy on reflection coefficients

Once again, let us consider an anisotropic **lower layer**. The effect of **elastic anisotropy** on reflection coefficients has been extensively described by both Banik (1987) and Thomsen (1986). Their results were reproduced with the greatest accuracy as shown in Figure 1.20a, where the upper layer is elastic isotropic, and the lower layer is either isotropic or anisotropic. Each group of curves shows a comparison between the analytical computation (+) of reflection coefficients using Banik approximations (1987) and the numerical computation (solid line). As expected with the current choice of parameters, the *elastic anisotropic* lower layer yields a *larger increase* in the reflection coefficient as a function of the angle of incidence than the elastic isotropic lower layer. However the effect of elastic anisotropy is relatively small when compared to the dramatic effects previously introduced by viscoelasticity.

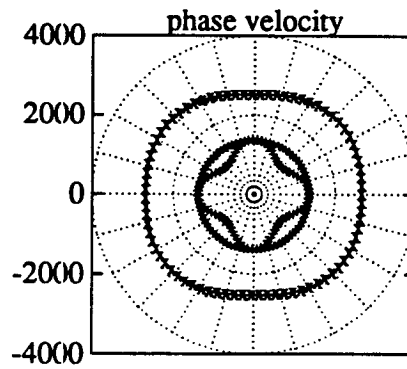
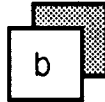
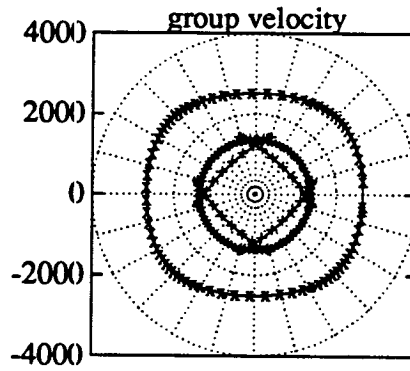
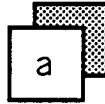


Figure 1.19: Elastic properties of the anisotropic material used for modeling : a) Group velocity, and b) Phase velocity.

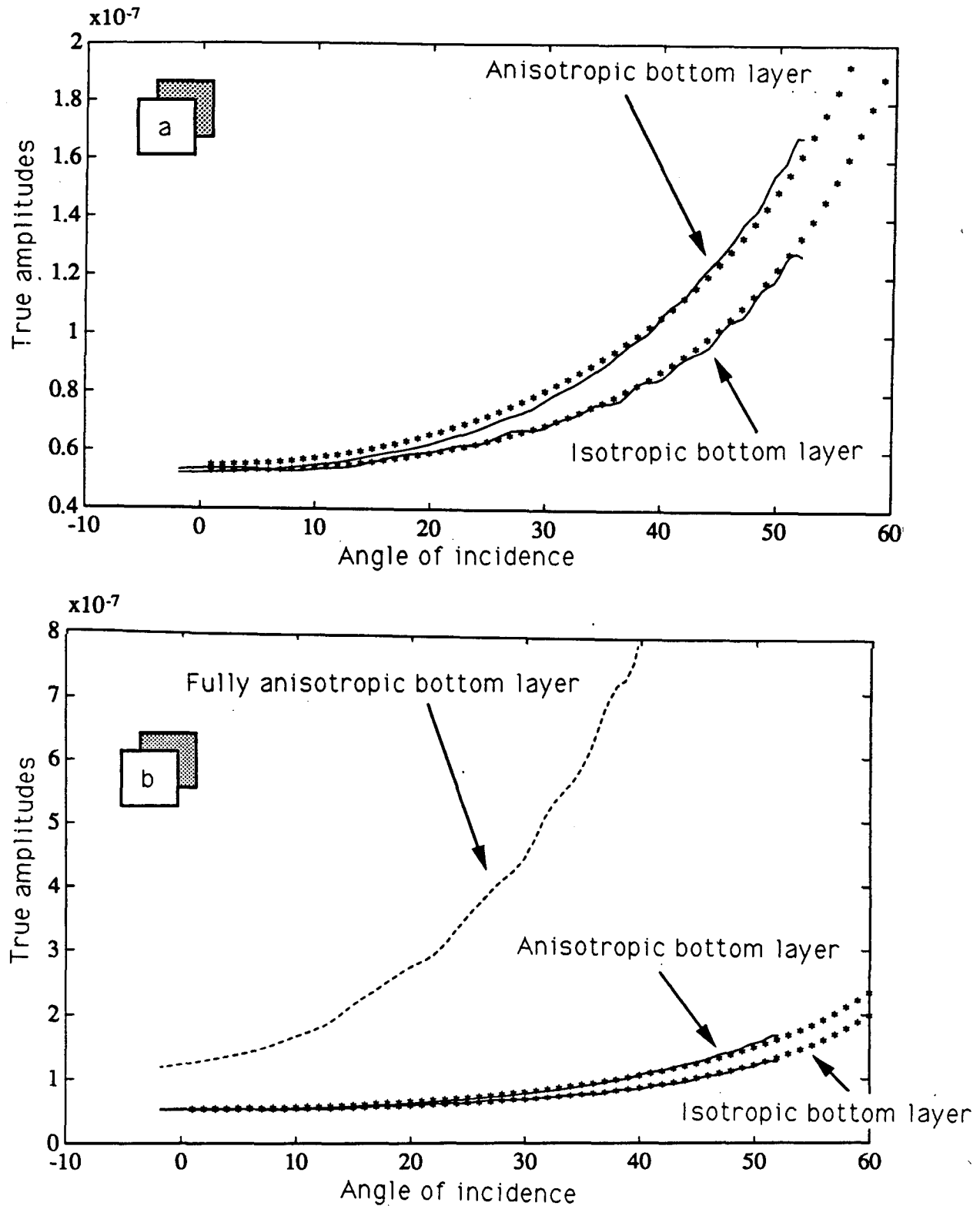


Figure 1.20: Effect of anisotropy on the reflection coefficient and on AVO measurements. Each curve displays a comparison between the numerical (-) and analytical (*) computation; a) where the reflecting (bottom) layer is isotropic or anisotropic, given an isotropic upper layer; b) where the bottom layer is viscoelastic anisotropic, given an isotropic upper layer (dashed line).

When considering a **fully anisotropic** bottom layer, with both elastic anisotropy and viscoelastic anisotropy, the reflection coefficient *increases more sharply* with offset than in the case of a viscoelastic isotropic bottom layer (Figure 1.20b) and more sharply than in the case of a Q-anisotropic bottom layer (figure 1.17b). This result may seem to contradict the previous result obtained, where a bottom layer with elastic-isotropic properties had more of an AVO increase than a bottom layer with viscoelastic-anisotropic properties (Figure 17b). However, it shows that in complex media, reflection coefficients introduce a **close coupling** between **elastic** and **viscoelastic** wave propagation phenomena, and that both phenomena should be incorporated together for rigorous seismic modeling, because their effects may cancel-out or reinforce each other - by *destructive* or *constructive* interference -, depending on the circumstances.

e.2) Effect of anisotropy on wave propagation

Let us choose a transversely isotropic **upper layer** with a $\delta = 0.1$. Figure 1.21 displays the reflected amplitudes after a geometrical spreading correction. The predicted results (+), and the actual numerical results (dashed line) differ, because of the wave propagation phenomena introduced by the intrinsic elastic anisotropy of the upper layer. The discrepancy is related to wave propagation phenomena introduced by the intrinsic elastic anisotropy of the **upper layer**.

Figure 1.21 was generated by using the receiver geometry described in Figure 1.13a and by monitoring the energy distribution of the down-going compressional wave front; it allows a comparison between an isotropic upper layer, and an anisotropic upper layer. For the parameters chosen, the anisotropic upper layer case displays less of an AVO increase than the isotropic upper layer case. In the isotropic case, the source radiates energy equally in all directions, and the amplitude decays along the wave front as time increases, because of geometrical spreading (Figure 1.22a). For the anisotropic upper layer case, the initial energy distribution along the wave front is not constant (Figure 1.22b). *Elastic anisotropy introduces a source radiation*

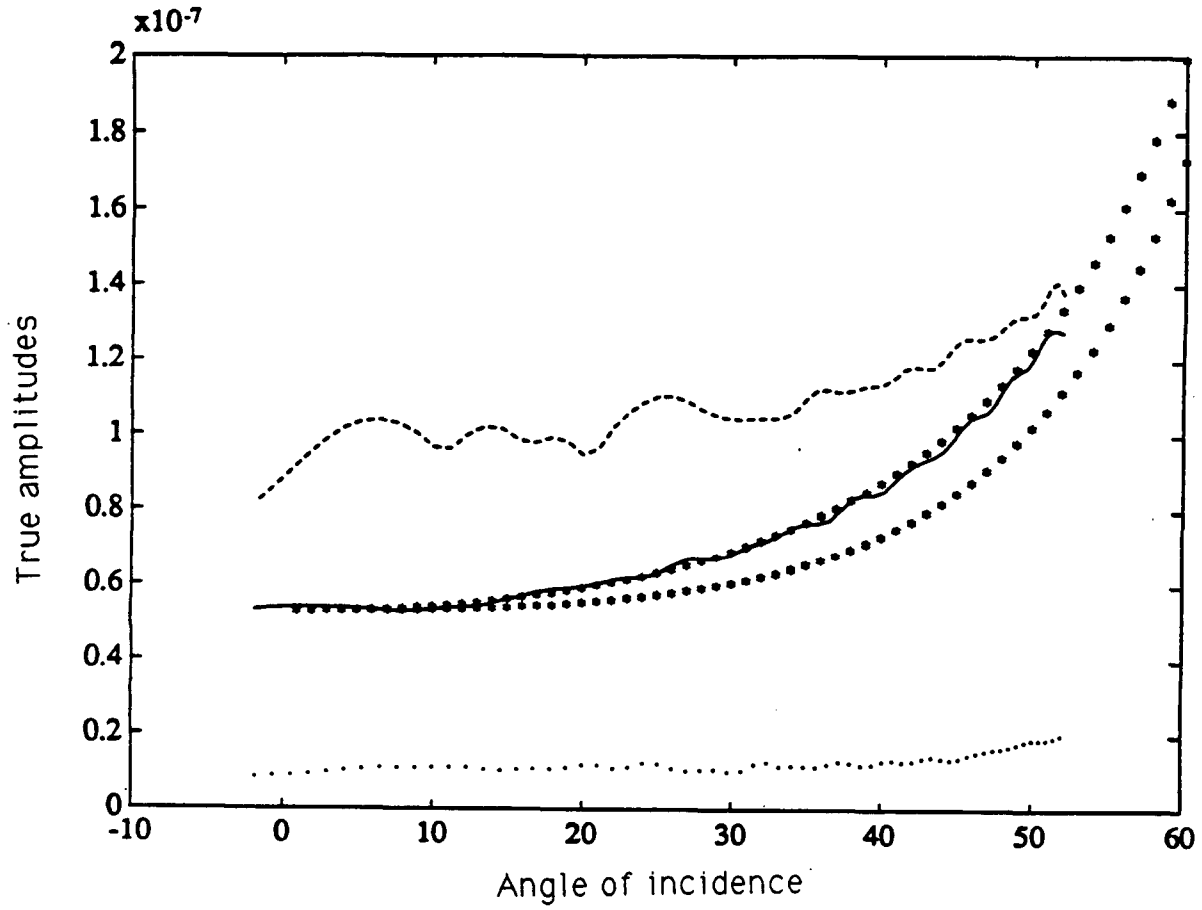


Figure 1.21: Effect of an anisotropic upper layer on the AVO measurement. The dashed line represents the modeling result for an anisotropic upper layer and the bottom curves (similar to figure 1.20) are included for comparison.

pattern that is not of equal amplitudes as a function of direction. The radiation pattern anisotropy explains the generation of shear waves by the buried pressure source (which, in an elastic isotropic earth, would be absent), the radiation pattern of the compressional waves, and the partition of energy between compressional and shear waves.

Also note that the energy distribution along the wavefront *shifts with time*. This is a particularly interesting result, due to the difference between group and phase velocities, which differentially focuses energy along the wavefront. With this in mind, it is clear that the apparent discrepancy between the numerical computation and the theoretical prediction (shown in Figure 1.21) is due to the **anisotropy of energy distribution along the wavefront**. This result can also be generalized to the case of attenuation anisotropy, where the upper layer would display Q anisotropy, whose effect would also be to differentially focus energy along the wavefront.

f) Results

The classical interpretation relating Amplitude Versus Offset (AVO) to Poisson's ratio and other petrophysical properties is based on the assumptions of elasticity and isotropy. In fact, the **direct** translation (with a minimum of modeling effort) of AVO trends into rock petrophysical properties such as Poisson's ratio can only proceed under the assumption that rocks are isotropic and elastic. This type of inversion is run routinely by contractors (Terra-Linda, Western-Atlas, Simon-Geolithic). However, as indicated by an increasing number of laboratory and field studies, the two assumptions of isotropy and elasticity are not always valid.

I extended the translation (or interpretation) of AVO trends to a layered medium with anisotropic and/or viscoelastic properties. When the earth is neither isotropic nor purely elastic, theory predicts that viscoelasticity and anisotropy lead to two types of AVO effects which can be large:

- 1) Reflection effects, which affect AVO trends at a given lithologic interface,

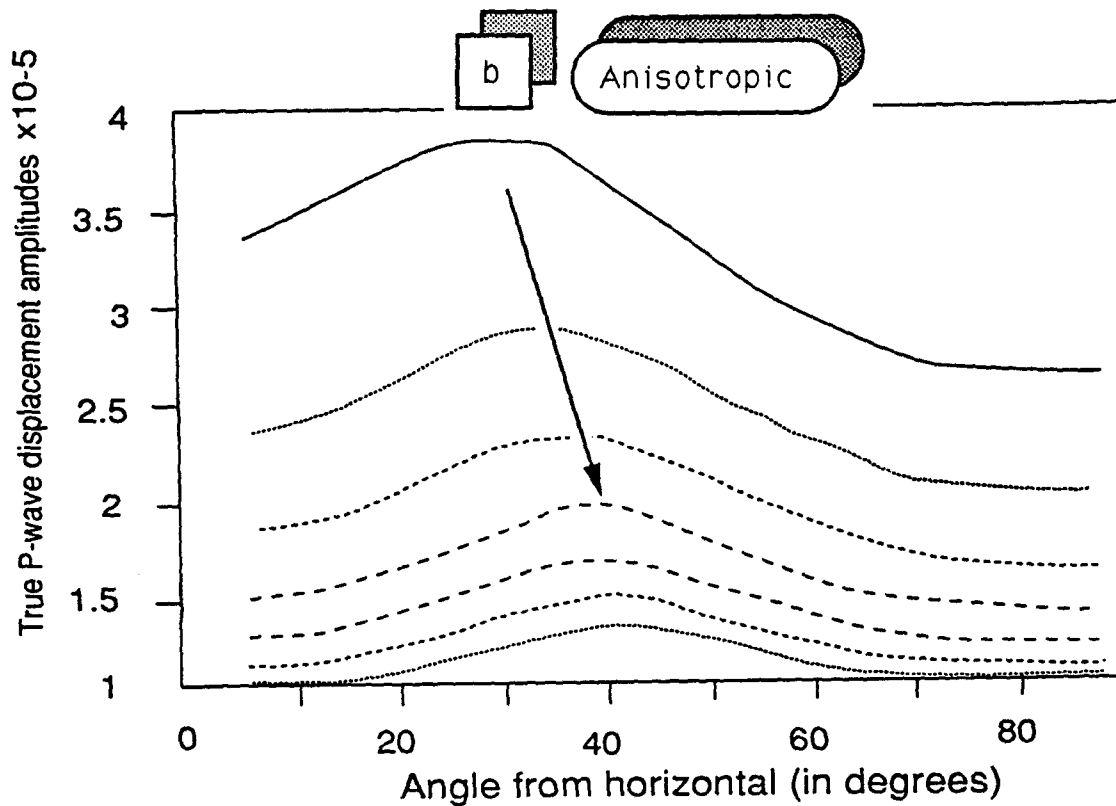
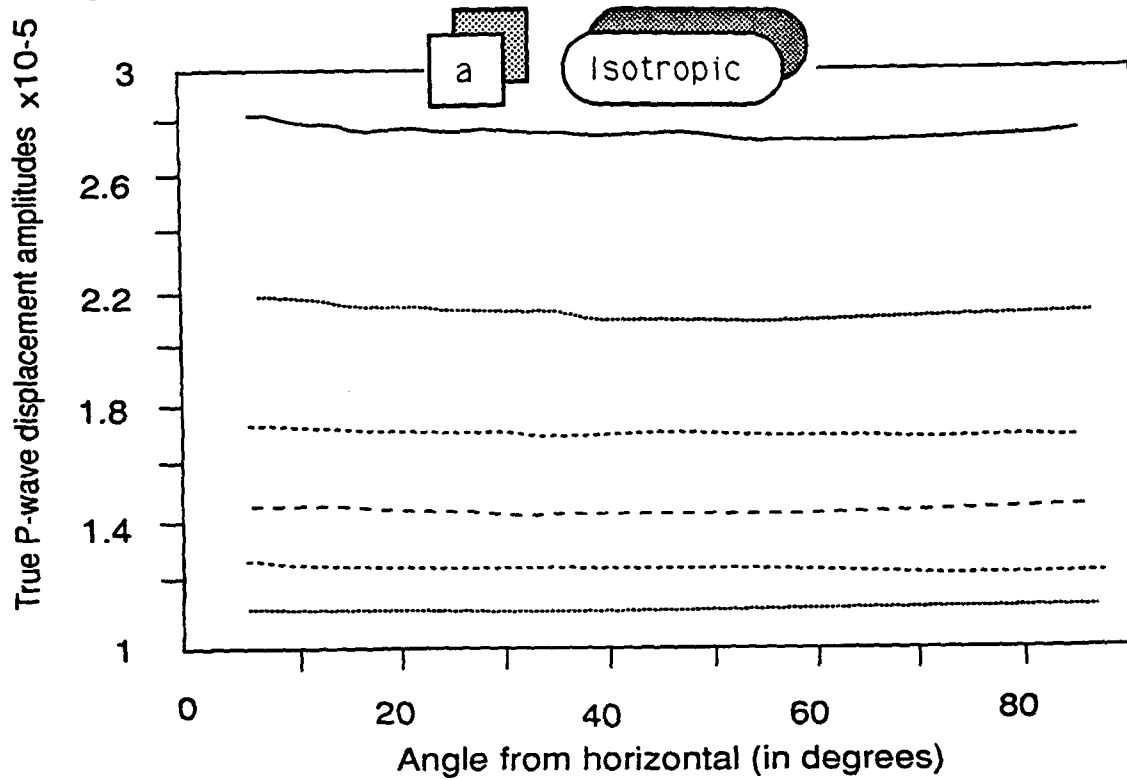


Figure 1.22: Energy distribution along the wavefront, using the receiver geometry in Figure 1.13a, in: a) an isotropic solid, and b) an anisotropic solid. Each of the curves corresponds to a separate wavefront, and the arrow indicates the direction of increasing times.

and

- 2) Propagation effects, which continuously alter the signal during propagation, because of energy focusing, and because of attenuation or dispersion.

* When viscoelasticity is taken into account, the following observations can be made:

- Contrasts in viscoelasticity do not appear to control the variations of reflection coefficients with incidence angle for small angles, but they certainly are a controlling factor of absolute amplitudes.
- For typical shallow reflector geometries, viscoelastic attenuation along the ray path can mask AVO increases.
- The effects of viscoelastic anisotropy are more subtle. Viscoelastic anisotropy can severely affect variations in reflection coefficients with angle of incidence, and is expected to yield a relative decrease in amplitude with offset, for a reflector displaying lower attenuation properties (or higher Q) in the horizontal direction than in the vertical direction. However, attenuation anisotropy can have very strong propagation effects, and can actually create a positive AVO anomaly for a reflection coefficient that would otherwise be constant with offset.

* On the other hand, anisotropy leads to:

- Changes in the characteristics of reflections, even for weak anisotropy (Thomsen, 1987, Banik, 1987), and
- Changes in the amplitude and phase of the signal, that occur during wave propagation.

Because anisotropy and anelasticity can lead to large changes in the phase of the wavelet and to preferential focusing of energy along the wavefront, and because the earth is neither purely elastic nor isotropic, I suggest to attempt to model these effects as accurately as possible in applications for detailed reservoir characterization.

g) Future work

Unfortunately, the results of the theoretical investigations on anisotropy and attenuation presented above were restricted to a level of simplicity which is not likely to be encountered in the field. In particular, I was not concerned with the interference of noise (be it random or systematic) and I did not account for complicated transmission effects, because the models included only one layer and one interface. Therefore, in part III of this thesis, more complex problems will be addressed with real data and multiple layers through the analysis of case studies.

I have shown that both viscoelasticity and anisotropy are key factors for the **quantitative interpretation of AVO trends**, because they contribute to the seismic energy partitioning at geological interfaces (the reflection coefficients), and because they continually induce propagation effects. Proper characterization of amplitude variations requires that the phenomena affecting the phase and amplitudes of the signal be modeled rigorously.

- In theory, attenuation and anisotropy make the amplitude determination of a seismic event somewhat dependent on wavelet phase changes which occur continually as the wavefront propagates. The good news is that changes in the phase of the signal occur continuously as the wavefront propagates, but can be **modeled in a deterministic manner**, by accounting for wave propagation in viscoelastic-anisotropic media.
- The bad news is that anisotropy and attenuation can be of the same order of magnitude as variations in reflection amplitudes with offset, and can make it

difficult to recover reflection coefficients along an interface, from *seismic data alone*. In practice, they create anisotropic radiation patterns and differentially focus the seismic energy distribution along the wavefront. In fact, it may not be possible to distinguish anisotropic effects from attenuation effects, from seismic data alone. **Integrated methods** ought to be sought as much as possible, in order to reduce the non-uniqueness in determining such parameters. One such method will be developed in detail in chapter 3.

All detailed reservoir characterizations based on modeling and interpretation of AVO trends, should attempt to account for anisotropy and viscoelastic attenuation; the interpreter should not only consider the reflecting target alone, but the full set of lithologies from the subsurface to the target, as well as the target itself. This is often an extremely difficult task, because of the difficulty in prescribing appropriate physical parameters, and requires the integration of multiple disciplines. However, whenever possible, this procedure should allow for a more robust extraction of lithology and fluid content.

IV)-SIMPLIFIED ZOEPPRITZ EQUATIONS FOR TRANSVERSELY ISOTROPIC MEDIA

The theory developed in the previous part has shown that the physical processes leading to AVO anomalies can be extremely complicated, and can sometime involve more than seven parameters per model layer (two velocities, three anisotropy parameters, and two Q values, for isotropic-Q models). From a practical viewpoint, it would be convenient to first examine the effects of some isolated parameters (such as changes in elastic velocities, densities, or transverse isotropy parameters) in a rapid forward modeling approach, and to iterate over different possibilities for reservoir models, before moving-on to the complicated full anisotropy cases (ie, elastic and anelastic anisotropy) presented above. Wave equation methods appear to be too slow, and it is difficult to use finite difference ray tracing (F.D.R.T.) for true amplitude calculations (Vidale, 1989, Van Trier, 1989). But analytical methods are applicable: in

fact, a generalization of the Zoeppritz equations to transversely isotropic media was presented by Daley and Hron (1977) and simplified by Thomsen for weak anisotropy (personal communication, to be published).

The exact formulas for reflection and transmission coefficients between two transversely isotropic media (Daley and Hron, 1977) are complicated, and as a consequence, are difficult to interpret in terms of the relative contributions of petrophysical parameters to the P-P reflected amplitudes.

However, for weak anisotropy, it can be shown that the equation for reflected P-P waves, reduces to (Thomsen, personal communication):

$$A_{RP} = \frac{1}{2} \left(\frac{\Delta\rho}{\rho} + \frac{\Delta V_P}{V_P} \right) + \frac{1}{2} \left(\frac{\Delta V_P}{V_P} + \delta_2 - \delta_1 \right) \tan^2(\theta) - \frac{2V_S^2}{V_P^2} \left(\frac{\Delta\rho}{\rho} + \frac{2\Delta V_S}{V_S} \right) \sin^2(\theta) - \frac{1}{2} (\delta_2 - \delta_1 - \varepsilon_2 + \varepsilon_1) \sin^2(\theta) \tan^2(\theta) \quad (11)$$

which reduces to Banik's expression for small angles (dropping higher order terms in θ and using the relationship $\Delta\delta = \Delta\varepsilon_P - 4\frac{\beta^2}{\alpha^2}\Delta\varepsilon_S$)

Thomsen's version of Daley and Hron's expressions for weak anisotropic reflections (Thomsen, to be published) can be readily applied as a first step; Thomsen's notation for transverse isotropy was reviewed in equations (10). The method is valid for weakly transverse isotropic media and should prove useful for quick iteration in forward modeling. In the case of transverse isotropy that is not weak, the parameter δ^* can be used instead of the parameter δ . The conversion between the two is given by (Thomsen, 1986):

$$\delta = \frac{1}{2} \left[\varepsilon + \frac{\delta^*}{\left(1 - \frac{V_S^2}{V_P^2}\right)} \right] = \frac{(C_{13} + C_{44})^2 - (C_{33} - C_{44})^2}{2C_{33}(C_{33} - C_{44})}$$

The following formulas for transmitted P-wave, reflected SV-waves, and transmitted SV-waves are included for completeness (after Thomsen, to be published):

$$\begin{aligned}
A_{TP} &= 1 - \frac{1}{2} \left(\frac{\Delta\rho}{\rho} + \frac{\Delta V_P}{V_P} \right) + \frac{1}{2} \left(\frac{\Delta V_P}{V_P} \right) \tan^2(\theta) + \frac{1}{2} (\delta_2 - \delta_1) \sin^2(\theta) \\
&\quad - (\delta_2 - \delta_1 - \varepsilon_2 + \varepsilon_1) \sin^4(\theta) + \frac{1}{2} (\varepsilon_2 - \varepsilon_1) \sin^2(\theta) \tan^2(\theta) \quad (12)
\end{aligned}$$

$$\begin{aligned}
A_{RS} &= -\frac{1}{2} \left(\frac{\Delta\rho}{\rho} + \frac{\Delta V_S}{V_S} \right) - \frac{1}{2} \left(\frac{\Delta V_S}{V_S} \right) \tan^2(\theta) + 2 \left(\frac{\Delta\rho}{\rho} + \frac{2\Delta V_S}{V_S} \right) \sin^2(\theta) \\
&\quad - \frac{1}{2} \frac{V_P^2}{V_S^2} (\delta_2 - \delta_1 - \varepsilon_2 + \varepsilon_1) \sin^2(\theta) \quad (13)
\end{aligned}$$

$$\begin{aligned}
A_{TS} &= 1 - \frac{1}{2} \left(\frac{\Delta\rho}{\rho} + \frac{\Delta V_S}{V_S} \right) + \frac{1}{2} \left(\frac{\Delta V_S}{V_S} \right) \tan^2(\theta) \\
&\quad - \frac{1}{2} \frac{V_P^2}{V_S^2} (\delta_2 - \delta_1 - \varepsilon_2 + \varepsilon_1) \sin^2(\theta) (1 - 2\sin^2(\theta)) \quad (14)
\end{aligned}$$

Expressing equations (11) through (14) in terms of contrasts in δ and ε by using

$$\tan^2(\theta) \sin^2(\theta) = \tan^2(\theta) - \sin^2(\theta)$$

and using

$$\Delta\delta = \delta_2 - \delta_1; \Delta\varepsilon = \varepsilon_2 - \varepsilon_1,$$

the equations take the form:

$$\begin{aligned}
A_{RP} &= \frac{1}{2} \left(\frac{\Delta\rho}{\rho} + \frac{\Delta V_P}{V_P} \right) + \left\{ \frac{1}{2} \frac{\Delta V_P}{V_P} + \frac{1}{2} \Delta\varepsilon \right\} \tan^2(\theta) \\
&\quad - \left\{ \frac{2V_S^2}{V_P^2} \left(\frac{\Delta\rho}{\rho} + \frac{2\Delta V_S}{V_S} \right) - \frac{1}{2} (\Delta\delta - \Delta\varepsilon) \right\} \sin^2(\theta) \quad (15)
\end{aligned}$$

The above formulation is not any simpler than that of Thomsen, **but it readily allows for evaluating the relative influence of contrasts in δ and ϵ** on the reflection coefficients. For completeness, the reflection coefficient for S waves (A_{RS}) and the transmission coefficients (A_{TP} and A_{TS}) become:

$$A_{TP} = 1 - \frac{1}{2} \left(\frac{\Delta\rho}{\rho} + \frac{\Delta V_P}{V_P} \right) + \left\{ \frac{1}{2} \left(\frac{\Delta V_P}{V_P} \right) + \frac{1}{2} (\Delta\epsilon) \right\} \tan^2(\theta) + \left\{ \frac{1}{2} (\Delta\delta - \Delta\epsilon) \right\} \sin^2(\theta) - (\Delta\delta - \Delta\epsilon) \sin^4(\theta) \quad (16)$$

$$A_{RS} = -\frac{1}{2} \left(\frac{\Delta\rho}{\rho} + \frac{\Delta V_S}{V_S} \right) - \frac{1}{2} \left(\frac{\Delta V_S}{V_S} \right) \tan^2(\theta) + \left\{ 2 \left(\frac{\Delta\rho}{\rho} + \frac{2\Delta V_S}{V_S} \right) - \frac{1}{2} \frac{V_P^2}{V_S^2} (\Delta\delta - \Delta\epsilon) \right\} \sin^2(\theta) \quad (17)$$

$$A_{TS} = 1 - \frac{1}{2} \left(\frac{\Delta\rho}{\rho} + \frac{\Delta V_S}{V_S} \right) + \frac{1}{2} \left(\frac{\Delta V_S}{V_S} \right) \tan^2(\theta) - \frac{1}{2} \frac{V_P^2}{V_S^2} (\Delta\delta - \Delta\epsilon) \sin^2(\theta) + \frac{V_P^2}{V_S^2} (\Delta\delta - \Delta\epsilon) \sin^4(\theta) \quad (18)$$

Of course, for accurate forward modeling applications using ray tracing, the exact expressions of Daley and Hron (1977) should be used. Thomsen's approximations, however, provide a level of physical understanding of the relative contributions of the anisotropic parameters, that is difficult to achieve from Daley and Hron. For example, for small angles, it appears from the equations that A_{RP} is primarily a function of **contrasts in V_P , V_S , and δ** , (since the terms in $\sin^2(\theta)$ and $\tan^2(\theta)$ are of the same order, and cancel-out the contributions of contrasts in ϵ). For slightly larger angles, the equation for reflected P-waves (developed from a Taylor series expansion) "reduces" to:

$$A_{RP} = \frac{1}{2} \left(\frac{\Delta\rho}{\rho} + \frac{\Delta V_P}{V_P} \right) + \theta^2 \left\{ \left(\frac{1}{2} \frac{\Delta V_P}{V_P} - 2 \frac{V_S^2}{V_P^2} \left(\frac{\Delta\rho}{\rho} + 2 \frac{\Delta V_S}{V_S} \right) \right) + \frac{1}{2} (\Delta\delta) \right\}$$

$$\begin{aligned}
& +\theta^4 \left\{ \frac{\Delta V_P}{3V_P} + \frac{2V_S^2}{3V_P^2} \left(\frac{\Delta\rho}{\rho} + 2\frac{\Delta V_S}{V_S} \right) + \left(\frac{1}{2}\Delta\epsilon - \frac{1}{6}\Delta\delta \right) \right\} \\
& +\theta^6 \left\{ \frac{17}{90} \frac{\Delta V_P}{V_P} - \frac{4}{45} \frac{V_S^2}{V_P^2} \left(\frac{\Delta\rho}{\rho} + 2\frac{\Delta V_S}{V_S} \right) + \left(\frac{1}{45}\Delta\delta + \frac{1}{6}\Delta\epsilon \right) \right\} + \dots \quad (19)
\end{aligned}$$

which also involves a term with contrasts in ϵ .

The methods presented or summarized in this section are based on ray tracing, and the algorithms can be executed quickly on an interactive workstation. Moreover, they can be seen as a generalization of the Zoeppritz equations to transversely isotropic media, because they are based on Snell's law, continuity of displacement, and continuity of stress across interfaces. They should prove useful to investigate AVO effects quickly through iterations in forward modeling, because they provide a quick way of running sensitivity analyses on anisotropy parameters (such as δ , ϵ , and γ) and their effects on AVO responses. However, the methods are based on ray tracing and as such, constitute high frequency approximations, which may not be accurate enough for **thin layer**, detailed models. They are ideal for testing the validity of preliminary reservoir models, and should be used **in conjunction with full waveform** (wave equation modeling) techniques for the *refinement* of these *reservoir models*. It should be noted that finite difference methods can also be a problem in the presence of fine layers, because of limitations in grid size and because of numerical artifacts. In those cases, reflectivity methods and integral methods would be preferred.

V)-CONCLUSIONS

In general, a signal propagating in a complex medium undergoes changes in its phase and spectral content; these changes are the product of interactions between a passing wave and the rock. Fortunately, seismic anomalies are usually robust enough that the modeling of seismic waveforms requires only the knowledge of "average properties" and of **contrasts** in velocities, densities, relative anisotropy, and Q at interfaces.

In my opinion, the **newly unvailed complexities in AVO modeling and interpretation** justify an in-depth research effort to help understand and delineate gas-related seismic anomalies. This endeavor requires a good balance between the implementation of conceptual modeling procedures on computers and the thorough analysis and re-processing (Yu, 1985) of a selected set of "key" data sets. In the following chapters (chapters 2 and 3), I establish a methodology and a constructive feedback, by which data-specific problems can be addressed and solved (chapters 4 and 5). The ultimate goal is to integrate the modeling of seismic amplitude anomalies within the geological framework of basin deposition and evolution for each dataset.

The need for a method of Integration and for a method of Estimating Petrophysical parameters:

I have shown that *many different algorithms exist* for simulating wave propagation in complex media. However, what is *lacking* is a *methodology to estimate crucial rock parameters* from a variety of rock properties, so that "exact" parameters can be prescribed for these modeling/inversion algorithms. It should now be clear to the reader that we, as petroleum geoscientists, **need a systematic and quantitative method** to derive some of the key parameters that may affect AVO responses - and in particular, anisotropy and attenuation -. We also need to derive a systematic procedure in establishing parameter variations, so that we can evaluate their effects on AVO responses (through sensitivity analyses). In chapter 2, I will show how "missing" rock properties can be estimated using a priori knowledge or a priori concepts and petrophysics, and in chapter 3, I will present a methodology for integration.

REFERENCES

- Aki, K., and Richards, P., G., 1980, Quantitative seismology: W. H. Freeman and Co., 153
- Backus, M., and Chen, R., 1975, Flat spot exploration: *Geophysical Prospecting*, **23**, 533,577.
- Banik, N., Lerche, I., and Shuey, R., 1989, Offset Dependent Amplitudes: Effects of Wavefront and Reflector Curvature in Homogeneous and Layered Media: *Pageoph*, vol. **130**, no. 1, 99-125.
- Banik, N., C., 1987, An effective anisotropy parameter in transversely isotropic media: *Geophysics*, **52**, 1654,1664.
- Bortfeld, R., 1961, Approximation to the reflection and transmission coefficients of plane longitudinal and transverse waves: *Geophysical Prospecting*, **9**, 485,502.
- Bourbie, T., 1982, Effect of attenuation on seismic reflections: *SRB* **14** .
- Carcione, J. M., 1987, Wave propagation in real media, Ph. D. thesis, Senate of Tel Aviv University.
- Carcione, J. M., Kosloff, D., and Kosloff, R., 1988, Viscoacoustic wave propagation simulation in the earth: *Geophysics*, **53**, 769-777.
- Crampin S., 1984, Effective Anisotropic Elastic constants for Wave propagation through cracked solids: *Geophys. J. R. Astr. Soc.* , **76**, 135,145.
- Daley, P., F., and Hron, F., 1977 : Reflection and transmission coefficients for transversely isotropic media: *Bull., Seis. Soc. Am.*, **67**, 661,675.
- Domenico, S. N., 1976, Effect of brine-gas mixture on velocity in an unconsolidated reservoir: *Geophysics*, **41**, 882,894.
- Domenico, S. N., 1977, Elastic properties of unconsolidated porous sand reservoirs: *Geophysics*, **42**, 1339,1368.
- Fung, Y. C., 1965, Foundations of solid mechanics: Prentice Hall, New York.
- Gassmann, F., 1951: Elasticity of porous media: *Vier. der Natur. Gesellschaft in Zurich*, Heft I.
- Gelfand, V., Ng, P., Nguyen, H., Larner, K., 1988, Seismic lithologic modeling of Amplitude-Versus-Offset data: paper presented at the ASEG/SEG meeting, Adelaide, 274,276.
- Gregory, A. R., 1976, Fluid saturation effects on dynamic elastic properties of sedimentary rocks: *Geophysics*, **41**, 895,921.
- Hosten, B., Deschamps, M., and Tittman, B.R., 1987: Inhomogeneous waves propagating in a lossy anisotropic solid. Application to the characterization of viscoelastic composite materials: *J. Acoust. Soc. Am.*, **82**, 1763,1770.

- Hudson, J.A., 1981, Wave propagation and attenuation of elastic waves in material containing cracks: *Geophys. J. R. Astr. Soc.*, **64**, 133-150.
- Jones, T., 1986, Pore fluids and frequency-dependent wave propagation in rocks: *Geophysics*, **51**, 1939,1953.
- Kjartanson, E., 1979, Constant Q-Wave Propagation and Attenuation: *J.G.R.*, **84**, 4737,4748.
- Koefoed, O, 1955, On the effect of Poisson's ratio of rock strata on the reflection coefficients of plane waves: *Geophysical Prospecting*, **3**, 381,387.
- Kosloff, D. and Baysal, E., 1982, Forward modeling by a Fourier method: *Geophysics*, **47**, 1402,1412.
- Liu, H. P., Anderson D.L., Kanamori H., 1976, Velocity dispersion due to anelasticity ; Implication for seismology and mantle composition: *Geophys. J. R. Astr. Soc.* , **47**, 41-58.
- Meissner, R., Stumpf, H., Theilen, F., 1985, Shear wave studies in shallow sediments, in: *Seismic shear waves, part B: Applications*, edited by G. Dohr, in *Handbook of Geophysical Exploration, section I: Seismic Exploration, Volume 15B*, Geophysical Press Limited, 224, 255.
- Ostrander, W., J., 1985, Plane-wave reflection coefficients for gas sands at non-normal angles of incidence: Paper presented at the 52nd Intern. Mtg. and Expos., SEG in Dallas.
- Ostrander, W., J., 1984, Plane-wave reflection coefficients for gas sands at nonnormal angles of incidence : *Geophysics*, **49**, 1637,1648.
- Ostrander, W., J., 1985, *Reflection Seismology: Acquisition and Processing*: Stanford University course notes
- Samec, P., and Blangy, J.P., 1992, Viscoelastic attenuation, Anisotropy, and AVO: *Geophysics*, **57**, 441, 450.
- Samec, P., 1991, Ph. D. Thesis, Stanford University, S.R.B., vol. **42**.
- Samec, P., Blangy, J.P., and Nur, A., 1990, Effects of Viscoelasticity and Anisotropy on AVO Interpretation: Paper presented at the annual International SEG meeting in San Francisco.
- Sengupta, M., 1989, Sensitivity analysis of Amplitude Versus Offset (AVO) method: Paper presented at the SEG convention.
- Shuey, R. T., 1985, A simplification of the Zoeppritz equations: *Geophysics*, **50**, 609,614.
- Tal-Ezer H., Carcione, J. M., Kosloff, D.,1990, An accurate and efficient scheme for wave propagation in linear viscoelastic media: *Geophysics*, **55**, No. 10, 1366-1379.
- Tal-Ezer H., Kosloff, D., and Koren, Z., 1987, An accurate scheme for seismic forward modeling: *Geophys. Prosp.*, **35**, 479-490.

- Tal-Ezer H., 1986, Spectral methods in time for hyperbolic equations: SIAM J. Numer. Anal., **23**, 11,26.
- Tatham, R., and Stoffa, P., 1976, Vp/Vs - A potential hydrocarbon indicator: Geophysics, **41**, 837,849.
- Thomsen, L., to be published, Weak anisotropic reflections: prepared for inclusion in Offset Dependent Reflectivity, edited by M. Backus.
- Thomsen, L., 1986, Weak elastic anisotropy : Geophysics, **51**, 1954,1966.
- Van Trier J., 1989, Finite-difference computation of travel times: Stanford Exploration project report, **57**.
- Vidale J., 1989, Finite-difference computation of travel times: Bulletin of the Seismological Society of America, **78**, 2062-2076.
- Waters, K., 1987, Reflection Seismology: A tool for Energy resource Exploration: John Wiley and sons, 538 pages.
- Winkler, K., and Nur, A., 1986, Pore fluids and seismic attenuation in rocks: Geophysical Research letters, v. 6, 1-4.
- Wright, J., 1987, The effects of transverse isotropy on reflection amplitude versus offset: Geophysics, **52**, 564,567.
- Yu, G., 1985, Offset-amplitude variation and controlled-amplitude processing: Geophysics, **52**, 2697,2708.

CHAPTER 2

DETERMINISTIC MODELING FOR AVO STUDIES:
THE CALCULATION OF "MISSING" ROCK PROPERTIES

"Is AVO the seismic signature of lithology?",

Fred Hilterman, 1990

ABSTRACT

It is well accepted that velocities in sediments depend on the intrinsic properties of their mineral constituents, on the in-situ state of the rocks, and on fluid content. The quantitative extraction of these properties from seismic must be model based. Therefore, one necessary step sought in this chapter is to design a deterministic modeling scheme in a forward sense, whereby a suite of properties (such as mineralogical content, porosity, fluid content, effective pressure, clay content, state of consolidation, ...) can be used quantitatively to arrive at the elastic velocities of the sediments under investigation. Information from non-biot velocity dispersion is also used to calculate intrinsic attenuation. In chapter 5, these methods will be used in conjunction with those of chapter 3, and applied to obtain the properties of reservoir sands from calibrated seismic data.

The objective sought here is to design systematic parameterization procedures that allow for a robust extraction of lithology and fluid content from petrophysical properties at the microscale. The approach involves the use of a rock physics database for *calibration* of log and core data, and the development of petrophysical modeling techniques for the *determination of "missing" rock properties*. My efforts are especially centered along two main directions: determining *shear velocities* on a depth by depth basis and obtaining average *attenuation values* for dominant lithologic layers.

I)-INTRODUCTION

The relevance of petrophysical properties to model-based interpretation of AVO trends is increasingly being recognized throughout the industry. However, there is to my knowledge no systematic modeling procedure based on sound petrophysical principles for detailed reservoir characterizations from AVO trends. This observation may have led geophysicists in the past to "over sell" the technique of pre-stack analysis, and to expose it to unreasonable expectations, because AVO can be very sensitive to a variety of factors. The work of chapter 1 has shown that both inelastic attenuation and anisotropy can significantly affect the behavior of reflection coefficients with offset; however, these two properties are extremely difficult, if not impossible, to obtain from seismic measurements alone. It is therefore necessary to use "outside information" such as logs and core measurements not only to constrain petrophysical parameters for inversion, but also as a calibration tool for a better definition of petrophysical properties from seismic data. One possible multi-disciplinary and integrated approach to the problem is presented in chapter 3. Crucial petrophysical properties which may not be *directly* obtainable from surface seismic data alone include permeability, anisotropy and anelasticity among others; permeability is the most important from a reservoir production perspective.

The modeling work of chapter 1 and recent advances in computer technology have demonstrated that it is rapidly becoming feasible to account for "all" aspects of wave propagation on an approximate basis. However, what is lacking is a systematic petrophysical interface that will serve as the tie between the actual rock properties and the seismic derived properties (figure 2.1) and therefore establish a bridge between seismic and lithology, or geophysics and geology; in that sense, rock physics should make it possible to view "AVO as the signature of lithology". In what follows, I will attempt to show the potential usefulness of petrophysical modeling in seismic modeling, and the importance of rock physics in understanding seismic properties: rock physics emerges as the necessary science to build alternative deterministic

models to be used for **sensitivity** analyses in AVO studies.

In this chapter, I present an integrated, systematic, and quantitative method for parameterization of rock properties **at the microscale**, based on sound petrophysical principles. Additional problems associated with *upscaling* to seismic wavelengths and transferring the properties *to the macroscale* will be addressed in chapter 3.

II)- RELEVANCE OF PETROPHYSICS TO AVO MODELING

1) Emphasis placed on integrated interpretation

Examples of the necessity for integration of methods for accurate reservoir characterization abound in the literature (Hoopes and Aber, 1989, Inouye and Williams, 1988, Robertson, 1989, Brown, 1986, among others). Traditional approaches emphasize that the benefits of integration are a better calibration of the seismic and as a result, a better final reservoir description. However, in this work, I integrate several methods not only to enable a better calibration of the seismic, but also to better understand the physics of wave propagation and the effects of petrophysical properties on the signature of the wavefield.

The integration step is an important one, because *it reduces the problem of non-uniqueness in lithological inversion*. As an example, and based on Marions' (1990) work on modeling of shaley sands, it is apparent that compressional velocity is a double-valued function of clay content (figure 2.2, bottom curve). With additional information coming from a thorough analysis of the depositional and diagenetic histories of a particular reservoir (this is called "a-priori information" by people working in seismic inversion), it may be possible to rule-out one of the two clay values corresponding to the same compressional velocity, and eliminate the non-unicity problem. The previous approach is a good example of the importance of integrated methods in seismic exploration. Hence, integration or cross-disciplinary interpretation can serve to better understand the physics of rocks, which is necessary to infer rock properties

and lithology.

2) Rock physics

Rock physics plays a central role in AVO modeling, because it can serve as the basis for integration through deterministic modeling and calibration of rock properties on a depth by depth basis at a well. The manner in which seismic amplitudes are affected by lithology, density, attenuation, frequency dispersion, environmental or in-situ conditions, fluids, and anisotropy can then be addressed systematically by sensitivity analyses.

a) Traditional rock physics

Velocities

Recent studies by Tosaya (1982) and Han et al (1986) have shown that the ultra-sonic compressional, V_p and shear, V_s velocities of shaley sands depend on clay content and porosity. From a collection of 80 different saturated sandstone samples from the Gulf coast, (with clay content ranging from 0 to 50 percent, and porosities comprised between 2 and 30 percent) they established the following statistical relationships between velocity, porosity (ϕ) and clay content (C):

$$V_p(Km/s) = 5.59 - 6.93\phi - 2.18C$$

and

$$V_s(Km/s) = 3.52 - 4.91\phi - 1.89C$$

and the following relationships for clean sands:

$$V_p(Km/s) = 6.08 - 8.06\phi$$

and

$$V_s(Km/s) = 4.06 - 6.28\phi$$

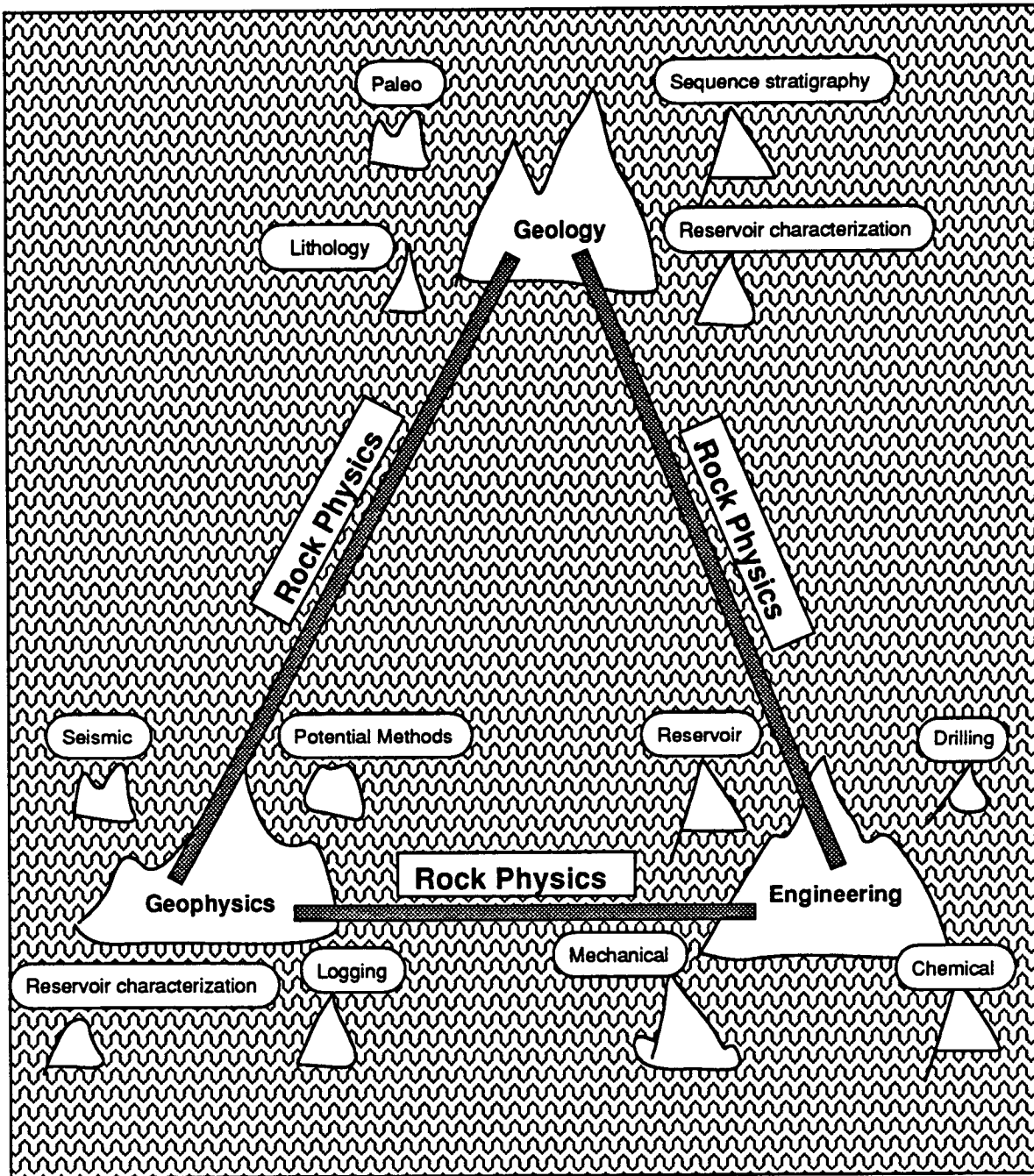


Figure 2.1: Concept: Rock physics can be used as a bridge between different disciplines; the disciplines can be seen as islands or archipelagoes - or as mountains for Norwegians! - ; each island - or mountain - has an "expert" standing on top of it. A bridge between seismic and lithology can be established; rock physics is one of the emerging sciences that should make it possible to view "AVO as the signature of lithology".

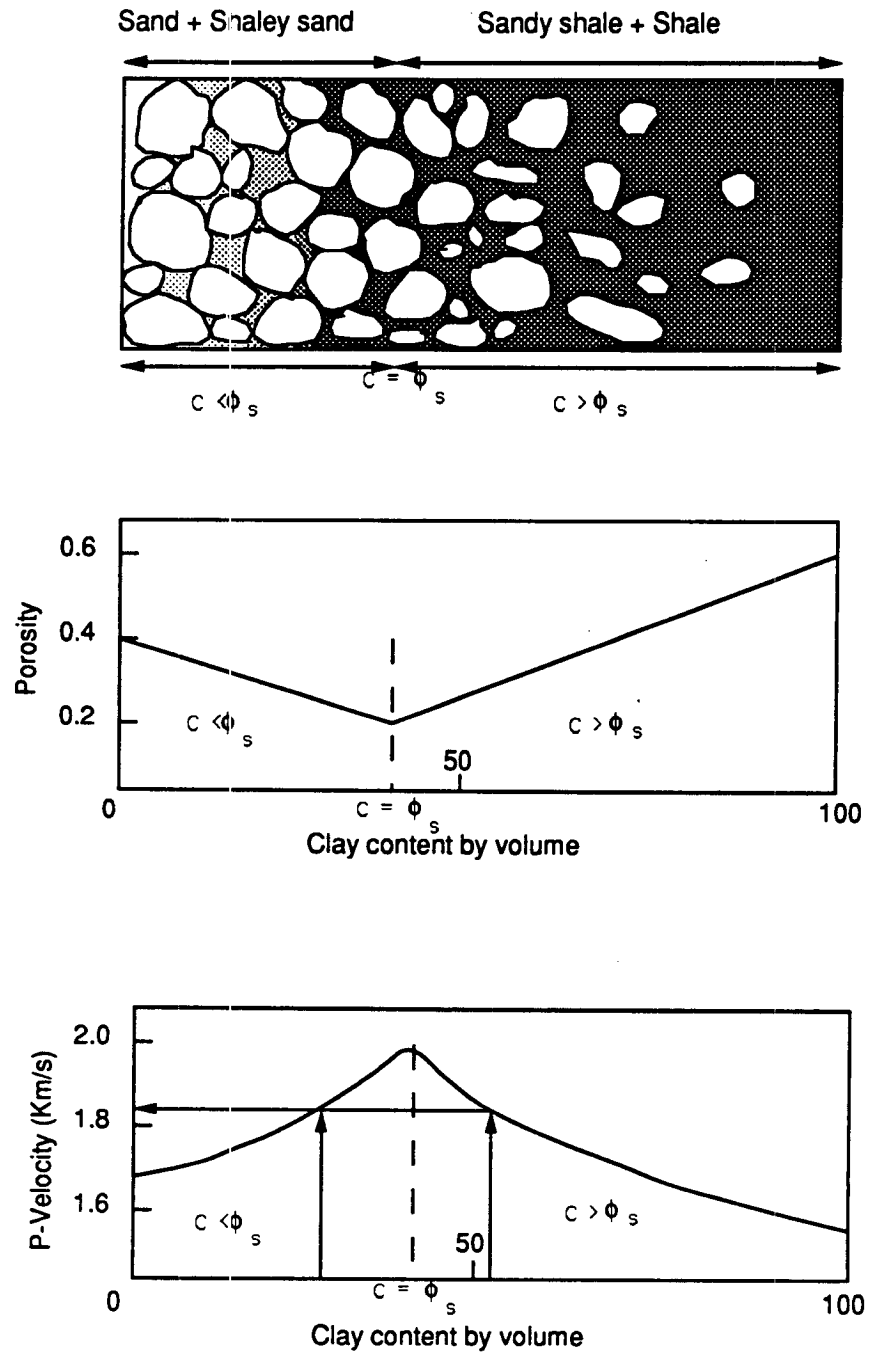


Figure 2.2: The topological model adopted by Marion (1990) for shaley sands shows that compressional velocities can be a double-valued function of clay content. Additional information or constraints on clay content (derived from logs or from a geologically plausible model) would allow for a unique lithological inversion (figure modified after Marion, 1990).

These relationships were determined empirically from least squares linear fits for confining pressures of 40 MPa and pore pressures of 1.0 MPa, and similar linear relationships - but with different regression coefficients - can be developed for different sets of in-situ conditions. Eberhard-Phillips et al. (1989) generalized the regressions to all pressures, by adding an effective pressure term.

Some of the rock parameters, such as porosity and clay content for example, can be interdependent. This means that the issue of clay location with respect to pore space is an important factor affecting velocities. For example, in shaley sandstone lithologies, it is convenient to assume that the primary sand porosity (or ϕ_s) is due solely to the space between the sand grains that are in contact; the porosity is then filled in part by clay particles, with volumetric concentration, c , so that the two properties porosity and clay content can no longer be considered as independent variables. - Clays that form a rim around sand grains are an exception, and can be conveniently modeled with a Hashin-Shtrikman bound -. Marion (1990) used this approach to model the effects of diagenetic clays on compressional velocities in shaley sands, by considering a microgeometrical model of clay *location* within the pore space and a bimodal grain size distribution. As shown in figure 2.2, sands and shaley sands (for $c > \phi_s$) can be modeled with a framework of sand grains and dispersed clay which simply fills the pore space. On the other hand, shales and sandy shales can be modeled as a suspension of sand grains floating in a shaley matrix (figure 2.2, for $c \leq \phi_s$). Using the following notation, c =clay content, ϕ_s =porosity of sand (sometimes also taken as the critical porosity, or ϕ_c), ϕ_{sh} =porosity of shale, K =bulk modulus, μ =shear modulus, ρ =density, and the following subscripts, w =water, fr =frame, fl =fluid, q =quartz and c =clay, for the effective mineral aggregate constituting the sand grains, one can obtain:

(a-1) for sands and shaley sands ($c \leq \phi_s$), the following equations hold:

$$\phi = \phi_s - c(1 - \phi_{sh})$$

$$\rho = \rho_q (1 - \phi_s) + c\rho_c (1 - \phi_{sh}) + \rho_w (\phi_s - c(1 - \phi_{sh}))$$

$$\frac{K}{K_q - K} = \frac{K_{fr}}{K_q - K_{fr}} + \frac{K_{fl}}{\phi_s (K_q - K_{fl})}; \text{ where}$$

$$\frac{1}{K_{fl}} = \frac{1 - c}{K_w} + \frac{c}{K_c}$$

$$\mu = \mu_{fr}$$

the clay is treated as a component of the pore space and stiffens the pore filling material, whereas the sand grains, which are taken as quartz and feldspar here, are load bearing.

(a-2) for **sandy shales and shales** ($c > \phi_s$), the sand grains can be modeled as suspensions within a clay matrix. This yields the well known isostress bound (Reuss, 1929) for suspensions:

$$\phi = c\phi_{sh}$$

$$\rho = \rho_q (1 - c) + c\rho_c (1 - \phi_{sh}) + c\phi_{sh}\rho_w$$

$$\frac{1}{K} = \frac{c}{K_{sh}} + \frac{1 - c}{K_q}$$

$$\frac{1}{\mu} = \frac{c}{\mu_{sh}} + \frac{1 - c}{\mu_q}$$

The concepts of a-1 and a-2 are illustrated in schematic form in figure 2.2, and work well for compressional waves (Marion, 1990). However, the model does not fit shear data well and, contrary to Marion's conclusions (1990, p. 51), the influence of the pore-filling material on the shear modulus cannot be neglected. To investigate this in more detail, I re-examined Hans' measurements on Gulf sandstones. Figure 2.3

displays the measured shear wave velocities as a function of clay content for several effective pressures. It is clear that clay location not only affects compressional wave velocities (as in Marion, 1990), but also shear wave velocities. The first part of the curves can be explained with the concept of stiffening of the shear frame modulus as clay gradually fills the pore space of the sand; however, the second part of the curve is expected to tend toward zero or a low value, since pure hydrated clays have very low shear moduli. Contrary to the case for compressional velocities, the isostress model - as used by Marion (1990) - cannot be used to model this part of the curve. It is also interesting to note that two peaks occur rather than one, as seen for P-waves; one occurs at a clay content of approximately 25-30 % and the other, more subtle, at approximately 40-45 %. The double peak effect observed may reflect more the dependency of μ_{fr} on porosity than on the pore filling mixture. The subject of shear velocities will be addressed in depth in section III.

Other properties

Renewed interest in the effects of pressure and temperature stem from the need to study fractured tight reservoirs and tar sands in association with thermal E.O.R. (Jones and Nur, 1983, Wang, 1988). Christensen and Wang (1985) found that compressional wave velocities increase and shear velocities decrease with increasing pore pressure, at constant effective pressure, in a rock containing 10% clay. Additional efforts need to be concentrated on the incorporation and modeling of the following environmental conditions: temperature, stress, fluid invasion, and effective pressure P_e . The good news is that in most cases, it is possible to model these effects, either deterministically or empirically, through the use of relationships derived from a database.

Fluid and saturation effects are the most interesting from an E&P point of view. Biot theory suggests that a change of compressional velocities of the order of several percent arises when partially saturating a low velocity water sand with gas. However, the effect of gas on shear waves is solely reflected in the density term, and leads

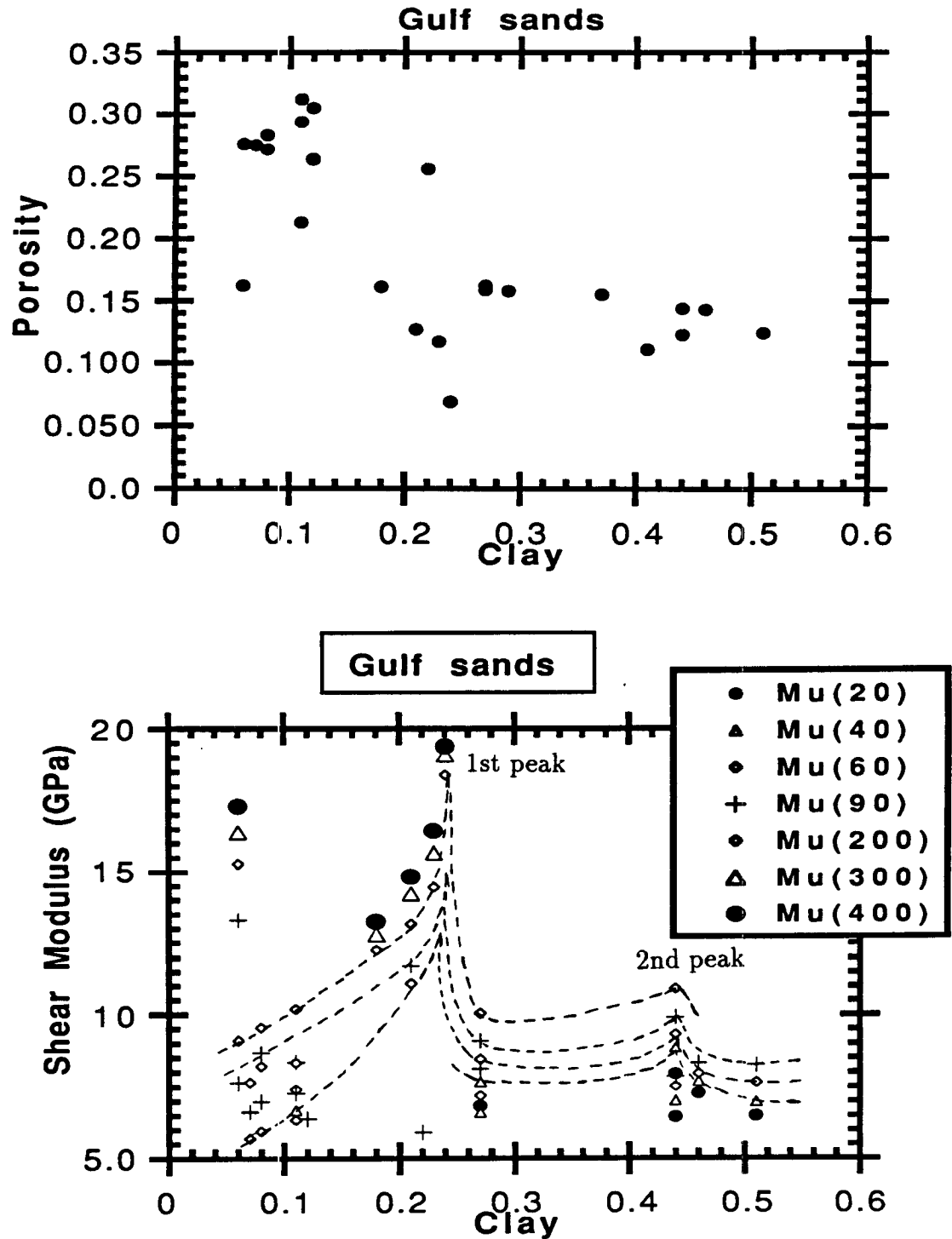


Figure 2.3: Example of the effects of clay location on shear wave velocities; the shear modulus is plotted at seven different effective pressures expressed in MPa. The data is from Han (1986). Much as for the case of compressional waves, shear waves (or shear moduli) exhibit a peak at a clay content of approximately 25%. A second peak is not as well defined, but nevertheless present at approximately 45%. It is absent on compressional wave data.

to the changes in Poisson's ratios observed between shallow gas sands ($\sigma=0.1$) and shallow water sands ($\sigma=0.3$). Other fluid saturation effects on elastic properties of sedimentary rocks are discussed in detail in Gregory (1976). The effects of fluid type and saturation can be incorporated in the modeling through the Biot-Gassman theory (Biot, 1956a, b, Gassman, 1951) and the Biot-Consistent theory (Thomsen, 1985).

Intrinsic seismic anisotropy has recently been studied in detail. Current work on shales has shown that, to a first approximation, shales can be considered transversely isotropic (Lo et al, 1985, Tosaya, 1982). Thomsen (1987) derived a practical set of parameters δ , ϵ , and γ to characterize transversely isotropic media. In chapter 1, I showed the importance of anisotropy in analyzing quantitatively AVO trends; therefore, whenever possible, anisotropy should be estimated for detailed model based interpretations.

b) Current directions in petrophysical studies

Recently, there has been an increasing amount of empirical evidence for anisotropy, and in particular for transverse isotropy in shales (Tosaya, 1982, Thomsen, 1986, Vernik and Nur, 1990), and for higher order anisotropy, such as azimuthal anisotropy in fractured rocks (Thomsen, 1987, Crampin, 1984). An increasing amount of research is also being carried-out on anelasticity or attenuation and velocity dispersion effects (Winkler, 1985, Jones, 1986). In particular, Jones (1986) re-introduced a "phenomenological" model to characterize frequency-absorption pairs and related dispersion to wave propagation for shear waves through the product of frequency times fluid viscosity. Concurrently, the emphasis in seismic petrophysical studies has shifted towards anisotropy (White et al, 1983, Lo et al, 1985, Rai and Hanson, 1988) and anelasticity (Johnston et al, 1979, Mavko and Nur, 1979, Kjartansson, 1979, Bourbie, 1982, Jones, 1986, Dvorkin, 1992). There also has been a growing interest in shear wave velocities, due to the need for better AVO modeling.

Other petrophysical parameters have also been shown to be important in the estimation of velocities and anisotropy. For example, as seen previously, clay location has

a strong effect on velocities, and Meissner (1978) and Passey et al. (1990) showed that there often is a good inter-relationship between organic richness, porosity, resistivity, and velocity.

Bounding methods can prove useful in the bracketing of bulk and shear moduli for cases where rock forming components exhibit relatively small contrasts in properties. A good summary of different methods was presented in Watt et al. (1976). Because of their importance, these are reviewed below.

c) Review of bounding methods

Velocities in shales and sands depend on the elastic moduli and densities of their mineral constituents (quartz and feldspar), on clay content, and on clay location. Bounding methods show that in addition to the suite of properties cited above, the velocities of shaley sands should also depend, to a lesser extent, on the microstructure of the clays.

It was shown by several authors that the Hashin-Shtrikman (Hashin, Z., and Shtrikman, S., 1963) bounds for multi-phase solids are a substantial improvement over the Voigt (Voigt, 1928) and Reuss (Reuss, 1929) bounds; these are reviewed in detail in the Bakken shale example (part II-3, this chapter). In fact, it was also shown (Walpole, 1966) that the HS bounds are the best bounds obtainable, with no prior knowledge of the microgeometry of the rock constituents, as long as these are randomly distributed. The HS bounds are reasonably close together, except when one of the constituents is comparatively weak (ie, clay) or rigid. When that is the case, it is possible to improve on the HS bounds with a minimum of geological information. The goal is to narrow the limits on the bounds of the moduli in order to examine and hopefully understand the *apparent* scatter in velocity measurements made in the lab on shale and sand mixtures. With limited quantitative information, the first approach is to derive bounds on elastic moduli, based on Miller's approach. Miller (1969) used statistical information based on one point and three point correlation functions to derive bounds for two-phase media, as functions of volume fraction and

Self-consistent approaches

Isotropic cases: In the self-consistent (SC) approach, it is assumed that the solution to the effect of many inclusions on one inclusion is given by the solution to a single inclusion surrounded by a uniform medium with the properties of the aggregate; this is the principle of "non-interaction". Explicit calculations using SC theory require an assumption of the shape of the inclusions as either needle-like, disk-shaped, or spherical. The equations are given by several authors (Hill, 1965, Wu, 1966, Walpole, 1966, O'Connell and Budiansky, 1974, among others). Moreover, because it is possible for inclusions to be connected, a second formulation was derived subsequently for interconnected porosity (Budiansky and O'Connell, 1980).

Transverse isotropy: Walpole (1969) derived bounds for anisotropic media and showed that the bounds actually coincide in the case of transverse isotropy. This leads to five constants to characterize a transverse isotropic medium. He also showed that the SC results are unreliable when both phases are incompressible and, more specifically, are in error for inclusion concentrations greater than 50 %.

In summary, the SC theory can be unreliable under extreme conditions, but, in general, it has the advantage of yielding practical approximations for moduli, when exact calculations are beyond any possibility. When in the presence of interconnected cracks, the self-consistent theory is not compatible with the Biot-Gassman theory, and use of the Biot-Consistent (BC) model (after Thomsen, 1985) is recommended (see part III-2, this chapter). Because no theoretical bounds have been derived for shear moduli, SC and BC predictions for shear moduli are understood to be deterministic and subject to propagation of errors; however, they do yield an approximate value of shear moduli, which is often better than having no information at all.

3) Rock physics used to approximate anisotropy:

The Bakken shale example

Review of anisotropy

Anisotropy has been shown to be a common occurrence in the Earth (Tosaya, 1982, Banik, 1984, Thomsen 1986, Sriram, 1984). Periodic layering of isotropic media leads to long wavelength homogeneous equivalents which have been discussed by Voigt (1928), Reuss (1929), Hill (1965), Backus (1962), Helbig (1981) among others. These models describe crustal anisotropies adequately, but as shown by Tosaya (1982), they can be in error when applied to intrinsically anisotropic shales.

Velocities have been related to the amount and type of clays present in a given rock. However, little or no work has been done to relate anisotropy on one hand, and clay content, clay type, and microstructure on the other hand. Meanwhile, rapid and continued improvement in high resolution seismic techniques is requiring a more sophisticated knowledge about the elastic behavior of rocks for a more quantitative interpretation. In particular, several examples in the literature (Banik, 1984 among others) have shown that neglecting anisotropic effects can lead to serious depth conversion errors in the presence of shales or shaley layers. Anisotropy will not only affect the time to depth conversion, but it will also affect the characteristics of the seismic wavelet (chapter 1); it should therefore be incorporated into the modeling process, whenever such information is available. However, because direct measurement of anisotropy is a rare occurrence in standard processing, and because it is subject to large uncertainties, one key issue for "proper" forward modeling is to approximate transverse isotropy from lithologic models based on rock composition.

A crucial problem in studies of anisotropy is to be able to separate mechanisms which relate to the scale of wave propagation. When dominant wavelengths ($\lambda = V/f$, where λ is wavelength, V is velocity in m/s, and f is frequency in Hz) are of the order of the size of the heterogeneities or smaller, most anisotropic effects are usually attributed to scattering; on the other hand, when heterogeneities are an order of

of a shape factor, G . The shape factor G has a simple geometric meaning, being $1/9$ for spherical shapes, $1/6$ for needle shapes, and $1/3$ for platey shapes. Unfortunately, Miller's equations are wrong in his paper (1969), in his errata (1971), and in the form provided by Watt (1976). The correct form is presented below:

$$K_+^* = K_2 \{ 1 + \nu_1 (\alpha - 1) - (\nu_1 (1 - \nu_1) (\alpha - 1)^2) \}$$

$$\left[\alpha - (\alpha - 1) \nu_1 + 2\gamma \left[1 - \frac{4}{3} \nu_1 + \frac{1}{3} \beta (4\nu_1 - 1) + 3(\beta - 1) (G_1 (1 - \nu_1^2) - \nu_1^2 G_2) \right] \right]^{-1} \}$$

for the upper limit on the bulk modulus, and

$$K_-^* = K_1 \{ \alpha + \nu_1 (1 - \alpha) - (\nu_1 (1 - \nu_1) (\alpha - 1)^2) \}$$

$$\left[1 + \nu_1 (\alpha - 1) + \frac{3}{8} \left(\frac{\alpha}{\beta\gamma} \right) \left[3(\beta - 1) \left[3(\nu_1^2 G_2 - (1 - \nu_1)^2 G_1) - \frac{4}{3} \nu_1 \right] + 3\beta - 1 \right] \right]^{-1} \}$$

for the lower limit on the bulk modulus, where the constant G_i is related to the dominant shape of the grains of phase i . In Miller's notation, ν_1 is the volume fraction of phase 1, and

$$\begin{aligned} \alpha &= \frac{K_1}{K_2} \geq 1 \\ \beta &= \frac{\mu_1}{\mu_2} \\ \gamma &= \frac{\mu_2}{K_2} \end{aligned}$$

As observed by Watt (1976), the Miller bounds are tighter than the Hashin-Shtrikman results. These principles can be applied to a shaley sands with various preponderant grain geometries, when clays are part of the matrix (or frame) and for pore filling clays. The third category of clays, pore lining clays, can simply be modelled using one of the Hashin-Shtrikman bounds.

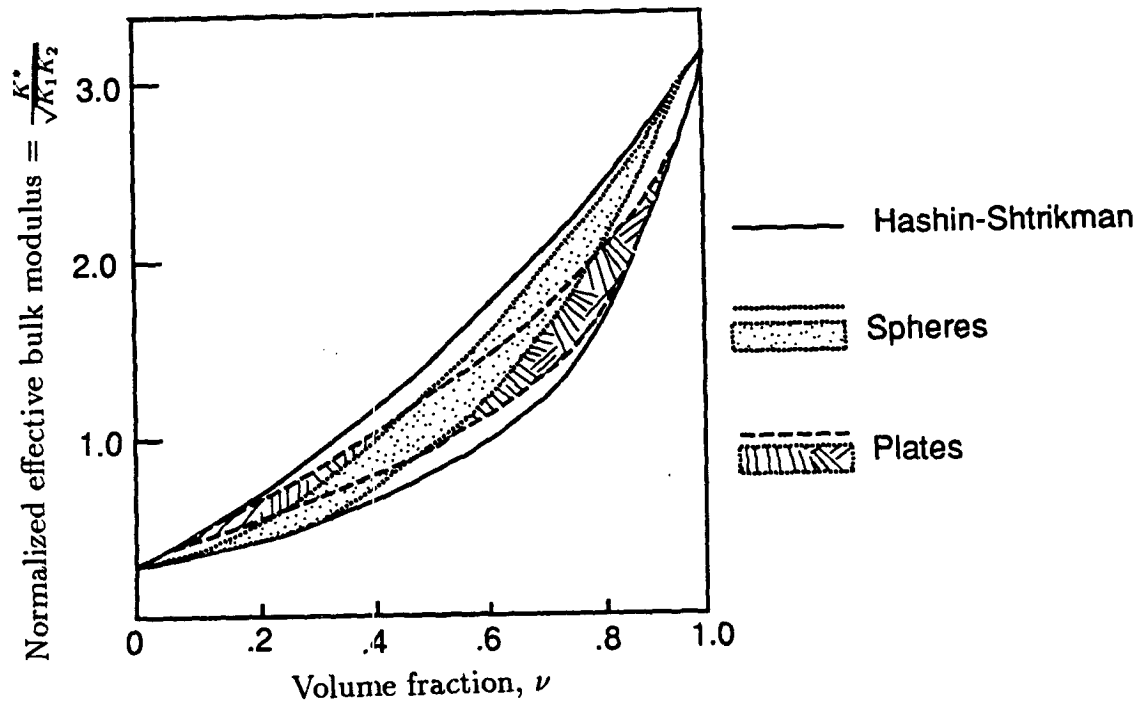


Figure 2.4: Normalized bounds on effective bulk moduli for spherical and platey geometries, and comparison to Hashin-Shtrikman bounds. Figure modified after Miller (1969), for $\alpha=10=\beta$ and $\gamma=1.0$. Note that the bounds do not overlap for concentrations below 20 % or above 80 %.

It is interesting to notice (figure 2.4) that the bounds for spherical and platey materials do not overlap for concentrations less than approximately 20 %, nor do they overlap for concentrations larger than approximately 75 %. The change in bulk modulus, which is solely attributable to the difference in clay microstructure, is largest for clay concentrations comprised between 25 % and 75 %; these are, by the way, the most common volume fractions encountered in hydrocarbon bearing shaley sands and sandy shales. In general, note that at small concentrations, platey geometries ($G=1/3$) yield greater bounds than needle geometries ($G=1/6$), which in turn yield larger bounds than spherical geometries ($G=1/9$).

Unfortunately, no equivalent bounds have been derived for shear moduli. This comes from the mathematical difficulty in manipulating the correlation integrals. But shear moduli are nevertheless expected to be a function of microstructure. Fortunately, deterministic, self-consistent methods can be used for more specific predictions of the shear moduli of rock aggregates.

magnitude smaller than the dominant wavelength, anisotropy can be modelled using long wavelength equivalent media. In the following study of the Bakken shale, the laboratory frequencies used were of the order of 1 MHz, and velocities were approximately equal to 4,000 m/s, so that the dominant wavelength is approximately 4 mm. Therefore, any microscale scale layering on a finer scale than 0.4 mm will be considered appropriate for the use of long wavelength equivalents. This appears to be the case, because most of the banding in the Bakken shale occurs on a micro-scale as can be observed on the cores.

Postma (1955), and Backus (1962) were among the first to show that a stacking of two alternating isotropic layers leads to an equivalent long-wavelength transverse isotropic medium (for more information, see the upscaling problem, in chapter 3). But the converse is not always true (Helbig, 1981): all transverse isotropic materials cannot be universally represented by an alternating set of isotropic layers. In fact, it is true, only under the condition - a "necessary" condition - that the P-wavefront is elliptical or that:

$$(C_{11} - C_{44})(C_{33} - C_{44}) - (C_{13} + C_{44})^2 = 0 \quad (1)$$

Elliptical anisotropy

The laboratory measurements of the Bakken shale (Vernik, 1990) did not verify equation (1); however, the reader will see (figures 2.5-2.9) that it was acceptable to first order to use an elliptical approximation. I first assume that the microstructure of the Bakken shale can be approximated by alternating isotropic thin layers, which consist of a silt-clay mixture on one hand, and kerogen on the other. I then apply isostress/isostrain concepts to the mixture (as in Blangy, 1990); this is shown in figures 2.5 and 2.6. Figure 2.5 is a summary of the concepts used in the work of Voigt (1928) and Reuss (1929), where ϵ and σ stand for strain and stress, K is % kerogen by volume, k and ec are the indices for kerogen and "effective clay". By setting isostrain conditions on a medium consisting of layered isotropic materials,

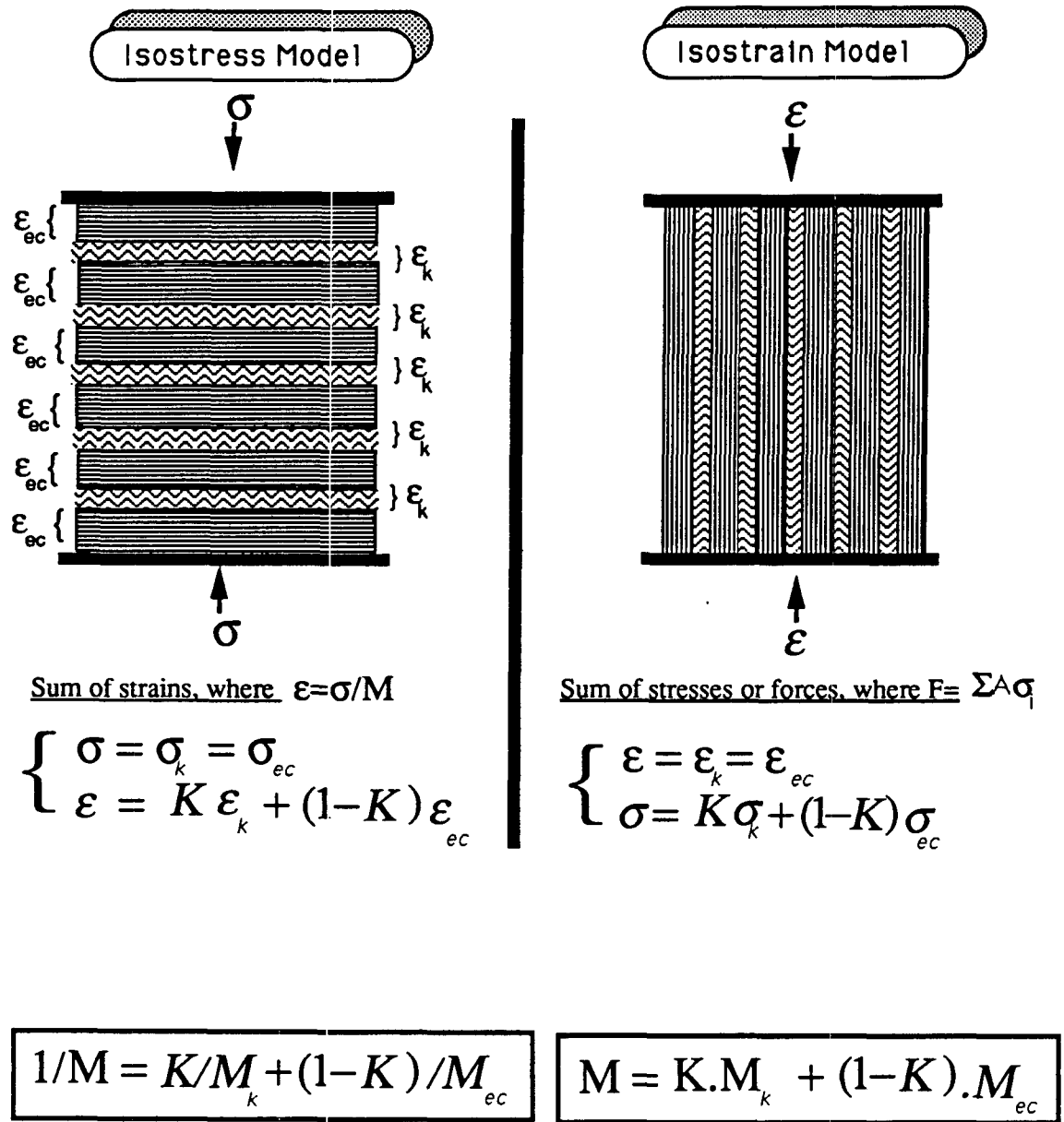


Figure 2.5: The familiar isostress (Reuss, 1929) and isostrain (Voigt, 1928) concepts have traditionally been used to define bounds on elastic moduli for suspensions and consolidated materials. As shown here, they can also conveniently be used to define theoretical velocities in directions perpendicular and parallel to bedding.

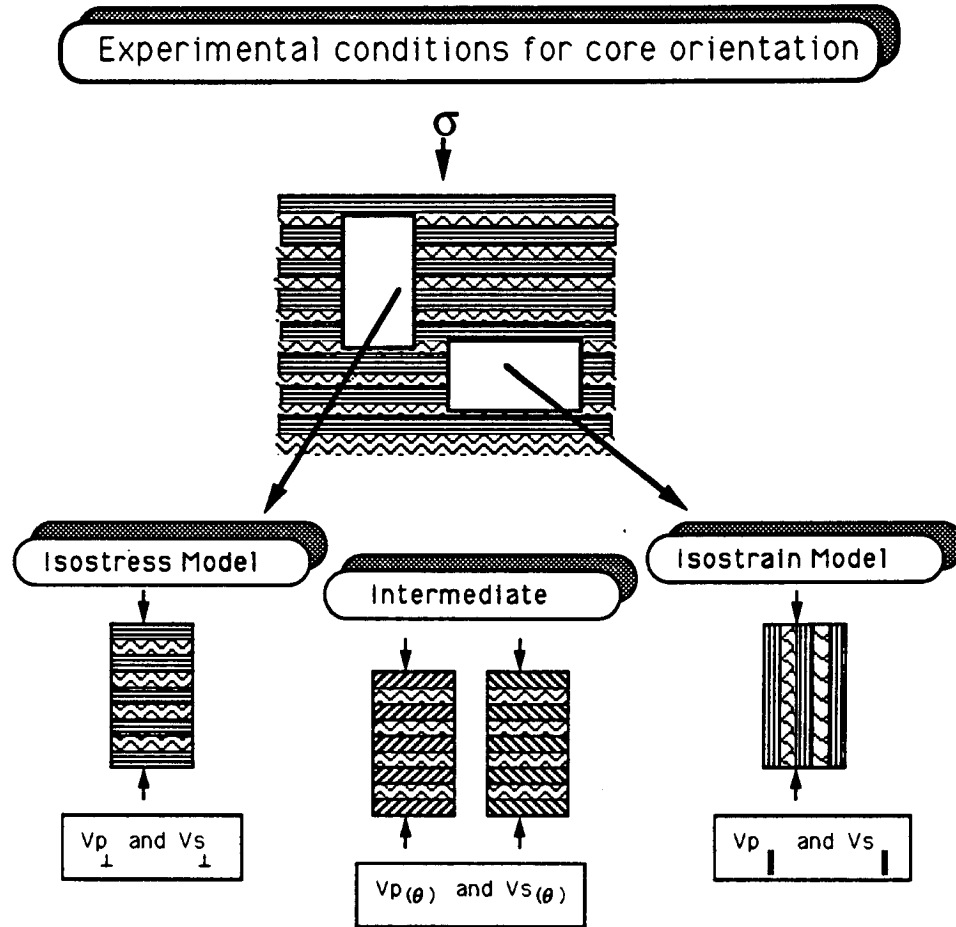


Figure 2.6: The directions in which core samples are taken can be related to the isostress and isostrain cases (and to any intermediate direction), when considering a finely layered medium to be elliptically isotropic.

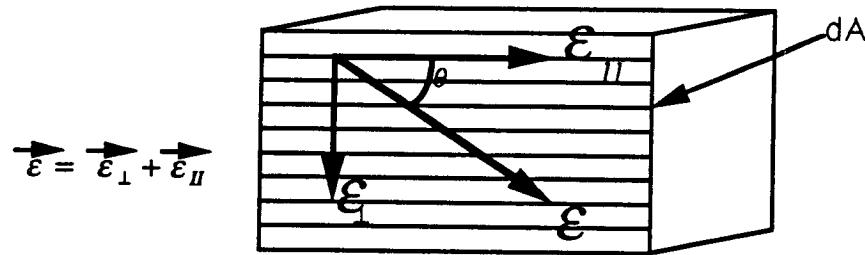


Figure 2.7: An idealized element of rock dA , where the total stress can be decomposed in 2-D into its normal and tangential components.

Voigt showed that elastic uniaxial moduli are expected to add in series; conversely, by setting conditions of isostress, Reuss arrived at a law of addition of elastic uniaxial moduli in parallel. In the experimental set-up shown in figure 2.6, I apply those principles to account for anisotropy due to micro-scale layering. A set of cores are retrieved at an arbitrary orientation from a block of shale which is considered to be laterally homogeneous; the cores oriented perpendicularly to the microlayers will be under pure isostress conditions, while those oriented parallel to micro-bedding will essentially be under isostrain conditions; in reality, the microbeds may not consist of truly isotropic layers, and the amount of departure from isotropy will affect the modeling results. By taking a sample at an arbitrary angle θ to the bedding, I obtain a hybrid between the Reuss and the Voigt models. A hybrid elastic modulus can be derived by examining the continuity of stress in 2-D:

According to figure 2.7, the total stress on an element of rock dA is decomposed in 2-D into its normal and tangential components (or into the sum of two uniaxial stresses): The "net isostress" component is $\sigma_{parallel} \sin \theta$, the "net isostrain" component is $\sigma_{perpendicular} \cos \theta$, and we have:

$$\sigma^2 = \sigma_{\text{perpendicular}}^2 \cos^2 \theta + \sigma_{\text{parallel}}^2 \sin^2 \theta$$

so that $M^2 = M_{\text{perpendicular}}^2 \cos^2 \theta + M_{\text{parallel}}^2 \sin^2 \theta$, where

$$M_{\text{perpendicular}}^2 = (p_1 M_1 + p_2 M_2)^2$$

$$M_{\text{parallel}}^2 = \left(\frac{p_1}{M_1} + \frac{p_2}{M_2} \right)^{-2}$$

therefore,

$$V_p = \sqrt{\frac{M}{\rho}} = \sqrt{\frac{\sqrt{(p_1 M_1 + p_2 M_2)^2 \cos^2 \theta + \left(\frac{p_1}{M_1} + \frac{p_2}{M_2} \right)^{-2} \sin^2 \theta}}{p_1 \rho_1 + p_2 \rho_2}} \quad (2)$$

Naturally, this general relationship is in agreement with the previous results (Reuss and Voigt): by letting $\theta = 0$, then $V_p = \sqrt{\frac{p_1 M_1 + p_2 M_2}{\rho}}$ (which is equivalent to the isostrain model), and by letting $\theta = \frac{\pi}{2}$, then $V_p = \sqrt{\frac{\left(\frac{p_1}{M_1} + \frac{p_2}{M_2} \right)^{-1}}{\rho}}$ (which is equivalent to the isostress model). Equation (2) is then used to generate the familiar plot of velocity versus angle to bedding, as can be observed in elliptically anisotropic media; predictions compare pretty well with the laboratory data at different propagation angles (figure 2.8).

The model can also be used to predict the variation in velocities with increasing kerogen content for wave propagation at a given, fixed angle θ to bedding. This is done by substituting p_2 into equation (2) for a given type of kerogen with properties ρ_2 and M_2 (figure 2.9). A sharp decrease in velocity results from the presence of kerogen. The velocity of the end point, corresponding to pure shale is coherent with previous laboratory measurements when extrapolated at 0 % porosity (Marion and Yin, 1988). Note that velocities at a 45 degree angle to bedding can be underestimated using this method, and especially so, if the shale is not really elliptically anisotropic; this is due to the fact that I am neglecting second order terms in the form of C_{13} or δ (see next section on transverse isotropy for more details). One may also expect the model to be able to characterize the amount of apparent anisotropy - defined as $'[V_{11}-V_{33}]/V_{11}'$ - as a function of kerogen content. However, the elliptical model did

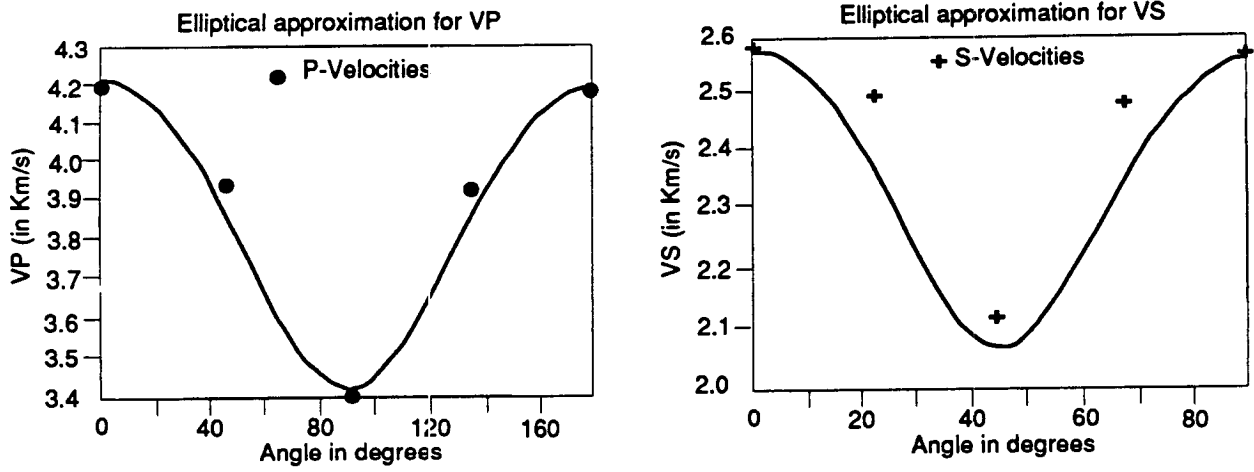


Figure 2.8: Elliptical isotropy was used as a first order approximation to model the effects of transverse isotropy observed in the Bakken shale (sample at depth 10164 ft from the Shell-Texel well). Both compressional and shear velocities are fairly well approximated as functions of direction; note however that velocities at 45 and 135 degrees are underestimated.

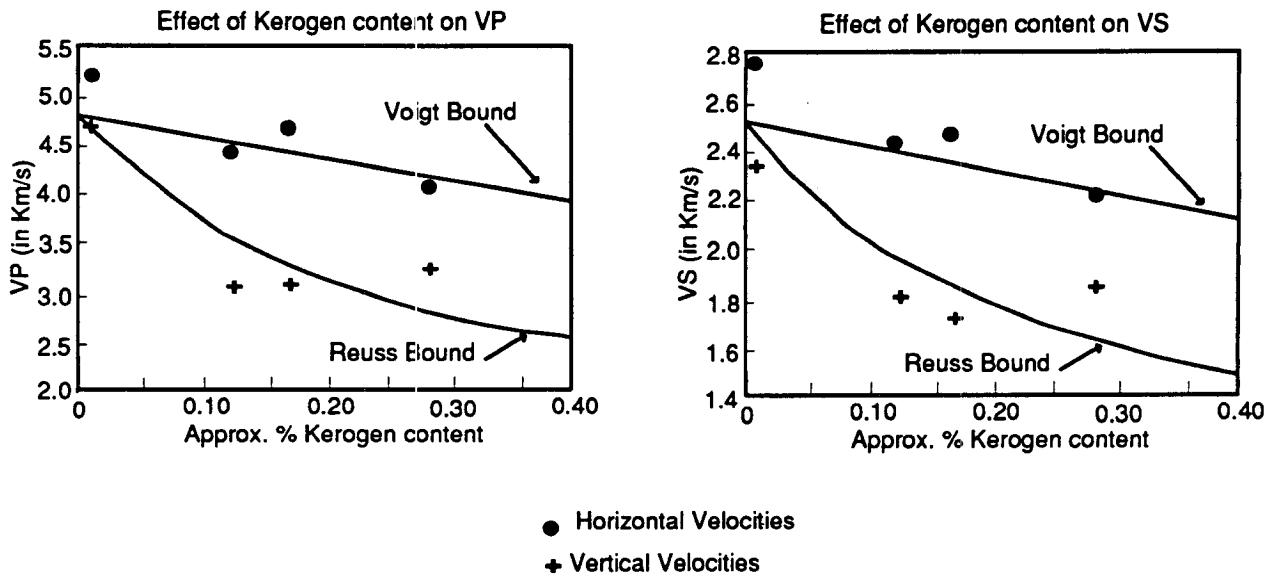


Figure 2.9: Elliptical isotropy was also used to model the effects of kerogen content on the Bakken shale. The simple model of velocity as a function of kerogen content agrees with laboratory observations made by Vernik (1990).

not quantitatively match the observed data, except for suggesting that anisotropy increases with increasing concentration of the weaker phase (here, kerogen). This is due to the fact that the Bakken shale is not truly elliptically anisotropic; therefore, I can get away with approximations in the calculation of first order quantities such as velocities, but not in the calculation of second order quantities, such as anisotropies, where parameters such as C_{13} or δ can no longer be neglected (see next section on transverse isotropy).

Because of depositional phenomena, one may expect that most shales would exhibit one axis of symmetry, perpendicular to bedding planes; this would yield five elastic constants as in transverse isotropy, or three planes of symmetry (arranged as: a plane of deposition (or plane 1), a plane in a direction parallel to flow and perpendicular to plane 1, and a plane in a direction perpendicular to flow and perpendicular to plane 1) and yielding nine elastic constants, as in orthorhombic anisotropy.

In summary, it would be possible to model the velocities in anisotropic shales with very simple concepts leading to elliptical anisotropy, when propagation occurs at either small or large angles to bedding. For the Bakken shale, the presence of kerogen is expected to have three main effects:

- decreasing V_p and V_s with increasing kerogen content,
- angle dependent velocities,
- and increased anisotropy with increasing kerogen content.

In using these simplifying concepts, I am actually computing a lower bound for anisotropy to be observed in the Bakken shale. The method yields results which are in agreement with the calculations of Levin (1978) for elliptical anisotropy. Levin (1978) or Berryman (1979) expressed phase velocities in an elliptically anisotropic solid as:

$$V^2 = V_1^2 \sin^2 \theta + V_2^2 \cos^2 \theta$$

It can be shown that the expression is equivalent to formula (2). In general, the elliptical approximation to velocity anisotropy can yield a good first order approximation for near horizontal and vertical propagation in flat layers. However, the velocities at steeper angles to bedding, and in particular velocities at 45 and 135 degrees, are underestimated (figure 2.8); this is due to the fact that for elliptical anisotropy, C_{13} is zero. In conclusion, it is often more reasonable to use a transversely isotropic model for most shales, rather than simple elliptical anisotropy.

Transverse isotropy

The previous discussion has shown that one must use caution when modeling anisotropy in shales. Several authors (Postma, 1955, Backus, 1962, Helbig, 1981) have calculated velocities for transversely isotropic media. Postma (1955) showed that a layered sequence creates transverse isotropy in the long wavelength. But the converse is false. Not all transversely isotropic materials can be modelled with a series of alternating micro-layers. In fact, Helbig (1983) showed that, in transversely isotropic media, only the wavefront of SH waves is always an oblate ellipsoid. Furthermore, he showed that when lamination is present, the wavefront of P waves can never be an ellipsoid. Daley and Hron (1977) calculated phase velocities for the general case of transverse isotropy ; phase velocities are described by the following equations:

$$V_p^2(\theta) = \frac{1}{2\rho} [C_{33} + C_{44} + (C_{11} - C_{33}) \sin^2\theta + D(\theta)]$$

$$V_{sv}^2(\theta) = [C_{33} + C_{44} + (C_{11} - C_{33}) \sin^2\theta - D(\theta)]$$

$$V_{sh}^2(\theta) = \frac{1}{\rho} [C_{66} \sin^2\theta + C_{44} \cos^2\theta]$$

where

$$D(\theta) = \left\{ (C_{33} - C_{44})^2 + 2 \left[2(C_{13} + C_{44})^2 - (C_{33} - C_{44})(C_{11} + C_{33} - 2C_{44}) \right] \sin^2\theta \right. \\ \left. + \left[(C_{11} + C_{33} - 2C_{44})^2 - 4(C_{13} + C_{44})^2 \sin^4\theta \right] \right\}^{\frac{1}{2}} \quad (3)$$

By introducing three new anisotropy parameters, δ' , ϵ , and γ defined below, Thomsen (1986), recast these velocities in terms of the more familiar velocities at normal incidence:

$$\alpha_0 = V_p(0) = \sqrt{\frac{C_{33}}{2\rho}}, \beta_0 = V_{sv}(0) = V_{sh}(0) = \sqrt{\frac{C_{44}}{2\rho}}, \epsilon = \frac{C_{11} - C_{33}}{2C_{33}}, \gamma = \frac{C_{66} - C_{44}}{2C_{44}}$$

$$\delta' = \frac{1}{2C_{33}^2} \left[2(C_{13} + C_{44})^2 - (C_{33} - C_{44})(C_{11} + C_{33} - 2C_{44}) \right], \text{ and } D'(\theta)$$

$$\text{where } D'(\theta) = \frac{1}{2} \left(1 - \frac{\beta_0^2}{\alpha_0^2} \right) \left\{ \left[1 + \frac{4\delta'}{\left(1 - \frac{\beta_0^2}{\alpha_0^2}\right)^2} \sin^2\theta \cos^2\theta + \frac{4\left(1 - \frac{\beta_0^2}{\alpha_0^2} + \epsilon\right)\epsilon}{\left(1 - \frac{\beta_0^2}{\alpha_0^2}\right)^2} \sin^4\theta \right]^{\frac{1}{2}} - 1 \right\}$$

to obtain the following equations:

$$\begin{aligned} V_p^2(\theta) &= \alpha_0^2 \left[1 + \epsilon \sin^2\theta + D'(\theta) \right] \\ V_{sv}^2(\theta) &= \beta_0^2 \left[1 + \frac{\alpha_0^2}{\beta_0^2} \epsilon \sin^2\theta - \frac{\alpha_0^2}{\beta_0^2} D'(\theta) \right] \\ V_{sh}^2(\theta) &= \beta_0^2 \left[1 + 2\gamma \sin^2\theta \right] \end{aligned}$$

These equations can further be simplified for the case of weak transverse isotropy (Thomsen, 1986) and involve a new parameter δ , defined as:

$$\delta = \frac{1}{2} \left[\epsilon + \frac{\delta'}{\left(1 - \frac{\beta_0^2}{\alpha_0^2}\right)} \right] = \frac{(C_{13} + C_{44})^2 - (C_{33} - C_{44})^2}{2C_{33}(C_{33} - C_{44})}$$

this parameterization yields:

$$\begin{aligned} V_p(\theta) &= \alpha_0 \left(1 + \delta \sin^2\theta \cos^2\theta + \epsilon \sin^4\theta \right) \\ V_{sv}(\theta) &= \beta_0 \left[1 + \frac{\alpha_0^2}{\beta_0^2} (\epsilon - \delta) \sin^2\theta \cos^2\theta \right] \\ V_{sh}(\theta) &= \beta_0 \left(1 + \gamma \sin^2\theta \right) \end{aligned}$$

where

$$\epsilon = \frac{V_p\left(\frac{\pi}{2}\right) - \alpha_0}{\alpha_0}; \quad \gamma = \frac{V_{sh}\left(\frac{\pi}{2}\right) - \beta_0}{\beta_0}; \quad \delta = 4 \left[\frac{V_p\left(\frac{\pi}{4}\right)}{V_p(0)} - 1 \right] - \left[\frac{V_p\left(\frac{\pi}{2}\right)}{V_p(0)} - 1 \right]$$

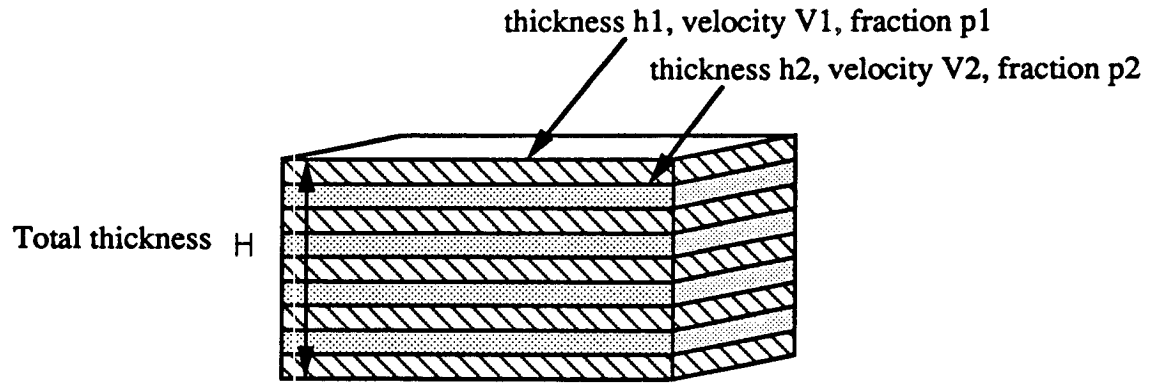


Figure 2.10: An idealized finely layered rock consisting of two isotropic and homogeneous flat layers with thicknesses H_i , velocity V_i , and fraction p_i .

Banik (1987) discussed the physical meaning of δ in detail, and related it to the difference between the P-wave anisotropy and the SV-wave anisotropy of the medium. In particular, for small δ , he showed that, at zero-offset,

$$V_p(0) = \alpha_0(1 + \delta)$$

One interesting application of the previous discussion on isostress/isostrain (or elliptical) anisotropy is that it is possible to use the simple model to approximate a lower bound on δ for weak transverse isotropy. Consider the case of two isotropic and homogeneous flat layers shown in figure 2.10. In the particular case of two isotropic and homogeneous layers, and in the absence of dip, we have:

$$V_{nmo} = \sqrt{\frac{\sum_i \Delta t_i V_i^2}{\sum_i \Delta t_i}} = \sqrt{\frac{\sum \Delta t_1 V_1^2}{\sum (\Delta t_1 + \Delta t_2)} + \frac{\sum \Delta t_2 V_2^2}{\sum (\Delta t_1 + \Delta t_2)}}$$

$$\text{since } \sum \Delta t_1 = \sum \frac{h_1}{V_1} = \frac{p_1 H}{V_1}$$

$$\text{then } V_{nmo} = \sqrt{\frac{p_1 V_1 + p_2 V_2}{\frac{p_1}{V_1} + \frac{p_2}{V_2}}}$$

I obtain a very simple relationships, expressing **isostress and isostrain** limiting velocities as a function of seismic interval velocities and seismic rms velocities for a layered medium with two alternating components:

$$V_{nmo} = \sqrt{V_{Voigt} \cdot V_{Reuss}}$$

(4)

This formula (4) expresses the familiar normal-moveout velocity in terms of the geometric average of the Voigt and Reuss bounds on velocities. Then, using the fact that $V_{nmo} = (1 + \delta) V_{perpendicular}$ and taking the isostress bound in the limit of normal incidence:

$$\text{letting } V_0 = V_{perpendicular} = \sqrt{\frac{1}{\rho} \left(\frac{\rho_1}{M_1} + \frac{\rho_2}{M_2} \right)^{-1}} \text{ where } M_1 = \rho_1 V_1^2 \text{ and } M_2 = \rho_2 V_2^2$$

then,

$$\delta = \frac{\sqrt{\frac{p_1 V_1 + p_2 V_2}{\frac{\rho_1}{V_1} + \frac{\rho_2}{V_2}}}}{\sqrt{\frac{1}{\rho} \left(\frac{\rho_1}{\rho_1 V_1^2} + \frac{\rho_2}{\rho_2 V_2^2} \right)^{-1}}} - 1 \quad (5)$$

where $\rho = p_1 \rho_1 + p_2 \rho_2$. Note that for $\delta < 0$, we have $\frac{p_1 V_1 + p_2 V_2}{\frac{\rho_1}{V_1} + \frac{\rho_2}{V_2}} < \frac{1}{\rho} \left(\frac{\rho_1}{\rho_1 V_1^2} + \frac{\rho_2}{\rho_2 V_2^2} \right)^{-1}$.

Next, I apply formula (5) to calculate lower bounds on δ for several hypothetical types of lithologies, given p_1 , p_2 , ρ_1 , ρ_2 , V_1 , and V_2 . The calculated values (presented in table 2.1) are of the same order of magnitude as those of Thomsen (1986). As discussed by Banik (1987), errors can be amplified, because the way in which δ is estimated involves the difference between quantities of the same order of magnitude.

Phase versus Group velocities

Care must be taken in understanding the differences between phase and group velocities in anisotropic media. In the laboratory, we usually measure group velocities,

	Volume Fraction 1	Volume Fraction 2	Vp1	Vp2	Density1	Density2	Delta	Wyllie-average Velocity
1	Hypothetical model for shale similar to <u>Bakken shale</u> (1=Mixture of clay & silt, 2=kerogen); $\Phi = 2\%$							
	0.2	0.8	4.5	2.0	1.5	2.6	.290	3.6
2	Hypothetical model for shale similar to <u>Cotton Valley shale</u> (1=silt, 2=clay); $\Phi = 4\%$							
	0.5	0.5	5.7	4.0	2.6	2.6	.031	4.7
3	Hypothetical model for shale similar to <u>Pierre shale</u> (1=silt, 2=clay); $\Phi = 15\%$							
	0.65	0.35	5.1	3.8	2.25	2.35	.076	4.5
4	Hypothetical model for sandstone similar to <u>Berea sand</u> (1=silt, 2=clay); $\Phi = 18\%$							
	0.95	0.05	5.0	3.5	2.2	2.3	0.006	4.7

Table 2.1: Calculated lower bounds on δ for several "type" lithologies.

which are associated with the arrival of most of the energy of the propagating wave. However, most theoretical treatments of anisotropy involve phase velocities. Therefore, in order to be able to relate theory and practice, one must convert from phase velocity to group velocity and vice-versa. The procedure is summarized in appendix A.

It is also worth to mention that large errors may be introduced in shear wave velocity measurements in the laboratory, when looking at rotational modes; this is due to the fact that rotational modes yield a mixture of shear velocities (V_{sh} and V_{sv}) and it is difficult to recover the true velocities of either mode. In fact, as recommended by Hearmon (1961), the elastic moduli should be averaged, when shear velocity is measured at an angle which is different from 0 or $\pi/2$ radians.

Future research on characterizing organic content seismically

The previous observations of anisotropy in the Bakken shale provided the necessary background to generate elastic synthetic seismogram responses of immature kerogen rich shales and those of mature kerogen-free shales. Preliminary synthetic work (Blangy, 1990) showed that one would expect a difference in total seismic amplitude between immature kerogen rich shales, and mature kerogen-free shales. Hence, in the future, it may be possible to map the state of maturation of organic rich rocks directly from calibrated seismic.

4) Reservoir heterogeneities

In general throughout the petroleum industry, there is an increase in awareness of the importance of reservoir heterogeneities, and this results in the modeling of the effects of microstructure. In the past, the modeling was done by making approximations on the particular geometries of grain shapes or by using networks, but more recently, advances in computer technology have enabled the direct calculation of elastic moduli for any pore geometry (Chen et al, 1990, Dvorkin et al, 1990).

Clearly, when the information is available, all of the effects listed above have to be incorporated into the modeling, inversion and interpretation of AVO anomalies, be-

cause they each contribute destructively or constructively to overall seismic responses.

One problem encountered when working with velocities is that compressional velocity changes reflect the effects of reservoir parameter changes on both shear and bulk moduli and on density, while shear velocity changes reflect both shear modulus and density changes. In order to relate changes in rock properties to lithology, it is necessary to decouple these effects, and we therefore recommend working with elastic moduli rather than velocities.

III)-DETERMINISTIC MODELING OF SHEAR VELOCITIES

As seen in chapter 1 (from figure 1.6), AVO responses of compressional waves are most sensitive to changes in shear velocities. Another compelling evidence of the importance of shear properties is that the P-wave velocity itself depends on the shear modulus more than on the bulk modulus by a factor of 4/3. Further evidence of the importance of shear properties comes from Poisson's ratio: as seen in chapter 1, once the compressional velocity structure of an area is known, it is essential to properly quantify Poisson's ratio in order to interpret AVO anomalies correctly. By definition, Poisson's ratio is defined as:

$$\sigma = \frac{1 \left(\frac{v_p}{v_s} \right)^2 - 2}{2 \left(\frac{v_p}{v_s} \right)^2 - 1} = \frac{1}{2} \frac{K - \frac{2}{3}\mu}{K + \frac{1}{3}\mu}$$

The change in Poisson's ratio can be expressed as follows:

$$\Delta\sigma = \left[\frac{\partial K}{\partial \mu} \right]_K \Delta K + \left[\frac{\partial \mu}{\partial K} \right]_\mu \Delta \mu = \frac{9}{2} \frac{1}{(3K + \mu)^2} [\mu \Delta \mu + K \Delta K]$$

This shows that reducing the uncertainties on the effective elastic moduli is an important consideration in AVO work; unfortunately, shear moduli are poorly understood.

Elastic modeling is necessary to invert AVO signatures quantitatively for lithology. Since shear waves play an important part in AVO modeling, and because shear measurements (via either core analysis or logs) are costly and seldom run, there is a need to develop methods for modeling shear wave velocities. Empirical modeling methods can be obtained from the literature or from sets of measurements for specific lithologies in specific geographical areas. Deterministic methods are attractive, because they allow an understanding of the fundamentals of rock properties; they also allow for sensitivity analyses to be run on shear velocities (for example, quantifying the effect of a change in porosity on V_s). In what follows, I present and summarize four different deterministic methods to calculate synthetic shear velocities; the notation used in this section appears at the end of this chapter, whenever it is not explicitly defined.

1) The Gregory-Pickett method

The Biot-Gassman equations in the low frequency limit are used as a starting point, where the compressional velocity can be expressed as the sum of a matrix component and a fluid component, and the shear modulus is independent of saturation:

$$V_p^2 = \frac{1}{\rho} \left(K_d + \frac{4}{3} \mu_d \right) = \frac{1}{\rho} \left\{ \underbrace{\left(K_d + \frac{4}{3} \mu_d \right)}_{\text{Matrix}} + \underbrace{\frac{\left(1 - \frac{K_d}{K_s} \right)^2}{\left(1 - \phi - \frac{K_d}{K_s} \right) \frac{1}{K_s} + \frac{\phi}{K_f}}}_{\text{Fluid}} \right\} \quad (6)$$

$$V_s^2 = \frac{\mu_b}{\rho}; \mu_b = \mu_d \quad (7)$$

Using the exact relationship for dry rocks derived by Fung (1965)

$$2\mu_d(1 + \sigma_d) = 3K_d(1 - 2\sigma_d) \quad (8)$$

I express the matrix components in terms of the dry rock's Poisson's ratio (σ_d) and

the dry frame moduli (K_d and μ_d):

$$K_d + \frac{4}{3}\mu_d = 3K_d \frac{1 - \sigma_d}{1 + \sigma_d} \quad (9)$$

and I find from equation (6) that:

$$\left(1 - \frac{K_d}{K_s}\right)^2 - \left(\rho V_p^2 - 3K_d \frac{1 - \sigma_d}{1 + \sigma_d}\right) \left(1 - \frac{K_d}{K_s}\right) + \phi \left(\rho V_p^2 - 3K_d \frac{1 - \sigma_d}{1 + \sigma_d}\right) \left(\frac{1}{K_s} - \frac{1}{K_f}\right) = 0 \quad (10)$$

this equation can also be expressed in a more convenient form as:

$$\begin{aligned} & \left(3 \frac{1 - \sigma_d}{1 + \sigma_d} - 1\right) \left(1 - \frac{K_d}{K_s}\right)^2 + \left(3\phi \frac{1 - \sigma_d}{1 + \sigma_d} \left[\frac{K_s}{K_f} - 1\right] - 3 \frac{1 - \sigma_d}{1 + \sigma_d} + \frac{\rho V_p^2}{K_s}\right) \left(1 - \frac{K_d}{K_s}\right) \\ & - \phi \left(3 \frac{1 - \sigma_d}{1 + \sigma_d} - \frac{\rho V_p^2}{K_s}\right) \left(\frac{K_s}{K_f} - 1\right) = 0 \end{aligned} \quad (11)$$

where we can identify an equation of the form:

$$aX^2 + bX + C = 0$$

where

$$a = 3 \frac{1 - \sigma_d}{1 + \sigma_d} - 1$$

$$b = 3\phi \frac{1 - \sigma_d}{1 + \sigma_d} \left[\frac{K_s}{K_f} - 1\right] - 3 \frac{1 - \sigma_d}{1 + \sigma_d} + \frac{\rho V_p^2}{K_s}$$

$$c = -\phi \left(3 \frac{1 - \sigma_d}{1 + \sigma_d} - \frac{\rho V_p^2}{K_s}\right) \left(\frac{K_s}{K_f} - 1\right)$$

and I solve this quadratic equation in X by posing:

$$X = \left(1 - \frac{K_d}{K_s}\right) \quad (12)$$

One can recognize that when solutions are real, there will be a positive solution and a negative solution to this equation, because the sign of the product of the

solutions is equal to the sign of the product of a and c; I therefore take only the positive solution; it is also the largest solution:

$$X = 1 - \frac{K_d}{K_s} = \frac{-b + \sqrt{b^2 - 4ac}}{2a} \quad (13)$$

Having solved for X, I obtain K_d from equation (12) as:

$$K_d = (1 - X) K_s$$

and substituting into equation (8) I obtain μ_d as

$$\mu_d = \frac{3}{2} K_d \left(\frac{1 - 2\sigma_d}{1 + \sigma_d} \right) = \frac{3}{2} (1 - X) K_s \left(\frac{1 - 2\sigma_d}{1 + \sigma_d} \right)$$

I then obtain:

$$V_s = \sqrt{\frac{\frac{3}{2} (1 - X) K_s \left(\frac{1 - 2\sigma_d}{1 + \sigma_d} \right)}{\rho}} \quad (14)$$

The Gregory-Pickett method generally gives accurate approximations of shear velocities in clean sands of good porosity; however, it should be noted that the method yields a μ_d that is directly related to K_d through σ_d , and therefore μ_d is a function of $(\phi, \sigma_d, V_p, K_f, \text{ and } K_s)$. V_s is therefore somewhat dependent on K_f , which is in disagreement with Biot's theory. However, for small changes in fluid type, fluid saturation, or porosity, the Gregory-Pickett method yields adequate results. For large changes in those parameters, the Gregory-Pickett method can prove inaccurate, because it does not follow Biot's theory. In those cases, I suggest to try to use the more complicated "Biot-Consistent" theory in calculating shear velocity.

The Castagna method

This method is a particular case of the Gregory-Pickett method and was used by Castagna et al. (1985). It is based on the observations of Pickett that the ratio of dry velocities V_p/V_s is independent of porosity, and is approximately equal to 1.53;

this is similar to assuming a Poisson's ratio of 0.125 in the Gregory-Pickett method, or to assuming that the K_d is equal to μ_d . Gassman's equations can then be solved for μ_d through a second degree equation, as in the Gregory-Pickett method.

2) The Biot-Consistent method

This method was published by Thomsen (1985) and makes minimal assumptions about the microscopic geometry of rocks. Biot (1956) showed that three independent state variables (rather than K_b and μ_b , as commonly used) are necessary to characterize a porous aggregate. The third variable is the fluid pressure, p_f ; in an undrained aggregate, one may equivalently specify the increment in pore volume: $\frac{\Delta V_p}{V}$

At this point, a new modulus, the pore incompressibility is defined as:

$$K_p = -V_p \frac{p}{\Delta V_p} = K_f \frac{p}{p_f} \quad (15)$$

Therefore, any porous aggregate which satisfies the Biot-Gassman equations has three characteristic moduli (K_b , μ_b , and K_p), which when specified define its elastic response for all saturations.

The Biot-Consistent method was derived for a rock containing substantial interconnected equant porosity and crack density, following Budiansky and O'Connell (1980) who expressed K_b , μ_b , and K_p (or $\frac{p}{p_f}$) as functions of K_f :

$$K_b(K_f) = K_s \frac{1 - \left(1 - \frac{K_f}{K_s}\right) \left(\frac{\phi_p}{1-a_B} + A_B \varepsilon\right)}{1 + \frac{K_f}{K_s} \left(\frac{a_B}{1-a_B} \frac{\phi_p}{\phi} + \frac{A_B \varepsilon}{\phi}\right)} \quad (16)$$

$$\mu_b(K_f) = \mu_s \left(1 - \frac{\phi_p}{1-b_B} - B_B \varepsilon\right) \quad (17)$$

$$\frac{p_f}{p}(K_f) = \frac{K_f}{K_b} \frac{\frac{\phi_p}{1-a_B} + A_B \varepsilon}{\phi + \frac{K_f}{K_b} \left(\frac{\phi_p}{1-a_B} + A_B \varepsilon - \phi_p\right)} \quad (18)$$

where ε is the fracture density (which can be related to the crack porosity, ϕ_c , for specific crack geometries), ϕ_p is the porosity due to the pores, and ϕ is the total porosity,

$$\begin{aligned}
 b_B &= \frac{2}{15} \frac{4 - 5\sigma}{1 - \sigma} \\
 a_B &= \frac{1 + \sigma}{3(1 - \sigma)} \\
 B_B &= \frac{32}{45} \frac{(1 - \sigma)(5 - \sigma)}{(2 - \sigma)} \\
 A_B &= \frac{16}{9} \frac{1 - \sigma^2}{1 - 2\sigma} \\
 \sigma &= \frac{1 - \frac{2\mu_b}{3K_b}}{2 + \frac{2\mu_b}{3K_b}} \tag{19}
 \end{aligned}$$

The parameter α_B is also defined after Geertsma (1957) and Nur and Byerlee (1971) as:

$$\alpha_B = 1 - \frac{K_b^*}{K_s} = 1 - \frac{K_d}{K_s} \tag{20}$$

It can then be shown (Thomsen, 1985) that:

$$\frac{p_f}{p} = \frac{K_f}{K_b^* \phi + \frac{K_f}{K_b^*} (\alpha_B - \phi + \phi \alpha_B)} \tag{21}$$

A summary of the procedure used in the Biot-Consistent algorithm is shown in figure 2.11a. The strength of the Biot-Consistent method lies in the fact that it does not assume any a-priori dry frame Poisson's ratio as a starting point. Instead, its value is arrived at by iteration and convergence; once σ^* (or σ_d : a * means a dry modulus in Thomsen's notation) has been obtained by convergence, the dry frame modulus K_b^* (or K_d) is also determined.

An example of the computation procedure is shown in figure 2.11b. Convergence of K_b (K_f) is achieved for $\sigma_d = 0.135$. The two compressional velocities V_{Hill} and V_{BC} correspond to values of K_b (K_f) in steps 6 and 8 of figure 2.11a. For $\sigma_d = 0.135$,

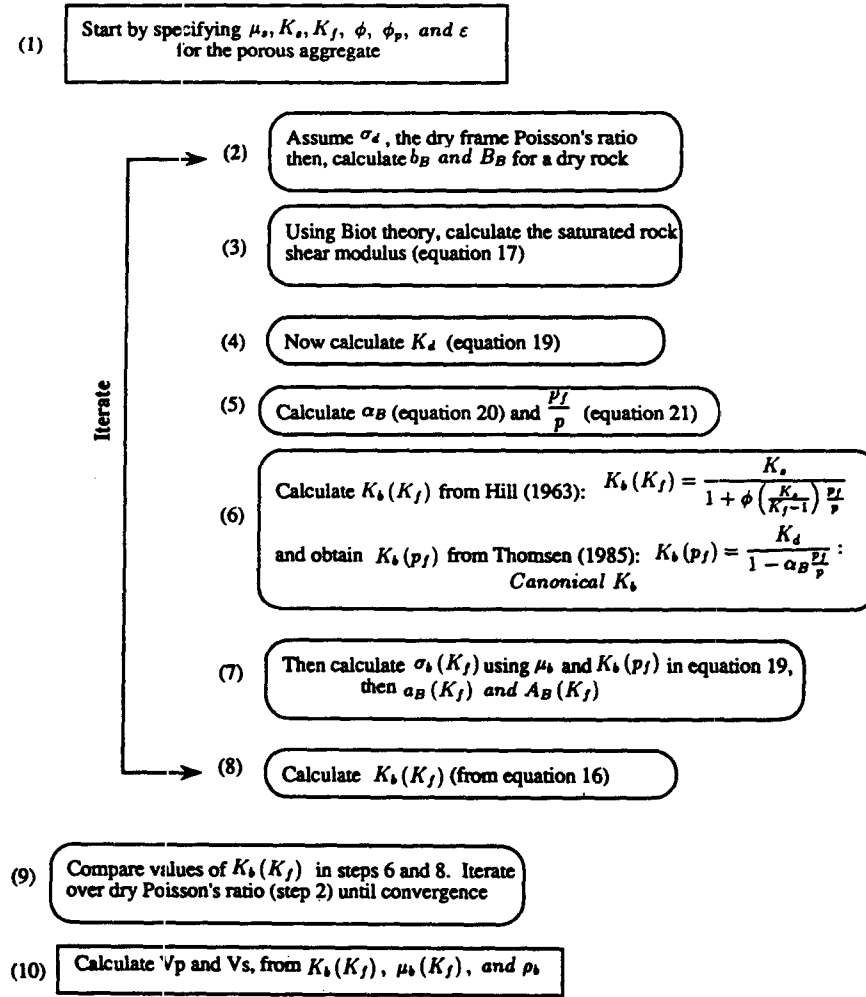


Figure 2.11a: Flow chart for the Biot-Consistent algorithm; after convergence, $\sigma^* = \sigma_d$ is determined, and $K_b^* = K_d$ is obtained. This procedure yields a dry frame bulk modulus which is completely decoupled (Thomsen, 1985).

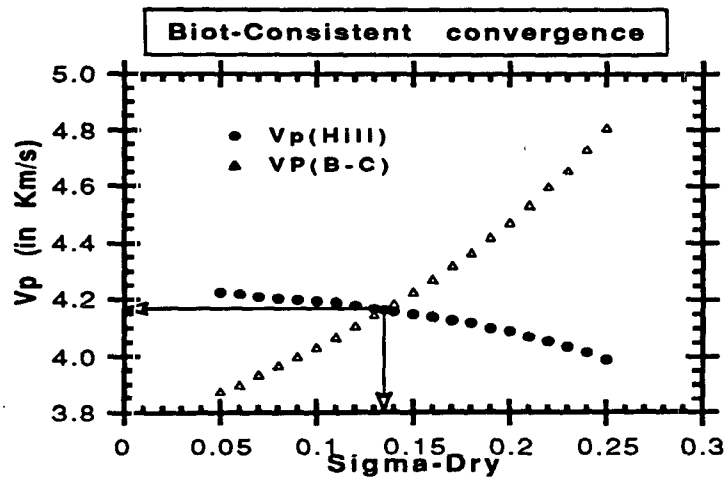


Figure 2.11b: Example calculation using the Biot-Consistent method.

they converge to $V_p = 4.17$ km/s; the aggregate parameters used were: $\mu_s=40$ GPa, $K_s=37$ GPa, $\phi=0.30$, $\phi_p=0.30$, $\phi_c=0$, $K_f=2.2$ GPa, $\rho_f=1$ g/cc, and $\rho_s=2.65$ g/cc. The method is valid for any aggregate made up of interconnected pores and cracks. The method allows for the calculation of the influence of interconnected secondary porosity on wetted dry frame bulk and shear moduli, and on compressional and shear velocities at full water saturation. It is apparent that in-situ fractures (variable ϵ) have a sizeable effect on the elastic behavior of rocks. The Biot-consistent method will not account for non-elastic behavior of rocks, for non-connected microcracks or pores, and for anisotropic media. It remains fairly cumbersome to use, because of the relatively large number of input parameters it requires for calibration.

3) The Krief method

This method is based on Pickett's (1963) observation that the ratio of slownesses for the P (Δt_p) and the S (Δt_s) waves is constant for a gas filled lithology, and changes with porosity for a water saturated lithology. This empirical observation, known as the Pickett relationship, can be expressed as:

$$\frac{V_{pd}}{V_{sd}} = \frac{V_{pma}}{V_{sma}} \quad (22)$$

Krief et al. (1990) summarize the theory of Biot on consolidation (1941) as yielding two equations:

$$\delta(V_f) = \frac{\delta(p)}{M} + \beta\delta(V_{fm})$$

$$\lambda_{fm} = \lambda_{sk} + \beta^2 M$$

where λ is the Lamé coefficient of the formation, β is the Biot coefficient (which measures the ratio of volume change of the fluid to the volume change of the formation under constant hydraulic pressure), M is a modulus, which measures the change in hydraulic pressure that is needed to force some fluid into the formation without inducing any change in the volume of the formation, and $\delta(V_f)$ is the variation in the

volume of the fluid as a function of changes $\delta(p)$ in hydraulic pressure and changes $\delta(V_{fm})$ in the volume of the formation.

He then incorporates the Gassman theory to show that:

$$K_{fm} = K_{sk} + \beta^2 M \quad (23)$$

$$K_{sk} = K_{ma} (1 - \beta) \quad (24)$$

$$\frac{1}{M} = \frac{\beta - \phi}{K_{ma}} + \frac{\phi}{K_f} \quad (25)$$

Krief et al. then use the Pickett relationship, which can be re-written as:

$$\frac{\rho_b V_{pd}^2}{\rho_b V_{sd}^2} = \frac{\rho_{ma} V_{pma}^2}{\rho_{ma} V_{sma}^2}$$

or as

$$\frac{K_{fm}}{\mu_{fm}} + \frac{4}{3} = \frac{K_{ma}}{\mu_{ma}} + \frac{4}{3}$$

and show that for a gas saturated lithology:

$$\frac{K_{fm}}{\mu_{fm}} = \frac{K_{ma}}{\mu_{ma}} \quad (26)$$

since, to a first approximation, at gas saturation, we have $M = 0$, I obtain:

$$\mu_{fm} = \mu_{ma} (1 - \beta) \quad (27)$$

In summary, the following two equations are obtained:

$$\rho_b V_p^2 = \rho_{ma} V_{ma}^2 (1 - \beta) + \beta^2 M \quad (28)$$

$$\rho_b V_s^2 = \rho_{ma} V_{sma}^2 (1 - \beta) \quad (29)$$

Using the dataset of Raymer et al. (1980), Krief et al. (1990) then show empirically that β is related to porosity through:

$$1 - \beta = (1 - \phi)^{\left(\frac{3}{1-\phi}\right)} \quad (30)$$

Krief et al. showed the usefulness of the method in obtaining accurate porosity values from full waveform data. In particular, the coefficient β allows for a smooth transition between formation properties at different states of compaction. Ward (1991) then used the method to obtain synthetic shear waves from a knowledge of porosity, by using equations (29) and (30).

4) The Calibrated Empirical Method: C.E.M.

a) Observations

The previous methods are not trivial, and it is somewhat difficult to readily see the physics that controls the effects of porosity on the shear modulus. After re-examination of the data from Han et al (1986) and Yin et al (1988) measured on Gulf sands, and the data from Troll (clean and loosely consolidated sands), I observe the following:

Figure 2.12 shows that the Troll sands have a much lower dry shear modulus than the consolidated samples of Han; in turn, the weak cementation in the Troll sands yields higher shear moduli than those observed in the packed Ottawa sands, which have no cement at all. This led me to subdivide sands and sandy shales into two groups: those that are consolidated, and those that are unconsolidated or loosely consolidated.

When *consolidated* sands are separated according to the amount of clay they contain, a strong linear trend is apparent between shear modulus and porosity. As seen in figures 2.12a and 2.12c, in general, a more consolidated rock has a higher shear modulus than a less consolidated rock, and exhibits a greater decrease in shear modulus with increasing porosity.

These linear trends appear to break down for *loosely consolidated* samples and for samples with large amounts of clay (figures 2.12b and 2.12d). Note that the trends observed on the saturated measurements (figures 2.12c and 2.12d) are not as clear as those observed on the dry measurements, because saturated measurements are subject to larger experimental uncertainties. The sands from Troll are loosely consolidated "clean" sands, exhibit a non-linear trend, and approximate a lower bound on modulus-porosity trends. Furthermore, if a line were to be fitted to the Troll data in a least squares sense, the slope of the line would be smaller than that for clean Gulf sands; this is due to the difference in consolidation between the two sand types, and indicates that the isostrain or Voigt concept is not applicable to loosely consolidated sediments; furthermore, the isostress or Reuss model for suspensions - which can be successfully applied to the modeling of bulk moduli in loosely consolidated rocks, as shown in figure 2.13b - is not directly applicable to the analysis of shear moduli, because the shear modulus "fluids" tends towards zero. In regressing both dry and saturated shear moduli versus porosity for unconsolidated rocks, I found it convenient to use an exponential function, as suggested by Bryan and Stoll (1988). The exponential fits are superimposed on figures 2.12b and 2.12d.

b) Empirical model

The previous observations led me to adopt the following empirical model for shear velocities in consolidated sands: If I assume that a sand can be represented by a bimodal distribution of "strong" framework grains and "weak" porosity filling material, it will have no shear strength when its critical porosity ϕ_c is reached and for porosities beyond ϕ_c ; in fact, under these conditions, the sand can be considered as a suspension of framework grains within a matrix of porosity filling fluid (air or water). In other words, I identify ϕ_c as the porosity below which the rock begins to have significant shear strength, and beyond which it has essentially no shear strength. Then, for porosities less than ϕ_c , I assume that μ_d is proportional to porosity and we require one calibration point for each lithology; this defines a calibration porosity and a calibration dry shear modulus (Figure 2.14a). A more consolidated rock has a higher

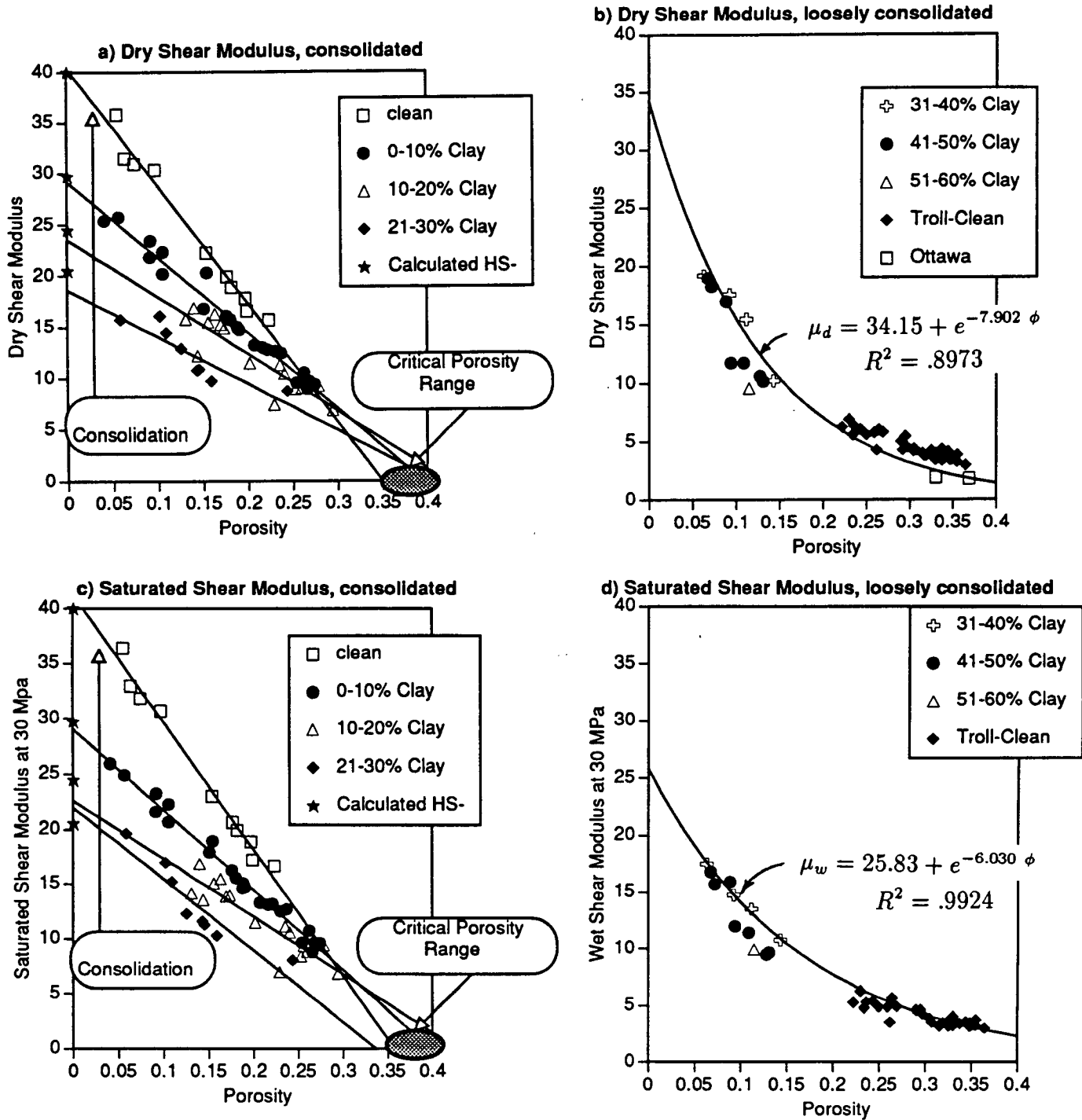


Figure 2.12: a) Data from Yin et al. (1988), and Han et al. (1986), showing dry dynamic shear moduli for consolidated sands as a function of porosity. Hashin-Shtrikman lower bounds are plotted as open squares on the y-axis, for "average" amounts of clay corresponding to 0 %, 5 %, 15%, and 25 %.

b) Data from Troll, Domenico (1976), Yin et al. (1988), and Han et al. (1986), showing dry dynamic shear moduli for less consolidated sands as a function of porosity; an exponential fit is superimposed.

c) Data from Yin et al. (1988), and Han et al. (1986), showing saturated dynamic shear moduli for consolidated sands as a function of porosity.

d) Data from Troll, Domenico (1976), Yin et al. (1988), and Han et al. (1986), showing saturated dynamic shear moduli for loosely consolidated sands as a function of porosity; an exponential fit is superimposed.

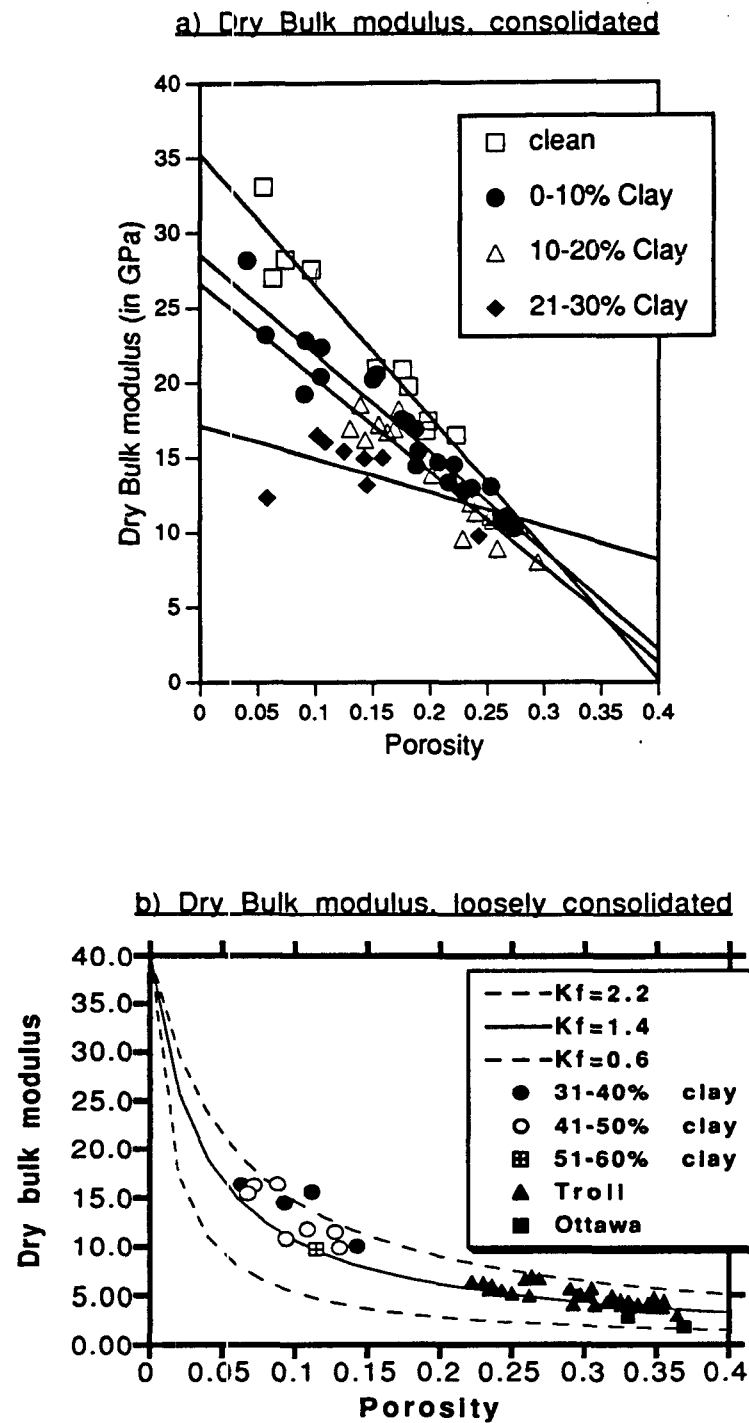


Figure 2.13: Comparison of dry bulk moduli for the Troll samples, Ottawa sands, Yin et al (1988), and Han's data.

a) For consolidated sands; the straight lines correspond to linear regressions for different lithologies.

b) for less consolidated sands; the theoretical curves represent the Reuss or isostress model for a suspension of sand grains in a matrix of fluid filled porosity, with bulk modulus K_f . Departures from the theoretical curves are most probably due to variations in the effective moduli of the fluid or the matrix.

shear modulus than a less consolidated rock (its calibration point is "higher"), and therefore exhibits a greater decrease in shear modulus with increasing porosity (larger slope). The postulated linear trend between porosity and dry shear modulus is valid under fixed conditions (in particular, at constant effective pressure and temperature) and can be expressed as:

$$\mu_d = \mu_m \left(1 - \frac{\phi}{\phi_c} \right); \phi \leq \phi_c \quad (31)$$

As porosity tends towards zero, μ_d tends toward μ_m , and all lithologies go through the point with coordinates $(\phi_c, 0)$. The effect of clay is to change the slope and intercept of the curve. According to the model, as the amount of clay (the "weak" component) increases, or as consolidation decreases, the overall dry shear modulus decreases and the slope of the curve (μ_m) decreases. It is also interesting to note from the data, a slight change in critical porosity from 0.36 for clean sands, to 0.38 for the sands with 0 % to 10 % clay content, to 0.40 for the sands with 10 % to 20 % clay content, and to 0.42 for the sands with 20 % to 30 % clay content (figure 2.12a).

Figure 2.14a shows what the empirical behavior of the shear modulus would be for less competent sands; these sands may consist of a mixture of sand and clay for example, for which μ_m is lower than 40 GPa. In the C.E.M. model, the first few percent of clay can be assumed to surround the quartz grains and drastically weaken the effective mineral modulus leading to $K_{q-eff}=39$ GPa and $\mu_{q-eff}=33$ GPa, in accordance with the observations of Han (1986). The remaining amounts of clay surround the weakened quartz grains in a manner which I assume is consistent with the Hashin-Shtrikman lower bound (figure 2.14b), where the average bulk and shear modulus of the clay are $K_{clay}=21$ GPa and $\mu_{clay}=7$ GPa ; in other words, μ_m is calculated as:

$$\mu_m = \mu_c + \frac{1 - c}{\frac{1}{\mu_q - \mu_c} + \frac{2c(K_c + 2\mu_c)}{5\mu_c(K_c + \frac{4}{3}\mu_c)}}$$

This is a good assumption, as seen from the Hashin-Shtrikman lower bounds calculated at zero porosity which are plotted as open squares on the y-axis (at 0 %

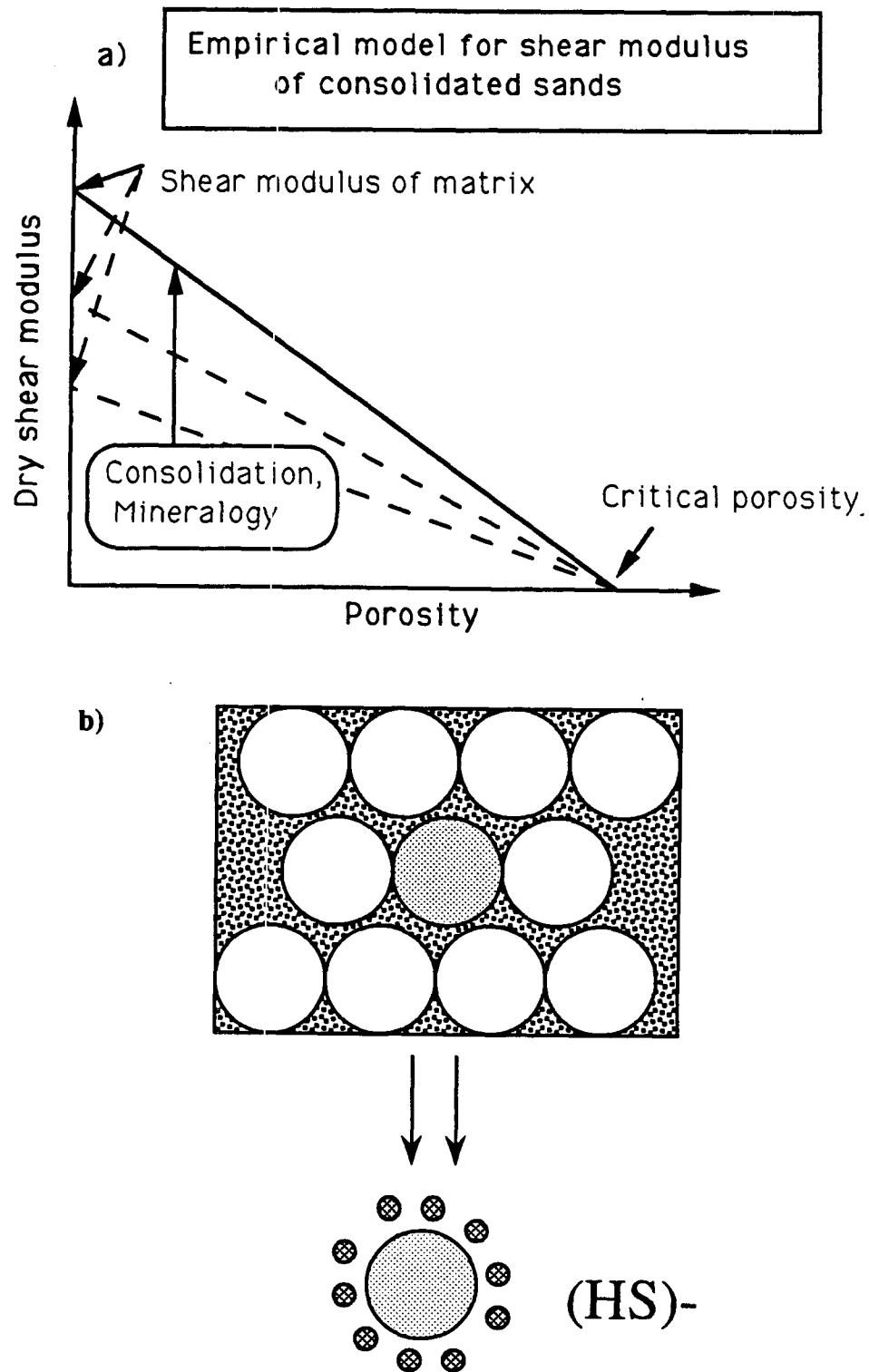


Figure 2.14: a) An empirical model for dynamic shear moduli as a function of porosity. A linear trend is defined; all lines pass through one point defined at critical porosity which has zero shear modulus; another point -of tighter porosity- defines the shear modulus for its specific lithology; the y-axis intercept defines the shear modulus of the matrix.

b) The clay content can be modeled to a first approximation as the Hashin-Shtrikman lower bound between quartz and clay, because clay can be assumed to surround the quartz grains and it is the weaker phase.

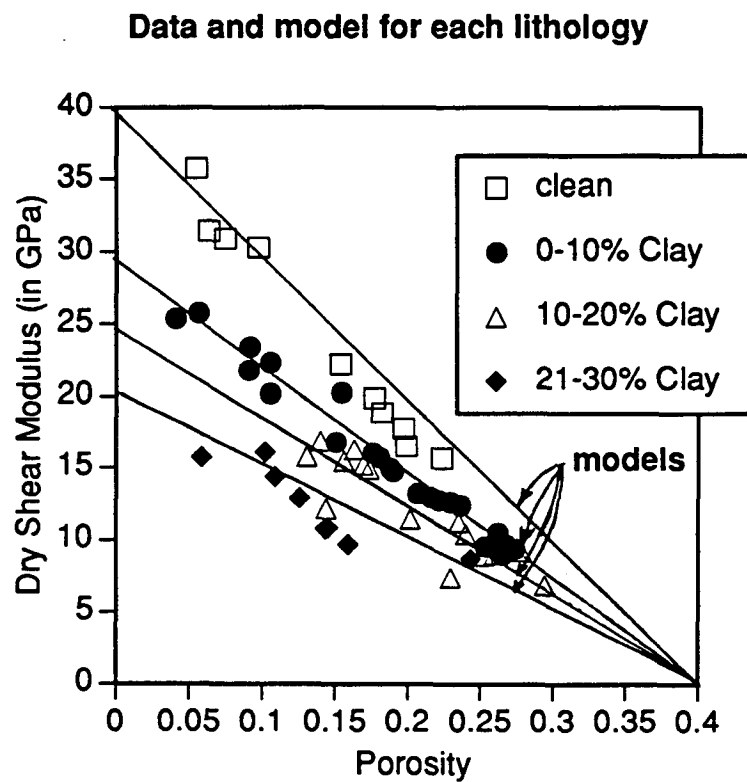


Figure 2.15: The model reproduces the two essential characteristics that are observed for the behavior of the shear modulus:

- A linear decrease with porosity, for a given mineralogy.
- A diminishing effect of increased amounts of clay on the reduction of the shear modulus; in other words, the first few percent of clay have the largest effect on the shear modulus, and any additional amount of clay result in less and less of a drop in shear modulus.

porosity) in figure 2.12a, for "average" amounts of clay corresponding to 0 %, 5 %, 15%, and 25 %, and correspond to the clay averages for the four arbitrary classes chosen (ie, 0 % clay, 0 %-10 % clay, 10 %-20 % clay, and 20 %-30 % clay). In a sense, the model can be seen as a type of "double embedding" method (Samstag and Morgan, 1991), where the matrix effective properties are evaluated in a first step through a Hashin-Shtrikman lower bound at zero porosity, and where the isostrain model is applied in a second step to incorporate the effects of porosity and those of the porosity filling material. Figure 2.15 shows that the model reproduces the two essential characteristics that were previously observed for the behavior of the shear modulus:

- A linear decrease with porosity, for a given mineralogy.
- A diminishing effect of increased amounts of clay on the reduction of the shear modulus; in other words, the first few percent of clay have the largest effect on the shear modulus, and any additional amount of clay result in less and less of a drop in shear modulus.

c) Comparison with other models

The empirical model defined above is equivalent to the isostrain or Voigt (1928) model, where the effective shear modulus of the rock forming components (a mixture of quartz and clay), and the shear modulus of a "weak" matrix (which is composed of water or air with only minor amounts of clay and with zero shear modulus) are averaged arithmetically:

$$\mu_d = \left(1 - \frac{\phi}{\phi_c}\right) \mu_m + \frac{\phi}{\phi_c} \mu_f \quad (32)$$

As μ_f tends to zero, then μ_d tends towards $\mu_m \left(1 - \frac{\phi}{\phi_c}\right)$, which is equivalent to the empirical model formulation in equation (31).

In order to test the model of equation (31), I compare it to the Krief et al. (1990) relationship for consolidated sands, to the Biot-Consistent model (Thomsen, 1985),

and to the Kuster-Toksoz (1974) model. The Krief model was derived from Biot principles, and a "Biot coefficient" β was found by fitting an empirical relationship similar in form to that of Raymer et al. (1980) for consolidated sands. This yields a formula of the type:

$$\mu_d = (1 - \beta) \mu_m; \text{ where } (1 - \beta) = (1 - \phi)^{\left(\frac{3}{1-\phi}\right)} \quad (33)$$

where β is known as the Biot coefficient. The Krief model has been shown to work well (Ward, 1991).

The Kuster-Toksoz scattering model (K-T) was derived for specific geometries. For spherical pores it yields a dry shear modulus equal to:

$$\mu_d = \frac{\mu_m (1 - \phi)}{1 + \phi \left(\frac{6K_m + 12\mu_m}{9K_m + 8\mu_m} \right)} \quad (34)$$

which is equivalent to the Hashin-Shtrikman upper bound and, for most rocks, tends towards:

$$\mu_d = \mu_m \left(\frac{1 - \phi}{1 + \phi} \right) \quad (35)$$

The Biot-Consistent (BC) model (section III-2) yields a shear modulus equal to (equation 17, using a fracture density $\epsilon=0$):

$$\mu_d = \mu_m \left(1 - \frac{\phi}{1 - b_B} \right)$$

in turn, this expression is approximately equal to $\mu_m (1 - 2\phi)$ for most rocks.

In order to back-out lithology effects, or the effects of μ_m , I compare the expressions for "normalized" dry shear moduli: $\frac{\mu_d}{\mu_m}$. Figure 2.16 shows the good agreement between my model (C.E.M.), the Biot-Consistent model, and the Krief model for porosities less than ϕ_c ; the Kuster-Toksoz model yields somewhat larger shear moduli for spherical pores, and would yield lower moduli if I was to use a different spectrum of pore aspect ratios. The parameters chosen for the models were those of clean sands: $\mu_m = 40$ MPa, and $\phi_c=0.40$.

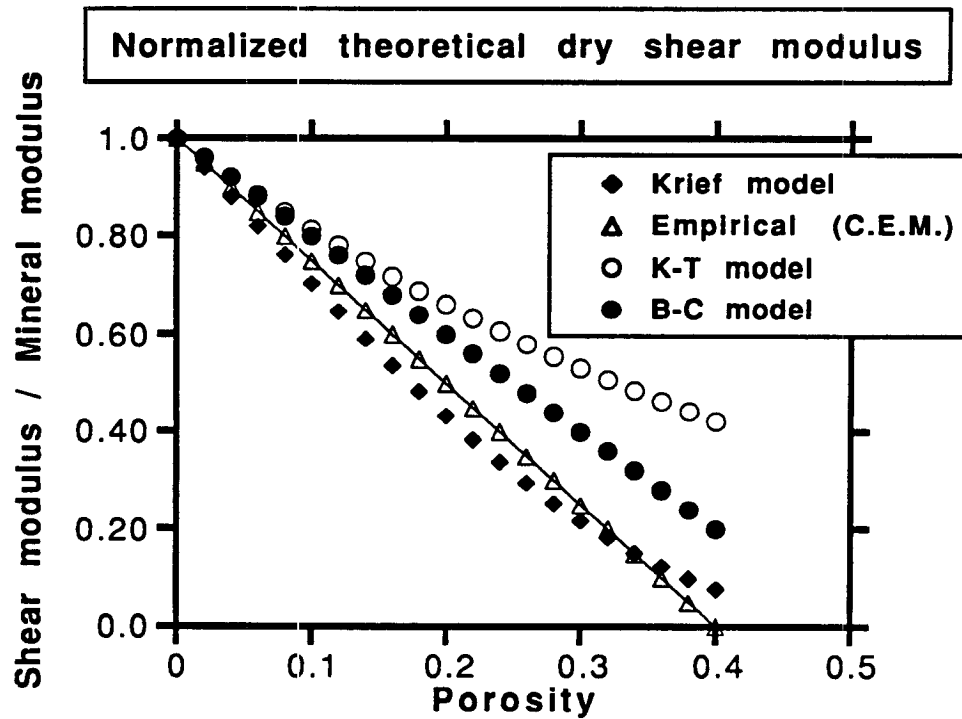


Figure 2.16: Comparison of modeled dry shear moduli between the empirical model, the Kuster-Toksoz (1974) model, the Biot-Consistent model (1985), and the Krief (1990) model. My model (C.E.M.) is simpler than existing models, yet it produces almost identical results to the other models, for porosities less than ϕ_c .

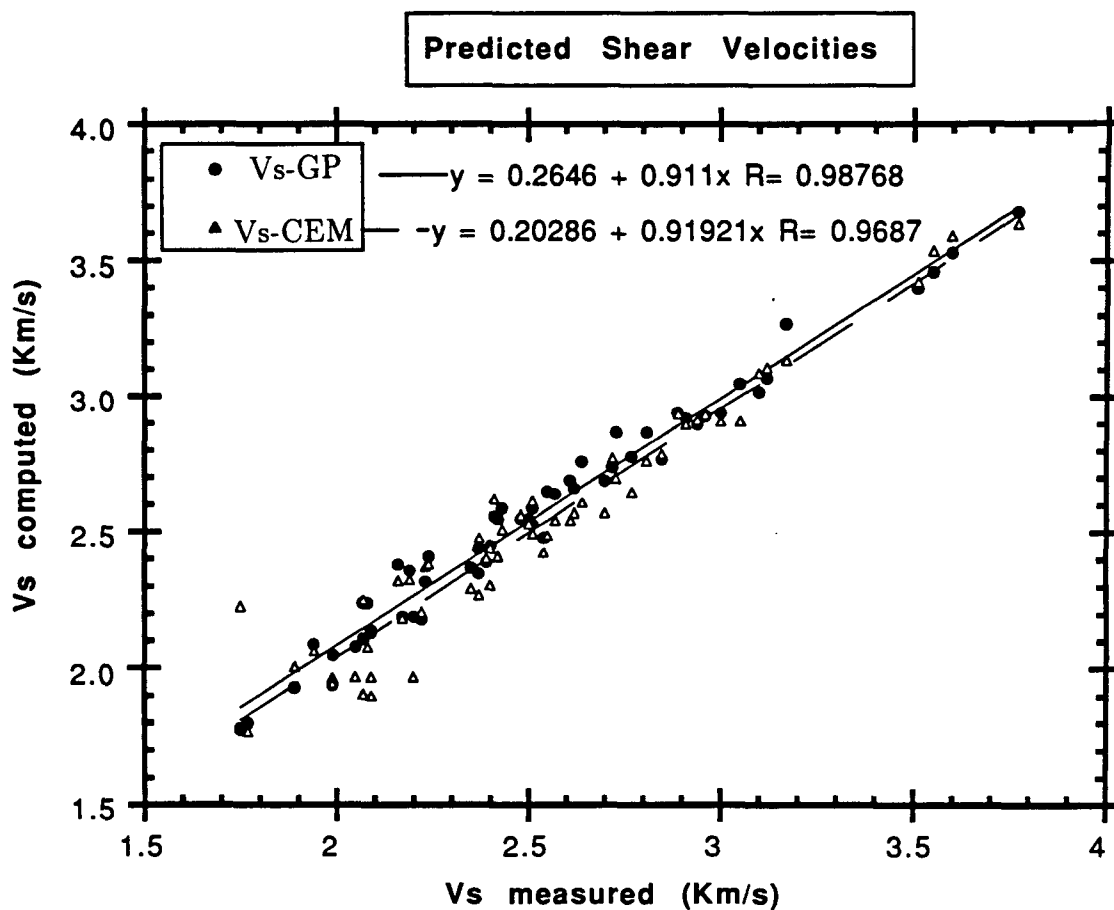


Figure 2.17: Comparison between my predictions of shear velocities (C.E.M.) to those made using the Gregory-Pickett method for the data of Han with less than 30 % clay. In general, the results are very good, the Gregory-Pickett method showing a slightly tighter linear trend, but overestimating the measured shear, while my predictions show a closer fit to the data. Note the C.E.M. method is not as accurate for the samples with the lowest shear velocities, which also correspond to the samples with the most clay. There is a trade-off between the knowledge of clay content and porosity, needed for the C.E.M. model, and the knowledge of V_p , porosity, and K_m needed for the Gregory-Pickett method.

I also compared shear velocity predictions made using the C.E.M. model to predictions calculated using the Gregory-Pickett method (see Castagna et al., 1985 for example). The method is based on the assumption that K_d is equal to μ_d ; this is similar to assuming that the dry V_p/V_s ratio is 1.53 (after Pickett, 1963) or to assuming a dry rock Poisson's ratio of 0.125. Gassman's equations can then be solved for μ_d through a second degree equation. The parameters needed for input are V_p , porosity, and the densities and bulk moduli of the matrix and fluid ρ_m , K_m , ρ_f , and K_f ; the dry shear modulus can then be used to calculate the shear velocity. Figure 2.17 compares my predictions of shear velocities to those made using the Gregory-Pickett method for the data of Han with less than 30 % clay. In general, the results are very good, the Gregory-Pickett method showing a slightly tighter linear trend, but overestimating the measured shear, while my predictions show a closer fit to the data. Note that my method (C.E.M.) is not as accurate for the samples with the lowest shear velocities, which also correspond to the samples with the most clay. It must be remembered that the C.E.M. method yields an upper bound on the expected shear velocities. In general, there is a trade-off between the knowledge of clay content and porosity, needed for the C.E.M. model, and the knowledge of V_p , porosity, and K_m needed for the Gregory-Pickett method.

As a final remark, recall that the Krief model showed that the dry shear modulus was equal to:

$$\mu_d = \mu_s (1 - \phi)^{\frac{3}{1-\phi}}$$

which can be expanded in a Taylor series (for small porosities, and dropping second order terms in porosity) as:

$$\mu_d = \mu_s \left\{ 1 - \phi \left(\frac{3}{1-\phi} \right) + \left(\frac{3}{1-\phi} \right) \left(\frac{3}{1-\phi} - 1 \right) \frac{\phi^2}{2} + \dots \right\} = \mu_s \{ 1 - 3\phi + \dots \}$$

while the Kuster and Toksoz model yields:

$$\mu_d = \mu_s \left(\frac{1-\phi}{1+\phi} \right)$$

which, for small porosities, can be expanded as:

$$\mu_d = \mu_s (1 - 2\phi + \dots)$$

and the Biot-Consistent method yields (approximately):

$$\mu_d = \mu_s (1 - 2\phi + \dots)$$

The C.E.M model shows that $\mu_d = \mu_s \left(1 - \frac{1}{\phi_c} \phi\right)$, where ϕ_c usually takes-on a value of 0.38 to 0.40. This empirical determination yields a value of $\frac{1}{\phi_c}=2.5$, which is intermediate between the values found with the Kuster and Toksoz and the Biot-Consistent model ($\frac{1}{\phi_c}=2$) and Krief ($\frac{1}{\phi_c}=3$) models.

d) Implications of the model

In summary, it can be stated that Biot defined a coefficient $\alpha = 1 - \frac{K_d}{K_m}$; Krief et al. (1990) generalized the concept to shear moduli, by introducing the coefficient $\beta = 1 - \frac{\mu_d}{\mu_m}$; they then found an empirical formulation for β (equation 33). The results of equation (31) show that for consolidated sands, $\beta = \frac{\phi}{\phi_c}$.

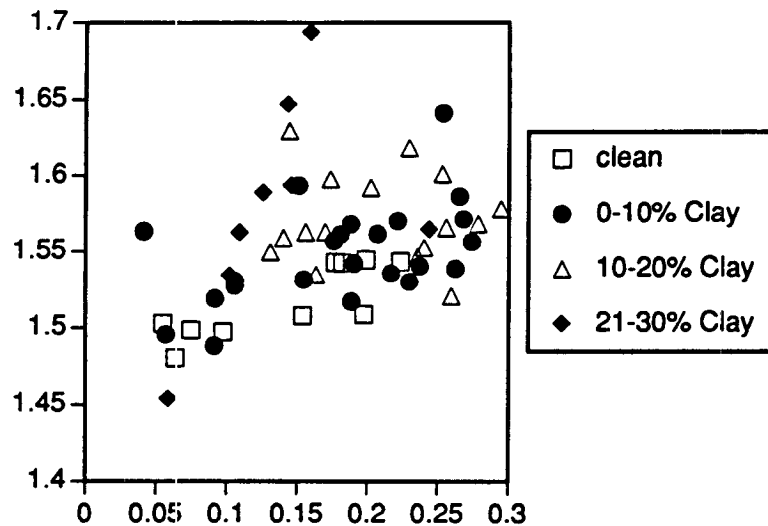
Let's consider the observations of Pickett (1963) - the dry V_p/V_s ratios are constant for all porosities -, and let's assume that equation (31) holds. Then, our assumptions yield a similar equation for the dry bulk modulus:

$$K_d = K_m \left(1 - \frac{\phi}{\phi_c}\right) \tag{36}$$

In fact, this trend can be recognized in figure 2.13a, where there is more scatter in the K_d data than was seen for the case of dry shear modulus. Then, for clean sands, the dry V_p/V_s ratio should be equal to:

$$\frac{V_p}{V_s} = \sqrt{\frac{K_d}{\mu_d} + \frac{4}{3}} = \sqrt{\frac{K_{ma}}{\mu_{ma}} + \frac{4}{3}} = \sqrt{\frac{38}{40} + \frac{4}{3}} = 1.51$$

Similar arguments would yield dry V_p/V_s ratios of 1.61 for sands with 5 % clay, 1.66 for sands with 15 % clay, and 1.71 for sands with 25 % clay, when using a Hashin-Shtrikman lower limit for the matrix moduli, as discussed in figures 2.14 and 2.15. The results from lab measurements are presented in figure 2.18a; the trend is in agreement with theoretical predictions, showing that the more clay in the sand, the higher the dry V_p/V_s ratio. However, note that the ratios are not quite constant with porosity.

a) Effect of clay content on dry V_p/V_s 

b) Effect of clay on dry bulk / dry shear modulus ratio

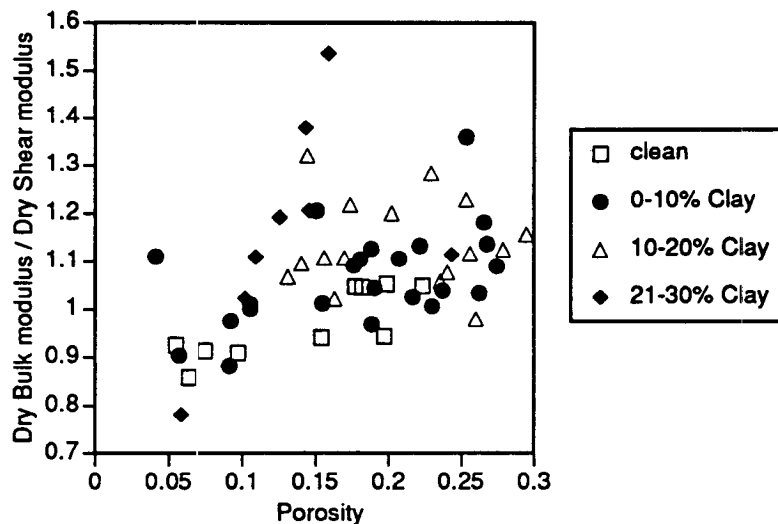


Figure 2.18: a) Dry V_p/V_s ratios plotted as a function of porosity for different sands at 30 MPa effective pressure. The data is in general agreement with Pickett's observation that dry V_p/V_s ratios are quasi constant with porosity. In general however, it appears that the larger the clay content, the larger the dry V_p/V_s ratio.

b) Dry ratio of bulk to shear modulus for the data from Gregory (1976), Domenico (1977), Han (1986 a,b), Yin et al. (1988), and Klimentos et al. (1990). Note that, as observed by Castagna et al. (1985) and to a first approximation $K_d = \mu_d$, but that in general, the ratio increases somewhat with clay content and porosity.

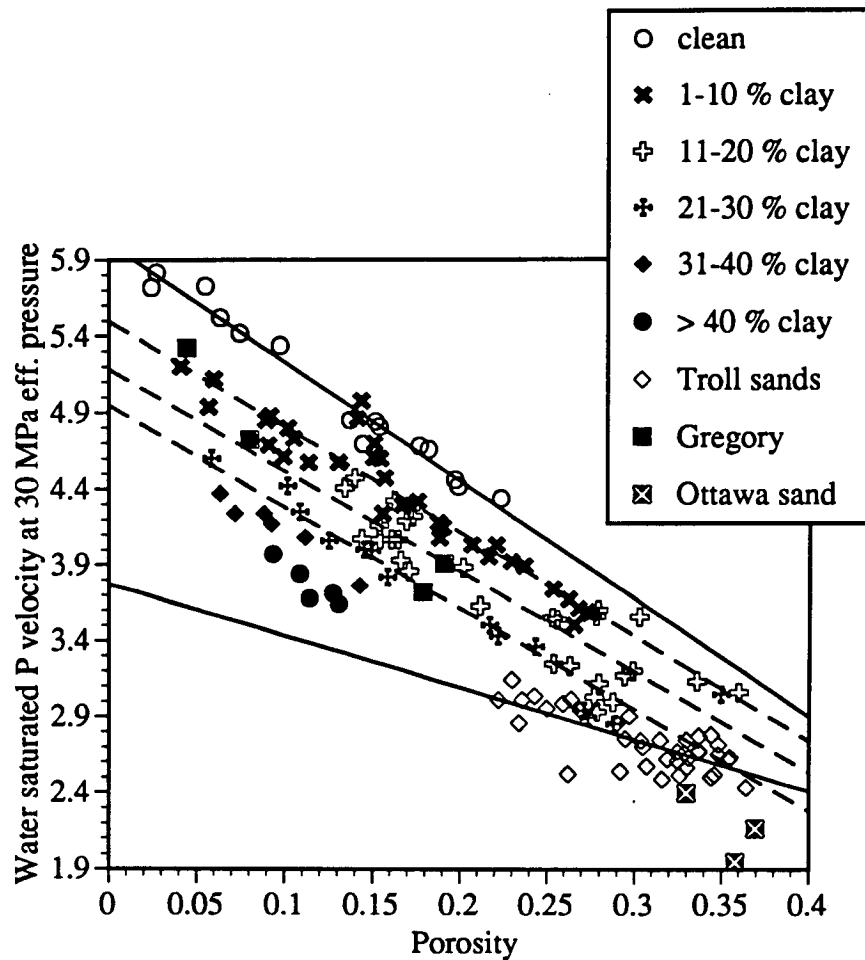


Figure 2.19: Comparison of velocity-porosity relationships for 100 % water saturated samples. Data are from Troll, Gregory (1976), Domenico (1977), Han et al (1986 a,b), Yin et al (1988), and Klimentos et al (1990).

It is interesting to note that the C.E.M. model implies that dry V_p/V_s is constant with porosity, and that K_d is approximately equal to μ_d (since K_{ma} is approximately equal to μ_{ma}) as observed by Castagna et al. (1985). Again, this observation is only an approximation, as seen in figure 2.18b.

The model can also help us understand the slopes of the velocity versus porosity curves, and in particular it explains why dry consolidated sands with different amounts of clays plot as more or less parallel trends (as seen figure 2.19). From equations (31) and (36), we have:

$$V_p = V_{pma} \sqrt{\frac{1 - \frac{\phi}{\phi_c}}{1 - \phi}}$$

$$V_s = V_{sma} \sqrt{\frac{1 - \frac{\phi}{\phi_c}}{1 - \phi}}$$

These equations reveal that the slope of the curves shown in figure 2.19 for varying amounts of clay content are very similar: $\frac{\delta V_p}{\delta \phi} = V_{pma} * f(\phi)$; where $f(\phi)$ is solely a function of porosity; neglecting density effects, the variations in the term V_{pma} due to variations in clay content from 0 % to 30 % is relatively small, and therefore, the change in slope is also small.

Finally, the model shows that V_p^2 is linearly related to V_s^2 for gas saturated sands. Indeed, for dry states, the model yields: $\mu_d = a\phi + b$; $K_d = c\phi + d$ so that

$$V_p^2 = AV_s^2 + B$$

where a, b, c, d, A, and B are constants.

In conclusion, my simple model (C.E.M.) for shear should prove useful for model-based seismic lithologic interpretation or inversion, for sensitivity analyses, and in cases where shear wave measurements were not available. However, it can only be used for fairly consolidated sands with less than approximately 30 % clay. When in the presence of shales or shaley sands of unknown composition and unknown state of consolidation, I recommend using the Castagna et al. (1985) "mud" formula: $V_P = 1.16V_S + 1.36$, where velocities are given in Km/s. The strength of this linear relationship comes from the fact the V_P and V_S properties of most clays fall close to a line connecting the water point to the quartz point on a V_P - V_S cross-plot; this line is called the "mud" line.

e) Applications of the model

Next, I test the model against full-waveform sonic results obtained in a well at Cajon pass, California. Since there is no data on frequency dispersion between ultrasonic and sonic frequencies, I chose to ignore these effects to a first approximation, and to use equation (31) "as is" for sonic saturated measurements.

The data is particularly bad in the shallow parts of the hole, and shear velocity picks from Schlumberger's SDT and an older 12 channel sonic tool differ substantially from Mobil's dipole shear measurements. Because the sands are arkosic, with varying amounts of Potassium feldspar, it was not possible to obtain an estimate of clay content from the natural gamma ray spectroscopy tool; a constant matrix shear modulus was assumed instead. To obtain a reasonable estimate of the wetted dry shear modulus, I used a crossplot of shear modulus obtained from the dipole shear measurements versus porosity for relatively "good" hole conditions; more specifically, constraints were imposed on the caliper, porosity, and density correction curves. The plot indicates that the overall matrix shear modulus of the sands is approximately 12.5 GPa and the critical porosity is around 0.45 (Figure 2.20a).

The synthetic shear results obtained by applying equation (31) are presented in figure 2.20b. It is surprising to see how well the data fits the measured shear velocities obtained with the dipole shear tool even though a constant matrix shear was assumed. The shear velocity data obtained from the two standard axisymmetric tools are not shown, because they strongly disagreed with the dipole shear results; this was probably due to the relatively large size and rugosity of the borehole. The Gregory-Pickett method of shear velocity determination (Castagna et al., 1985) is also shown for comparison. My synthetic shear results track the dipole shear velocities almost peak for peak throughout the interval and are for the most part closer to the measured shear than the synthetics obtained with the Gregory-Pickett method.

In general, the C.E.M. method yields good estimates of the shear velocity; these synthetic shear values can be regarded as upper bounds on shear velocities. Since our method is based on the shear modulus of the frame (μ_m) and on porosity, it is subject to errors if these properties are not well known. The Gregory-Pickett method on the other hand, requires knowledge of the frame bulk modulus (K_m), porosity, and V_p , and is subject to errors in the estimate of these three properties; it also makes the assumption that dry V_p/V_s is 1.53, which is not always true as seen in figure 2.18a, and also yields estimates of shear velocities which are too high, as seen in figure 2.17.

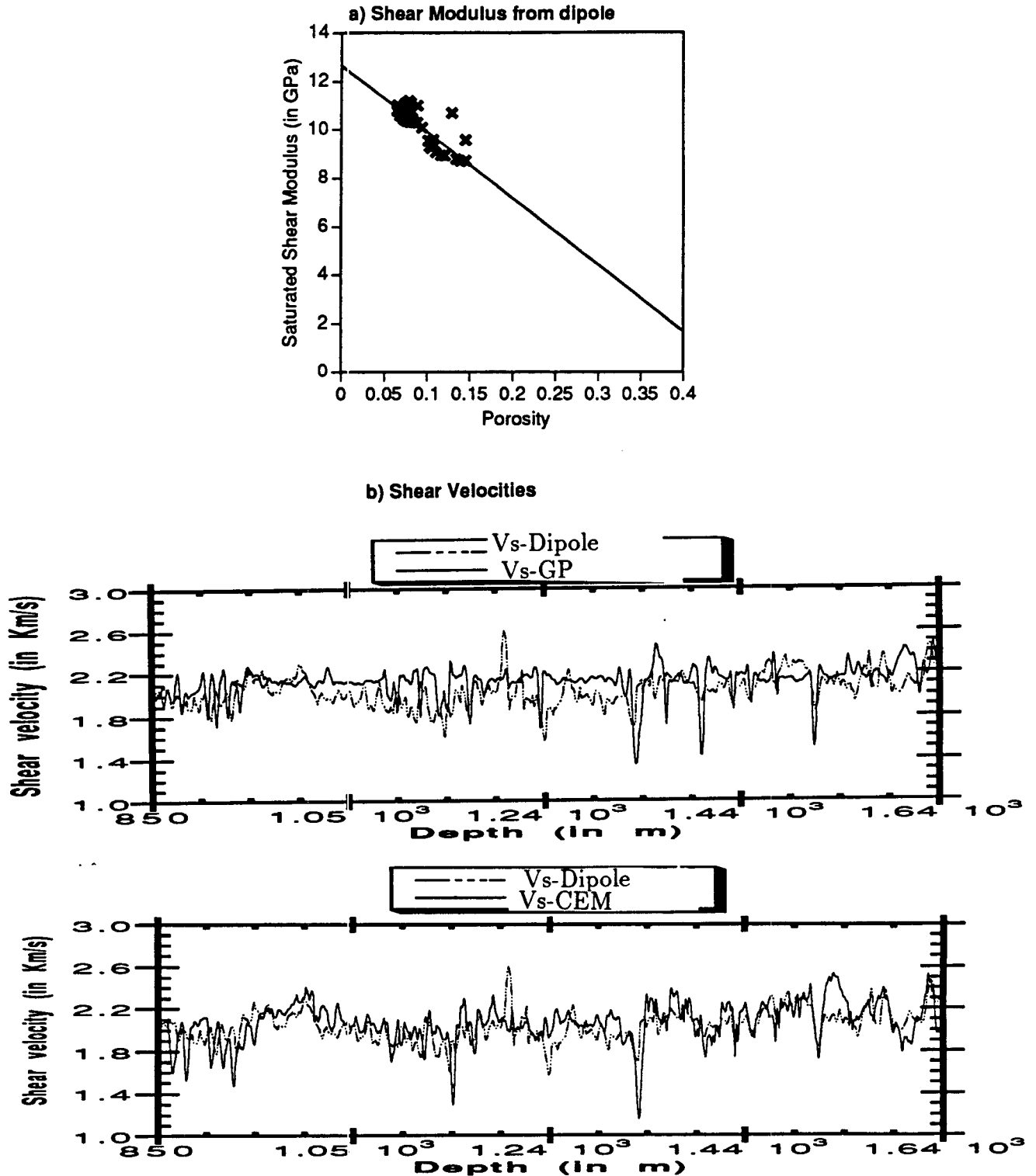


Figure 2.20: a) Crossplot of shear modulus obtained from the dipole shear measurements versus porosity for relatively "good" hole conditions. This indicates that the overall matrix shear modulus of the sands is approximately 12.5 GPa and the critical porosity (ϕ_c) approximately 0.45.

b) Agreement between the model for shear velocities (as calculated from equation 31) and the shear velocities measured via Mobil's dipole tool. Synthetic shear estimates using the Gregory-Pickett method (Castagna et al. 1985) are also plotted for comparison.

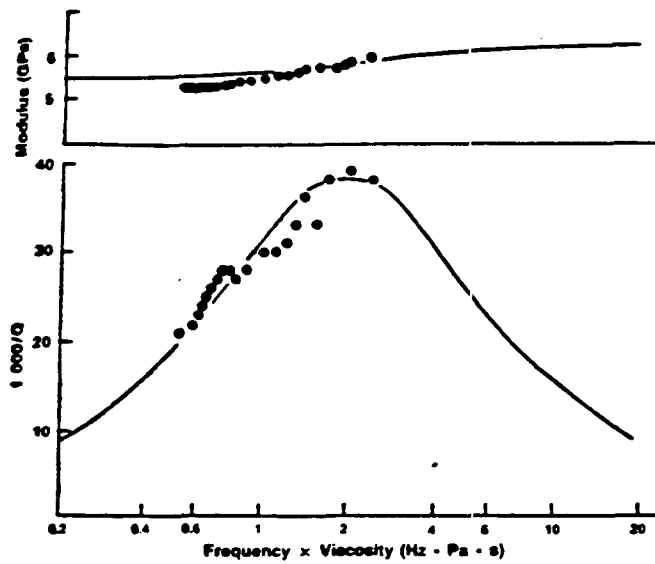
The advantage of the Gregory-Pickett method is that it incorporates intrinsically the effects effective pressure through the use of the compressional velocity; however, for lithologic inversion purposes it may be better to try to dissociate in-situ related effects, such as pressure and temperature, from compositional and fluid effects. In conclusion, the C.E.M. method appears to be sound for consolidated rocks with less than 30 % clay; further work is required to understand shear velocities in unconsolidated sediments, in sediments with more than 30 % clay, and under low effective pressures (less than approximately 10 MPa).

The proposed empirical model for dynamic shear moduli (and shear velocities) as a function of porosity in consolidated sands compares well to existing and more complicated models, and is consistent with isostrain concepts. It also predicts reasonably well the shear velocities obtained from a dipole tool in consolidated sands.

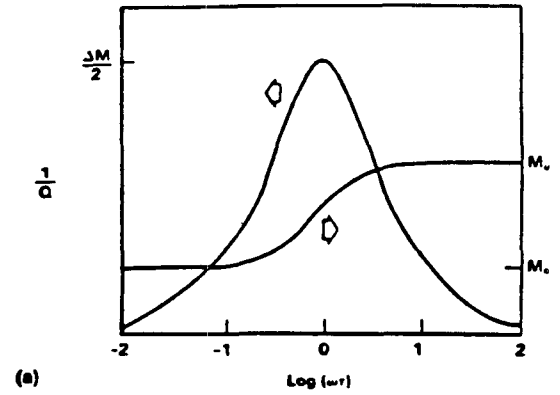
In conclusion, the models presented here should be used on a depth by depth basis to obtain rock properties at the microscale; they are ideal for use with logs that have been calibrated with core data for example. They are particularly useful in modeling the changes in wetted dry frame moduli of reservoir rocks. Chapter 3 will discuss how to bridge these properties over to the seismic domain, by upscaling and averaging to seismic wavelengths.

IV)-DETERMINISTIC MODELING OF VISCOELASTIC ATTENUATION

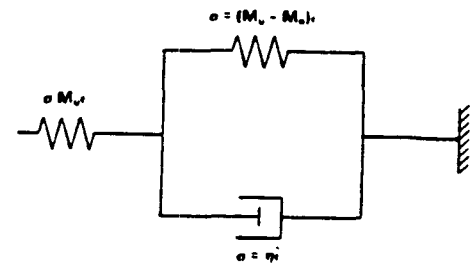
The results of chapter 1 show that, because the earth is attenuative, interpreting reflection seismic data in terms of simple elastic models may give rise to an apparent and false degree of detail which would otherwise be smoothed-out when using viscoelastic models; this concept was first expressed by Kennett in 1975. One of the challenges of reservoir characterization then becomes to determine attenuation values for building more accurate models of the earth. I am referring to intrinsic attenuation, which is a property of rocks, as opposed to "extrinsic" attenuation, which is



Seismic shear attenuation and shear modulus measured as a function of frequency times pore fluid viscosity in a Berea sandstone. The confining pressure was 10 mPa and the pore pressure was 4.5 mPa. The pore fluid was water. Temperature varied from 20°C to 120°C.



(a)



(b)

(a) Frequency-dependent modulus and attenuation of a standard linear solid. (b) Spring and dashpot model of standard linear solid.

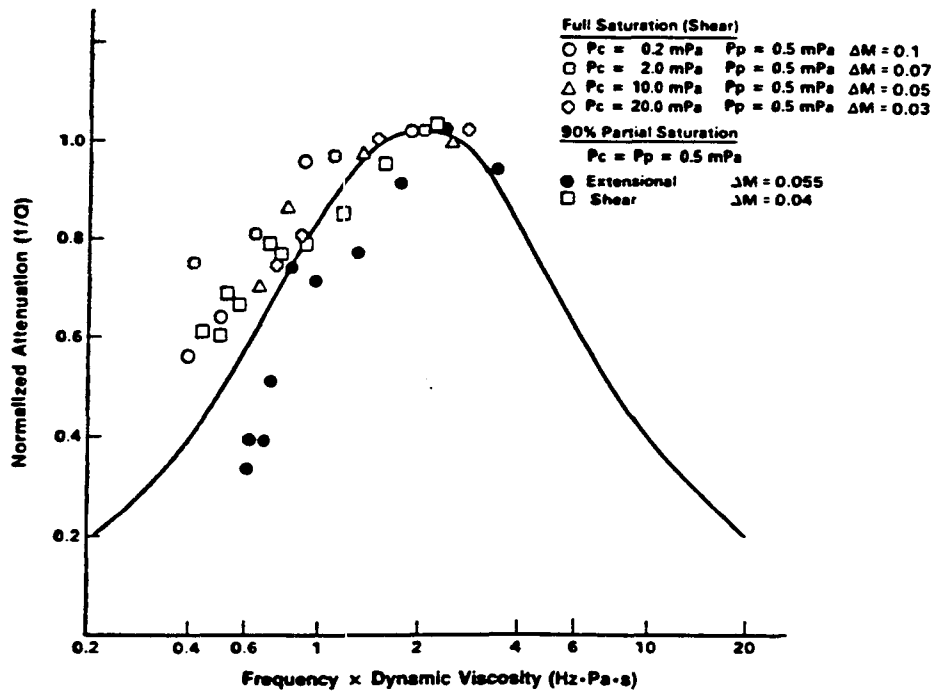


Figure 2.21: The Standard linear solid (Liu et al., 1976) can be used to quantify the effects of attenuation on velocities; figure modified after Jones (1986).

mostly due to scattering (Shoenberger and Levin, 1974, Spencer et al, 1982, Menke and Dubendorff, 1985). Large amounts of extrinsic attenuation can be observed in areas with thin alternating beds, such as sand-shale sequences in a turbidite facies, so that the reflectors lose their continuity and brightness. This suggests that attenuation is related to lithological cycles and that, like seismic velocity, it is a function of scale. In other words, areas with alternating thin bedded sedimentation have, in general, a higher attenuation than areas of transitional sedimentation (Spencer et al., 1982). This type of "attenuation" is mostly related to transmission effects through thin beds, rather than to the intrinsic attenuation of the sediments themselves. According to Waters (1987), intrinsic attenuation accounts for approximately one third to one half of the total attenuation found in seismic work.

There are some areas in the world (offshore Gulf of Mexico for example, Unocal, Personal communication) that exhibit a strong correlation between the presence of gas and areas of anomalously high seismic intrinsic attenuation. These are commonly referred to as "shadow zones", beneath gas sands. Because of these zones, seismic attenuation has been studied extensively. In general, geophysicists assume a linear frequency dependence of absorption over all frequencies. This may be an oversimplification, but is useful nevertheless. Furthermore, laboratory studies of absorption in partially gas saturated rocks is generally larger than that for either complete gas saturation or complete brine saturation (Frisillo and Stewart, 1980, Murphy, 1982).

One challenge facing geoscientists in the future is to try to use information from intrinsic attenuation as an aid in lithologic identification on stacked sections, and as a tool for reservoir characterization. Unfortunately, seismic intrinsic attenuation is not well understood. A myriad of mechanisms have been proposed for intrinsic attenuation, including: matrix anelasticity (frictional dissipation at grain boundaries, Walsh, 1966), thermoelastic attenuation (Savage, 1966, Kjartansson, 1979), fluid flow (dissipation in a fully saturated rock due to motion of the frame with respect to inclusions, Biot, 1956), combined fluid losses and frame losses (Stoll and Brian, 1970, Keller, 1989), intercrack flow or squirting flow (Mavko and Nur, 1975, O'Connell

and Budiansky, 1977), partial saturation effects due to gas-pocket squeezing (White, 1975, Dutta and Ode, 1979, Dutta and Seriff, 1979), intracrack flow (Mavko and Nur, 1979), and a whole family of effects related to geometry (scattering off pores as in Kuster and Toksoz, 1974, and thin bed effects, as in Spencer et al, 1977); a series of other papers use self-consistent theory to predict attenuation. These are reviewed in Toksoz and Johnston (1981) and Bourbie et al (1987).

The truth is that it is likely that different mechanisms affect attenuation under different conditions of saturation, pressure, and frequency. A comprehensive theory including and accounting for all mechanisms under all conditions is not available today. However, it is generally accepted that intrinsic attenuation is mostly due to viscous fluid flow mechanisms in the pore space, because it appears to be a function of frequency, and because its behavior appears to fit a Zener-type model (Murphy, 1982, Jones, 1983). A combination of Biot theory with squirt flow and intracrack flow would therefore be desirable; unfortunately, it is not currently available, but it is an active area of research (Dvorkin and Nur, 1992). The good news is that, for all practical purposes, the phenomenological model relating dispersion to attenuation (Liu et al., 1976) can be used conveniently, in relating seismic velocities to seismic attenuations at different frequencies.

As evidenced by both theoretical and experimental findings, attenuation is not independent of frequency for saturated rocks as postulated by Kjartansson (1979). In fact, large peaks in attenuation have been observed in the low to mid KHz range (Murphy, 1982, Jones and Nur, 1983). This information can be used to calibrate dispersion effects between seismic, sonic, and laboratory frequencies as in Winkler (1985).

Winkler (1985) and Jones (1986) summarized the duality between viscoelastic attenuation and velocity dispersion by re-introducing a phenomenological model relating dispersion to attenuation (Liu et al., 1976) for shear waves through the product of frequency times fluid viscosity (figure 2.21). I use this type of approach to calculate

"average-Q" values from the discrepancy between "average-velocities" at different frequencies for a given lithological layer; in what follows, I will refer to "average" velocities for a lithologic interval, and I will use velocity dispersion results to back-calculate "average Q". This method assumes that all of the non-Biot dispersion is due to squirt flow type attenuation. The calculation of individual or local Q values is not a goal here, since it is extremely variable. Budiansky and O'Connell (1980) show that average Q values of composites can be calculated when crack to pore flow relationships are known. However, this includes terms in the power of three and makes Q calculations highly uncertain. As a last remark, Spencer et al (1982) defined Q_e (the effective Q) as the time-weighted average of the dissipation in the different rock types being traversed by a wave:

$$\frac{1}{Q_e} = \sum_{Interval} \frac{1}{Q_i} \frac{t_i}{t_{total}}$$

where the interval refers to a depth interval for VSP work, but could also refer to a seismic time interval, corresponding to the time that it takes a wave to travel within an interval of interest.

Practical considerations:

In prospect areas, velocity dispersion data can typically be obtained from: 1) a combination of check shot information (high quality velocity estimates at seismic frequencies) and log data, or 2) from core velocity data at in-situ conditions and from check shot data, or 3) from the pressure dependency of velocities (as in Mavko and Jizba, 1991). However, methods which obtain velocity dispersion from core data suffer from the possibility of undersampling, because core data is seldomly obtained in a continuous way.

Biot dispersion:

Using Biot theory (Biot, 1956a, 1956b), it is possible to calculate low and high-frequency limiting velocities for saturated rocks; this yields a value for "Biot-dispersion", which was defined as the percentage difference between the Biot low and high fre-

quency limits (Winkler, 1985). The expressions for the Biot low and high frequency limiting velocities have been used extensively in the past and can be found in Biot, 1956a and 1956b, Winkler, 1985, and Han, 1986 among others. The Biot absorption peak is usually found in the Megahertz range or higher, depending on fluid viscosity.

Local flow dispersion:

"Apparent dispersion", is defined as the percentage difference between measured ultrasonic velocities and the low-frequency Biot limit (Winkler, 1985) which is measured at seismic frequencies. When the apparent dispersion is greater than the Biot-dispersion, I assume that all of the difference in dispersion can be accounted for by a local flow relaxation mechanism (O'Connell and Budiansky, 1977, Mavko and Nur, 1979), which can be modelled by a Zener model, a constant Q model or a near constant Q model (for more details, see Bourbie et al, 1987), much in the same way as Winkler (1985) presented it. In otherwords, I attribute all of the non-Biot dispersion to the local flow mechanism; the local flow dispersion is given by the difference between the measured saturated ultrasonic velocities and the calculated Biot high frequency velocity limit; the local flow attenuation peak is usually found in the Kilo-hertz range or lower range, depending on fluid viscosity. The relaxation mechanism yields approximate average Q values for the lithologies under investigation, as follows: For a continuous distribution of relaxations frequencies over a limited frequency band, we have:

$$\frac{1}{Q} = \frac{2\Delta V}{V_0 \text{Ln} \left(\frac{\tau_1}{\tau_2} \right)} \tan^{-1} \left(\frac{\omega (\tau_1 - \tau_2)}{1 + \omega^2 \tau_1 \tau_2} \right) \quad (37)$$

where $\frac{\Delta V}{V_0}$ is the total velocity dispersion, ω is angular frequency, and the relaxations are distributed over relaxation frequencies $\omega_1 = \frac{1}{\tau_1}$ and $\omega_2 = \frac{1}{\tau_2}$; τ_1 and τ_2 are the corresponding relaxation times. For a single relaxation, the equation simplifies and we have:

$$\frac{1}{Q} = 2 \frac{\Delta V}{V_0} \frac{\omega \tau}{1 + \omega^2 \tau^2}$$

To solve equation (37) for modulus as a function of attenuation Q, I use the

following approximation to the Kramers-Kronig equations:

$$\frac{\delta \text{Log}(M)}{\delta \text{Log}(f)} = \frac{2}{\pi Q}$$

and integrating, I obtain:

$$M(f) = M(0) + \left[\frac{M_{inf} - M_0}{\frac{2}{\pi} \int_{-inf}^{+inf} \frac{dh}{Q(h)}} \right] 10 \left[\frac{2}{\pi} \int_{-inf}^h \frac{dh}{Q(h)} \right]$$

where M_{inf} denotes the high frequency modulus and M_0 denotes the low frequency modulus.

These equations are sufficient to reconstruct $Q(f)$ from $M(f)$ and $M(f)$ from $Q(f)$. Note that local dispersion is expected to be greater than Biot dispersion for most rocks. As a final remark, note that the case of infinite- Q corresponds to the elastic case, with zero non-Biot dispersion. In general, it can be said that the local flow mechanism has not been developed enough theoretically to make rigorous predictions of Q ; however, it has been shown to yield good results in explaining semi-quantitatively recent experiments (Winkler and Nur, 1979, Murphy, 1982, Jones and Nur, 1983), and will be used in chapters 5 and 6 to determine semi-quantitative values of Q for viscoelastic seismic modeling.

Other methods for determining Q :

The literature is rich in discussions of different ways to measure Q . Good summaries are given in Toksoz and Johnston (1981) and Bourbie et al (1987). In general, there are three categories of methods:

- In-situ methods, which include VSPs and full waveform log analysis; these are usually based on spectral ratio or rise time methods
- Empirical methods from the laboratory; these include pulse echo and transmission techniques (spectral ratios and rise time) which use wave propagation phenomena, stress relaxation (Spencer, 1981) which uses stress strain cycle curves, and methods using vibrations such as pendulum methods (Peselnick and Outerbridge, 1961), or resonant bar techniques (Murphy, 1982, Jones, 1983, Lucet, 1989)

- Several correlations have been observed between velocities and attenuation: For instance, Waters (1987) showed that there is a general relationship of the form: $\frac{1}{Q_p} = \frac{C}{V_p^2}$, where $C = 10^6$ approximately for P waves.

The attenuation of shear waves is usually higher than that of P-waves for rocks with high $\frac{V_p}{V_s}$ ratios, ie for either dry or 100 % saturated rocks (Waters, 1987), and Waters concludes that if the previous attenuation-velocity relationship also holds for S-waves, then the attenuation of S-waves should be approximately four times greater than the attenuation of P waves, for a rock with a $\frac{V_p}{V_s}$ ratio of 2. Additionally, Kennett (1975) showed that $\frac{Q_s}{Q_p} = \frac{4}{3} \left(\frac{V_s}{V_p}\right)^2$, which is consistent with the laboratory observations made on sediments by McDonal et al (1958). Typical values recorded by McDonal et al for the Pierre shale were $Q_p=32$, $Q_s=10$, $V_p=2152$ m/s, and $V_s=792.5$ m/s, for a Poisson's ratio of $\sigma=0.42$. According to Waters (1987), the work of McDonal et al shows that rocks have internal friction, which implies a Q proportional to frequency to the first power, as opposed to viscoelastic solids, for which Q is proportional to frequency to the second power. Winkler and Nur (1979) show that $\frac{Q_p}{Q_s} > 1$ for fully saturated rocks, while $\frac{Q_p}{Q_s} < 1$ for partially saturated rocks.

It is generally accepted that within the seismic bandwidth, attenuation is not a strong function of frequency, so that most Q models are relevant to tying Q's at different frequencies. In subsequent chapters, non-Biot dispersion will be used to calculate semi-quantitative values of Q, which I will assume remains constant in the low frequency range.

V)-CONCLUSIONS

I have reviewed and developed methods to determine local shear velocities and "average" Q values that will serve for detailed deterministic modeling of seismic AVO responses. Shear velocities can be determined for consolidated sediments with good accuracy on a lithologic, depth by depth basis at a well, while Q values can only be obtained for dominant depth averaged intervals, and are not as accurate. Fortunately, the effect of attenuation on reflection coefficients is not as pronounced as that of velocities, and the knowledge of absolute values of intrinsic attenuation is not required, since the contrast in Q - or relative change in Q, on a scale of dominant layers several meters thick - is sufficient in studying AVO behaviors (see chapter 1).

The best approach to the determination of "missing" properties consists in a combination of deterministic methods and empirical methods, which are used to calibrate the deterministic model results; yet this approach remains expensive and is still not widely spread in industry. I will nevertheless use the combined approach in chapter five.

Notation used for synthetic shear modeling in part III:

K_d : wetted dry bulk modulus

μ_d : wetted dry shear modulus, also equal to μ , the saturated shear modulus

K : bulk modulus of the rock under fluid saturation

K_m : bulk modulus of the matrix (or grain) material

μ_m : shear modulus of the matrix (or grain) material

K_f : bulk modulus of the fluid (inverse of its compressibility)

ϕ : porosity of the rock

ϕ_c : critical porosity of the rock

α : Biot coefficient used to relate dry and mineral (or matrix) bulk moduli.

β : By analogy, "Biot coefficient" used in Krief (1990) model, to relate dry and mineral (or matrix) shear moduli.

REFERENCES

- Biot, M., 1956a, Theory of propagation of elastic waves in a fluid saturated porous solid; I-Low frequency range: *J. Acoust. Soc. Am.*, **28**, 168,178.
- Biot, M., 1956b, Theory of propagation of elastic waves in a fluid saturated porous solid; II-Higher frequency range: *J. Acoust. Soc. Am.*, **28**, 179,191.
- Blangy, J.P., 1990, Modeling of anisotropy in shales for AVO studies: S.R.B., vol. **40**, paper M.
- Bourbie, T., Coussy, O., and Zinsner, B., 1982, Acoustics of porous media: Gulf publishing company, Editions Technip, 334 pages.
- Bourbie, T., 1982, Effects of attenuation on reflections: Ph. D. thesis, Stanford University, SRB report vol. **14**.
- Brown, A., 1986, Interpretation of three-dimensional seismic data: AAPG Memoir **42**.
- Bryan, G.M., and Stoll, R.D., 1988, The dynamic shear modulus of marine sediments: *J. Acoust. Soc. Am.*, **83**, vol. 6, 2159, 2164.
- Budiansky, B., and O'Connell, R., 1976, Elastic moduli of a cracked solid: *Int. J. Solids Structures*, vol. 12, p. 81-97.
- Budiansky, B., and O'Connell, R., 1980, Bulk dissipation in heterogeneous media: *Solid Earth Geophys. and Geotech.*, vol. 42, p. 1-10.
- Castagna, J.P., Batzle, M.L., and Eastwood, R.L., 1985, Relationship between compressional-wave and shear-wave velocities in clastic silicate rocks: *Geophysics*, **50**, 571,581.
- Chen, Q., Nur, A., Mavko, G., and Dvorkin, J., 1990, Modeling effective elastic moduli of porous rocks: S.R.B., **40**, paper C.
- Christensen, N., Wang, H., 1985, The influence of pore pressure and confining pressure on dynamic elastic properties of Berea sandstone: *Geophysics*, **50**, 207-213.
- Crampin S., 1984, Effective Anisotropic Elastic constants for Wave propagation through cracked solids: *Geophys. J. R. Astr. Soc.* , **76**, 135,145.
- Domenico, S. N., 1976, Effect of brine-gas mixture on velocity in an unconsolidated reservoir: *Geophysics*, **41**, 882, 894.
- Dutta, N. C., and Ode, H., 1979a, Attenuation and dispersion of compressional waves in fluid filled rocks with partial gas saturation (White model)-Part I: Biot theory: *Geophysics*, **44**, 1777, 1788.
- Dutta, N. C., and Ode, H., 1979b, Attenuation and dispersion of compressional waves in fluid filled rocks with partial gas saturation (White model)-Part II: Results: *Geophysics*, **44**, 1788, 1805.
- Dutta, N. C., and Sheriff, A.J., 1979, On White's model of attenuation in rocks with partial gas saturation: *Geophysics*, **44**, 1806, 1812.

- Dvorkin, J., and Nur, A., 1992, Dynamic poroelasticity: A unified theory with the squirt and the Biot mechanisms: S.R.B., 50, paper P.
- Dvorkin, J., Mavko, G., Jizba, D., and Nur, A., 1990, Modeling the granular structure of rocks: S.R.B., 40, paper D.
- Eastwood, R.L. and Catagna, J.P., 1986, Interpretation of V_p/V_s ratios from sonic logs: in Shear Wave Exploration, Geophysical Developments, No. 1, 139, 153.
- Eberhardt-Phillips, D., Han, D., Zoback, M., 1989, Empirical relationships among seismic velocity, effective pressure, porosity, and clay content in sandstone: Geophysics, vol. 54, No. 1, pp. 82-89.
- Frisillo, A., and Stewart, T., 1980, Effect of partial gas/brine saturation on ultrasonic absorption in sandstone: J. G. R., 85, 5209, 5211.
- Fung, Y. C., 1965, Foundations of solid mechanics: Prentice Hall, New York
- Gardner, G. H., and Harris, M. H., 1968, Velocity and attenuation of elastic waves in sands: Trans. 9th Annual Log. Sympos., Paper M.
- Gassman, F., 1951: Elasticity of porous media: Shear-wave exploration, Geophysical Developments, No. 1, 139, 153.
- Gregory, A. R., 1976, Fluid saturation effects on dynamic elastic properties of sedimentary rocks: Geophysics, 41, 895,921.
- Han, D-H, Nur, A., and Morgan, D., 1986a, Effects of porosity and clay content on wave velocities in sandstones: Geophysics, 51, 2093, 2107.
- Han, D-H, 1986b, Effects of porosity and clay content on acoustic properties of sandstones and unconsolidated sediments: Ph. D. thesis, Stanford University, SRB report vol. 28.
- Hashin, Z., and Shtrikman, S., 1963, A variational approach to the elastic behavior of multiphase materials: J. Mech. Phys. Solid, 11, 127, 140.
- Helbig, K., 1981, Systematic classification of layer-induced transverse isotropy: Geophys. Prospecting, vol.19, pp. 550-577.
- Helbig, K., 1983, Elliptical anisotropy - Its significance and meaning: Geophysics, vol. 48, pp. 825-832.
- Hill, R., 1965, A self-consistent mechanics of composite materials, J. Mech. Phys. Solids, Vol. 13, p. 213-222.
- Hilterman, F., 1990, Is AVO the seismic signature of lithology? A case history of the Ship Shoal-South Addition: T.L.E., 6, June, 15, 22.
- Hoopes, R., Aber, W., 1989, Integrated multianalysis procedure that qualifies DHI's; a case history in the Louisiana Kackberry trend: paper presented at the 59th SEG convention, Dallas

- Inouye, F. Williams, G., 1988, An integrated approach to seismic interpretation: paper presented at the ASEG/SEG conference, Adelaide, 91,93
- Johnston, D.H., Toksoz, M.N., and Timur, A., 1979, Attenuation of seismic waves in dry and saturated rocks: I- Laboratory measurements: *Geophysics*, vol. 44, pp. 681-690.
- Johnston, D.H., Toksoz, M.N., and Timur, A., 1979, Attenuation of seismic waves in dry and saturated rocks: II- Mechanisms: *Geophysics*, vol. 44, pp. 691-711.
- Jones, T., 1986, Pore fluids and frequency-dependent wave propagation in rocks: *Geophysics*, **51**, 1939,1953.
- Jones, T., and Nur, A., 1983, Velocity and attenuation in sandstone at elevated temperatures and pressures: *Geophys. Res. Lett.*, **10**, 140,143.
- Jones, T., 1983, Wave propagation in porous rock and models for crustal structure: Ph. D. thesis, Stanford University, SRB report vol. 19.
- Keller, J. D., 1989, Acoustic wave propagation in composite fluid saturated media: *Geophysics*, **54**, No. 12, 1554, 1563.
- Kennett, B. L., 1975, The effects of attenuation on seismograms: *Bull. Seis. Soc. America*, **65**, no. 6, 1643, 1652.
- Kjartasson, 1979, Attenuation of seismic waves in rocks and applications in energy exploration: Ph. D. thesis, Stanford University, SRB report vol. 8.
- Koefoed, O, 1955, On the effect of Poisson's ratio of rock strata on the reflection coefficients of plane waves: *Geophysical Prospecting*, **3**, 381,387.
- Krief, M., Garat, J., Stellingwerff, J., and Ventre, J., 1990, A petrophysical interpretation using the velocities of P and S waves (full-waveform sonic): *The Log Analyst*, november-december, 355, 369
- Kuster, G. T., and Toksoz, M. N., 1974, Velocity and attenuation of seismic waves in two-phase media, part I: theoretical formulations: *Geophysics*, **39**, no. 5, 587, 606.
- Kuster, G. T., and Toksoz, M. N., 1974, Velocity and attenuation of seismic waves in two-phase media, part II: experimental results: *Geophysics*, **39**, no. 5, 607, 618.
- Levin, F.,1979, Seismic velocities in transverse isotropic media: *Geophysics*, vol. 44, pp. 918-936.
- Liu, H. P., Anderson D.L., Kanamori H., 1976, Velocity dispersion due to anelasticity ; Implication for seismology and mantle composition: *Geophys. J. R. Astr. Soc.*, **47**, 41, 58.
- Lo, T., Coyner, K., and Toksoz, N., 1985, Experimental determination of elastic anisotropy of Berea sandstone, Chicopee shale, and Chemsford granite: *Geophysics*, **51**, 164,171.
- Lucet, N., 1989, Vitesse et atténuation des ondes élastiques soniques et ultrasoniques dans les roches sous pression de confinement: Ph. D. thesis, IFP, Paris VI,

- McDonal, F. J., Angona, F. A., Mills, R. L., Sengbush, R. L., Van Nostrand, R. G., and White, J. E., 1958, Attenuation of shear and compressional waves in Pierre shale: *Geophysics*, vol. 23, No. 3, 421, 439.
- Marion, D., Nur, A., Yin, H. and Han, D., Compressional velocity and porosity in sand-clay mixtures: submitted to *Geophysics*.
- Marion, D., 1990, Acoustic, mechanical, and transport properties of sediments and granular materials: Ph. D. thesis, Stanford University, SRB report vol. 39.
- Mavko, G., and Nur, A., 1979, Wave Attenuation in Partially Saturated Rocks: *Geophysics*, 44, 161,178.
- Mavko, G., and Nur, A., 1975, Melt squirt in the aesthenosphere: *J.G.R.*, 80, 1444, 1448.
- Mavko, G., and Jizba, D., 1991, Estimating grain-scale fluid effects on velocity dispersion in rocks: *Geophysics*, 56, no. 12, 1940, 1949.
- Meissner, F., F., 1978, Petroleum geology of the Bakken Formation, Williston Basin, North Dakota and Montana, in *The economic geology of the Williston basin: Montana Geological Society, 1978 Williston basin symposium*, 207,227.
- Menke, W., and Dubendorff, B., 1985, Discriminating intrinsic and apparent attenuation in layered rock: *Geophys. Res. Lett.*, vol. 12, no. 10, 721, 724.
- Miller, M.N., 1969, Bounds for effective bulk modulus of heterogeneous materials, *J. Math. Physics*, Vol. 10, N. 11, 2005, 2013.
- Murphy, W., 1982, Effects of microstructure and pore fluids on the acoustic properties of granular sedimentary materials: Ph. D. thesis, Stanford University, SRB report vol. 16.
- Murphy, W. F., 1982, Effects of partial water saturation on attenuation in Massilon sandstone and Vycor porous glass: *J. Acoust. Soc. Am.*, vol 71, 1458, 1468.
- Nur, A., and Simmons, G., 1969, Stress induced velocity anisotropy in rock; an experimental study: *J. G. R.*, 74, 6667,6674.
- Nur, A., and Byerlee, J.D., 1971, An exact effective stress law for elastic deformation of rock with fluids: *J. Geophys. Res.*, v. 76, 6414, 6419.
- O'Connell, R., and Budiansky, B., 1977, Viscoelastic properties of fluid-saturated cracked solids: *J. Geoph. Res.*, v. 82, No. 5719, 5736.
- O'Connell, R., and Budiansky, B., 1974, Seismic velocities in dry and saturated cracked solids: *J. Geophys. Res.*, vol. 79, p. 5412-5426.
- Ostrander, W., J., 1984, Plane-wave reflection coefficients for gas sands at nonnormal angles of incidence: *Geophysics*, 49, 1637,1648.
- Passey, Q. R., Creaney, S., Kulla, J. B., Moretti, F. J., and Stroud, J. D., 1990, A practical model for organic richness from porosity and resistivity logs: *A.A.P.G.*

- Bulletin, **74**, no. 12, 1777,1794.
- Peselnick, L., and Outerbridge, W., 1961, Internal friction in shear and shear modulus of Solenhofen limestone over a frequency range of 10 cycles per second: *J. Geophys. Res.*, vol. 66, 581, 588.
- Pickett, G. R., 1963, Acoustic character log and their application in formation evaluation: *J.P.T.*, *Trans. AIME*, **15**, June, 659, 667.
- Postma, G.W., 1955, Wave propagation in stratified medium: *Geophysics*, **20**, No. 4, 780, 806.
- Rai, C., and Hanson, K., 1988, Shear-wave velocity anisotropy in sedimentary rocks: A laboratory study: *Geophysics*, **53**, 800,806.
- Raymer, L. L., Hunt, E. R., and Gardner, J. S., 1980, An improved sonic transit time to porosity transform: *SPWLA, 21st Annual Logging Symposium Trans.*, paper P.
- Reuss, A., 1929, Berechnung der Fließ Grenze von Mischristallen auf Grund der Plastizitätsbedingung für Einkristalle: *Zeitschrift für Angewandte Mathematik und Mechanik*, vol. 9, 49, 58.
- Robertson, J. D., 1989, Reservoir management using 3-D seismic data: *J.P.T.*, **7**, 663,667.
- Samstag, F. J., and Morgan, F. D., 1991, Induced polarization of shaly sands: Salinity domain modeling by double embedding of the effective medium theory: *Geophysics*, vol. 56, 1749, 1756.
- Savage, J., 1966, Thermoelastic attenuation of seismic waves by cracks: *J. Geophys. Res.*, v. 71, 3929, 3938.
- Shoenberger, M., and Levin, F., 1974, Apparent attenuation due to intrabed multiples: *Geophysics*, **39**, 278,291.
- Spencer, T.W., Sonnad, J., and Butler, T., 1982, Seismic Q - Stratigraphy or dissipation: *Geophysics*, v. 47, no. 1, 16, 24.
- Spencer, J.W., 1981, Stress relaxation at low frequencies in fluid saturated rocks: Attenuation and modulus dispersion: *J. Geophys. Res.*, 1803, 1812.
- Stoll, R.D., and Bryan, G.M., 1970, Wave attenuation in saturated sediments: *J. Acous. Soc. Am.*, v. 47, 1440, 1447.
- Thomsen, L., 1987, Reflection seismology over azimuthally anisotropic media: *Geophysics*, **53**, 304,313.
- Thomsen, L., 1986, Weak elastic anisotropy : *Geophysics*, **51**, 1954,1966.
- Thomsen, L., 1985, Biot-Consistent elastic moduli of porous rocks; low-frequency limit: *Geophysics*, **50**, 2797,2807.
- Toksoz, N., and Johnston, D., 1981, Seismic wave attenuation: *SEG, Geophysics Reprint Series No. 2*, 459 pages.

- Tosaya, C., and Nur, A., 1982, Effects of diagenesis and clays on compressional velocities in rocks: *Geophys. Res. Lett.*, **9**, 5,8.
- Tosaya, C., 1982, Acoustic properties of clay bearing rocks: Ph. D. dissertation, S.R.B. vol. **15**, 106,130.
- Vernik, L., and Nur, A., 1990, Ultrasonic velocity and anisotropy of some petroleum source rocks; the Bakken formation, Williston basin, North dakota: S.R.B. vol. **40**, paper K.
- Voigt, W., 1928, *Lehrbuch der Krystallphysik*, Taubner, Leipzig.
- Walpole, L., 1969, On the overall elastic moduli of composite materials: *L. Mech. Phys. Solids*, Vol. 17, p. 235-251.
- Walpole, L., 1966, On the bounds for the overall elastic moduli of inhomogeneous systems, I, *J. Mech. Phys. Solids*, Vol. 14, p. 151-162.
- Walsh, J.B., 1966, Seismic wave attenuation in rock due to friction: *J. Geophys. Res.*, v. 71, 2591, 2599.
- Wang, 1988, Wave velocity in hydrocarbons and hydrocarbon saturated rocks - with applications to EOR monitoring: Ph. D. dissertation, SRB vol **34**
- Ward, 1991, Synthetic shear wave sonics for seismic methods: S.E.G. Workshop on Lithology, St. Louis, extended abstract
- Waters, K., 1987, *Reflection Seismology: A tool for Energy resource Exploration*: John Wiley and sons, 538 pages.
- Watt, J.P., Davies, G.F., and O'Connell, R.J., 1976, The elastic properties of composite materials: *Rev. Geophys. Sp. Phys.*, **14**, 541, 560.
- White, J. E., Martineau-Nicoletis, L., and Monash, C., 1983, Measured anisotropy in Pierre shale: *Geophysics*, v. 31, No. 5, 709, 725.
- White, J. E., 1975, Computed seismic speeds and attenuation in rocks with partial gas saturation: *Geophysical Prospecting*, v. 40, 224, 232.
- Winkler, K., 1985, Dispersion Analysis of Velocity and Attenuation in Berea Sandstone: *J. Geoph. Res.*, v. 90, No. B8, 6793, 6800.
- Winkler, K., and Nur, A., 1979, Pore fluids and seismic attenuation in rocks: *Geophysical Research letters*, v. 6, 1, 4.
- Wyllie, M. R., Gregory, A. R., and Gardner, L. W., 1958, An experimental investigation of factors influencing elastic wave velocities in porous media: *Geophysics*, **23**, no. 3, 459, 493.
- Wu, T., 1966, The effect of inclusion shape on the elastic moduli of a two-phase material, *Int. J. Solids Structures*, Vol. 2, p. 1-8.
- Yin, H., Han, D-H, Nur, A., 1988, Study of velocities and compaction on sand-clay mixtures: Stanford University, SRB report vol. **33**.

CHAPTER 3

DETERMINISTIC MODELING FOR AVO STUDIES: AN
INTEGRATED APPROACH

"In any petrophysical consideration it is important to first type the rock",

G. E. Archie, 1952.

ABSTRACT

In the past, traditional seismic interpretation techniques relied mostly on the use of velocity analyses in combination with qualitative seismic amplitude observations. A significant amount of additional valuable information can be derived from quantitative analyses of seismic pre-stack amplitudes. However, to recover this information **quantitatively**, it is necessary to design a systematic and integrated petrophysical interface that serves as the tie between the actual rock properties and the seismic derived properties. The rock physicist's knowledge can then be used as the essential element to tie classical high resolution seismic and well log data, with a knowledge representation system - the "dictionary" - that allows to infer in-situ rock properties such as lithology and porosity, and to some extent permeability and fluid saturation or fluid type.

An **integrated deterministic modeling** approach is developed for seismic synthetics. All of the information available from logs, core measurements, check shot data, and seismic is integrated in four main steps:

- a) The determination of rock properties at specific depths
- b) Environmental corrections for the calculation of in-situ properties
- c) Calibration of core data with "continuous" petrophysical properties, inferred from well-log data; this step also serves as an empirical calibration of petrophysical models
- d) Frequency and scale-dependent corrections.

The modeling approach developed here can be used for two purposes: In a first step, it can be used to **calculate overall rock properties** at seismic frequencies at a given well; this is the straight forward and more direct application. In a second step, it provides the methodology for sensitivity analyses of petrophysical parameters away from that well, for **extrapolation of reservoir properties**. In this case the information from logs, core measurements, check shot data, and seismic is not only integrated, but used as a tool for a better definition of changes in petrophysical properties as we move away from a control well. This involves the construction of a "different" rock, with attributes (such as porosity, mineralogy, fluid content, effective pressure, consolidation, ...) that have a high probability of existence in an area laterally adjacent to a well.

Three topics are particularly emphasized:

- The determination of major lithologic "zones" at a well and the reconciliation between chronostratigraphic and lithostratigraphic boundaries at the megascale
- The **classification** of sedimentary rocks at the microscale (or the scale of investigation of core and log data) for establishing geologically consistent parameter variations
- The **up-scaling** of properties from the microscale to the macroscale (the scale of seismic wavelengths); this step involves the calculation of a smooth tranverse isotropic long wavelength equivalent (STILWE) medium, which is equivalent to a series of finely layered media.

The techniques outlined present systematic and quantitative methods of determining petrophysical parameters at seismic scales, and allow for sensitivity analyses on those parameters; they serve as an ideal integration step in defining rock properties prior to detailed model-based lithologic interpretations of seismic data.

I)-INTRODUCTION

The need for integration

It has become apparent that information other than seismic data can be immensely valuable in characterizing a particular reservoir seismically (see chapter 2, section II-1 for example). To that effect, logs are probably the most valuable. However, logs alone are not sufficient to complete the picture, and it is often necessary to pull-in information from core analyses and geological descriptions of rocks. The systematic study of AVO trends in relationship to petrophysical properties requires the integration of such analyses from different disciplines and differs substantially from the bright spot technology of the mid 1970s (Backus and Chen, 1975). Borehole information is very accurate in the depth direction, yet has low lateral penetration, while seismic has low vertical resolution but allows for large scale lateral investigations (for example, see Poggiagliolmi and Lowden, 1990, or de Buyl et al., 1988). By including and integrating all of the available information, it may be possible to calibrate the seismic data very precisely, thus making it possible to distinguish subtle stratigraphic features from a small change in the trend of reflection coefficients with angle of incidence. However, this approach requires the analysis of high quality, high resolution seismic and petrophysical data.

The need for a systematic procedure for integration

The relevance of petrophysical properties to AVO modeling and interpretation is increasingly being recognized throughout the industry. However, there is to my knowledge no systematic and integrated modeling procedure based on sound petrophysical principles; this may be the reason why geophysicists often "oversold" the technique of pre-stack analysis in the past. More often than not, a large number of petrophysical information regarding shear velocities, intrinsic attenuation, and anisotropy is unknown. As a result, the non-uniqueness in the lithologic interpretation of seismic amplitudes is compounded, and the interpretation is often subject to unreasonable expectations. Chapters 1 and 2 reviewed the main factors affecting velocities and seis-

mic amplitudes with offset. It is therefore necessary to take into account as many of those parameters as possible, and to use them as calibration tools in order to achieve a better definition of petrophysical properties from seismic data.

The seismic interpreter typically works with a depositional model in mind. He then generates several plausible working models of facies variations or petrophysical variations, and uses the principle of "least astonishment" to arrive at a few select model possibilities around a given well. The objective sought here is to quantify his/her model parameters, in order to determine which is the "best" model, by comparison with the seismic data.

The work presented here is an attempt to translate detailed changes in facies properties to changes in rock properties. This requires the prior recognition of the rock facies, its classification, the calculation of new rock properties from other sets of measured rock properties, and the up-scaling of rock properties to seismic scales of investigation via the construction of equivalent macroscale media. The deterministic modeling approach proposed here is summarized in figure 3.1.

II)- IN-SITU PROPERTIES FROM LOGS AND CORES: LITHOLOGIC "ZONING"

Well logs constitute the ideal starting point from which to build a petrophysical model, because they provide a dense amount of quantitative data in digital form. Depending on their type, well-logs have a vertical sampling rate which varies from one half of a foot (0.152 m) to two feet (0.608 m). This means that, in general, logs will have a vertical resolution of one half a foot or worse.

Log measurements are complicated by the fact that they can only investigate petrophysical properties in a shallow ring around the wellbore, and that they are severely affected by environmental conditions (wellbore quality, drilling fluid invasion, etc). But once calibrated with core measurements, well logs allow for rock properties to be inferred on a quasi-continuous depth record in a well, and thus constitute the

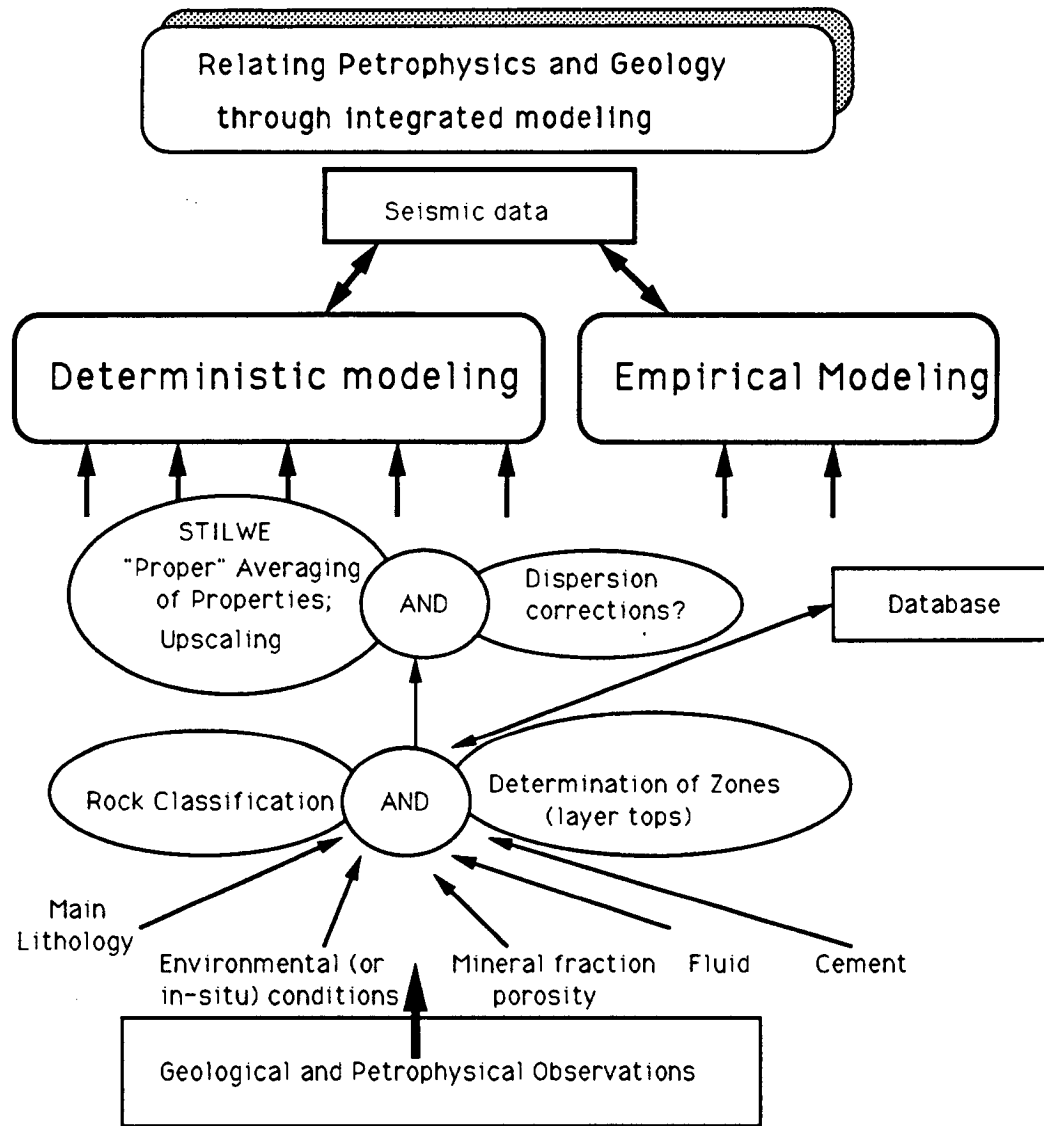


Figure 3.1: A deterministic approach: showing a flow chart of a methodology using deterministic modeling and its calibration via empirical modeling, to relate petrophysics and geology. The four individual steps (Lithologic "zoning", rock classification, upscaling via the calculation of STILWE, and dispersion corrections) will be examined thoroughly in this chapter.

ideal basis from which to build petrophysical models of the earth at the microscale. For all practical purposes, well logs can be seen as a suite of rock properties sampled at intervals of 1/2 foot for a given well. The properties sampled by the logs can be "mapped" into actual rock properties by comparison with core data, using either empirical or theoretical relationships or a combination of both, and I will use this calibrated log data as a starting point.

Depending on their availability, the types of logs involved are the Spontaneous Potential (SP), Gamma Ray (GR), Caliper (CALI), Sonic (DT), Density (RHOB), Resistivities (ILD, ILM, SFLU, LLD, LLS), Porosity (NPHI). This first set of logs can be used in their raw form, but must be edited and calibrated with cores, to yield a good starting point for building a model. In general, three levels of editing can be identified, mechanical, interpretative, and modeling (for more details, see Ausburn, 1977). Other useful information can also be incorporated, such as shear wave information (DTS), and the Natural (NGT) or the Induced gamma ray spectroscopy (GST), which enable partial mineralogical inversions. This second set of logs can be used for mineralogic fractions and direct shear wave readings in the model building steps. For the purposes of this chapter, I will start from a set of edited and calibrated logs.

There are two major schools of seismic interpretation: one school is based on lithostratigraphic boundaries, and speculates that changes in lithology give rise to seismic reflections; the other, based on chronostratigraphic boundaries, relates reflections to hiatus (or times of non-deposition and erosion) and speculates that reflections are due to variations in sedimentation patterns, regardless of rock type. Vail et al (1977) state that: "Primary seismic reflections are generated by stratal surfaces which are chronostratigraphic, rather than by boundaries of arbitrarily defined lithostratigraphic units, many of which commonly transgress geologic time". Both approaches can be reconciled, in the sense that, in general, hiatus are the locus of major unconformities, which separate major facies. Nevertheless, it is agreed upon that changes in acoustic impedance give rise to reflections. Therefore, in defining the major petrophysical layers for a forward model, I will use a criterium of impedance contrasts.

Figure 3.2 illustrates the processing flow which enables us to determine a set of model layer boundaries (the layer tops) from calibrated logs. The logs are first read-in, de-spiked and filtered. This step is crucial, because logs can often be extremely noisy. The type of filtering has been the subject of many controversies, and I use a median filter with adjustable window length), followed by a de-spiking filter, which is a weighted average adaptive filter using the error function (for more information, cf Mathis, 1987). An impedance log is then calculated from the available information; ideally, this would be a combination of sonic and density logs, but pseudo-sonic or pseudo-density logs can also be used, depending on the availability of logs, on the quality of the logs, and on borehole conditions); for example, when density logs are not available, a pseudo-density log can be calculated via Gardner's relation (Gardner, 1974), and pseudo-sonic logs can sometimes be calculated from resistivity logs (Brito dos Santos et al., 1988). The impedance log is ordered by decreasing impedance contrast and the interpreter decides on a number "n" of layer boundaries; the "n" largest impedance contrasts are then used to define "n" user-defined layer boundaries, the layers being subject to a minimum thickness requirement; usually, this minimum thickness is on the order of the detection limit of a thin bed or approximately one eighth of a wavelength or less (Widess, 1973); a factor of one tenth of the dominant wavelength is therefore considered safe. The layer boundaries determined from impedance contrasts are then refined manually to depth-match neighboring lithologic boundaries. Once the layer boundaries have been defined, deterministic modeling steps can be initiated for each of the model layers.

Environmental corrections (Pe, T)

I assume that the logs have already been corrected for borehole effects, and that they are representative of "true" rock properties. Therefore, when quantifying certain environmental effects in generating new models for sensitivity analyses (such as pressure effects or temperature effects), I extract empirical relationships from core measurements, and correct the logs accordingly for these. In a sense, the logs are calibrated from core analyses. For example, in creating variations in effective pressure for a given formation, I would empirically determine changes in properties (due to changes in effective pressure) from core measurements, and transfer these changes to the logs, within the interval of interest. Therefore, core information is necessary for a quantitative calibration of logs.

Default values are used for log readings in the case of bad washouts or poor wall stability, by monitoring changes in the caliper readings. These default values are determined in connection with the classification of lithologies that follows in part III.

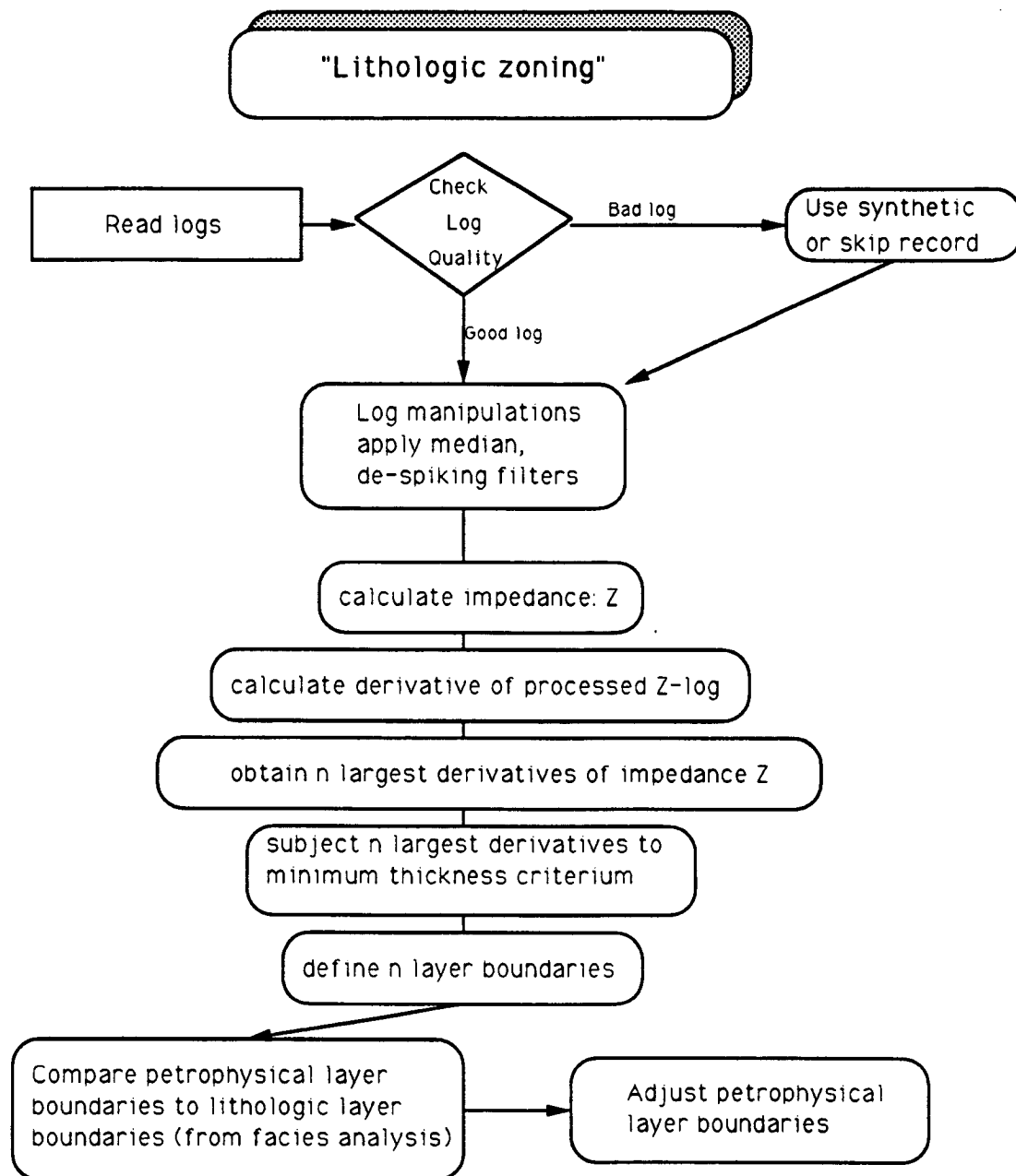


Figure 3.2: "Lithologic zoning": the processing flow which allows the conversion from calibrated logs to a set of model layer boundaries. The logs are first read-in, de-spiked and filtered using a combination of methods. Petrophysical boundaries are then refined manually to match neighboring lithologic boundaries.

III)- CLASSIFICATION OF SEDIMENTARY ROCKS FOR ESTABLISHING PARAMETER VARIATIONS

In part II, I defined layer boundaries, which were delimited by large contrasts in impedance. Because a priori, there is no reason for these boundaries to define changes in lithology, I showed the importance of calibrating them to known lithologic boundaries. The next step is to classify each of these seismic "zones" according to their dominant lithology.

The problem of classification of sedimentary rocks has been tackled by many authors. In general, sandstones are best classified according to their texture and mineralogical composition; fortunately for us, composition has proved most useful for classification; most authors make the distinction between cementing minerals and framework minerals, and use the detrital components to define different sandstone classes (Dott, 1964, Pettijohn, 1975 among others). As shown by Pettijohn (1975), most families of sands can be classified using a generalized ternary diagram, involving quartz, feldspar, rock fragments, and matrix. The classification scheme of Dott (1964) was generalized by Pettijohn (1975) and will be adopted here. Figure 3.3 shows an ideal classification of terrigenous sandstones, where clay constitutes the matrix. Folk's dual maturity concepts (1951) are incorporated, with a horizontal textural axis, and a vertical compositional axis. The parameter "ratio" is calculated as the sand-clay ratio from gamma-ray logs for example, and serves as the basis for the classification. The exact cut-offs between different classes can be determined somewhat arbitrarily and should remain user-defined, as is shown in the flow chart of figure 3.4. In the absence of information on the rocks under investigation, the recommended default values for the classification are:

- $wackll$ (or clay-sandstone lower limit) = 15 %; below this limiting clay content, the rock is assigned to be a sandstone (either clean or dirty)
- $wackul$ (or clay-sandstone upper limit) = 75 %; above this limiting clay content, the rock is assigned to be a mudstone, claystone, or shale

- p_{orm} (or upper limit on porosity of consolidated mudstone) = 20 %; with effective porosities above this limit (and clay-sand ratios comprised between w_{ackul} and w_{ackll}), the rocks are treated as wackes, otherwise they are assigned to claystones or other lithologies; this type of reasoning is valid for compacted and consolidated claystones and mudstones only
- p_{ormss} (or minimal sandstone porosity) = 15 %; with clay-sand ratios typical of arenites, the rocks are treated suspiciously and are cross-checked for other lithologies, if their effective porosity is less than p_{ormss} .

It is worth noting that, from a geological point of view, the classification remains incomplete, because it does not reflect changes in the depositional environment, and because it should also reflect *textural* attributes and the character of *cements*; but from a petrophysical perspective, this classification should serve its purpose well.

IV)- UP-SCALING AND EQUIVALENT TRANSVERSELY ISOTROPIC MEDIA

The key to deterministic modeling is to recognize that "average" rock properties are a function of the scale of investigation. This is due to the fact that the averaging process is scale dependent. I define four scales of lithologic investigations: the megascopic or basin scale, which involves depositional environments and reflector geometry, the mesoscopic, which is the field or prospect scale, and involves hydrocarbon indicators and rock type, the macroscopic or reservoir scale, which involves pore fluids, fracture orientation, and pressure among other properties, and the microscopic or core scale, which involves mineralogy, and pore geometries for example. In this particular section, I deal with up-scaling rock properties from the **microscale** (where I start from core and well-log scales) to the **seismic scale** (which can be considered at the macroscopic or mesoscopic scale). This is an extremely important step to master, because my ultimate goal is to relate elastic properties to lithology at the two different scales.

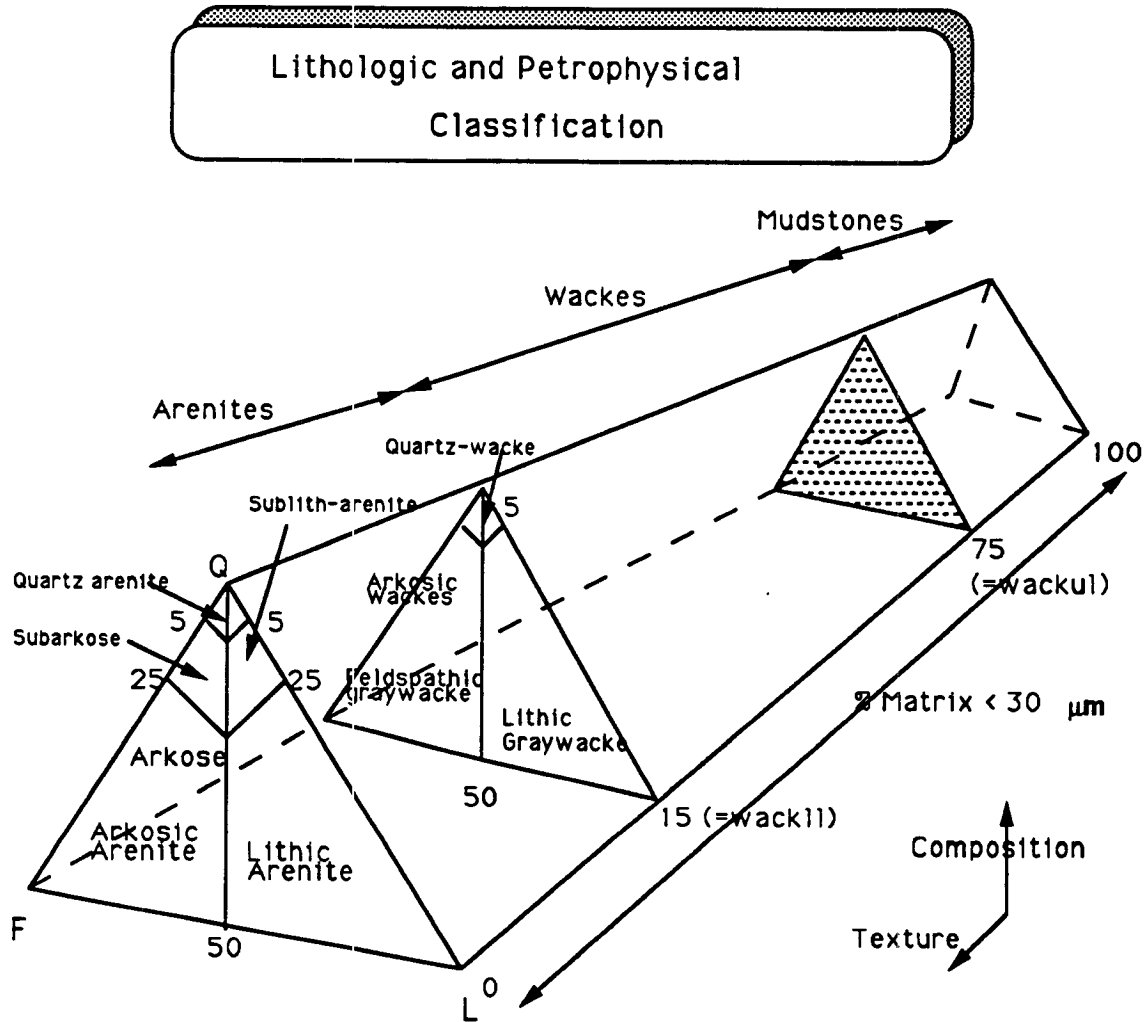


Figure 3.3: Classification of sedimentary rocks according to their texture and mineralogical composition; a distinction is first made between cementing minerals and framework minerals, and the detrital components are used to define different sandstone classes. It is convenient to use a generalized ternary diagram, involving quartz, feldspar, rock fragments, and matrix. I adopt the generalized classification of terrigenous sandstones modified from Pettijohn, 1975, where clay constitutes the matrix; the horizontal axis representing texture, and the vertical axis expresses composition. Exact cut-offs between different classes are determined arbitrarily and are user-defined.

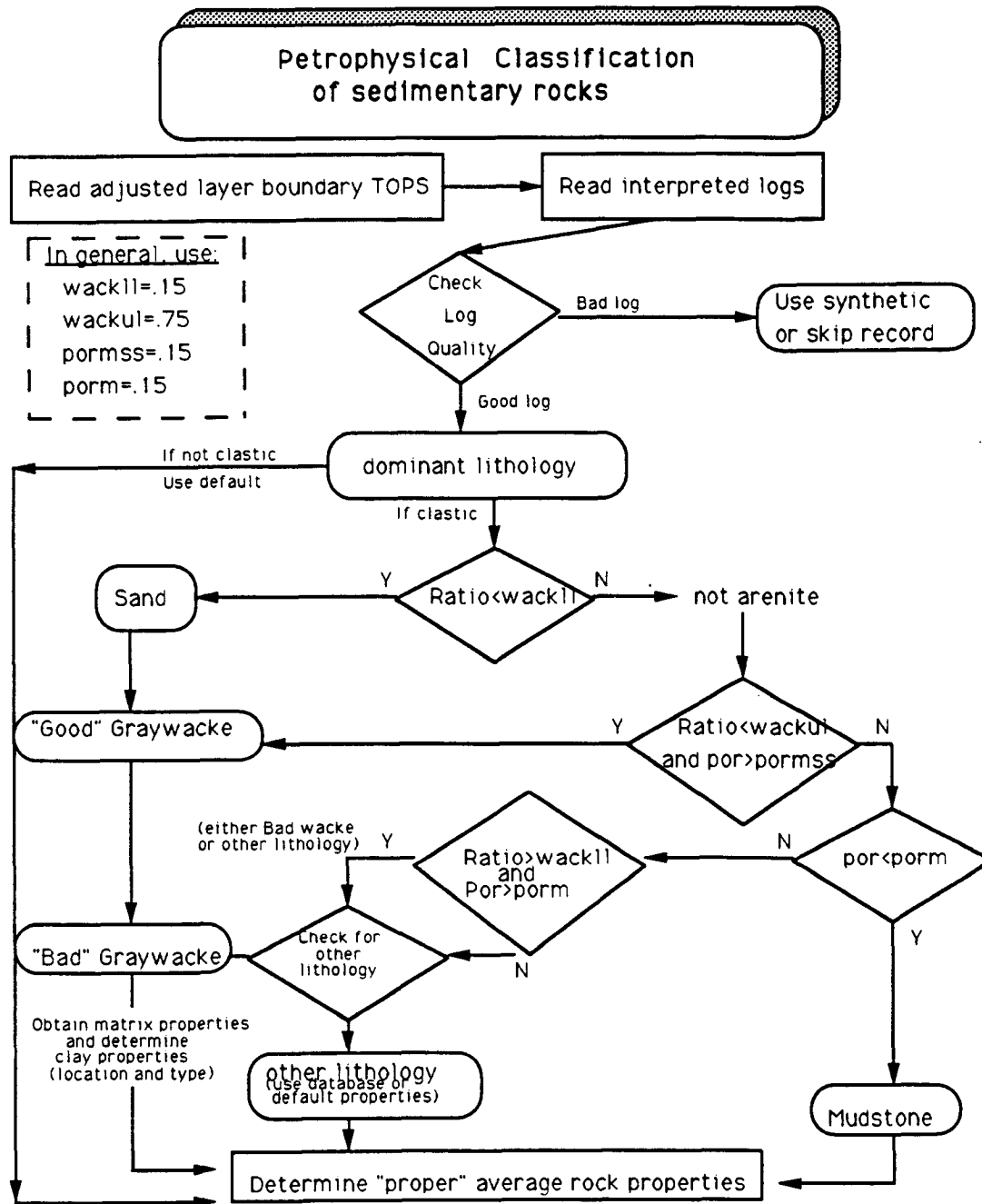


Figure 3.4: Classification of sedimentary rocks: Flow chart

Because average rock properties are scale dependent, the act of modifying the properties of a given series of micro-layers (or a portion of a model layer) will not affect the properties of the model or macro-layer in the same way as those of the microlayers which constitute it; in other words, during sensitivity analyses, each change in petrophysical property, when calculated at a micro-scale on a local depth basis (from logs for example), needs to be up-scaled to the mega-scale and transformed into a change in the properties of a model layer. This generally involves the calculation of a new smooth long wavelength transversely isotropic equivalent (STILWE) medium, for each iteration in the sensitivity analysis.

In what follows, I assume that we are in the presence of flat layers at the well, and that the highest level of anisotropy of these layers is transverse isotropy; furthermore, all of these layers have parallel axes of symmetry.

1) For a series of isotropic homogeneous microlayers

It was shown by Backus (1962) that a set of thin horizontal isotropic layers can be approximated by a single, smooth transversely isotropic *long* wavelength equivalent (STILWE) medium. The averaging method can be seen as a physical way, as opposed to a statistical way, to upscale the rapid variations (due to micro-layering) at the logging scale, to the larger seismic scale (which is based on impedance contrasts). The result is a medium which can be considered as the "long wavelength equivalent" transversely isotropic medium, whose wavelength is very much larger than the fine-layered medium, and whose density is the arithmetic average of densities over thickness (figure 3.5). The question of what is defined as "long-wavelength" has been the subject of much controversy; a thin bed was defined as a bed with thickness below one eighth of the dominant wavelength (Widess, 1973); more recent work (Carcione et al, 1991) has shown that the ratio $R = \frac{\lambda}{d}$ - where λ is the dominant wavelength and d is the spatial period of a system consisting of two alternating thin layers - was around 8 for an epoxy-glass system and between 5 and 6 for a limestone-sandstone system. This means that any "zone" with thickness t less than $t = \frac{\lambda}{2R}$ (or approximately $d = \frac{\lambda}{10}$)

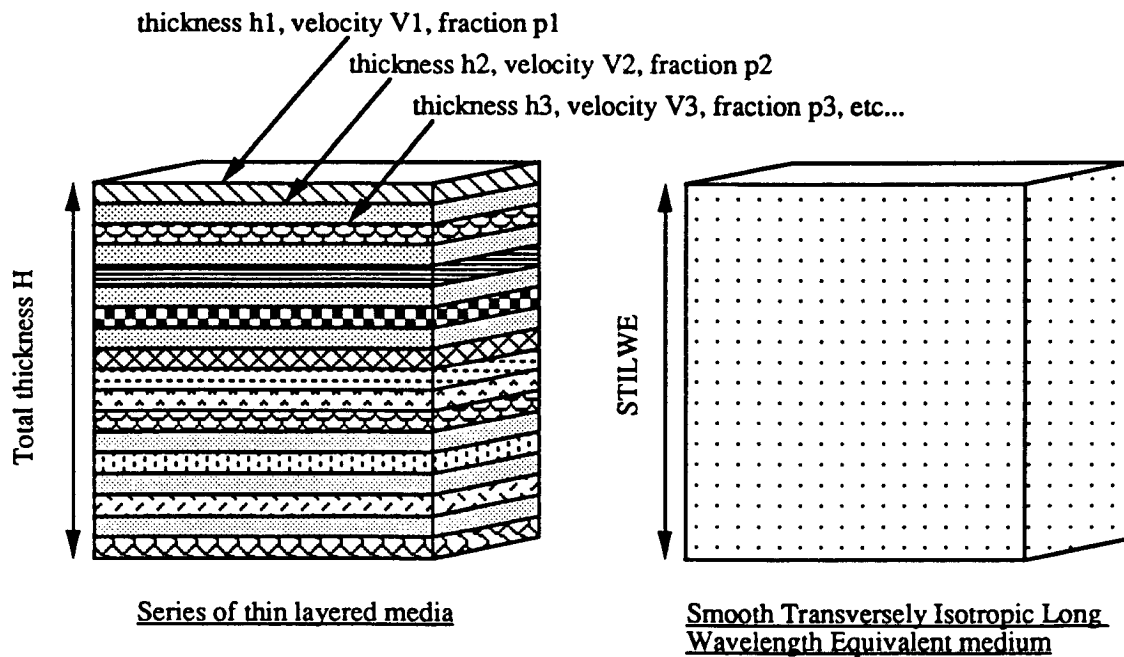


Figure 3.5: Schematic of the smooth transversely isotropic long wavelength equivalent (STILWE) concept; usually, the h_i are less than $d = \frac{\lambda}{10}$ or so (Widess, 1973, Carcione et al, 1991); see text for more details.

can be considered as a thin bed; the factor of two is due to the fact that the system has two components and I assume that $d = t_1 + t_2 = 2t$ for maximum anisotropy.

In the up-scaling from logs, I consider each depth sample (1/2 ft or 0.152m) to be a separate layer; this, by the way, implies that I am attempting to build-up macrolayers from a knowledge of microlayers that are as thin as the logs will allow me to "see" them. I then up-scale to a series of macrolayers that were defined as "zones"; this is rigorous, since the microlayer spacing (1/2 ft or 0.152m) is well below one tenth of a dominant wavelength.

Backus defined five constants and a sixth redundant one, A, B, C, F, L, and M, as follows:

$$A = \left\langle \frac{4\mu(\lambda + \mu)}{\lambda + 2\mu} \right\rangle + \left\langle \frac{1}{\lambda + 2\mu} \right\rangle^{-1} \left\langle \frac{\lambda}{\lambda + 2\mu} \right\rangle^2 = C_{11}$$

$$B = \left\langle \frac{2\lambda\mu}{\lambda + 2\mu} \right\rangle + \left\langle \frac{1}{\lambda + 2\mu} \right\rangle^{-1} \left\langle \frac{\lambda}{\lambda + 2\mu} \right\rangle^2 = C_{12} = C_{11} - 2C_{66}$$

$$C = \left\langle \frac{1}{\lambda + 2\mu} \right\rangle^{-1} = C_{33}$$

$$F = \left\langle \frac{1}{\lambda + 2\mu} \right\rangle^{-1} \left\langle \frac{\lambda}{\lambda + 2\mu} \right\rangle = C_{13}$$

$$L = \left\langle \frac{1}{\mu} \right\rangle^{-1} = C_{44}$$

$$M = \langle \mu \rangle = C_{66} \text{ where the symbols } \langle \rangle \text{ mean weighted average.}$$

The previous expressions can be converted into functions of Lamé's constants, by using the well known relationship:

$$\lambda + 2\mu = K + \frac{4}{3}\mu$$

for isotropic media, to obtain the following averages over bulk and shear moduli:

$$C_{11} = \left\langle \frac{4\mu \left(K + \frac{\mu}{3} \right)}{K + \frac{4}{3}\mu} \right\rangle + XY^2$$

$$C_{12} = \left\langle \frac{2\mu \left(K - \frac{2}{3}\mu \right)}{K + \frac{4}{3}\mu} \right\rangle + XY^2 \quad (1)$$

$$C_{13} = XY \quad (2)$$

$$C_{33} = X \quad (3)$$

$$C_{44} = \left\langle \frac{1}{\mu} \right\rangle^{-1} \quad (4)$$

$$C_{66} = \langle \mu \rangle \quad (5)$$

where

$$X = C_{33} = \left\langle \frac{1}{K + \frac{4}{3}\mu} \right\rangle^{-1} \quad (6)$$

$$Y = \left\langle \frac{K - 2\mu}{K + \frac{4}{3}\mu} \right\rangle \quad (7)$$

2) For a series of transversely isotropic homogeneous microlayers

Here again, the upscaling from microlayers defined by the log sampling of 1/2 ft is rigorous, since it is well below one tenth of the dominant seismic wavelength.

However, each microlayer can be transversely isotropic, and I use Helbig's relationships (1981), expressing the averaging in terms of the five constants L, M, R, S, and T:

$$R(i) = \frac{1}{C_{33}}; R = \langle R(i) \rangle \quad (8)$$

$$\frac{1}{L(i)} = \frac{1}{C_{44}(i)}; \frac{1}{L} = \langle \frac{1}{L(i)} \rangle \quad (9)$$

$$M(i) = C_{66}(i); M = \langle M(i) \rangle \quad (10)$$

$$T(i) = \frac{1}{2} \left(1 - \frac{C_{13}(i)}{C_{33}(i)} \right); T = \langle T(i) \rangle \quad (11)$$

$$S(i) = \frac{1}{4} \left(\frac{C_{13}^2(i)}{C_{33}(i)} - C_{11}(i) \right) + C_{66}(i); S = \langle S(i) \rangle \quad (12)$$

The conversion back to elastic constants is given by:

$$C_{11} = \frac{(1 - 2T)^2}{R} + 4(M - S); C_{13} = \frac{1 - 2T}{R} \quad (13)$$

$$C_{33} = \frac{1}{R}; C_{44} = L; C_{66} = M \quad (14)$$

This formulation has the advantage of being valid for any transversely isotropic medium, including intrinsically anisotropic media.

3) Convenient notation for transverse isotropy

Since Thomsen's (1986) notation for transverse isotropy is convenient and offers more physical insight on anisotropy than other notations, I can transform the equations of Backus or those of Helbig to convert the averaged results to Thomsen's notation, via the following equations for general transverse isotropy:

$$\varepsilon = \frac{C_{11} - C_{33}}{2C_{33}}$$

$$\gamma = \frac{C_{66} - C_{44}}{2C_{44}}$$

$$\delta^* = \frac{1}{2C_{33}^2} \left[2(C_{13} + C_{44})^2 - (C_{33} - C_{44})(C_{11} + C_{33} - 2C_{44}) \right]$$

(The parameter δ^* is used for general transverse isotropy, and δ for weak transverse isotropy; they are related by the following relation (Thomsen, 1986):

$$\delta = \frac{1}{2} \left[\epsilon + \frac{\delta^*}{\left(1 - \frac{\beta_0^2}{\alpha_0^2}\right)} \right] = \frac{(C_{13} + C_{44})^2 - (C_{33} - C_{44})^2}{2C_{33}(C_{33} - C_{44})}$$

When a series of alternating layers are transversely isotropic to begin with and are to be averaged using formulas (8)-(14), the δ^* , ϵ and γ parameters can be combined to form equivalent transversely isotropic media. As experienced by Levin (1988), this is not an easy analytical task when using Thomsen's notation. However, the previous formulas can be used to achieve digital averaging of Thomsen's parameters through the following two steps:

* First the parameters V_P (vertical P-wave velocity), V_S (vertical S-wave velocity), δ^* , ϵ , and γ are converted to five elastic constants for transverse isotropy, according to:

$$C_{33} = \rho V_P^2$$

$$C_{44} = \rho V_S^2$$

$$C_{11} = (1 + 2\epsilon) \rho V_P^2$$

$$C_{12} = C_{11} - 2C_{44}(2\gamma + 1) = (1 + 2\epsilon) \rho V_P^2 - 2\rho V_S^2(2\gamma + 1)$$

$$C_{13} = \sqrt{\frac{2\delta^* C_{33}^2 + (C_{33} - C_{44})(C_{11} + C_{33} - 2C_{44})}{2}} - C_{44}$$

(and

$$C_{66} = \frac{C_{11} - C_{12}}{2}$$

* Second, these elastic constants are used in the Helbig-type averaging. The application of this method is in the "proper" averaging of thin layers that are intrinsically transversely isotropic, and it yields final STILWE parameters that are related to Thomsen's notation rather than Helbig's.

In the future, it may be feasible to consider microlayers with orthorhombic symmetry, and to calculate long wavelength equivalents to those microlayers. The expressions for such averaging have already been published in Sun and Li, 1988; they will not be considered here, because at present, we do not have the technology to determine orthorhombic rock properties at the microscale on a dense depth sampling; however, data for V_P and V_S anisotropies of rock forming minerals, have been published (Babuska, 1981), thereby creating a possibility, in the future, of using these averaging formulas, if the composition of the rock and the orientation of its mineral constituents are known at the microscale.

V)-DISPERSION CORRECTIONS OF MODULI

An increasing amount of evidence shows that sonic and ultrasonic velocities tend to be higher than seismic velocities under similar conditions. This is sometimes called positive drift and is believed to be related to frequency dependent wave propagation (Ward and Hewitt, 1977, Jones, 1986). I believe that frequency dependence is a fact, even if the various models used to characterize absorption, dispersion, and other loss mechanisms are not fully understood. I therefore adopt the idea that velocities have to be corrected for frequency effects, prior to seismic modeling.

The observation that dispersion is negligibly small in dry formation led numerous authors to associate it with some type of fluid flow mechanism. Winkler (1985) showed how Biot theory can be used to calculate velocity dispersion and absorption due to the Biot mechanism and to local fluid flow mechanisms, provided that both dry and saturated measurements are available. I suggest to use the Biot equations to calculate velocity dispersion, and then to calibrate seismic for Q , using a simple model of frequency-dependent attenuation such as the one adopted by Liu et al. (1976) and Jones (1986). This assumes that individual relaxation mechanisms can be modeled by a standard linear solid (Zener model) and generalizes the results to a distribution of relaxations over a frequency band (see chapter 2, part IV or Bourbie et al, 1987 for more details).

In some cases, such as for fused glass beads for example, it may prove that the effects of frequency-dependent Q are negligible when compared to Biot dispersion, or that Biot dispersion itself is negligible; this would make the total dispersion corrections null.

After going through the steps that I have just outlined, the geoscientist should have a good idea of rock types and specific rock properties present at a given well. The information available from that well can then be used for the generation of precise synthetic seismic gathers to be compared with real seismic data in the vicinity of the well. The procedure for seismic-based extrapolation of rock properties away from an existing well will be treated in the next section.

VI)-POTENTIAL APPLICATIONS

1) Calculation of average bulk properties at a well

The left hand side of figure 3.6 summarizes the procedure that I have just outlined to build a rigorous reservoir model for detailed seismic analyses. The approach is straight forward: microlayer properties are first determined at the log sampling rate (1/2 ft or 0.152m); each log reading is assumed to represent a microlayer, whose properties are derived from calibrated log information. In the next step, the boundaries of macro-zones or "model layers" are determined from a combination of geological input and impedance contrasts. Finally, the properties of each macrolayer are calculated from the up-scaling of log-derived properties within that particular macrolayer. In a last step, the elastic properties of the macrolayers are adjusted for viscoelastic behavior, and intrinsic attenuation values are calculated from velocity dispersion information.

2) Extrapolation of average bulk properties away from a well

The classification scheme developed in part II can be used in sensitivity analyses to change the properties of the lithologies under investigation (within the range of properties of their lithologic class). The concept of perturbation analysis is illustrated

in the center of figure 3.6; parameter variations are implemented within a given zone of interest at the microscale, on a depth by depth basis (ie, at the sampling rate of the well logs), and this gives rise to overall changes in the bulk properties of the zone at the macroscale, through the calculation of a new STILWE medium in the zone undergoing the change. The method of calculation of these new bulk properties is based on a combination of the modeling techniques which best match the laboratory data, and on empirical relations derived for the lithologies under investigation. It is crucial to emphasize that empirical validation of petrophysical models on a field-wide (or basin-wide) basis is of primary importance. In particular, experimental data allows for the calibration of wetted dry frame moduli and for the computation of dispersion factors.

VII)-CONCLUSIONS

I have developed a possible approach to deterministic modeling for seismic elastic synthetics. Logs are first used to define major lithologic boundaries and model layers are defined based on an impedance criterium and a minimum thickness criterium. Information from logs, core measurements, check shot data, and seismic is then integrated and used to construct smooth long wavelength equivalent transversely isotropic media for each of the layers. Each layer is parameterized as a function of two vertical velocities, V_P , and V_S , density, and three anisotropy parameters, δ , ϵ , and γ .

There are two possible applications of the modeling approaches developed here:

- The first application is in the calculation of average bulk rock properties at seismic frequencies at a given well. This will enable the generation of the "best possible" synthetic matches to seismic data at a well.
- The second application provides a way to construct new rock types for sensitivity analyses of petrophysical parameters away from the well. This involves the construction of a new type of rock that has a high probability of existence in an area that is laterally adjacent to a well.

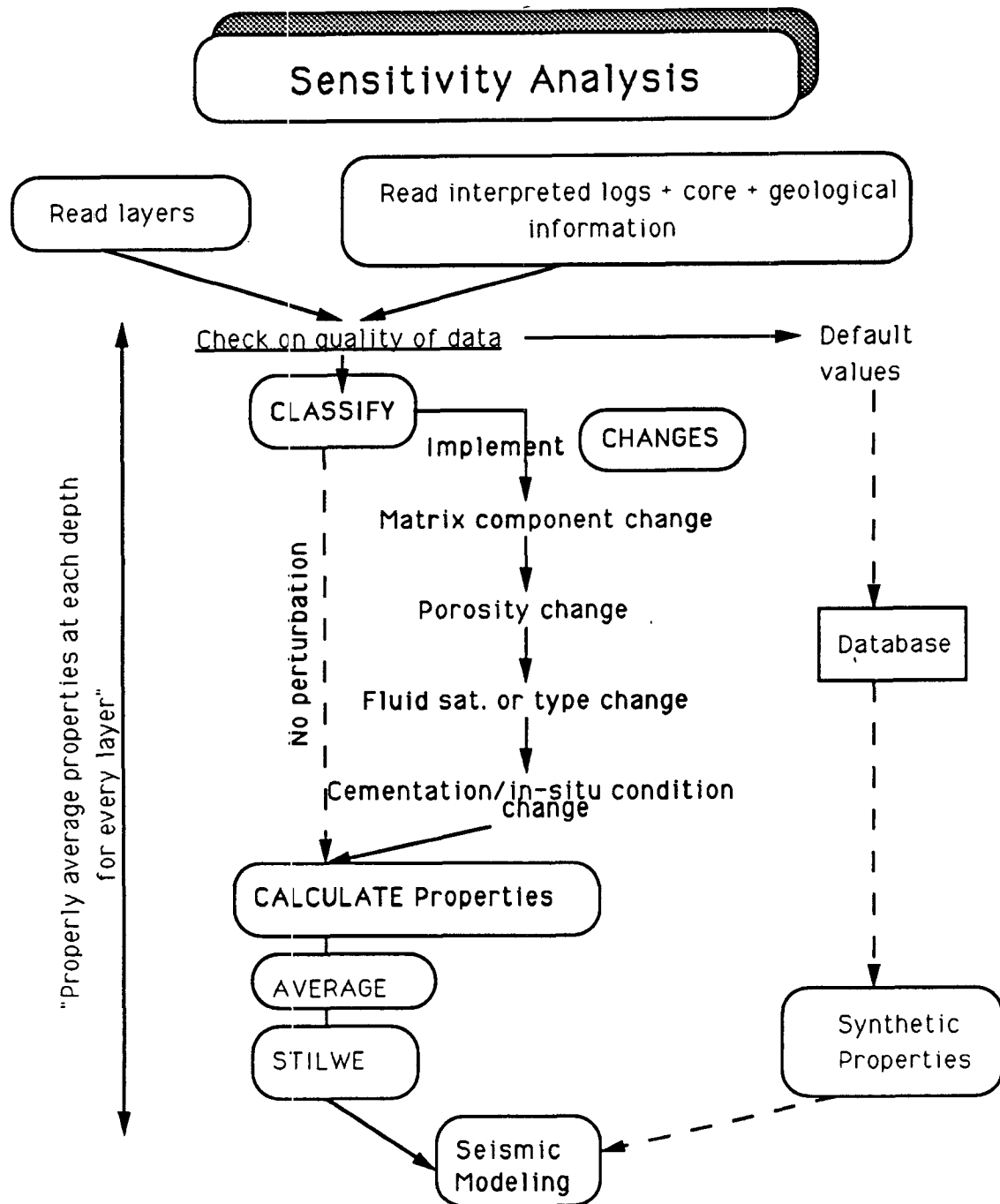


Figure 3.6: Implementing parameter variations: these are implemented within a given zone of interest, on a depth by depth basis; overall changes in the bulk properties of the zone are calculated at each depth sample and are then up-scaled to seismic wavelengths, according to the methods described in part IV.

As a final remark, the modeling approach presented here is part of a *continuously* evolving process; its purpose is to design and implement a methodology for bridging petrophysics and geology and tying seismic and lithology. The method serves as an ideal integration step in defining rock properties prior to synthetic modeling, and will be used in chapter 5.

REFERENCES

- Archie, G. E., 1952, Classification of carbonate reservoir rocks and petrophysical considerations: Bull. A.A.P.G., v. **36**, no. 2, 278,298.
- Ausburn, B., 1977, Well log editing in support of detailed seismic studies: SPWLA 18th Annual Logging Symposium, June 5-8, paper F.
- Babuska, V., 1981, Review Article: Anisotropy of vp and vs in rock-forming minerals: J. Geophys., **50**, 1, 6.
- Backus, G., 1962, Long wave elastic anisotropy produced by horizontal layering: J. Geophys. Res., **67**, 4427, 4440.
- Backus, M., and Chen, R., 1975, Flat spot exploration: Geophysical Prospecting, **23**, 533,577.
- Banik, N., C., 1987, An effective anisotropy parameter in transversely isotropic media: Geophysics, **52**, 1654,1664.
- Biot, M., 1956a, Theory of propagation of elastic waves in a fluid saturated porous solid; I-Low frequency range: J. Acoust. Soc. Am., **28**, 168,178.
- Biot, M., 1956b, Theory of propagation of elastic waves in a fluid saturated porous solid; II-Higher frequency range: J. Acoust. Soc. Am., **28**, 179,191.
- Bortfeld, R., 1961, Approximation to the reflection and transmission coefficients of plane longitudinal and transverse waves: Geophysical Prospecting, **9**, 485,502.
- Bourbie, T., 1982, Effect of attenuation on seismic reflections: SRB **14** .

- Brito dos Santos, W.L., Ulrych, T.J., and Lima, O.A.L., 1988, A new approach for deriving pseudovelocity logs from resistivity logs: *Geophysical Prospecting*, **36**, 83, 91.
- de Buyl, M.m Guidish, T., and Bell, F., 1988, Reservoir description from seismic lithological parameter estimation: *J.P.T.*, April, 475, 482.
- Carcione, J. M., Kosloff, D., and Behle, A., 1991, Long-wave anisotropy in stratified media: A numerical test: *Geophysics*, **56**, No. 2, 245, 254.
- Daley, P., F., and Hron, F., 1977 : Reflection and transmission coefficients for transversely isotropic media: *Bull., Seis. Soc. Am.*, **67**, 661,675.
- Domenico, S. N., 1976, Effect of brine-gas mixture on velocity in an unconsolidated reservoir: *Geophysics*, **41**, 882,894.
- Domenico, S. N., 1977, Elastic properties of unconsolidated porous sand reservoirs: *Geophysics*, **42**, 1339,1368.
- Dott, R., H., 1964, Wacke, graywacke and matrix - What approach to immature sandstone classification?: *Jour. Sed. Petrology*, v. **34**, No. 3, 625, 632.
- Folk, R., L., 1951, Stages of textural maturity in sedimentary rocks: *Jour. Sed. Petrology*, v. **21**, No. 1, 127, 130.
- Gardner, G.H.F., Gardner, L.W., and Gregory, A.R., 1974, Formation velocity and density - The diagnostic basics for stratigraphic traps: *Geophysics*, **39**, no.6, 770, 780.
- Gassmann, F., 1951: Elasticity of porous media: *Vier. der Natur. Gesellschaft in Zurich*, Heft I.
- Gelfand, V., Ng, P., Nguyen, H., Larner, K., 1988, Seismic lithologic modeling of Amplitude-Versus-Offset data: paper presented at the ASEG/SEG meeting, Adelaide, 274,276.
- Gregory, A. R., 1976, Fluid saturation effects on dynamic elastic properties of sedimentary rocks: *Geophysics*, **41**, 895,921.
- Han, D., Nur, A., and Morgan, D., 1986, Effect of porosity and clay content on wave velocity in sandstones: *Geophysics*, **51**, 1093,2107.
- Hoopes, R., Aber, W., 1989, Integrated multianalysis procedure that qualifies DHI's; a case history in the Louisiana Kackberry trend: paper presented at the 59th SEG convention, Dallas
- Inouye, F. Williams, G., 1988, An integrated approach to seismic interpretation: paper presented at the ASEG/SEG conference, Adelaide, 91,93
- Jones, T., and Nur, A., 1983, Velocity and attenuation in sandstone at elevated temperatures and pressures: *Geophys. Res. Lett.*, **10**, 140,143.

- Jones, T., 1986, Pore fluids and frequency-dependent wave propagation in rocks: *Geophysics*, **51**, 1939,1953.
- Kjartanson, E., 1979, Constant Q-Wave Propagation and Attenuation: *J.G.R.*, **84**, 4737,4748.
- Koefed, O, 1955, On the effect of Poisson's ratio of rock strata on the reflection coefficients of plane waves: *Geophysical Prospecting*, **3**, 381,387.
- Levin, F., 1988, Discussion on: "Weak elastic anisotropy", by L. Thomsen, 1986: *Geophysics*, **53**, No. 4, 558,560.
- Liu, H. P., Anderson, D., L., and Kanamori, H., 1976, Velocity dispersion due to anelasticity: Implication for seismology and mantle composition: *Geophys. J. R. Astron. Soc.*, 41,58.
- Marion, D., 1990, Acoustical, mechanical, and transport properties of sediments and granular materials: Ph. D. dissertation, SRB vol **39**
- Mathis, G., L., 1987, Smoothing spectral gamma logs: A simple but effective technique: *Geophysics*, **52**, 363,367.
- O'Connell, R. J., and Budiansky, B, 1977, Viscoelastic properties of fluid saturated cracked solids: *J. Geoph. Res.*, **82**, 5719,5735.
- Ostrander, W., J., 1982, Plane-wave reflection coefficients for gas sands at non-normal angles of incidence: Paper presented at the 52nd Intern. Mtg. and Expos., SEG in Dallas.
- Ostrander, W., J., 1984, Plane-wave reflection coefficients for gas sands at nonnormal angles of incidence : *Geophysics*, **49**, 1637,1648.
- Pettijohn, F. J., 1975, *Sedimentary rocks: third edition*, New York, Harper and Brothers.
- Poggiagliolmi, E., and Lowden, D., 1990, An integrated approach to reservoir petrophysical parameters evaluation: Paper presented at the annual International EAEG meeting in Florence, 74, 75.
- Sengupta, M., 1987, Sensitivity analysis of Amplitude Versus Offset (AVO) method: Paper presented at the SEG convention.
- Strandenes, S., and Blangy, J.P., 1991, Factors influencing velocities in porous rocks - theory versus experiment: this volume.
- Shuey, R. T., 1985, A simplification of the Zoeppritz equations: *Geophysics*, **50**, 609,614.
- Sun, C.T., and Li, S., 1988, Three-dimensional effective elastic constants for thick laminates: *J. of Composite Materials*, vol. **22**, July, 629, 639.
- Thomsen, L., 1985, Biot-consistent elastic moduli of porous rocks: Low frequency limit: *Geophysics*, vol. **50**, 2797, 2807.

- Thomsen, L., 1986, Weak elastic anisotropy: *Geophysics*, **51**, No. 10, 1954, 1966.
- Thomsen, L., Weak anisotropic reflections: manuscript prepared for "Offset dependent reflectivity" to be published.
- Tosaya, C., and Nur, A., 1982, Effects of diagenesis and clays on compressional velocities in rocks: *Geophys. Res. Lett.*, **9**, 5,8.
- Vail, P.R., Todd, J.M., Sangree, J.B., 1977, Chronostratigraphic significance of seismic reflections, in *Seismic stratigraphy - applications to hydrocarbon exploration: A.A.P.G. Memoir*, **26**, 99, 116.
- Wang, 1988, Wave velocity in hydrocarbons and hydrocarbon saturated rocks - with applications to EOR monitoring: Ph. D. dissertation, SRB vol **34**
- Ward, R. W., and Hewitt, M. R., 1977, Monofrequency borehole travel time survey: *Geophysics*, **42**, no. 6, 1137, 1145.
- Widess, M.B., 1973, How thin is a thin bed?: *Geophysics*, **38**, no. 6, 1176, 1180.
- Winkler, K., 1985, Dispersion analysis of velocity and attenuation in Berea sandstone: *J. Geophys. Res.*, **90**, 6793, 6800.
- Winkler, K., and Nur, A., 1986, Pore fluids and seismic attenuation in rocks: *Geophysical Research letters*, v. 6, 1,4.
- Wright, J., 1987, Short note: The effects of transverse isotropy on reflection amplitude versus offset: *Geophysics*, **52**, no. 4, 564, 567.

INTRODUCTION TO PARTS II AND III: APPLICATIONS

(1) General approach: Difficulties

The applicability of integrated, model-based, seismic interpretation methods to field data for reservoir characterizations remains difficult, because of several factors, including:

- 1) The **modeling methods** themselves, which are often computationally slow and generally do not allow for interactive adjustment of parameters
- 2) The relative difficulty in obtaining **realistic petrophysical properties**, including shear wave velocities, attenuation and anisotropy
- 3) **Differences in the scales of investigation**, which more often than not lead to layer induced anisotropy, due to the juxtaposition of finely layered media at the seismic scale; this problem is compounded by the need for integration of different disciplines in order to reduce the non-uniqueness in seismic interpretation.

Fortunately, the revolution in computer science has helped us get around the first problem; algorithms have been improved, CPUs are now faster or operate in parallel, and memory has become more readily available. The second problem is approached with the use of an increasing number of petrophysical measurements in the calibration of indirect techniques (chapters 1, 2 and 3) for reservoir detection and characterization. The third problem has been recognized and addressed (chapter 3) and hopefully, will be more routinely incorporated in the interpretation of seismic properties at different scales in the future.

(2) Applied work:

The modeling techniques developed in part I are applied to **real data** and form the basis for model based interpretation of several areas within the Troll West oil province. As can be seen by the relative size of parts II and III, this thesis places great emphasis on the analysis of real data:

- The first task (chapter 4) is to analyze and interpret a large 3-D **stacked**, migrated, seismic survey shot in 1989 over the Troll West area in the North Sea.
- Second (chapter 5), I apply the petrophysical-based modeling techniques to pre-stack data to attempt a more detailed **reservoir characterization** than was possible from stacked data alone. One can see that in the future, the model-based interpretation techniques may also be routinely incorporated into reservoir management studies for the monitoring of fluid flow during production.

(3) The role of geology/geophysics:

In general, the role of geology/geophysics can be seen as four fold:

- 1) To observe or to describe
- 2) To compare with established and well understood models
- 3) To interpret, on a regional and local context
- 4) To predict, meaning to delineate the extent of the reservoir, and to monitor its production

Hence, the immediate role of geology/geophysics is to expand the natural resource base, and if possible, to monitor the extraction of the mineral resources.

A variety of data types exist to achieve these four roles, but because seismic measurements provide a way of remote sensing the earth at reservoir depths and because they are the most common form of measurement used in the O&G industry, chapters 4 and 5 concentrate on seismic methods. However, note that seismic methods are **not** necessarily the most sensitive to certain crucial rock properties, such as fluid saturation. Additionally, borehole information is very accurate in the depth direction, but has a limited lateral penetration, whereas seismic has low vertical resolution but allows for large scale lateral investigations. Therefore, in order to utilize the power of seismic data to its full extent, it must be calibrated to well data: **accurate calibration** of seismic data is the **key** to the quantitative extraction of lithologic parameters.

**INTRODUCTION TO PART II: APPLICATIONS-1:
3-D INTEGRATED STACKED INTERPRETATION AT TROLL WEST**

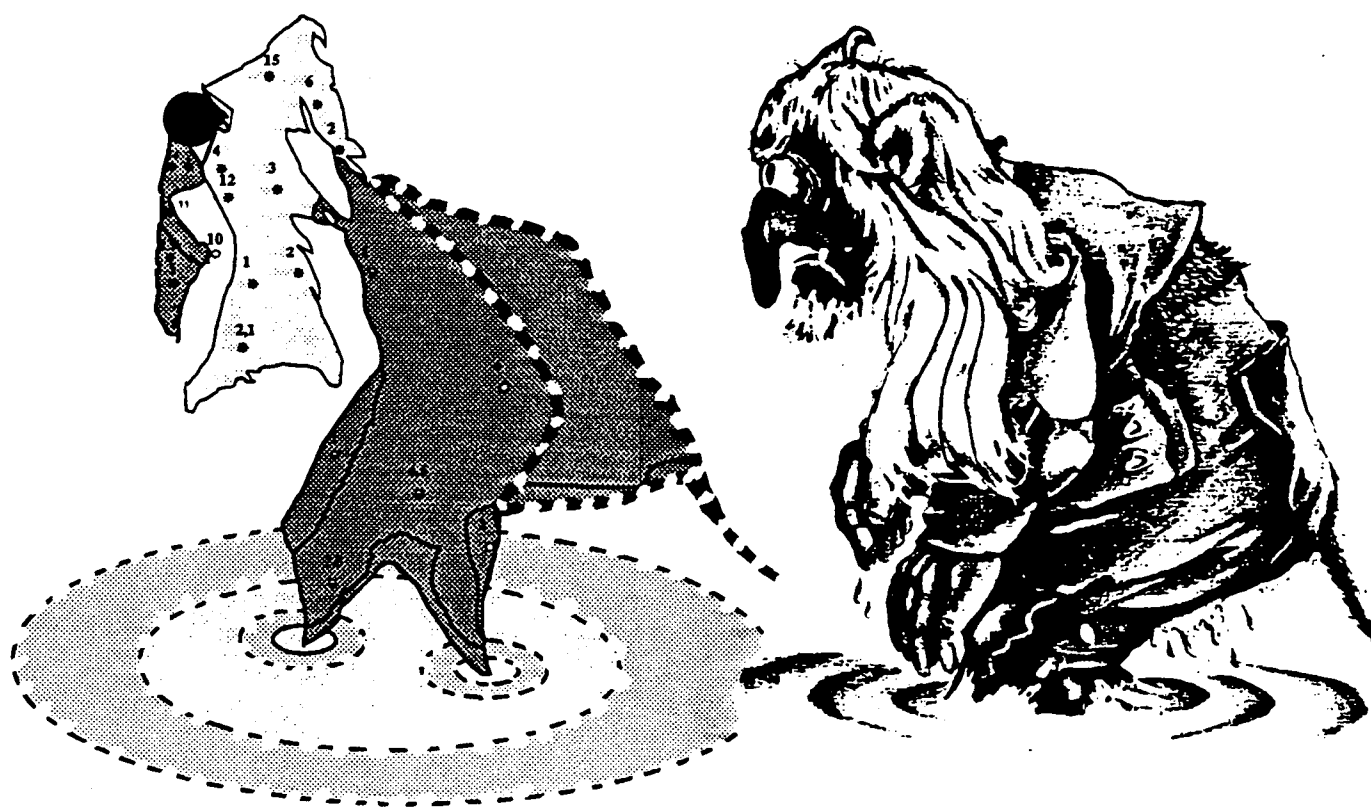
In chapter 4, I establish relationships from rock properties to geology, including dominant lithology and depositional environment, and map-out subtleties that are of interest for reservoir characterization in the Troll West Oil province.

One must always keep in mind that, within the seismic realm, structural information has to be mapped-out first, and only then can the interpreter go-on to investigate more subtle stratigraphic nuances. My first effort is therefore directed toward establishing the main structural controls of the field; I then define the general stratigraphy and look at lateral variations in stacked amplitudes and other complex seismic attributes; these allow for the accurate mapping of the stratigraphic components of the hydrocarbon traps. Because the data quality is good, it is feasible to carry the analysis one step further and to study pre-stack seismic behaviors, which allow a more detailed reservoir characterization than that available from stacked seismic attributes alone.

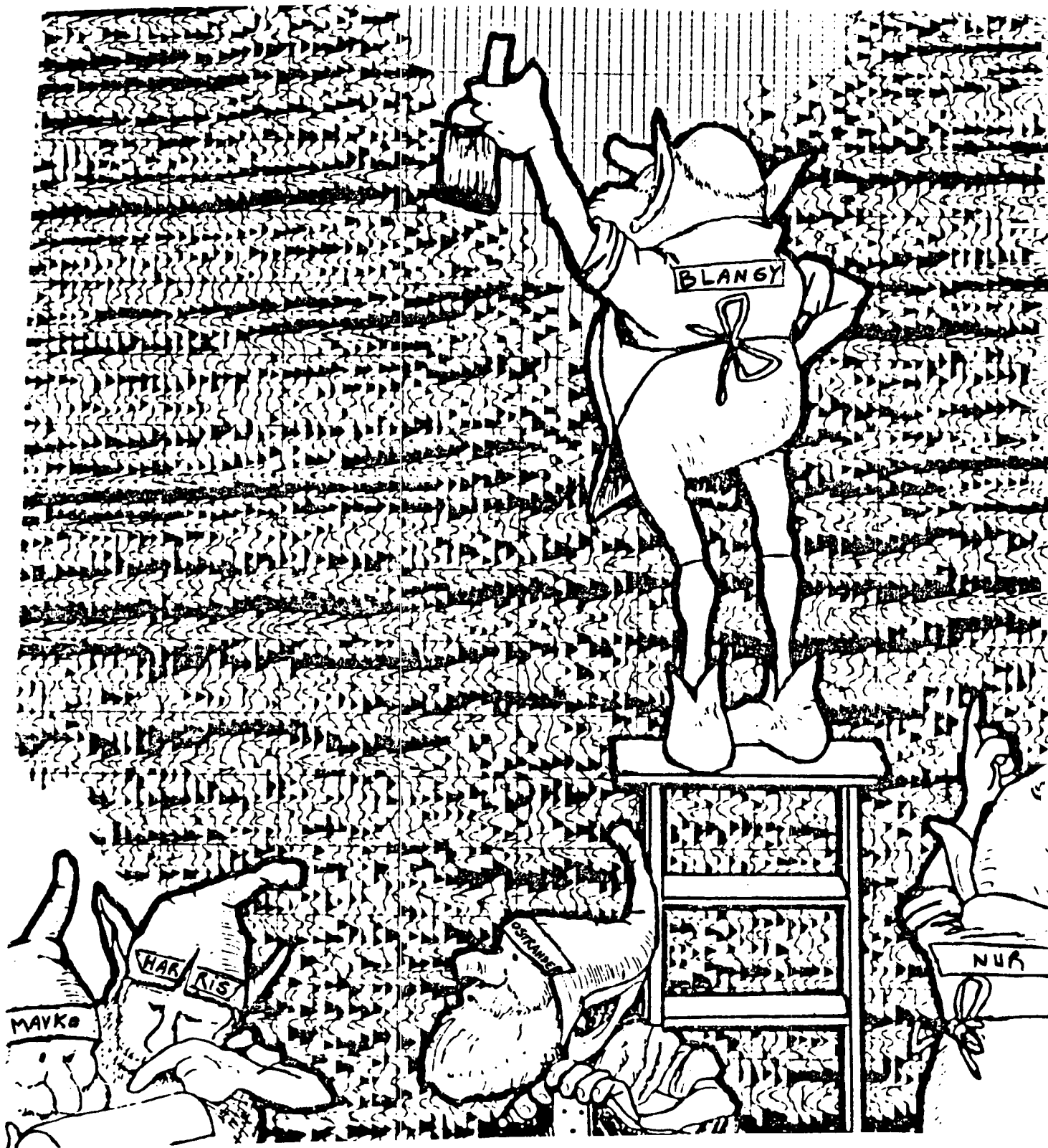
The Troll West Oil province, being a shallow reservoir with high quality seismic and well data, is a candidate of choice for a detailed integrated reservoir geophysical investigation. Moreover, the field has not yet entered its full production phase, which is scheduled to begin by early 1996, according to Norsk Hydro. Therefore, the potential for calibrated geophysical data to contribute towards the optimal production of the field is an exciting challenge.

While proceeding with the analysis of the Troll West Oil province, I seek to solve problems that are specifically associated with this reservoir; however, my goals are general and in doing so, I try to devise a general approach or methodology, to the analysis of integrated projects like Troll, and to suggest procedures that can be used in similar studies elsewhere.

TROLL ?



Introduction figure for parts II and III: Troll comparison.



Fill-in page

This page was inserted for esthetic purposes only, and does not necessarily reflect the author's opinion or his state of mind. It is NOT an integral part of the thesis at Stanford University, and was obtained from a series of "reliable" sources out there.

CHAPTER 4

THE TROLL WEST OIL PROVINCE: AN INTEGRATED 3-D SEISMIC STACKED MIGRATED INTERPRETATION

"Imagination is more important than knowledge", **Albert Einstein.**

"Oil is first found in the minds of men", **Wallace E. Pratt.**

ABSTRACT

First, I review the geological setting and regional structural features of the Troll field. This is followed by a description of the reservoir units in terms of depositional environment and lithologic facies. The hydrocarbon traps are structural with a stratigraphic component: the reservoir consists of a series of middle Jurassic shallow marine deposits prograding to the west and south over horst and graben blocks that are bounded by syndepositional normal faults associated with an aulacogen of Permian through Cretaceous age.

Second, I present the results of a detailed and integrated 3-D stacked migrated seismic interpretation of the Troll West Oil Province. Well-log information is tied to the seismic grid at well control points, thus enabling the correlation of sedimentary cycles identified on well logs to intra-formational reflectors. Structure contour maps are generated, including the top of Cretaceous strata, the top of reservoir "Sognefjord" sands, and the top of Brent sands, together with an isopach map of the Sognefjord Formation.

In a third and last step, I use pattern recognition techniques to assess the relative importance of several seismic attributes with respect to detecting reservoir heterogeneities. Using these attributes, a feasibility study is undertaken to: 1) classify the top of the Sognefjord sands, and 2) detect subtle, stratigraphic changes within the

Sognefjord reservoir units.

An **automatic unsupervised classification** was then run on a set of diagnostic complex seismic attributes. The procedure yields clusters of data, which identify areas of heterogeneity within the reservoir. A "training set" was then extracted from several sections around key wells. This training set was used for **supervised classification** of the reservoir along time slices and along the time-flattened Sognefjord horizon. The presence of a gas cap in the Sognefjord sands over much of the West Oil province creates strong anomalies in seismic attributes (such as amplitude, phase and frequency) at the top of the Sognefjord, which are easily recognized by the pattern recognition techniques. Examination of the same attributes at the Sognefjord/Fensfjord boundary reveals complex patterns, which may or may not be possible to relate to subtle changes in reservoir properties. The outcome of future production drilling may shed light on these apparent seismic trends.

The work with stacked migrated seismic data presented here provides a complete 3-D **structural** framework of the reservoir and a preliminary **stratigraphic** understanding, from which more detailed 2-D **pre-stack** seismic stratigraphic analyses can be carried-out. The work also demonstrates that it is **feasible** to use **pattern recognition** of migrated post-stack seismic attributes in identifying sub-units within the reservoir, even if some of the more subtle lithologic information was lost during the stacking process.

(I) INTRODUCTION

The characteristics of the Troll reservoir, the availability of high quality 3-D seismic data, and the relative abundance of well data, make it an ideal candidate for an integrated case study of reservoir description involving seismic, well logs, and core data.

Troll field description

The Troll field is a giant oil and gas field situated off the western coast of Norway. It was discovered in 1979 and was primarily considered as a gas field until recently,

when commercial oil reserves were found through horizontal drilling in the so-called Troll West Oil Province. The Troll field is considered to be the second largest offshore gas field in the North sea, with over 40 tcf of recoverable gas. It is located on the NW edge of the Horda platform, adjacent to the Bergen high, offshore western Norway, approximately 80 Km WNW of Bergen (figure 4.1). Because it is adjacent to the Norwegian trench, it has unusually large water depths of close to 340 m. The reservoir sands occur at approximately 1500 meters depth. The oil leg forms a rim of varying thickness beneath the gas zone. The thickness of the oil column varies from a few meters, up to more than 20 meters; a maximum oil column of 28m is found in the northern part. Horizontal drilling techniques have made it technically possible to produce the oil from this relatively thin zone at a profit. Due to the large size of the field (770 sq Km or 270 sq mi), the oil reserves are also large, and are estimated to be approximately 1.4 billion barrels recoverable (Halbouty, 1982), with total estimated O & G reserves of 8.9 bbls equivalent, thus ranking the field as the 36st largest in the world. For optimal reservoir management, the oil must be produced prior to gas exploitation.

The reservoir sands at Troll are shallower and the trap is structurally simpler than those found in North Sea structural hydrocarbon reservoirs which occur along a N-S axis located west of Troll. Due to the shallow depth and simple structure of the Troll West oil province, recently acquired 3-D seismic data (1989) over this field is very good. The reservoir sands are essentially clay free, of simple mineralogical composition, and as such can be considered as isotropic in the absence of microlayering. A detailed mineralogical analysis of these sands is presented in chapter 5. The micaceous sands of the reservoir have strikingly different permeabilities from their clean counterpart, and their mapping is essential to optimize the production of the field.

Very small pressure differences are observed between oil zones in adjacent fault blocks in the Troll West oil province, but in general, it is accepted that there are little to no permeability barriers between fault compartments, indicating non-sealing faults. This is also supported by the fact that there are no large jumps in fluid levels

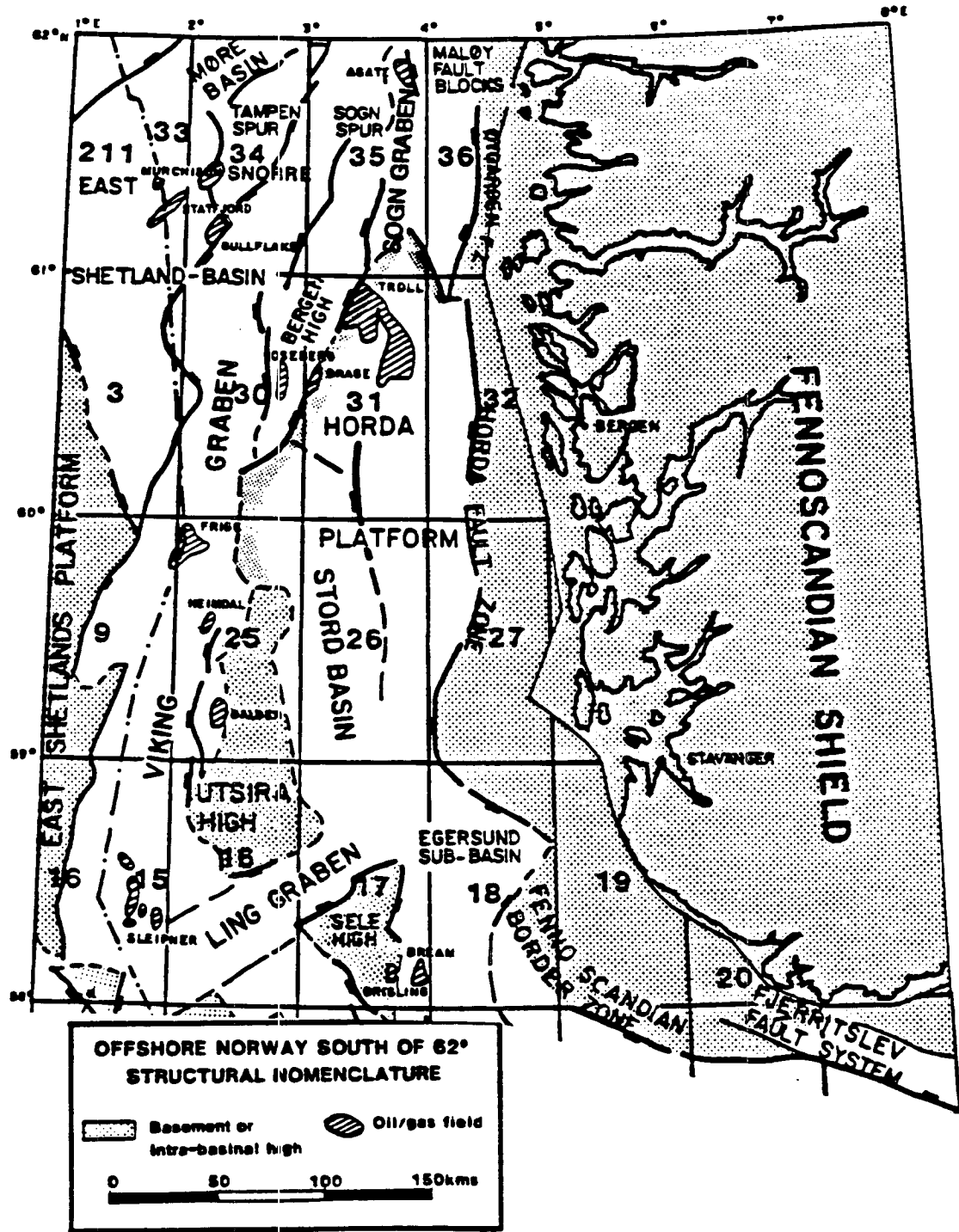


Figure 4.1: The Troll field is located on the NW edge of the Horda platform, adjacent to the Bergen high, offshore Western Norway. The field is located to the East of the North-South trend formed by most of the other fields in the North sea. It is associated with unusually deep waters of upwards of 350 m (figure adapted from Norsk Hydro, Joint Geological review, 1988).

across the Troll West Oil Province (see table 4.5).

Carbonate layers occur in a variety of ways, from small nodules to laterally extensive vertical permeability barriers of calcite. These constitute 6-8 % of the total rock volume. Carbonate cements, consisting mostly of calcite, occur in all major lithologies within the reservoir. Unfortunately, they act as permeability barriers wherever they are present.

In the following, I first review the structural and depositional aspects of the field as a whole, and then focus on the integration of well log and seismic data for the interpretation of a 3-D survey, acquired in 1989 over the Troll West Oil province. I also investigate the use of seismic attributes and pattern recognition techniques for more detailed structural and stratigraphic interpretations.

(II) GLOBAL SETTING AND REGIONAL STRUCTURAL CONTROL

1) The North Sea

The North Sea basin underwent a complex geologic evolution from Cambrian through recent time (Glennie, 1986, Ziegler, 1989, 1990, Klemperer and Hobbs, 1992). A phase of tensional tectonics, associated with the opening of the north Atlantic began during Permian. The North Sea rift system per se initiated during the Triassic and developed fully during the Jurassic and Cretaceous, where it dominated most other depositional controls. Today's configuration of the oceanic crust in the North Sea shows a zone of maximum crustal thinning which coincides with the Viking and Central grabens. According to Blundell and Gibbs (1990), the Moho rises from a depth of approximately 35 Km under the coast of Norway, to about 20-25 Km under the Viking and Central grabens. Furthermore, Ziegler (1990) calculates coefficients of crustal extension, β , of 1.05 for the Horda platform and 1.15 for the Viking graben at the base of the Jurassic.

Permian sedimentation was rift-related, with continental clastics and evaporites, extending through middle Triassic. Deposition of anaerobic marine sediments fol-

lowed and continued until late Jurassic. Cretaceous and Tertiary deposits were also dominantly marine.

The tectonic framework of the North Sea led to the development of two main hydrocarbon provinces: 1) a southern province, where Permian Rotliegendes sandstones are capped by Zechstein evaporites, and 2) a northern province, where Jurassic sands occur along a north-south rift axis. The **Troll** field lies to the **East** of this main trend, and as a result, has had a different depositional and diagenetic history than the other fields of the northern North Sea.

2) Structural and depositional controls at Troll

a) Structure

Troll is bounded to the west by the N-S-trending Bergen high, which is part of the Northern Viking graben (60°30'N to 62°00'N). To the north, it is bounded by a complex transform fault zone which connects the Viking graben to the Sogn graben. It is also bounded to the south, by the Stord graben, and to the east, by the Oygarden fault zone. As shown in figure 4.2, the **Troll** field can be conveniently sub-divided into three major fault blocks:

- a north-south fault block consisting of the **Troll East gas province**,
- a northwest-southeast fault block called the **Troll West gas province** and
- a northwest-southeast fault block, the **Troll West oil province** , which is separated from the **Troll West gas province** by a major controlling fault.

Figure 4.2 also indicates the location of major wells at **Troll** and the thickness of the oil zone, as interpreted and contoured from well log resistivities and neutron-density cross-overs.

b) Regional stratigraphy (depositional controls)

The North Sea central graben/Viking graben system is an aulacogen or failed rift which initiated during Permian times. At the end of the lower Jurassic, a large

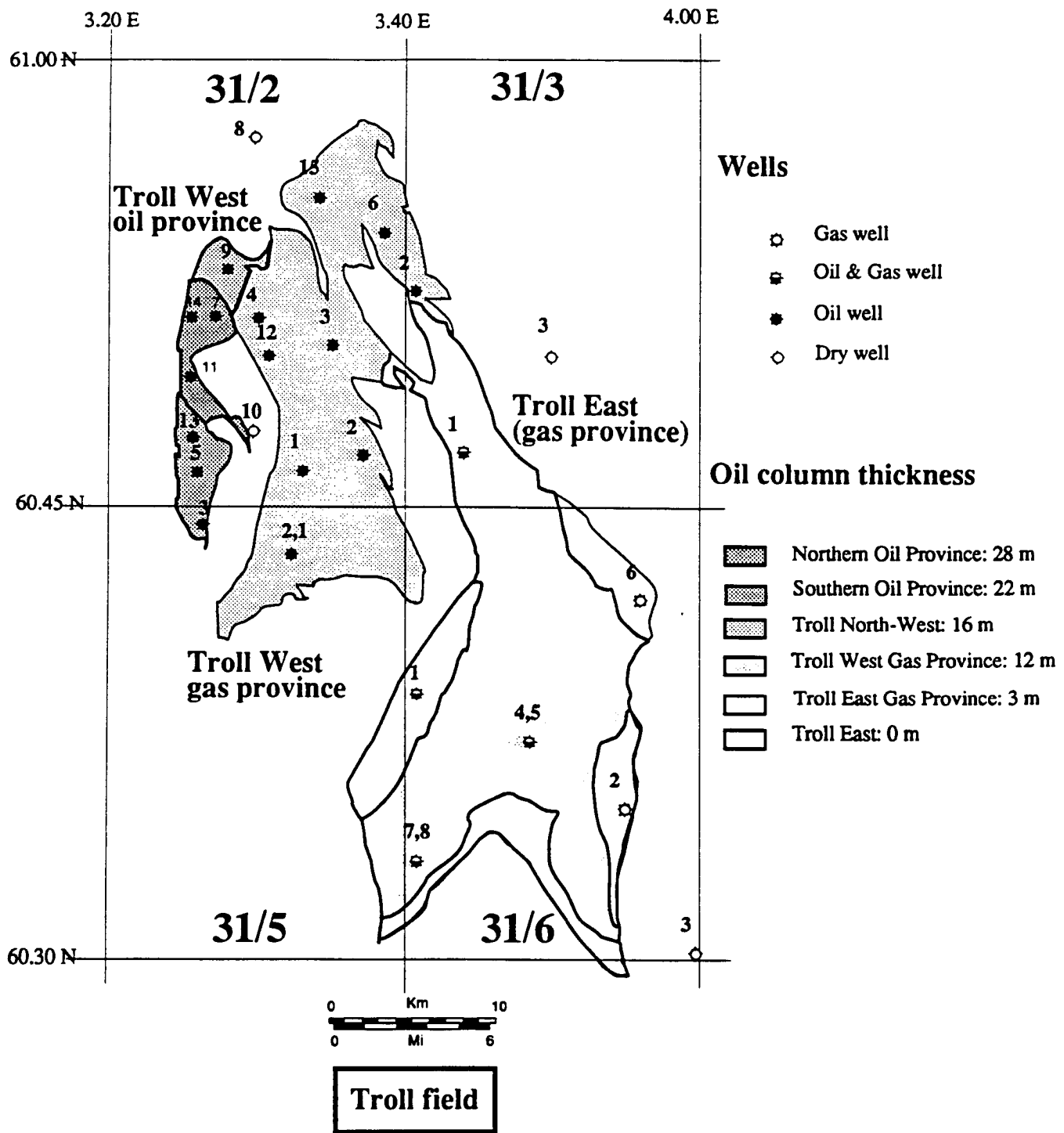


Figure 4.2: Map of the Troll field showing the location of wells and the thickness of the oil column. As can be seen, a substantial amount of oil is present in the western part. Troll is considered the second largest gas field in the North Sea, with an estimated 43 tcf of recoverable gas.

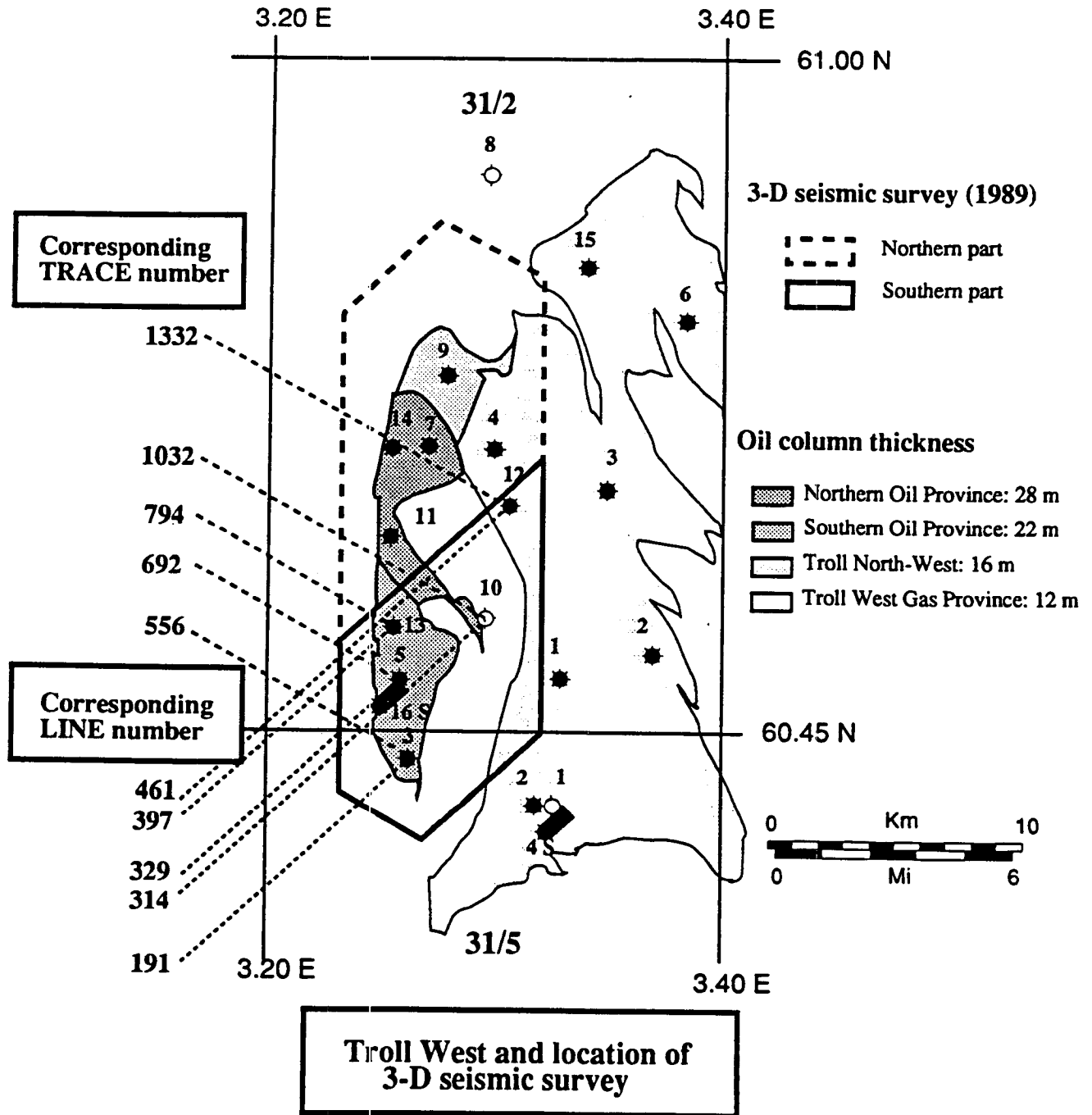


Figure 4.3: Close-up on the Troll West Oil province, showing the layout of the 3-D survey shot in 1989 (losange shape). The southern part was interpreted. It is estimated that over 1 billion barrels of oil are present. The relatively thin nature of the reservoirs makes the oil production difficult, but horizontal wells are profitable. Well 31/5-1 is an old well that was re-spudded and renamed well 31/5-2. It is located next to well 31/5-4S which will be studied in detail in chapter 5.

rift dome uplifted at the triple junction between the Central graben, the Viking graben, and the Moray Firth fault complex. This uplift enabled the progradation and build-out of Middle Jurassic deltaic **Brent** sands. The axis of the Viking graben was progressively offset in a dextral motion during Middle and Late Jurassic and produced a set of NE-SW trending faults.

During Callovian (**Late Jurassic**) time, a major rise in relative sea level led to the widespread deposition of marine shales of the **Viking Group** throughout the basin. This was accompanied by local deposition of shallow marine sands around intrabasinal highs and on the flanks of the basin. The **Sognefjord** sands consist of one such shallow marine sequence. Continued rifting at the end of Late Jurassic led to the easterly tilted fault blocks that constitute the hydrocarbon traps at Troll today.

Late Jurassic and Early Cretaceous times were often dominated by restricted, anoxic sea bottom conditions and led to the organic rich clay deposits of the **Draupne Formation**, which are equivalents of the Kimmeridge clay for the main rift (Dore et al., 1985). Fault movement and block tilting toward the east continued throughout the Cretaceous, creating a complex and intricate series of unconformities. As a result, upper Jurassic and Cretaceous units are often missing in the western part of the field. Rifting ceased by the end of the Cretaceous and led to the **widespread** deposition of **Tertiary** claystones.

In this study, I concentrate on the **Troll West Oil Province** (figure 4.3); it is divided into a series of horst and graben blocks which are bounded by Northwest-Southeast faults. In general, the hydrocarbon traps consist of eastwardly tilting fault blocks. A major saddle feature divides the Troll West oil province into a northern and a southern province. The hydrocarbon reservoir sands consist mainly of Middle to late Jurassic (Oxfordian-Tithanian) deltaic and shallow marine sands of Troll West. However, continental clastics of late Triassic age (Carmian-Norian-"Reuper") and Lower Cretaceous (Aptian-Albian) deeper marine clastics and carbonates can also be found in other parts of Troll (Ziegler, 1989, Ziegler and van Hoorn, 1989). The

reservoir section belongs to the Viking Group, which is normally sub-divided into the Heather, Krossfjord, Fensfjord, Sognefjord, and Draupne Formations. The Sognefjord sands form the high quality oil and gas bearing reservoir sands of the Troll West Oil Province.

3) Key parameters in the evolution of hydrocarbon traps at Troll

In general, hydrocarbon traps require the following three key parameters: 1) a reservoir structure, 2) the proper source rock/maturation and migration history, and 3) a seal. All three are present at Troll:

- The structures are typical horst and graben features. They formed during continued late Kimmerian (Late Jurassic) fault block movements which involved block rotation and tilting to the east, resulting in the erosion or non deposition of Upper Jurassic and Cretaceous sediments, specially in the west.
- The source rock is the Draupne Formation, a Kimmeridge clay equivalent at Troll. According to the source rock maturation work of Thomas et al. (1985), the Troll "kitchen" was located to the WNW of the field and migration of oil occurred as early as Upper Cretaceous/Lower Tertiary. A substantial amount of lateral migration of oil, up to 40 Km, has been documented by Thomas et al., 1985; this migration was synchronous with block tilting towards the east.
- The complex erosion pattern of eastwardly tilted blocks implies a laterally changing seal, going from Upper Jurassic claystones to Cretaceous marls to Tertiary claystones from east to west within each block sequence. Much of the Upper Cretaceous strata is absent over the Troll West Oil Province.

Tilting of the field toward the west began in late Jurassic/Late Cretaceous times and peaked during Late Tertiary. As a result, gas expulsion, migration and entrapment occurred in Late Tertiary times during subsidence towards the west; this led to the widespread displacement of oil by gas, in an eastward direction.

4) Discovery of the Troll field and future plans

The Troll field was first discovered in 1979 with well 31/5-1 shown in figure 4.2. This particular well was later shut-in and re-spudded as well 31/5-2. The target was the crestal high of a horst block in the Troll West gas province. A flat bright spot had been identified on the stacked migrated data and suggested a possible gas-liquid contact around well 31/2-1. This was later interpreted as the spill-point of the structure (Gray, 1987). The seismic bright spot is prominent and can be correlated over much of the Troll West gas province and Troll East gas province. Unfortunately, it is difficult to identify in the Troll West oil province.

As a result of licensing round PL54 in 1979, Shell acquired operatorship of block 31/2 with a 35 % interest. Statoil acquired a 50 % interest, and Norsk Hydro, Conoco, and Superior Oil each obtained a 5 % interest. Troll East forms the largest gas structure, and was discovered in 1983. Blocks 31/3, 31/5, and 31/6 were awarded as a result of PL85, from which Statoil obtained 85 %, Norsk Hydro 9 %, and Saga 6 %. Today, the appraisal of the field is complete, with a total of 15 wells having been drilled in block 31/2 by the end of 1984. According to Norsk Hydro, development of the Troll field in the future will involve (1) the production of oil from the Troll West oil province, which should be under full production by early 1996, and (2) full scale gas production from Troll East, which is also supposed to begin in 1996. In the meantime, as part of the "Troll-Oseberg Gas Injection Project", partial production of gas has already begun from Troll East. This project consists in producing and transporting gas via pipeline to the Oseberg field for injection. The gas from the Troll West Gas Province will be produced subsequently, but no firm decision has yet been made as to the production of oil from that area. As a final remark, it is interesting to note that most of the gas to be produced from Troll has already been contracted for consumption in western Europe.

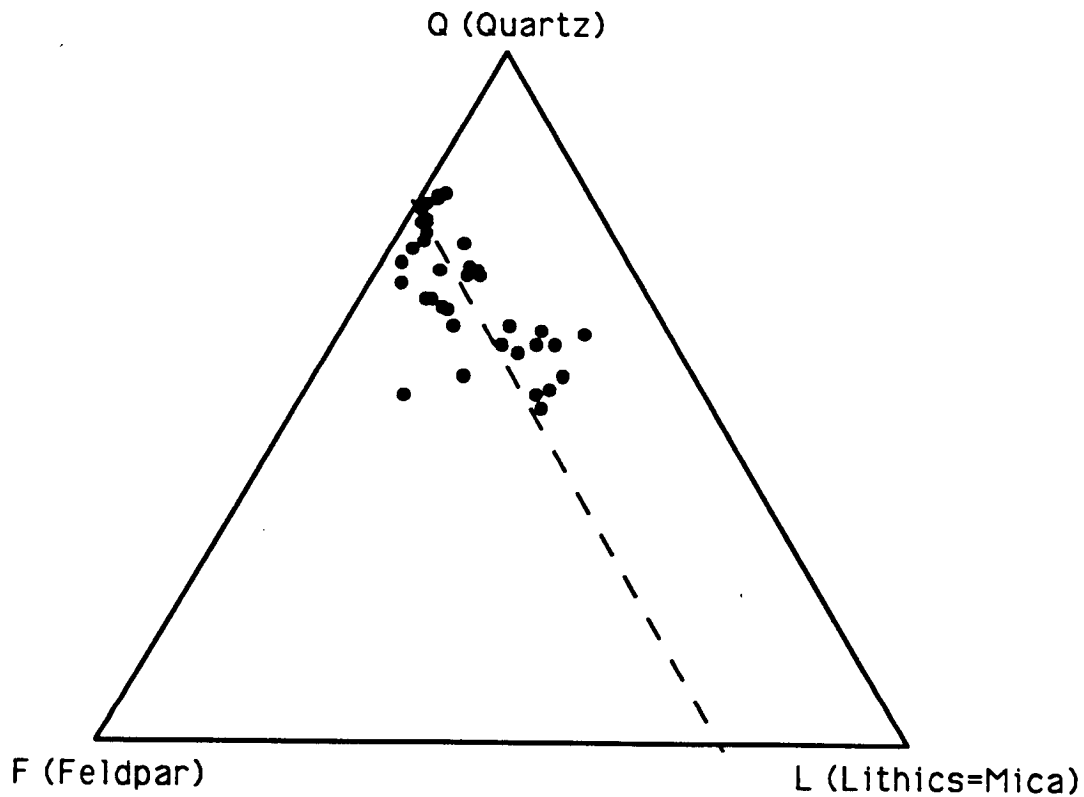
(III) RESERVOIR DESCRIPTION

1. General description

The reservoir sands consist of a section of up to 350 meters thick of Middle/upper Jurassic shallow marine deposits from the Viking Group. They represent a period of transgression over earlier Jurassic sediments, changing from marginal marine to higher energy conditions. Sediment supply was from coastal distributaries, located just east of Troll. The best sands are clean, loosely consolidated, with excellent porosities ranging up to 40 %, and extremely high permeabilities sometimes in excess of 10 Darcies. Overall, shale beds seem to be absent from the reservoir sand units.

From the core analyses in chapter 5, I determined that the mineralogy of the sands is that of typical sub-arkoses, with an approximately constant concentration of feldspars at around 20 %. The concentration in micas can be unusually high, ranging from 5 % to 20 % as analyzed from well 31/5-4S (see figure 4.4 and chapter 5). The mapping of micaceous layers is important, because they are characterized by lower permeabilities. Furthermore, the micaceous sands are thought to restrain the movement of fluids between fault blocks, because they have higher pore entry pressures than cleaner sands (Norsk Hydro, personal communication).

The mineralogic point counting from thin sections presented in chapter 5 shows two types of sands: (1) "clean" sands, which have a mica content of less than 5 %, and (2) micaceous sands, which have a mica content comprised between 5 and 20 %. Because the mica sands have greatly reduced permeabilities, they are borderline economical, and preference will be given to producing the clean sands (Norsk Hydro, personal communication). Because the field has not yet entered its production phase, the mapping of the clean sands is important for designing the optimal recovery program. The carbonate cemented horizons also pose a problem in producing the field, because they play a critical role in controlling fluid flow during production, since they act as permeability barriers. Unfortunately, they are usually discontinuous, except for those occurring at major facies boundaries, and may vary



Sognefjord sands at well 31/5-4S

Figure 4.4: Ternary diagram showing the global composition of the Sognefjord reservoir sands. The mineralogical analyses were carried-out on 38 samples from well 31/5-4S (chapter 5), and show typical sub-arkosic sands with varying amounts of mica. The sands are fairly immature. Note that overall, the amount of potassium feldspar is relatively constant, at approximately 20 %.

laterally in thickness. I present detailed analyses of the lithologies encountered at the six wells within the studied 3-D seismic grid (and at well 31/5-4S) in appendix B and in chapter 5.

2. Subdivisions within the reservoir

The Sognefjord Formation contains over 90 % of the hydrocarbons in the Troll field, with the Fensfjord Formation being the second most important reservoir rock after Sognefjord sands. According to Norsk Hydro (Joint Geological report, 1988), the Fensfjord is interpreted as a progradational shoreface facies, with a series of small units coarsening upwards, ranging from micaceous siltstones to medium grained sands. The Sognefjord represents a shoreface transgression, followed by progradation across the shelf, with alternating cycles of low energy, more distal, fine micaceous silts coarsening upwards into medium to coarse grained clean sands. As a result of the progradation towards the west across the Horda platform, the Sognefjord upper boundary is diachronous. Figure 4.5 shows a schematic type stratigraphic section of the Sognefjord along with log responses for the area. Well 31/2-5 was used as the **type well**. The reservoir facies descriptions were obtained from core descriptions, courtesy of Norsk Hydro, while fluid contacts were identified from well logs. For a look at the detailed log responses within the Sognefjord Formation for the six wells present within the 3-D survey area, refer to Appendix B. Well 31/2-5 shows a gas thickness of 43 m, oil thickness of 21.5 m, and major formation tops at 1532 m (K-T boundary), 1536 m (Sognefjord), 1692 m (Fensfjord), and 1956 m (Brent).

According to Norsk Hydro (Joint Geological report, 1988) five major facies sequences can be identified within the Sognefjord throughout the Troll field. They correspond to five different depositional environments:

- a) Low energy marine, which led to the deposition of fine grained micaceous sands. This is considered to be the normal shelf sedimentation environment.
- b) Moderate energy marine, which originated fine to medium grained sandstones. These contain micas and some drapes of clay and organic material,

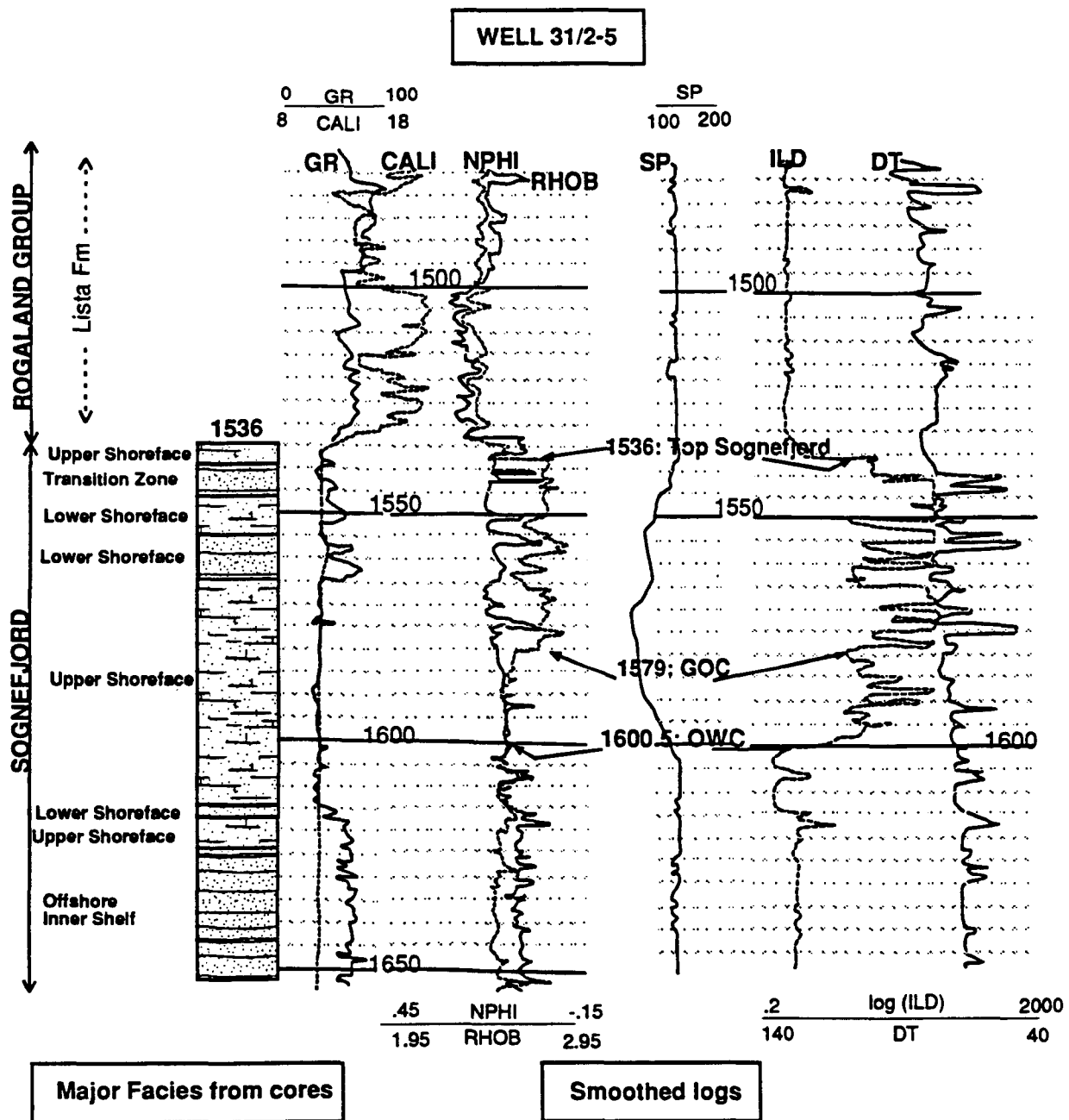


Figure 4.5: Schematic stratigraphic column at the "type" well 31/2-5. Facies were interpreted by Norsk Hydro from core logs (Joint Geological report, 1988). Thin calcite stringers can be identified on the sonic and density logs (see appendix B for more details on individual log responses).

and are mostly found in Troll East.

- c) High energy marine which deposited clean, medium to coarse grained, and moderately sorted sands.
- d) Tidally influenced marine, which resulted in cross-bedded sands with draping of clay units. Double mud drapes are associated with channel deposits and in general, these deposits exhibit high angle cross lamination.
- e) Storms, which deposited poorly sorted and inhomogeneous sands. The distribution of grain sizes, their structural organization and the thickness of individual beds depend on the strength and duration of the storms, on the distance from the source, and on the depositional depth.

Well-based paleogeographic reconstructions at Troll West (Hellem et al., 1986) show that the southern part of the Troll West Oil Province formed a structural high and, at times, a topographic high during deposition. This led to active westward shoreface progradation and northward sand ridge migration, which are characterized by thick, upward coarsening sequences of moderate to high energy conditions.

The normal depositional environment at Troll West during Sognefjord times was dominated by low energy marine conditions. This led to the five facies sequence types described previously. Two dominant types of facies associations are present, both being of upward coarsening cycles: (1) facies types a through d, which are related to transport by water bottom currents and (2) facies types a, b, and e, which are related to storm processes. Cycle (1) is dominant at Troll West. Each upward coarsening cycle shows a bimodal distribution of sediments, in both grain size and lithology. The cycles initiate with a more silty and micaceous base, grading into coarser and cleaner sands. In defining a facies model, I have therefore picked the two main lithologies - micaceous sands and clean sands - within each upward coarsening depositional cycle (Appendix B).

In general, it is found that silty and micaceous sands have porosities comprised

between 20 % and 30 %, with permeabilities of less than 1 D. The fine to coarse grained clean sands have porosities of 25-40 % with permeabilities of up to 10 Darcies. The latter are the target sands for production, because the micaceous sands are not always continuous, and cannot be produced economically. I therefore map the location of both of these sand types from combined well and seismic data.

3. Mineralogy and Diagenesis

Figure 4.4 summarizes the mineralogic analysis that I made at well 31/5-4S, from point counting of thin-sections; chapter 5 includes details of the analysis, which I performed in the Stanford Rock Physics laboratory. The figure shows that the sands are typical arkoses to sub-arkoses. Note that overall, the amount of potassium feldspar is relatively constant at approximately 20 %. The sands are textural immature, as can be seen by the individual grains which are sub-angular to sub-rounded, by the large amount of well preserved feldspars, and by the preservation of relatively fragile components, like amber (see chapter 5); all of this indicates that the source rock was likely a nearby granitic mass. The following summarizes the occurrence of the major mineral components that I found from the thin-section analysis:

- Quartz: occurs as monocrystalline to polycrystalline grains.
- Feldspar: mainly orthoclase, but microcline, plagioclase and microperthite can be present.
- Mica: present in various amounts; mainly muscovite, with some biotite and chlorite. Generally randomly oriented, but can occur as laterally extensive laminae, possibly forming permeability barriers. Correlates with finer grained deposits, and generally contributes to a higher gamma ray response on logs.
- Rock fragments and shell fragments, can occur in local concentrations of up to 30 %. These are usually associated with higher energy deposits, such as the larger grain sized sands.

- **Carbonate:** calcite layers can occur in all stratigraphic intervals. According to Norsk Hydro (Joint Geological report, 1988), trends in the location or areal extent of the calcite intervals seem to correlate to eustatic sea level changes (maximum flooding surfaces and sequence boundaries from the Haq et al. curves) in Troll East. Additionally, carbonate cement occurs in a variety of forms, from small nodular layers to pervasive cemented layers; this leads to carbonate cemented horizons, with laterally varying thicknesses.

Kaolinite can also be found; it is the dominant authigenic mineral, and occurs in concentrations of up to 20 % (data from Norsk Hydro, 1988, Troll Joint geological review). Furthermore, according to Norsk Hydro, changes in kaolinite content seem to correlate to the original concentration in muscovite, thereby supporting the diagenetic origin of the kaolinite.

In summary, the mineralogic content, the average shape of the grains, and their relatively well preserved state, contribute to the observation that the reservoir rocks are fairly immature and have been weathered from a nearby granite mass. Two types of sands can be identified at Troll West:

- **Clean sands:** which occur as medium to coarse grained, well sorted, arkosic sands with no preferred mineral orientation. Their mica content is generally less than 5 %, and they have the highest permeabilities and porosities. They are the targets for production, when their thickness is greater than 12 m.
- **Micaceous sands "of Troll West"**, which occur as very fine to medium grained, moderately to well sorted sands, with mica concentrations of 5 % to 20 %, showing no apparent preferred orientation (in contrast to those found at Troll East).

(IV) MAJOR STRUCTURAL CONTROLS

In general, three types of "fractures" can be identified at Troll:

- macrofaults
- single fractures
- swarms of fractures

Single fractures and swarms of fractures are identifiable on logs and in core samples, but their role with respect to permeability is difficult to assess. Unfortunately, they cannot be readily identified on seismic. Macrofaults have throws in excess of 10-15 meters and can be easily identified on seismic sections, as seen in the horst and graben blocks on figure 4.6. Most faults are normal faults with large amounts of offset, but they sometimes show evidence of reversals (see fault interpretation section in part V). Some of the faults can be identified as major bounding faults, such as the one colored in red in the eastern part of line 328, trace 1200, figure 4.6. This fault correlates across the entire Troll province and is considered a major boundary. It also exhibits the greatest amount of rotation and eastwardly block tilting. The structural evolution of the Troll West Oil Province will be discussed in detail in part V.

(V) 3-D INTERPRETATION OF THE TROLL WEST OIL PROVINCE

In the following, I present a summary of a detailed 3-D interpretation of the 1989 3-D seismic survey shot over the Troll West Oil Province. The interpretation provides a good general 3-D structural framework from which to build for future detailed 2-D pre-stack analyses of selected parts of the reservoir.

1) Classical 3-D Interpretation of stacked migrated data

a) Survey layout

Figure 4.3 is a close-up on the Troll West Oil province, showing the layout of the 3-D survey shot in 1989 (losange shape). The highlighted southern part was interpreted

Processing sequence Troll NH-8901

- 1) Reformat, edit
- 2) Minimum phase designation
- 3) Amplitude recovery
- 4) Adjacent trace summation
- 5) CMP sort
- 6) First VELAN
- 7) DMO
- 8) Multiple attenuation in F-K domain
- 9) Predictive deconvolution
- 10) Second VELAN
- 12) Stack
- 13) Gun and cable static correction
- 14) In-line F-K migration
- 15) In-line residual F-X migration
- 16) T/q attenuation compensation
- 17) Spectral balancing
- 19) Time variant filtering
- 20) Cross-line F-X migration

Table 4.1: Processing sequence used by CGG for the 1989 3-D seismic survey over the Troll West Oil Province.

here. The data was shot by Geco in 1989 and processed by Compagnie Generale de Geophysique for Norsk Hydro. A constant goal was set to recover amplitudes as "truly" as possible. The processing sequence is summarized in table 4.1.

The stacked migrated data was loaded on a Landmark IBM RT based system. The dynamic range of the seismic amplitude traces was scaled and clipped to a range of 8 bit integer values on input using the Batch Control Monitor. This is an important step and was first done dynamically on a test subset of the data. Because the seismic amplitude data appeared to be normally distributed, only the 98th percentile and above were clipped. This resulted in a display with most of the total amplitude range being converted in a range from -127 to 128. Amplitudes are displayed on a color scale ranging from dark red (peaks) to dark blue (troughs) in figures 4.6, 4.9-4.11 and figure 4.13. The southern part of the survey consists of a set of 453 lines, numbered from 36 to 488, and 1420 traces, numbered from 161 to 1580. Only the even numbered lines were loaded and interpreted. The trace spacing is 12.5m and the line spacing is 18.75m. Working in a coordinate system of line number / trace number is easier than working with UTM coordinates, so the former system was used here. The coordinates

Vertical well coordinates (Longitude and latitude)					
Well	31/2-13	31/2-5	31/2-10	31/2-12	31/5-3
Latitude	60 DEG 47'14 N	60 DEG 46'16 N	60 DEG 47' 39N	60 DEG 50'06 N	60 DEG 44'37 N
Longitude	3 DEG 26' 03E	3 DEG 25'53 E	3 DEG 29'40 E	3 DEG 30'48E	3 DEG 26'21 E

Horizontal well coordinates (Longitude and latitude)		
Well	31/5-4S	31/2-16S
Latitude	60 DEG 43'16 N	60 DEG 46' 00 N
Longitude	3 DEG 33'43 E	3 DEG 25'27 E

Well coordinates and Gas-Oil contacts (ms)							
Well	31/2-13	31/2-5	31/2-10	31/2-12	31/5-3	31/2-16S	31/5-4S
Line	397	329	314	461	191	(318)	outside 3D
Trace	794	692	1032	1332	556	(640)	outside 3D
GOC	1656	1650	dry	1656	1656	1656	-

Table 4.2: Well coordinates (in line number, trace number coordinate system), and fluid contacts in ms, two way travel travel time, at the six major control wells within the 3-D surveyed area; the seventh well, well 31-5-4S, was used for core analysis (see chapter 5 for details).

of the wells drilled within the interpreted 3-D survey area are indicated in table 4.2.

b) Procedure

The seismic interpretation was performed on dip-lines, perpendicular to structural strike, because they have a better S/N than strike-lines (which will be referred to as "traces"); this can be seen in figure 4.13. The data was interpreted every 10th dip-line, with denser picking immediately around well control points; in-fill lines were interpreted subsequently; the accuracy of the picks is estimated at about 1-2 ms. I used the 3-D seismic interpretation approach which is summarized in table 4.3. The approach is based on establishing ties between well-log picks and seismic horizons, as shown in figures 4.9, 4.10 and 4.11 of part e). The interpreted horizons are then correlated across the field, by tying around seismic loops. The well log picks used for correlation to the 3-D seismic are summarized in tables 4.2, 4.4, and 4.5. Well 31/2-13 has a 45 degree hole deviation and well 31/2-16S is horizontal. Ties between well-logs and seismic are crucial and will be discussed in part e) for all wells encompassed within

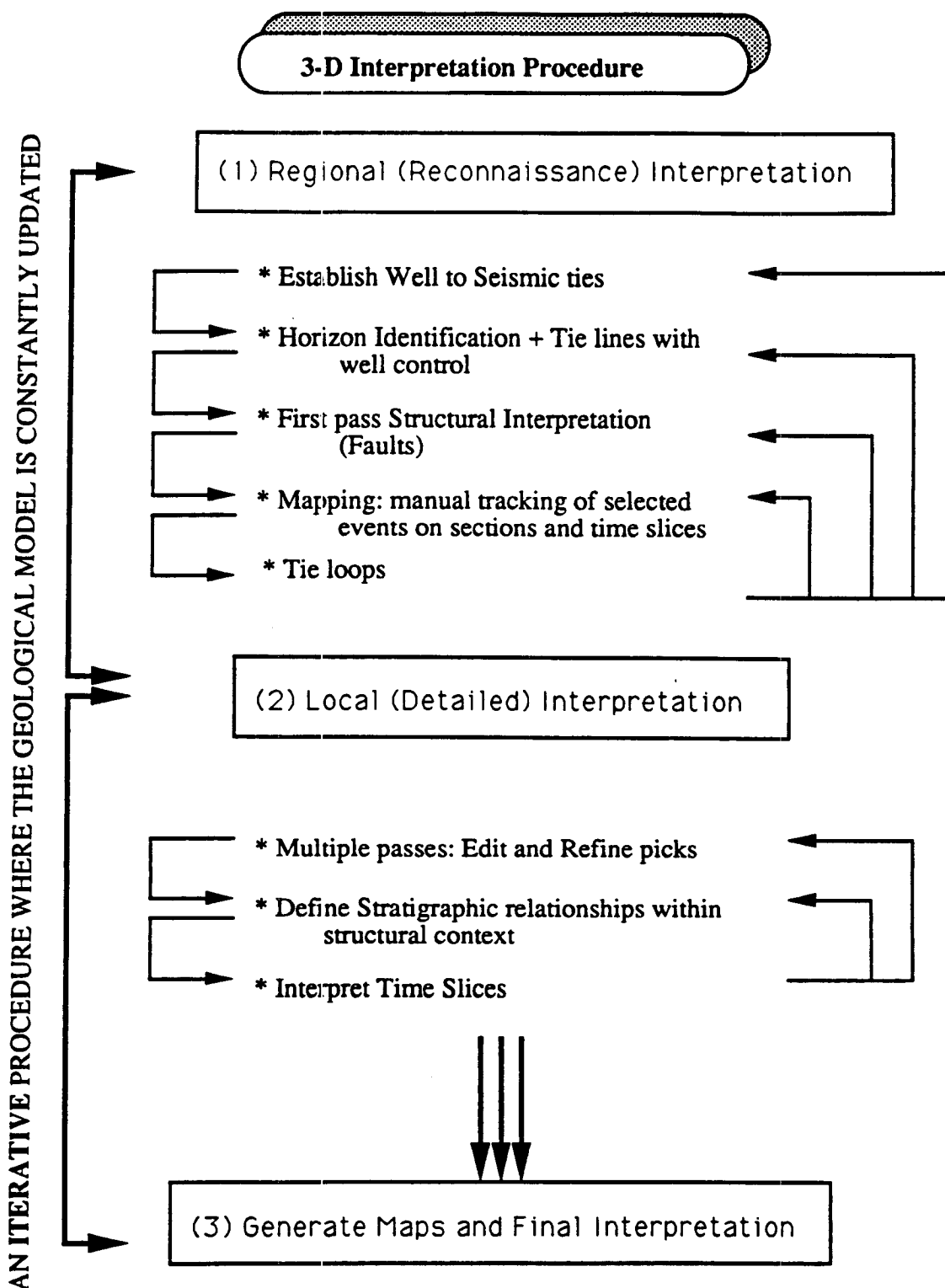


Table 4.3: The standard 3-D seismic interpretation approach is based on tying horizons on cross-line and in-line sections, around an area. Formation tops from well log picks serve as reference points, and loops are first established around well control points; areas which are remote from wells are then interpreted based on correlations of seismic character.

Formation Picks			
Formation	Well Number	Depth (m-TVD)	Travel time (ms)
Bottom Quaternary	31/2-13	513	628
-	31/2-5 and 2-16S	517	622
-	31/2-10	515	610
-	31/2-12	523	616
-	31/5-3	508	624
Top Oligocene	31/2-13	783	868
-	31/2-5 and 2-16S	786	862
-	31/2-10	739	826
-	31/2-12	730	820
-	31/5-3	780	866
Top Balder	31/2-13	1335	1442
-	31/2-5 and 2-16S	1345	1432
-	31/2-10	1305	1404
-	31/2-12	1204	1300
-	31/5-3	1340	1430
Bottom Tertiary	31/2-13	1523	1612
-	31/2-5 and 2-16S	1532	1604
-	31/2-10	1534	1626
-	31/2-12	1354	1452
-	31/5-3	1537	1622
Top Draupne	31/2-13	-	-
-	31/2-5 and 2-16S	-	-
-	31/2-10	1564	1654
-	31/2-12	-	-
-	31/5-3	1547	1634
Top Sognefjord	31/2-13	1526	1622
-	31/2-5 and 2-16S	1536	1612
-	31/2-10	1600	1680
-	31/2-12	1365	1470
-	31/5-3	1555	1638
Top Fensfjord	31/2-13	1670	1728
-	31/2-5 and 2-16S	1692	1736
-	31/2-10	1797	1808
-	31/2-12	1541	1626
-	31/5-3	1718	1754
Top Brent	31/2-13	-	1910
-	31/2-5 and 2-16S	1956	1912
-	31/2-10	-	2016
-	31/2-12	-	1832
-	31/5-3	1992	1940

Table 4.4: Formation picks in m, below sea floor, and in ms, two way travel time, at the six major control wells within the 3-D surveyed area.

Fluid Contacts (m-TVD)						
Contact type	31/2-13	31/2-5	31/2-16S	31/2-10	31/2-12	31/5-3
GOC	1568	1579	1579	-	1570.5	1572.5
OWC	1593?	1600.5	1600.5	-	1582.0	1593.5
GWC	-	-	-	-	-	-

Table 4.5: Fluid contacts in m (below sea floor) at the six major control wells within the 3-D surveyed area. Well 31/2-13 is deviated, and well 31/2-16S is horizontal.

the 3-D survey. Because the cap rock can occur as a shalier unit (Draupne Formation or a Kimmeridge clay equivalent of Late Jurassic age), as a claystone (Lista Fm. of Paleocene or Sele Fm. of Paleocene), or as a limestone or marl (part of the Balder Fm. of Paleocene) - all of which are from the Rogaland Group -, it was mapped loosely as "Bottom Tertiary" or K-T from the 3-D seismic.

I interpreted the seismic at Troll West with a depositional model corresponding to an early rifting stage, beginning in early Triassic, peaking during late Jurassic-early Cretaceous, and ending during Paleocene times (Ziegler and van Hoorn, 1989). In tying loops around key wells, I up-dated the general depositional model on a local scale. The following steps were completed:

- A reconnaissance mapping phase, where the outline of the field was defined and specific areas of interest were identified. This was mainly an exercise in structural interpretation.
- A more detailed mapping phase, where the validity of the depositional model was verified and the quality of the seismic picks was upgraded, through detailed and systematic line ties and in-fill picking. This was followed by a careful, partial mapping of key intra-formational reflectors in order to identify more subtle stratigraphic relationships such as those lithologies associated with changes in

mica content. These relationships will be discussed in detail below, in part e).

c) Horizon interpretation

The main horizons picked for interpretation were:

* **Base of the Quaternary.** This marker appears in bright yellow and is highly continuous. It defines a major truncating angular unconformity.

* **Top of the Oligocene.** This continuous marker appears in orange and is the site of a major unconformity. Small scale faulting appears to have ceased at the end of Oligocene times.

* **Intra-Oligocene.** This event is colored in red. It is highly discontinuous, yet marks a change in seismic character, going from low amplitude, discontinuous, transparent-like events to fairly continuous high amplitude, faulted events.

* **Top of the Balder.** This event is colored in purple; it is highly continuous, and was identified from well control points.

* **Base of the Tertiary or K-T boundary.** This event appears in green. It is usually a strong and continuous event and is strongly diachronous, due to widespread deposition of claystones in the east, with limestones and marls being deposited in the west. The Upper Cretaceous/lower Tertiary units drape over the paleotopography.

* **Top of the Draupne.** This event appears in dark blue. Because of Kimmerian related erosion, it has often been eroded around local highs and is relatively thin when present. It was completely removed from the most western part of the Troll West Oil Province. The Draupne was identified from well control points.

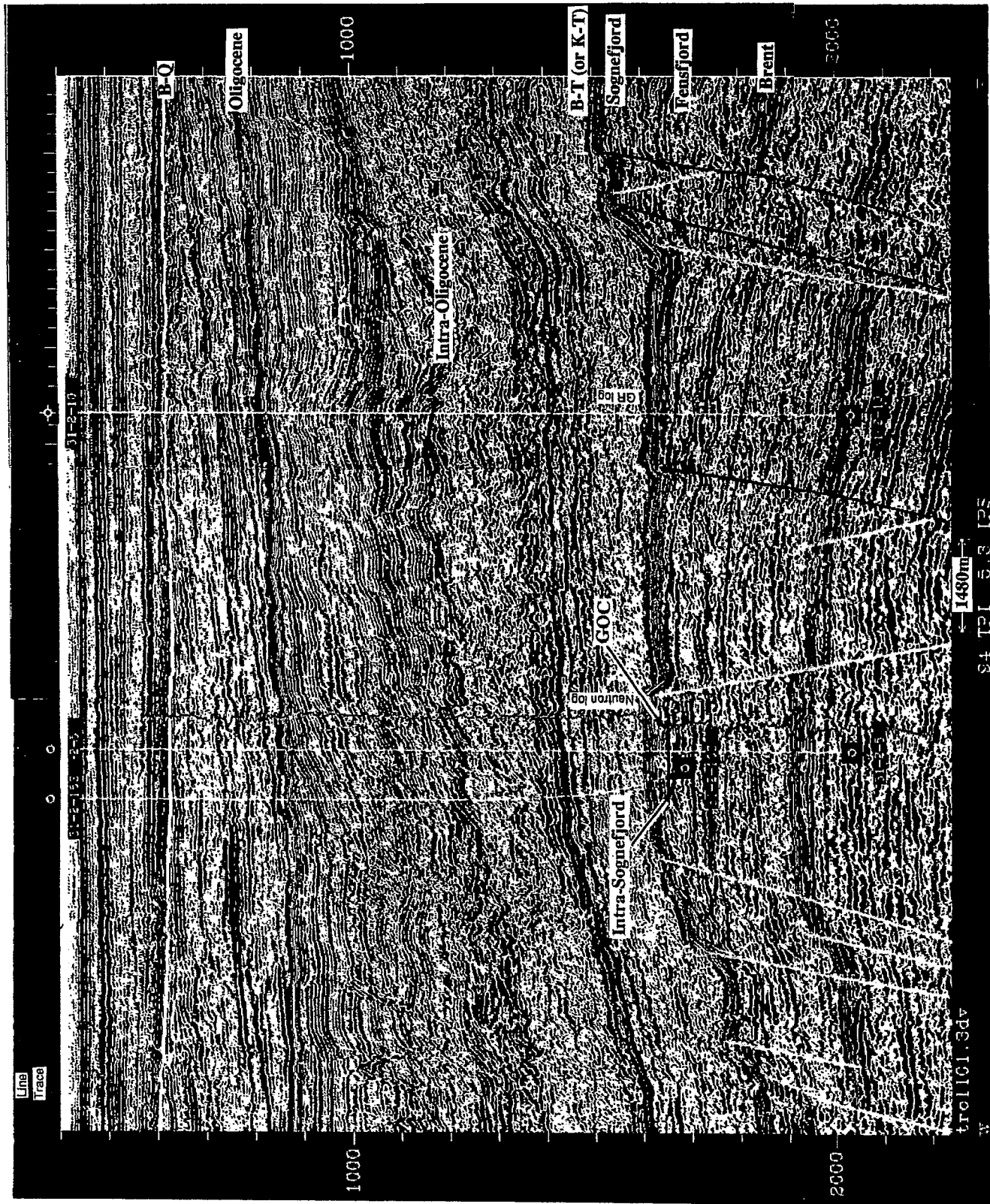
* **Top of the Sognefjord.** This event appears in brownish-red. It has also been eroded, specially around local highs and in the western end of the field. It was identified from well control points. The Sognefjord Formation consists of a series of southwest advancing sands which are successively off-lapped through the westward and northward progradation of a shoreface sand facies. They are identified on logs as thick coarsening upward units. There is seismic evidence of progradation towards the west across the Horda platform. As a result, the top of the Sognefjord is strongly

Figure 4.6: Line 328 shot through well 31/2-5, the "reference" well for the Troll West Oil Province, with interpreted horizons and faults. The log displayed at well 31/2-5 is the neutron porosity log; note the gas-oil-contact (GOC) level from the sharp kick in the neutron log, and the presence of a strong intra-formational reflector, just below the GOC. This intra-formational reflector corresponds to a shift in the gamma-ray log, as seen in figure 4.10 at well 31/2-5, and can be correlated to a subtle change in lithology from micaceous sands to clean sands at the boundary between cycles ZA-4.2 and ZA-4.3 (appendix B-4).

The faults define major horst and graben features, typical of rifted "basement involved" normal faulting provinces. Differential thickening of units is sometimes seen on the downthrown blocks near the faults. Rollover anticlines are rare in the reservoir section, because the faults are high angle planar (not listric) at shallow depths. Some evidence of "drag" along faults on the downthrown side, also known as "compaction folds" is present over horst blocks as seen in the western end of the figure, near the K-T boundary. A major bounding fault was identified in red to the East (around trace 1200); it is associated with a larger amount of block rotation and eastwardly tilting than other faults.

There was no evidence of any inverted structures in Tertiary times that may have been associated with compression due to the Alpine orogeny. Such structures were documented by Biddle and Rudolf (1988) in the Stord basin, west of the Horda platform, and south of Troll. Yet some evidence suggests that some of the normal faults were reactivated as reverse faults around late Cretaceous, possibly associated with compression around that time (Subhercynian orogeny?). This can be seen in the Western part of figure 4.6, on the third "normal" fault from the left (around trace 460), which shows a decreasing amount of offset with depth, and practically no offset at all at the Brent level.

Note: This figure is a reduced reproduction of the larger figure featured in my Ph.D. thesis. For a detailed view of the seismic line under full scale, refer to the original thesis by contacting Stanford University.



diachronous: clean sands pinch-out and interfinger with micaceous silts towards the west (figure 4.6).

* **Top of the Fensfjord.** This event is colored in light blue. The Fensfjord unit consists of thin upward coarsening sequences through shoreface progradation. The top of the Fensfjord appears as a fairly continuous event, but with varying brightness. It can sometimes be seen to dim-out, and was identified from well control points.

* **Top of the Brent.** This marker appears in dark green. It is bright, easy to traverse, and was identified from well control points.

d) Fault interpretation

The macrofaults are easily identifiable from reflector terminations and truncations in the survey area. They are, for the most part, normal syndepositional growth faults that are high angle and planar at shallow depths, becoming somewhat more listric with depth. The faults define major horst and graben features, typical of rifted "basement involved" normal faulting provinces (Bally, 1983). Differential thickening of units is sometimes seen on the downthrown blocks near the faults. Rollover anticlines are rare in the reservoir section, because the faults are high angle and planar at shallow depths. Some evidence of "drag" or "compaction folding" is present in the hanging wall of some fault blocks (see western end of figure 4.6, trace 460, near K-T boundary).

Some faults initiated during early Permian times and became inactive by Middle Jurassic time (see figure 4.6, in center, trace 900, right after Brent deposition); others were either reactivated or were continually active from Permian through the end of the Cretaceous; and others were active from late Jurassic until late Cretaceous (see figure 4.6, trace 400, in the western end after Brent deposition). There was no evidence in the Troll area of any inverted structure in Tertiary times that may have been associated with compression during the Alpine orogeny; such structures were documented by Biddle and Rudolf, in 1988, in the Stord basin, to the west of the Horda platform, and to the south of Troll. However, some evidence may suggest that

a few of the normal faults were reactivated as reverse faults around late Cretaceous, possibly during the Subhercynian orogeny. These can be seen in the western part of figure 4.6, where the third "normal" fault from the left (around trace 460), shows a decreasing amount of offset with depth and practically no offset at all at the Brent level.

The largest fault separating the Troll West Oil Province from the rest of the Troll field (as identified in the eastern part of line 328, around trace 1200) was identified as a controlling fault. It has, associated with it, the largest amount of block rotation and eastward tilting in the area. Note that the Upper Jurassic and Cretaceous units overlying the Sognefjord sands pinch-out updip. The main episode of rifting appears to have ceased by Tertiary times, when sedimentary units formed a conformable blanket over the paleotopography. Pervasive faulting is also present after the formation of the hydrocarbon traps of Troll, in Oligocene times for example (see figure 4.6, in a time window from 900 ms to 1300 ms).

I interpreted and correlated the largest faults on the seismic data from line to line to define important fault plane strike and dip directions in 3-D. Figure 4.7 summarizes the different phases of the structural development of the Troll field, and compares the present day structure of the field to six paleostructures. For reference, the top of the Sognefjord Formation has been highlighted and marked with an arrow. The figure was obtained using a horizon flattening technique on a key line (line 330) extracted from the 1989 3-D seismic survey. Note that the figure represents seismic time sections, but it is still assumed to be fairly representative of depth relationships, because of the relatively flat and laterally continuous nature of the strata. The following observations can be made:

- (f+g) Fensfjord and Sognefjord datum Syndepositional tectonism was of minor importance inside the Troll area. However, differential subsidence kept up with sediment input to maintain low energy conditions in Troll West throughout deposition of the Fensfjord and Sognefjord in Middle to late Jurassic times.

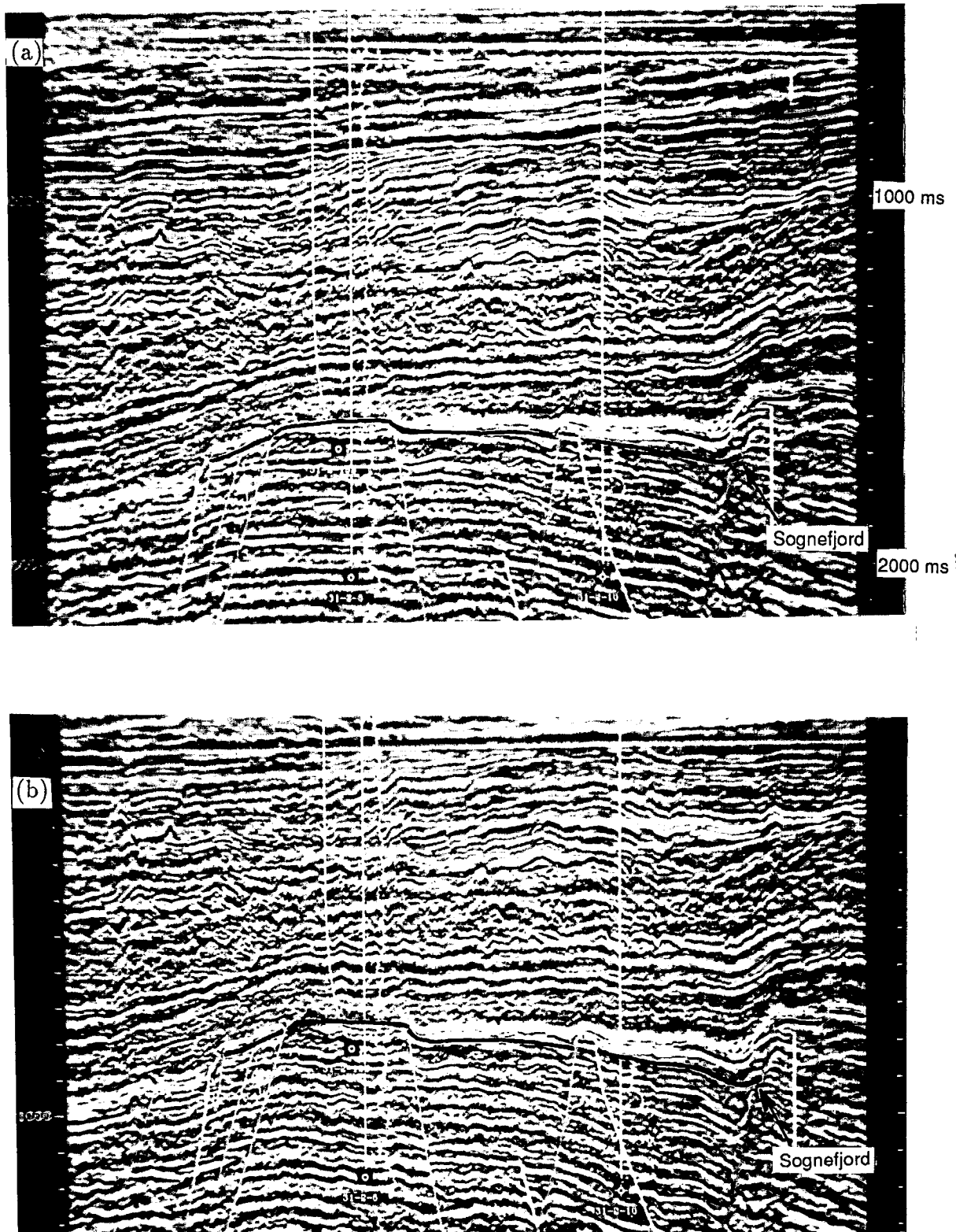


Figure 4.7: The structural development of the Troll field as illustrated through horizon flattening on line 330 of the 1989 3-D seismic survey. The darkened horizon indicated with an arrow is the top of the Sognefjord. The present day structure of the field is compared to six paleostructures: (a) Present day sea floor datum (b) Oligocene datum

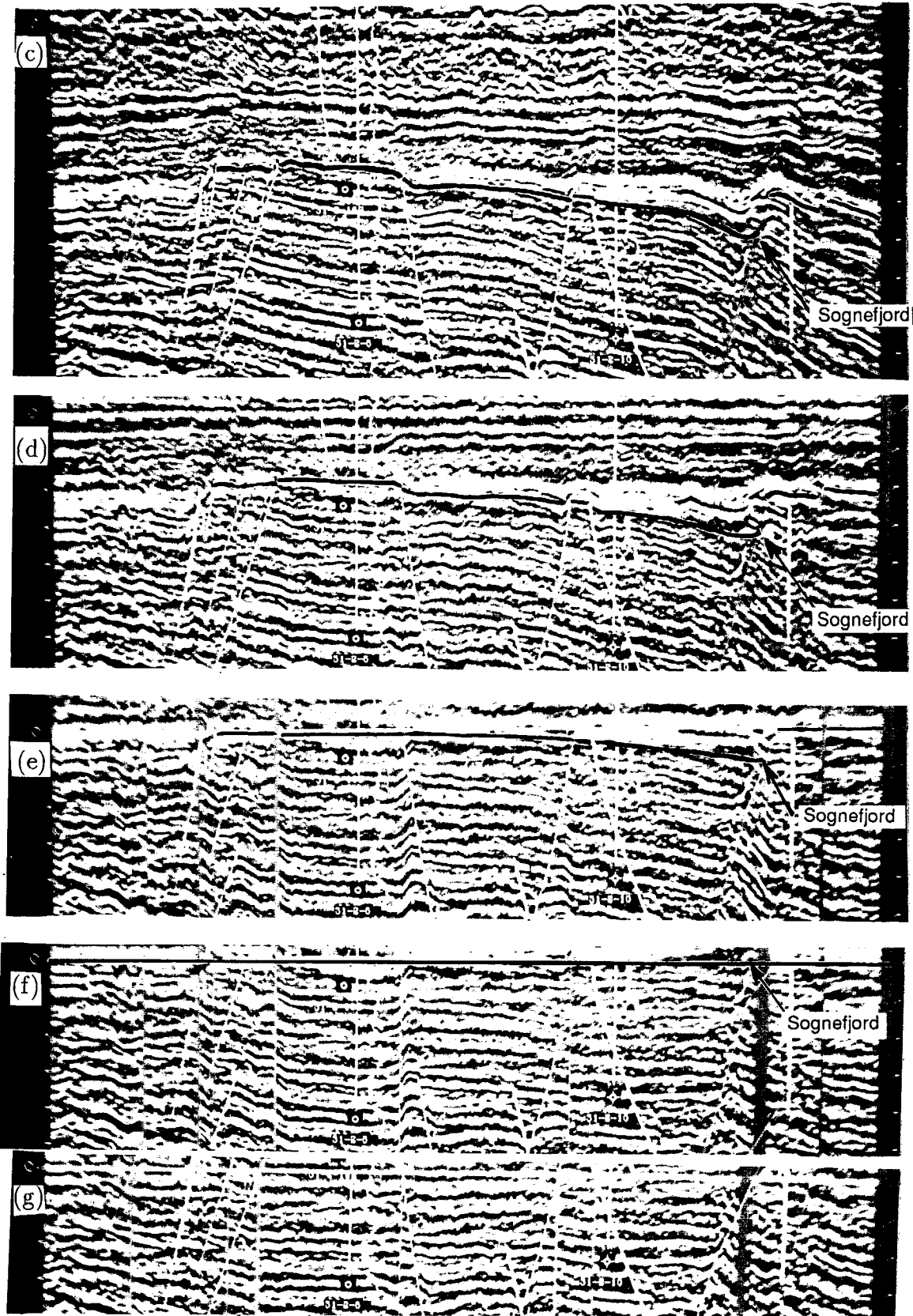


Figure 4.7 (continued):(c) Intra-Oligocene datum (d) Balder datum (e) Bottom Tertiary datum (f) Sognefjord datum (g) Fensfjord datum.

Block tilting to the east is particularly obvious on the major bounding fault to the east.

- (e) K-T datum Faulting and accompanying subsidence created the Troll structure in late Jurassic to Cretaceous times. The Draupne Formation and Cretaceous sediments which formed onlapping wedges over the Sognefjord were exposed along highs and eroded in the west. They are thin, but still present in the east.
- (c+d) Balder and Intra-Oligocene datum Continued subsidence apparently enlarged the Troll structures until this time.
- (b) Oligocene A new episode of normal faulting during Late Oligocene times affected shallow Oligocene beds. Faulting during this period does not appear to cut into older strata; a possible explanation is that Lower Oligocene beds (those below the Intra-Oligocene reflector marked on figure 4.6) are dominantly shaley units and very ductile; they can accommodate most faulting through folding and internal deformation. Thus, the shales "shield" deeper strata from faulting events. This is a commonly observed phenomenon in the North Sea.
- (a) Bottom-Quaternary and Present sea floor Westerly tilting of the whole area during late Tertiary times resulted in decreased structural closure and possibly erosion in the east. Quaternary sediments form a depositional blanket over the entire area. There is some evidence of westward progradation of both late Tertiary and Quaternary deposits.

e) Correlation of depositional cycles identified on logs with seismic

e-1) Troll West Oil Province

During Late Jurassic, a major, "long term", rise in relative sea level led to the deposition of marine shales of the Viking Group throughout the North Sea, and to the local deposition of shallow marine sands around intrabasinal highs and on the flanks

of the basin. The **Sognefjord** sands consist of a shallow marine sequence deposited along the western flank of the Horda platform, which formed an intrabasinal high.

According to Norsk Hydro (1988), the deposition of the Sognefjord sands is thought to have been dominated by eustatic sea level changes. They document that the sands were deposited during a period extending roughly from 155 my ago (Callovian stage) until 135 mybp (early Cretaceous). Figure 4.8a includes a digitized version of the Haq et al. (1988) curves of relative sea level for the North Sea. These curves were derived from data in Southern England and represent an extension of the Vail et al. (1977) curves; they are thought to be valid for the North Sea basin. Undoubtedly, the "long term" trend in sea level, which I highlighted as supercycles ZA-3 and ZA-4 in figure 4.8a corresponds to the time of deposition of the Sognefjord sands.

Next, I attempt to correlate shorter term depositional cycles at Troll to small changes in relative sea level. The difficulty in the correlation comes from the lack of data to decouple the influence of three factors that could have possibly controlled the deposition of the Sognefjord sands: (1) changes in relative sea level (the Vail et al. approach, 1977), (2) syndepositional tectonism (faulting and subsidence), and (3) changes in sediment supply to the area (the Galloway, 1989, school of thought). It is clear that any predepositional structure, in the form of paleotopography along the Horda platform, would have influenced current patterns by creating higher energy conditions, thereby initiating the deposition of coarser grained sediments. Similarly, the sediment supply (which, according to Norsk Hydro, 1988 came from the NE), could have been affected by changes in the climate or changes in the topography of the source area. With these uncertainties in mind, I proceeded in identifying depositional cycles within the Sognefjord facies from well-logs and in correlating these to the Haq et al. (1988) curves.

As part of the global rise in relative sea level of cycles ZA-3 and ZA-4, I identified a total of seven depositional "short-term" subcycles within the Sognefjord sands over the **Troll West Oil Province**. I believe these correspond to slight shifts in

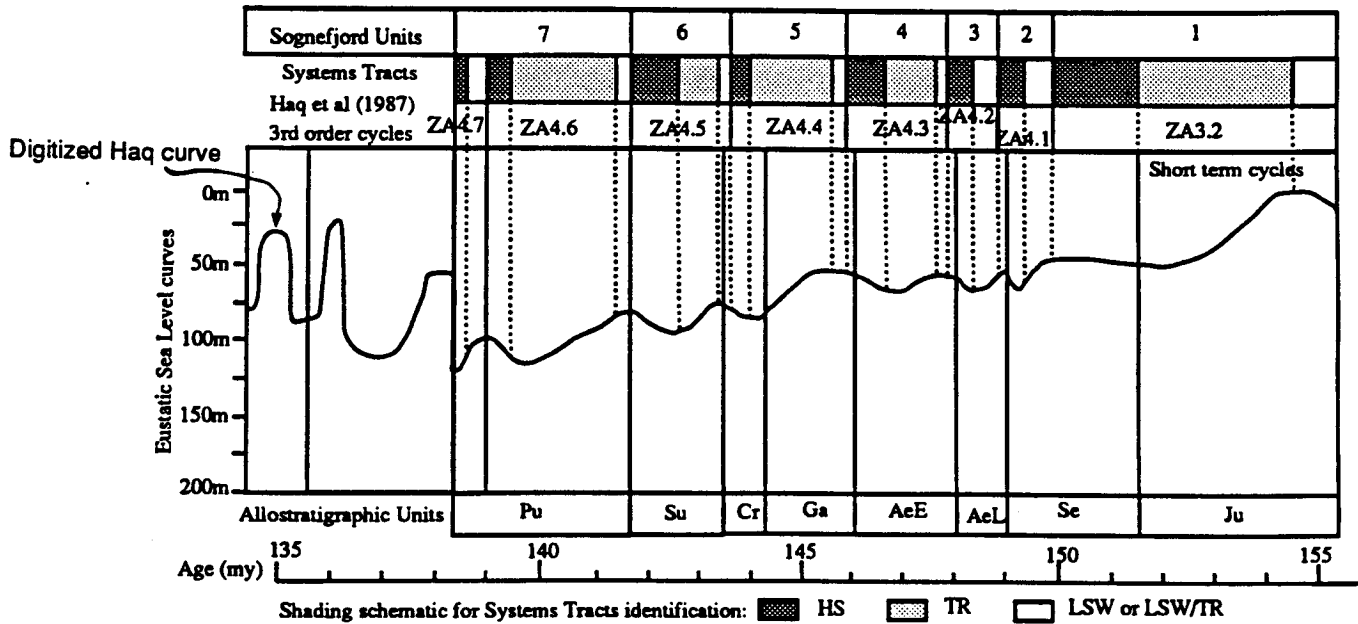
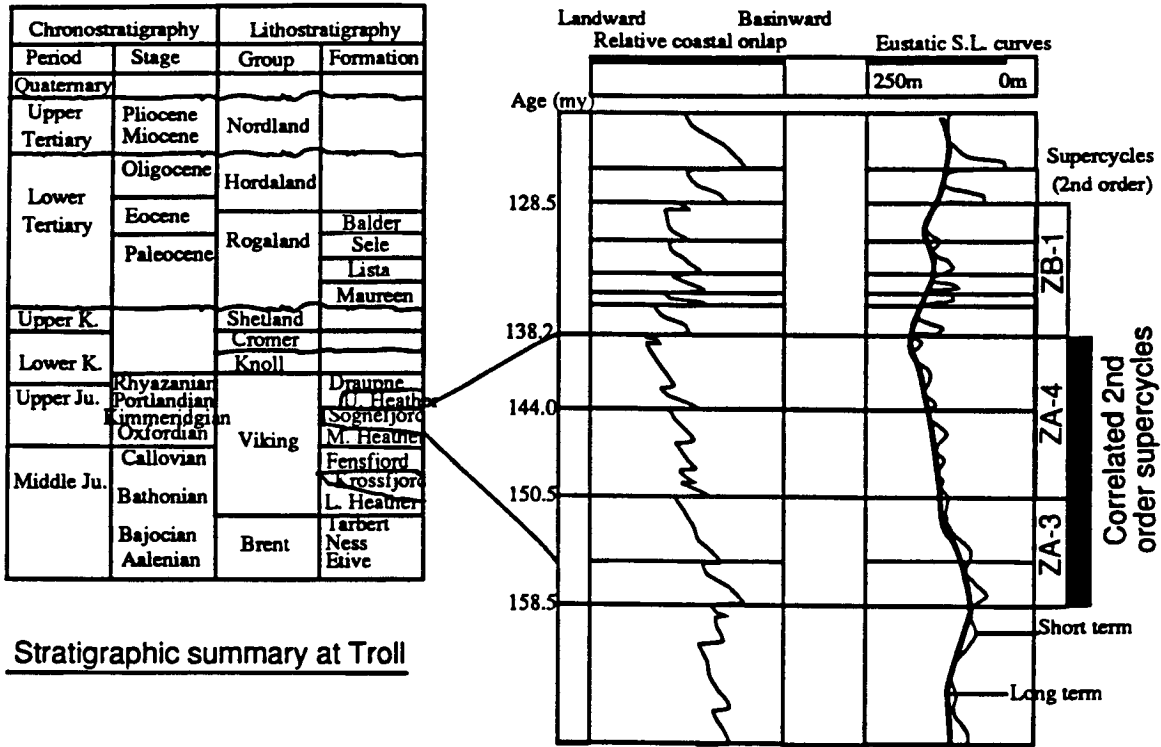


Figure 4.8:
 a) Stratigraphic summary over the Troll area (top left), and correlation of allostratigraphic units within the Sognefjord Formation with long term cycles in relative sea level (top right).
 b) Short term (bottom) eustatic sea level curves as digitized from Haq et al. (1987); HS=High Stand deposits, TR=Transgressive deposits, and LSW=Low Stand Wedge deposits. I used "absolute" ages (data from Norsk Hydro, summarized in appendix B-9) for correlation of depositional cycles observed at Troll with the Haq curves.

sedimentation cycles from lower to upper shoreface. The cycles are presented in appendix B for seven wells. I first identified the depositional sequences in log-derived lithostratigraphic sections and tied them to the biostratigraphic correlations of Norsk Hydro (1988), which is summarized in appendix B-9. The allostratigraphic units were determined on the basis of lowest and highest appearance of index dinocyst taxa (data from Norsk Hydro, 1988). In turn, I used the biostratigraphic and absolute age information to establish the chronostratigraphic significance of the units, by direct correlation to the Haq curves at each of the wells present in the Troll West Oil Province (appendix B-10). Figure 4.8b shows a correlation of the seven depositional cycles which were identified at Troll West, to the Haq curves in digitized form. The allostratigraphic units and the final Sognefjord units are specific to Troll West (this study), whereas the relative sea level curves, the third order cycles, and the systems tracts were digitized from Haq et al. (1988). The biostratigraphic zonation and data on "absolute" age from Norsk Hydro makes these correlations possible.

Haq et al. (1988) estimate dating errors within the Jurassic to 3 my, but for the present study, I had no information on the uncertainty in the dating of events within the Sognefjord subcycles. The reader should keep in mind that the ages of the third order cycle boundaries are at or near the presumed scale of biostratigraphic resolution (3 my), and that the correlations of cycles are subject to a level of uncertainty of plus or minus one cycle.

Undoubtedly, a set of characteristic short-term cycles can be identified on well logs (appendix B). However, it is not clear whether they correlate to third order cycles of changes in relative sea level. The cycles correspond to slight shifts in the depositional environment from lower shoreface to upper shoreface, and may very well be accounted for by changes in the sediment supply, rather than changes in eustasy. In other words, correlations in absolute ages are not sufficient to establish the relationship of the sedimentation cycles observed at Troll. Before establishing the origin of the cycles with confidence, I recommend (after Vail and Wornardt, 1990) incorporating additional data, including paleobathymetric data, and data on

abundance and diversity of nannofossils and planktonic forams.

If these cycles were of eustatic origin, each cycle would be marked with a rapid rise in sea level. Each third order cycle would typically comprises three systems tracts, a low stand wedge, a progradational or transgressive component, and a high stand systems tract, which would have relative durations as indicated on figure 4.8b (Haq et al., 1988).

e-1.1) Calcite stringers

The accurate prediction of the lateral extent of calcite cemented horizons is crucial, because it plays a controlling factor in fluid flow during production. Previous workers at Norsk hydro have partially correlated two well cemented horizons. They occur near major facies changes, one at the top of the Sognefjord, at the boundary between supercycles ZA-4 and ZB-1, and the other, near the top of the Fensfjord, at the boundary between cycles ZA-3.1 and ZA-3.2 (appendix B-4). These can sometimes be inferred indirectly by association with seismic intra-formational reflectors representing major cycle boundaries. For example, the boundary between cycles ZA-4.2 and ZA-4.3 at well 31/2-5 shown in appendix B-4 appears in figure 4.6, just beneath the GOC. Additionally, some evidence of progradation to the west around trace 600 in figure 4.6 helps in identifying this boundary as a possible low stand wedge (erosional surface). This shows that it may be viable to map some of the more prominent micaceous layers and possibly infer the location of calcite cemented horizons directly from stacked migrated seismic data.

Next, I present the relationship of depositional cycles to intra-formational reflectors in detail, by zooming-in on several wells.

e-1.2) Depositional cycles and intra-formational reflectors

At Troll West, the low stand and the high stand components are difficult to identify, and it is not clear whether the cycles respond to a change in relative sea level or to a change in sediment supply. Nevertheless, each cycle is thought to represent

a progradation episode of the shoreface across the shelf. A cycle usually begins with low energy, more distal, micaceous silts corresponding to coastal progradation. These coarsen upwards into clean sands, forming transgressive intervals. This is in agreement with commonly accepted sequence stratigraphic concepts (Vail et al., 1977, Haq et al., 1987, Vail and Wornardt, 1990). The more distal micaceous silts, corresponding to slope fan or the base of the prograding complex within the low stand systems tract and to the transgressive systems tract, have high gamma ray characteristics. On the other hand, the cleaner and coarser transgressive sands, which correspond mostly to the prograding complex of the low stand systems tract and to the high stand systems tract, have low gamma ray responses (see appendix B and chapter 5). Note, from appendix B, that different parts of the systems tracts are preserved at different locations: for example, cycle 4.2 appears as a slope fan or as the base of a prograding complex (low stand systems tract) at well 31/2-5, as a prograding complex (low stand systems tract) at wells 31/2-12 and 31/2-10, and as a transgressive systems tract at well 31/5-3.

Figures 4.9-4.11 show a one to one correspondence between the presence of micaceous layers (as inferred from gamma ray logs), or of calcite stringers (as inferred from sonic and density logs), and intra-Sognefjord reflectors, as seen on seismic. The logs shown in the figures are gamma ray logs, which, for clarity, have been shifted to the right of actual well locations. In the following, log and seismic characteristics at wells 31/5-3, 31/2-5, 31/2-10, and 31/2-12 are examined in detail:

- The seismic data at well **31/5-3** (at the top of figure 4.9) exhibits an intra-formational reflector (red trough) at the boundary between cycles ZA4.1 and ZA4.2 at approximately 1724 ms. It is overlain by another subtle intra-formational reflector occurring at 1710 ms and marking the ZA4.2/ZA4.3 boundary. Two other intra-formational reflectors can be seen, one at approximately 1686 ms representing the boundary between cycles ZA4.3 and ZA4.5, and the other at approximately 1660 ms, representing the boundary between cycles ZA4.5 and ZA4.6 of appendix B-6. The gas oil contact (GOC) reflection at approximately

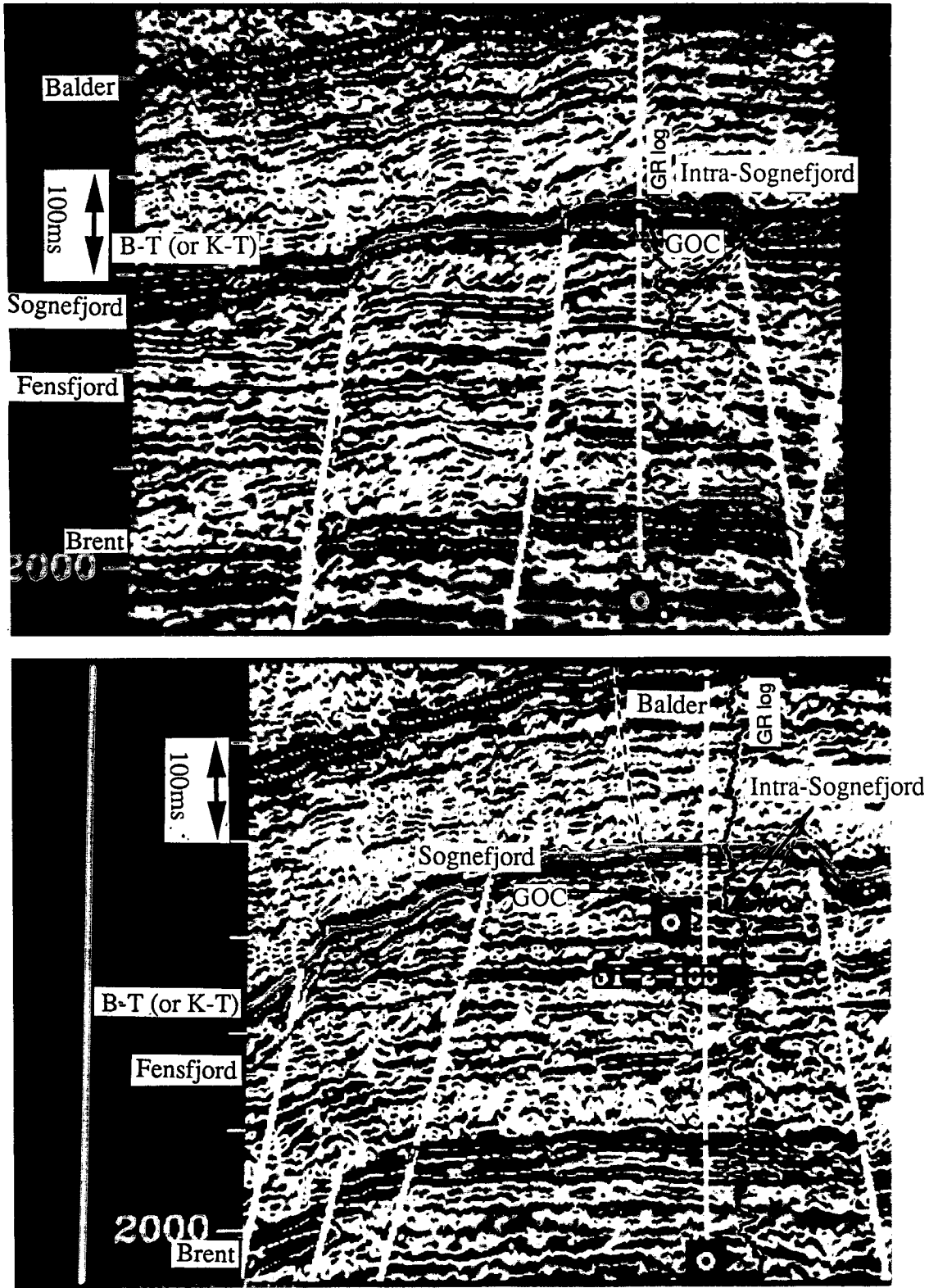


Figure 4.9: Well to seismic ties for well 31/5-3 (top figure) through line 190 and well 31/2-16S (bottom figure) through line 318. Well 31/2-16S is horizontal, and for clarity its location is dashed and only tops are indicated (no logs). It is next to well 31/2-5, which is also plotted with its depth to time converted Gamma ray log to the right. For detailed correlations of intra-formational reflectors to changes in lithology, refer to text.

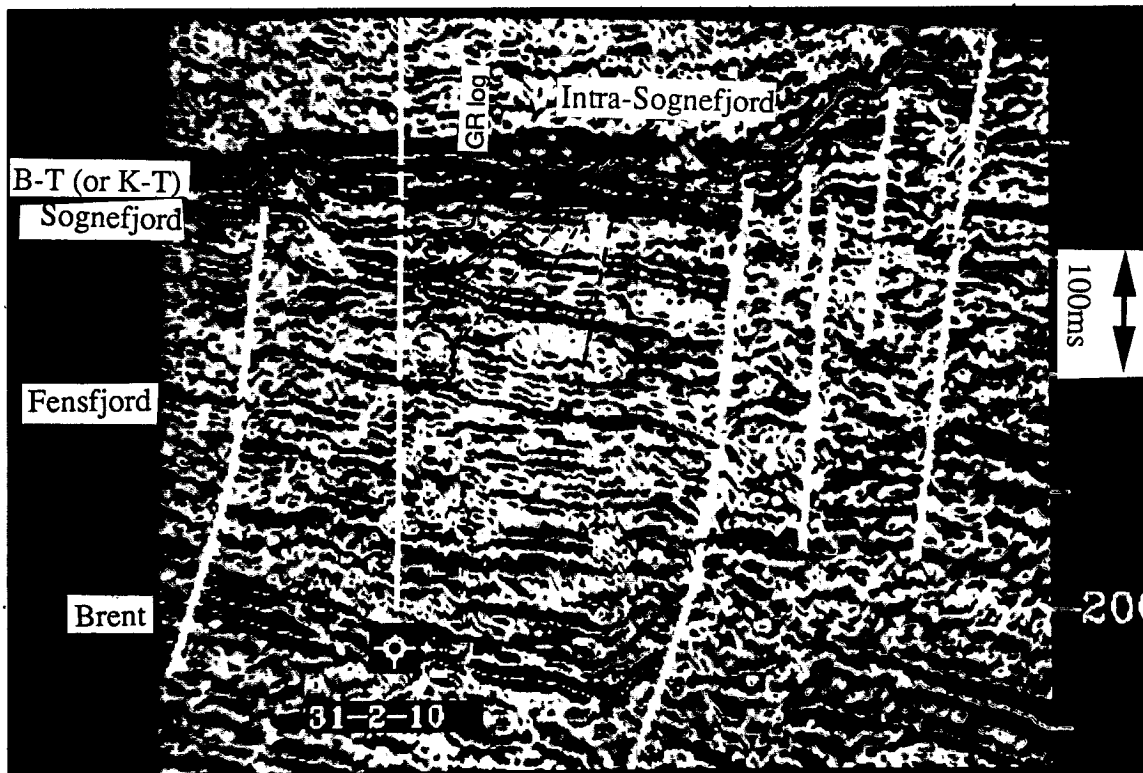
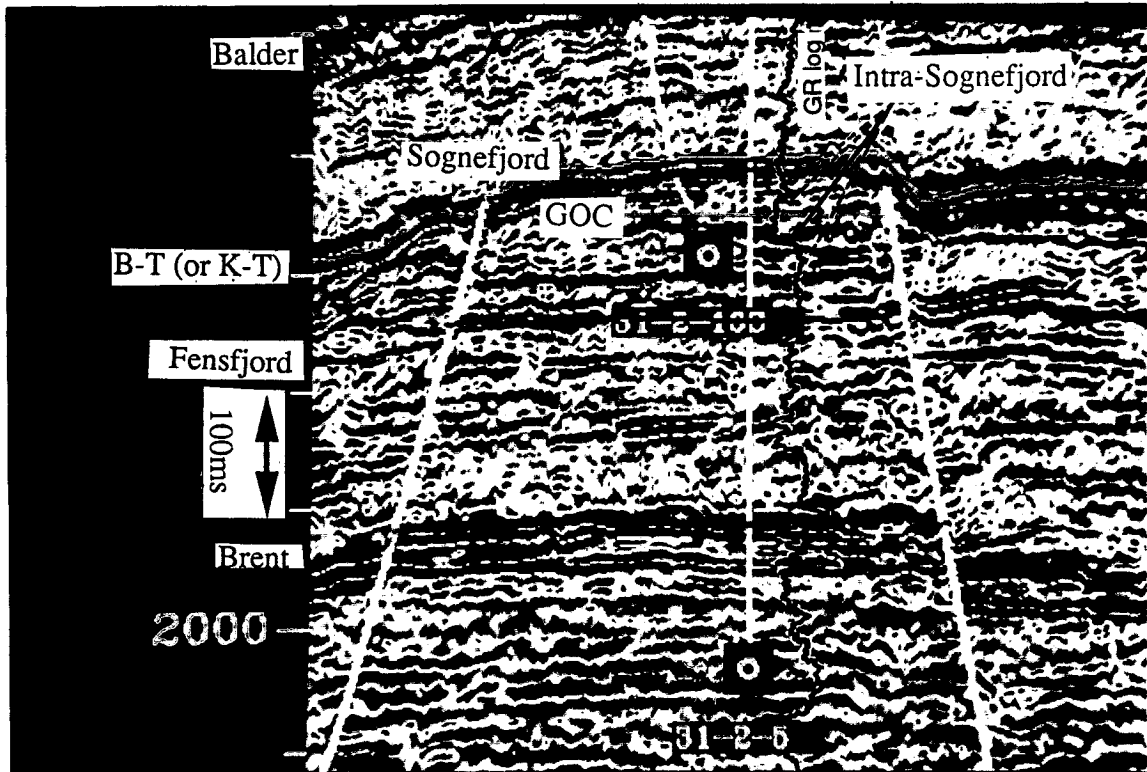


Figure 4.10: Well to seismic ties for wells 31/2-5 (top figure) through line 328 and well 31/2-10 (bottom figure) through line 314. Depth to time converted gamma ray logs are superimposed. For detailed correlations of intra-formational reflectors to changes in lithology, refer to text.

1656 ms obliterates subtle reflections within the top of the Sognefjord around well 31/5-3 and affects the ZA4.3/ZA5.5 boundary.

- Because of their proximity, the seismic responses at wells **31/2-16S** (bottom of figure 4.9) and **31/2-5** (top of figure 4.10) are similar. The prominent intra-formational reflector at approximately 1672 ms marks the boundary between cycles ZA4.2 and ZA4.3. Note that this reflection is probably also undergoing constructive and destructive interference with the GOC reflection immediately above it. Two other, more subtle intra-formational reflectors overlay it. One of them at approximately 1638 ms which corresponds to the lithologic change from unit 4C to unit 5M within cycle ZA4.4. The other possibly reflects the presence of calcite layers at approximately 1622 ms (1554 m depth) and marks the boundary between cycles ZA4.4 and ZA4.5 of appendix B-4.
- Well **31/2-10**, shown at the bottom of figure 4.10, was drilled updip of a tilted structure and was dry. The seismic data shows a prominent intra-formational reflector at approximately 1714 ms corresponding to the boundary between cycles ZA4.2 and ZA4.3 of appendix B-2. It is underlain by a thin micaceous unit occurring within unit 3C at approximately 1744 ms. Note that the boundary between cycles ZA4.1 and ZA4.2 is transitional in this area and does not lead to a strong intra-formational reflector. Several other weak intra-formational reflectors can be seen. One occurs at approximately 1786 ms and can be correlated to the boundary between units 2M and 3M. The boundary between units 5C and 6M within cycle ZA4.5 can also be correlated to a local intra-formational reflector at approximately 1688 ms (appendix B-2). Two "new" discontinuous intra-formational reflectors appear downdip and to the East of the well, but they are absent at well 31/2-10. One is located above the ZA4.2/ZA4.3 boundary, at approximately 1716 ms on trace 1068, while the other, is located below the ZA4.2/ZA4.3 boundary, at approximately 1802 ms on trace 1073.
- Well **31/2-12**, shown in the bottom of figure 4.11, was drilled on the easternmost high of the Troll West Oil Province, and it is technically part of the Troll

West Gas Province. It shows a prominent intra-formational reflector at approximately 1564 ms, corresponding to the boundary between cycles ZA4.1 and ZA4.2 of appendix B-1. Another prominent intra-formational reflector occurs at 1508 ms and indicates the boundary between cycles ZA4.2 and ZA4.3. It marks the top of unit 4M, a micaceous unit. Three additional subtle intra-formational reflectors can be identified at this well. One occurs at approximately 1586 ms and corresponds to the boundary between cycles ZA3.2 and ZA4.1 of appendix B-1, possibly reflecting the presence of thin calcite layers. Another, at approximately 1494 ms, marks the boundary between cycles ZA4.4 and ZA4.5 which shows several calcite layers (appendix B-1). A third intra-formational reflector is present at 1522 ms and occurs within the upper part of unit 3C, marking the presence of calcite layers. This reflector gains strength in the downdip direction, to the east of the well.

In summary, intra-formational reflectors mark the presence of micaceous units and of calcite layers, and usually occur at boundaries marked by slight shifts in the depositional environment. In general, they indicate lithologic changes that are laterally discontinuous and that can be identified on seismic data, via correlation at well locations with time converted log responses. Interestingly, certain intra-formational reflectors, such as the one appearing on the seismic between units 2M and 3M at well 31/2-10, are chronostratigraphic and do not have large and obvious lithostratigraphic expressions on logs (see appendix B-2, at the boundary between units 2M and 3M!). The work presented here shows that it is feasible to use seismic intra-formational reflectors in assessing reservoir quality. Because intra-formational reflectors play such an important role in reservoir development at Troll West, future work involving 3-D seismic data sets should include a study of their distribution.

e-2) Troll Gas provinces

The Haq curves were also used successfully by Norsk Hydro in the **Troll Gas provinces** during well-log based basin modeling studies (1988, Joint geological re-

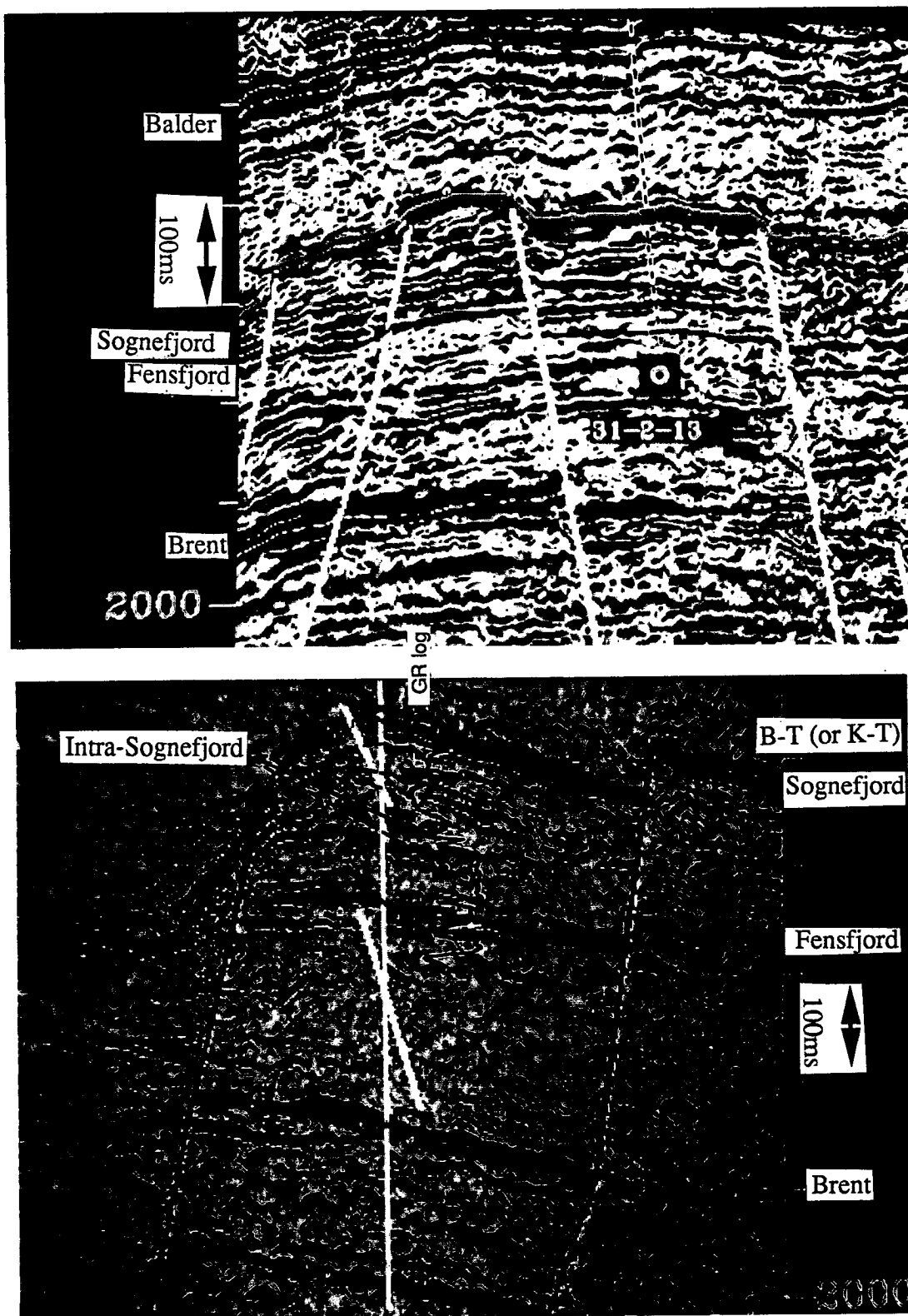


Figure 4.11: Well to seismic ties for wells 31/2-13 (top figure) through line 396 and well 31/2-12 (bottom figure) through line 460, which is plotted together with its depth to time converted gamma ray log. Well 31/2-13 is deviated, and for clarity its location is dashed and only tops are indicated (no logs). For detailed correlations of intra-formational reflectors to changes in lithology, refer to text.

view of Troll). In particular, carbonate cemented zones were shown to occur in areas of marked facies changes or near erosional unconformities. Most calcite cemented zones are therefore related to time/facies zones within the reservoir. Nearly 80 % of the maximum flooding surfaces and sequence boundaries showed a facies characteristic of normal marine and restricted marine environments. The conclusion of an extensive study in the Troll Gas provinces (Read report, 1988) was that 70-75 % of the maximum flooding surfaces and 60-65 % of the sequence boundaries are carbonate cemented, and that some of them can be correlated between adjacent wells. However, statistical regressions on all carbonate cemented horizons showed trends "that could not be assigned any singular factors, except that they were generally more frequent in transgressive tracts than in high stand wedges". Moreover, distinguishing between lateral and stratigraphic variations in facies from well data alone can be difficult. Hence, one easily sees the potential usefulness of seismic data in delineating the micaceous and/or carbonate cemented horizons. Note that some of the thinner lithologic intervals fall below the traditional resolution limit of migrated seismic data.

Limitations of seismic resolution

A short comment on the limitations of seismic resolution at Troll is appropriate. Traditional wisdom enables us to vertically resolve beds as thin as 1/4 of a wavelength (Widess, 1973, Sheriff, 1977) in thickness, with a horizontal resolution of at least as small as 1/2 of a Fresnel zone for migrated seismic data (Neidell and Poggiagliolmi, 1977). For the Sognefjord sands, with compressional wave velocities of 3000 m/s, occurring at approximately 1500 ms, and having a dominant frequency of close to 50 Hz (see figure 4.12), this yields a vertical resolution limit of:

$$\frac{\lambda}{4} = \frac{V}{4f} = \frac{3000}{4(50)} = 15 \text{ m},$$

and a horizontal resolution of at least:

$$\frac{r_f}{2} = \frac{V}{8} \sqrt{\frac{t}{f_d}} = \frac{3000}{8} \sqrt{\frac{1.5}{50}} = 65 \text{ m}.$$

The events identified as intra-formational reflectors on the seismic data have lateral continuities in excess of one half of a Fresnel zone and usually correspond to the

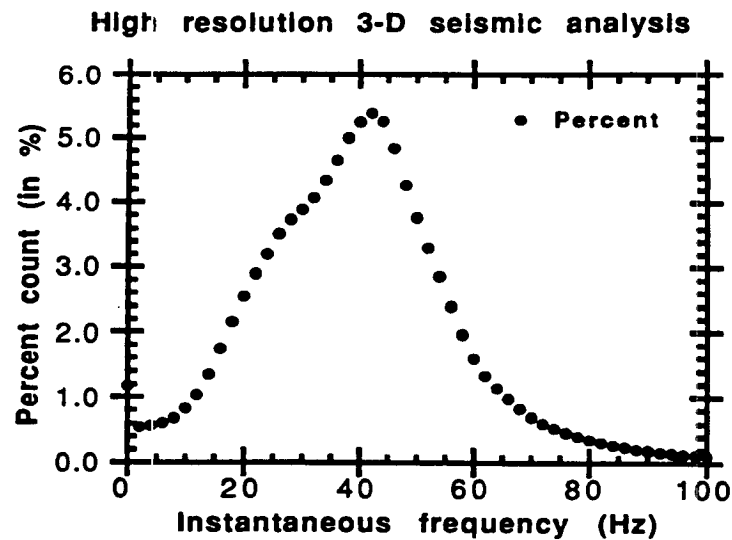


Figure 4.12: Distribution of instantaneous frequencies across the 1989 3-D seismic survey over the Troll West oil province, within a time window centered around the Sognefjord from 1500 ms to 1800 ms.

boundary between beds that are thicker than 15 m (see appendix B). However, some of the intra-formational reflectors were attributed to the presence of thin calcite beds or of micaceous sands, which are below the traditional vertical resolution limit of seismic. These beds cannot be resolved, but can nevertheless be detected. On the other hand, because dating errors within the Jurassic are approximately 3 my, the ages of third order cycle boundaries are at or near the scale of biostratigraphic resolution. In conclusion, the largest pitfalls in the correlation of eustatic sea level cycles to seismic data at Troll West lie mostly in the limits of biostratigraphic resolution, and not in the limits of seismic resolution.

f) results

Tying the horizon picks around faults is an iterative process that can prove time consuming. An example tie-loop between line 190, through well 31/5-3, and line 328, through well 31/2-5, is shown in figure 4.13. Once the seismic picks were refined

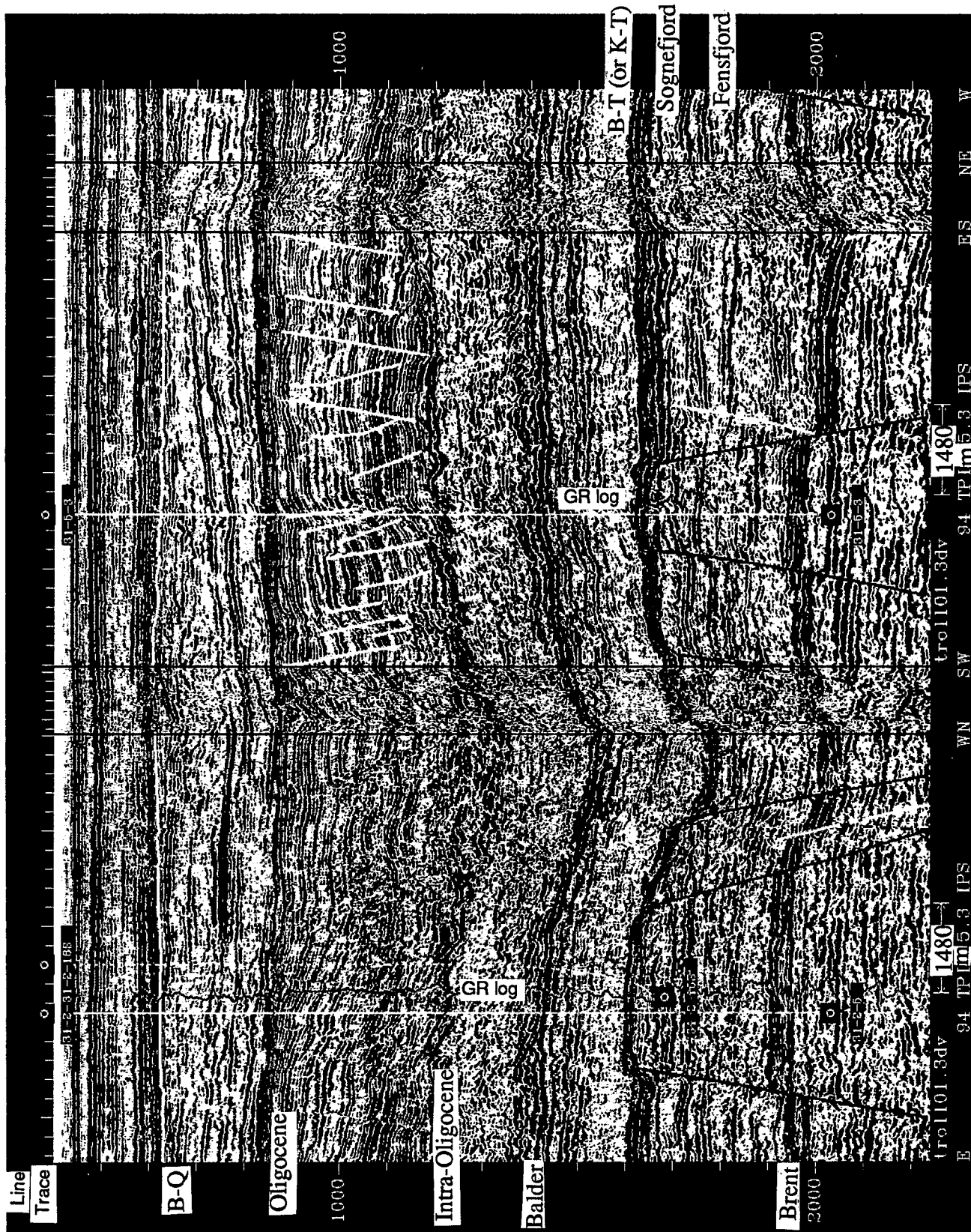


Figure 4.13: Tie-loop through line 190 through well 31/5-3 and line 328 through well 31/2-5 from the 1989 3-D seismic survey, showing the main seismic picks. Note the better S/N obtained from dip lines as opposed to strike lines.

to the point that they tied on selected dip lines in arbitrary directions of traverse, the intervening dip lines were interpolated and contour maps were generated. These maps included the base of the Tertiary (K-T boundary), the top Sognefjord, the top of the Fensfjord, the top of the Brent, and an isopach map of the reservoir. Maps of the top Sognefjord and top Fensfjord are presented in figure 4.14, where contours are in variable density format. A structure contour map of the top of the Brent and an isopach map of the Sognefjord are shown in figure 4.15. Here, two different color scales are used to emphasize the importance of color displays. The maps are consistent with the general geological framework and depositional environments, with Sognefjord sands being thickest to the south and to the east.

2) Exotic 3-D Interpretation of stacked migrated data

Following the generation of 3-D structural contour and isopach maps from stacked seismic travel times, a set of complex seismic trace attributes were computed. A thorough discussion of complex trace attributes can be found in Taner et al., 1979, Bodine, 1984, and Shtivelman et al, 1986. A 3-D seismic dataset such as the Troll 1989 survey is ideal for using trace attributes in relating small changes in seismic character to the stratigraphy in terms of depositional units and reservoir quality.

2.a) Interpretation of complex trace attributes

For a given area, seismic attributes may correlate spatially with secondary in-situ parameters such as porosity, clay/sand ratio or mica content, gas content, etc. The idea is to validate a correlation on a local scale such as that around a well location for example, and then to generalize it to other parts of the reservoir, assuming that other conditions (overburden properties and in-situ conditions for example) remain the same elsewhere.

The dominant properties of seismic attributes and their main uses are summarized in table 4.6, which I compiled from a combination of Taner et al. (1979), Bodine (1984), Shtivelman et al. (1986), and Sonneland and Barkved (1989). I extracted the

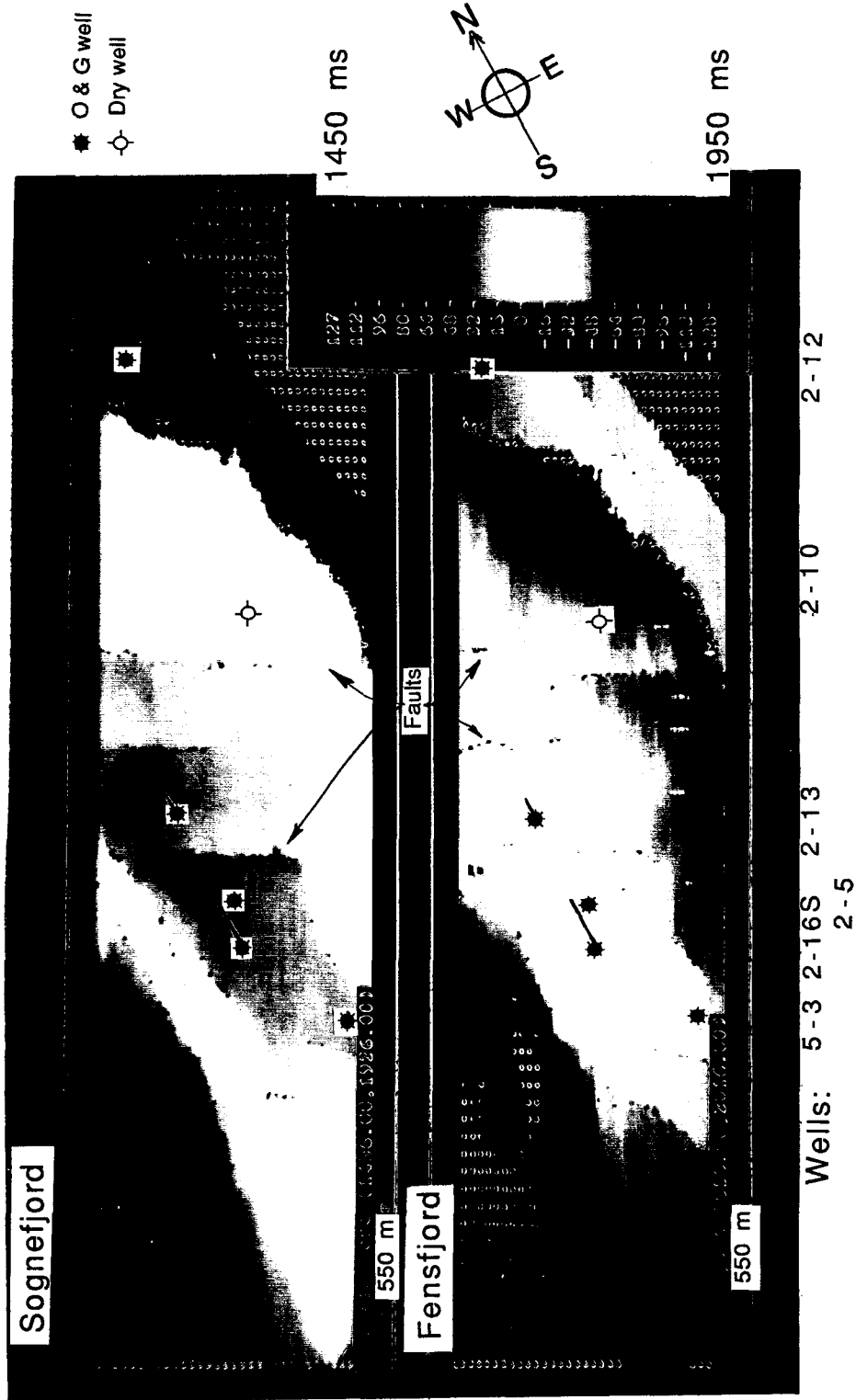


Figure 4.14: Structure contour maps of the top of the Sognefjord and top of the Fensfjord (variable density format, with color scale as indicated). For clarity, fault heaves were not plotted.

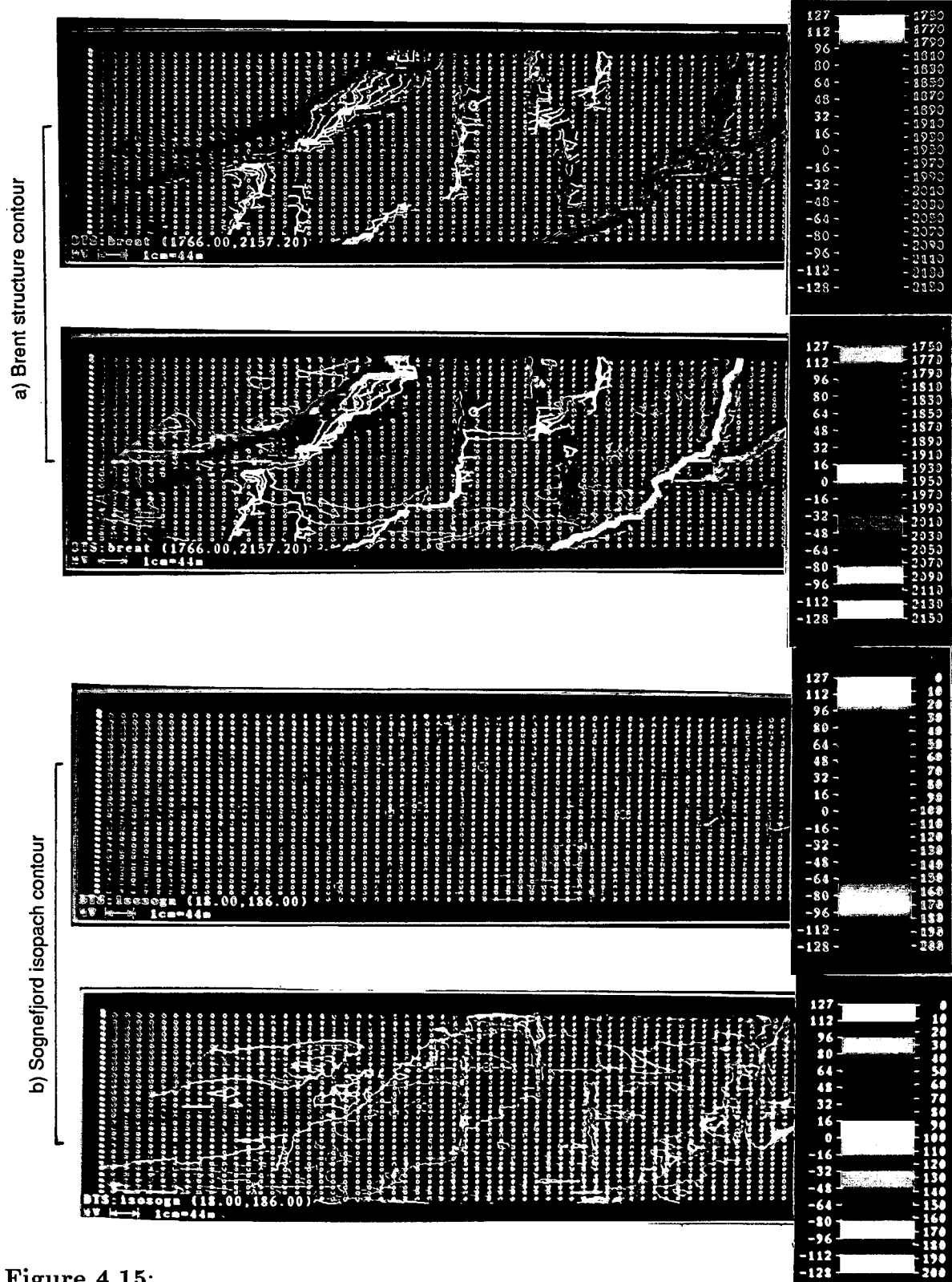


Figure 4.15:
 a) Brent: Structure contour map of the top of the Brent, with fault heaves indicated in red. Color scale as indicated in top two figures.
 b) Sognefjord: Isopach map of the Sognefjord sands. Note that the Sognefjord thins-out on local highs (horst blocks), specially in the westernmost part of the field; color scale as indicated in bottom two figures.
 Two different color scales were used for each map, to emphasize the importance of color displays.

General seismic attribute properties	
Property	Common usage
Areal association	Geological setting Depositional patterns Depositional environment
Reflector geometry	Geological setting Depositional patterns Bedding patterns (transport direction) Depositional environment Depositional processes Erosional patterns
General seismic character	Continuity Gross lithology

Specific seismic attribute properties	
Seismic Attribute	Common usage
Polarity	Lithologic contrast
Amplitude	Lithology Continuity of beds Porosity Bed thickness Fluid type
Interval velocity	Lithology Porosity Fluid type?
Instant. frequency	Bed thickness Lithology Fluid type?
Response frequency	same as above using dominant properties
Instant. phase	Continuity of beds
Response phase	same as above using dominant properties
Reflection strength	Lithology Continuity of beds Porosity Bed thickness (including thin bed detection)
Group time	Outline of features
Perigram (group phase)	Inner structure of features
AVO	Lithology Fluid content Porosity Bed thickness (including thin bed detection)
Waveform	Lithology Lateral continuity Porosity Bed thickness (including thin bed detection)

table 4.6: Summary of seismic trace attribute properties and characteristics.

following attributes in a 300 ms window around the Sognefjord reservoir:

- **Reflection strength.** It is somewhat larger than the largest absolute value of the migrated (stacked) amplitudes. All phase information is removed from the data. It can be indicative of lithology, bed continuity and thickness, and porosity.
- **Instantaneous phase** is indicative of the continuity of beds.
- **Instantaneous frequency** is used for lithology and bed thickness studies.
- **Quadrature** is used for bed thickness and continuity.
- **Apparent polarity** at envelope peaks, weighted by amplitude is used for bed thickness and continuity, and lithologic contrasts.
- **Response phase** (instantaneous phase at envelope peaks) helps in determining continuity of beds, based on dominant wavelet properties in the vicinity of local peak amplitudes.
- **Response frequency** (instantaneous frequency at envelope peaks) helps in determining lithology and bed thickness, based on dominant wavelet properties in the vicinity of local peak amplitudes.
- **Group time section** (envelope with DC removed) represents zones of energy concentration and gives an estimate of average characteristics (the outline) of the structure on a seismic section.
- **Perigram** (cosine of instantaneous phase) represents the inner structure on a seismic section.
- **Product** (product of group time section and perigram) highlights common features between group time section and perigram.

Scaling is an important issue during the calculation of seismic attributes, because the screen image is confined to a dynamic range of 8 bits. Most scaling is done on

output, using statistical analysis on a subset of the data in much the same way as for the input of the original seismic amplitude data. However, certain attributes need special scaling which can be predicted without statistical analysis. For example, instantaneous and response frequency must be scaled below the Nyquist frequency; instantaneous and response phase should be confined to -180 and +180 degrees, and the perigram should have limits of -1 and 1.

Time horizon slices

After computing complex trace attributes, time horizon slices were extracted at the top of the Sognefjord and top of Fensfjord units. Figure 4.16 shows the extracted stacked seismic amplitudes, together with instantaneous frequency and instantaneous phase at the top of the Sognefjord unit. Other horizon-consistent complex seismic attribute slices (as listed above) were also extracted. Note that well 31/2-10 encountered wet Sognefjord sands and that it is associated with a low amplitude, dim-spot, appearing in white, as compared to the rest of the survey area, which has a gas cap present. In fact, figure 4.16 shows that wells 31/5-3, 31/2-16S, 31/2-5, 31/2-13, and 31/2-12 all exhibit high negative amplitudes appearing in red, because they are associated with the presence of gas at the top of the Sognefjord. This is a good example of **direct hydrocarbon detection** from 3-D seismic data. Note that the large controlling fault to the east forms the eastern boundary of the water zone, while the western boundary of the water zone is stratigraphic and does not correspond to a particular fault. This is in agreement with the fact that the faults are believed to be non-sealing. The trap appears to be filled to its spill point. The gas zone also exhibits different phase and frequency characteristics from the water zone (figure 4.16), but these features are more difficult to observe than from seismic amplitudes.

Individually, single attribute time-flattened horizons give rise to only marginal improvements over the stacked migrated amplitude attribute horizons from which they were derived. Therefore, I ran pattern recognition tests on joint sets of attributes along time-flattened horizons.

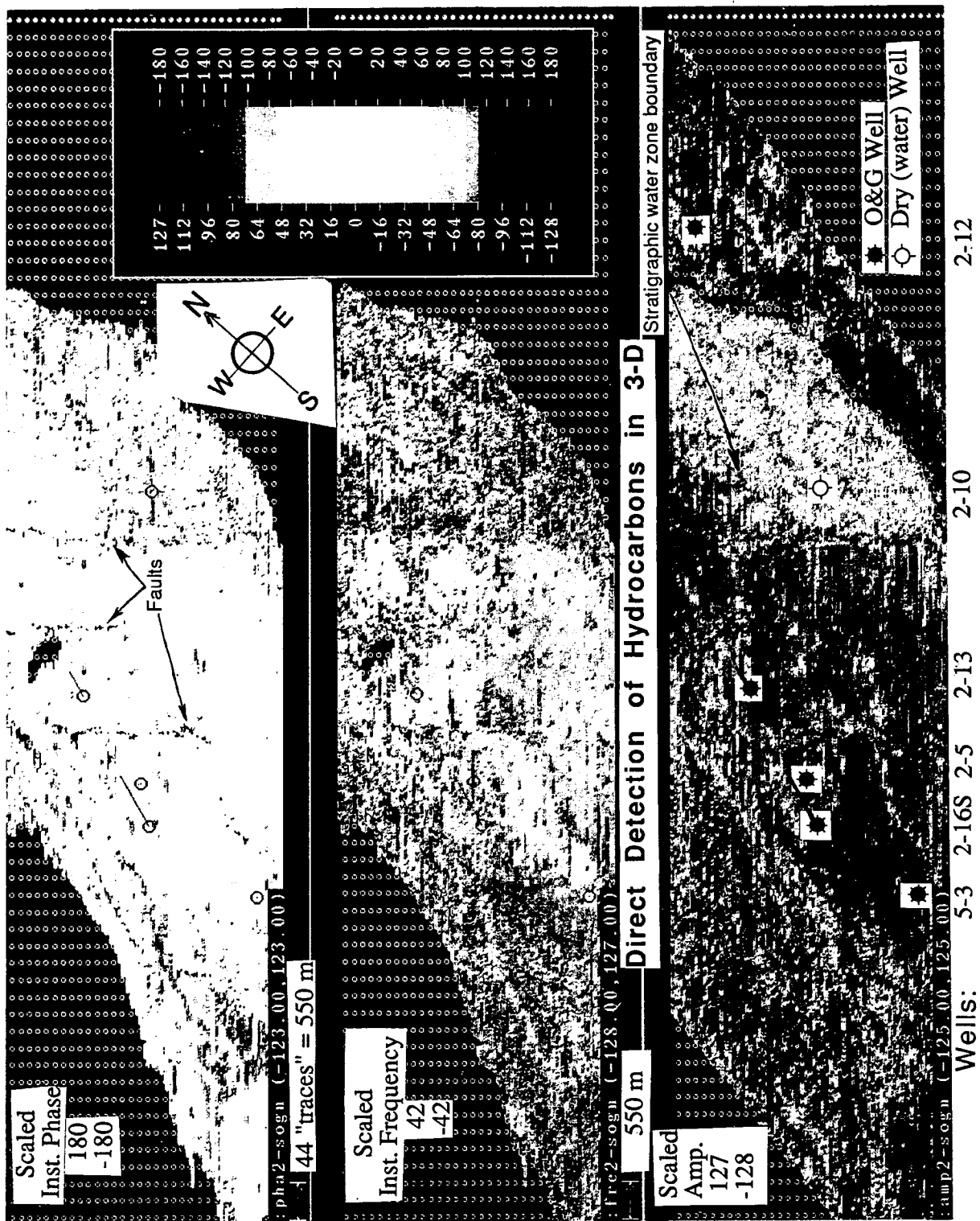


Figure 4.16: Flattened time-horizons slices showing stacked migrated amplitudes, instantaneous frequency, and instantaneous phase at the top of the Sognefjord. Well 31/2-10 is wet and is associated with a low amplitude appearing in white; all other wells (31/5-3, 31/2-16S, 31/2-5, 31/2-13, and 31/2-12) exhibit bright amplitudes associated with the presence of gas and appear in red. This is a good example of direct hydrocarbon detection using 3-D seismic data.

2.b) Pattern recognition of clusters of complex trace attributes

There is no single post-stack complex seismic attribute that will tell us everything that we need to know about the reservoir. Therefore, not only is it necessary to examine the seismic attributes individually, but one must also look at them jointly. This can be achieved by "combining" attributes in a statistical fashion, using clustering, and by "compacting" discriminatory information, using factor analysis.

Five of the complex attributes extracted in part 2.a were analyzed jointly in a horizon-consistent manner at the top of the Sognefjord and the Fensfjord units. This was done using general image analysis software adapted from the Stanford Remote Sensing Laboratory. Each attribute was assigned a single channel, and the data were treated as a single "satellite" image, having five different bands of information. The data were first displayed individually, and then "stretched" on all five channels.

1) Methodology

Statistical methods have been the subject of much research in the oil industry (Bois, 1980, 1981, Aminzadeh, 1987, Dumay and Fournier, 1988, Simaan and Aminzadeh, 1989). The methods used in the following analysis are based on the combination of two statistical methods: (1) statistical clustering, and (2) factor analysis:

- **Statistical clustering** groups points in an n-dimensional space, according to their euclidian distance in that n-space. In our case, $n=5$ is the number of different attributes considered. This yields a certain number of "characteristic" classes in the n-dimensional space.
- **Factor analysis** reduces the information from the n-dimensional space to a new "compact" space of lesser dimension, by computing the most efficient way to summarize the information contained initially. The data or points are then projected onto the new space which is built through a linear combination of the n-starting attributes. Discriminant factor analysis or principal component

analysis is carried-out in such a way to minimize the distortion of information when transferred from n-space to a space of lesser dimension. In that way, the points in the new space can be used to reconstruct most of the initial information in n-dimensions.

The procedures are summarized in figure 4.17.

2) Data analysis

At this point, several attributes were cross-plotted versus one another, to identify which were most independent. I decided that three eigenvectors, formed from linear combinations of the initial five channels, were sufficient to perform the discrimination analysis adequately. The data were then clustered, based on statistical classes, which were defined interactively on a workstation.

Unsupervised clustering

A first pass classification was run using unsupervised clustering to outline areas of the reservoir with different statistical attributes. This procedure highlighted differences in reservoir characteristics, which may otherwise not have been easily detected on conventional seismic sections. One disadvantage of this type of clustering is that the classes established usually do not have a one to one correspondence with the lithologic boundaries that the interpreter is trying to identify.

Supervised clustering

Geophysicists and geologists who work in specific areas develop a talent for recognizing changes in waveform characteristics on seismic data and in using this information in their interpretation. To capture the essential features to be used for discrimination using an artificial intelligence (AI) approach, we need to examine the data around certain key training wells. In the training step, the data around selected wells are first examined to determine if discrimination is possible among the traces, and to calibrate the traces to the properties seen at the learning wells. The learning traces are then used in a predictive step to classify other parts of the reservoir,

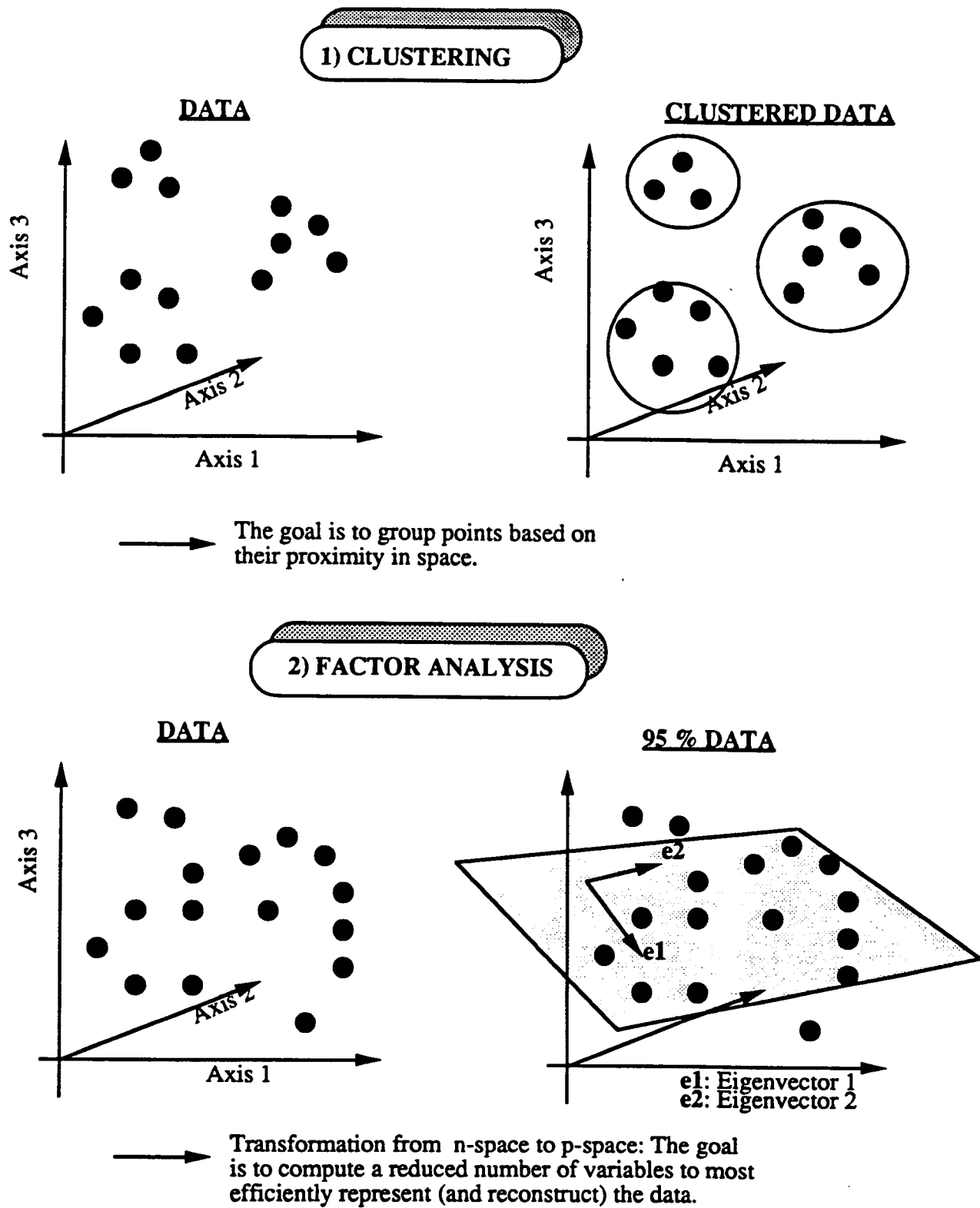


Figure 4.17: Principles of statistical clustering and factor analysis.

away from the reference wells, using pattern recognition. Unfortunately, differences in trace character which are due to lithology are superimposed on any acquisition and processing artifacts in the data.

The choice of the training traces is crucial. One needs to define small sets of reference seismic traces at key wells to carry-out subtle differentiations of possible "sub-facies" within the Sognefjord facies. However, we also want these traces to have enough discrimination power to differentiate between all of the traces present on the section, so that most of the image is classified. In other words, we need to design our training sets such that they carry compact information, and yet have just the right amount of discriminating power to identify key properties in the Sognefjord, while classifying the entire seismic horizon. For these reasons, an interactive environment is necessary for the optimal selection of training traces around the control wells.

As a final remark, keep in mind that seismic data reflects changes in the properties of both the overburden and the reservoir. Therefore, any change that may be observed in the character of seismic reflections, can be explained by changes in either the seal or the reservoir, or both.

In this feasibility study, wells 31/2-5, 31/2-16S, 31/2-13 and 31/2-10 were used as training sets for classification of the horizon-flattened seismic image at the top of the Sognefjord. Figure 4.18a shows the superposition of three seismic attributes from the time-flattened horizon map defined at the top of the Sognefjord. These are instantaneous frequency in red, stacked amplitude in green, and instantaneous phase in blue. The stratigraphy and rock properties are well known at the control wells. The results of the supervised classification clearly indicate the presence of gas as seen in figure 4.18b, together with the extracted training sets, appearing as solid boxes in figure 4.18a. A similar study was undertaken to classify the top of the Fensfjord sands. Results were mixed and no clear trend in seismic attributes was found. This was possibly due to the fact that the Fensfjord/Sognefjord boundary corresponds to the contact between clean sands at the top of the Fensfjord and micaceous sands at

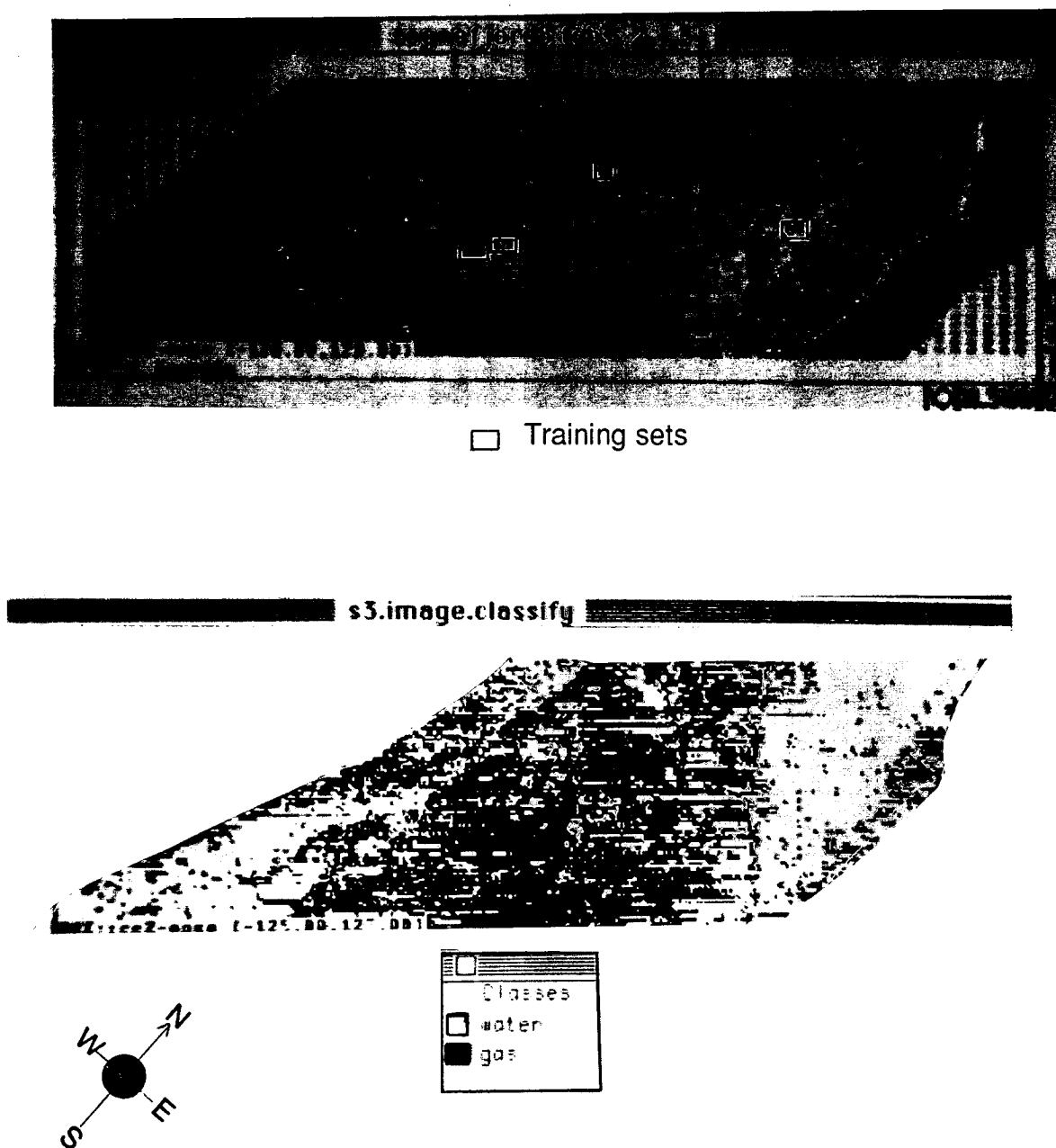


Figure 4.18:

a) Superposition of three seismic attributes (instantaneous frequency in red, stacked amplitude in green, and instantaneous phase in blue) from the time-flattened horizon map defined at the top of the Sognefjord. Note the locations from which training sets were extracted (wells 31/5-3, 31/2-16S, 31/2-5, 31/2-13, and 31/2-10).

b) Supervised classification of seismic attributes from the time-flattened horizon map defined at the top of the Sognefjord. Training properties were extracted from the boxes outlined above. The gas zone can easily be differentiated from the water zone.

the base of the Sognefjord (2M or 3M sands) throughout the entire 3-D survey area. Therefore, no clear differentiation can be seen at that contact.

(VI)-CONCLUSIONS

I have identified the major structural controls over the Troll West Oil province. Several horst blocks have been drilled, showing significant amounts of oil and gas. The detailed integrated 3-D seismic interpretation presented in this chapter reveals that stratigraphic components combine with structural trends to create reservoir heterogeneities throughout the field. In particular, prograding cycles (parasequences) appear to correlate with eustatic sea level changes and often lead to subtle seismic intra-formational reflectors. Detailed studies of calibrated seismic responses at key wells show that the boundary between cycles ZA4.2 and ZA4.3 usually leads to the strongest intra-formational reflector within the Troll West area. However, it does not seem to correlate to either the highest rate of sea level rise or to the highest magnitude of sea level rise for that time period (figure 4.8). This observation leads to a fundamental question regarding eustatic sea level changes: why does the ZA4.2/ZA4.3 boundary appear the strongest on seismic sections, and could this possibly be related to the driving mechanism behind sedimentation cycles? The answer may lie in the interaction through time between the tectonic and subsidence components of the sedimentation cycles observed here.

In order to study stratigraphic relationships and direct hydrocarbon indicators in detail at Troll West, we need to examine the pre-stack seismic data as well as the stacked migrated data. Detailed pre-stack seismic analyses dictate that we concentrate on a small subset of the data, and integrate seismic velocities with core and log analyses, in order to establish direct correlations with rock properties such as mineralogy, cementation, fluid content, and local changes in in-situ conditions.

REFERENCES

- Aminzadeh, F., 1987, Pattern recognition and image processing: Handbook of Geophysical Exploration, section I, Seismic Exploration, Vol. 20, 568 pages.
- Bally, A.W., 1983, Seismic expression of structural styles: AAPG, studies in geology series #15, v. 2.
- Biddle, K.T., and Rudolf, K.W., 1988, Early Tertiary structural inversion in the Stord Basin, Norwegian North Sea: J. of Geological Society, London, v. 145, 603, 611.
- Blundell, D.J., and Gibbs, A.D., 1990, Tectonic Evolution of the North sea Rifts: Oxford science publications, 272 pages.
- Bodine, J.H., 1984, Waveform analysis with seismic attributes: Proceedings of the 54th Annual SEG meeting, Atlanta.
- Bois, P., 1981, Determination of the nature of reservoirs by use of pattern recognition algorithm with prior learning: Geophysical Prospecting, 29, 687, 701.
- Bois, P., 1980, Autoregressive pattern recognition applied to the delineation of oil and gas reservoirs: Geophysical Prospecting, 28, 572, 591.
- Bolle, L., and Henningfeld, H., 1990, Troll: Norway's Giant offshore gas field: Giant Oil and Gas Fields of the Decade 1978-1988 Conference, September 9-12, Stavanger, Norway.
- Brown, A., 1986, Interpretation of three-dimensional seismic data: AAPG Memoir 42.
- Chew, K. J., 1990, Oil and Gas Developments in Europe in 1989: AAPG Bulletin, v. 74, 240,256.
- Cross, T.A., and Lessenger, M.A., 1988, Seismic stratigraphy, in G.W. Wetherell, A.A. Albee, and F.G. Stehli, eds., Annual Review of Earth and Planetary Sciences, v. 16, 319, 354.
- Denham, J. I., and Nelson, R. H., 1986, Short note: Map displays from an interactive interpretation: Geophysics, 51, 1999,2006.
- Dore, A.G., Vollset, J., and Hamar, G.P., 1985, Correlation of the offshore sequences referred to the Kimmeridge Clay Formation - Relevance to the Norwegian sector: in Petroleum Geochemistry in Exploration of the Norwegian Shelf, The Norwegian Petroleum Society, Graham and Trotman.
- Dumay, J., and Fournier, F., 1988, Multivariate statistical analyses applied to seismic facies recognition: Geophysics, v. 53, no. 9, 1151, 1159.
- Galloway, W.E., 1989a, Genetic stratigraphic sequences in basin analysis I: Architecture and genesis of flooding-surface bounded depositional units: AAPG Bulletin, v. 73, 125, 142.

Galloway, W.E., 1989b, Genetic stratigraphic sequences in basin analysis II: Application to Northwest Gulf of Mexico Cenozoic Basin: AAPG Bulletin, v. 73, 143, 154.

Gardner, G. H. F., L. W. Gardner, and A. R. Gregory, 1974, Formation Velocity and density-the diagnostic basis of stratigraphic traps, Geophysics, 39, pp.770-780.

Geertsma, J., 1961, Velocity-log interpretation: The effect of rock bulk compressibility: Society of Petroleum Engineers J. (AIME) , v. 1, 235, 248.

Glennie, K.W., 1986, Introduction to the Petroleum Geology of the North Sea: Blackwell scientific publications, second edition, 278 pages.

Gray, D.I., 1987, Troll: in Geology of the Norwegian Oil and Gas Fields, The Norwegian Institute of Technology, Graham and Trotman.

Halbouty, M. T., 1982, The Deliberate Search for the Subtle Trap: AAPG Memoir 32.

Haq, B.V., Hardenbol, J., and Vail, P.R., 1988, Mesozoic and Cenozoic chronostratigraphy and eustatic cycles: in "Sea level changes: an integrated approach", 71, 108.

Haq, B.V., Hardenbol, J., and Vail, P.R., 1987, Chronology of fluctuating sea-level since the Triassic: Science, 234, 1156, 1167.

Hellem, T., Kjemperud, A., and Ovrebo, O.K., 1986, The Troll field: a geological/geophysical model established by the PL085 group: in Habitat of hydrocarbons on the Norwegian continental shelf, The Norwegian Petroleum Society, Graham and Trotman, 217, 238.

Klemperer, S.L., and Hobbs, R.W., in press (1992), The B.I.R.P.S. Atlas of deep seismic reflection profiles around the British Isles: Cambridge University Press, 198 pages + 99 seismic sections.

Neidell, N.S., and Poggiagliolmi, E., 1977, Stratigraphic modeling and interpretation - Geophysical principles and techniques, in Seismic stratigraphy - applications to hydrocarbon exploration: A.A.P.G. Memoir, 26, 389, 416.

Norsk Hydro A.S., 1988, Troll: Joint Geological review.

Osborne, P., and Evans, S., 1987, The Troll field: reservoir geology and field development planning: in North sea Oil and Gas reservoirs, The Norwegian Institute of Technology, Graham and Trotman.

Simaan, M., and Aminzadeh, F., 1989, Artificial Intelligence and Expert Systems in Petroleum Exploration: in Advances in Geophysical Data Processing, Vol. 3, 307 pages, Jai Press Ltd.

Sonneland, L., and Barkved, O., 1990, Use of seismic attributes in reservoir characterization: North sea Oil and Gas reservoirs, II, The Norwegian Institute of Technology, Graham and Trotman.

Pickett, G. R., 1963, Acoustic character logs and their applications information evaluation, Jour. Pet. Tech., pp. 659-667.

Read A.S., 1988, Sediment sequences, sea-level fluctuations, and carbonate cemented horizons in the Troll field reservoir, report.

Sheriff, R.E., 1977, Limitations on resolution of seismic reflections and geologic detail derivable from them, in *Seismic stratigraphy - applications to hydrocarbon exploration*: A.A.P.G. Memoir, 26, 3, 14.

Shtivelman, V., Landa, E., and Gelchinsky, B., 1986, Phase and group time sections and possibilities for their use in seismic interpretation of complex media: *Geophysical Prospecting*, 34, 508-536.

Spencer, A.M., 1987, *Geology of the Norwegian Oil and Gas Fields: The Norwegian Petroleum Society*, Graham and Trotman.

Taner, M. T., Koehler, F., and Sheriff, R. E., 1979, Complex seismic trace analysis: *Geophysics*, 44, 1041-1063.

Taner, M. T., and Sheriff, R. E., Application of Amplitude, Frequency, and Other Attributes to Stratigraphic and Hydrocarbon Determination: *AAPG, Memoir 26*, 301-327.

Thomas, B.M., Moller-Pederson, P., Whitaker, M.F., and Shaw, N.D., 1985, Organic facies and hydrocarbon distributions in the Norwegian North sea: in *Petroleum Geochemistry in Exploration of the Norwegian Shelf*, The Norwegian Petroleum Society, Graham and Trotman.

Vail, P.R., and Wornardt, W.W., 1990, Well log-seismic sequence stratigraphy: an integrated tool for the 90's: in Armentrout, J.M., and Perkins, B.F., editors, *Sequence Stratigraphy as an exploration tool: Concepts and Practices in the Gulf Coast: Gulf Coast SEPM Foundation, 11th Annual Research Conference, Abstracts*, 379, 388.

Vail, P.R., Mitchum, R.M., Todd, J.M., Widmier, Thompson III, S., Sangree, J.B., Bubb, J.N., and Hatlelid, W.G., 1977, *Seismic stratigraphy - applications to hydrocarbon exploration*: A.A.P.G. Memoir, 26, 29-212.

White, R.E., 1991, Properties of instantaneous seismic attributes: *Geophysics*, T.L.E., July issue, 26, 32.

Widess, M.B., 1973, How thin is a thin bed?: *Geophysics*, 38, no. 6, 1176, 1180.

Ziegler, P. A., 1990, *Geological Atlas of Western and Central Europe*: Shell Internationale Petroleum Maatschappij B.V., 239 pages.

Ziegler, P. A., 1990, Tectonic and palaeogeographic development of the North sea rift system: in *Tectonic Evolution of the North sea Rifts*, edited by Blundell and Gibbs.

Ziegler, P. A., 1989, Evolution of the North Atlantic - An overview: *A.A.P.G. Memoir*, 46, 111-129.

Ziegler, P. A., and van Hoorn, B., 1989, Evolution of the North sea rift system: *A.A.P.G. Memoir*, 46, 471-500.

**INTRODUCTION TO PART III: APPLICATIONS-2:
A DETAILED INTEGRATED PRE-STACK RESERVOIR STUDY
OF THE TROLL WEST OIL PROVINCE**

One key goal in reservoir characterization is to obtain estimates of the elastic parameters of a reservoir. This is a seismic imaging problem, which consists mostly in a series of advanced pre-stack depth migrations. Subsequently, the state-of-the-art consists in relating observed seismic properties to rock properties through approximations such as the Bortfeld approximation. This has traditionally been called "inversion" (Hampson, 1991). Another approach is to use iterative forward modeling, starting from rock properties, building a model, and matching seismic responses. This is known as the "forward modeling" approach. The approach that I have developed in part I of this thesis belongs to the second category. By iterative forward modeling, one can arrive at a final earth model. In that sense, it can be seen as an inversion for lithology, physical states, and pore fluid type. Applications of this approach to reservoir characterization include: (1) reservoir extension, (2) direct hydrocarbon detection, and (3) reservoir production.

In chapter 5, I integrate the currently available tools used in geology, rock physics, seismic, and engineering in order to test the methodologies developed in part I, using a field data set from industry.

I concentrate on reservoir characterization for reservoir management, and in particular, on the use of **petrophysics** for calibration of seismic at wells and for **extrapolating** reservoir properties away from those wells. In that sense, the techniques developed here are different from existing reconnaissance AVO techniques developed previously by companies like Western Geophysical, Cogniseis, and Simon-Geolithic, among others. Instead, they are part of "exploitation" or "development AVO" and are not subject to the same pitfalls as "Recon AVO", because they are based on a fine-tuned knowledge of geology and rock properties at calibration wells. However, they remain subject to the interpreter's knowledge base, to the quality of the data,

and to its "true amplitude" processing. To some extent, I tend to agree with the concept that the least you "do to the data", the better-off you are for inversion. However, it is necessary to achieve a decent S/N ratio through processing, to be able to interpret the essential components of the data. This observation justifies the fact that I carried-out my own processing steps on pre-stack seismic gathers, as well as the exact duplication of the processing steps to synthetic seismic data.

An increasing amount of effort is currently being directed toward the integration of geophysical methods with geological and engineering techniques in order to use seismic data more quantitatively for the design, optimization, and monitoring of the production of oil reservoirs (Geoffrey et al, 1989, Johnstad et al, 1990, Lines et al, 1989, Justice et al, 1989, Nur, 1987, Robertson, 1989, Seymore et al, 1989, Wang, 1988). The successful outcome of these studies is dependent on many factors, among which are:

- a detailed characterization of the sediments,
- a reliable reservoir geological and geophysical model,
- dense data coverage and high quality seismic and well data,
- and the establishment of a reliable rock physical model for the reservoir and the overburden.

Some of these issues imply a working understanding of petrophysics, such as frequency dispersion phenomena, accounting for scale averaging in the integration of diverse data, such as induced anisotropy at the seismic scale, a good working knowledge of intrinsic and extrinsic attenuation, etc. In fact, our current state of knowledge dictates that we further address and understand these issues through more studies of the relations between seismic and sedimentary facies (Cross and Lessenger, 1988) before geophysical data can be routinely used quantitatively in detailed production work.

Fortunately for us, seismic anomalies are often robust enough that we do not need to understand secondary effects in order to make intelligent decisions based on them. For example, in chapter 1, I showed that contrasts in intrinsic attenuation can distort the character of a reflection at an interface. The effects of Q contrasts on AVO responses add-on as second order terms and are most pronounced when velocity contrasts are small at an interface. Luckily, mother earth is often such that interfaces with small impedance contrasts also exhibit small attenuation contrasts, so that the error made in neglecting attenuation contrasts is usually small. It is precisely this robustness of seismic anomalies that has enabled the success of relatively "simple" integrated studies in some shallow reservoirs. By introducing more accurate models that account for issues such as scale differences between laboratory and seismic field measurements, dispersion, anisotropy, and limited seismic resolution, we stand to better characterize reservoirs with calibrated geophysical data.

The theoretical results of chapter 1 on anelasticity and anisotropy are encouraging, but have not dealt with many of the problems encountered with field data. The problems associated with seismic acquisition and processing conditions have been the subject of much research, in order to establish the best possible processing methods to enhance S/N ratios, and differentiate noise from wave propagation effects (Yu, 1985, Dey-Sarkar et al, 1988). In what follows, I test the methodologies for integration developed in part I, by analyzing a complete data set from the Troll field. More specifically, I use seismic and well data to investigate to what extent geophysical data can be used in reservoir characterization for the design of oil production from the Troll West oil province. The case history that follows depends on sound petrophysical analyses and on an AVO modeling approach described in part I, chapters 1, 2, and 3. It includes the automatic filtering and blocking of logs, proper averaging and up-scaling to seismic wavelengths, the determination of shear velocities in the absence of full waveform logs, the calculation of "average" Q values for dominant layers, the interactive implementation of "reasonable" variations in petrophysical parameters within a seismic facies for sensitivity analyses, and the iterative generation of synthetic

seismograms.

In short, the approach is to investigate changes in reflection signature from the reservoir as a function of changes in important lithological parameters such as porosity, fluid saturation, fluid flow and permeability. In a sense, the **detailed iterative forward modeling approach** achieves two things:

- it recasts the geophysical inversion process in its natural geological settings, by including the maximum amount of a-priori information
- and it makes use of petrophysics to convert seismic waveform properties into stratigraphic and lithologic information.

I hope that this type of approach will generate new ideas for geologists, geophysicists and engineers and that it will help them converge towards a common goal: the mapping of reservoir heterogeneities from high resolution seismic data for reservoir characterization and management.

REFERENCES

- Cross, T.A., and Lessenger, M.A., 1988, Seismic stratigraphy, in G.W. Whetherell, A.A. Albee, and F.G. Stehli, eds., Annual Review of Earth and Planetary Sciences, v. 16, 319, 354.
- Dey-Sarkar, S.K., Svatek, S.A., and Crewe, O.W., 1986, Prestack Analysis: Data Processing: S.E.G. Expanded Abstracts from the 56th Annual meeting in Houston, 339, 341.
- Geoffrey, A.D., Fisher, D.A., 1989, Detailed fault interpretation of 3D seismic data for EOR planning: S.E.G. Expanded Abstracts from the 59th Annual meeting in Dallas, Vol. 2, 747, 749
- Hampson, D., 1991, AVO inversion, theory and practice, Geophysics, TLE, June, 39, 42.
- Johnstad, S.E., Seymore, R.H., Dunlop, K.N.B., 1990, The feasibility of monitoring fluid movements during production from a Norwegian oilfield using repeated seismic surveys: Paper presented at the 52nd E.A.E.G. Conference in Copenhagen, Denmark.
- Justice, J.H., Vassiliou, A.A., Singh, S., Ranganayaki, P.S., Cunningham, P.S., Solanki, J.J., and Allen, K.P., 1989, Recent developments in geophysics for reservoir characterization: S.E.G. Expanded Abstracts, 59th Annual meeting in Dallas, V. 1, 549, 550.
- Lines, L.R., Fackson, R., and Covey, J.D., 1989, Seismic velocity models for heat zones in Athabasca tar sands: S.E.G. Expanded Abstracts from the 59th Annual meeting in Dallas, V. 2, 751, 753
- Nur, A., 1987, Seismic rock properties for reservoir description and monitoring: in G. Nolet (ed) Seismic Tomography, 203, 237.
- Robertson, J.D., 1989, Reservoir management using 3D seismic data: S.E.G. Expanded Abstracts from the 59th Annual meeting in Dallas, V. 2, 897.
- Seymore, R.H., King, G.A., Dunlop, K.N.B., and Uden, R.C., 1990, The potential contribution of surface seismic surveys to the monitoring of offshore oil fields: Paper presented at the 51st E.A.E.G conference in Berlin, F.R.G.
- Wang, Z., 1988, Wave velocities in hydrocarbons and hydrocarbon saturated rocks, with applications to EOR monitoring: PhD Thesis Stanford University, SRB report, V. 34
- Justice, J.H., Vassiliou, A.A., Singh, S., Ranganayaki, P.S., Cunningham, P.S., Solanki, J.J., and Allen, K.P., 1989, Recent developments in geophysics for reservoir characterization: S.E.G. Expanded Abstracts from the 59th Annual meeting in Dallas, Vol. 1, 549-550
- Yu, G., 1985, Offset-amplitude variation and controlled-amplitude processing: Geophysics, 52, 2697, 2708.

"THE GEOPHYSICIST, GOD BLESS HIM"

A geophysicist is a person who passes as an exacting expert on the basis of being able to turn out with prolific fortitude infinite strings of incomprehensible formulae calculated with micromatic precision from vague assumptions derived from debatable figures which are based on inconclusive experiments carried out with instruments of problematic accuracy by persons of doubtful reliability and questionable intellect for the avowed purpose of confounding a hopeless group of fanatics known as geologists!

Fill-in page

This page was inserted for esthetic purposes only, and does not necessarily reflect the author's opinion or state of mind. It is NOT an integral part of the thesis at Stanford University, and was obtained from a series of "reliable" sources out there.

CHAPTER 5

AN INTEGRATED SEISMIC RESERVOIR CHARACTERIZATION AT TROLL WEST

"If facts conflict with a theory, either the theory must be changed or the facts",

Benedict Spinoza.

ABSTRACT

Iterative model-based integrated seismic pre-stack lithologic interpretation is used for reservoir characterization at Troll. Critical questions relating to the production and development of the Troll West oil province include the recognition of calcite cemented layers, the differentiation between clean and micaceous sands, and the possibility of predicting fluid movement associated with hydrocarbon production. Modeling results show that:

- The lateral extent of calcite cemented layers can be predicted from model-based integrated seismic interpretation work
- The differentiation between clean and micaceous sands is difficult. However, since the top and bottom of the micaceous units are often associated with calcite, their presence can be inferred indirectly
- The prediction of fluid movement associated with the production of hydrocarbons and in particular, the identification of coning around wells, is a key goal. Synthetic studies are encouraging, because they show that subtle differences in seismic signatures are expected at production wells before and after coning.

My approach is based on petrophysics and seismic modeling. It involves the integration of core analyses, log analyses, petrophysical interpretation, true amplitude

reprocessing of seismic, and pre-stack, AVO modeling. Lithologic models were systematically built from the microscale to the seismic scale, which involved **three phases of investigation**, corresponding to the following three types of measurements:

- A comprehensive **core measurement** program undertaken to calibrate ultrasonic responses to changes in lithology, porosity, and fluid content at in-situ reservoir conditions.
- **Log measurements**, which average heterogeneities on the order of core dimensions to a scale of a few feet. These measurements correlate well to the core results, except in areas of thin-interbedded *calcite* stringers, where "average sonic" logs tend to be faster than ultrasonic core velocities. Logs were also used to estimate total *muscovite* content in the Sognefjord sands and *fluid effects*, which were seen to be consistent with the Biot-Gassman theory. Correlations between velocity, porosity, and lithology were established from well logs allowing a transformation of lithologic variations into velocity changes at the log scale of investigation.
- **Seismic elastic macro-models** were built from log and core data at well control points. These detailed 1-D lithologic models compared favorably with **seismic data**. More complicated 2-D models were also investigated. Because of the lack of structural features in the overburden and the relatively flat reflectors under investigation, a 1-D approach appears valid. Results show that subtle changes in lithology, such as the presence of calcite and/or micaceous layers and changes in porosity, can be mapped from seismic data.

The iterative lithologic modeling approach was also shown to have potential in extracting quantitative information that can assist in **reservoir production**. Sensitivity analyses were carried-out for production monitoring. The analyses involved the use of more general "**Lithologic models**" that incorporated fluid properties and in-situ conditions, to evaluate these effects on seismic properties. Model results showed

that fluid movements are associated with subtle differences in seismic signatures. In the future, these small changes in seismic character may be used to identify coning around wells.

In summary, integrated 1-D seismic lithologic models can be used effectively at Troll to extract quantitative information that can be used to support or refute certain reservoir properties inferred from depositional models or reservoir simulations.

INTRODUCTION

Difficult conditions at Troll

The geographical extent of the North Sea includes boundaries defined by the straights of Dover/Calais in the south, the gaps between Scotland-Orkney and Shetland in the west, the 62 degree parallel in the north, and the Skagerrak/Kattegat boundary in the east. This eastern boundary is defined by a northeasterly line from cape Skagen to the swedish coast. These boundaries were set by the International Hydrographic bureau and are shown in figure 5.1.

As seen in the chapter 4, the general shape of the North Sea basin is controlled in part by NW-SE faults reflecting a structural trend as old as Permian. However, present day sea floor topography reflects Pleistocene events, when large glaciers excavated the Norwegian trough and the Skagerrak, which was probably the site of an older river valley at that time. The Troll field is located in the Norwegian trench in waters of 350m depth (figure 5.1). Sea floor sediments around Troll consist mostly of muds (Veenstra, 1970), creating difficult conditions for the production of hydrocarbons. These conditions are made the more difficult by relatively strong average surface currents and water flow rates, as shown in figure 5.1.

During the past 20 years, offshore production in the North Sea has skyrocketed from practically nothing to an average of 2.5 mbpd of oil and 100 mcmpd of gas. This was achieved by seeking deeper targets and by designing new advanced production

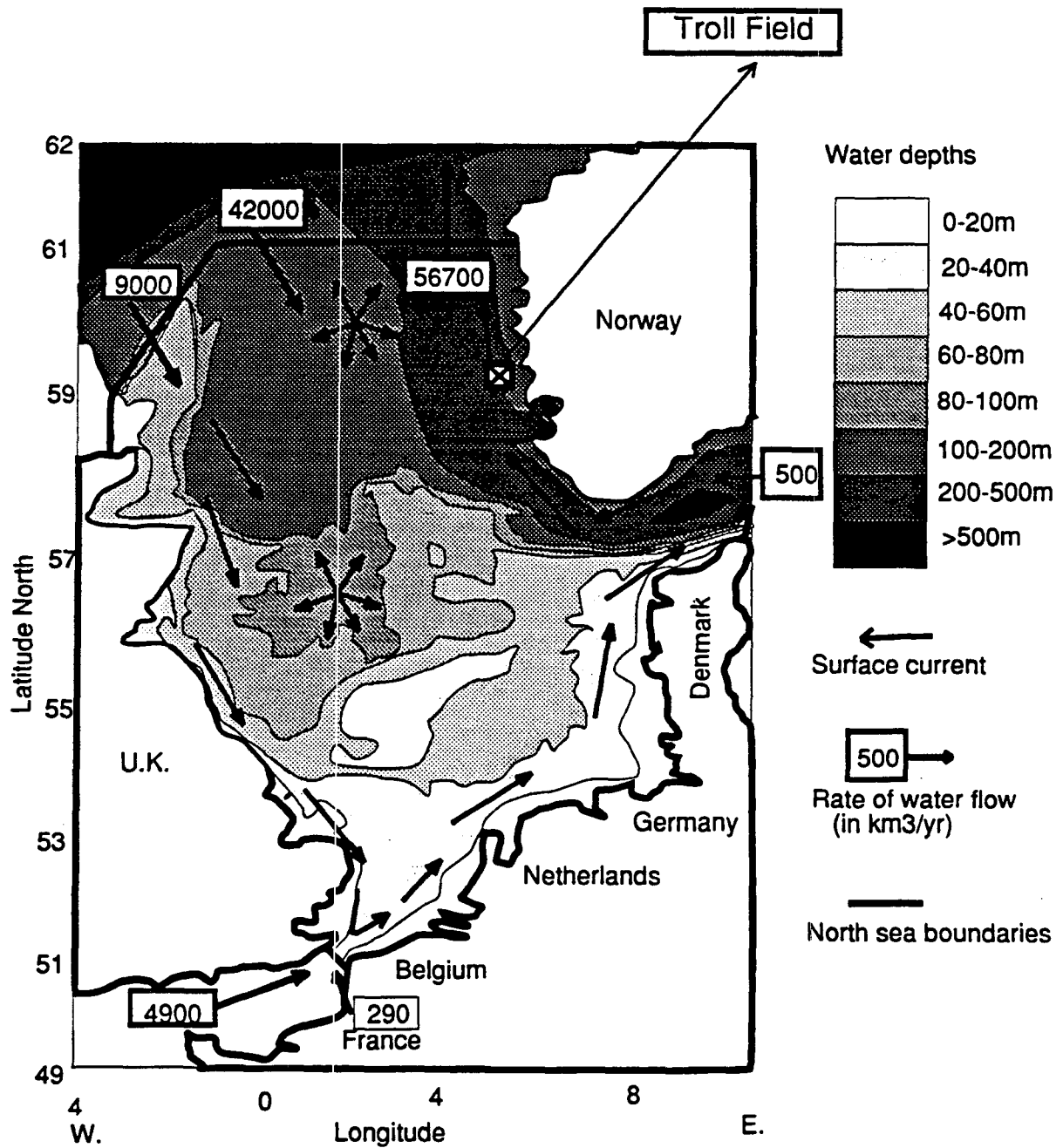


Figure 5.1: Hydrographical boundaries, average water depths, and average currents in the North sea; figure modified after Eisma (1987) and Eisma and Kalf (1987).

facilities, such as steel jackets, concrete gravity platforms, underwater manifold systems, and sub-sea pipelines. As North Sea exploration pushes further north, from the southern U.K. sector to the northern norwegian sector, newer production technologies will become necessary, with emphasis on remote controlled production facilities on the sea floor. According to Norsk Hydro, such an underwater network is scheduled for production at Troll.

Today, geoscientists have the opportunity to influence production plans through better characterization of reservoir units. This forms an exciting new challenge for those geoscientists. Ideally, the approach would involve the iteration of reservoir models by geologists, geophysicists, and engineers, and comparing results through seismic, well testing and production data. Unfortunately, it is not possible for a single student to achieve this kind of iteration in a university environment. Therefore, the work presented here should only be seen as a concept-proving feasibility study, from geoscience to engineering.

(I) CORE ANALYSIS AND ULTRASONIC ELASTIC VELOCITIES AT THE TROLL WEST WELL 31/5-4S

1) Motivation for laboratory work

In chapter 2, I showed that some properties of consolidated rocks could be modelled accurately. However, because the productive Sognefjord sands are only loosely consolidated, the theory developed in chapter 2 to calculate shear velocities cannot be applied with much accuracy. Therefore, an extensive laboratory program was undertaken to empirically establish a detailed and reliable physical model of the reservoir sediments at Troll West. With data from laboratory measurements, a physical model can be built to better understand the effects of lithology, porosity, pore pressure, and fluid content on seismic velocities.

2) Origin of the core samples

A pilot well (31/5-4S) was drilled in conjunction with one of the recent horizontal wells in the Troll West Oil province. Core plugs were selected at 2m intervals from an 80m cored section in the Sognefjord sands. Reservoir layers are practically horizontal with the core plugs being taken perpendicular to bedding. Unfortunately, two core plugs were damaged, leaving a total of 38 samples available for this study. Figure 5.2 shows measured core porosities at atmospheric pressure, together with computed grain densities. The depths used for reference are measured cable depths, along well 31/5-4S, which is highly deviated. The porosities range from about 25 % to 40 % and grain densities average 2.6 g/cc to 2.65 g/cc. Three different high porosity sand zones can be identified: from 1720m to 1735m, from 1670m to 1695m, and from 1652m to 1658m, approximately. The lower porosity sections correlate well to the gamma ray log, as shown in appendix B-7.

3) Sample preparation and measurement set-up

Due to lack of cement, the core samples required careful preparation to prevent the loose sands from disintegrating. The samples were re-cut under liquid nitrogen to a diameter of 2.54 cm and a length of approximately 5 cm; they were then mounted in lead sleeves with sealing metal screens at both ends. The metal screens were used to hold the samples in place during the cleaning and preparation phases prior to the actual measurements. Once put into a jacket, the samples were thoroughly cleaned of their oil content with toluene.

After a first cleaning attempt, the measured porosities led to unreasonable apparent densities and didn't match previous laboratory porosity measurements made on similar core samples. The samples were then re-cleaned thoroughly by soaking in toluene for several days and replacing the dirty "clouded" toluene several times. The samples were considered clean when it appeared that residual oil could no longer be dissolved in the toluene. After the second cleaning, a significant increase in apparent porosities was apparent, especially in the oil zone. Figure 5.3 shows a comparison

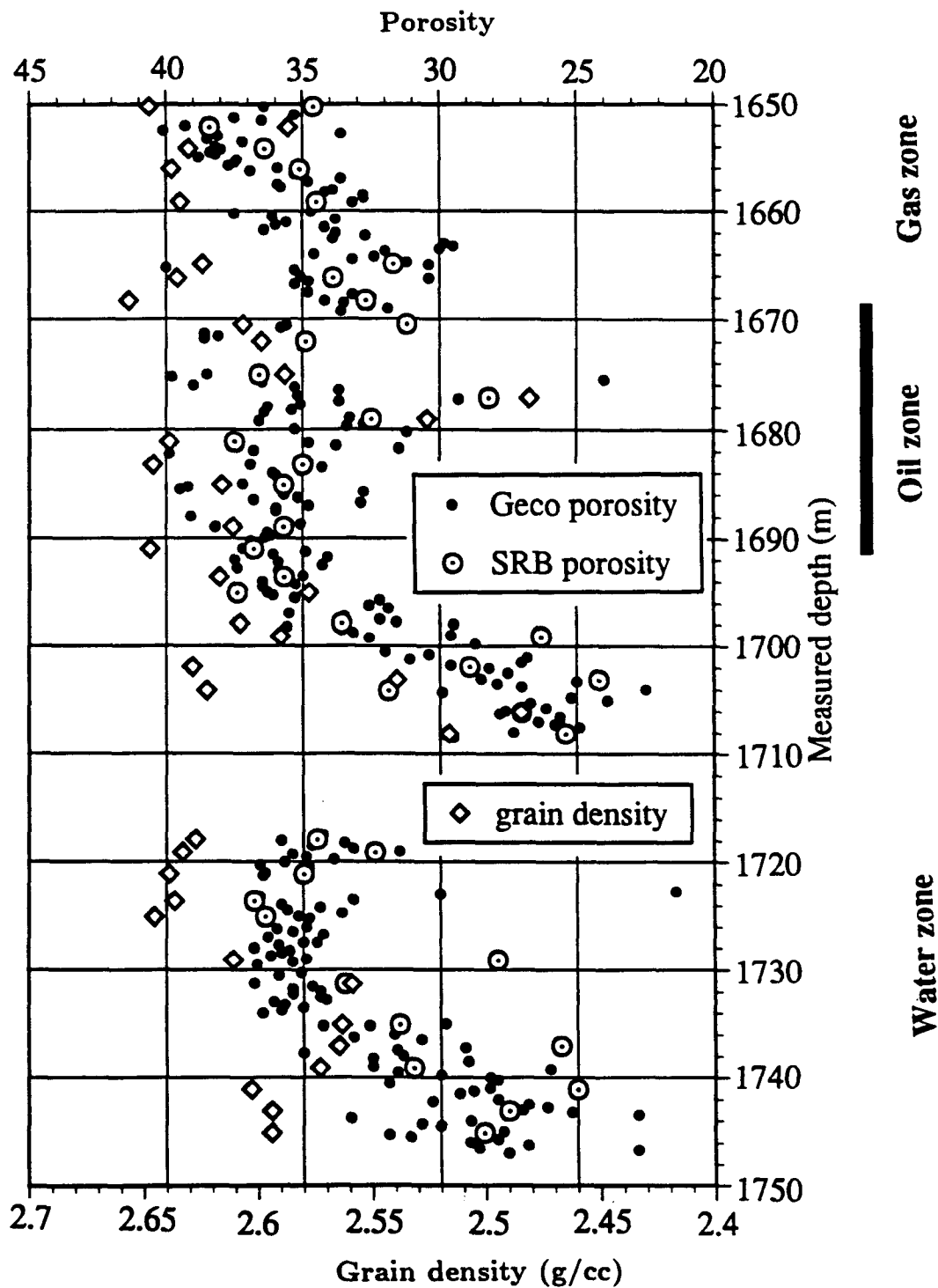


Figure 5.2: Troll porosities from well 31/5-4S measured at the S.R.B. laboratory compare well with porosities measured by Geco Corelabs (on a 25 cm basis); a computed grain density scale is superimposed on the x-axis.

between the measured porosities before and after the second cleaning attempt. This clearly demonstrates the importance of a thorough cleaning procedure before proceeding with further measurements, in order to eliminate any residual oil from the pore space.

Prior to helium-porosity measurements, the samples were oven dried at low temperature (approximately 40 degrees C) for up to ten days, while their respective weights were monitored. Since their weight decreased due to the evaporation of fluids, they were considered dry when their weight stabilized. The final porosity results were consistent with those measured on similar samples by Geco Corelabs in Stavanger (figure 5.2).

The measurement set-up used for ultrasonic elastic velocities was identical to that built by C. Tosaya (1982), and later used by Marion (1989) and Vernik (1990), along with other S.R.B. members. It is based on a standard pulse transmission technique, with a P-wave transducer of central frequency 1 MHz, and a shear wave transducer of central frequency 0.6 MHz. Both the pore pressure and the confining pressure were controlled individually, along with the temperature inside the pressure vessel. The metal screens used during preparation of the samples were removed to achieve better coupling to the transducers. Net sample lengths, volumes, and weights were also computed.

4) Overview of the measurement program

The following measurements were obtained in the laboratory:

(1) Dry compressional and shear wave velocities at confining pressures of 5, 10, 15, 20, 25 and 30 MPa. Here, the confining pressure is equal to the effective pressure, because there is no pore pressure.

(2) Compressional and shear wave velocities in fully water saturated samples, with pore pressure equal to 15 MPa, under confining pressures of 20, 25, 30, 35, 40, and 45 MPa, yielding effective pressures of 5, 10, 15, 20, 25, and 30 MPa, respectively.

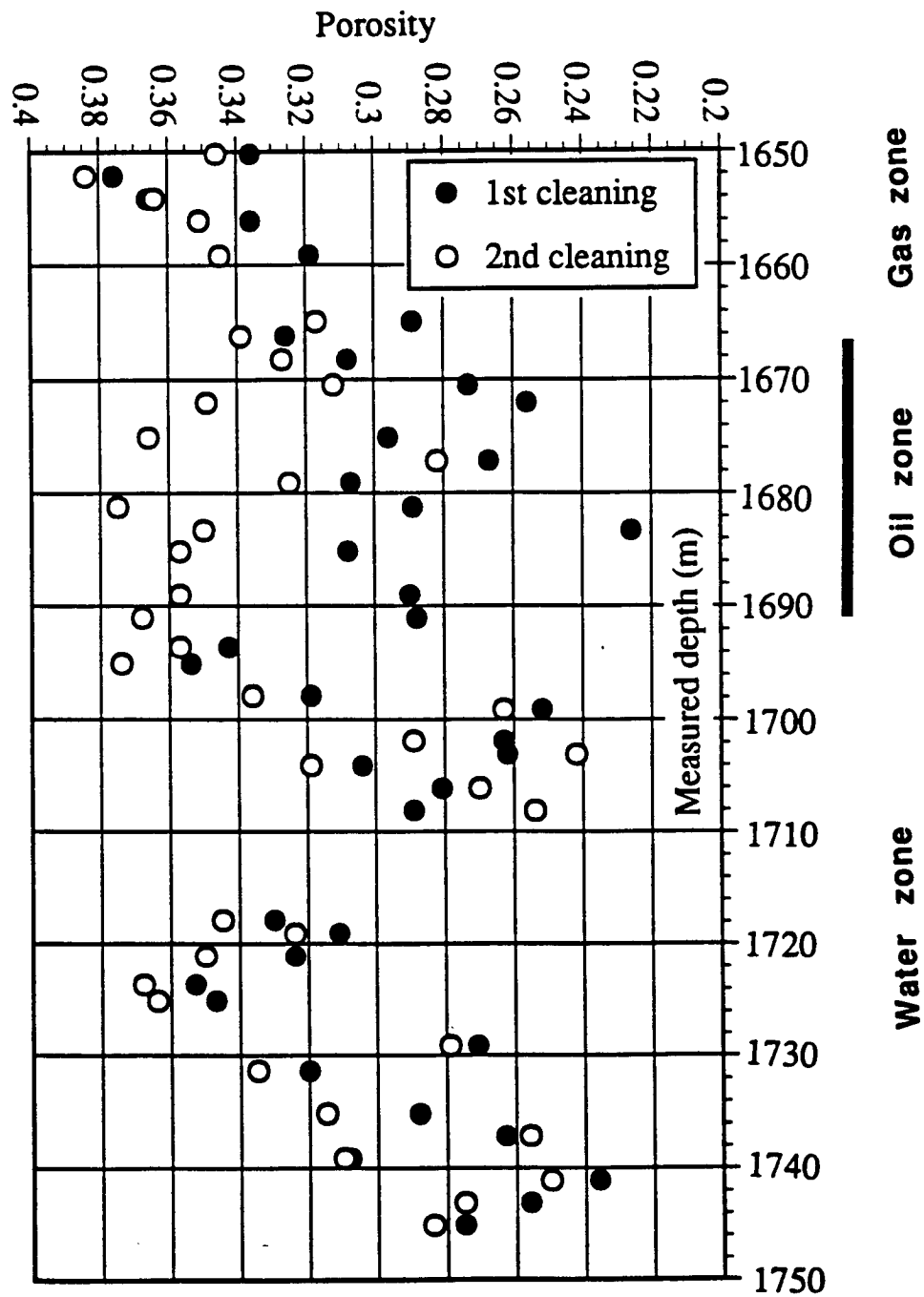


Figure 5.3: Measured apparent porosities at Troll, after 1st and 2nd cleaning attempts. A significant increase in apparent porosities occurs in the oil zone after the second cleaning.

(3) Compressional and shear wave velocities in selected fully oil saturated samples, under the same conditions as for the water saturated samples.

(4) Compressional and shear wave velocities in selected fully oil saturated samples under different temperature conditions. Here, the confining and pore pressures were held at 45 MPa and 15 MPa, respectively, yielding an effective pressure of 30 MPa.

5) Data corrections

Before picking the final traveltimes, the samples were taken through several pressure cycles, until apparent travel times stabilized. Velocities were determined only during the pressure downloading cycle. Usually, the apparent travel times stabilized after the first pressure cycle.

For a given effective pressure, ultrasonic velocities are obtained by dividing the true length of the sample by measured traveltime. Since a sample changes both length and porosity due to a change in effective pressure, accurate measurements of true sample length and porosity are necessary to obtain good experimental results at ultrasonic velocities. This is especially important in the Troll sands, because the samples undergo both permanent and elastic deformations during pressure cycling.

a) permanent deformation

Length and porosity changes were monitored versus pressure, because a significant amount of compaction occurs with pressure, due to the loose consolidation of the samples. In addition to the stress induced elastic deformation, permanent deformation also took place, as evidenced by a significant reduction in length after the samples had been pressurized through several cycles. On the average, measured permanent vertical strain deformation increased with increasing porosity. Typical permanent strain values of 0.015 were observed for the lower porosity samples, with up to 0.03 being observed for the larger porosity samples. These changes were accounted for on a sample by sample basis.

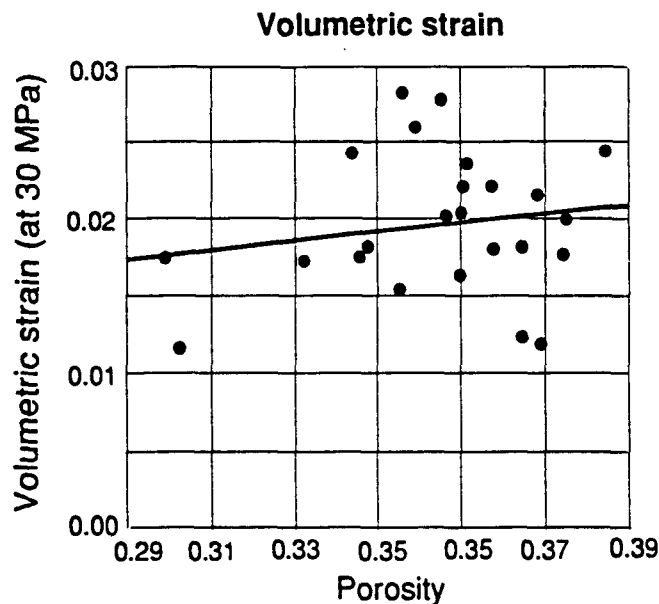


Figure 5.4: Measured volumetric strains at 30 MPa effective pressure.

b) elastic deformation

To estimate the amount of elastic deformation with pressure, the amount of water expelled from the pore space with increasing pressure was monitored at the end of each core experiment. From this measurement, a reversible volumetric strain was computed. It is reasonable to attribute the volumetric change to a reduction of the pore space, by assuming that the grain compressibility is negligible. A linear stress-strain relationship was also assumed. For each sample, the elastic change in length (which is due to vertical strain) is obtained under the assumption of isotropy, as $1/3$ of the volumetric strain. Figure 5.4 shows the volumetric strain versus porosity at 30 MPa effective pressure. The values are scattered, but a weak overall trend showing increasing volumetric strain with increasing porosity can be observed. A constant value of 0.02 for volumetric strain at 30 MPa was subsequently used for all of the samples in computing length and porosity corrections with effective pressure. This assumption led to a constant absolute decrease in porosity for samples measured at 30 MPa compared to those measured at atmospheric pressure.

c) total deformation

The corrected length for each sample at each effective pressure is obtained from the sum of permanent and elastic deformations. Figure 5.5 shows the velocity-porosity relationship for dry compressional and shear velocities at all pressures, before and after applying porosity and length corrections with increasing effective pressure. One can observe that these corrections are significant, especially at the highest effective pressures, and thus should always be applied for this type of loosely consolidated sandstones. In the following analysis, all of the measurements have been corrected for deformation with effective pressure.

6) Measurement accuracy and repeatability

In general the data quality was satisfactory for both compressional and shear wave modes. S-wave velocities in the higher porosity water saturated samples was not as good, but nevertheless acceptable. The accuracy of the velocity data at the highest effective pressures was estimated to be within 2 % for the dry and oil saturated P and S velocities and for the water saturated P velocities. The corresponding accuracy for the water saturated S velocities was estimated to be within 3 %.

Dry velocities were re-measured at all effective pressures before making the water and oil saturated measurements. The results agreed very well, indicating that the measurements were highly repeatable.

7) Thin section analysis

One thin section constructed from grain mounts was generated for each of the 38 core samples. The disadvantage of this procedure is that it is difficult to detect and quantify any calcite cementation in the samples. The grains were stained to enable the identification of K-feldspar and calcite. The main minerals found in the Troll sands are quartz, feldspar, and muscovite. I chose to identify only these main minerals in the point counting of the thin sections. However, other minerals do occur in small amounts, and these were grouped as "unclassified". These rare minerals

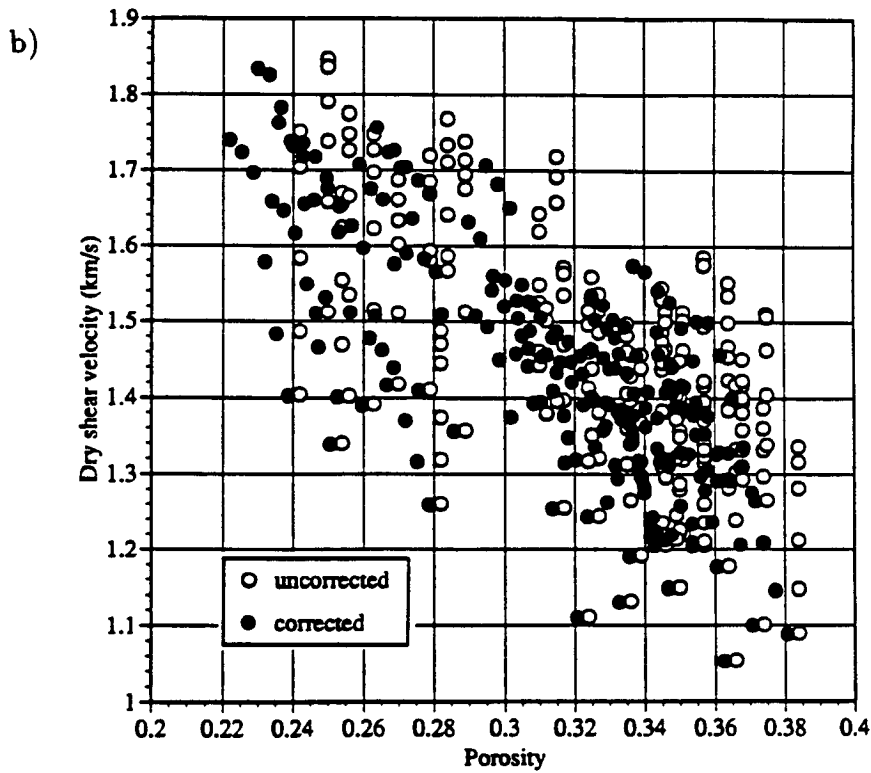
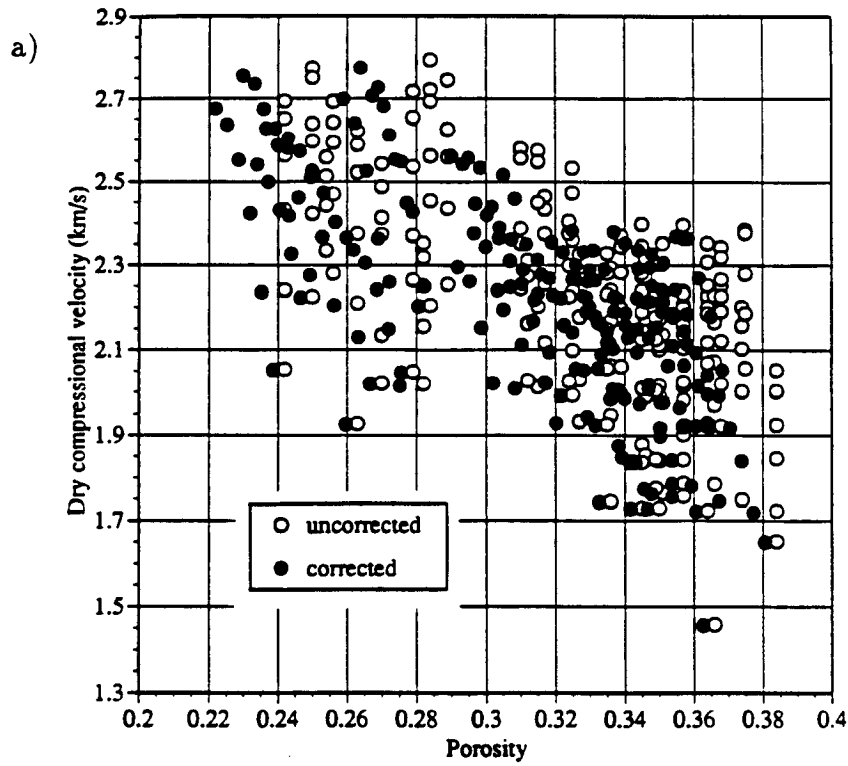


Figure 5.5: a) Dry compressional velocities (at all effective pressures) before and after porosity and length corrections.
 b) These corrections were also applied to shear velocities.

include rock fragments of igneous and metamorphic origin, accessory heavy minerals, and organic material. Bioclasts were also found. In general, these "unclassified" minerals were found in larger concentrations in the coarser grained sands, which were deposited under higher energy conditions (see chapter 4). It was frequently observed that the feldspars had been altered on their surface to kaolinite and, occasionally, that the muscovite had also been altered superficially to kaolinite. No attempt was made to quantify the amount of diagenetic clays present, but it was relatively small. For better statistics, we used a minimum number of 500 total point counts for each thin section. The thin sections were point-counted independently twice, with the results agreeing to within a few percent. Therefore, the analyses carried-out in the following work will refer to "true" mineralogic compositions as seen by us under the polarizing microscope.

Figure 5.6 shows the results of the point counting. These results agree with previous mineralogical analyses done by Norsk Hydro at other wells at Troll (Norsk Hydro, Joint Geological report, 1988). Quartz is the dominant constituent, with a volume percentage varying between 50 % and 80 %. Surprisingly, the amount of feldspar is quasi-constant in all of the samples (as seen figure 5.6), with an average value of approximately 20 %. This was seen previously in the ternary diagram of figure 4.4, chapter 4. 20 % is a very high concentration, and indicates that the sand originated from a nearby granite mass. The overall good state of preservation and the presence of sub-angular grains also indicate proximity to the source. The mica content varies from 0 % in the "clean" sandstones up to 25 % in highly micaceous parts of the reservoir. Figure 5.6 also shows that the mica concentration tends to be higher in areas immediately above and below the oil zone, thus suggesting a possible relationship between the mica content and the thickness of the oil column. This may have been related to the higher pore entry pressure required to saturate micaceous sands with oil (as compared to clean sands) during fluid migration.

Figure 5.7 shows the relationship between the computed matrix mineral density of the cores and the mineral composition of each thin section as obtained from point

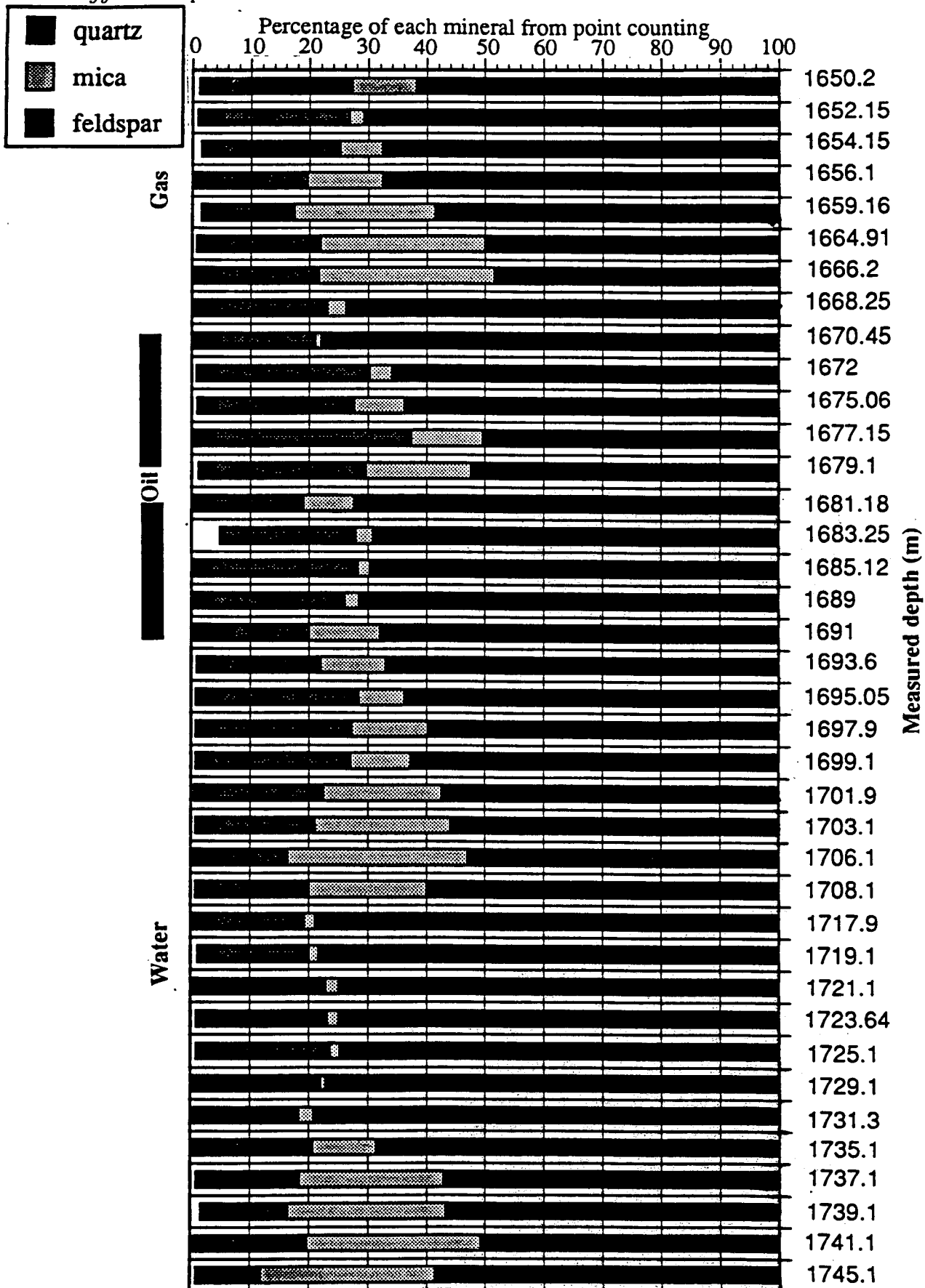


Figure 5.6: Dominant mineral compositions of the Sognefjord sands. The feldspar content is almost constant at approximately 20 %. Note that the mica content is higher in areas immediately above and below the oil zone.

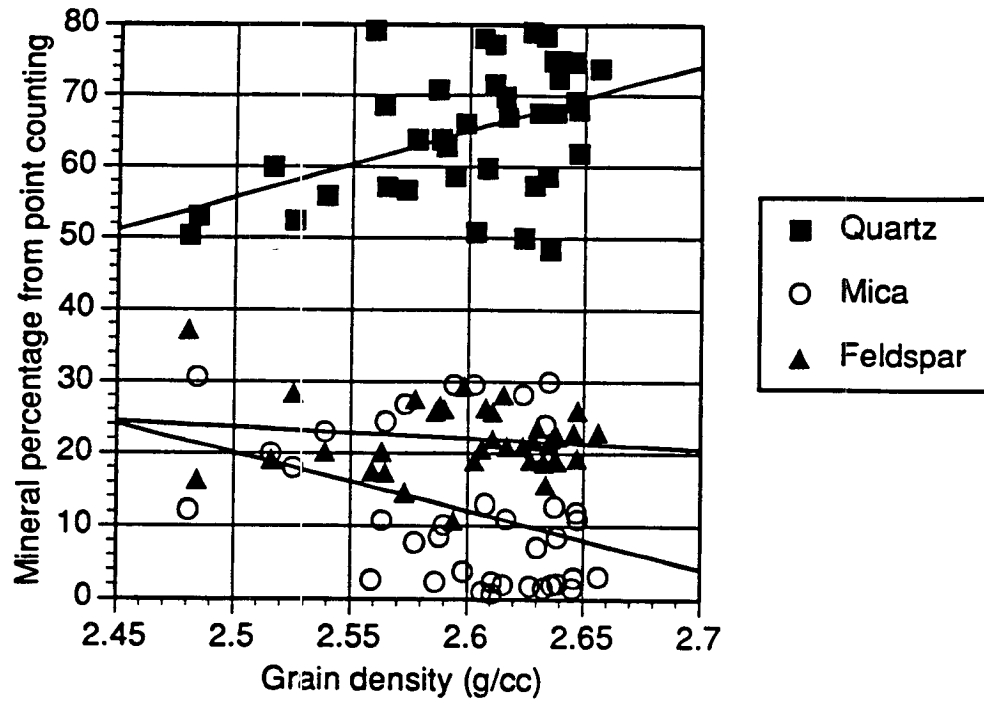


Figure 5.7: Grain density versus mineralogy of the Sognefjord sands.

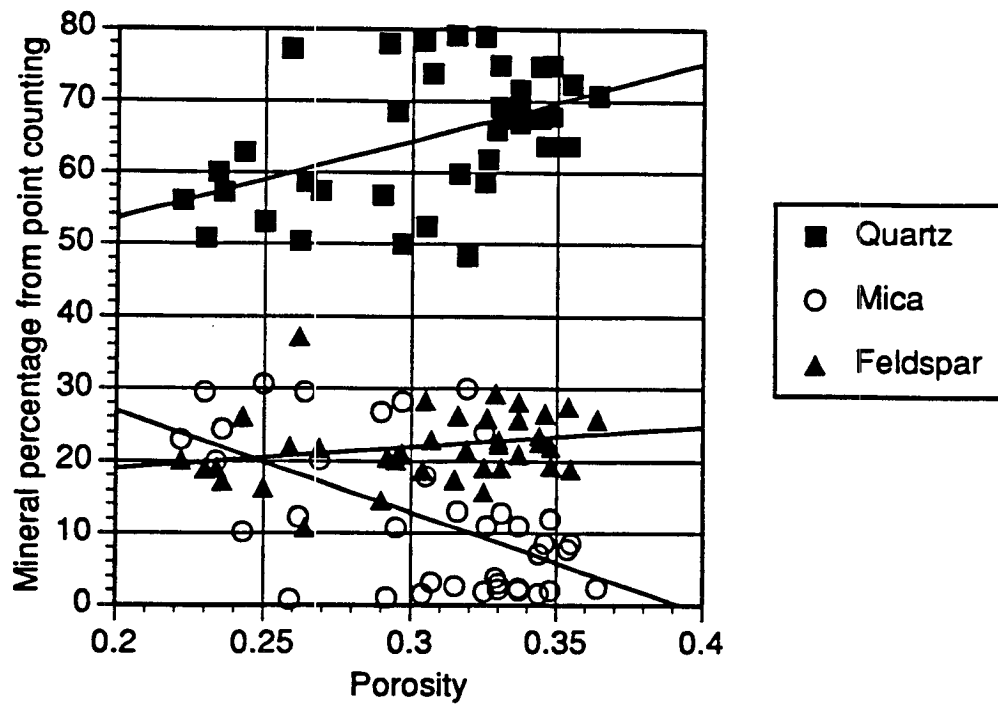


Figure 5.8: Dominant mineralogy versus porosity for the Sognefjord sands.

counting. Note that the mineral density generally has values between 2.6 g/cc and 2.65 g/cc in the mica free sands, while in the low quartz-high mica sands, the mineral density can drop to values below 2.55 g/cc.

Figure 5.8 shows that there is a close relationship between mineral composition and porosity. Linear fits are shown for each mineral type. The fits are quite poor, with (R^2 on the order of 0.2, so the equations are not listed. However, some general trends can be seen. The amount of feldspar shows little variation with porosity, and the high porosity sands have higher quartz content and lower mica content, on average. On the other hand, the lower porosity sands tend to contain less quartz and more mica.

I also observed large variations in grain size, ranging from fine grained highly micaceous sandstones, with average grain size less than 0.1 mm, to coarse grained rocks consisting mainly of quartz and feldspar, with average grain size of 0.4-0.5 mm. The coarse grained sandstones contain quartz in mono and poly-crystalline forms. The highest amount of quartz is found in the coarse grained samples, while the micaceous sands are generally restricted to the fine to medium grained sands (figure 5.9). Note also, in the lower graph of figure 5.9, that the highest porosity is not necessarily found in the coarsest sands, but rather in the low mica medium grained sands.

On the basis of flow properties (see part V, this chapter), I distinguish between four classes of sands for reservoir characterization. These are coarse grained clean sands, medium grained clean sands, medium grained micaceous sands, and fine grained micaceous sands. The best reservoir sands are the clean sands.

Thin sections from grain mounts

In the following analyses, the samples from well 31/5-4S are labelled by their depth in the well.

a) Coarse grained sands:

Figure 5.10 shows micro photographs of thin sections for typical coarse grained

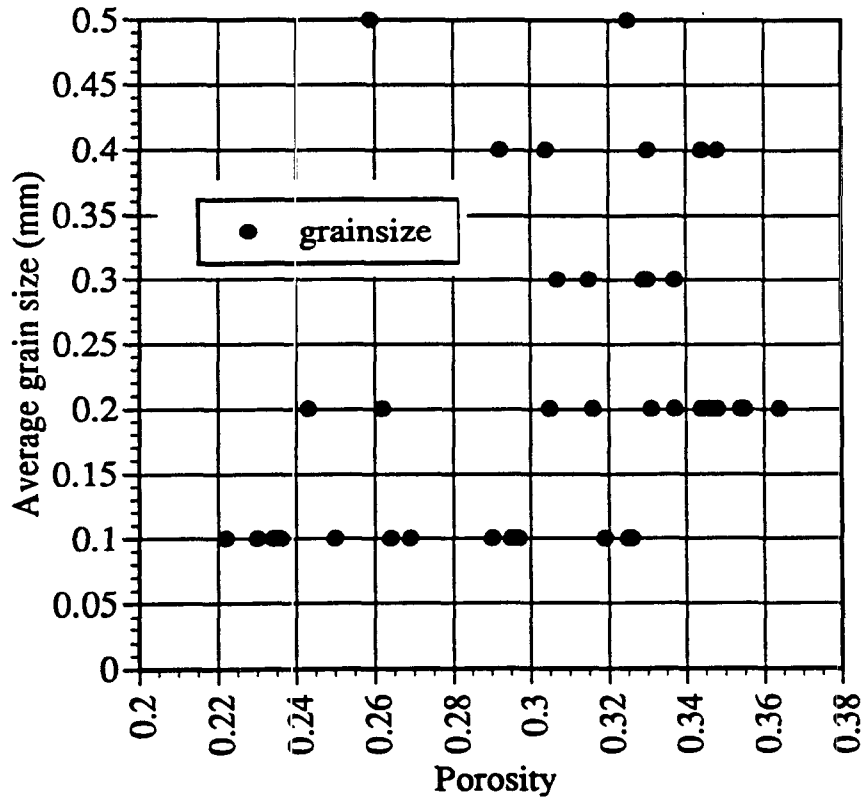
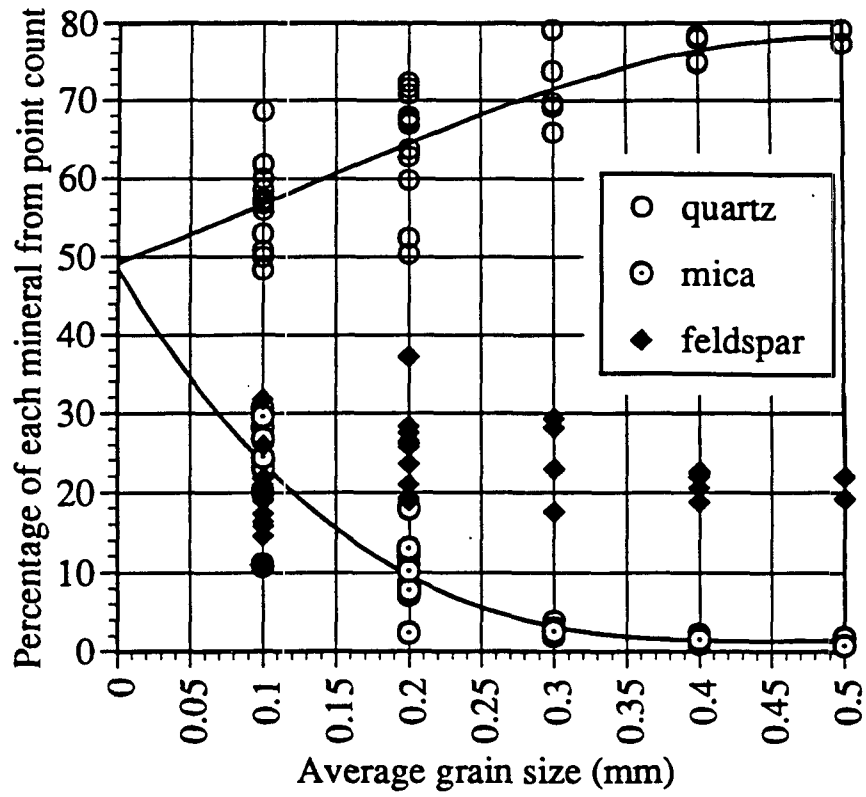


Figure 5.9: Dominant mineralogy versus grain size for the Sognefjord sands.

samples. The magnification in all of the photos is approximately 100, with each unit in the pictures representing 0.16 mm. Figures 5.10 a and b show pictures in cross-polarized and plane polarized light, respectively, of sample 1719.1. Figure 5.10 c shows sample number 1670.45 in plane polarized light and figure 5.10 d shows a different portion of the same sample in cross polarized light. The porosity at atmospheric pressure for samples 1719.1 and 1670.45 are 32.4 % and 31.2 %, respectively. The feldspar grains are easily identified by their darker color compared to the colorless quartz (figures 5.10a and 5.10b, at F5 and D7, and figure 5.10c, at C2 and G5). Figure 5.10d displays quartz in both mono-crystalline (coordinates B-2.5) and poly-crystalline (coordinates B-6) forms.

b) Medium grained sands:

Figure 5.11 shows pictures of medium grained samples. Figure 5.11a shows a portion of sample 1652.12 in cross polarized light. This sample contains practically no mica. Figure 5.11b shows an example of a medium grained micaceous sample (1693.6) in cross polarized light. Multicolored iridescent elongated flakes are characteristic of the mica, with a typical example shown in figure 5.11b at D4. Figures 5.11c and 5.11d are from different portions of sample 1652.15, shown in cross polarized and plane polarized light, respectively. Alterations of the feldspar crystals are seen as dark material sitting on top of the grains (i.e. figures 5.11c and 5.11d at D7), especially in the plane polarized light in figure 5.11d. The medium grained clean sands, of which 1652.15 is a typical example, normally contain the highest porosities in the Troll West oil province. The porosity of sample 1652.15 is 38.4 % while the porosity of sample 1693.6 is 35.7 %.

c) Fine grained sands:

The highest mica content is normally found in the fine grained sands, and figures 5.12 a,b,c,d show typical examples of highly micaceous samples. These pictures are taken from samples 1737.1 (figure 5.12a), 1708.1 (figure 5.12b) and 1666.2 (figures 5.12c and 5.12d), all in cross polarized light. The respective porosities of these samples

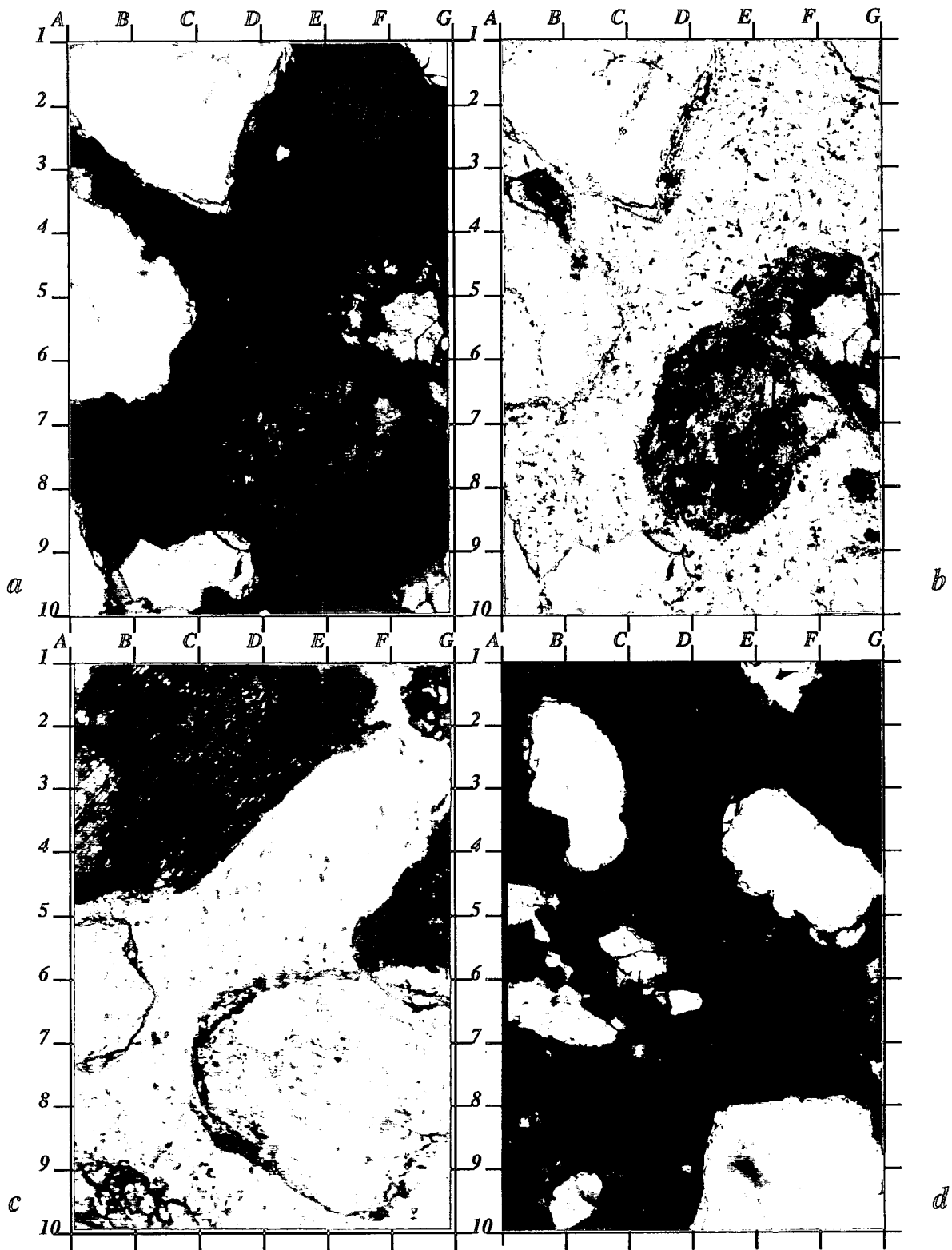


Figure 5.10: Micro photograph of thin sections of typical coarse grained clean Sognefjord sands at well 31/5-4S.

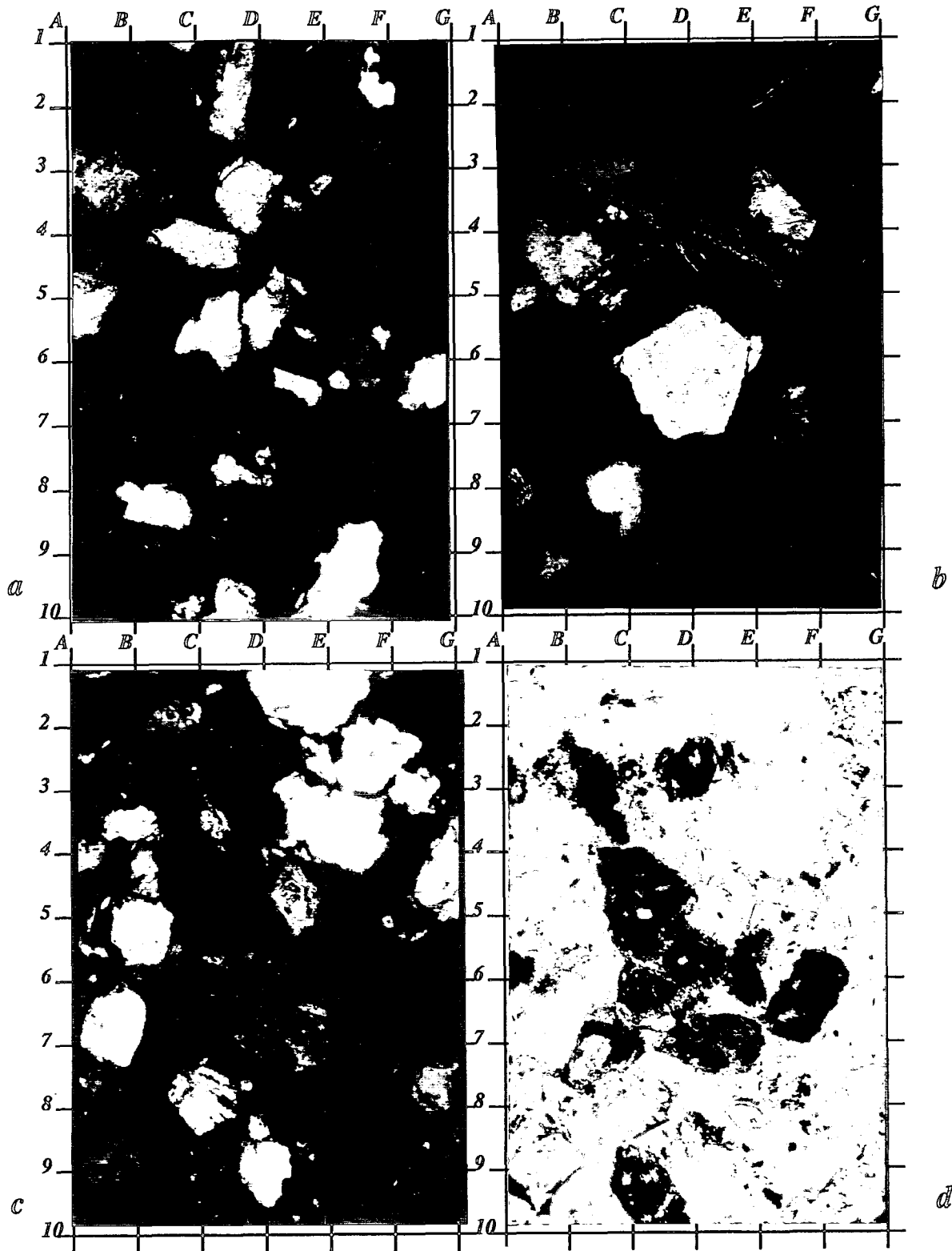


Figure 5.11: Micro photographs of thin sections of typical medium grained clean and micaceous Sognefjord sands at well 31/5-4S.

are 25.6 %, 25.4 % and 33.9 %, while the mica content is 20 % or more in all samples. The mica is normally randomly oriented, but it can occasionally be aligned in parallel laminae. An example of preferred orientation can be seen in figure 5.12c, where the orientation of the mica flakes is along the SW/NE axis of the picture.

d) Weathering at the surface of grains:

Figure 5.13 shows examples of weathered feldspar and possibly weathered mica. Figures 5.13a and 5.13b were taken in cross polarized and plane polarized light for a portion of sample 1677.15. The dark material (seen in figure 5.13b from B4 to D7 and from E6 to F6) sitting in between grains and on top of some of the grains is thought to be diagenetic kaolinite, from weathered feldspar. This particular sample contains significant amounts of diagenetic clay, compared to the rest of the samples. The velocities measured in this sample were anomalously low, and we believe that it was due to the large amount of altered feldspar. Figures 5.13c and 5.13d, were taken from sample 1741.1, and show another example where both feldspar and mica appear to have been altered.

Thin sections from pore casts

To study the pore geometries of the Troll sands, a subset of the samples were selected for the construction of blue epoxy pore casts. Blue epoxy was injected into the jacketed samples to fill the pore space. Thin sections were then made from these injected samples. The pore space is consequently colored blue in the micro photographs. Figure 5.14 shows microphotographs of blue epoxy thin sections from sample number 1719.1 on the top, and from sample number 1670.45 on the bottom. The magnification in figures 5.14a and 5.14c on the left is 40, with each unit in the pictures representing 0.36mm. The pictures on the right hand side (5.14b and 5.14d) are magnified 100 times, where each unit corresponds to 0.144mm. The samples shown in figure 5.14 are coarse grained clean sandstones with porosities of 32.4 % and 31.2 %, respectively. From these pictures we see that the pore space is very open, consisting mainly of high aspect ratio pores, with a small number of low aspect ratio

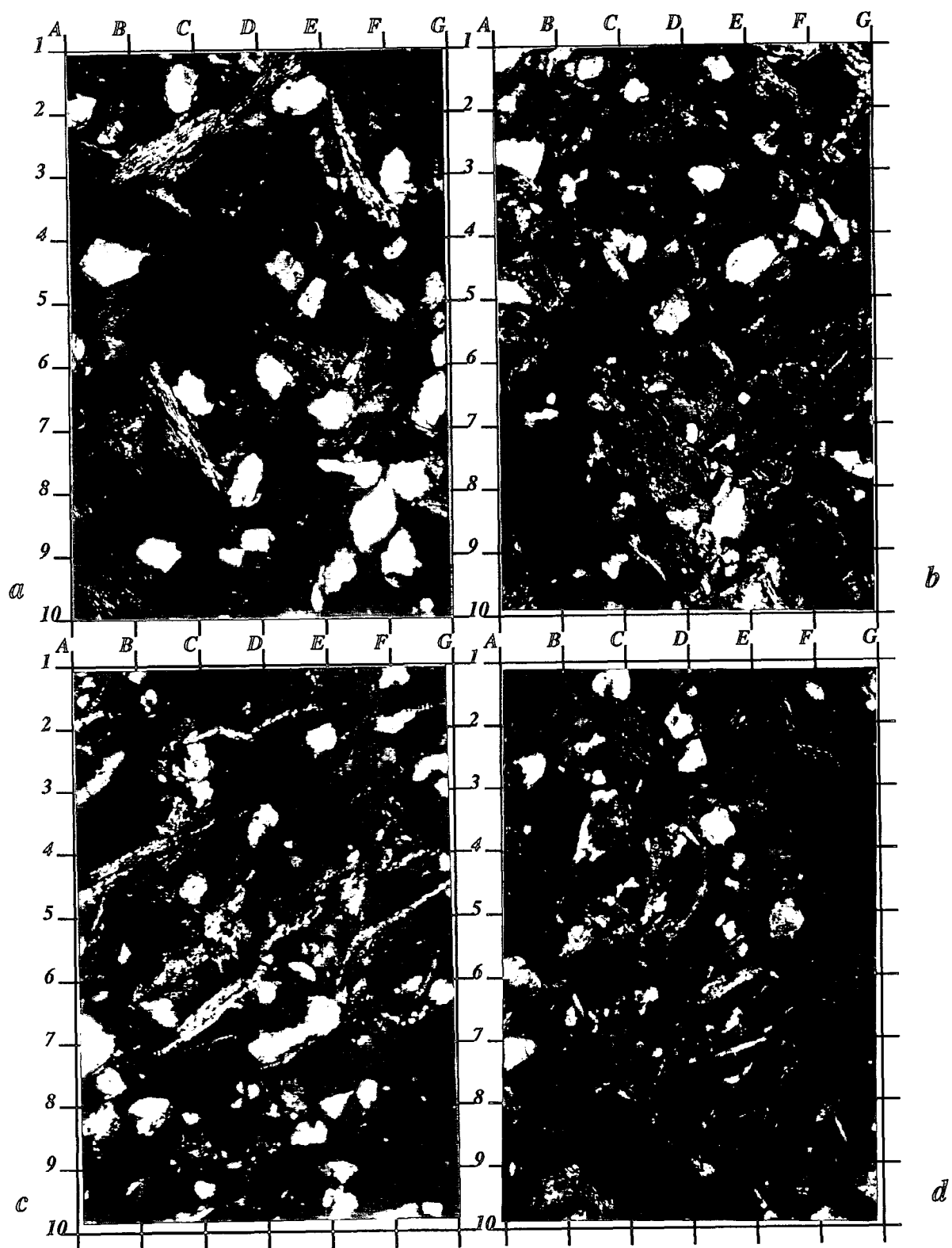


Figure 5.12: Photos of thin sections of highly micaceous fine grained Sognefjord sands at well 31/5-4S.

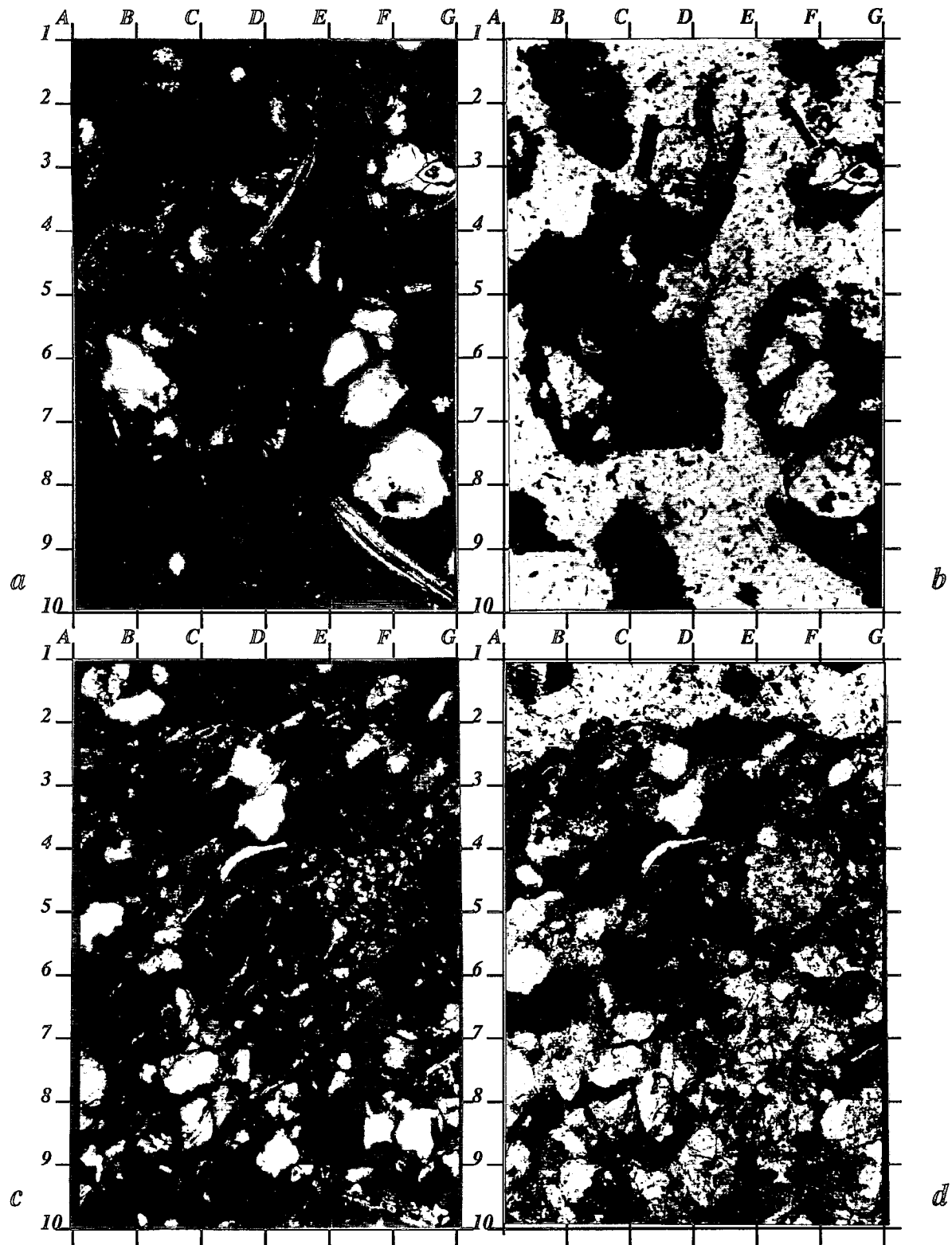


Figure 5.13: Micro photographs of thin sections displaying high amounts of altered feldspar and/or mica at well 31/5-4S.

pores occurring at grain contacts. The grains are angular to subrounded, and some of the samples show evidence of weak cementation (figure 5.14b at L3 and L4).

Figures 5.15a and 5.15b are taken from sample 1652.15, a medium grained clean sample with a porosity of 38.4 %. Magnifications are identical to those in figure 5.14. Figures 5.15c and 5.15d are obtained from sample number 1745.1, a fine grained highly micaceous sample. The dark material in these pictures is altered mica and feldspar. Note in figure 5.15d that altered minerals partly fill the pore space, leading to reduced porosity, as compared to the clean samples. An example of mica grains filling the pores between the quartz grains can be seen in figure 5.15d at K12. Figures 5.14 and 5.15 reveal that the sizes of the pores and grains are fairly constant in all of the samples and that the grains are usually well sorted.

Figure 5.16 shows additional interesting features of the Sognefjord sands at well 31/5-4S:

- (a) A good example of surficial alteration of a feldspar under cross-polarized light in sample 1725.1. The blotchy pattern over striated plagioclase feldspar is characteristic, with plagioclase feldspars being rare in the Sognefjord.
- (b) Shell fragment, which is most likely a brachiopod in sample 1739.1.
- (c and d) A good example of amber in a medium grained clean sand from sample 1739.1. Amber appears in reddish-brown under both cross-polars (c) and plane polarized light (d).
- (e and f) Sample 1670.45 shows a muscovite grain deformed by a quartz grain in a blue epoxy pore cast. It is difficult to tell whether the deformation is the result of the thin-section process itself, whether it occurred during the pressuring cycles of the ultrasonic measurements, or whether it is a true feature of the sand.
- (g and h) Sample 1670.45 shows allogenic muscovite obstructing porosity. One can understand why the micaceous sands are not as permeable as the clean sands.

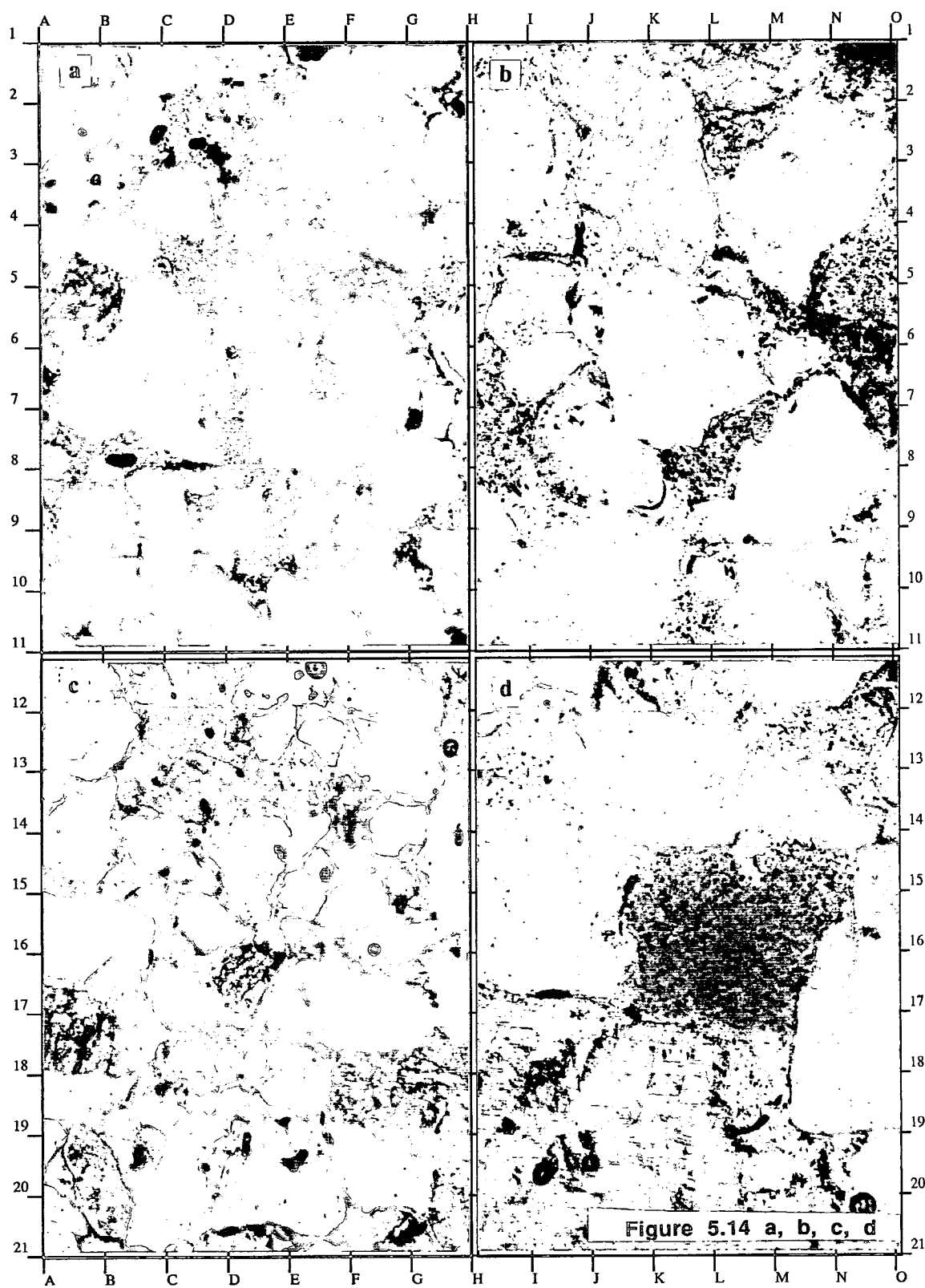


Figure 5.14: Micro photographs of blue epoxy thin sections showing pore geometries of coarse grained clean sands at well 31/5-4S.

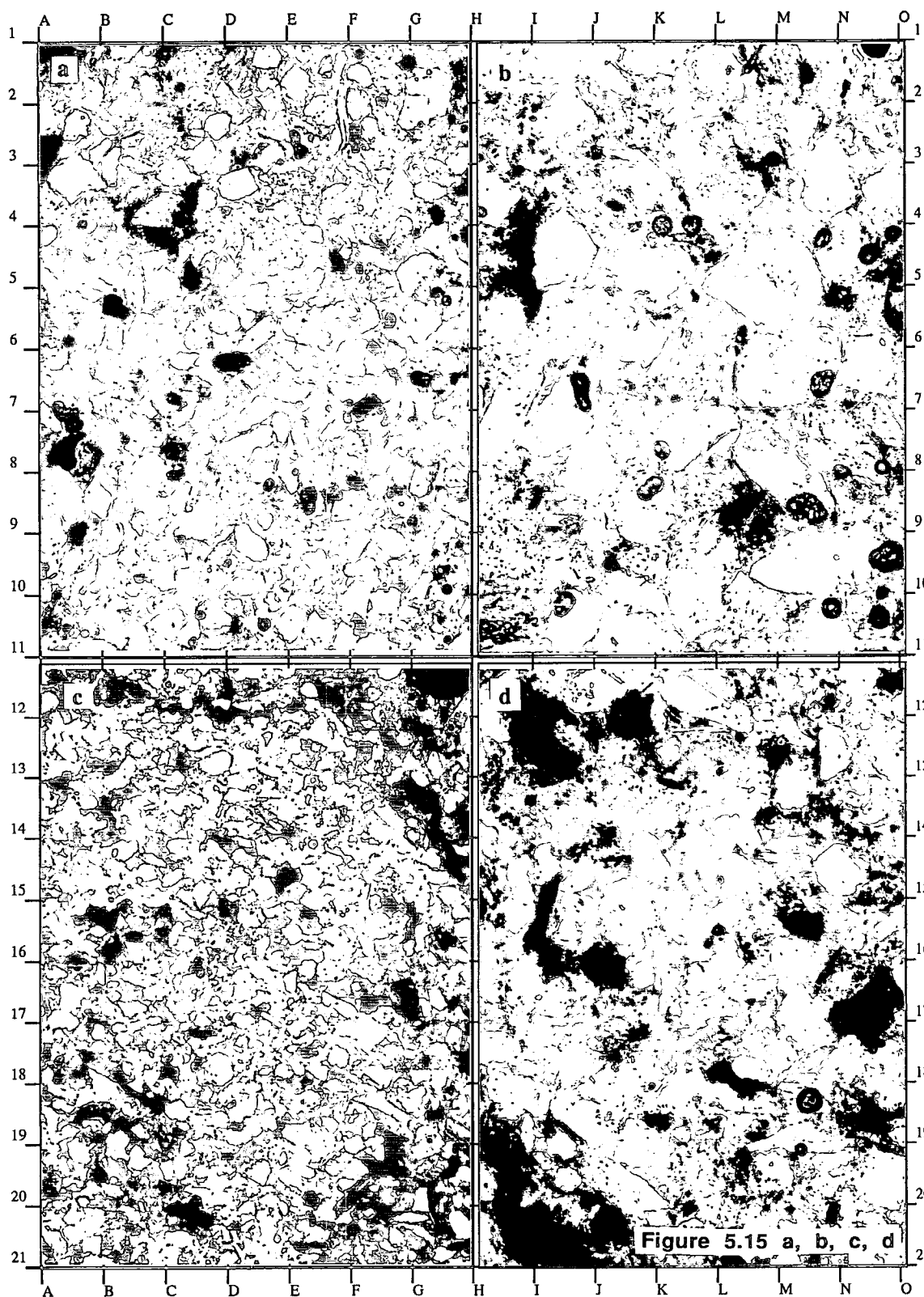


Figure 5.15: Micro photographs of blue epoxy thin sections showing pore geometries of medium grained clean sands and fine grained highly micaceous sands at well 31/5-4S.

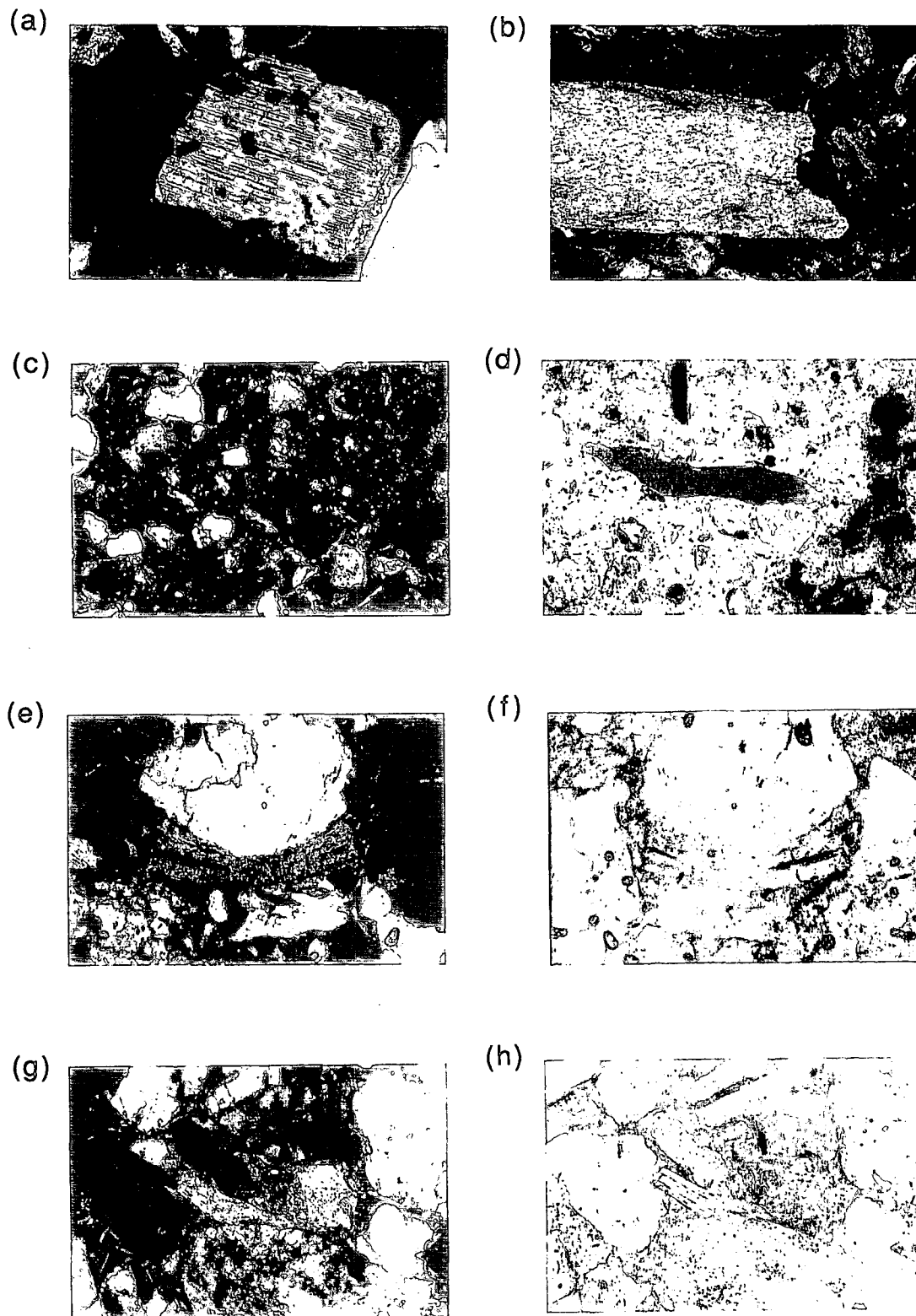


Figure 5.16: Additional features observed in the Sognefjord sands: (a) surficial alteration of a feldspar (sample 1725.1); (b) fragment of a brachiopod (sample 1739.1); (c+d) amber (sample 1739.1); (e+f) muscovite grain deformed by a quartz grain (sample 1670.45); (g+h) allogenic muscovite obstructing porosity and lowering permeability.

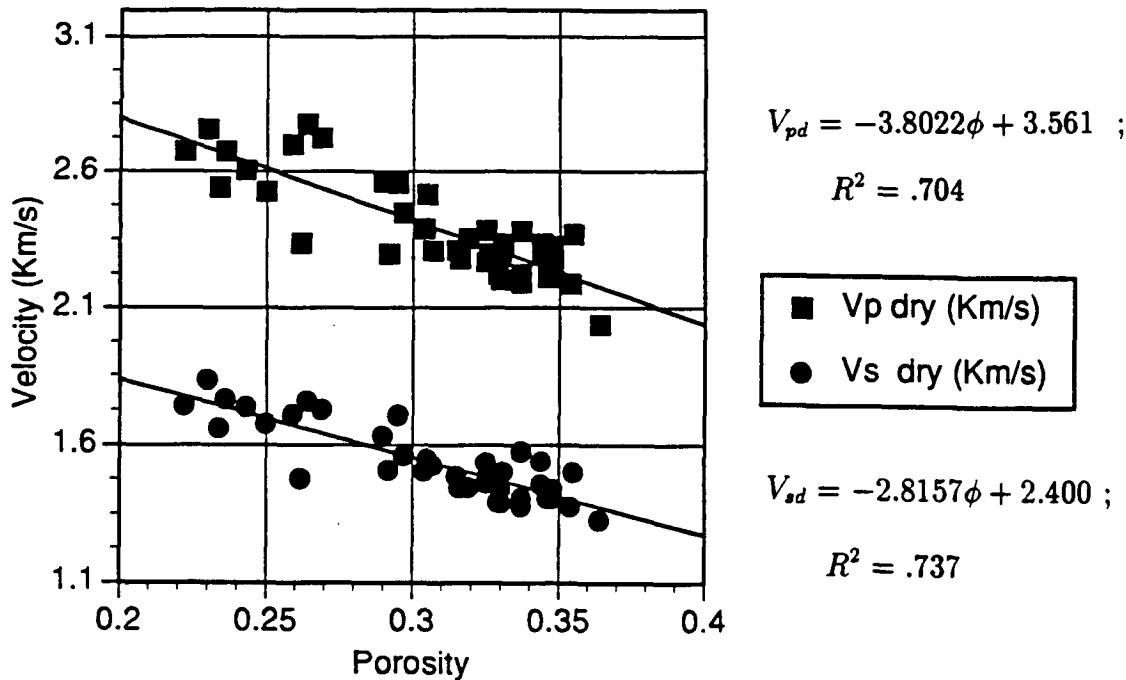


Figure 5.17: Dry compressional and shear wave velocities at 30 MPa effective pressure.

8) Velocity variations with porosity and mineralogy

The full set of ultrasonic velocities, together with main mineral composition, are given in appendix C. Figure 5.17 shows the dry compressional and shear wave velocities as a function of porosity at 30 MPa effective pressure. The dry P-wave velocities range from about 2100 m/s for the highest porosity up to about 2800 m/s for the lowest porosities. The corresponding range of S-wave velocities is from 1300 m/s to 1800 m/s. Figure 5.18 shows the velocities obtained for the fully water saturated case at 30 MPa effective pressure. The saturated P-wave velocities range from about 2500 m/s for the higher porosity sands, up to 3100 m/s for the lower porosity sands, while the S-wave velocities are lower than those in the dry state, due to increased bulk density. The saturated S-wave velocities range from 1100 m/s up to 1600 m/s at the lowest porosities. Figure 5.19 shows that there is a linear relationship between the compressional and shear wave velocities at 30 MPa effective pressure. The upper line in this figure corresponds to the dry state, while the lower curve was obtained

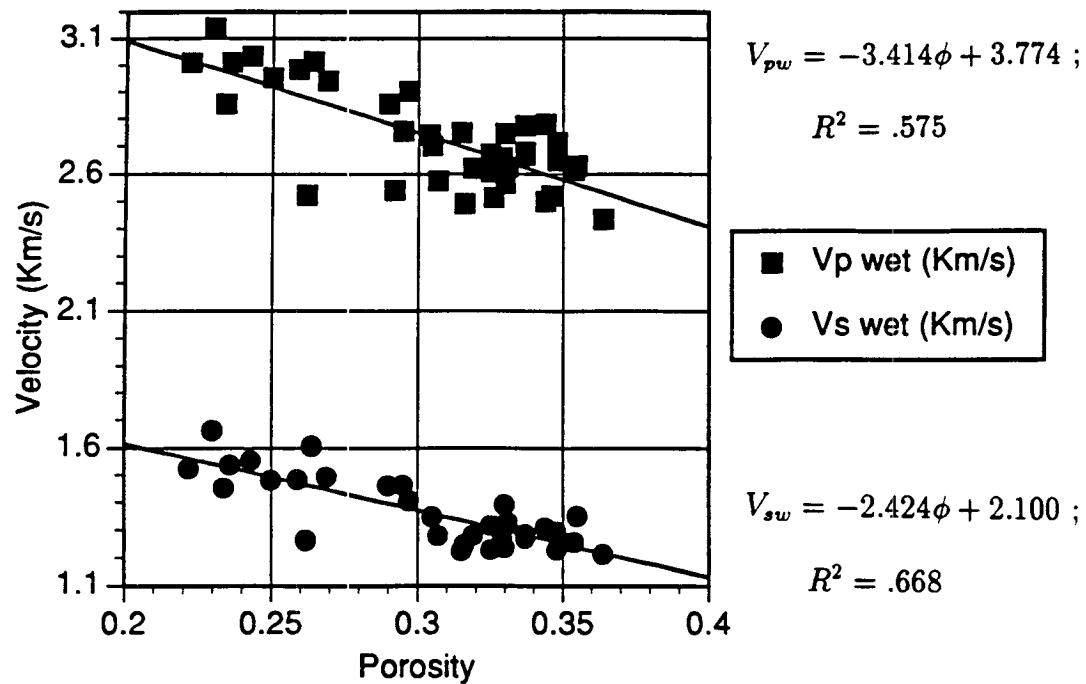


Figure 5.18: Fully water saturated compressional and shear wave velocities at 30 MPa effective pressure.

for the fully water saturated case.

8-a) Porosity

When investigating velocity-porosity relationships from figures 5.17 and 5.18, the expected strong influence of porosity is easily seen. However, some scattering is apparent in the data.

8-b) Mica content

In figure 5.20 the dry sample velocity data are sub-divided into groups with varying mica content. The clean sands contain less than 5 % mica. The samples labeled limestone were classified from the core-log descriptions obtain from geologists at Norsk Hydro. There is no clear systematic trend with varying mica content. At porosities greater than 30 %, the dry P-wave velocities in the clean sandstones seem, on the average, are marginally lower than those in the micaceous samples. However, this effect is not observed in the water saturated samples.

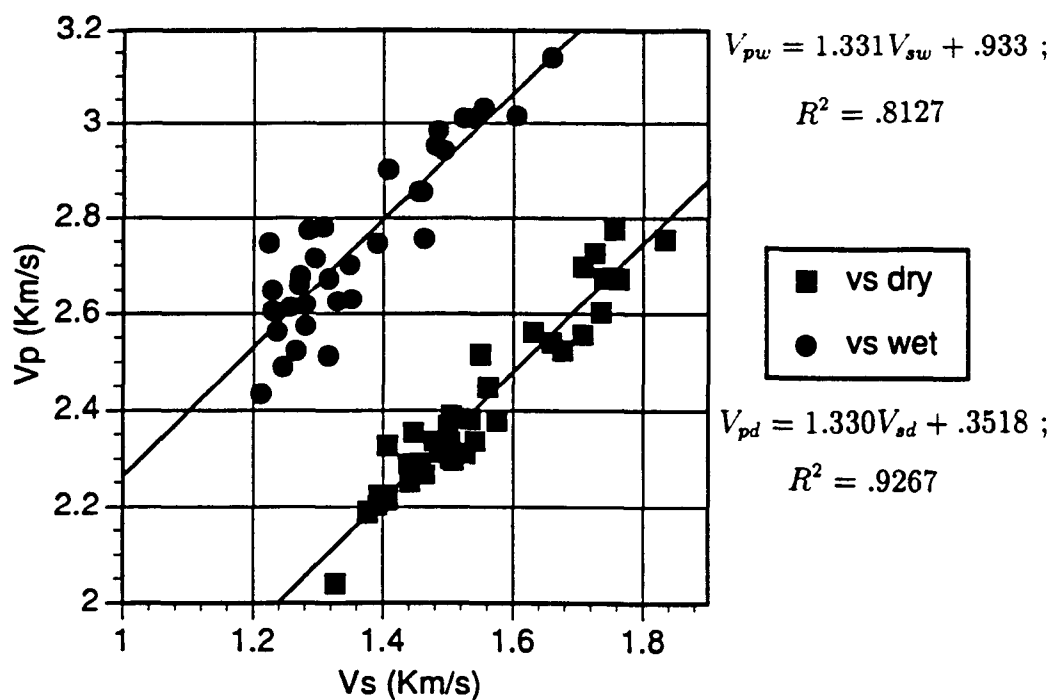


Figure 5.19: Compressional versus shear wave velocity at 30 MPa effective pressure for the Sognefjord sands.

8-c) Feldspar content

Although the samples are practically free of clay, I observed from thin sections that occasionally small amounts of potassium feldspar (mostly orthoclase) had weathered to kaolinite. One could therefore expect a higher probability of encountering small amounts of clay in the samples with the higher amounts of feldspar. In figure 5.21, I have divided the data into groups with varying amounts of feldspar for dry samples. Least squares linear fits are shown through samples containing less than 20 % feldspar and greater than 20 % feldspar. The trend indicates that samples containing high amounts of feldspar have slightly lower velocities. This is consistent with the observed surficial alteration of orthoclase grains. The corresponding data for the water saturated samples are shown in figure 5.22. Results for the water saturated shear wave velocities are not as good and can be explained by the higher measurement uncertainty in these data.

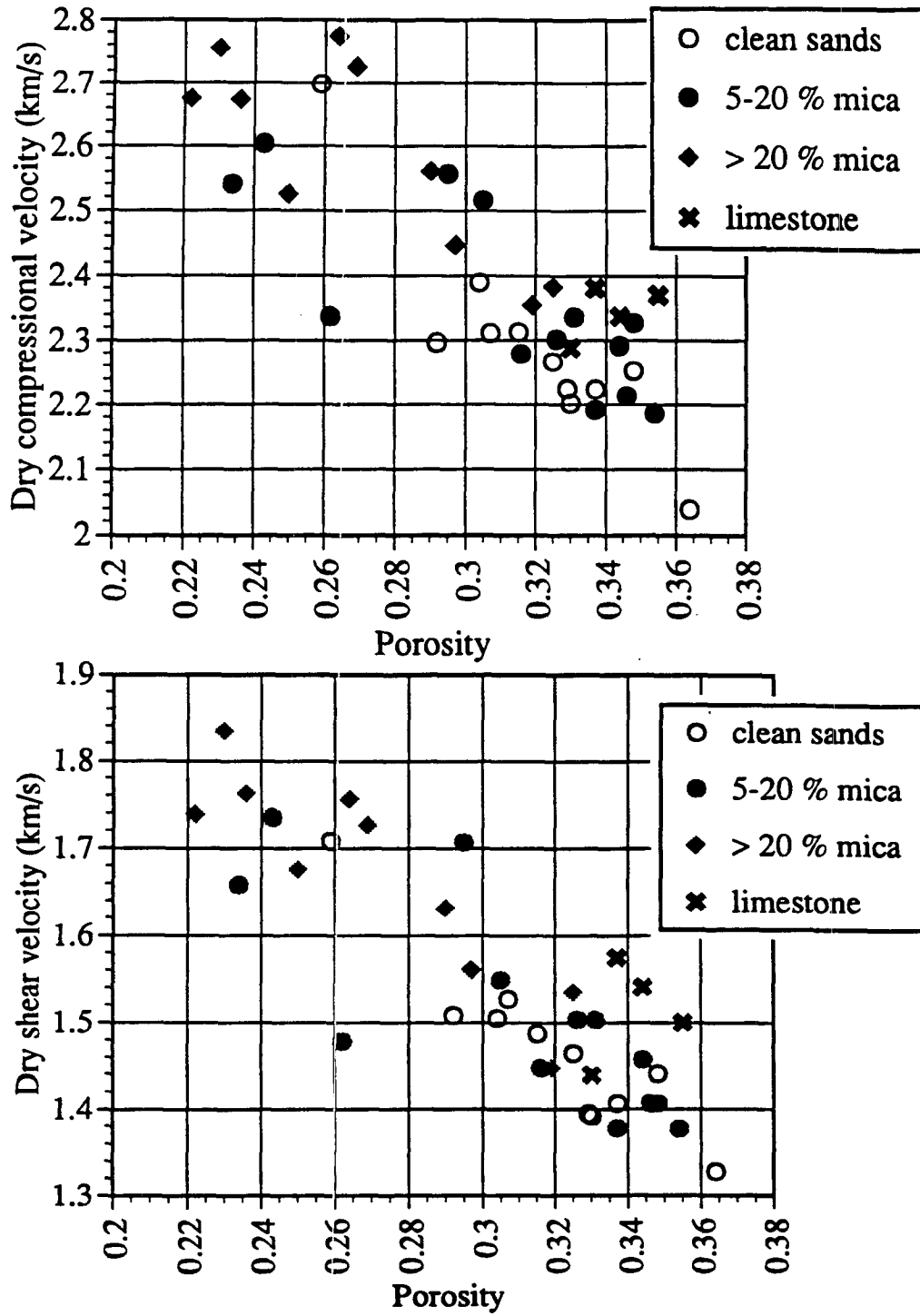


Figure 5.20: Velocity-porosity versus mica content; dry samples.

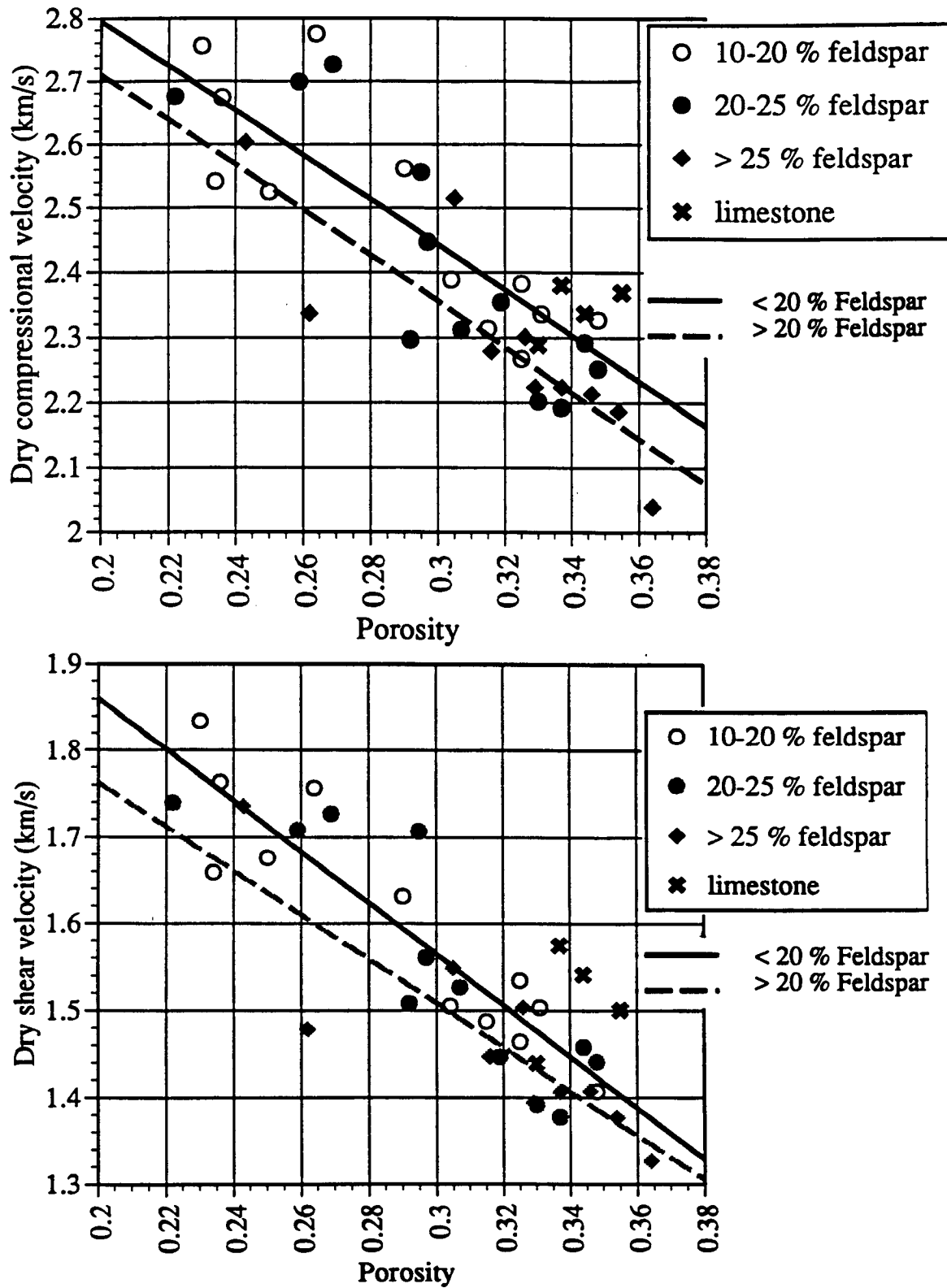


Figure 5.21: Velocity-porosity versus feldspar content; dry samples.

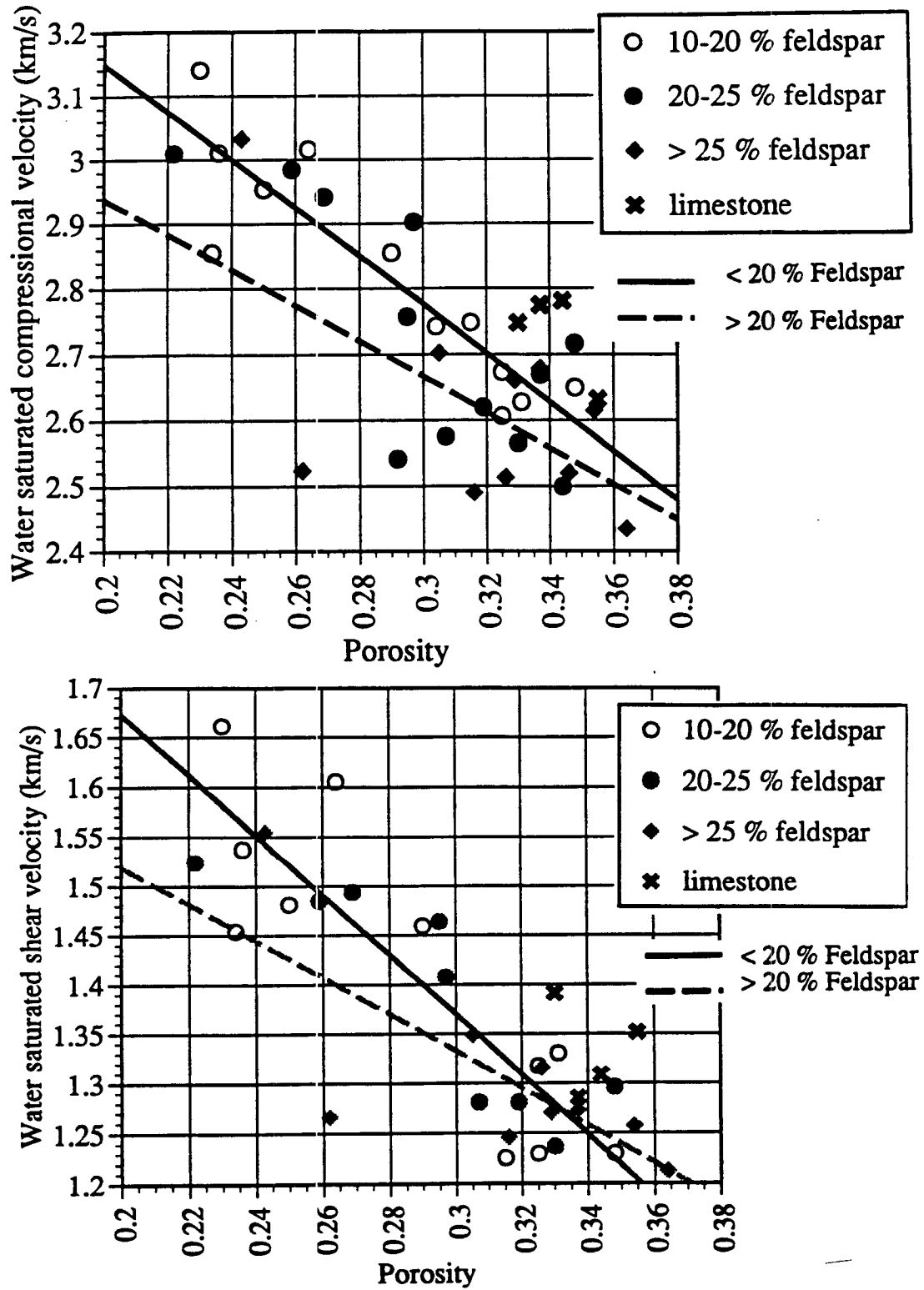


Figure 5.22: Velocity-positivity versus feldspar content; saturated samples.

8-d) The "bad news"

The examples above show that while mica content may marginally increase the dry compressional velocities, this effect may be obscured by the amount of feldspar present. A high amount of feldspar may marginally lower both compressional and shear wave velocities, possibly due to small amounts of authigenic clays. Since the amount of feldspar generally shows no correlation to porosity or grain size (figures 5.8 and 5.9), its effect may be present in all lithologies within the reservoir sands. Consequently, for a given velocity and porosity, it is not possible to relate the velocity directly to the amount of mica. Therefore, and unfortunately, the effects of variations in mineralogy on the velocities are generally so small that they will not be distinguishable from seismic data.

8-e) The "good news"

I showed that mica content is related to porosity in the Troll sands, with higher porosity correlating to lower amounts of mica. Fortunately, since porosity is also strongly related to velocity, there is an indirect relationship between velocity and mica content. This can be seen from figure 5.23, which shows the dry and water saturated compressional and shear wave velocities as a function of mica content. The least squares fits through each measurement series are shown, indicating that velocities generally increase with increasing mica content.

Unfortunately, it was not possible to quantify the amount of calcite cementation in the samples, due to the procedure used when generating thin sections. Based on the core descriptions, a few samples were marked as possibly containing calcite. It is not possible to develop a velocity/calcite relationship here, but we can qualitatively state that velocities are expected to increase with calcite cementation.

9) Velocity variations with pressure

In the analyses of the ultrasonic velocities that follow, there is no subdivision of the data into different lithologies.

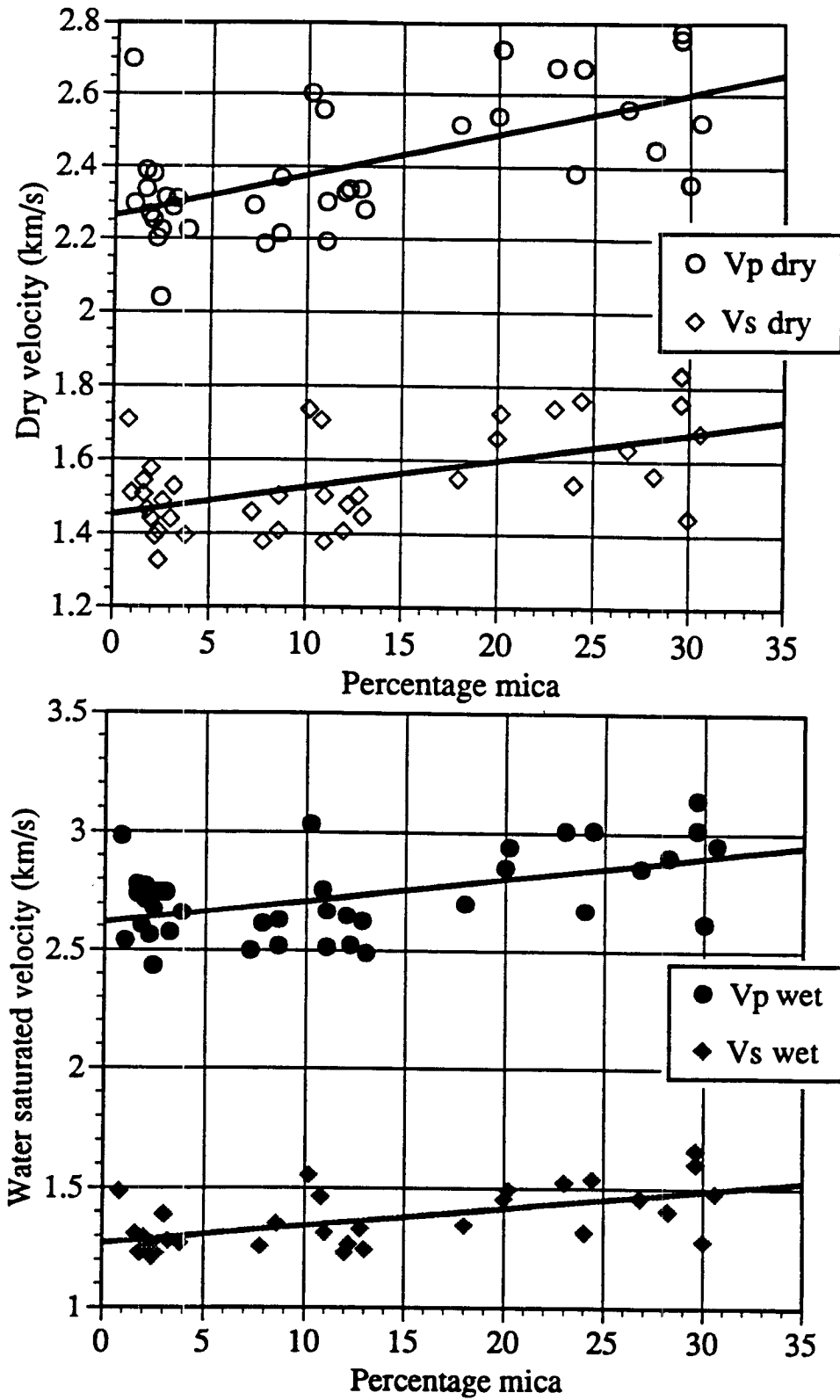


Figure 5.23: Dry and water saturated compressional and shear velocities versus mica content.

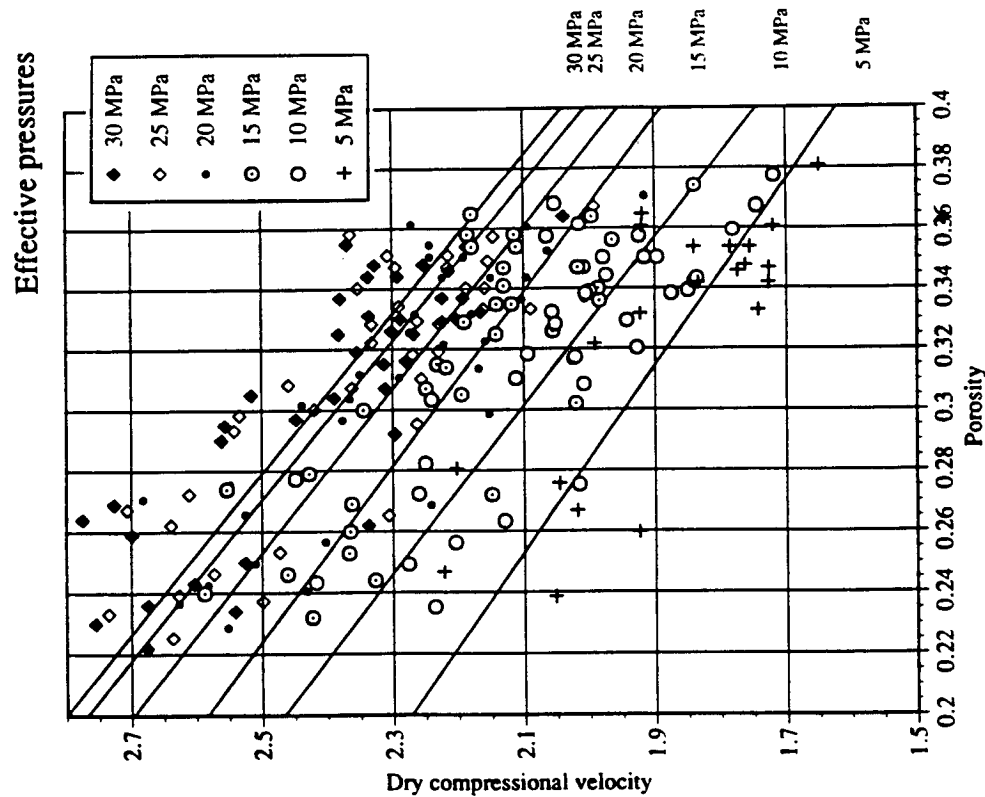


Figure 5.24: Dry compressional velocities at 30, 25, 20, 15, 10 and 5 MPa effective pressures.

Figures 5.24 and 5.25, respectively, show the dry P-wave and S-wave velocities for all of the measured samples at all pressures. In these figures, each measurement series is plotted with different symbols, and consists of data obtained at one effective pressure. Recall that the accuracy of the velocities at the lower effective pressures is less than that at the higher pressures. Also, keep in mind that there are less data points at the lower pressures, because it was not always possible to pick a reliable travel time at those pressures. Although the data may appear to be quite scattered when viewed jointly, consistent average trends are present. Least squares linear fits, determined for each data series, appear as lines which are practically parallel to each other. Note that dry P-wave velocities respond faster to pressure changes than dry S-wave velocities. There is a strong velocity dependence on pressure, and on the average, dry P-wave velocities decrease by approximately 500 m/s (22 %) between effective pressures of 30 MPa and 5 MPa. The corresponding drop in S-wave velocities is about 250 m/s (16 %).

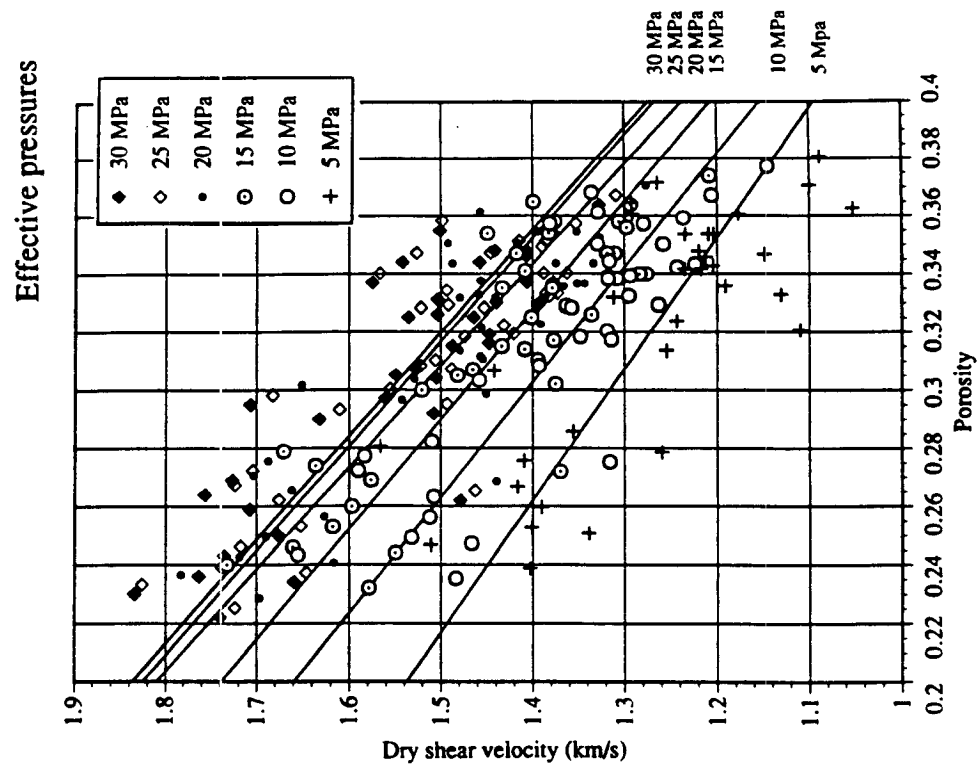


Figure 5.25: Dry shear wave velocities at 30, 25, 20, 15, 10 and 5 MPa effective pressures.

Similar curves can be observed for fully saturated measurements as seen in figures 5.26 and 5.27. However, the dependence of the saturated P-wave velocities on effective pressure is greatly reduced compared to the dry case, showing a total drop of approximately 350 m/s (12 %) between 30 MPa and 5 MPa effective pressures. On the other hand, water saturated S-wave velocities drop slightly faster with effective pressure, than dry S-wave velocities. The total reduction in S-wave velocity is approximately 270 m/s between the highest and the lowest effective pressures (20 %).

The most obvious feature in figures 5.24 and 5.25 is the large pressure dependence of the dry P-wave velocities. Although the curves tend to level-out at higher pressures, an increase in velocity with increasing pressure characterizes these samples. The shape of these curves indicates uniform compaction of an opaque pore space. This is in contrast to crack rich rocks that show large initial velocity increases with increasing effective pressure, followed by small velocity increases at the higher pressures, due to the closing of the thin cracks. Since the curves have not leveled-off completely at 30

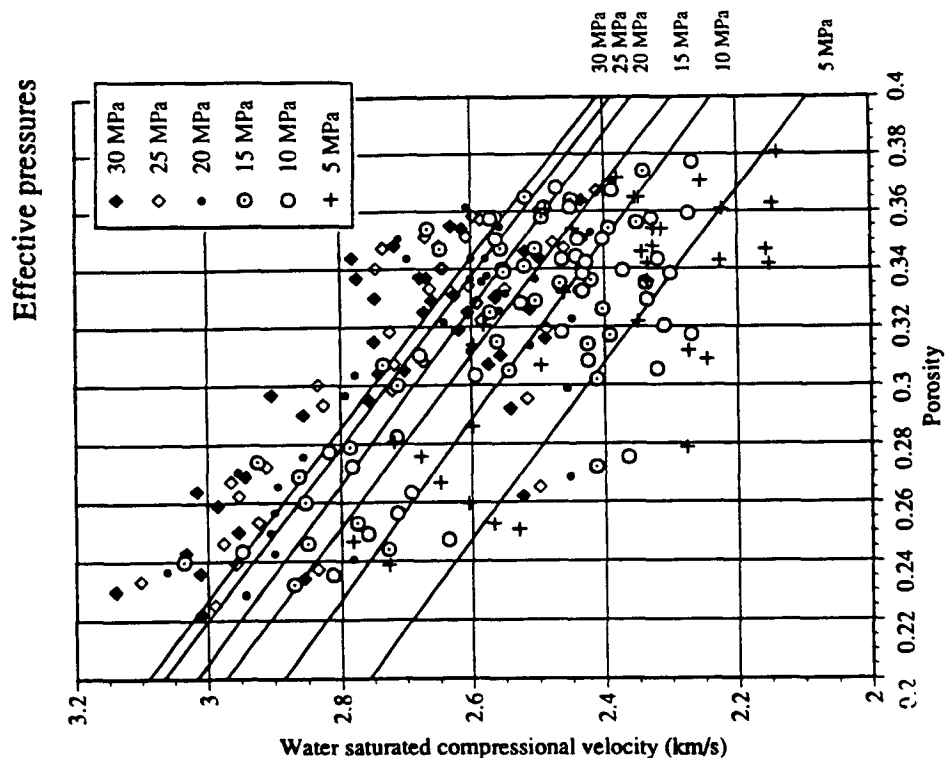


Figure 5.26: Fully saturated compressional velocities at 30, 25, 20, 15, 10 and 5 MPa effective pressures.

MPa effective pressure, this means that there is still a certain amount of compressible pore space at that pressure in the Troll sands.

10) V_p/V_s relationships

Figure 5.28 shows the V_p/V_s ratios for the dry measurements, plotted as a function of porosity. Here again, each data series corresponds to measurements taken at one effective pressure with least squares linear fits computed to show average trends in the data. Although the data are scattered, the V_p/V_s ratios tend to increase with increasing porosity. For the Troll sands it is reasonable to assume that the higher the porosity, the looser and more unconsolidated the sample. It is also known that unconsolidated samples tend to have higher V_p/V_s ratios than more consolidated samples (Gregory, 1976). The V_p/V_s ratios at the higher effective pressures are approximately 1.55. There is a small but significant decrease in the V_p/V_s ratios with decreasing effective pressure, with the V_p/V_s ratios at the lower effective pressures

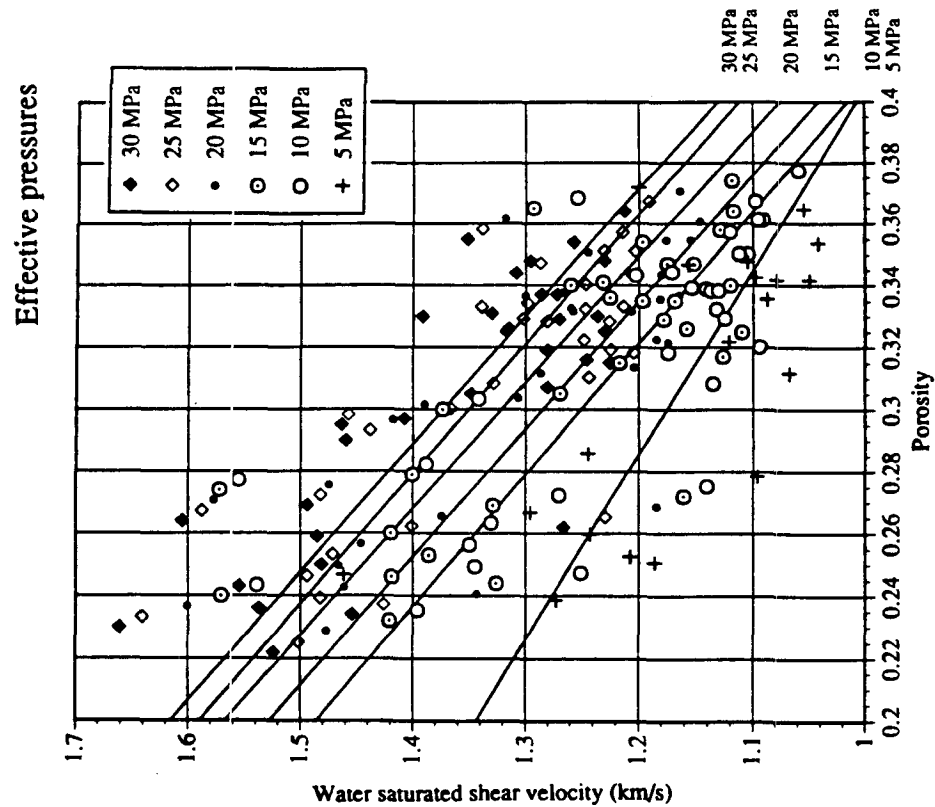


Figure 5.27: Fully saturated shear wave velocities at 30, 25, 20, 15, 10 and 5 MPa effective pressures.

decreasing to about 1.45. This is consistent with the fact that dry S-wave velocities decrease slower than dry P-wave velocities with effective pressure (section 9 above).

Figure 5.29 shows the corresponding V_p - V_s ratios for the fully saturated measurements. There is a stronger dependence on porosity, with a significant increase in V_p - V_s ratio with increasing porosity. Part of the increase in the V_p - V_s ratio is due to decreasing consolidation with increasing porosity for these sands. Normally, one would not expect the V_p - V_s ratios in unconsolidated materials to depend on effective pressure. However, we can observe a small increase in V_p - V_s ratio with decreasing effective pressure, opposite to the trend defined by the dry measurements. This is consistent with the fact that saturated S-wave velocities decrease faster than saturated P-wave velocities with effective pressure (section 9 above).

11) Measurements in oil saturated samples

Ten representative samples were selected for measurement under oil saturation.

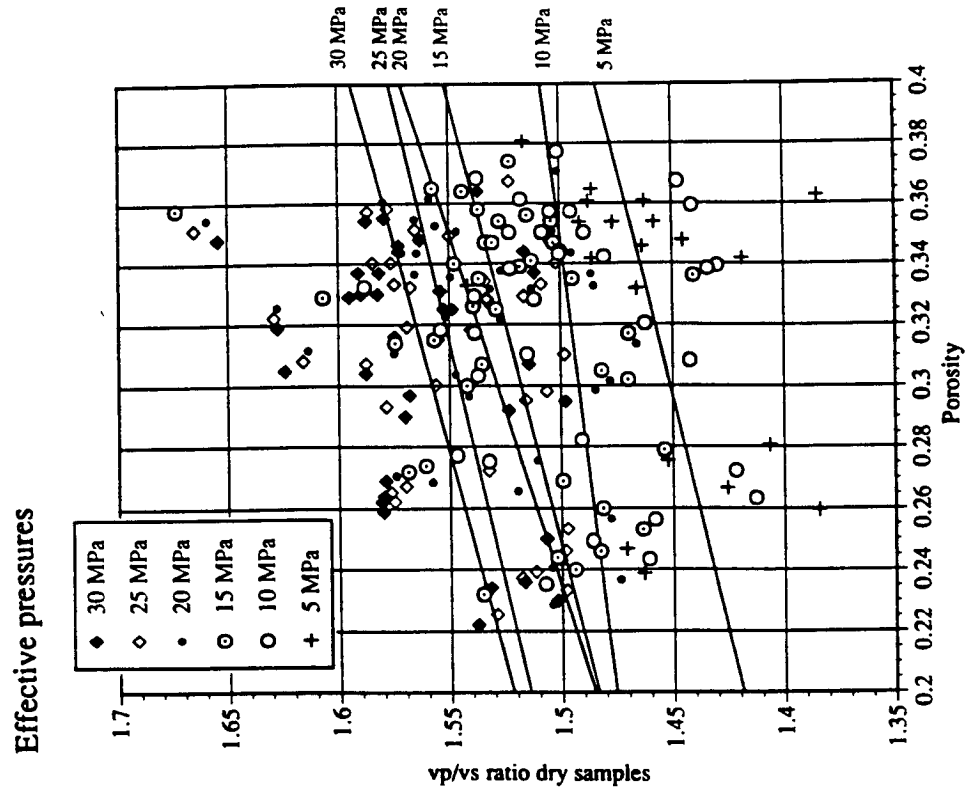


Figure 5.28: Dry Vp-Vs ratios at 30, 25, 20, 15, 10 and 5 MPa effective pressures.

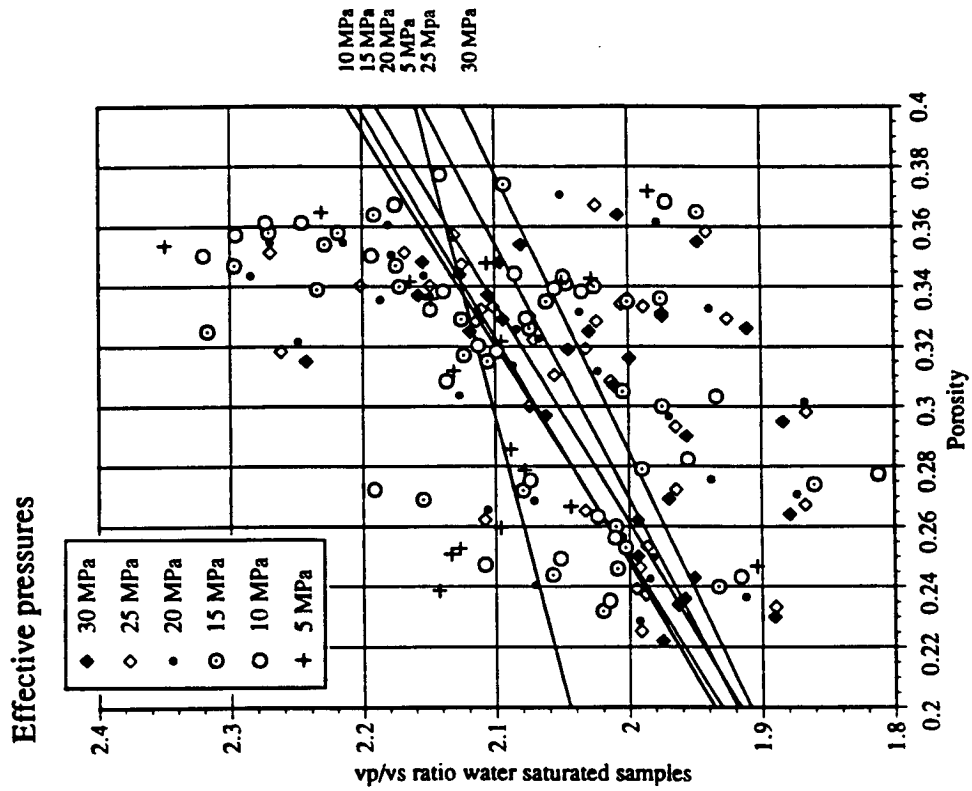


Figure 5.29: Water saturated Vp-Vs ratios at 30, 25, 20, 15, 10 and 5 MPa effective pressures.

Crude oil from the actual reservoir (courtesy of Norsk Hydro) was used for these measurements. The Troll West oil is a light hydrocarbon with an API gravity of approximately 25 degrees, a viscosity of about 1.5 cp, and a density of 0.878 gr/cc. The oil saturated measurements were done in a second round of measurements, and a careful selection was made to avoid samples that had been damaged in the first round of dry and water saturated measurements. Before the samples were oil saturated, the dry velocities were re-measured and compared to the first run. These second results agreed well with the first. Figure 5.30 shows the P-wave and S-wave velocities obtained for the fully oil saturated samples. The corresponding water saturated velocities are shown in the same graphs, with least squares linear fits being plotted for each group of measurements. For P-wave velocities, oil saturated velocities appear slightly higher than water saturated velocities. S-wave velocities seem to be unaffected by the difference between water and oil. These are expected to be slightly larger than water saturated S-wave velocities, because of the density difference between the oil (0.88 g/cc) and the water (1.0 g/cc). However, the apparent differences between water and oil saturated P-wave and S-wave velocities are within the uncertainty of the measurements (they appear to be less than 50 m/s for P-wave velocities, and a lot less for S-wave velocities). For all practical purposes, sands fully saturated with pure oil or water will be considered to have the same velocities at Troll.

12) Effect of temperature

Figure 5.31 shows changes in P-wave and S-wave velocities due to increasing temperature in three oil saturated samples. Confining pressure was held constant at 45 MPa and pore pressure at 15 MPa, yielding an effective pressure of 30 MPa. A weak decrease in P-wave and S-wave velocity can be seen from a room temperature of 30 degrees C to a reservoir temperature of 60 degrees C. This difference amounts to approximately 100 m/s for compressional velocities and about 50-75 m/s for shear-wave velocities. These results agree well with previous laboratory measurements reported by Wang (1988) in unconsolidated Ottawa sands.

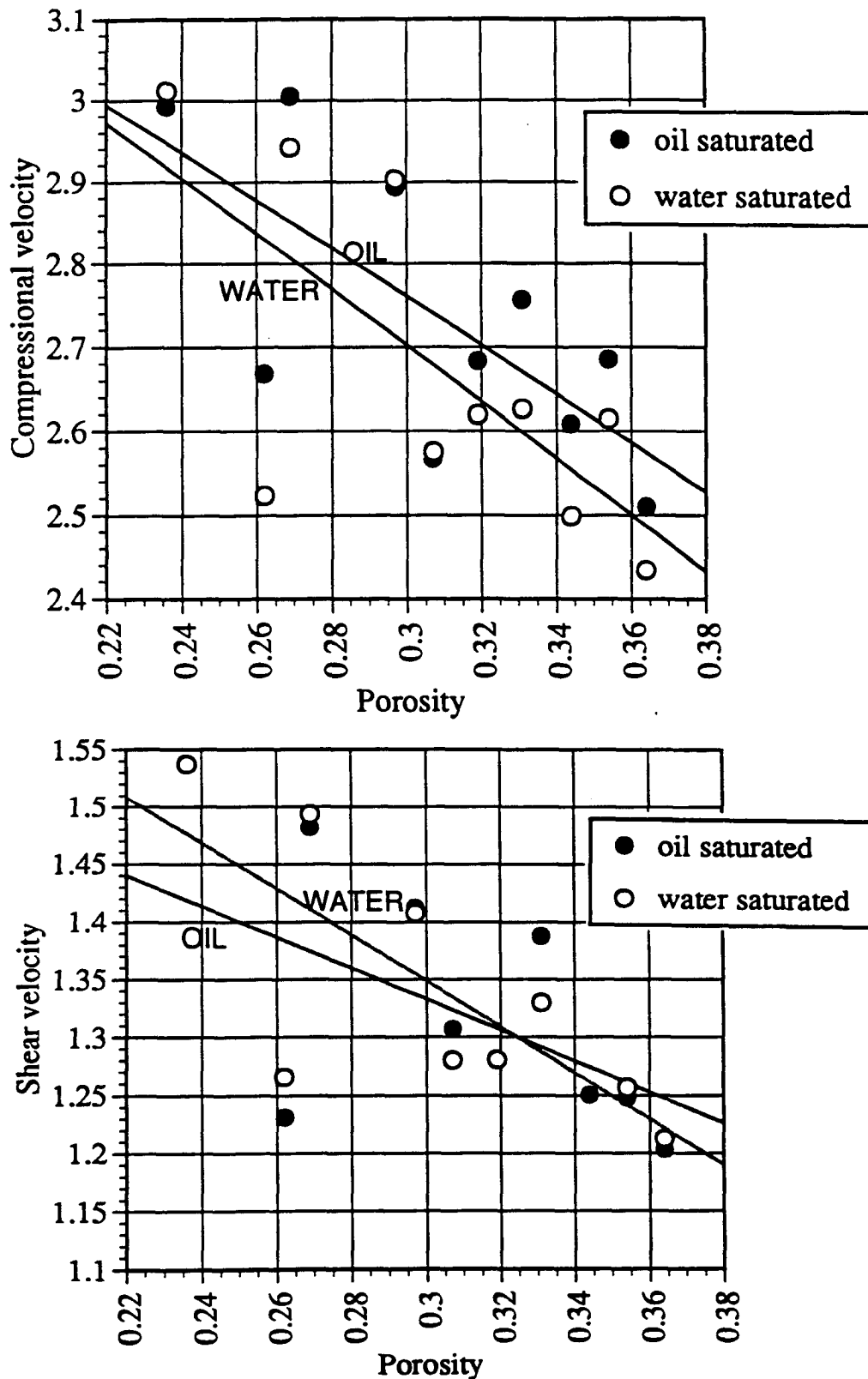


Figure 5.30: Oil and water saturated compressional and shear velocities at 30 MPa effective pressure.

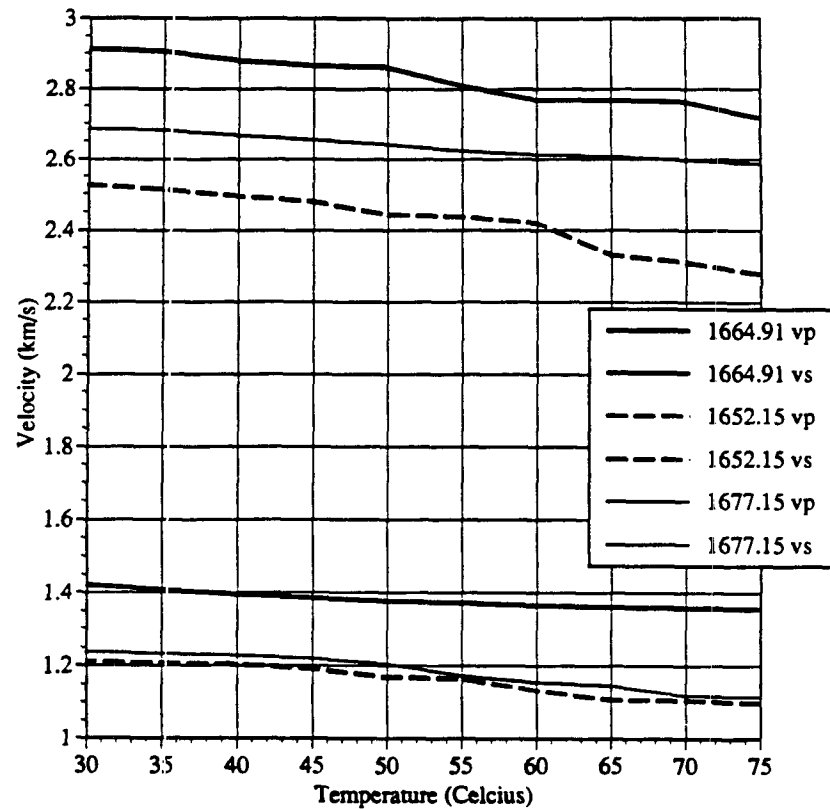


Figure 5.31: Compressional and shear wave velocities in oil saturated samples as a function of temperature at 30 MPa effective pressure.

13) Other measurements!

Special attention was given to the detectability of "FUN" fluids directly from seismic. Sample 1741.1 was chosen for this special occasion. Figure 5.32 shows the difference in velocities under full saturation for water, cognac, and champagne at room temperature. Clearly, the full champagne "liquid" saturation was not immediately possible, because of the presence of many bubbles, making the champagne mixture a highly compressible fluid. Full saturation was achieved after de-bubbling for some time. Apart from the obvious economic potential if those fluids were ever to be found in-situ, it is interesting to note that fluids such as cognac and champagne at full saturation behave like "heavier" fluids than water.

14) Dispersion

Comparison between ultrasonic measurements (MHz) and seismic measurements (less than 100 Hz) are frequently complicated by frequency dispersion. It is usually

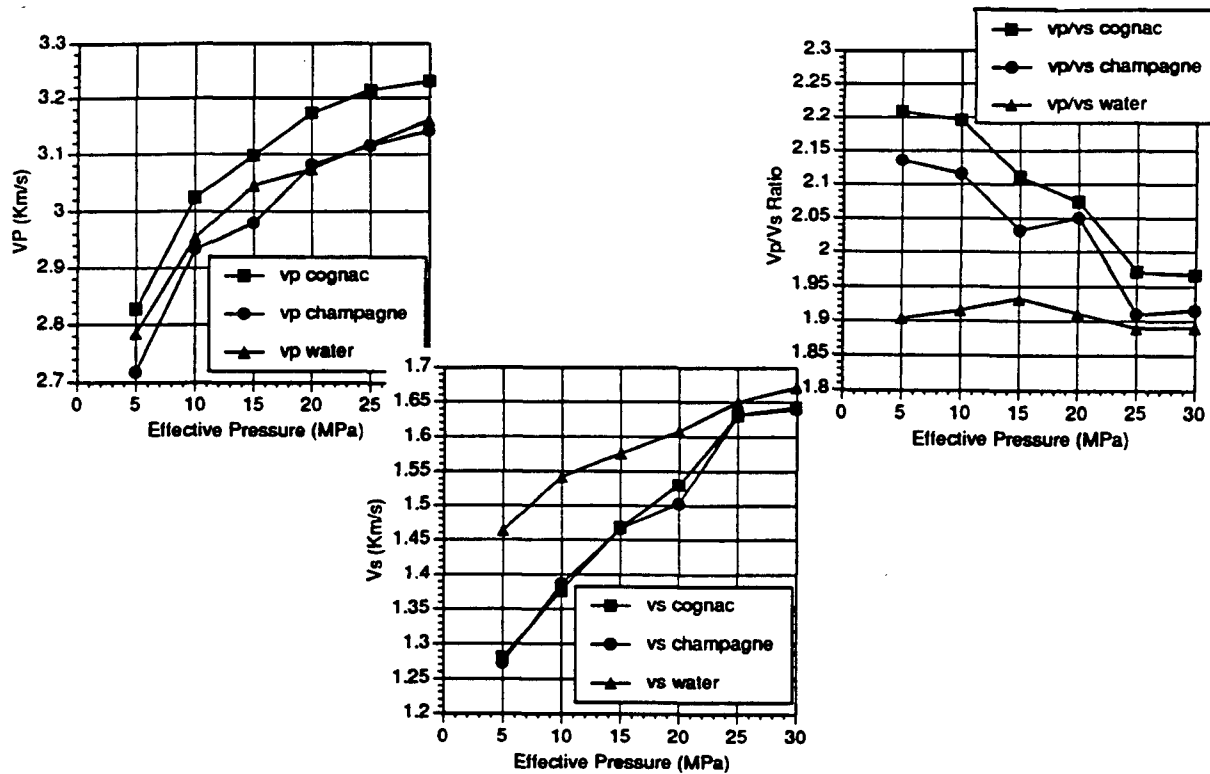


Figure 5.32: Other data! Velocities under full saturation for water, cognac, and champagne at room temperature.

assumed that dispersion is negligible in dry rocks, so that dispersion is restricted to the case of saturated rocks and is related to fluid flow (chapter 2). Dispersion is commonly thought of as a combination of Biot dispersion, caused by large scale average fluid motion relative to the matrix (Biot, 1956 a,b) and of "squirt flow" or local fluid flow on the scale of individual grains (Mavko et al, 1990 a,b). Figure 5.33 shows the water saturated P-wave and S-wave velocities measured at 30 MPa effective pressure, together with the predicted fully saturated velocities, using Biot theory and the measured dry velocities. A constant value of 43 MPa was used for the matrix bulk modulus for all of the samples, so the results must be viewed for the dataset as a whole. In general, measured and predicted results are very close. It should be mentioned that the calculated velocities are from the Biot low frequency equations and that there is practically no difference between the Biot low and high frequency results for these sandstones. Shear wave velocities predicted from Biot theory are always slightly higher than the measured S-wave velocities. This may be caused by chemical alteration effects which take place during initial water saturation.

Another comparison done at an effective pressure of 10 MPa yielded similar results. The agreement between Biot theory and the observed velocities indicates that the ultrasonic wave velocities obtained from these samples can be considered in the low frequency range for the Biot mechanism and that they can be used in direct comparison with measurements at sonic frequencies. Any difference between laboratory derived velocities and seismic velocities would be due to a local flow mechanism involving intrinsic attenuation. The results also indicate that these samples have a rather open pore space with few low aspect ratio pores, since fluids appear to be relaxed at low effective pressures.

15) Comparison with other data

In figure 5.34, I compare the measurements from this experiment to some previously published results. The Troll data shown are fully water saturated P-wave velocities at 30 MPa effective pressure. Other data are from Gregory (1976), Domenico (1977), Han (1986 a,b), Klimentos et al. (1990) and Yin et al (1988). The data from Gregory are cemented sandstones, but no information was available regarding clay content. The Ottawa sands are from Domenico and Yin, and consist of high porosity loose sands that have been artificially packed together.

All other data represent a variety of samples, including clean sands, shaley sands, and sandy shales from the data sets of Han and Klimentos. In general, the clean sandstones are consolidated samples, while the clay bearing sandstones range from consolidated to loosely consolidated samples. The data from Klimentos were obtained at 40 MPa effective pressure, a 2% reduction was applied to the velocities to correct for effective pressure differences. Figure 5.26 shows an approximate 1% velocity increase in the compressional-wave velocities between 25 and 30 MPa, indicating that the 2% reduction in the velocities for Klimentos data should be adequate. The clay bearing sandstones have been divided into groups according to their origin, Han data set or Klimentos data set. As was shown in figure 2.18, chapter 2, the data can also be regressed linearly according to their lithologic classes or clay content, regardless of

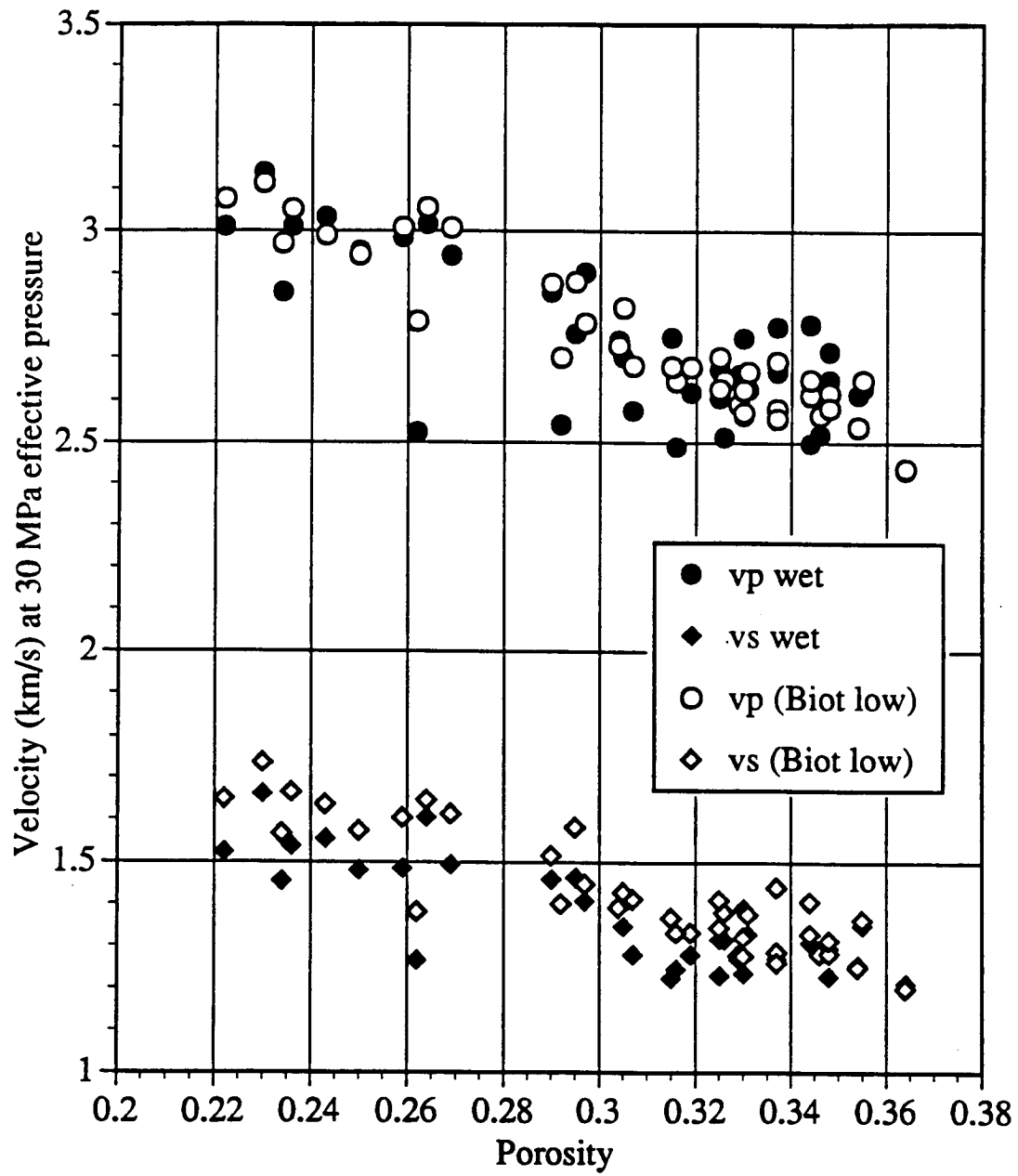


Figure 5.33: Measured water saturated compressional and shear velocities at 30 MPa effective pressure compared to velocities computed from Biot low frequency expressions.

their origin (see chapter 3 on classification of sedimentary rocks).

The results show that the Troll samples generally have lower velocities than the clean sandstones and the clay bearing sandstones from Han and Klimentos. For porosities between 25 % and 30 %, some of the clay bearing sandstones (11-30% clay) have velocities close to those of the Troll sands. These samples are from a very shallow interval (625 meters) of the Klimentos dataset, and consequently, there is reason to believe that these samples are fairly unconsolidated. Note that the velocities of the Troll samples decrease slower with increasing porosity, than the other data in figure 5.34. As a result, the slope of the regression of velocity versus porosity for the Troll sands is smaller than that for other more consolidated sands. The Ottawa sands have the lowest velocities, and are the most unconsolidated samples in the figure. Figure 5.35 shows the same comparison based on the fully water saturated shear wave velocities. No S-wave velocities were available for the Klimentos data set. Similar observations to those made for P-wave velocities can be made for S-wave velocities (figure 5.35).

The Troll sands are considered clean sandstones, as opposed to clay bearing sandstones. It is interesting to note that all of the "dirty" clay bearing sandstones of Han and Klimentos are confined between a straight line fitted through the clean consolidated sandstones (of Han and Klimentos) and a straight line fitted through our clean unconsolidated sandstones (those of Troll). These results indicate that the degree of consolidation or cementation is a crucial parameter that should be considered when investigating velocity/porosity relationships. Furthermore, the effect of consolidation can overwhelm that of clay, as was examined in detail in chapter 2.

Figure 5.36 shows V_p - V_s ratios for the saturated data shown in figures 5.34 and 5.35. Although the data is scattered, there is a consistent trend, showing the lowest V_p - V_s ratios for the clean consolidated sandstones and the highest V_p / V_s ratios for the unconsolidated Ottawa sands. The V_p - V_s ratio increases with both porosity and clay content (Han, 1986 a). According to Han, the effect of porosity is larger than

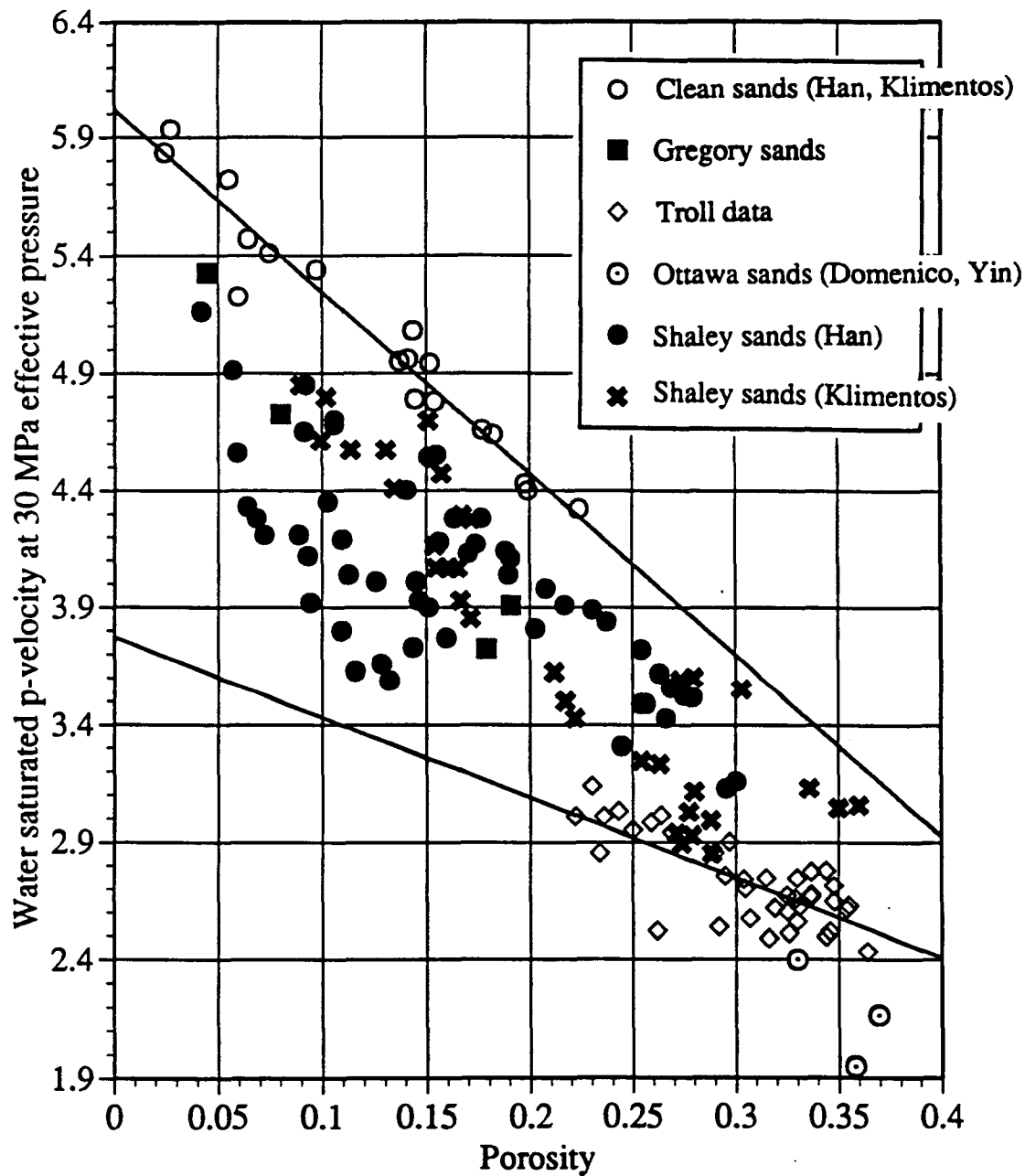


Figure 5.34: Comparison of different measurements of water saturated P-wave velocities in various sandstones at 30 MPa effective pressure; data from Troll, Domenico (1977), Gregory (1976), Han (1986), Klimentos et al (1990), Yin et al (1988).

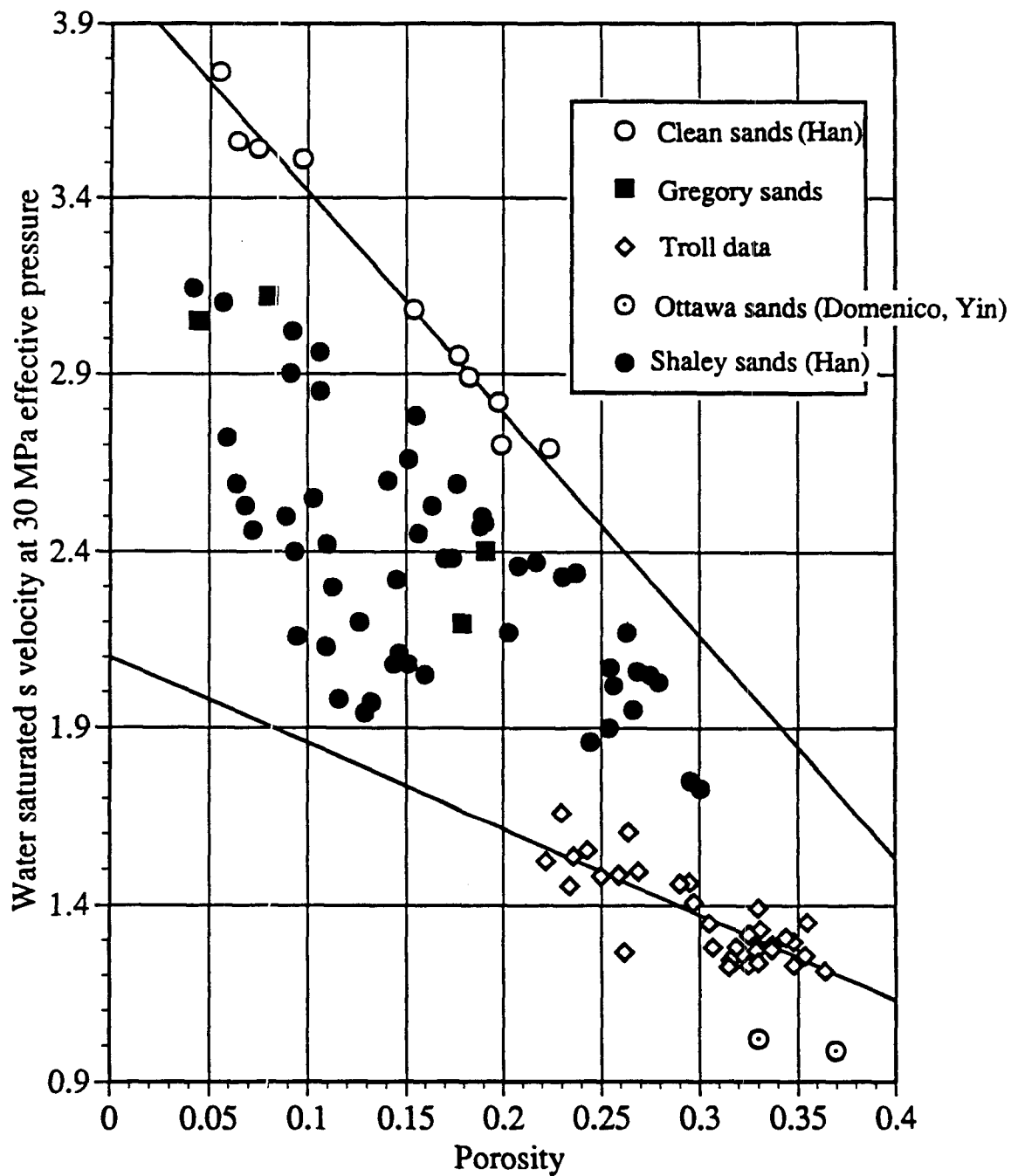


Figure 5.35: Comparison of different measurements of water saturated S-wave velocities in various sandstones at 30 MPa effective pressure; data from Troll, Domenico (1977), Gregory (1976), Han (1986), Yin et al (1988).

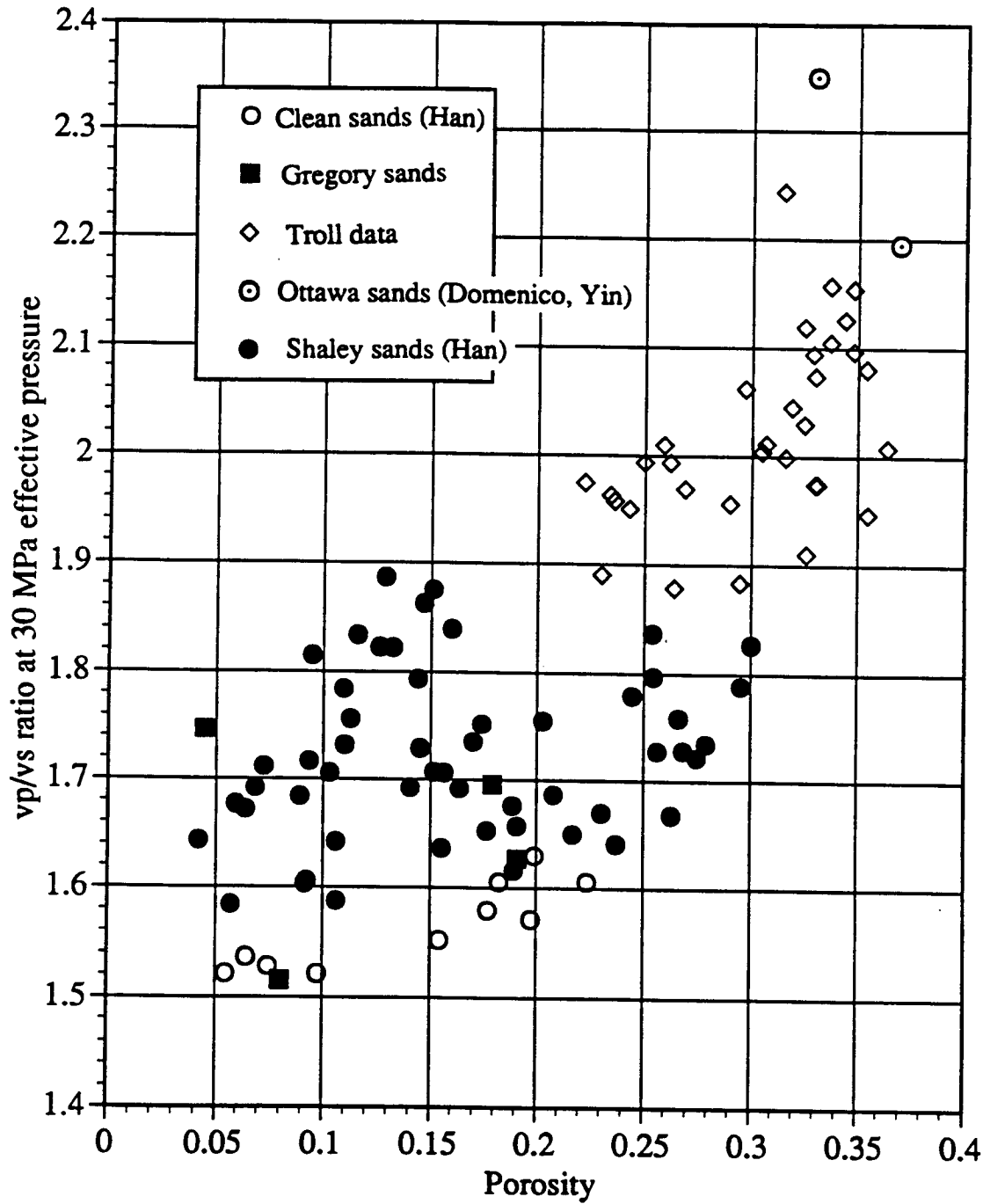


Figure 5.36: Comparison of Vp-Vs ratios in various water saturated sandstones at 30 MPa effective pressure; data from Troll, Domenico (1977), Gregory (1976), Han (1986), Yin et al (1988).

that of clay content. It can be seen that the Vp-Vs ratios from the Troll samples are consistently higher than those of Han, and that they have a greater dependence on porosity. The Troll data fits well with previous observations that the Vp-Vs ratio in unconsolidated, brine saturated sandstones are greater than 2 (Gardner and Harris, 1968). These results support the fact that the Troll samples are less consolidated than the samples from Han.

16) Defining rock parameters for Sognefjord sands

Typical mineral compositions for the Sognefjord sands include 72% quartz, 18% potassium feldspar (mostly orthoclase), and 10% muscovite; the elastic moduli of these components are: $K_{quartz} = 38$ GPa, $\mu_{quartz} = 44$ GPa, $K_{feldspar} = 65$ GPa, $\mu_{feldspar} = 28$ GPa, $K_{msc} = 52$ GPa, and $\mu_{msc} = 31$ GPa (appendix D). When those mineral moduli are combined to obtain the arithmetic mean of the Hashin-Shtrikman (HS) upper and lower bounds of a three component aggregate, the resulting model does not fit the data well over the large observed range of porosities. The HS upper bound and the HS lower bound do not fit the data well either. It appears that one would need an intermediate model that would be in agreement with the HS upper bound for low porosities and closer to the HS lower bound for higher porosities. One possible explanation for this discrepancy is that most theoretical models do not account for cementation effects (see chapter 2). Intuitively, one might expect the matrix moduli in a "zero porosity loosely consolidated sand", otherwise known as the y-intercept of a modulus-porosity crossplot, to be lower than that of a well cemented sand with the same mineralogy. In conclusion, because there is no existing single model that can reproduce the velocity versus porosity behavior of both consolidated and unconsolidated sands, I revert to empirical modeling of the velocities in loosely consolidated Sognefjord sands.

Linear regressions were fitted through the water saturated Sognefjord sands at 30 MPa for the porosities in the range from 20% to 40%), yielding the equations shown in figure 5.37. Projecting to zero porosity, these linear empirical relations yield matrix

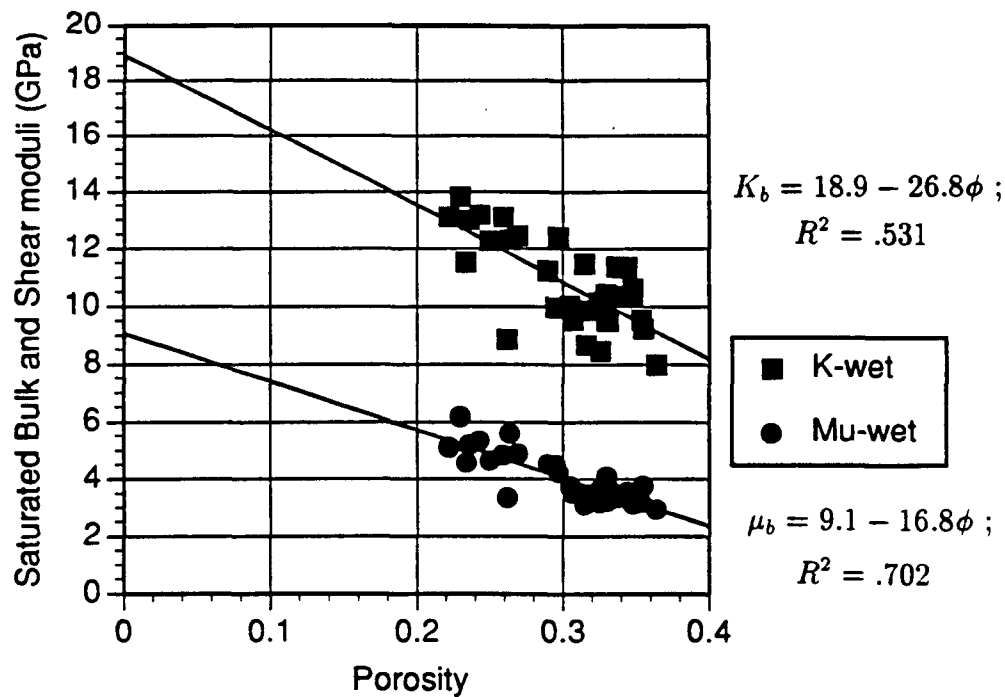


Figure 5.37: Water saturated bulk and shear moduli as a function of porosity for Sognefjord sands at 30 MPa effective pressure.

bulk and shear moduli for loosely consolidated Sognefjord sands equal to 19 GPa and 9 GPa respectively. These estimated values of pure matrix moduli allow for modeling of the data obtained in the laboratory experiment. In chapter 2, I showed that presently, it is not possible to quantitatively take into account the effects of cementation nor chemical effects in theoretical models. In fact, there is no petrographic scheme that can simultaneously classify a rock in terms of mineralogy, pore geometry, cementation, confining pressure, and pore fluid. However, by calibration to experimental data, "effective" matrix parameters can be introduced for the Sognefjord sands.

In all respects, theoretical equations which involve only porosity terms cannot accurately describe the velocities of all porous rocks. Subdivisions according to lithology, cementation, and in-situ conditions of pressure and temperature are necessary.

17) Summary of the core measurement program

A comprehensive ultrasonic laboratory measurement program was designed to

establish a detailed and reliable rock physical model of the Sognefjord reservoir sands from well 31/5-4S. The main results are:

- High amounts of potassium feldspar can lower elastic (P and S wave) velocities due to the presence of small amounts of associated diagenetic clay. Because this velocity difference is small, it is doubtful that such subtle changes can be detected from seismic data.
- High amounts of muscovite marginally increase P-wave velocities for a given porosity; high amounts of mica also decrease porosity and therefore increase velocities. Because of non-uniqueness, it is not possible to deduce the mineral composition of the reservoir rocks from their velocity alone. However, since the amount of mica is related to porosity and because we found that feldspar concentration is approximately 20 % throughout, it is possible to establish an indirect velocity/mica relationship through porosity. This relationship yields an increase in velocity for increasing mica content. Such a relationship could be used with seismic data to map regional variations in the mica content within different Sognefjord cycles between wells.
- A quasi-linear relationship was observed between compressional and shear wave velocities, with a different slope for the dry and the water saturated cases
- Measured ultrasonic velocities in water saturated samples are similar to those computed from the Biot low frequency expressions, for all effective pressures.
- Velocities in loosely consolidated Sognefjord sands have a weaker dependency on porosity than those in other well cemented sands.

The empirical-petrophysical-lithological model derived in this section will next be used for seismic lithologic modeling of AVO trends at Troll West. This involves the calibration and lithologic interpretation of well logs, the development of formulations for effective parameters of the reservoir and seal, and full waveform forward modeling of AVO responses.

(II) LOG ANALYSIS AND INTERPRETATION AT WELL 31/5-4S

The key to detailed and quantitative interpretations of lithologies from seismic data lies in its calibration, via well logs and core data. This implies that well logs are central to seismic lithologic interpretation. Thus, logs must be quality-checked and processed to provide the best possible image of in-situ properties for the lithologies under investigation, a fact that has been recognized for some time (Ausburn, 1977). Better results yet can be obtained by calibration of logs to core data, as is done in the following section at well 31/5-4S.

1) The litho-density log: Comparison of core and log porosities at well 31/5-4S

Two logs are available for estimating porosities throughout the interval from 1650m to 1750m: the compensated neutron log (CNL) and the density log. I chose not to use the sonic log here, because it will later be used independently to estimate fluid content. The CNL is not adequate for inferring porosities throughout the interval, because the zone contains gas, oil and water, and the CNL reacts primarily to the concentration of $[H^+]$. On the other hand, the density log is of good quality in the interval, having a good caliper and a small " $\Delta\rho$ " curve. Figure 5.38 compares core measured and log-derived porosities at well 31/5-4S. There is good agreement between the density log-derived porosities (assuming a sandstone matrix density of 2.65 g/cc) and the core measured porosities outside of the gas zone. The density log underestimates porosity in the gas zone. Note that if we wrongly assume that the gas zone is actually water saturated, with a fluid of density 1.04 g/cc (dashed line in figure 5.38), the porosities are overestimated.

2) The sonic log: Comparison of core and log velocities

Figure 5.39 compares core measured and log-derived P-wave velocities at well 31/5-4S. Because thin-sections showed very large open pores, and because velocities from Biot low and high frequency limits were similar, I did not apply any dispersion correction to either the log or core velocities. The raw sonic log which appeared very

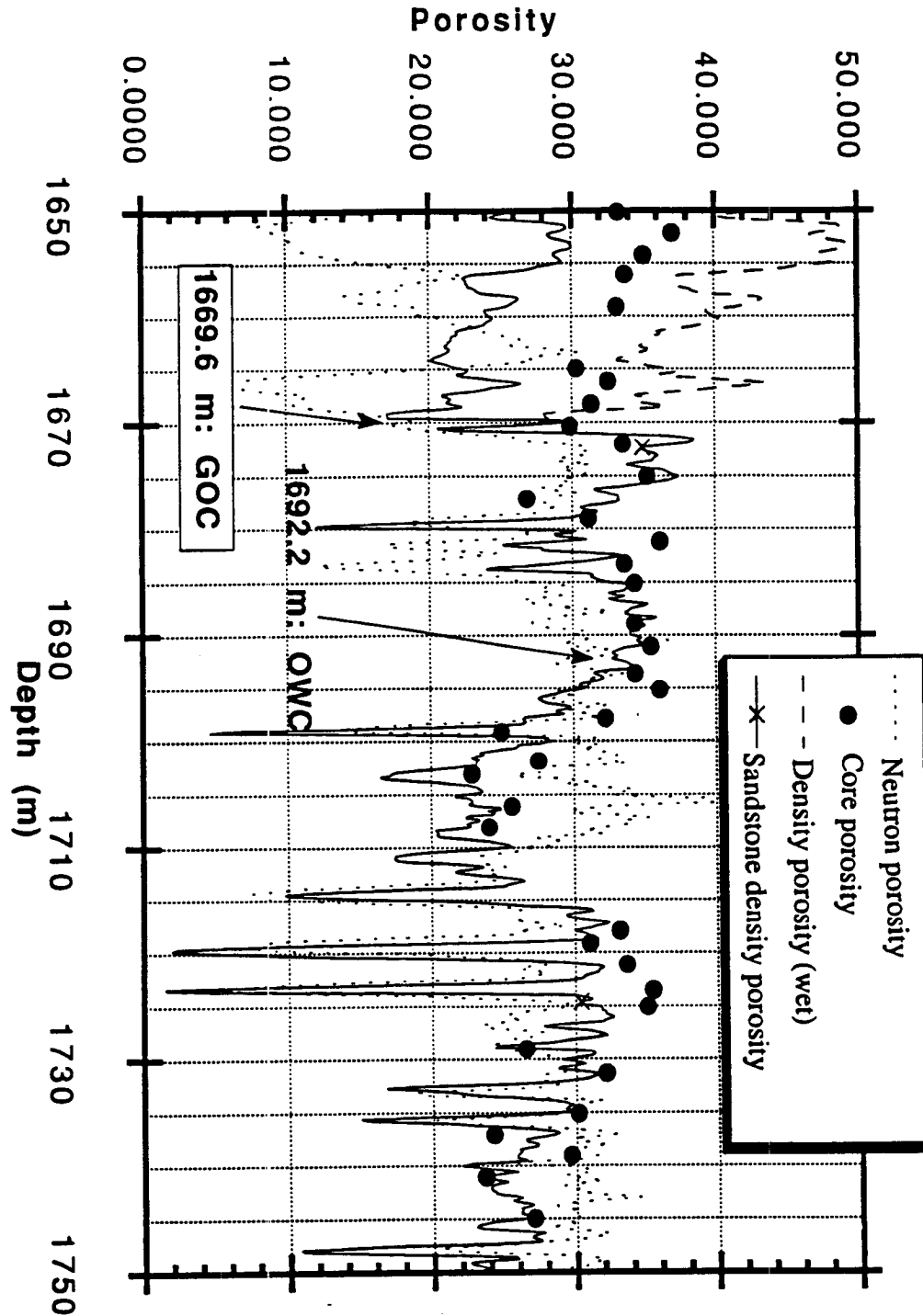


Figure 5.38: Comparison between core measured helium porosities, and log-derived porosities at well 31/5-4S. The neutron-density cross-over marks the GOC (at 1669.6 m), while the OWC (at 1692.2 m) was identified from resistivity logs (Appendix B-7). Best matches are achieved using the density log and a sandstone matrix in liquid saturated zones. Both the CNL (dotted) and the density (solid) log underestimate porosities in the gas zone. If we wrongly assume that the gas zone is actually water saturated with a fluid of density 1.04 g/cc (as in the dashed line), the density derived porosities are overestimated in the gas zone.

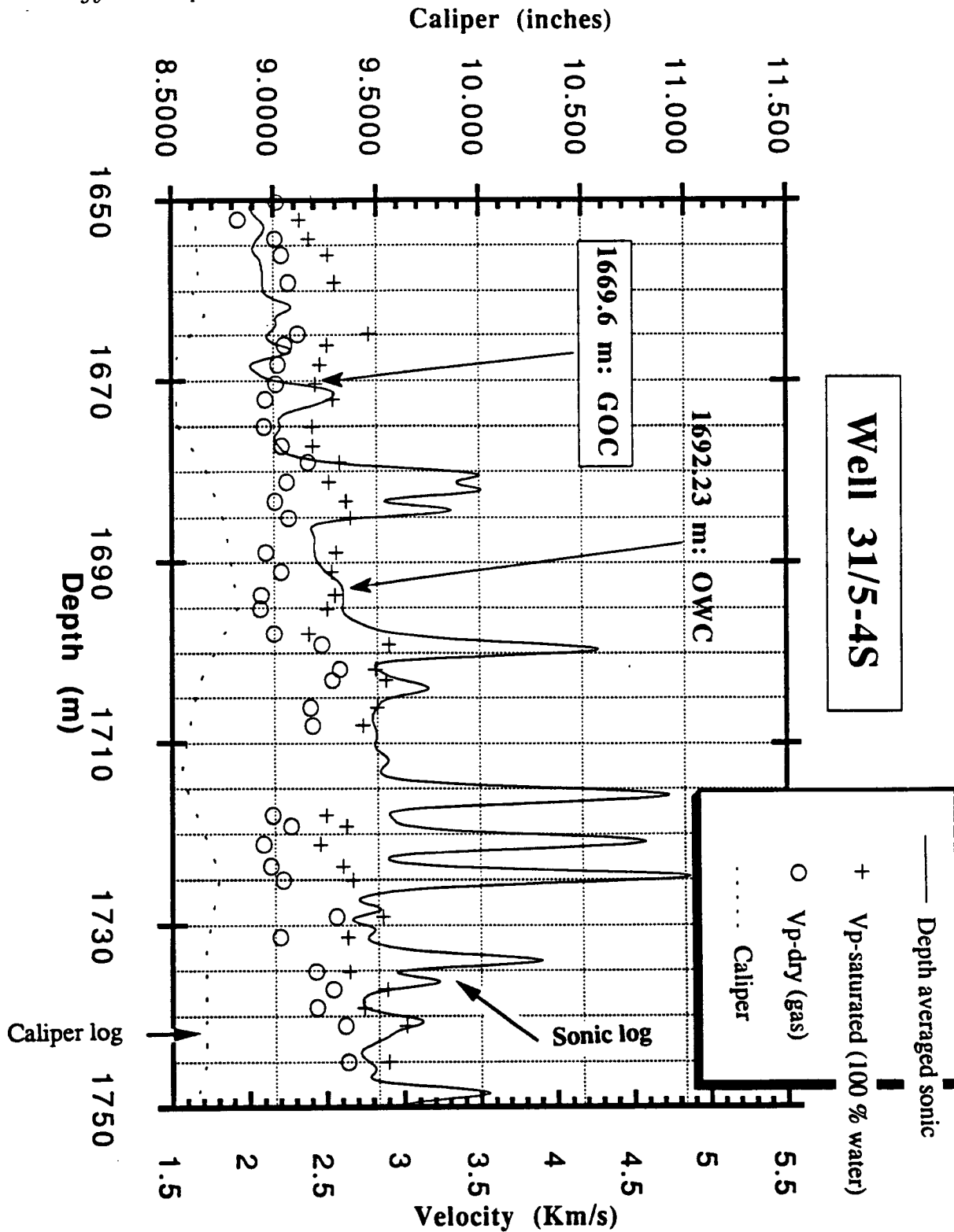


Figure 5.39: Comparison between core measured and log-derived P-wave velocities at well 31/5-4S. Because thin section analyses show practically no low aspect ratio pores present in the sandstones, and because velocities from the Biot low and high frequency limits are similar, no dispersion corrections were applied to either the log or core velocities. The GOC exhibits a bulk shift (this is truly a Gassman effect) and correlates well with figure 5.38. Note the good agreement for velocities in the gas zone (above 1669.6 m), for velocities in the "dead" oil zone (below 1678 m), and for velocities in the water zone (below 1792m).

noisy at first, was edited using two passes through a 7 point median filter, followed by two passes through a 7 point running average filter. This had a net smoothing effect. Because I had more confidence in core velocities measured under higher effective pressure conditions, I used the core velocities measured at 30 MPa effective pressure and corrected them for pressure (using figure 5.26) down to reservoir conditions at approximately 1500 m vertical depth. Since there is no overpressuring at Troll West, we have:

$$P_e = P_{confining} - P_{pore} = P_{lithostatic} - P_{hydrostatic} = gh(\rho - 1.04) \approx 15 \text{ MPa}$$

where g is the acceleration of gravity and h is depth. The open circles ("O") in figure 5.39 indicate dry velocities corresponding to 100 % gas saturation, while the "+" signs mark liquid saturated velocities corresponding to either 100 % oil or 100 % water saturation. The compressional-wave velocities for both liquid saturated and dry samples are in good agreement with those derived from the sonic in areas where the caliper indicates good hole conditions. Note that the gas oil contact (GOC) occurs at 1669.6 m, as seen from the classical neutron-density cross-over in figure 5.38. It is interesting to observe that the GOC appears on the sonic as a subtle bulk shift. If we didn't know where the GOC was located, we would probably miss it on the sonic. However, with independent information from other logs, the sonic confirms the presence of a GOC through a small bulk shift increase in P-wave velocities. Note how the sonic matches the dry core velocities above the GOC, and the saturated core velocities below the GOC. The discrepancies within the oil and water zones (1681m-1684m, 1715m-1725m, and 1731m-1736m) are due to the fact that carbonate rich layers were not sampled in the core measurement program. On the other hand, the sonic tool "averages" refracted velocities over a distance of several feet and incorporates the effects of higher velocity calcite shoulder beds. This is a scaling problem, where the sonic includes both vertical and lateral heterogeneties that are not necessarily sampled by the cores, and results in somewhat higher "average" sonic velocities than core velocities. There is no evidence of an OWC from the sonic at 1692 m. This is not surprising, since there was practically no difference in oil and water saturated P-wave

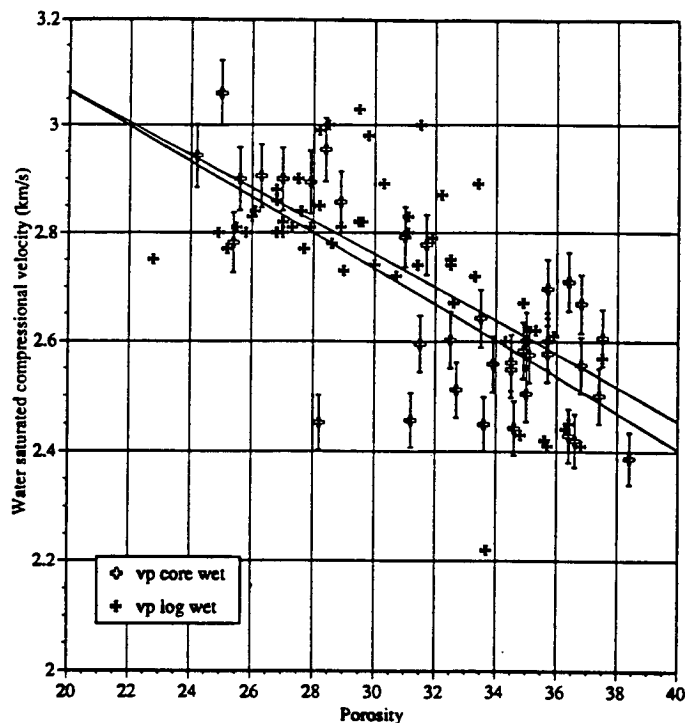


Figure 5.40: Comparison between core measured and log-derived P-wave velocities at Troll. Some scatter is present, but statistical regressions (best linear fits) for log and core velocities versus porosity are in good agreement.

velocities as observed from core measurements (figure 5.30).

It is worth noting that there is some disagreement between core and sonic velocities between 1674m and 1677m. Here, sonic velocities appear to be lower than those measured in oil saturated cores. According to Biot theory, as little as 5-10% gas can cause a substantial drop in the P-wave velocity, so I speculate that this zone may be partially gas saturated. The neutron and density logs shown in figure 5.38 also show some weak indication of gas in that zone.

Figure 5.40 confirms that core measured and log-derived velocities are similar in cleaner parts of the Sognefjord sands lacking calcite cementation. The figure shows velocity-porosity relationships as determined independently from both core and log data. The core data is from well 31/5-4S, while the sonic log data are taken from Sognefjord sands in several wells. As expected, some scatter is present in the data, but statistical regressions for log and core velocities versus porosity are in good agreement.

3) Mapping lithologic changes with logs

In chapter 4, I used geophysical log information, in a semi-quantitative manner, to correlate depositional cycles within stratigraphic units across the Troll West Oil Province. Since the major minerals encountered in the Sognefjord sands have a relatively constrained range of physical properties, a more quantitative inversion for lithology can be attempted from a set of diagnostic log properties.

a) The NGS: Correlation to MUSCOVITE content

The Natural Gamma Ray Spectroscopy (NGS) tool detects the natural gamma ray emissions of various energies from a given formation. The individual contributions of three radioactive elements, Thorium, Uranium, and Potassium, are then calculated from the total energy spectra. I assume that the K, U, and Th curves supplied by Schlumberger are the best possible, and that statistical errors associated with the actual measurements have been minimized (Serra et al, 1980).

The NGS has traditionally been used as an improved shale indicator for a better estimate of clay percentages. This is obtained by subtracting the uranium component from the total gamma ray response, because uranium salts contained in connate water can precipitate onto a permeable formation and because uranium is also associated with organic materials. The NGS has also been used as an indicator of the paleoenvironment, since it enables clay typing. For example, illite is generally associated with calm, deep marine deposition, and kaolinite is more indicative of higher energy environments.

Sognefjord sands are arkosic, and as such are primarily composed of quartz, feldspar, and mica. The more micaceous sand layers can be identified by their higher gamma ray log response, because of their high potassium content. Both the gamma ray and the K curves correlate to total muscovite content, as is shown in figure 5.41. The K curve shows a small improvement over the total gamma ray response in its correlation to muscovite content throughout the Sognefjord, except for the zone be-

tween 1735m and 1745m, which also happens to contain less than 20% orthoclase. Note that there is only a weak correlation of the two log types, total gamma ray count and K curve, with feldspar content, but that the correlation with mica content is good. The correlation should come as no surprise, since we had observed from thin-section analyses (figure 5.6) that the orthoclase content was practically constant in the Sognefjord sands. This means that we can assume that the dominant reason for the change in potassium content in the Sognefjord sands is from variations in muscovite concentration (table 5.1).

Table 5.1: Potassium bearing minerals (modified after Serra et al, 1980)

Main Potassium rich minerals		
Mineral	Composition	K content by weight (%)
Feldspars		
Microcline	$KAlSi_3O_8$, Triclinic	16 to 10.9
Orthoclase	$KAlSi_3O_8$, Monoclinic	14 to 11.8
Plagioclases	(Albite, Anorthite)	0.54
Sheet Silicates		
Muscovite	$KAl_2(Si_3AlO_{10})(OH)_2$	9.8 to 7.9
Biotite	$K(Mg, Fe)_3(AlSi_3O_{10})(OH)_2$	10.1 to 6.2
Illite	$K_{1-1.5}Al_4(Si_{7-6.5}Al_{1-1.5})O_{20}(OH)_4$	8.3 to 3.5
Glauconite	$K_2(Mg, Fe)_2Al_6(Si_4O_{10})_3(OH)_{12}$	5.8 to 3.2
Other clays		
Montmorillonite	-	0.6 to 0
Kaolinite	-	1.49 to 0

From the core measurement program, micaceous sands were found to have lower porosities (figure 5.23), making it possible to establish an indirect velocity/mica relationship at well 31/5-4S. Figure 5.42 shows the same sort of inverse relationship between mica content and porosity at a different well, well 31/2-5. In the bottom part of figure 5.42, muscovite content was obtained by using the gamma ray log, as calibrated from well 31/5-4S. Note that two distinct families of lithologies can be identified from logs at wells 31/5-4S and 31/2-5: clean, high porosity sands, and micaceous sands with lower porosities.

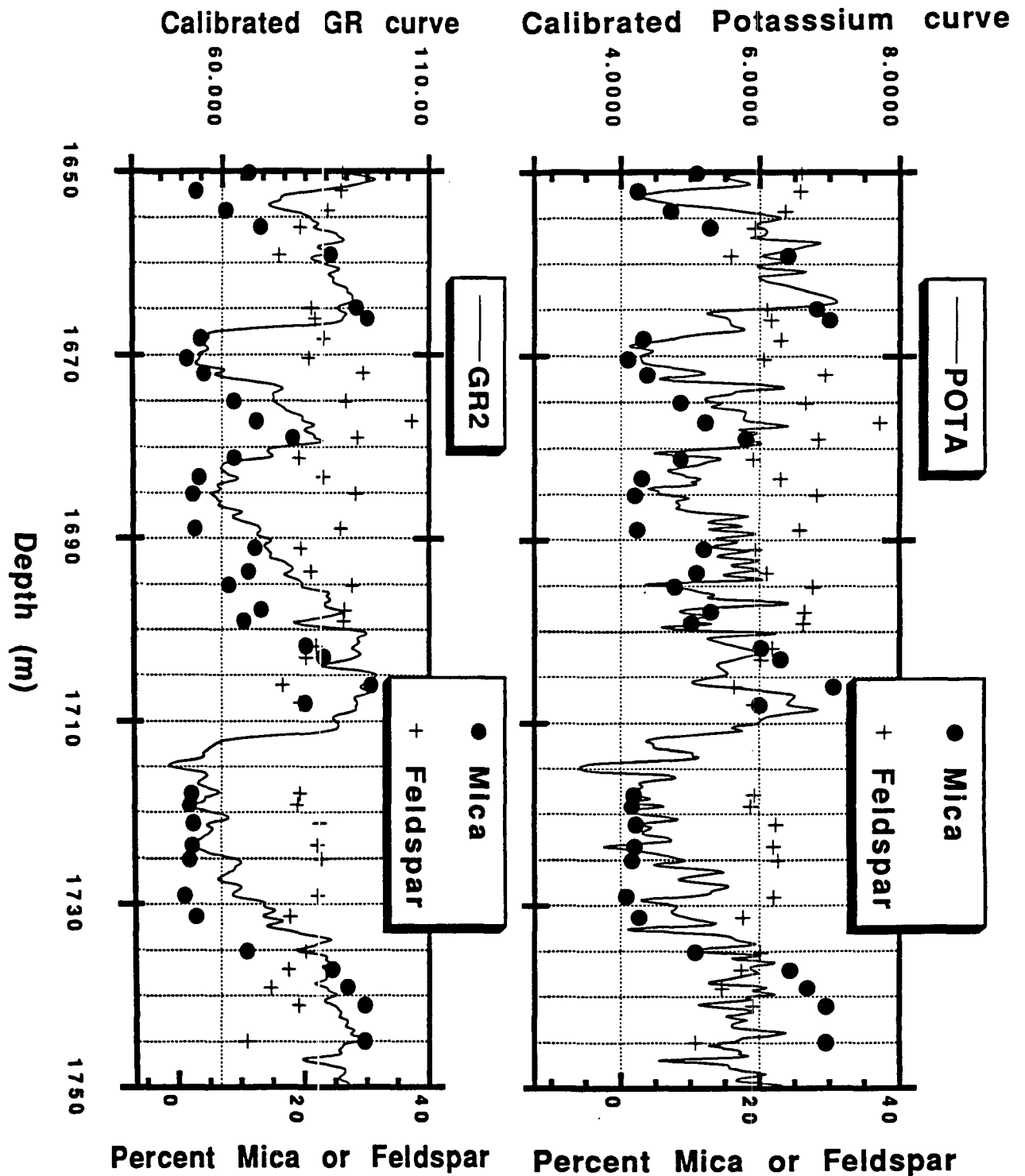


Figure 5.41: Correlation at well 31/5-4S, between the potassium content obtained from the NGT, the total gamma ray count, and the mica content, as identified from point counting on thin-sections. Note that the feldspar (orthoclase) content is almost constant at approximately 20 %; the best correlation to mica (muscovite) content is obtained through the potassium curve.

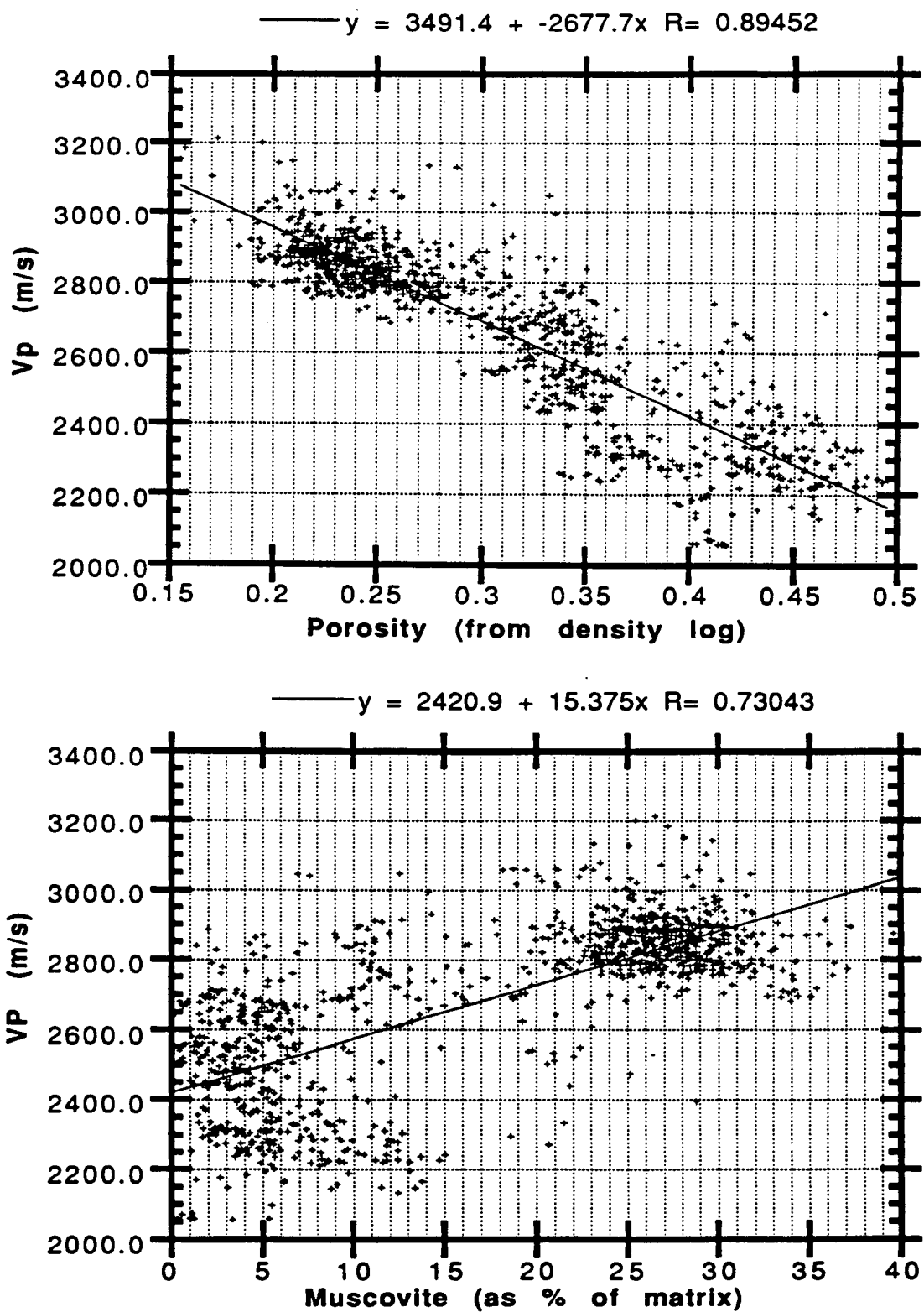


Figure 5.42: Indirect velocity-mica relationship for sands from well 31/2-5. The mica content was obtained using calibration relationships obtained from logs at well 31/5-4S (figure 5.41). Two distinct families of lithologies can be identified: clean high porosity sands, and micaceous sands with lower porosities. As in the case with core data, the mica rich sands have higher P-wave velocities and lower porosities.

b) The lithodensity and sonic: Correlation to CALCITE

In contrast to the micaceous sands, calcite cemented intervals or thin limestone stringers influence the sonic and density responses directly. Calcite cemented zones appear as layers with significantly higher velocities and densities, as indicated in figures 5.38 and 5.39. In conclusion, logs are useful tools in determining mica content and in locating thin calcite beds at Troll West.

Caveats:

Note that the potassium-muscovite correlation is not as straightforward as it may appear, because arenaceous rocks such as the arkosic and sub-arkosic sands found at Troll are fairly immature and may contain varying amounts of feldspars and micas. One might expect the amount of potassium feldspar to vary both vertically and horizontally within the Sognefjord Formation. This is due to the fact that sediments were derived from a tectonically active area which was undergoing rapid erosion and were transported only short distances in a rapidly subsiding basin. However, it is probably safe to invert the logs for mineral composition on a local scale, within depositional cycles in the neighborhood of a well. As a final remark, because of the correlation between the K-curve and muscovite content, it would be preferable to use the Th-curve as a clay indicator, when attempting to quantify the small amounts of clay present in the Sognefjord sands.

In addition, a "synergetic" approach to log analysis for lithologic inversion was also attempted, but with little success. This procedure consisted of inverting a set of simultaneous equations representing log responses, for their lithologic coefficients. This system of equations, written in matrix form, is shown below:

$$\begin{bmatrix} \rho_b \\ \Delta t \\ \phi_n \\ Th \\ U \\ K \\ 1 \end{bmatrix} = \begin{pmatrix} \rho_Q & \rho_{Msc} & \rho_{Orth} & \rho_{Ca} & \rho_w & \rho_o & \rho_g \\ \Delta t_Q & \Delta t_{Msc} & \Delta t_{Orth} & \Delta t_{Ca} & \Delta t_w & \Delta t_o & \Delta t_g \\ HI_Q & HI_{Msc} & HI_{Orth} & HI_{Ca} & HI_w & HI_o & HI_g \\ TH_Q & TH_{Msc} & TH_{Orth} & TH_{Ca} & 0 & 0 & 0 \\ U_Q & U_{Msc} & U_{Orth} & U_{Ca} & 0 & 0 & 0 \\ K_Q & K_{Msc} & K_{Orth} & K_{Ca} & 0 & 0 & 0 \\ 1 & 1 & 1 & 1 & 1 & 1 & 1 \end{pmatrix} \begin{bmatrix} V_Q \\ V_{Msc} \\ V_{Orth} \\ V_{Ca} \\ V_w \\ V_o \\ V_g \end{bmatrix}$$

The zero values in the square matrix indicate that the radioactivity contributions of the pore fluids are assumed negligible, compared to those of the solid mineral components. I first tried inverting the matrix when the system was underdetermined ($n+1 < m$, where n is number of logs and m is number of unknown components) using a least squares approach (Doveton and Cable, 1979), and then by direct inversion when the system had a unique solution ($n+1 = m$). The results were not satisfactory. This was probably due to the fact that the sediments are loosely consolidated and that linear relationships, such as Wyllie's time average equation, are only approximations and cannot be applied here.

In conclusion, I have shown that it is possible to establish a realistic reservoir model from correlation of lithologies to well logs and core data. **Quantitative estimates of dominant lithologies, porosity, and fluid content** can be established with a certain level of confidence. Note that sensitivity analyses of the volumetric model to rock properties were not done here. My next step is to calculate "missing" rock properties from the available information.

4) Calculation of "missing" properties

A continuous synthetic shear wave log was calculated in the overburden from the individual log components, using the Gregory-Pickett method presented in chapter 2. The empirical shear wave velocity relationships established during the core mea-

surement program were used to complete the synthetic shear wave log within the Sognefjord. The complete synthetic shear wave log was then used with the rest of the petrophysical information for log blocking, averaging and up-scaling, as described in chapter 3. Next, Q-values for each of the layers were calculated following the method presented in chapter 2. Note that the uncertainty in the Q parameters remains high. However, because dispersion is small at Troll, Q is high and has only minor effects. This implies that, for all practical purposes, we can use elastic synthetic models at Troll. There remains the question as to whether Q is low within the gas zone itself. This can be resolved through sensitivity analyses by comparing synthetic and seismic CDP gathers (Sengupta and Rendleman, 1991).

Use of calibrated logs at other wells

The key factors used in the lithologic calibration of logs at Troll are: the percent quartz, calcite, and mica by volume, and the total porosity. Unfortunately, well 31/5-4S is just southeast of the Troll West Oil Province under investigation (see map in figure 4.3). However, it also happens to be the only well for which actual core samples were obtained for complete petrophysical studies. Since the facies properties between well 31/5-4S and other wells of the Troll West Oil Province are very similar (Norsk Hydro, personal communication), I used the calibration results obtained at well 31/5-4S to characterize the petrophysical properties of the Sognefjord sands at other wells in the study area. An example was given in figure 5.42. In the following sections, well 31/2-5 will be examined in detail. Properties inferred from calibrated logs at the "microscale" will be up-scaled to seismic wavelengths and used to generate seismic synthetic AVO responses.

(III) CONTROLLED TRUE AMPLITUDE PROCESSING

Due to the large volumes of raw seismic data and the economic significance of well 31/2-5, I concentrate on a small area around this "type" well, described in chapter 4.

Why re-process the pre-stack data?

The application of AVO interpretation techniques to field data remains difficult (Yu, 1985, Dey-Sarkar, 1988, Mazzotti, 1990), because of interference problems and the need for improved S/N ratios in the pre-stack domain. The re-processing of real data is important, because it allows for controlled and enhanced pre-stack S/N ratios in conjunction with modeling/inversion.

In modeling seismic anomalies, I used a full solution approach, and tried to incorporate "coherent noise", such as multiples and P-S conversions in the seismic synthetics. The processing steps adopted for the real data were then duplicated to the synthetic seismic data. I performed the data analysis using ProMAX, a commercial processing package from Advance Geophysical. The de-multiplexing steps from SEG-D format and conversion to SEG-Y were done using Cogniseis' Disco package on Jon Claerbout's Convex system.

Model-assisted processing

A reasonable goal in a seismic stratigraphic interpretation is to remove the structural effects and to be left with the purely stratigraphic components of a petroleum trap. In order to recover interval velocities and "true amplitudes" in a stratigraphic sense, one has to first decouple the structural component of a trap. This can be done effectively at well 31/2-5 by working in the CDP domain, because there is practically no structure above the zone of interest, and because the reflectors under study are several cable lengths long (figure 4.6). The reservoir zone is also assumed to be flat, so that the dips of subtle features such as those of intra-formational reflectors described in chapter 4 are ignored.

Models are useful in determining the factors contributing to constructive/destructive interference within a particular zone of interest. For example, at well 31/2-5, I compare a seismic synthetic gather obtained using primary reflections only, shown in figure 5.43a, with a synthetic gather obtained using primaries and multiples only

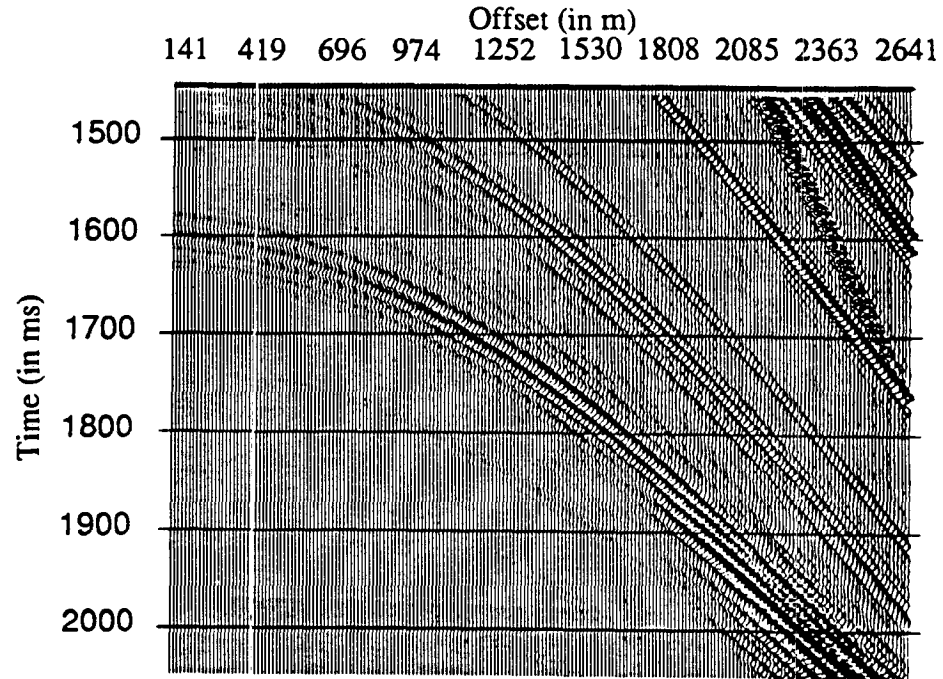


Figure 5.43: a) Primaries only model at well 31/2-5; close-up in the reservoir zone.

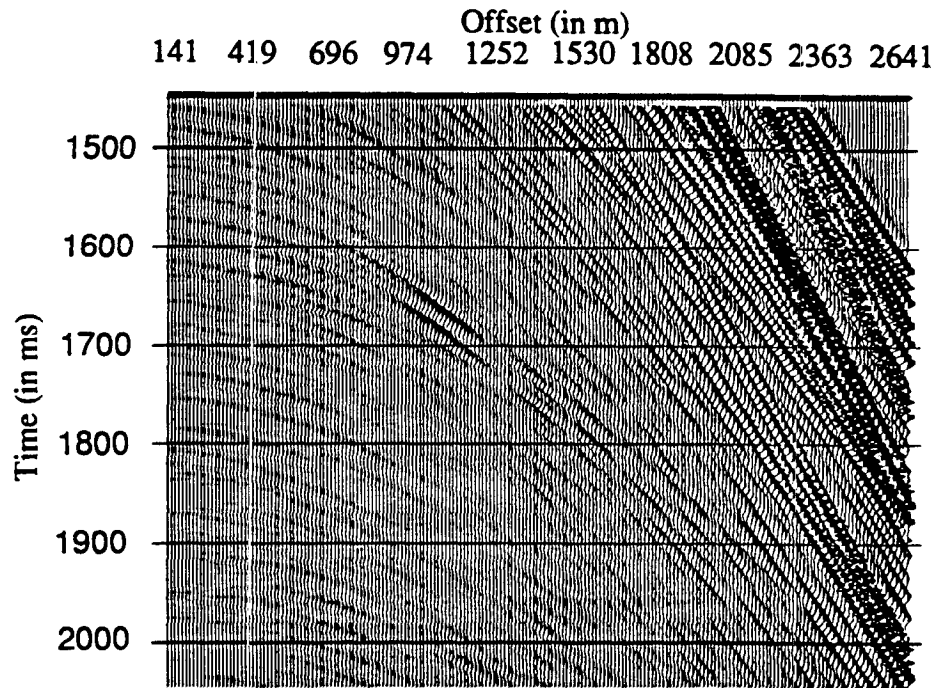


Figure 5.43: b) Primaries and multiples model at well 31/2-5; close-up in the reservoir zone.

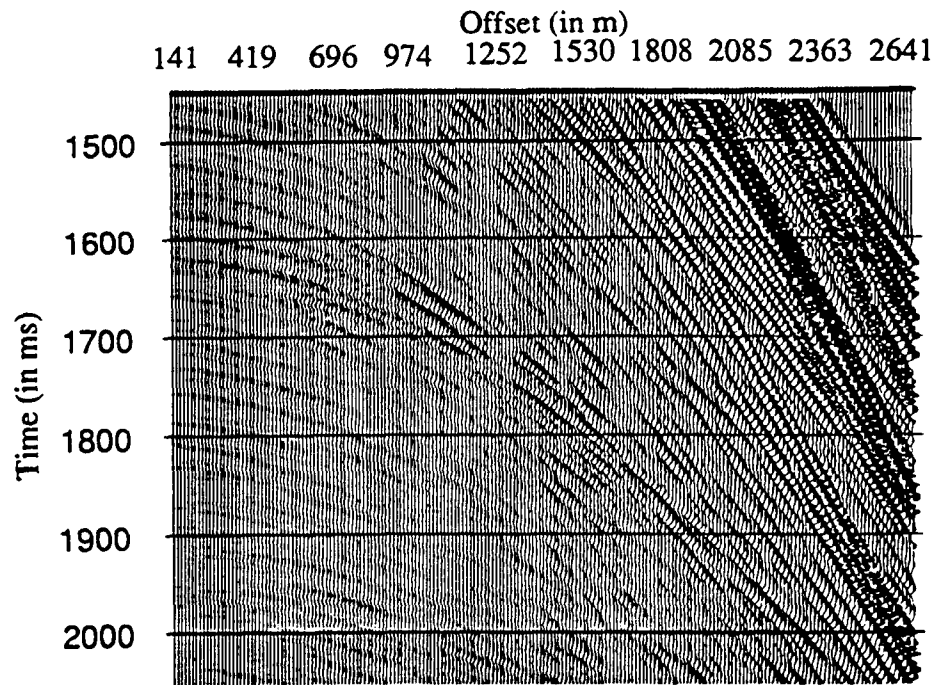


Figure 5.44: a) Full waveform model at well 31/2-5; close-up in the reservoir zone.

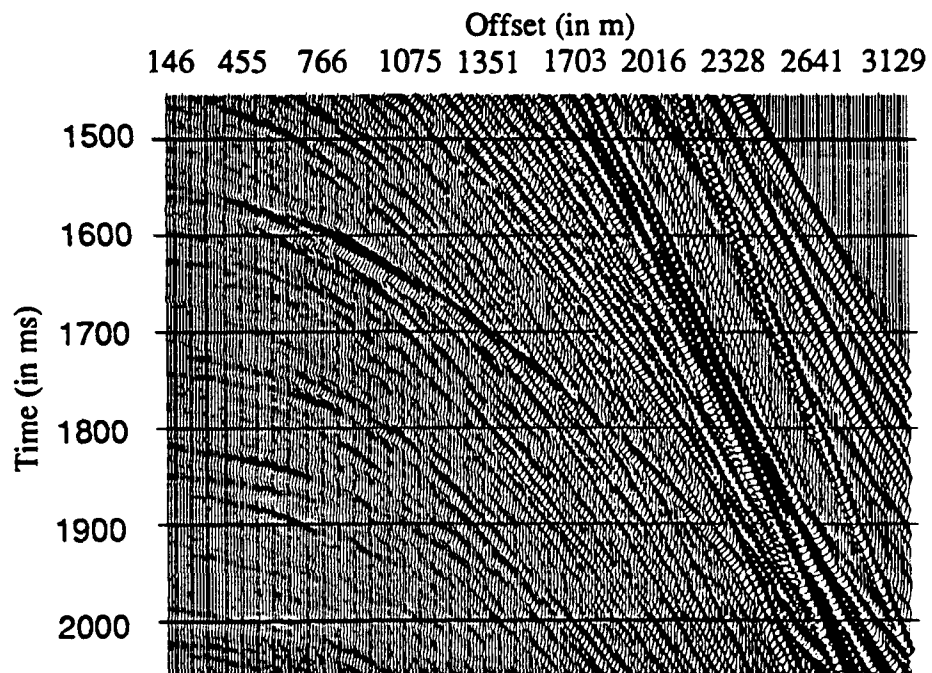


Figure 5.44: b) raw CDP supergather at well 31/2-5; close-up in the reservoir zone.

(figure 5.43b), with another synthetic gather obtained using a full solution including primaries, multiples, and conversions (shown in figure 5.44a), and with a real CDP gather. From the figures, it is clear that long period multiples (and possibly P-S conversions) add to the overall seismic response observed from about 1500 to 1800 ms, and interfere with the primary P-wave reflections from the top of the reservoir.

When modeling seismic data, it is recommended to either use solutions including only P-wave reflections, or to use the full seismic response. In the construction of all subsequent seismic synthetic pre-stack gathers, I use the full seismic solution. Preliminary processing pre-stack synthetic seismic data revealed that deconvolution operators were not effective in suppressing long period multiples. The model results showed that F-K filters are somewhat effective in removing long period multiples, but they also affect AVO responses to some extent. F-K filters were therefore applied to both the field seismic data and the synthetic seismic data.

The main processing steps involved de-multiplexing, geometry installation, deconvolution, F-K filtering, partial offset CDP stacking, and amplitude and phase balancing via inverse Q-filtering. Several tests were also done to establish reasonable binning and partial summing parameters. This partial summing was used to enhance S/N ratios and create supergathers as shown in figures 5.45 and 5.46.

(IV) PETROPHYSICS AND AVO FOR RESERVOIR CHARACTERIZATION

In A.A.P.G. Memoir 32 (1982), Halbouty, challenged earth scientists to bring forward new ideas and concepts to "deliberately search for the subtle trap". This endeavor was partly the result of the fast progress that had been made in previous years in seismic stratigraphy, and reflected the need to summarize and evaluate existing technology at that time. Since then, remarkable progress has been made in understanding seismic wave propagation and the tools available today can be extremely powerful in hydrocarbon exploration when used appropriately.

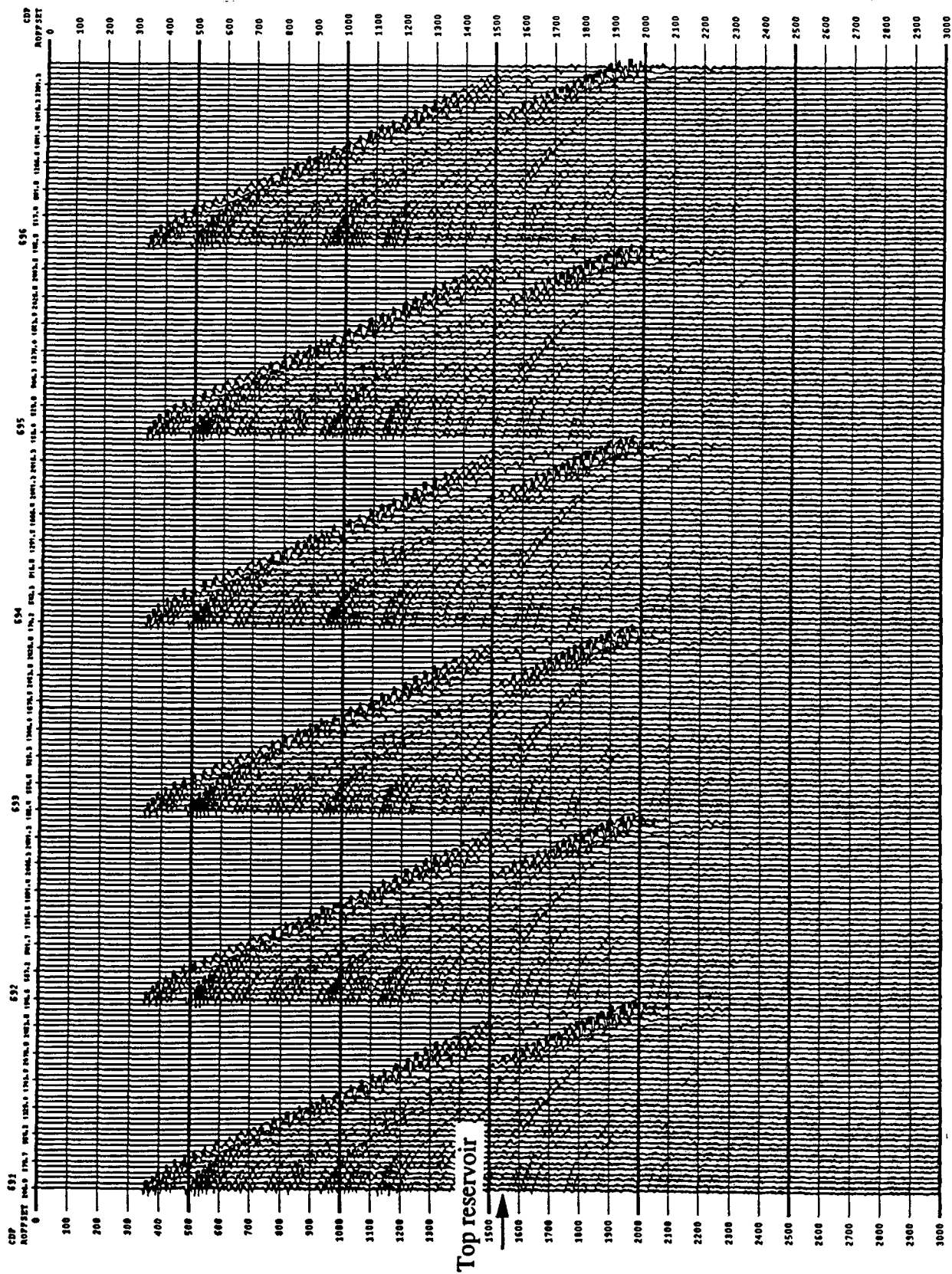


Figure 5.45: CDP gathers in the vicinity of well 31/2-5. Spherical divergence was applied and all traces were scaled by a constant common factor.

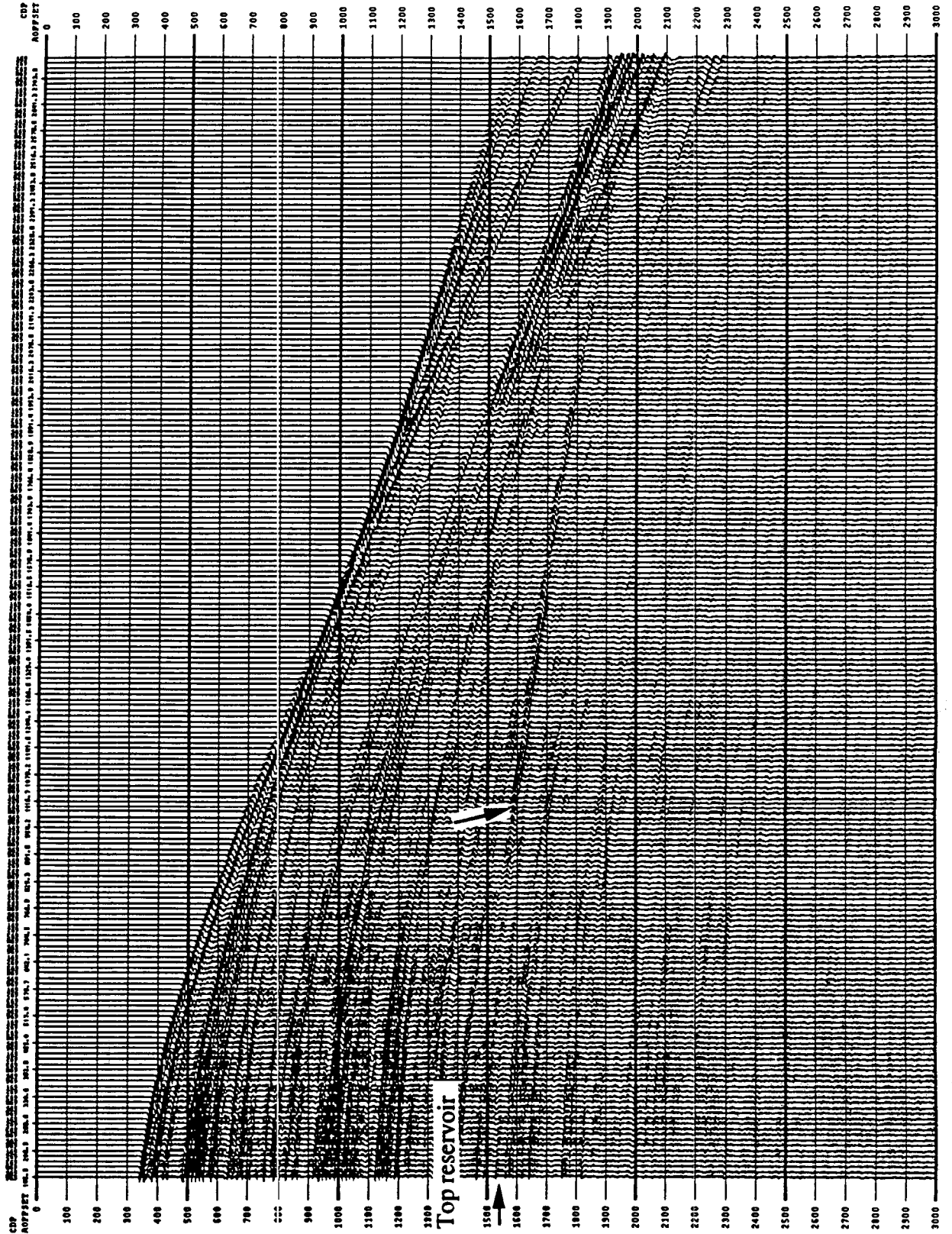


Figure 5.46: CDP supergather in the vicinity of well 31/2-5. Spherical divergence was applied and all traces were scaled by a constant common factor.

The use of AVO can be regarded as a powerful seismic method for extrapolating lithology changes away from well control. Before this method can be used in sensitivity analyses for the interpretation of model responses, two important conditions must be fulfilled:

- Factors influencing reflection coefficients must be identified, separated, and quantified in lithologic terms.
- The quality of the data must be such that AVO variations can be extracted reliably from the seismic data.

The first condition dictates the establishment of a reliable model of the subsurface. Unfortunately, a large number of variations in reservoir properties can give rise to the same, non-unique, AVO response in a reservoir zone. Forward modeling is typically used to investigate the many factors that can influence AVO responses. When iterating over several forward models, it is the accuracy of the geological and petrophysical models that allows for additional constraints on the seismic model, thus reducing the inherent non-unicity in the inversion process.

For the second condition, the seismic data must have a high signal to noise ratio (S/N) and must be carefully processed to ensure that observed AVO responses reflect elastic properties in the subsurface, rather than acquisition or processing artifacts.

(1) Preliminary model

My first step was to obtain some basic knowledge of the usefulness of AVO at Troll. This was in preparation for a more detailed investigation of how AVO techniques can be used to map reservoir quality between wells.

Figure 5.47 shows the model of the overburden that was used in the preliminary analysis. The model was constructed by "hand" blocking from well log data. The sonic and density logs from well 31/2-5 are shown together with the P-wave and

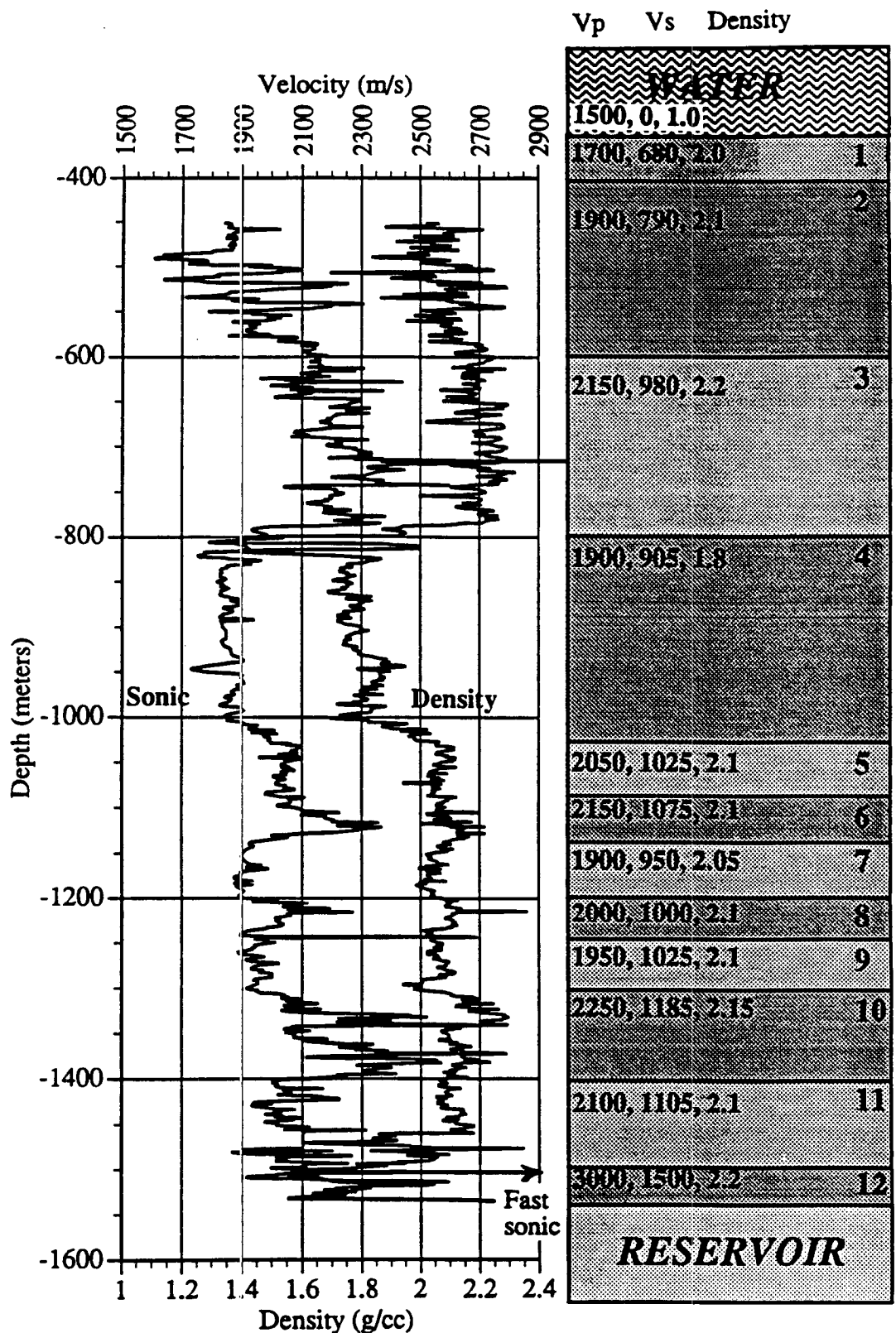


Figure 5.47: Geological model of the overburden used in the preliminary AVO modeling.

S-wave velocities and densities assigned to each layer in the model. For this preliminary model, S-wave velocities in the overburden were estimated based on empirical relationships for V_P/V_S in the different formations. Within the reservoir, beginning at 1536 meters, I use velocities obtained from the core measurement program. I assume the layering to be horizontal and isotropic, and do not consider the effects of intrinsic attenuation. I concentrate on reflections from the top reservoir (1536 m) and the gas/oil contact (GOC at 1578 m). The variations in reflection angle with offset and depth are shown in figure 5.48. Figure 5.49 shows the variations in reflection coefficient with offset for the top reservoir (top figure) and the GOC (bottom figure). In this model, the P-wave and S-wave velocities for the gas zone are 2300 m/s and 1500 m/s, respectively, while the corresponding velocities for the oil zone are 2700 m/s and 1300 m/s. Note that, as indicated previously in layer 12 of figure 5.47, the seal being a marl, it has large P-wave and S-wave velocities. Figure 5.49 shows an expected strong increase in reflected amplitude with increasing offset from both the top reservoir and the gas oil contacts. The relatively high velocities in the reservoir seal causes a negative reflection from the top reservoir. Spherical divergence effects are included in the curves shown.

Considerations of anisotropy

Anisotropy in the seal and overburden

Wright (1987) demonstrated that anisotropy can severely alter AVO responses with respect to the isotropic case. Kanestrom & Stordal (1991) established a transversely isotropic model of the overburden, based on well data and refracted data from a long cable seismic experiment at Troll. They found the ratio between horizontal and vertical P-wave velocities to be 1.10-1.15. Figure 5.50 (from Kanestrom & Stordal, 1991) shows a CDP gather at Troll. The vertical axis is reduced traveltimes ($t = t[\text{observed}] - \text{offset}/v$, where $v = 2100$ m/s) in seconds, and the horizontal axis is source-to-receiver offset in km. Computed arrival times for a refracted P-wave based on isotropic model and transversely isotropic models are shown at the top of the

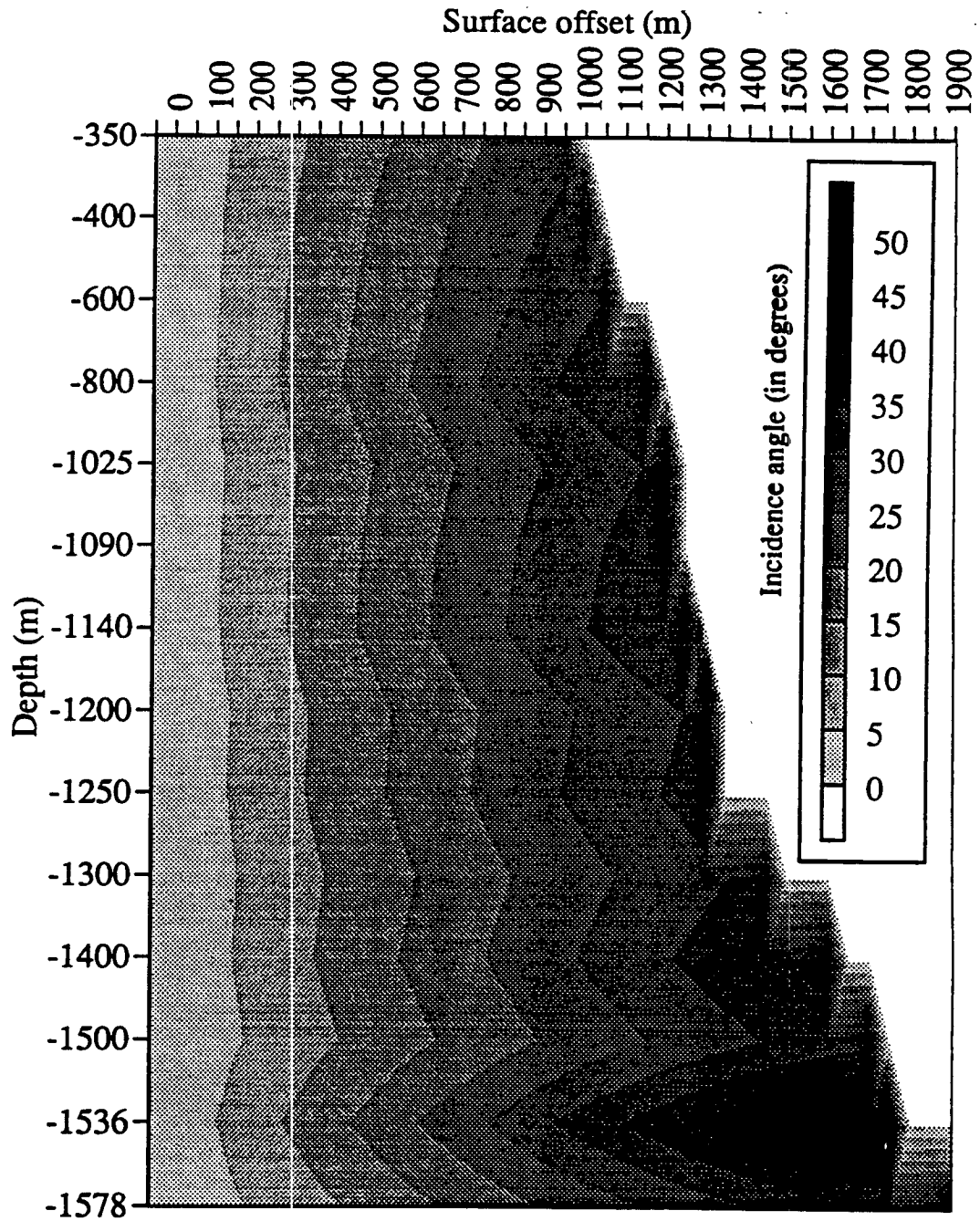


Figure 5.48: Variations in reflection angle with depth and surface offset, based on the isotropic velocity model of figure 5.47. The vertical scale is non linear.

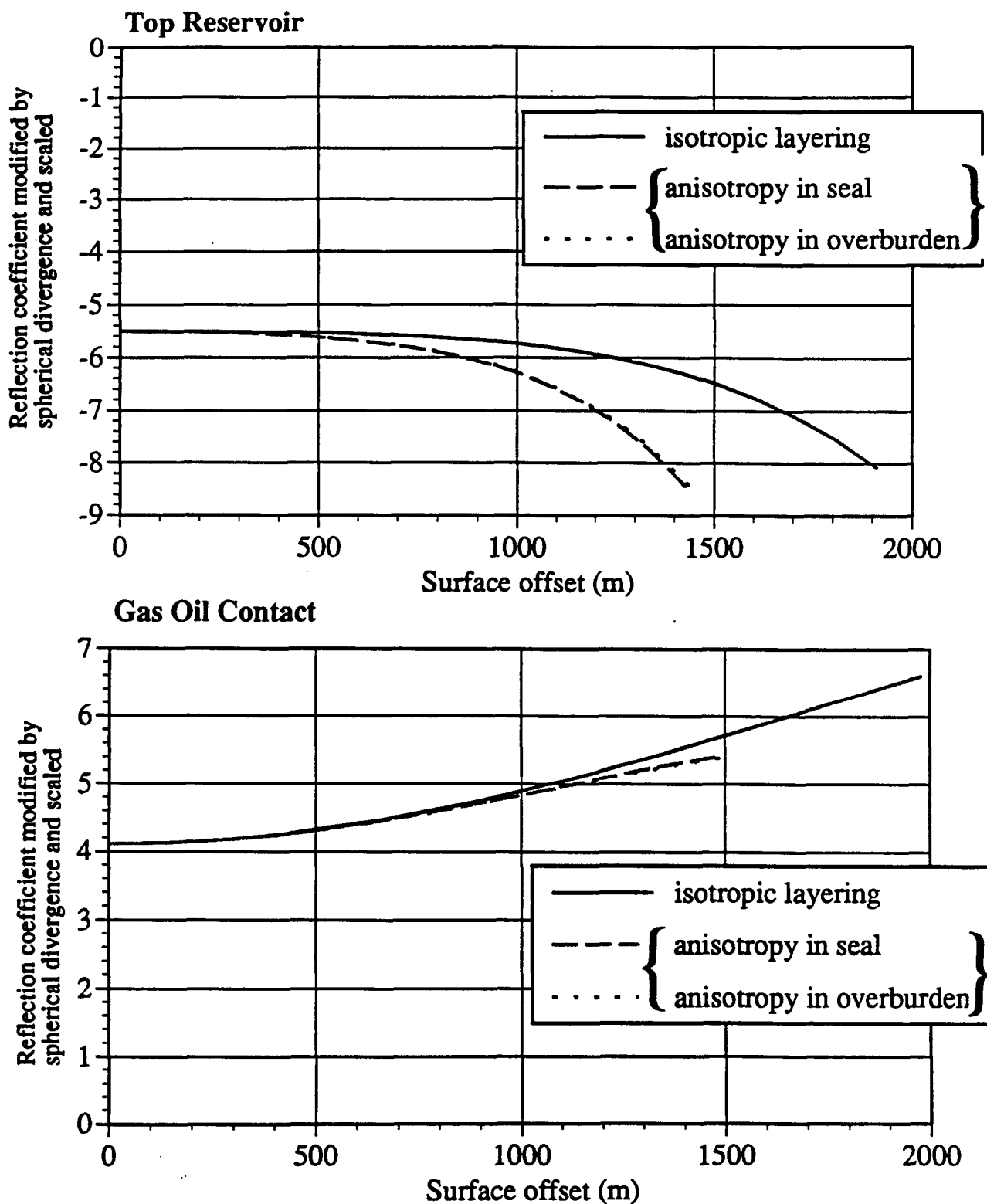


Figure 5.49: AV0 responses from the top of the reservoir and from the GOC for different models of the overburden.

figure. A reflected event with a zero offset traveltime of 1.38 s can be compared with modeled traveltimes for the isotropic and a transversely isotropic models. Good agreement is obtained between observed and computed traveltimes for the transversely isotropic model. At large offsets the discrepancy between the isotropic and transversely isotropic model shows differences in the arrival times of more than 100 ms.

I have adopted Kanestrom & Stordal's P-wave anisotropy parameters to investigate how the AVO response is affected by transverse isotropy in the overburden. Reflections from the top reservoir and the gas oil contact are computed by introducing a P-wave and S-wave anisotropy ($\epsilon_P = \frac{V_{P\text{-vertical}} - V_{P\text{-horizontal}}}{V_{P\text{-horizontal}}}$ and $\epsilon_S = \frac{V_{S\text{-45}} - V_{S\text{-vertical}}}{V_{S\text{-vertical}}}$, after Banik, 1987) of 0.1 in layers 4-11 (figure 5.47), ϵ_P and ϵ_S equal to 0.15 / 0.1 in layer 3, and 0.2 / 0.1 in layer 12 (the seal). The response from this model is labeled anisotropy in overburden on figure 5.49. Another response in figure 5.49 is obtained by assuming that only the seal (layer 13) is transversely isotropic. As expected, the curves show that anisotropy in the overburden or seal has little effect on the AVO response from the gas oil contact. On the other hand, anisotropy in the seal gives rise to a stronger increase in reflected amplitude with offset from the top of the reservoir. In summary, anisotropy in the overburden has no effect on the AVO response from the top reservoir, but anisotropy in the seal itself does affect the AVO response.

Anisotropy in the reservoir

So far, I have assumed that the reservoir behaves isotropically. This seemed reasonable, since the Troll sands themselves were considered isotropic at the micro scale. However, the presence of thin calcite cemented zones complicates the picture at seismic scales. Figure 5.51 shows a model of the gas zone in well 31/2-5, as obtained from core descriptions with sonic and density logs plotted to the left of the model. The calcite layers have a thickness of up to 3 meters. It is known that a system of periodically layered media may introduce transverse isotropy if the thickness of the individual layers are small compared to the seismic wavelength of interest. Carcione

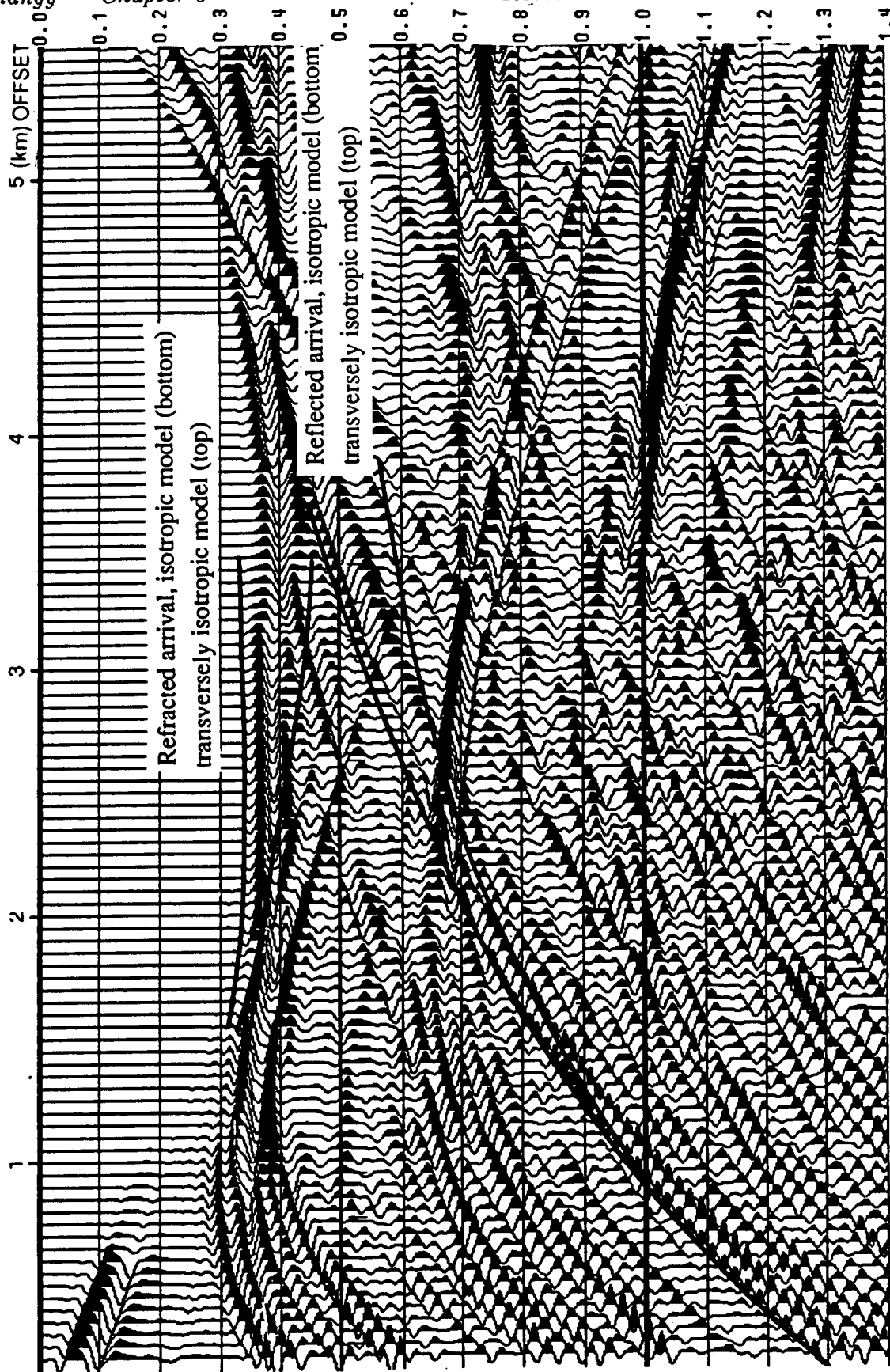


Figure 5.50: Reduced travel time CDP gather at well 31/2-5. Modeled arrival times for refracted and reflected arrivals in the isotropic and transversely isotropic cases are superimposed on the actual data (after Kanestrom & Stordal, 1991).

et al. (1991) investigated the conditions for which this situation may occur, and found that dominant wavelengths of 5 or 6 times greater than layer thicknesses would suffice. As seen in chapter 4, the dominant frequency in the 3-D seismic data at the reservoir level is approximately 50 Hz, which is more than 10 times the average thickness of the layers in figure 5.51. The Backus formulations (1962) were used in their generalized form (White, 1965) to compute the elastic parameters of a transversely isotropic equivalent replacement layer for the thin beds (see details in chapter 3). This resulted in anisotropy parameters ϵ_P and ϵ_S equal to 0.1083 and 0.04, respectively, for the layer model shown in figure 5.51. A polar plot of the corresponding P-wave and S-wave phase velocities is shown in figure 5.52 for this transversely isotropic replacement layer. Figure 5.53 shows the AVO responses from the top reservoir and the gas oil contact for the transversely isotropic gas zone where the seal is either isotropic or anisotropic. The main effect of the layer induced anisotropy is to reduce the reflection coefficients, from both the top reservoir and the gas oil contact interfaces.

The prediction of clean versus micaceous sands is an important goal in the Troll West Oil Province, because the presence of mica restricts fluid flow in the reservoir. Because oil is the primary target for production in the Troll West Oil Province, I will now examine the effects of mica content in the oil zone on expected AVO responses. The mica content in the gas zone will be held constant. From figure 5.23, clean oil sands correspond to P-wave and S-wave velocities of 2600 m/s and 1250 m/s, respectively, while a high mica content increases the corresponding velocities to 2900 m/s and 1500 m/s, respectively. AVO responses for these two scenarios can be viewed in figure 5.54, in the case of both an isotropic and a transversely isotropic gas zone. In both cases the reflection coefficients and AVO behaviors change due to the mica content, while transverse isotropy does not affect the relative AVO responses much. This demonstrates the importance of being able to separate the individual factors that influence AVO responses, and shows possible non-uniqueness problems for inversion.

So far, I have shown that anisotropy is important only if it occurs in the layer

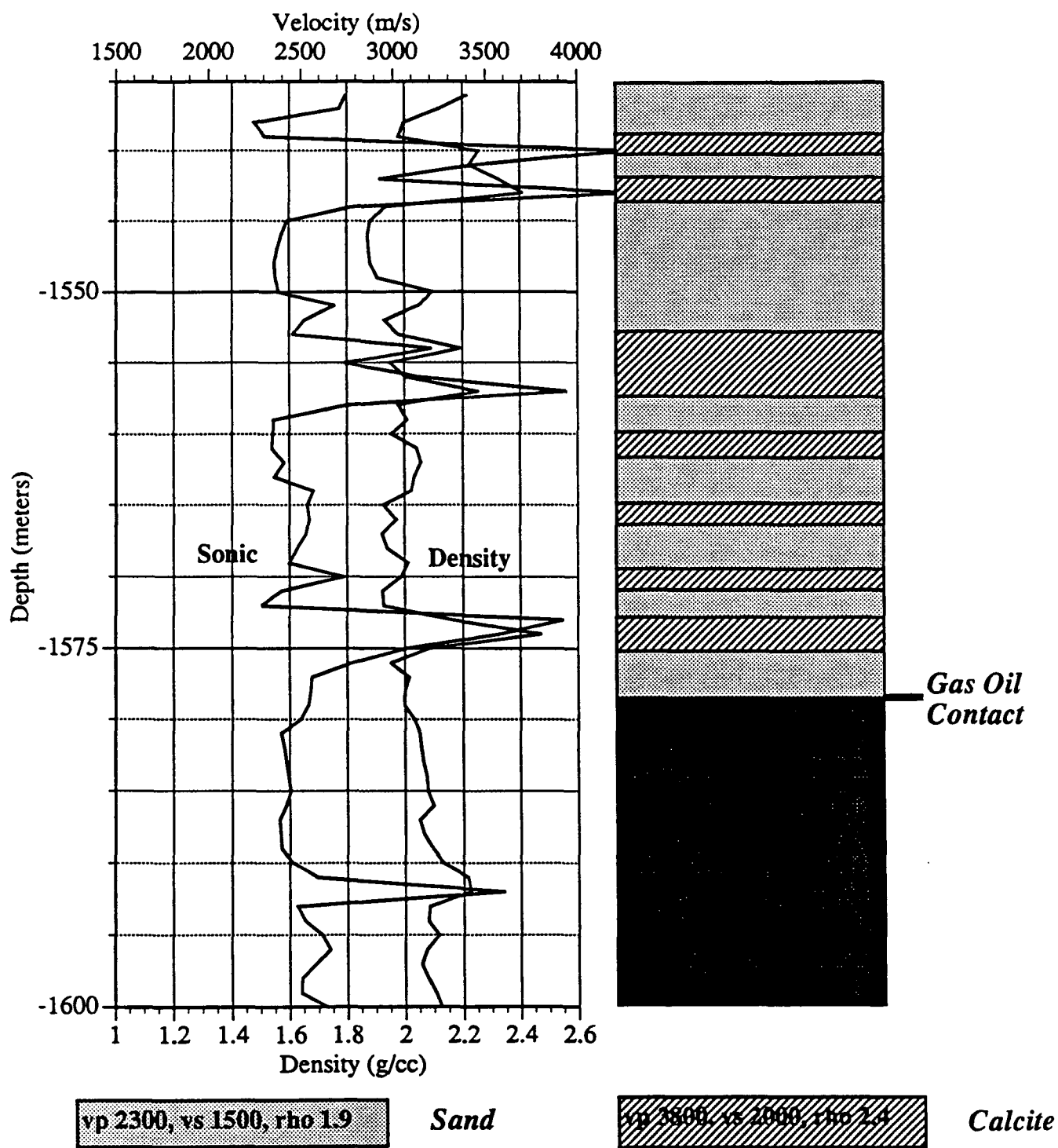


Figure 5.51: Preliminary model of the reservoir zone, based on well 31/2-5. Layer induced transverse isotropy is introduced in the gas zone by alternating low velocity sand layers and high velocity calcite layers.

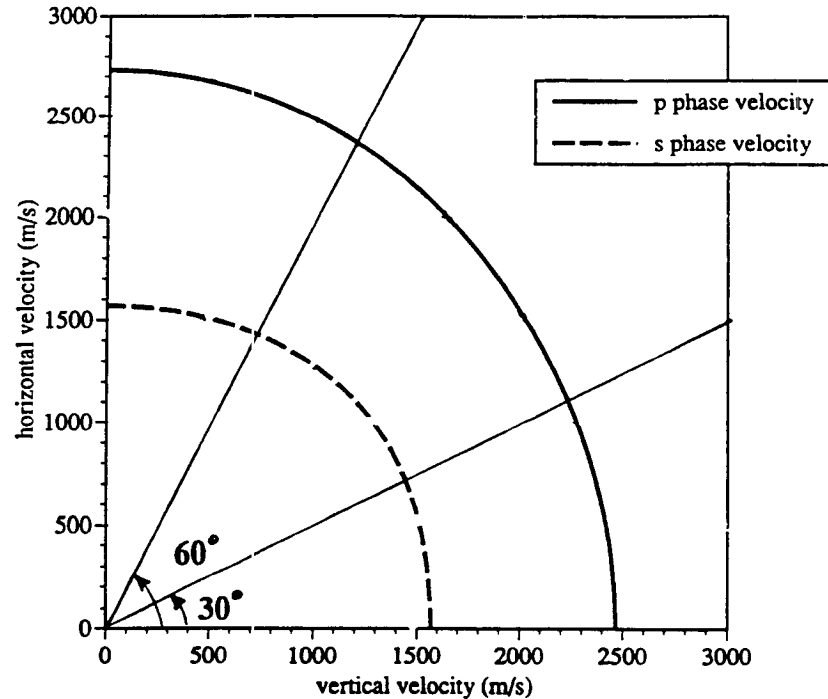


Figure 5.52: Phase velocities in the transversely isotropic gas zone, produced by layer induced anisotropy.

immediately above or below the interface of interest. One may conclude the following:

(1) Above the interface: If the seal is anisotropic, this can lead to a stronger increase in AVO. At well 31/2-5, the seal is thin and there is a question as to what extent it can be fully "seen" by seismic waves.

(2) Below the interface: Layer induced transverse isotropy in the reservoir zone may marginally increase the reflection coefficients from the top reservoir and the gas/oil contact, particularly at larger incidence angles. This effect may be present if a sufficient number of high velocity calcite cemented layers occur in the reservoir. However, the effect of calcite-induced transverse isotropy on AVO is small. On the other hand, large concentrations of mica in the oil zone will influence the reflection coefficients, and are expected to influence the relative shape of the AVO response curve.

2) Building of a detailed geological/petrophysical reservoir model

I now build more accurate models to determine the parameters that influence AVO in Sognefjord sands, and whether AVO analysis is feasible at Troll West.

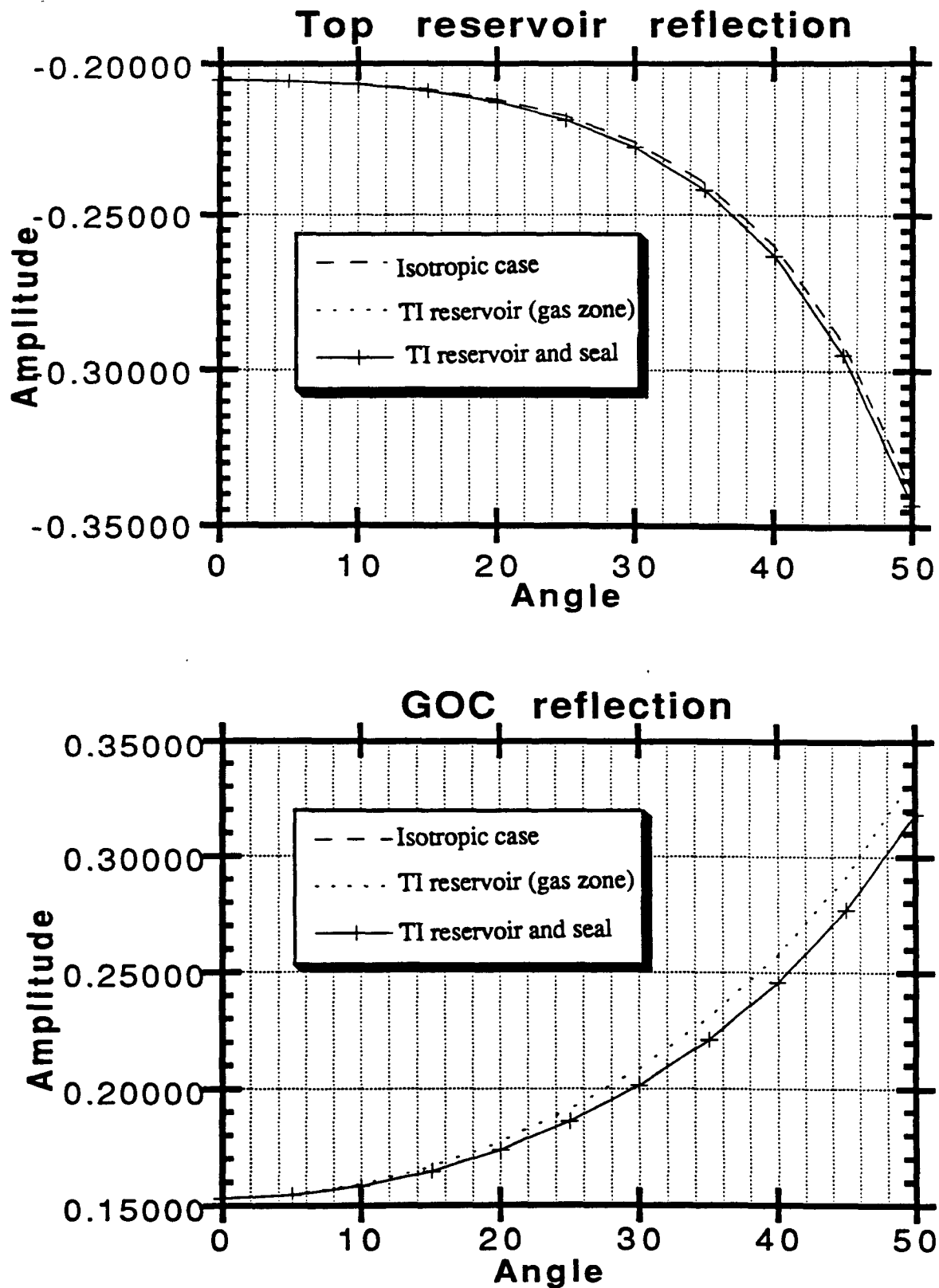


Figure 5.53: AVO responses from the top of the reservoir and from the GOC for various models of the gas zone and the seal.

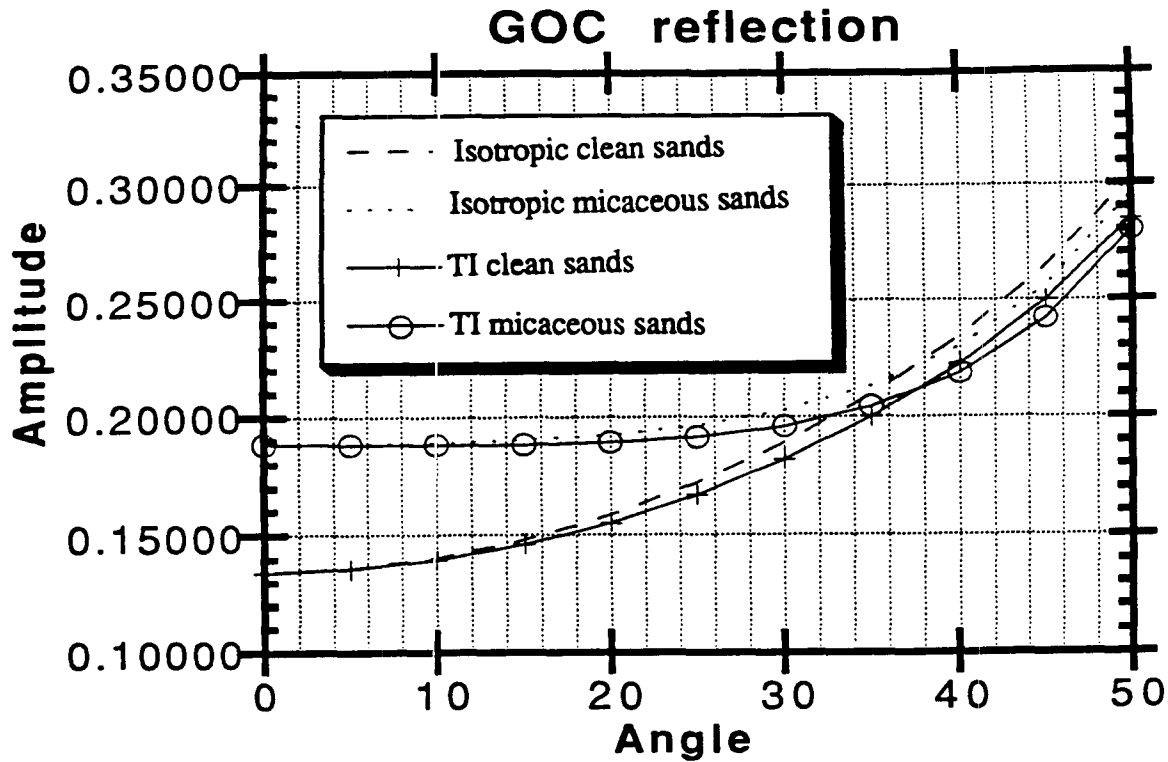


Figure 5.54: AVO responses from the GOC for an isotropic or transversely isotropic gas zone, and for a clean or micaceous oil zone.

Several steps were implemented to build a complex "more realistic" geological model of the earth at well 31/2-5, and to assign appropriate petrophysical properties to model layers. These include:

- Automatic log blocking, based on impedance contrasts
- Averaging porosity, density, and sonic within each layer
- Calculating missing properties from elemental compositions
- Adjusting the properties of the shallowest layers through iterative guesses, due to the fact that logs start at 451m depth and unfortunately, do not reach the ocean bottom floor. These are important, because they generate long period water bottom multiples and their associated peg-legs that interfere with primary reflections within the reservoir zone (figure 5.44b). Unfortunately, it is almost impossible to obtain the properties of these shallow layers correctly. It is nevertheless worthwhile to approximate them.

The model

The final model consists of 199 layers from sea level down to a depth of 2470 m. The layers are, on average, thinner than one tenth of a wavelength, and no Backus-type averaging was necessary. Figure 5.55 represents the detailed model in the reservoir zone. As expected, it agrees with well-logs and the stratigraphic column shown in appendix B-4, which are plotted at the same scale. The top of the reservoir was simulated at a depth of 1537.5 m, with a seal consisting of a thin marl. Several thin calcite layers are included within the reservoir zone. The GOC (1580 m) and the OWC (1601.5 m) are also featured. Note that, because the impedance log was blocked automatically based on a threshold of impedance contrasts, and because the GOC has a relatively small impedance contrast compared to the rest of the sedimentary column, the model does not account for the small bulk shift in compressional wave velocities observed on the sonic, or that in the density log at the GOC. The same observation can be made for the OWC. In other words, the model does not account for the subtle change in impedance at the GOC nor the OWC. On the other hand, because S-wave velocities were generated empirically, the model does account for a change in S-wave velocity at the GOC. In this model, the top of the Fensfjord occurs at 1694.5 m depth.

Single interface coefficients

Because the model doesn't "see" a clear GOC or the OWC, I will concentrate on reflections from the top of the reservoir only. Single interface reflection coefficients from the top of the reservoir are similar to those discussed in the previous section (preliminary model).

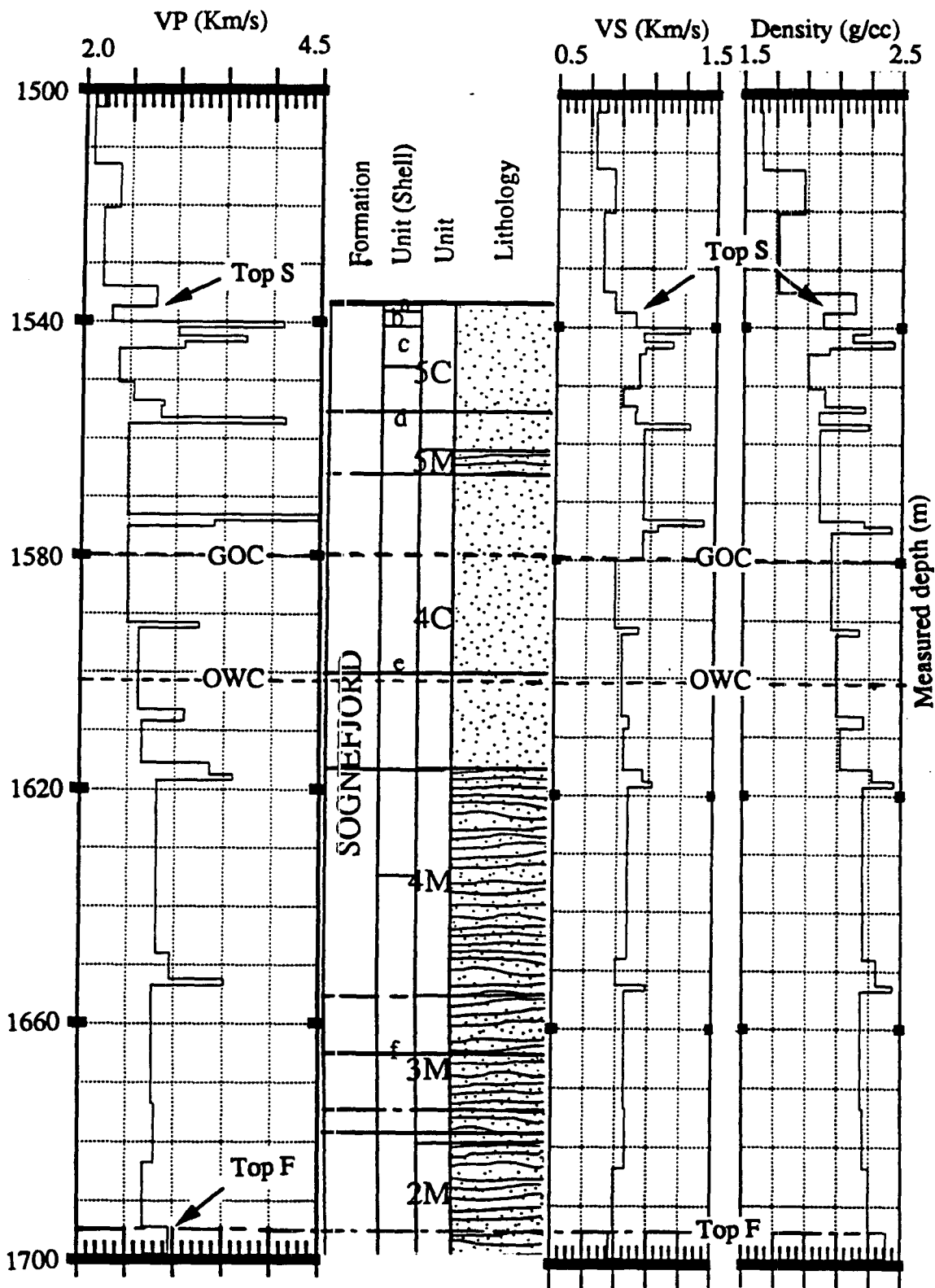


Figure 5.55: Close-up on the reservoir model. The model compares well to the log data and stratigraphic column shown in Appendix B-4 and is plotted at the same scale.

Effective reflection coefficients, generation of synthetic seismograms
and model-based interpretation

In all of the subsequent modeling work, I assume a homogeneous earth with flat layers. The flat layer assumption is reasonable at Troll West and leads to simplifications. For example, when the assumption holds, shot profiles are equivalent to CDP gathers. In the following, I therefore compare synthetic shot profiles, which are equivalent to synthetic CDP gathers, with real CDP gathers.

In generating synthetic seismograms, an explosive source was simulated at a depth of 4 m and a hydrophone cable was hypothesized at a depth of 6 m. The near offset is placed at 141 m, with a group interval of 12.5 m. These parameters reflect the actual recording conditions during the 1989 survey. Because of limitations in computer memory, I used a total of 201 hydrophones groups only, yielding a maximum offset of 2641 m for the synthetic seismic gathers. As we will see, the actual seismic CDP supergathers under investigation have a near offset of 145.9 m, which includes a small lateral offset of the cable from the center of the ship, and consist of a total of 240 traces separated by 12.5 m, for a maximum offset of 3129 m. For comparisons between model and live data, I used a cut-off in offset of approximately 1750m. Additionally, all both real and synthetic seismic gathers underwent the same processing sequence, including: spherical divergence correction, statics, and F-K "demultiple" filtering.

Five key model responses were investigated at well 31/2-5, using full waveform modeling including primaries, multiples and P-S converted modes:

- (1) Well 31/2-5, under "in-situ" conditions
- (2) Replacement of clean sands by micaceous sands (equivalent to an decrease in porosity)
- (3) Replacement of micaceous sands by clean sands (equivalent to an increase in porosity)
- (4) Replacement of calcite layers by clean sand layers

- (5) Replacement of gas zone by water zone

An additional (6th) response was modeled for a hypothetical well to the east of well 31/2-5 along the same dip line, in the Troll West Gas Province.

A 2-D dip-line was shot through well 31/2-5. The seismic brute stack is shown in figure 5.56 and helps identify the target zone of interest. It is similar to line 328 of the 3-D survey, shown in figure 4.6 of chapter 4. The CDP numbering convention adopted here differs from the numbering of "traces" in the 3-D survey of chapter 4. This difference in numbering convention is due to the shooting geometry of the 3-D survey, which involved a dual source, dual streamer configuration. To obtain CDP numbers consistent with the "trace" numbers of chapter 4, roughly multiply the new (2-D) CDP number of chapter 5 by a factor of two. For example, well 31/2-5 occurs approximately at CDP 355 (more exactly, at trace 692 on 3-D). The location of a fictitious well to the east, in the westernmost horst block of the Troll West Gas Province occurs around CDP 691 (trace 1382 on 3-D). This horst block represents the southern extension of the block where well 31/2-12 was drilled. Both CDP locations are shown by an arrow in figure 5.56.

(1) In-situ conditions around well 31/2-5. Figure 5.57 shows the full waveform synthetic CDP gather, and figure 5.58 shows the corresponding processed real seismic data. As shown, the match for reflections from the top of the reservoir is poor. Note the absence of a clean AVO increase from the top of the reservoir (gas) zone at approximately 1540 ms on the CDP supergathers. This observation can be explained with simple concepts. At well 31/2-5, the K-T boundary occurs as a prominent reflector at approximately 1532 m. On the other hand, the top of the Sognefjord, and therefore the top of the gas, occurs at 1536 m. This implies a small depth difference of only 4 meters between the strong K-T reflector and the top of the reservoir. Conventional seismic methods can resolve thin beds of up to a quarter wavelength ($\frac{\lambda}{4}$). For a dominant frequency of 50 Hz, and a velocity of 2000 m/s, this implies a resolution limit of 10 m or so. We are well below the resolution limit of conventional seismic, and the reflection from the top of the gas destructively

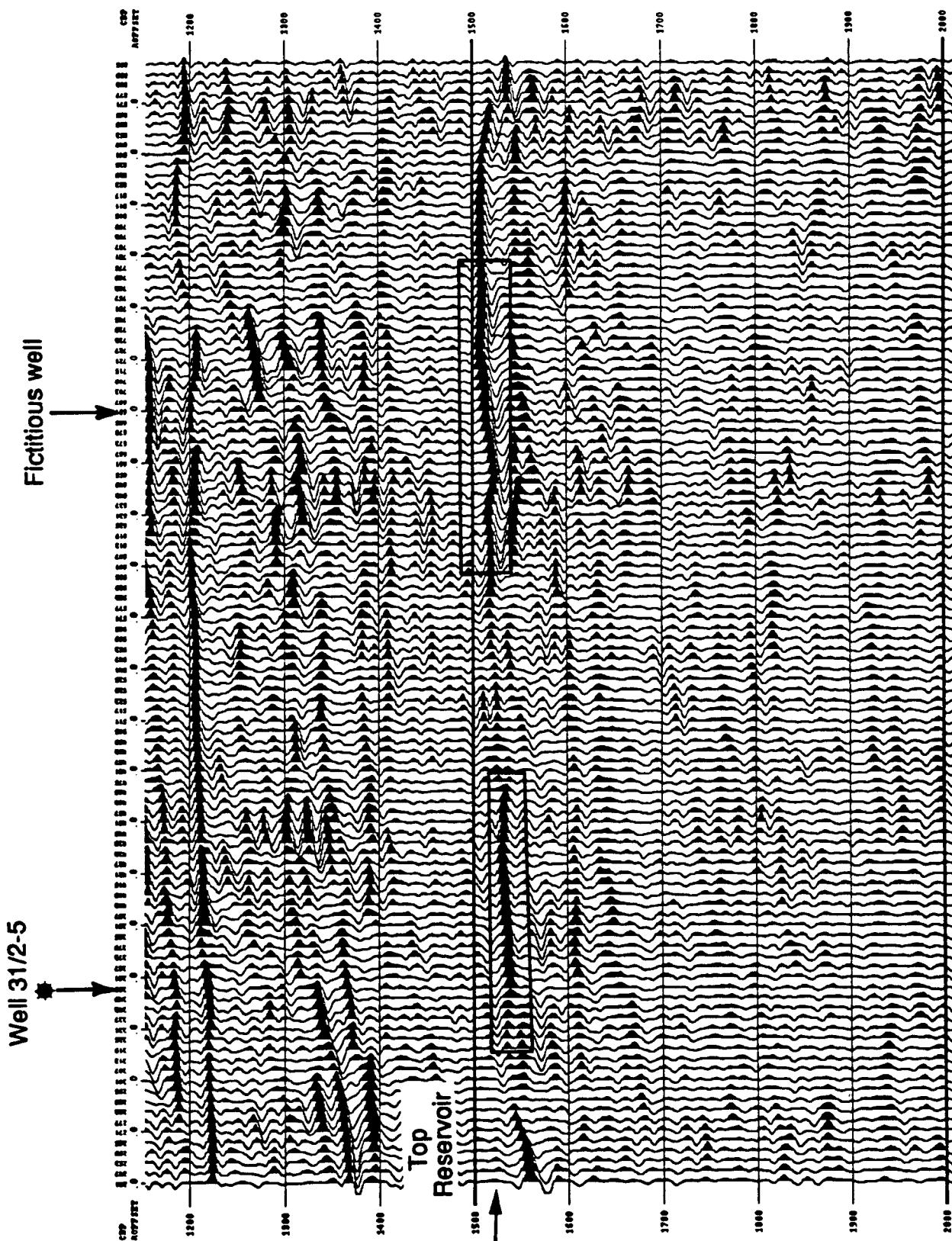


Figure 5.56: Brute stack, after processing steps including sort, supergather binning, spherical divergence correction, statics and F-K "demultiple" filtering. The two locations outlined will be studied and modeled in detail.

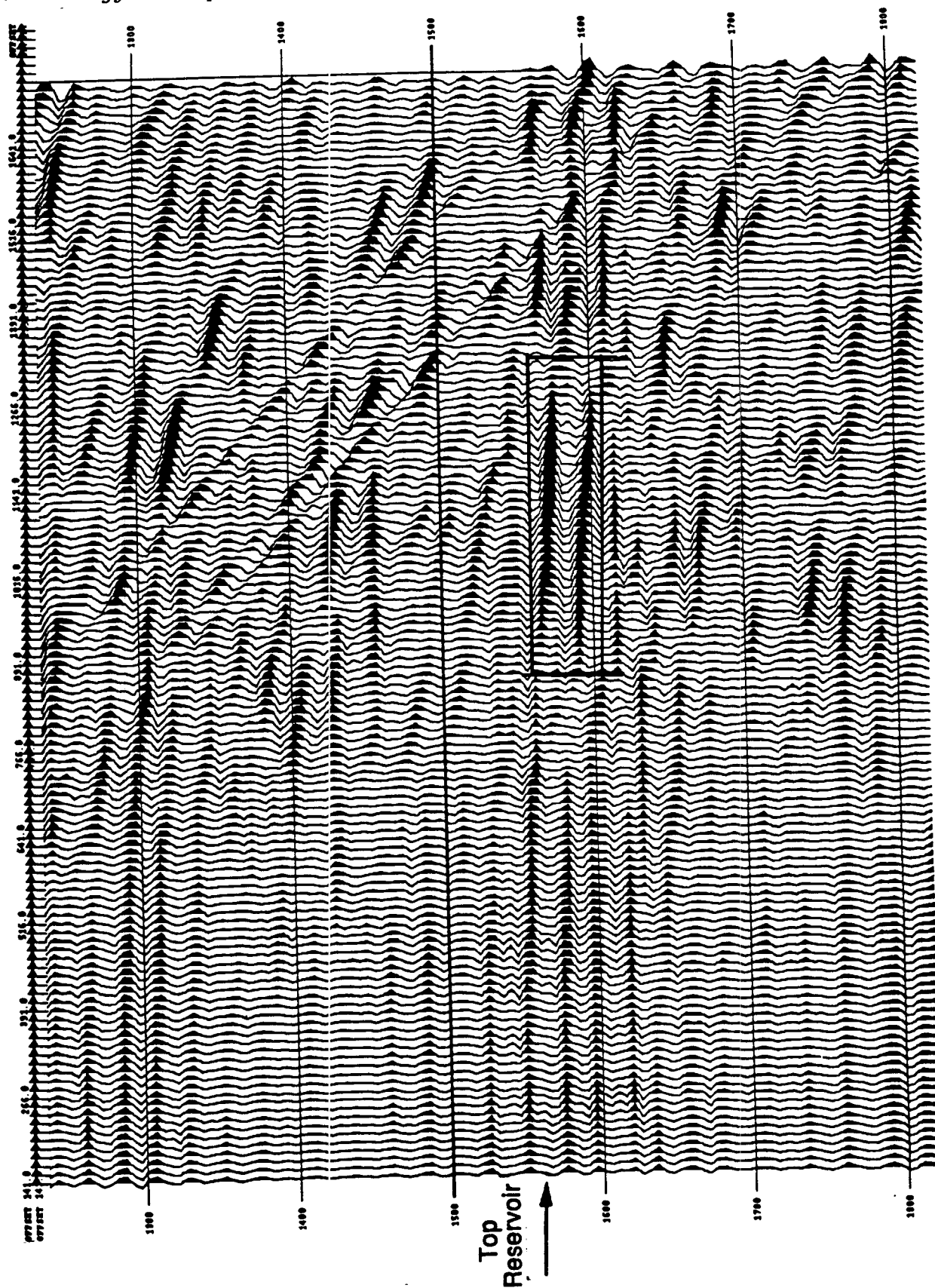


Figure 5.57: Full waveform seismic synthetic CDP gather at well 31/2-5; close-up on the reservoir zone.



Figure 5.58: Seismic CDP supergather within the vicinity of well 31/2-5 (approximately CDP 355); close-up on the reservoir zone.

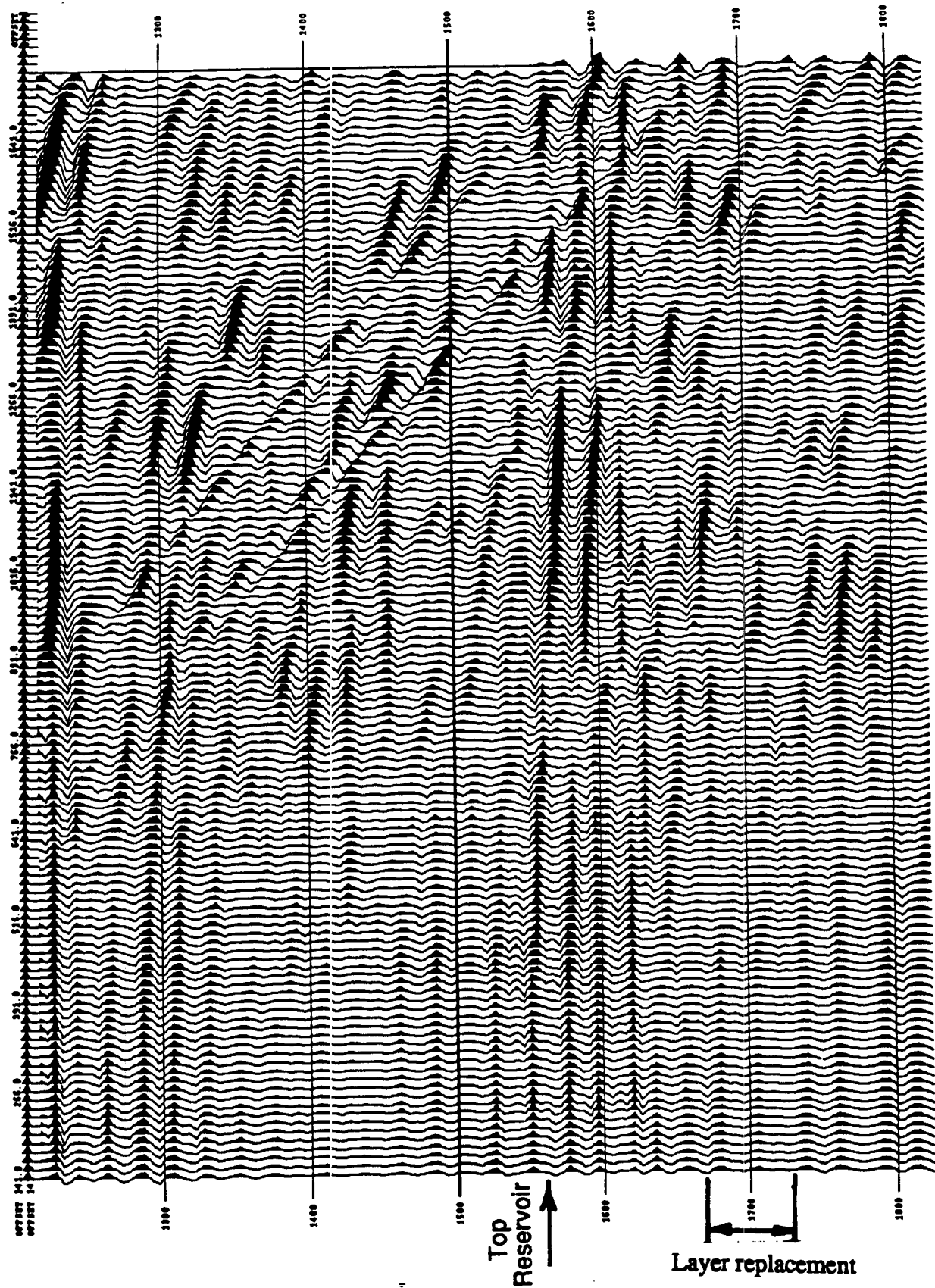


Figure 5.59: Full waveform seismic synthetic CDP gather at well 31/2-5 with no micaceous layers present within the Sognefjord.

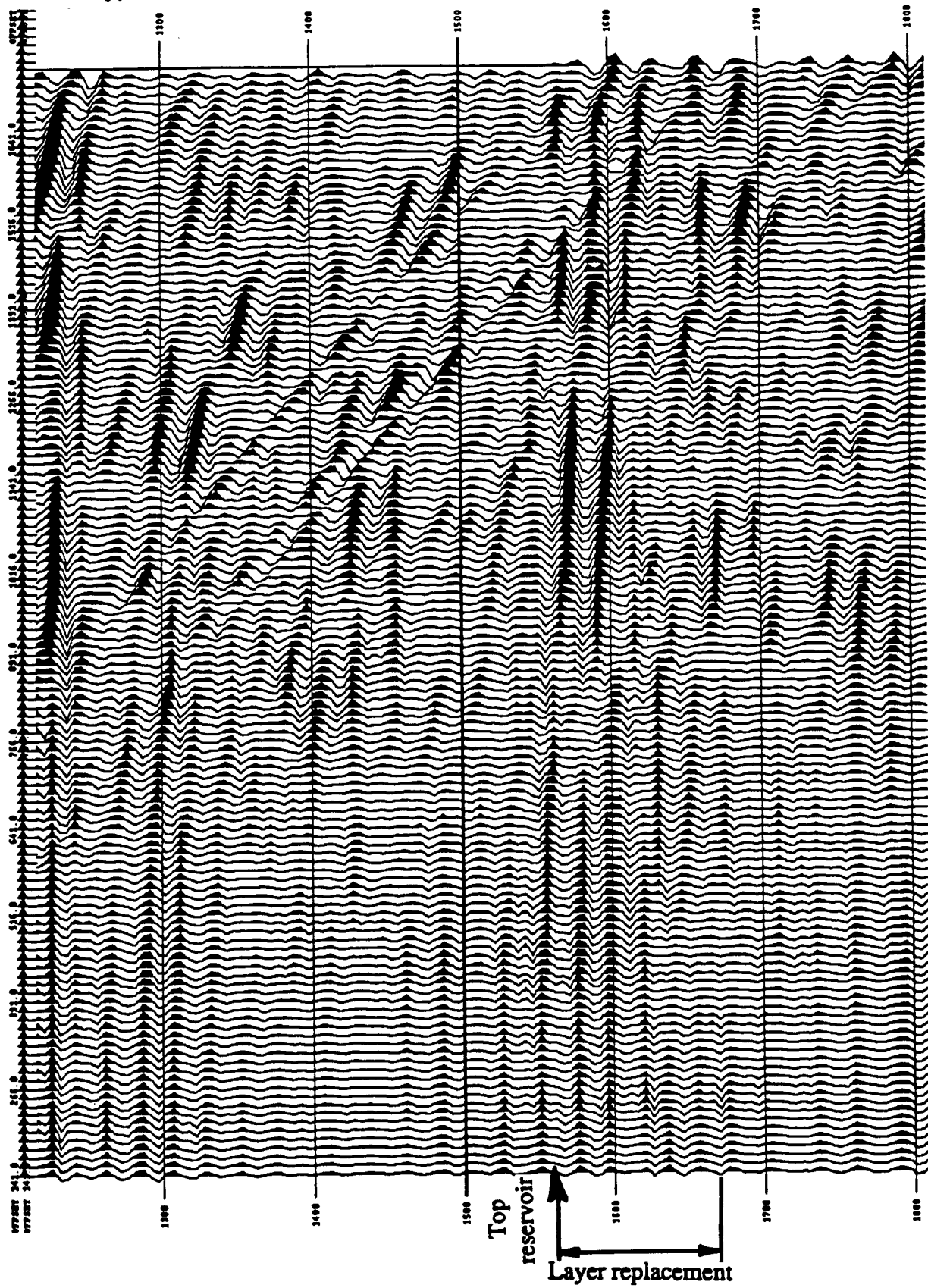


Figure 5.60: Full waveform seismic synthetic CDP gather at well 31/2-5 with only micaceous layers present within the Sognefjord.

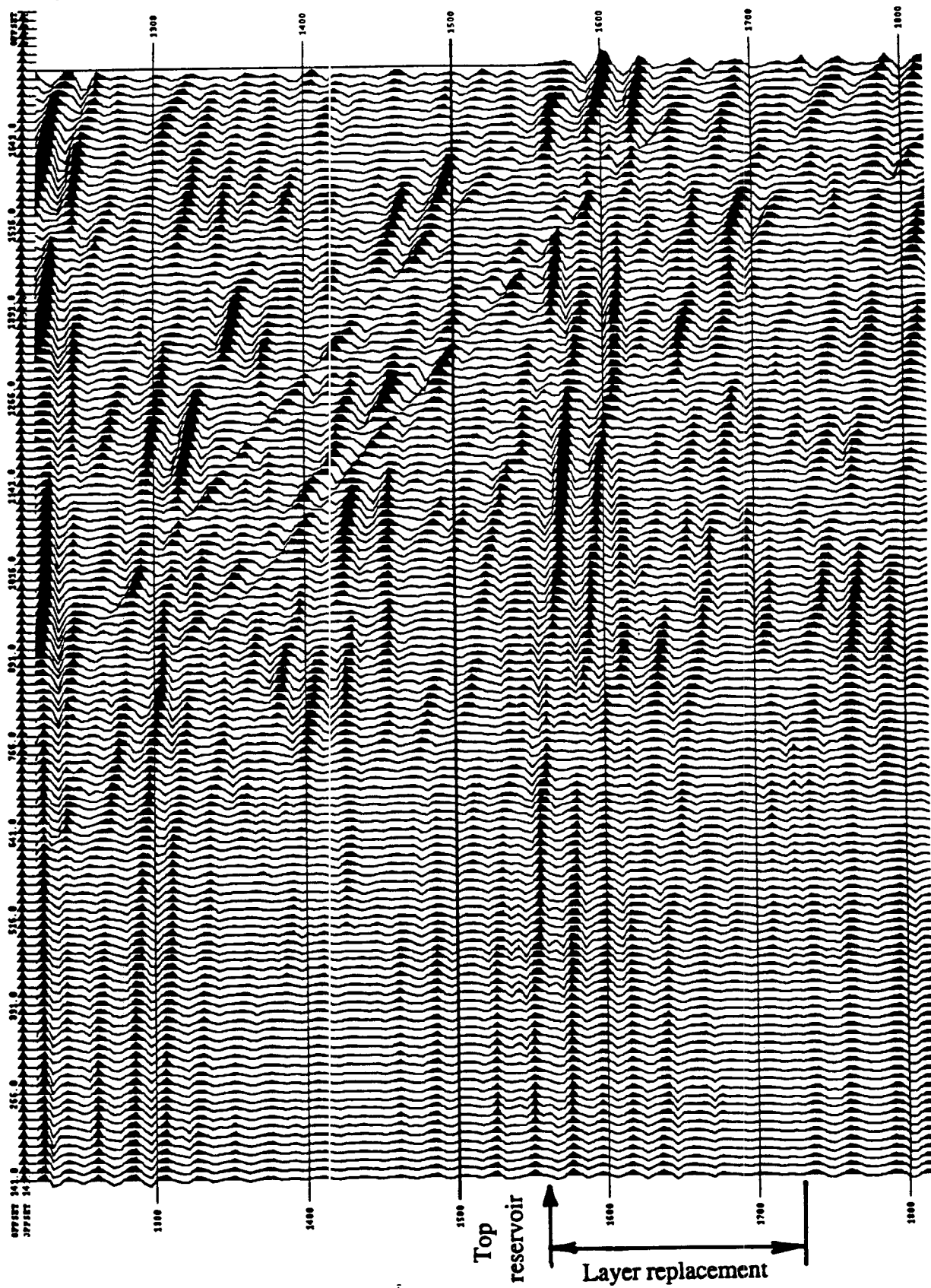


Figure 5.61: Full waveform seismic synthetic CDP gather at well 31/2-5 with no calcite layers present.

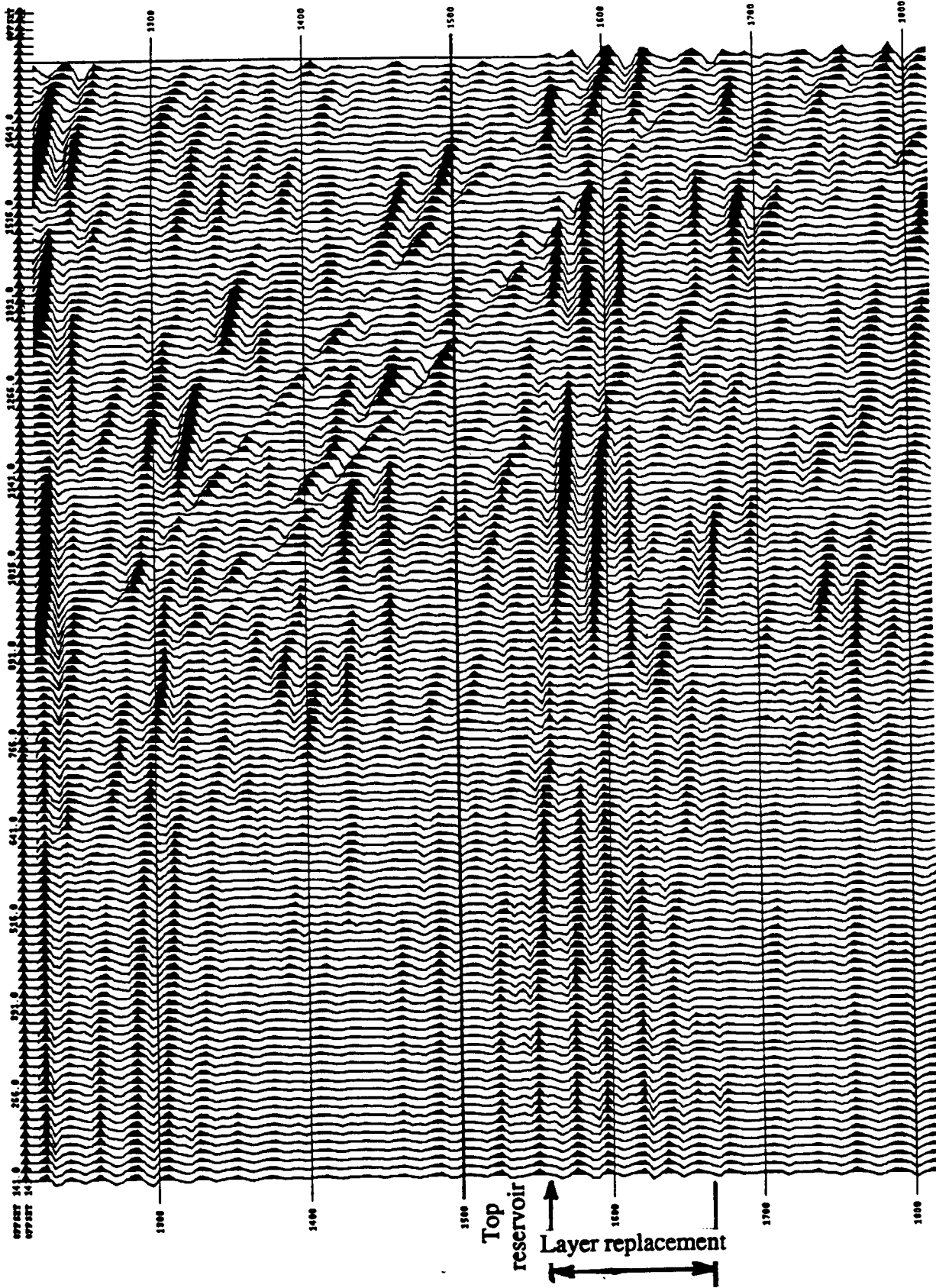


Figure 5.62: Full waveform seismic synthetic CDP gather at well 31/2-5 with no gas present.

of reflectors at 1680 ms.

(5) Replacement of gas zone by water zone. When there is no gas present within the Sognefjord, the response illustrated in figure 5.62 is to be expected. The replacement of gas by water occurs in the gas zone, from 1550 ms to 1670 ms. Comparison with figure 5.57 shows small differences. In particular, note slightly lower frequencies and amplitudes in the near to mid offset amplitude build-up at about 1630 ms, and slightly stronger reflections at about 1650 ms.

(6) Fictitious well to the east. Next, I concentrate on the area corresponding to the easternmost part the line of figure 5.56. Note from figure 5.56, that contrary to the location of well 31/2-5 (CDP 355) which shows no bright spot at the top of the gas zone, this new location (CDP 691) presents a strong negative reflection, just below the K-T boundary. A CDP supergather was extracted around CDP 691 and is shown in figure 5.63. Note the strong increase in AVO, which may be associated with the presence of gas. Unfortunately, there is no well present in that part of the block. Note however, that well 31/2-12, which is located further north in the same fault block, has a large gas column. Because the present CDP location (CDP 691) is contained within the southern extension of the block on which well 31/2-12 was drilled, I built a simple lithologic model from the combination of data from wells 31/2-5 and 31/2-12. In particular, the model used was a modification of the one shown in figure 5.55, with two additional layers, 6M and 6C of 10 m total thickness at the top of the Sognefjord in accordance with well 31/2-12 (see Appendix B-1). The thickness of the marly unit serving as the seal was also increased by 7.5 m in accordance with chapter 4, table 4.4. The relative thicknesses of 2 shallower layers were also adjusted. A full waveform synthetic CDP gather was generated using the same acquisition geometries as previously and is shown in figure 5.64. Note that this synthetic gather shows a strong AVO increase and agrees with the observed behavior at the corresponding real CDP supergather shown in figure 5.63.

interferes with that from the K-T boundary. In fact, it appears to be drowned-out by that strong reflector. This is apparent in the brute stack of figure 5.56 and in the CDP supergather of figure 5.58. In conclusion, the presence of gas may still be detected at well 31/2-5, but it is characterized by a subtle pattern of amplitude interference between the K-T boundary and the gas reflection at the top of the reservoir, rather than a strong AVO increase.

(2+3) Effects of changes in mica content inferred from porosity variations. Several empirical relationships have been suggested in the past to describe the dependence of velocity on porosity. The two best known are the Wyllie time average equation (Wyllie et al., 1956) and the Raymer equation (Raymer et al., 1980). However, as pointed-out previously, equations that incorporate only porosity terms cannot accurately describe velocities in all porous rocks. Therefore, when establishing porosity changes within the Sognefjord sands, I used the results of the core measurement program. Figures 5.59 and 5.60 show the expected seismic responses of pure clean sands or pure micaceous sands, respectively, for the Sognefjord interval. In figure 5.59, the time interval from 1670 ms to 1730 ms corresponds to the location where clean sands were substituted for micaceous sands. When comparing to the original response of figure 5.57, note the presence of slightly stronger, and sometimes new subtle low amplitude reflectors. In figure 5.60, the time interval from 1560 ms to 1670 ms corresponds to the location where micaceous sands have been substituted for clean sands. The net effect is to give rise to slightly larger amplitudes in existing reflections at near offsets, specially around 1650 ms.

(4) Replacement of calcite layers. Figure 5.61 shows the full waveform seismic synthetic CDP gather after the the calcite layers shown in the reservoir model in figure 5.55 have been replaced by sand. This replacement occurs throughout a time interval from 1550 ms to 1730 ms, corresponding to the Sognefjord Formation. Note the following subtle changes in reflection character: weaker reflections at 1600 ms, the absence of near to mid offset amplitude build-up at about 1630 ms, thus reinforcing the amplitude build-up from mid to far offset at about 1630 ms, and the weakening

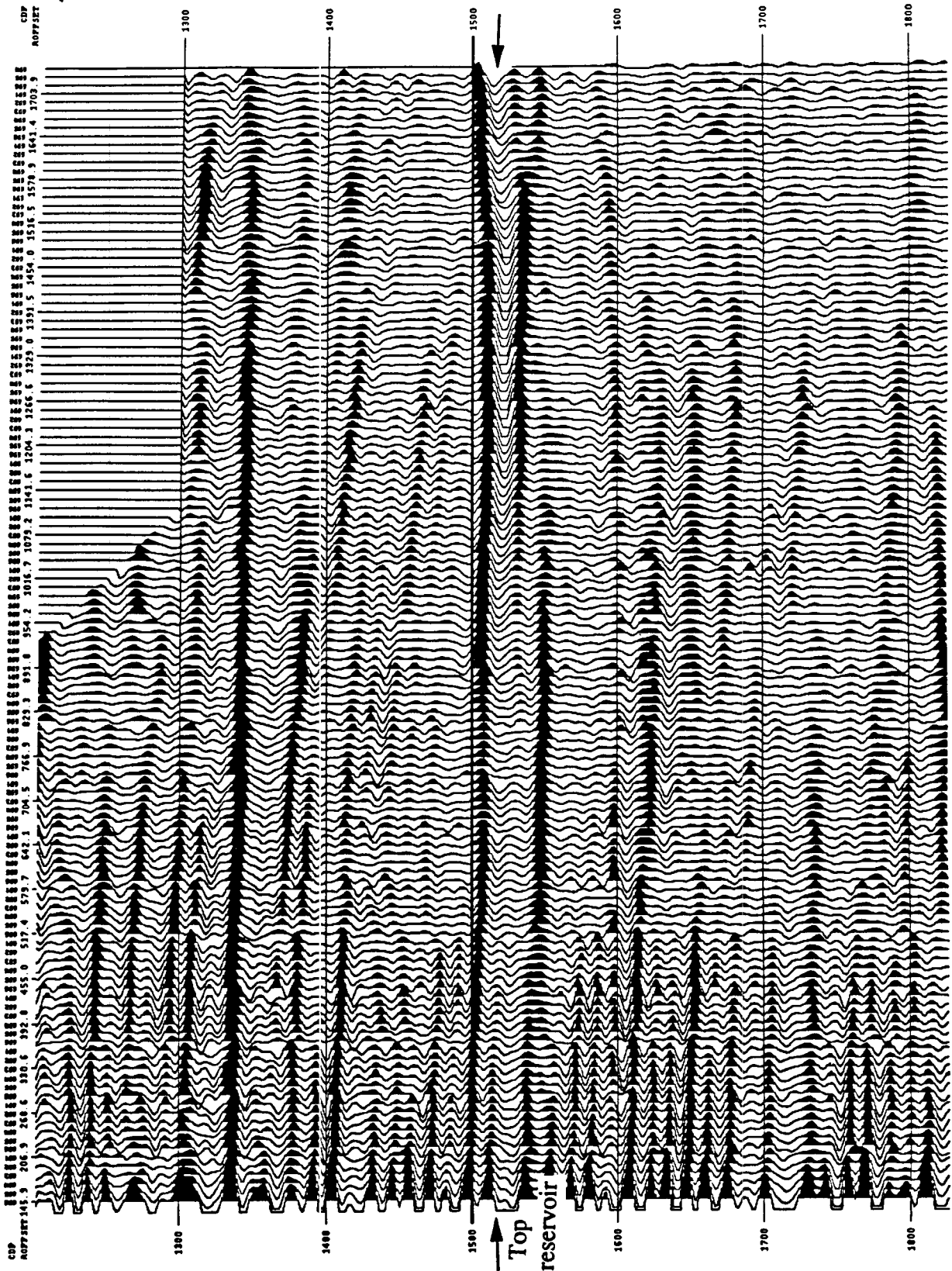


Figure 5.63: CDP supergather in the westernmost part of the Troll West Gas province, corresponding to the southern extension of the block where well 31/2-12 was drilled (approximately CDP 691); close-up on the reservoir zone.

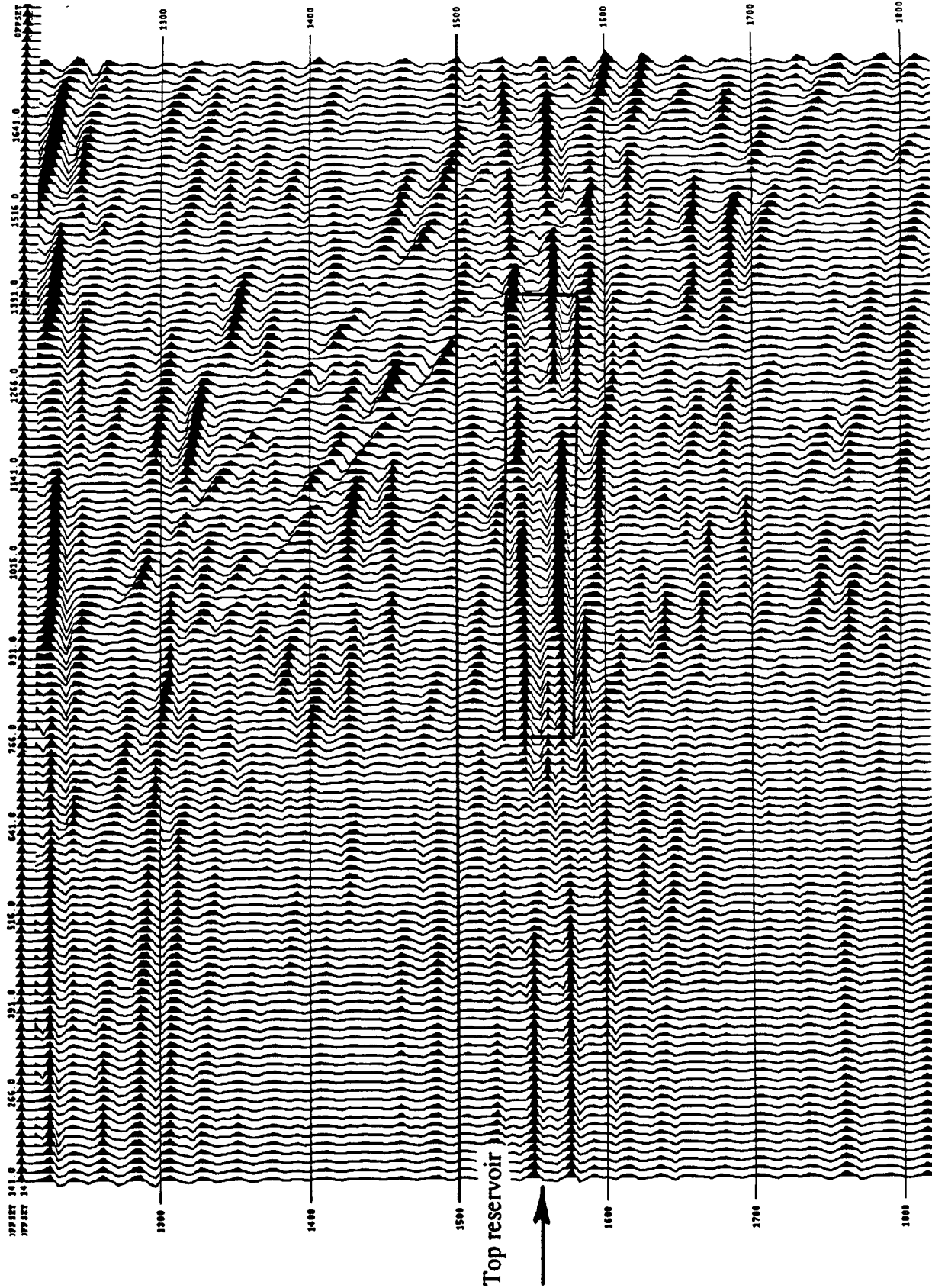


Figure 5.64: Full waveform seismic synthetic CDP gather of the westernmost part of the Troll West Gas province, at approximately CDP 691; close-up on the reservoir zone.

Conclusions on AVO modeling

The results of the modeling of AVO responses, via full waveform synthetic CDP gathers reveal that seismic reflection signatures are often very complex.

- At CDP 355 (well 31/2-5), there appears to be no increase in AVO for the reflection from the top of the reservoir, even though it is gas saturated. This can be explained by the relative proximity of the marly seal and the K-T boundary to the top of the reservoir (less than 4 m). They give rise to reflections which destructively interfere with that from the top of the gas zone. The destructive interference behavior was successfully reproduced in the synthetic gathers. However, the match between synthetic and real gathers are rather poor at this location. Furthermore, sensitivity analyses on the amount of mica/calcite present show that subtle features are expected due to the presence of such layers.
- On the other hand, at CDP 691, there is a large increase in AVO for the reflection from the top of the reservoir. This AVO increase corresponds to that which is expected from the top of the gas zone. This is because the top of the marly seal is several tens of meters above the top of the reservoir, and thus interferes very little with the reflection from the top of the gas zone. This AVO behavior is successfully reproduced on synthetic gathers.

The previous results show that we still do not fully understand all of the mechanisms involved in "real" seismic data. Semi-quantitative lithologic results can be obtained with AVO, but true quantitative parameter inversion from AVO is still a dream for the future. In summary, AVO remains a "risk reducer" and should be used, in conjunction with other techniques, as one of many tools for exploration and development.

(V) PETROPHYSICS AND AVO FOR RESERVOIR MANAGEMENT

1) Environmental management

According to Larminie (1987), from 1979 to 1984, the total oil production from the North Sea was 574 Mt, of which 1.78 Mt were spilled. The larger spills included one spill of close to 1 Mt and five spills of approximately 55 t each. These had large environmental impacts. Long term low-level ("chronic") oil inputs from the discharge of drill cuttings and oil-based muds are also considered to have some impact on the environment (Larminie, 1987). Potential environmental repercussions of oil spills are numerous and require that the accidental discharge of hydrocarbons into the North Sea be minimized. They also require that potential conflicts with other users of the North Sea, such as fisheries and recreation, be resolved. Because of the risks involved, environmental management now plays a major role in most organizations. It consists of two main phases: environmental impact assessment (EIA), and a monitoring program. Time and space preclude a detailed review here, but for more information, refer to UKDOE (1985). However, in the following, I will address the potential of monitoring production, via seismic surveys.

2) Difficult production conditions

When the Troll field was first discovered, the technology for producing the oil from the field was lacking. However, because of the large areal extent of the field, oil reserves are enormous (approximately 1 bbls recoverable). Recent improvements in hydrocarbon recovery techniques have made the production of the thin Troll oil-zone profitable by means of horizontal drilling. Two horizontal wells were recently drilled in the area: wells 31/2-16S and 31/5-4S. Well 31/2-16S was drilled adjacent to well 31/2-5. It penetrated 502 m of reservoir, and is located only a few meters above the oil water contact. A long term production test was successfully carried out at well 31/2-16S and a peak production rate of 25,000 barrels per day was achieved for an extended time. At the end of the production test, a repeat seismic survey was acquired over the previous recorded seismic survey in the vicinity of well 31/2-5 to

investigate the possibility of monitoring fluid flow in the reservoir during production and to investigate the extent of coning around the test well. This is a first attempt to use seismic data for the design and monitoring of the production of the field. Previous studies on the use of seismic during hydrocarbon recovery have been recently published (Geoffrey et al., 1989, Johnstad et al., 1990, Lines et al., 1989, Seymore et al., 1989, Wang, 1988).

3) Production parameters

a) Permeability-porosity and permeability-mica content relationships

For production purposes, it is convenient to establish two families - or "Flow Units" in the Sognefjord sands: **Clean sands** and **Micaceous sands**.

The clean sands occur as either coarse or medium grained, while the micaceous sands occur as either medium or fine grained. Figure 5.65 was obtained in conjunction with the core analysis program. It shows that the two families of sands have different permeability characteristics. The medium grained clean sands present the best reservoir quality, possibly because they are better sorted than the coarse grained clean sands. The second best quality sands consist of coarse grained clean sands. In general, micaceous sands have poorer permeability characteristics and will not be produced, at least in the immediate future.

Figure 5.66 shows the direct correlation of mica content to permeability. The model data (open symbols) were obtained using the following procedure:

- (1) assume a bi-modal distribution of grains within the Sognefjord sands: either quartz (and orthoclase), or muscovite.
- (2) assume that most of the muscovite can be considered as "pore filling".
- (3) use the Kozeny-Carrnan equations (Carman, 1956) to describe permeability:

$$k = A \frac{\phi^3}{T^2 S^2}$$

where k , T , ϕ , and S are permeability, tortuosity, porosity and specific surface area of the sands, and A is an empirical constant.

Muscovite can reduce permeability through different ways: a reduction in porosity, an increase in specific surface area, an increase in tortuosity, through blocking of pore throats, and through weathering to kaolinite. Kaolinite clay would act to reduce permeability in much the same way as the muscovite, but also through swelling. A similar approach was followed by Marion (1990) for Gulf sands.

In the Sognefjord sands, the tortuosity of the quartz-muscovite mixture is obtained by:

$$T = T_s T_c = T_s \left[\frac{c}{\phi_c} (T_{msc} - 1) + 1 \right]$$

where ϕ_c is the critical porosity of clean Sognefjord sands and is assumed to be approximately 0.40. The tortuosity of the muscovite, in the pore space (T_{msc}), is assumed to be a linear function of the amount of muscovite present within the pore space (c). Additionally, the specific surface area of the quartz-muscovite mixture is obtained as a linear function of muscovite content:

$$S = S_s + cS_{msc}$$

where S is specific surface area and c is the concentration in muscovite.

Since the procedure involves only porosity and muscovite content, a rough estimate of permeabilities can be obtained from well logs. This was done using a value of $A=20$, $S_{msc}=S_s=0.15$ and $T_{msc}=T_s=1.5$. In other words, I assumed that the primary effect of muscovite is to reduce porosity. Permeability prediction results are shown in figures 5.66 and 5.67.

b) Elastic properties and fluid content:

In preparation for seismic modeling of fluid flow during production, compressional-wave velocity differences in Sognefjord sands due to fluid saturation were calculated

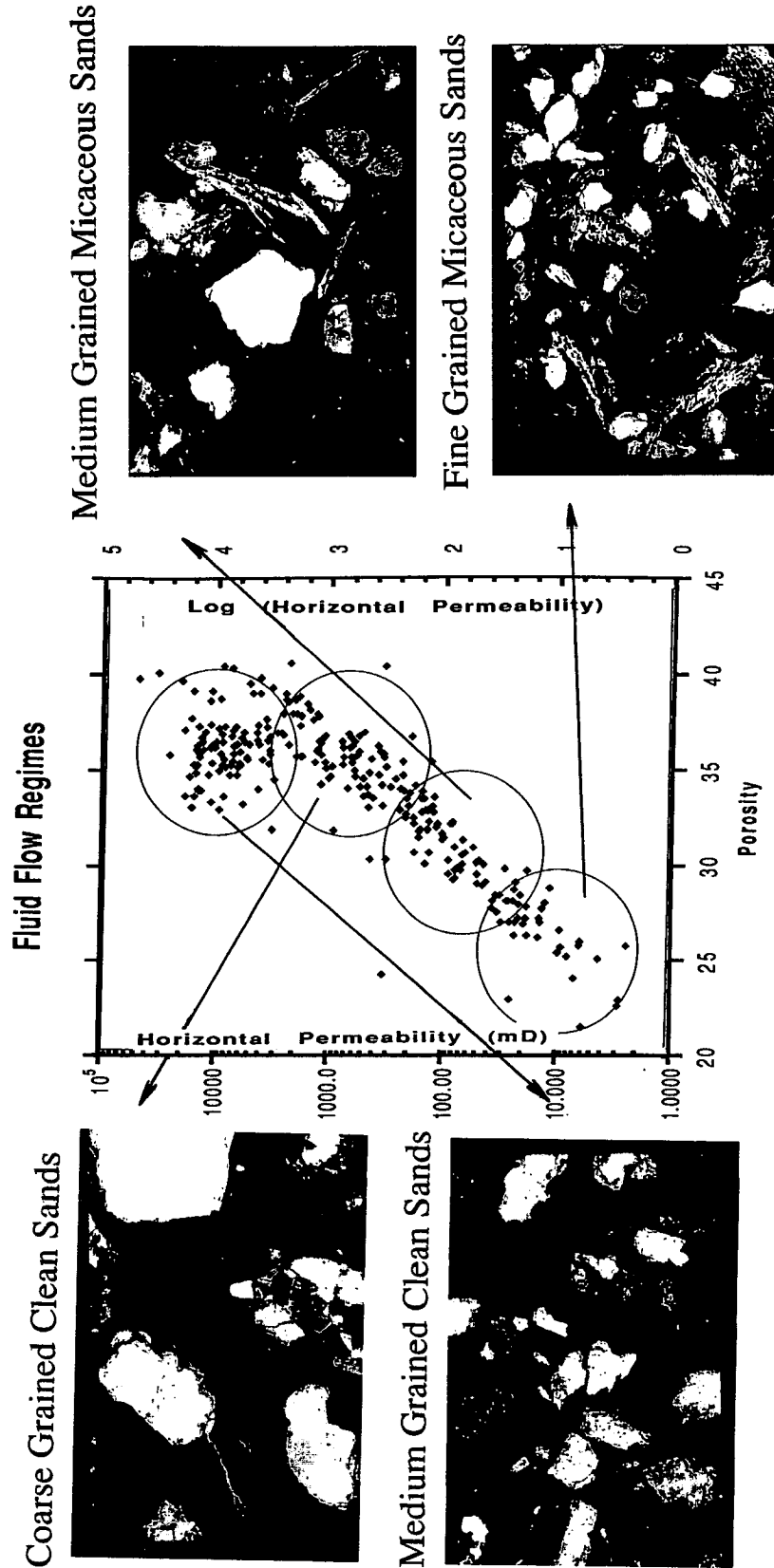


Figure 5.65: Permeability versus porosity data as measured on cores by Geco for all of the samples at well 31/5-4S.

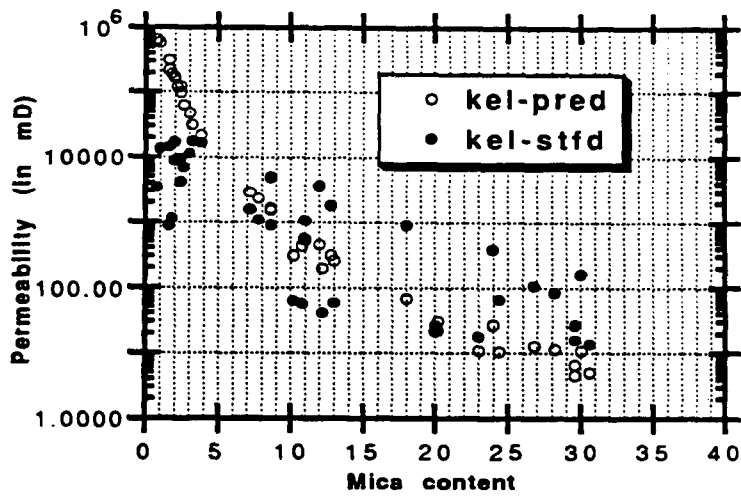
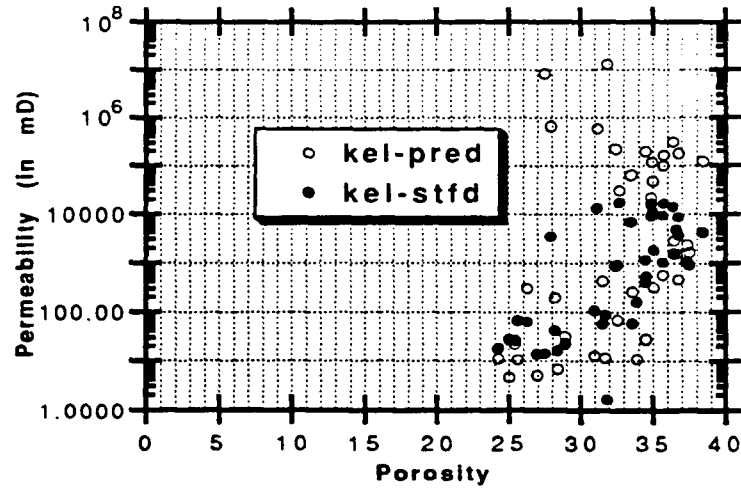


Figure 5.66: Permeability versus porosity and permeability versus muscovite content as measured on cores in the core measurement program (dark symbols) and as predicted from cores (open symbols) at well 31/5-4S.

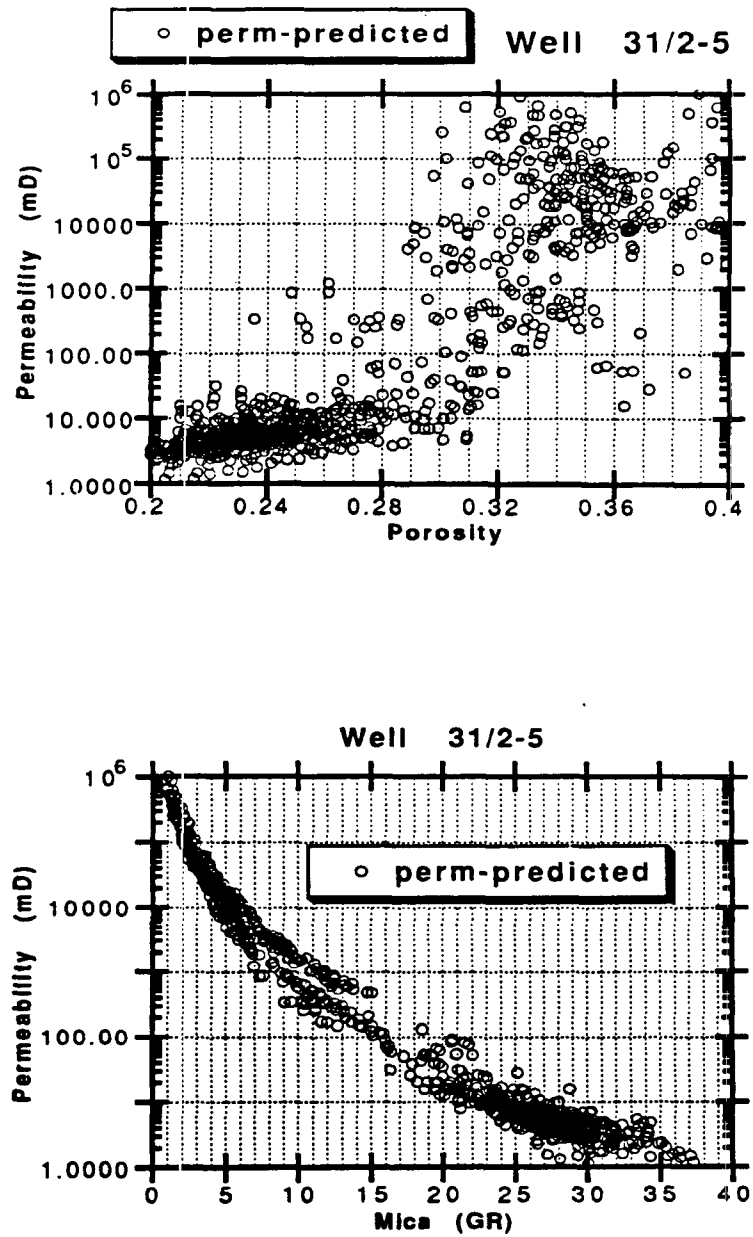


Figure 5.67: Permeability versus porosity and permeability versus muscovite content as inferred from logs at well 31/2-5; note the two distinct groups of sands present: clean sands and micaceous sands.

using Gassman's relation, bulk densities were adjusted using the mixing law, and shear wave velocities were obtained via density changes. The equations used for calculating the acoustic properties of a mixture of oil and gas were:

$$\frac{1}{K_f} = \frac{s}{K_g} + \frac{1-s}{K_o}$$

and

$$\rho_f = s\rho_o + (1-s)\rho_g$$

where K_f is the fluid bulk modulus, K_o , the oil bulk modulus, K_g , the gas bulk modulus, s the overall gas saturation, and ρ stands for density. K_o and K_g were obtained from fluid compressibilities under fixed pressure-volume-temperature conditions.

c) Fluid contacts, in-situ conditions and hydrocarbon properties:

We saw in chapter 4 that all fault blocks have a common OWC. Two main oil groups are found in the area, one with an API value of 24.7 degrees, and the other with a value of 28.4 degrees. These API values are relatively low when compared to the rest of the North Sea. This is thought to be due to bacterial degradation of the hydrocarbons in the reservoir. Corresponding viscosities are 1.22 and 1.48 cp, and hydrocarbon densities are obtained from the formula $API = \frac{141.5}{API+131.5}$. The natural gas is dry, consisting of more than 90 % methane with low normal alkane content. Pore pressure within the reservoir is thought to be hydrostatic, and reservoir temperatures do not vary much laterally. Factors related to higher seismic attenuation, such as gas or the presence of a non-uniform gaseous phase coming out of solution during oil production, were not considered.

d) Model results of fluid flow

Since the oil drainage will be gravity based, it would be useful to map the extent of the gas coning zone around producing wells. In fact, a seismic monitoring survey is planned for that purpose, in hope of detecting travelttime and/or amplitude differences

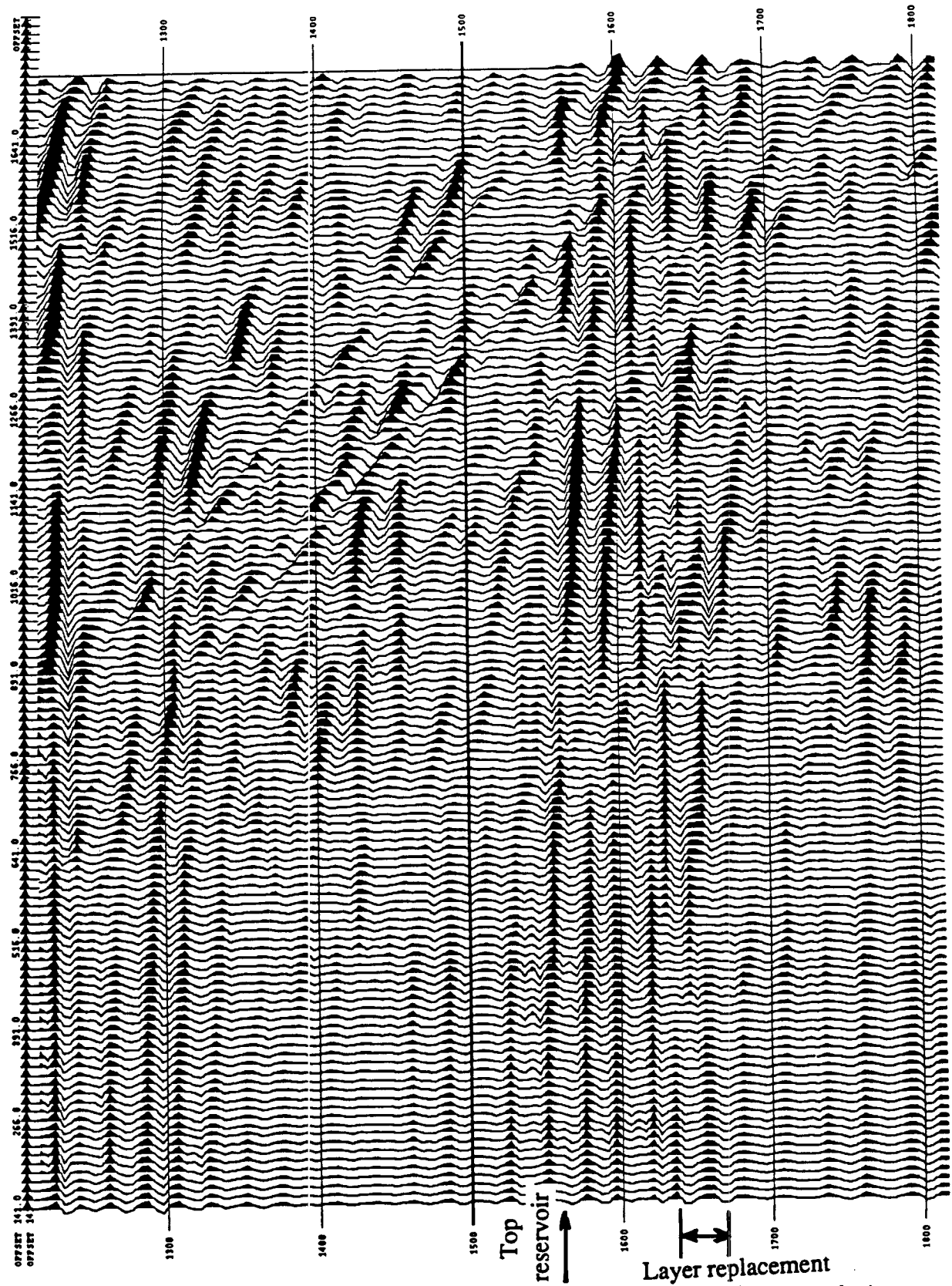


Figure 5.68: Full waveform seismic synthetic CDP gather at well 31/2-5, simulating gas coning in the Sognefjord.

in the gas-oil contact after coning around the horizontal production wells. The shape of the coning zone is expected to be closely related to the presence of calcite layers and micaceous sands, because they greatly reduce permeabilities.

Figure 5.68 shows the expected synthetic CDP seismic response at well 31/2-5, after the oil interval has been replaced with gas. This situation would correspond to the case where the well would have completely "coned-out", in the sense that most of the oil around the well would have been recovered and the gas cap would have expanded into the oil zone. In the actual reservoir, the oil layer would not be completely replaced by a gas layer, but since a 5-10 % gas saturation is sufficient to change compressional-wave velocities (Biot-Gassman effect), this is not a bad approximation. In any case, the model provides insight into the best possible conditions under which one might be able to detect a change in seismic signatures due to oil production. When comparing figure 5.68 to figure 5.57, one can notice subtle differences in the interval from 1550 ms to 1570 ms, corresponding to the depth interval where the oil was substituted for gas. In particular, the reflector at about 1560 ms at near offsets appears to be lower apparent frequency and to have gained amplitude due to oil displacement by gas. In the future, it remains to be seen whether such a subtle feature can be identified on the actual seismic monitor survey.

SUMMARY AND CONCLUSIONS

A model-based integrated seismic pre-stack interpretation was used for reservoir characterization at Troll. Critical questions addressed here included the recognition of calcite cemented layers, the differentiation between clean and micaceous sands, and the possibility of predicting fluid movement associated with hydrocarbon production.

The approach is based on petrophysics and seismic modeling and involves the integration of core analyses, log analyses, petrophysical interpretation, true amplitude reprocessing of seismic, and pre-stack (AVO) modeling. Lithologic models were systematically built from the microscale to seismic scales, involving three phases of

investigation, corresponding to three different scales:

- A comprehensive **core measurement** program was undertaken at well 31/5-4S to calibrate ultrasonic responses to changes in lithology, porosity, and fluid content at in-situ reservoir conditions. The results of the core analyses showed that clean sands and micaceous sands have different porosities, velocity and density characteristics, and that fluid effects can be approximated using the Biot-Gassman theory. These results justified further comparisons with other measurements at other scales, and in particular at the log and seismic scales.
- The core measurements were in good agreement with **log measurements** from well 31/5-4S. Log measurements average heterogeneities on the order of centimeters to a scale of a few feet. Local departures between log and core results can be explained in these terms, specially in areas of thin-interbedded calcite stringers, where "average sonic" logs tend to be faster than ultrasonic core velocities. Most reservoir sand units within the Sognefjord can be thought of as ternary systems, with quartz, feldspar, and muscovite as end members. Results from thin-sections analyses showed that the amount of orthoclase is quasi-constant; variations in the potassium log can therefore be attributed to changes in the amount of muscovite, a potassium aluminosilicate). As a result, the potassium log, and the gamma ray log to a lesser extent, were calibrated and used to estimate the total muscovite content. This enabled the mapping of clean versus micaceous sands from logs at wells. Correlations between velocity, porosity, and lithology were also established from well logs. These correlations allowed the transformation of lithologic variations into velocity changes at the scale of investigation of logs. Variations in fluid content were also mapped from logs. Dry core velocities and sonic measurements agreed well within the gas zone, while liquid saturated core velocities agreed in the oil and water zones.
- Building detailed macro-models from microscale observations at well control points and comparing them to seismic data is essentially a 1-D approach. It

is valid here, because most structural features are not present in the overburden, and because the areal extent of the reflectors under investigation is large. Although there is some mismatch between the real seismic and synthetic CDP gathers, integrated 1-D seismic lithologic models can be used at Troll by knowledgeable geoscientists in extracting quantitative information that will support or refute certain reservoir properties inferred from facies models.

The presence of gas can be inferred from pre-stack (AVO) responses whenever the thickness of the seal is large enough to prevent destructive interference with reflections from the top of the gas saturated sands. In addition, synthetic results show that thin calcite beds and micaceous units which are associated with a decrease in porosity, give rise to characteristic seismic responses.

Reservoir characterization

In a final step, the modeling approach was shown to have potential in extracting quantitative information that can assist field production. This involved the use of more general "lithologic models" that incorporate **fluid properties** and in-situ conditions. Synthetic results show subtle changes in seismic signature, due to the flow of fluid.

REFERENCES

- Ausburn, B., 1977, Well log editing in support of detailed seismic studies: SPWLA 18th Annual Logging Symposium, June 5-8, paper F.
- Backus, G.E., 1962, Long-wave Elastic Anisotropy Produced by Horizontal Layering: *J. Geoph. Res.*, 67, 4427-4440.
- Banik, N.C., 1987, An Effective Anisotropy Parameter in Transversely Isotropic Media: *Geophysics*, 52, 1654-1664.
- Biot, M.A., 1956a, Theory of propagation of elastic waves in a fluid saturated porous solid. I. Low frequency range: *J. Acoust. Soc. Am.*, 28, 168, 178
- Biot, M., 1956b, Theory of propagation of elastic waves in a fluid saturated porous solid; II-Higher frequency range: *J. Acoust. Soc. Am.*, 28, 179, 191.
- Brandt, H., 1955, A study of the speed of sound in porous granular materials: *J. Applied Mechanics*, 22, 479, 486.
- Brown, A. R., Wright, R. M., Burkart, K. D., Abriel, W. L., McBeath, R. G., 1986, Tuning effects, lithological effects and depositional effects in the seismic response of gas reservoirs: *Geophysical Prospecting*, 34, 623, 647.
- Carman, P.C., 1956, Flow of gasses through porous media: New York, Academic Press.
- Claerbout, J. 1985, Fundamentals of Geophysical Data Processing: Blackwell Scientific Publications, 106, 114.
- Daley, P., F., and Hron, F., 1977 : Reflection and transmission coefficients for transversely isotropic media: *Bull., Seis. Soc. Am.*, 67, 661, 675.
- Domenico, S. N., 1977, Elastic properties of unconsolidated porous sand reservoirs: *Geophysics*, 42, 1339-1368
- Doveton, J. H., and Cable, H. W., 1979, Fast matrix methods for the lithological interpretation of geophysical logs: in *Geomathematical and Petrophysical studies in Sedimentology*; D. Gill and D. F. Merriam editors, Oxford, 101, 116.
- Dawson-Grove, G.E., 1977, Gas is where you find it: paper presented at the S.P.W.L.A. 18th Ann. Mtg., paper O.
- Domenico, S. N., 1976, Effect of brine-gas mixture on velocity in an unconsolidated sand reservoir, *Geophysics*, v. 41, pp. 882-894.
- Eisma, D., 1987, The North sea: an overview: Environmental effects of North Sea oil and gas developments, proceedings of a royal society discussion meeting held in Feb. 1986, 1-24.
- Eisma, D., and Kalf, J., 1987. Dispersal, concentration, and deposition of suspended matter in the North sea: *J. Geol. Soc. London*, 144, 161-178.

- Gardner, G.H.F., Harris, M.H., 1968, Velocity and attenuation of elastic waves in sands: Trans. 9th Annual Log Symp., Paper M
- Geertsma, J., 1961, Velocity-log interpretation: The effect of rock bulk compressibility: Society of Petroleum Engineers J. (AIME) , v. 1, pp. 235-248.
- Gelfand, V., Ng, P., Nguyen, H., Larner, K., 1988, Seismic lithologic modeling of Amplitude-Versus-Offset data: paper presented at the ASEG/SEG meeting, Adelaide, 274,276.
- Geoffrey, A.D., Fisher, D.A., 1989, Detailed fault interpretation of 3D seismic data for EOR planning:S.E.G. Expanded Abstracts from the 59th Annual meeting in Dallas, Vol. 1,549-550
- Gregory, A. R.,1976, Fluid saturation effects on dynamic elastic properties of sedimentary rocks: Geophysics, 41, 895-921
- Han, D-H, Nur, A., and Morgan, D., 1986a, Effects of porosity and clay content on wave velocities in sandstones: Geophysics, 51, 2093, 2107.
- Halbouty, M., 1982, The deliberate search for the subtle trap: A.A.P.G. Memoir 32, 351 pages.
- Han, D-H, 1986b, Effects of porosity and clay content on acoustic properties of sandstones and unconsolidated sediments: PhD Thesis Stanford University, SRB report Vol. 28
- Hoopes, R., Aber, W., 1989, Integrated multianalysis procedure that qualifies DHI's; a case history in the Louisiana Kackberry trend: paper presented at the 59th SEG convention, Dallas
- Inouye, F. Williams, G., 1988, An integrated approach to seismic interpretation: paper presented at the ASEG/SEG conference, Adelaide, 91,93
- Justice, J.H., Vassiliou, A.A., SiUden, R.C., 1989, The potential contribution of surface seismic surveys to monitoring offshore oilfields: Paper presented at the 51st
- Kanestrom,R., Stordal,T.,1991, Pavisning av Seismisk Anisotropi pa Norsk Sokkel: "Detection of Seismic Anisotropy in the Norwegian Continental Shelf:" Norsk Hydro Internal Report.
- Klimentos,T., McCann, C., 1990, Relationship among compressional wave attenuation, porosity, clay content, and permeability in sandstones: Geophysics, 55, 998, 1014.
- Larminie, F., G., 1987, The history and future of North Sea oil and gas: an environmental perspective: Environmental effects of North Sea oil and gas developments, proceedings of a royal society discussion meeting held in feb. 1986, 27-32.
- Lines,L.R., Fackson, R., and Covey, J.D., 1989, Seismic velocity models for heat zones in Athabasca tar sands: S.E.G. Expanded Abstracts from the 59th Annual meeting in Dallas, V. 2, 751, 753
- Marion, D., 1990, Acoustic, mechanical, and transport properties of sediments and

- granular materials: Ph. D. thesis, Stanford University, SRB report vol. 39.
- Mazzotti, A., 1990, Pre-stack amplitude analysis, methodology, and application to seismic bright spots in the Po valley, Italy: *Geophysics*, **55**, 157,166.
- Mavko, G.M., Jizba, D., 1990b, Estimating grain scale fluid effects on velocity dispersion in rocks: SRB report Vol. 40
- Nur, A., 1987, Seismic rock properties for reservoir description and monitoring: in G. Nolet (ed) *Seismic Tomography*, pp 203-237
- Picket, G. R., 1963, Acoustic character logs and their applications information evaluation, *Jour. Pet. Tech.*, pp. 659-667.
- Raymer, D.S., Hunt, D.R., Gardner, J.S., 1980, An improved sonic transit time-to-porosity transform: paper presented at the S.P.W.L.A. 21st Ann. Mtg., paper P.
- Sengupta, M.K., and Rendleman, C.A., 1991, Case study: The importance of gas leakage in interpreting amplitude-versus-offset (AVO) analysis: *Geophysics*, **56**, 1886, 1895.
- Serra, O., Baldwin, J., and Quirein, J., 1980, Theory, interpretation and practical applications of natural gamma ray spectroscopy: S.P.W.L.A., 21st Annual Logging Symposium, 1980, Q1, Q30.
- Seymore, R.H., King, G.A., Dunlop, K.N.B., and Uden, R.C., 1989, The potential contribution of surface seismic surveys to monitoring offshore oilfields: Paper presented at the 51st E.A.E.C conference in Berlin, West Germany
- Thomsen, L., 1986, Weak elastic anisotropy : *Geophysics*, **51**, 1954,1966.
- United Kingdom Department of Energy, 1985, Development of oil and gas resources of the U. K.: (The "Brown book"), London.
- Yin, H., Han, D-H., Nur, A., 1988, Study of velocities and compaction on sand - clay mixtures: SRB Vol. 33
- Wang, Z., 1988, Wave velocities in hydrocarbons and hydrocarbon saturated rocks with applications to EOR monitoring: PhD Thesis Stanford University, SRB report Vol 34
- White, J.E., 1965, *Seismic waves: Radiation, transmission, and attenuation*: New York, McGraw-Hill Book Co.
- Wright, J., 1987, The Effect of Transverse Isotropy on Reflection Amplitude Versus Offset: *Geophysics*, **52**, 564-567.
- Wyllie, M.R., Gregory, A.R., and Gardner, A.L.W., 1956, Elastic wave velocities in heterogeneous and porous media: *Geophysics*, **21**, 41, 70.

GENERAL CONCLUSIONS

(1) Model-based Integrated Seismic Lithologic Interpretation

I have shown that model-based seismic lithologic interpretation has become feasible with today's understanding of rock physics and that it carries a lot of potential for the quantitative extraction of reservoir parameters. In a sense, combined true amplitude processing and integrated lithologic modeling have brought a new quantitative dimension to seismic interpretation. In particular, they allow for accurate calibration of seismic data at existing well locations and allows for the extrapolation of geological properties away from these known control points.

The process of translating subtle seismic parameters into reservoir description and production parameters is complex and I consider it risky business when used by itself as an exploration tool, because of its inherent non-uniqueness. It is truly a development tool which requires the careful and systematic integration of geophysics, geology, and engineering, and which is greatly facilitated through the use of analytical quantitative methods based on **rock physics** (figure 6.1). The key lies in the accurate **calibration** of seismic data. Where a priori data is available, physical models can provide adequate control over the calibration at all scales. In other areas, where there is a lack of well control or where petrophysical models have not been established, geostatistics may prove useful.

(2) An Inter-disciplinary Effort

Now more than ever, integrated seismic modeling appears as the tool of choice with which to test geological hypotheses prior to drilling. Because of the need to reduce the non-uniqueness of elastic parameter inversion, and because of the need for LITHOLOGIC inversion, the successful outcome of the technique requires the joint application of fundamental principles and creative interpretation techniques. Undoubtedly, computers will facilitate integration, but the final responsibility lies with of the geoscientist. These observations require that professionals not only work in groups, as in Masters (1989), but also that they be cross-trained.

Issues in Rock Physics
addressed in this thesis for the **quantitative**
extraction of lithologic properties from seismic

● **Seismic Calibration at wells**

- Log blocking, based on impedance contrasts or other criterium
- Rock classification (petrophysical and geological)
- "Properly" averaging rock properties and up-scaling
- Calculating "missing" properties

● **Extrapolation of seismic properties away from wells**

- All of the above, plus
- Implement perturbations for "average" rock properties

● **General issues**

- How to average rock properties for quantitative up-scaling
- Study the effects of lithology (matrix fraction) on seismic properties
- Study the effects of intrinsic attenuation
- Incorporate iso-stress/strain concepts
- Study the effects of anisotropy
- Model the effects of location of fine grained minerals (muscovite or clay)
- Attempt to characterize the diagenetic overprint (cementation, compaction, effective pressure changes)
- Estimation of shear velocity: Comparison of Shear velocities from different methods
- Determination of attenuation Q_s and Q_p
- Study the effects of porosity and clay on K_d and μ_{ub} and modify the
- Study the effects of fluid type and fluid saturation
- Study the effects of interrelationships between rock properties
- Study the relationship between porosity, lithology, permeability and fines (mica content)

Figure 6.1: Rock Physics as a quantitative tool for Integration.

Reflection seismic methods are, and will continue to be, the key geophysical tool for imaging heterogeneities in the subsurface of the earth. Integration of multi-disciplinary data reduces the non-uniqueness of the interpretation process. It also allows for the combined benefits of borehole information which is very accurate in the vertical direction, and of seismic data which has a large scale lateral resolution. By integrating all of the available information, seismic data can be precisely calibrated, thus making it possible to distinguish subtle stratigraphic features. **Rock physics** can provide the tools for **quantitative** integration of these different data types across scales of investigation (figure 6.1). In that sense, rock physics emerges as an ideal tool to provide the bridge between reservoir characterization and the actual geology of the subsurface.

(3) An Exciting time to be involved in Geosciences

Twelve years ago, Sheriff (1980) stated:

"Every little wiggle has a meaning of its own. This is our underlying faith, that details of seismic waveshapes can tell us the details of the nature of the earth. But their voices are obscured by many irrelevancies. They speak in a high-noise environment, and we have been able to decipher only a small portion. However, things are looking up: better techniques are lessening the irrelevancies, and we are learning to read".

As of today, we have learned a lot and we have come full circle. We have seen individual disciplines, such as petroleum geology, stratigraphy, seismic interpretation, basin analysis, geophysics, petroleum engineering, and reservoir engineering pushed to their limit, giving rise to new ideas or to refinements in older ones. It is interesting to note that each discipline evolved rapidly on its own but eventually became faced with resolution problems. Today, these individual professions depend on one another to advance the understanding of specific reservoirs. Integrated seismic interpretation is an exciting field to be in, because we are beginning to take advantage of the revolution in workstation and database technology, extracting more and more quantitative information from seismic data. Yet we still have a lot to learn, and I believe that

most of it will come through inter-disciplinary efforts.

(4) Looking ahead

I have identified and addressed two great challenges in any AVO modeling/interpretation work:

- integration (of scales and disciplines)
- lithologic inversion (rather than elastic parameter inversion)

These challenges arise from the need to reduce non-uniqueness in the interpretation of AVO signatures, specially when the data arise from imperfectly known wavelets and are contaminated by noise. However, when consistent with the structural information contained in stacked sections, model-based AVO interpretation appears as one of many promising tools for the refinement of stratigraphic models. In that sense, I believe that AVO will be integrated with modern seismic-stratigraphy and that it will be incorporated into 3-D seismic analyses for quantitative reservoir characterizations and descriptions.

In the future, the joint application of geology, geophysics, and petroleum engineering will undoubtedly lead to the optimization of hydrocarbon recovery from existing oil fields. We have already witnessed a shift in emphasis in the geosciences during the mid-1980's and early 1990's from exploration to reservoir description and characterization. The next shift will probably involve another transition from reservoir characterization to production and monitoring (figure 6.2). In that context, the direct mapping of oil saturation in a reservoir from seismic (Meissner and Hegazy, 1981, Wright, 1986) holds promise as technology evolves and data quality continues to improve. Quantitative model based AVO interpretation can prove to be an excellent tool in the identification of lithology, porosity, and the presence of gas associated with hydrocarbon deposits, yet the mapping of fluid saturation from AVO remains elusive: in fact, theory dictates that we work with both compressional and shear waves in order to map saturation directly, and thereby separate fizz water from economical

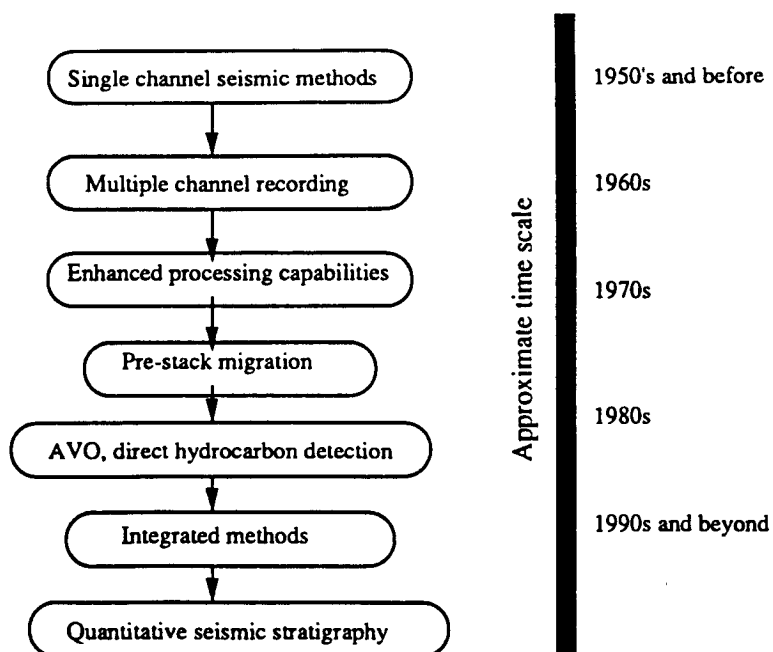


Figure 6.2: Evolution of surface seismic methods.

gas/hydrocarbon accumulations. Therefore, the use of seismic as a production tool will require the furtherance of multi-disciplinary integration and the quantitative use of shear waves. From there-on, it is only a small step to imagine complete integration between seismic and reservoir engineering, where 3-D grids would represent detailed up-scaled models of petroleum reservoirs in terms of saturation, permeability, porosity, in-situ conditions and seismic elastic properties.

Having shown that quantitative model-based seismic lithologic interpretations is rapidly becoming feasible with today's understanding of petrophysics, I conclude that the petroleum geoscientists of tomorrow will look for increasingly subtle changes in seismic waveform signatures to support/refute their understanding of reservoirs and the fluids that they contain. In that sense, there will be a need for the joint application of fundamental quantitative petrophysical principles and the reliance on creative interpretations. This will require a good sense of balance between science and art, coupled with the ability in going from the general to the specific, and will ultimately rely on the interpreter's educated decision and good judgement.

REFERENCES

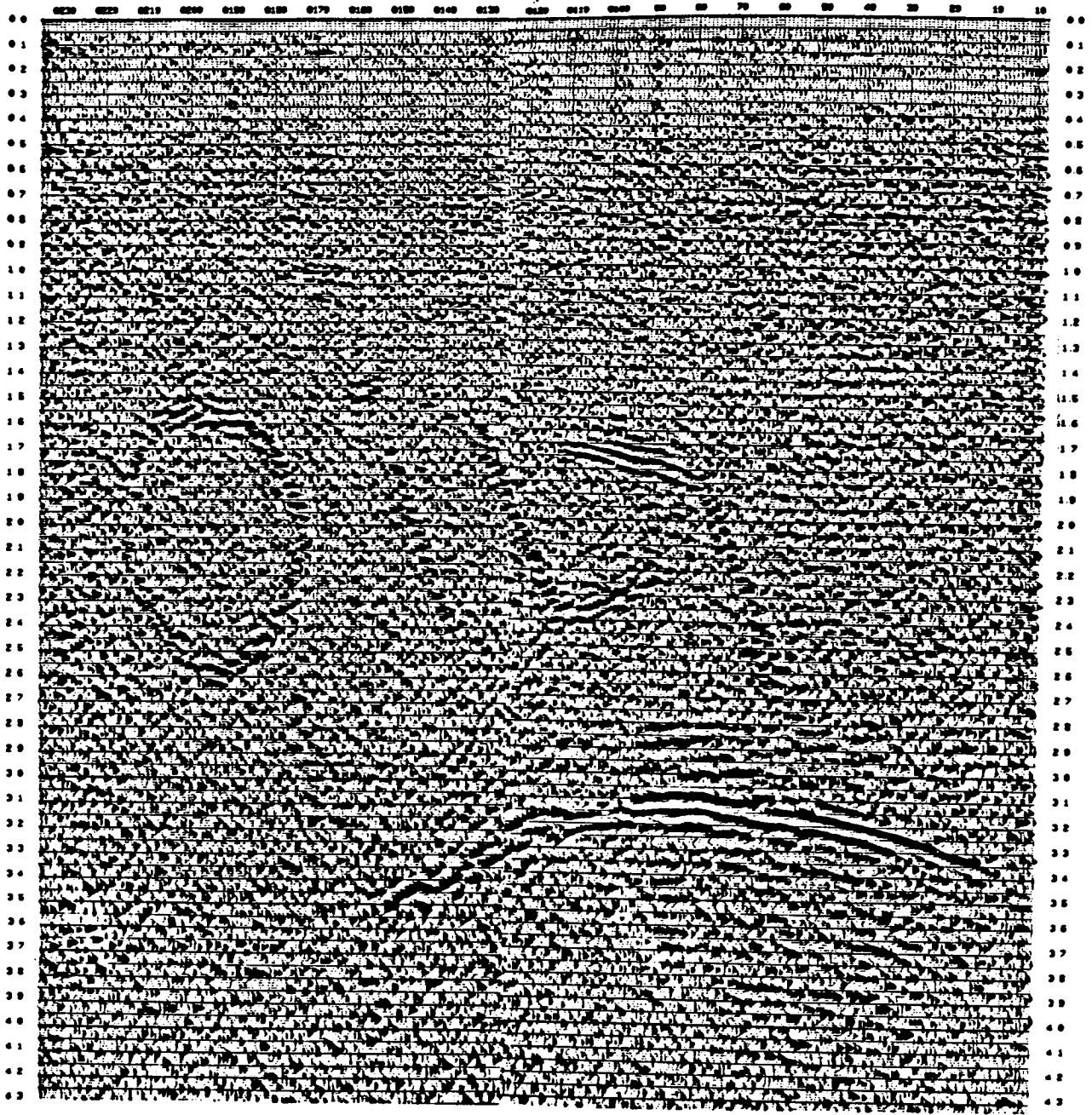
Masters, J.A., 1989, Exploration De-Organization: paper presented at a major American oil company on November 9

Meissner, R., and Hegazy, M.A., 1981, The ratio of the PP to the SS reflection coefficient as a possible future method to estimate oil and gas reservoirs: *Geophysical Prospecting*, vol. 29, 533, 540

Sheriff, R.E., 1980, *Seismic Stratigraphy*: International Human Resources Development Corporation, publishers, 227 pages

Wright, J., 1986, Short Note: Reflection coefficients at pore-fluid contacts as a function of offset: *Geophysics*, vol. 51, 1858, 1860

Seismic for beginners:



Fill-in page

This page was inserted for esthetic purposes only, and does not necessarily reflect the author's opinion or his state of mind. It is NOT an integral part of the thesis at Stanford University, and was obtained from a series of "reliable" sources out there.

APPENDIX A: PHASE AND GROUP VELOCITIES

Care must be taken in understanding the differences between phase and group velocities in anisotropic media. In the laboratory, we usually measure group velocities, which are associated with the arrival of most of the energy of the propagating wave. However, most theoretical treatments of anisotropy involve phase velocities. Therefore, in order to be able to relate theory and practice, one must convert from phase velocity to group velocity and vice-versa. This is done through the general relationship (after Berryman, 1979):

$$V^2 [\Phi (\theta)] = v^2 (\theta) + \left(\frac{dv}{d\theta} \right)^2 \quad (1)$$

where v is phase velocity, θ is phase angle, V is group velocity, and Φ is group angle.

For the case of elliptical anisotropy, we have (after Levin, 1979)

$$v^2 = v_1^2 \sin^2 \theta + v_2^2 \cos^2 \theta$$

which is equivalent to formula (2 of chapter 2), and we obtain by differentiating:

$$2v \frac{dv}{d\theta} = [v_1^2 - v_2^2] \sin (2\theta)$$

we then get:

$$V^2 = v^2 + \left[\frac{\sin (2\theta) (v_1^2 - v_2^2)}{4v^2} \right]^2 \quad (2)$$

(where V and v are group and phase velocities respectively).

For wave propagation at angles to bedding of 0 and $\pi/2$ radians in transversely isotropic media, group and phase velocities are equal. However, when looking at propagation at $\pi/4$ radians, the additive term on the right hand side of equation (2) is not negligible. For example, in the case of the Bakken shale of chapter 2 (with group velocities of 4.2 Km/s at 0 radians and 3.4 Km/s at $\pi/2$ radians), the term yields a 2 % difference in the estimate of the phase velocity. This is greater than the uncertainty in the velocity measurement itself.

* For the case of transverse isotropy, we use the equations of Daley and Hron (1977) listed in chapter 2. Differentiating, we obtain:

$$\left(\frac{\delta v_p}{\delta \theta}\right) = \frac{1}{4\rho v_p(\theta)} \frac{\sin 2\theta \left[(C_{13} + C_{44})^2 + (C_{11} - C_{33}) - (C_{33} - C_{44})(C_{11} + C_{33} - 2C_{44}) \right] + 2\sin^3\theta \cos\theta \left[(C_{11} + C_{33} - 2C_{44})^2 - 4(C_{13} + C_{44})^2 \right]}{D(\theta)}$$

which can be combined with equation (2) to yield group velocity. This type of system of equations can be easily solved iteratively for C_{13} , using a non-linear regression like the Newton-Raphson method. The special cases of velocities at a 0, 45, and 90 degree angles simplify considerably and are listed below:

* At 0 and $\pi/2$ radians, Group (V) and Phase (v) velocities are equal:

$$\begin{aligned} v_p^2(0) &= V_p^2(0) = \frac{C_{33}}{\rho} \\ v_p^2\left(\frac{\pi}{2}\right) &= V_p^2\left(\frac{\pi}{2}\right) = \frac{C_{11}}{\rho} \\ v_{sv}^2(0) &= V_{sv}^2(0) = \frac{C_{44}}{\rho} \\ v_{sv}^2\left(\frac{\pi}{2}\right) &= V_{sv}^2\left(\frac{\pi}{2}\right) = \frac{1}{4\rho} (C_{33} - C_{11} + 4C_{44}) \\ v_{sh}^2(0) &= V_{sh}^2(0) = \frac{C_{44}}{\rho} \\ v_{sh}^2\left(\frac{\pi}{2}\right) &= V_{sh}^2\left(\frac{\pi}{2}\right) = \frac{C_{66}}{\rho} \end{aligned}$$

* At $\pi/4$ radians, Group (V) and Phase (v) velocities also simplify:

$$\begin{aligned} v_p^2\left(\frac{\pi}{4}\right) &= \frac{C_{11} + C_{33} + 2C_{44} + \sqrt{4(C_{44} + C_{13})^2 + (C_{11} - C_{33})^2}}{4\rho} \\ V_p^2\left(\frac{\pi}{4}\right) &= v_p^2\left(\frac{\pi}{4}\right) + \frac{1}{(4\rho v_p\left(\frac{\pi}{4}\right))^2} \left\{ C_{11} - C_{33} + \frac{\frac{1}{2}(C_{11} - C_{44})^2 - \frac{1}{2}(C_{33} - C_{44})^2 - (C_{13} + C_{44})^2}{\sqrt{(C_{44} + C_{13})^2 + \frac{1}{4}\left(\frac{C_{11} - C_{33}}{2}\right)^2}} \right\}^2 \end{aligned}$$

$$v_{sv}^2 \left(\frac{\pi}{4} \right) = \frac{C_{11} + C_{33} + 2C_{44} - \sqrt{4(C_{44} + C_{13})^2 + (C_{11} - C_{33})^2}}{4\rho}$$

$$V_{sv}^2 \left(\frac{\pi}{4} \right) = v_{sv}^2 \left(\frac{\pi}{4} \right) +$$

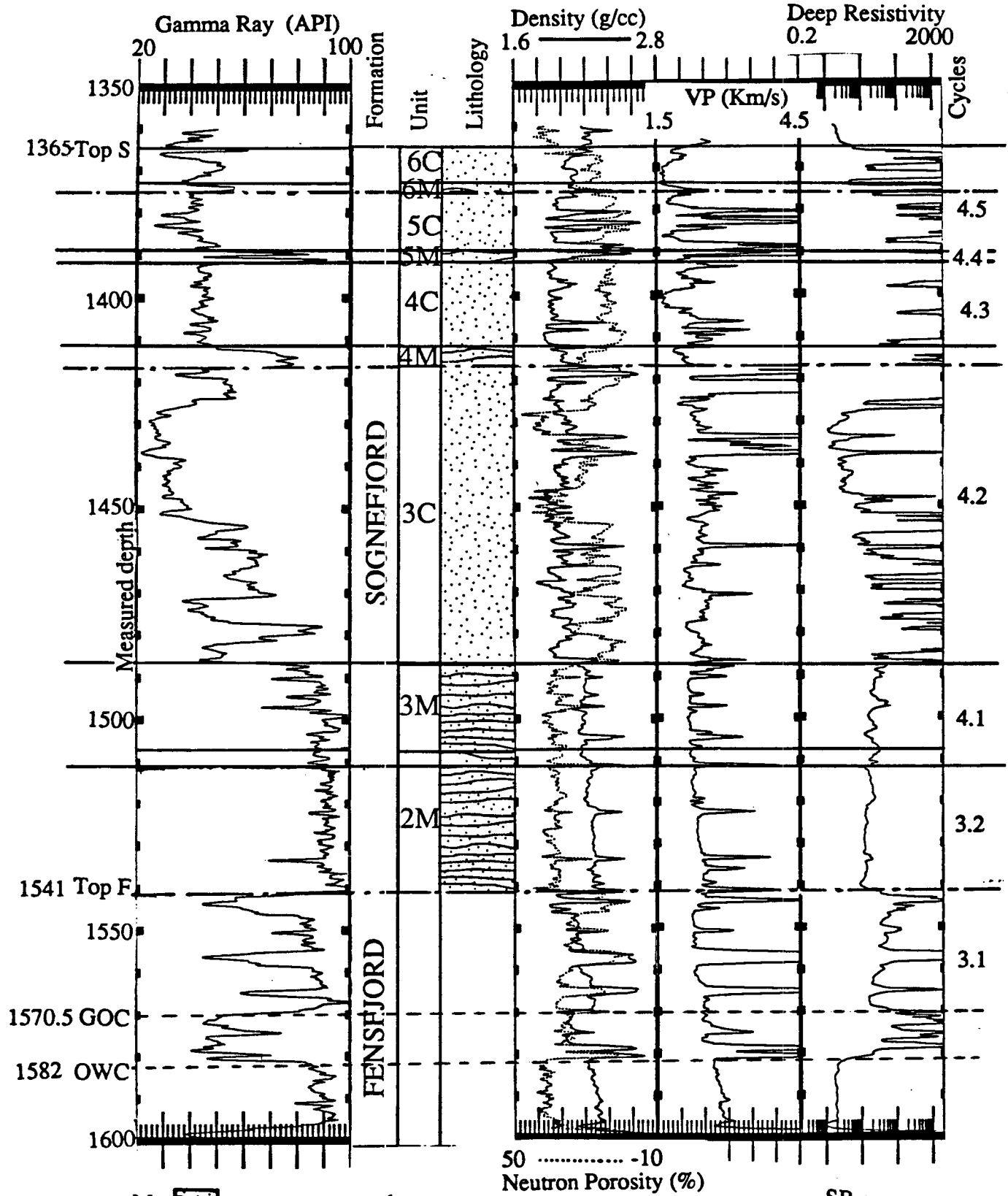
$$\frac{1}{(4\rho v_p \left(\frac{\pi}{4} \right))^2} \left\{ C_{11} - C_{33} + \frac{(C_{13} + C_{44})^2 + \frac{1}{2}(C_{33} - C_{44})^2 - \frac{1}{2}(C_{11} - C_{44})^2}{\sqrt{(C_{44} + C_{13})^2 + \frac{1}{4}(C_{11} - C_{33})^2}} \right\}^2$$

$$v_{sh}^2 \left(\frac{\pi}{4} \right) = \frac{C_{66} + C_{44}}{2\rho}$$

$$V_{sh}^2 \left(\frac{\pi}{4} \right) = \frac{C_{66} + C_{44}}{2\rho} + \frac{\rho (C_{66} - C_{44})^2}{2(C_{66} + C_{44})}$$

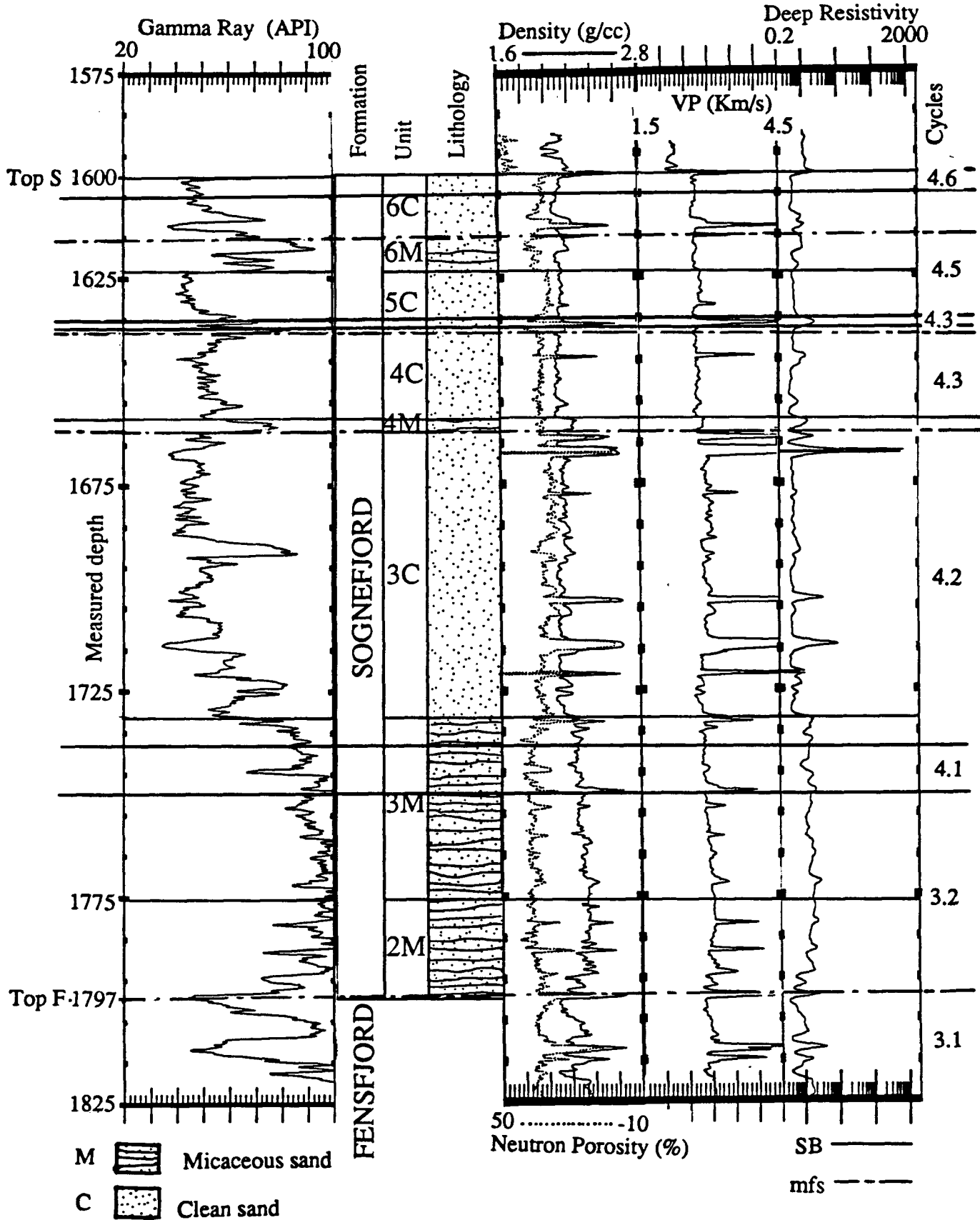
**APPENDIX B: WELL LOGS AND STRATIGRAPHIC
CORRELATIONS AT TROLL WEST**

(All depths appear in measured depth and in m, unless specified
otherwise in parentheses)

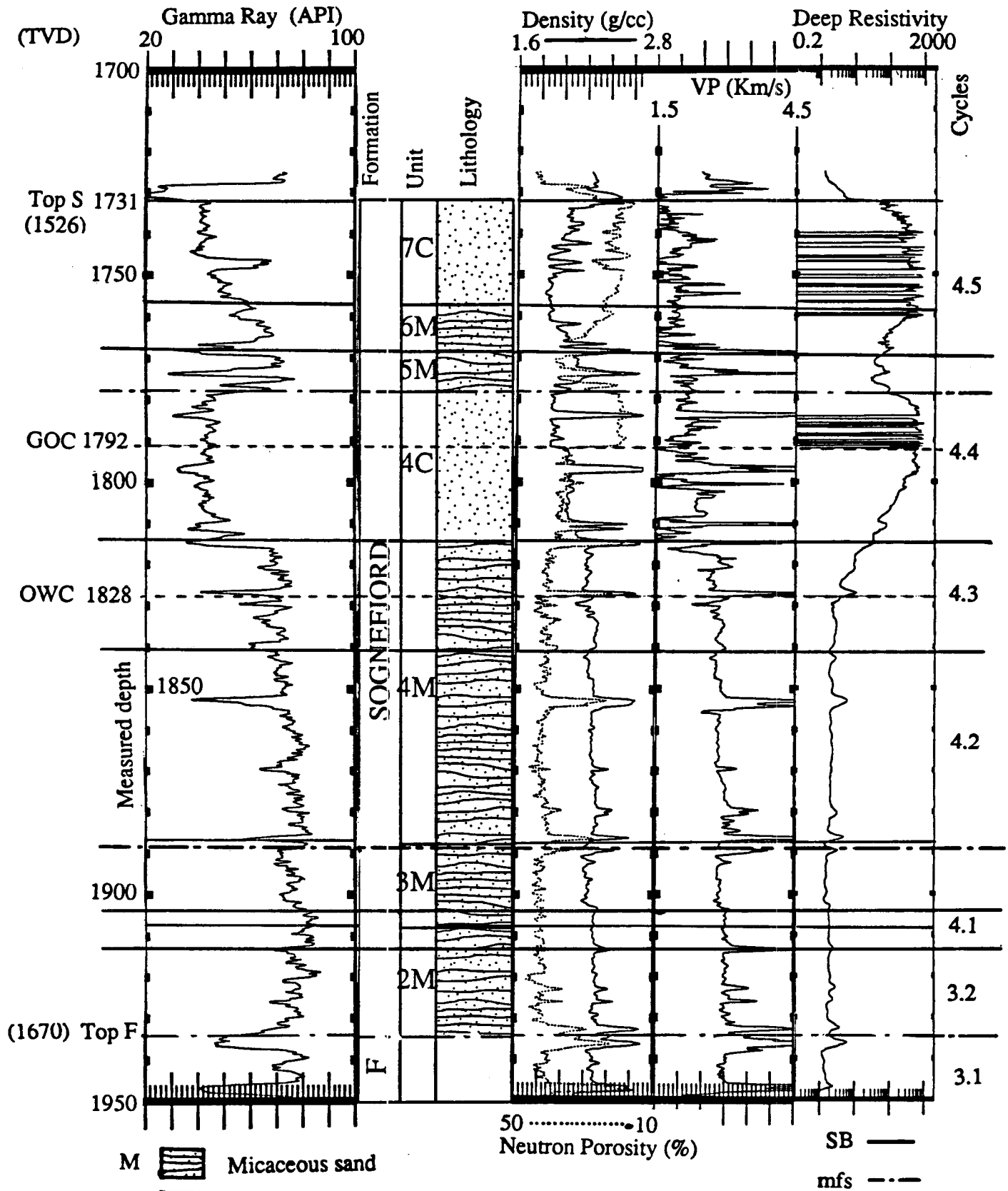




M Micaceous sand
 C Clean sand
 Appendix B.1: Well 31/2-12

SB
 mfs

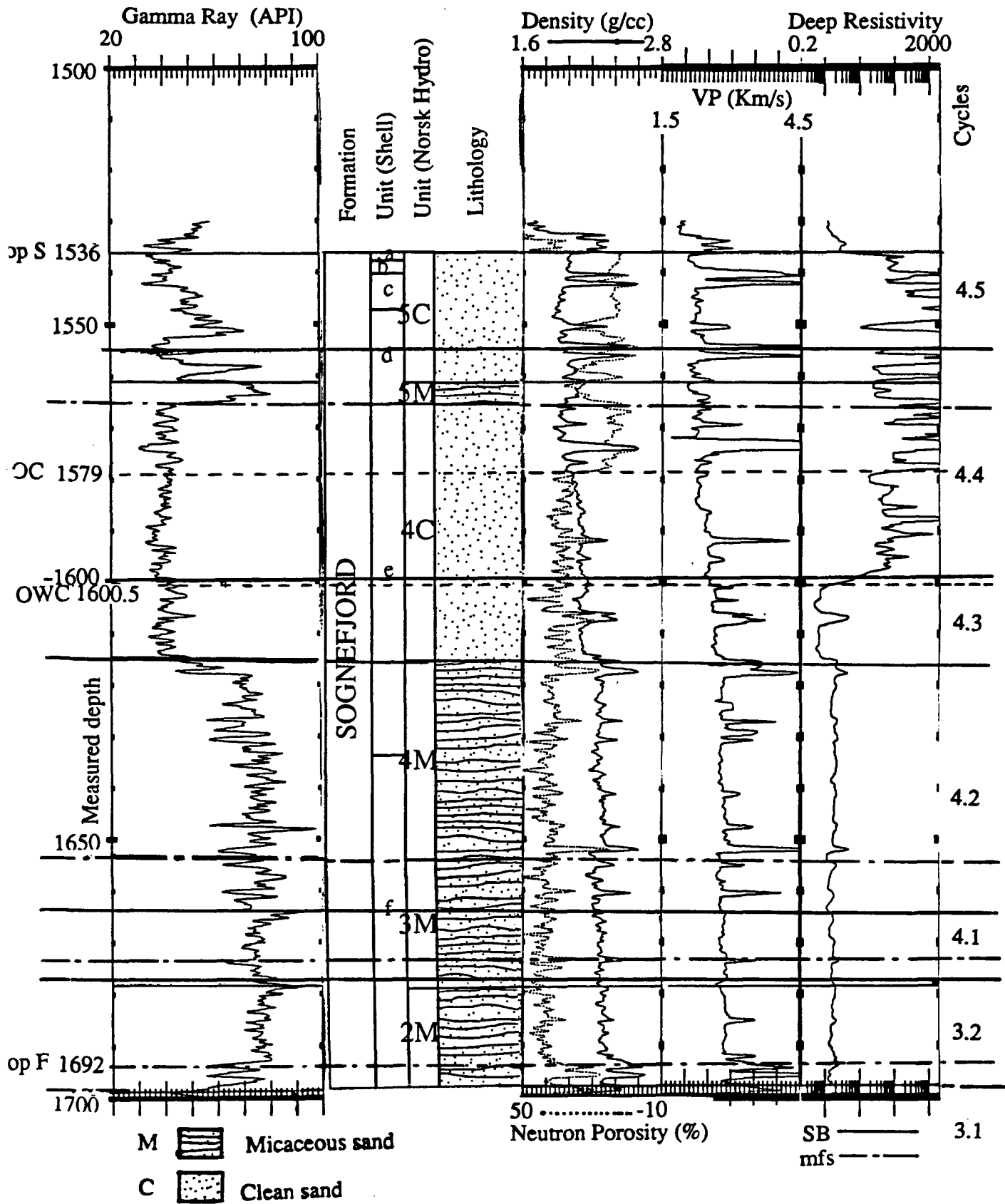


Appendix B.2: Well 31/2-10

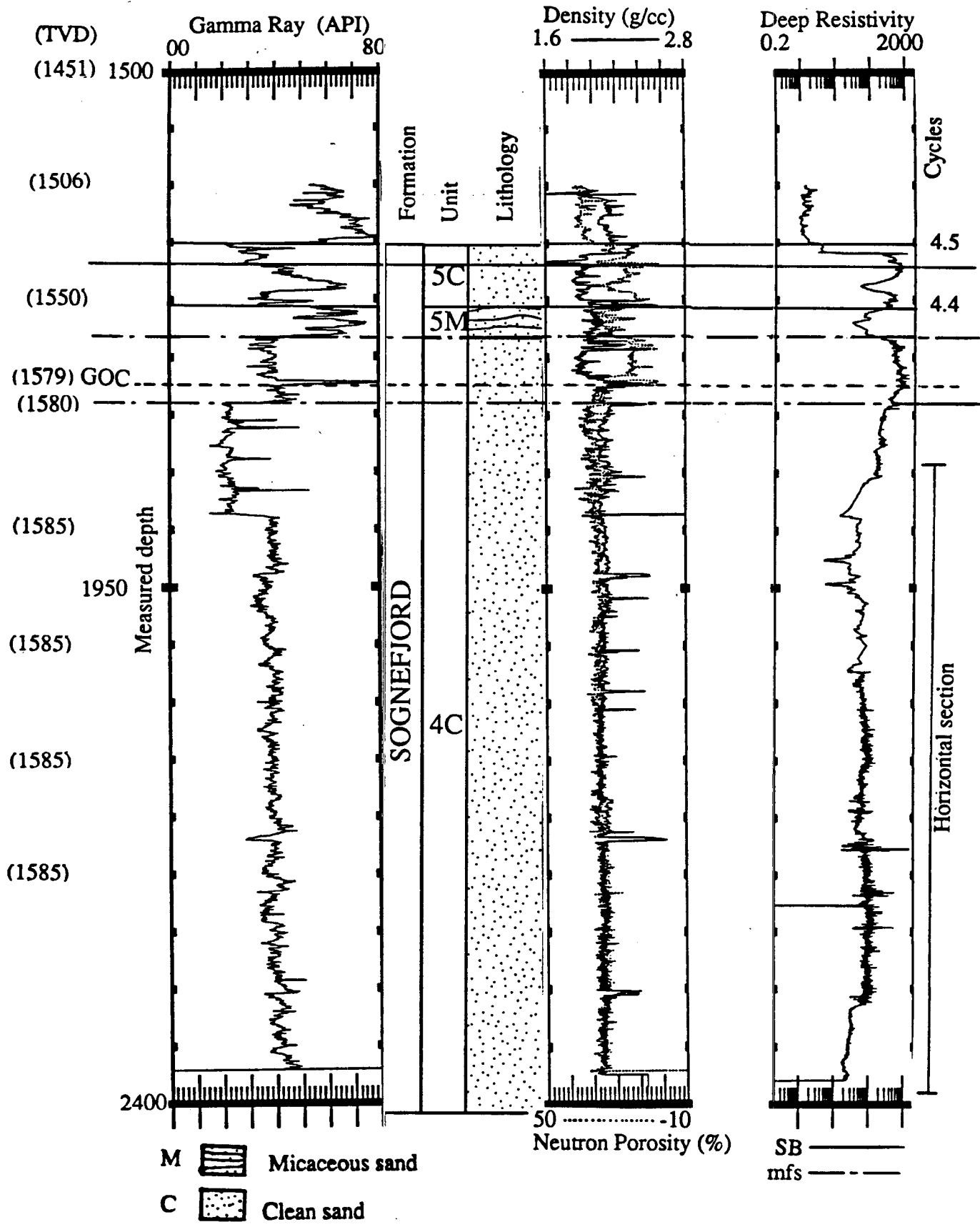


M  Micaceous sand
 C  Clean sand

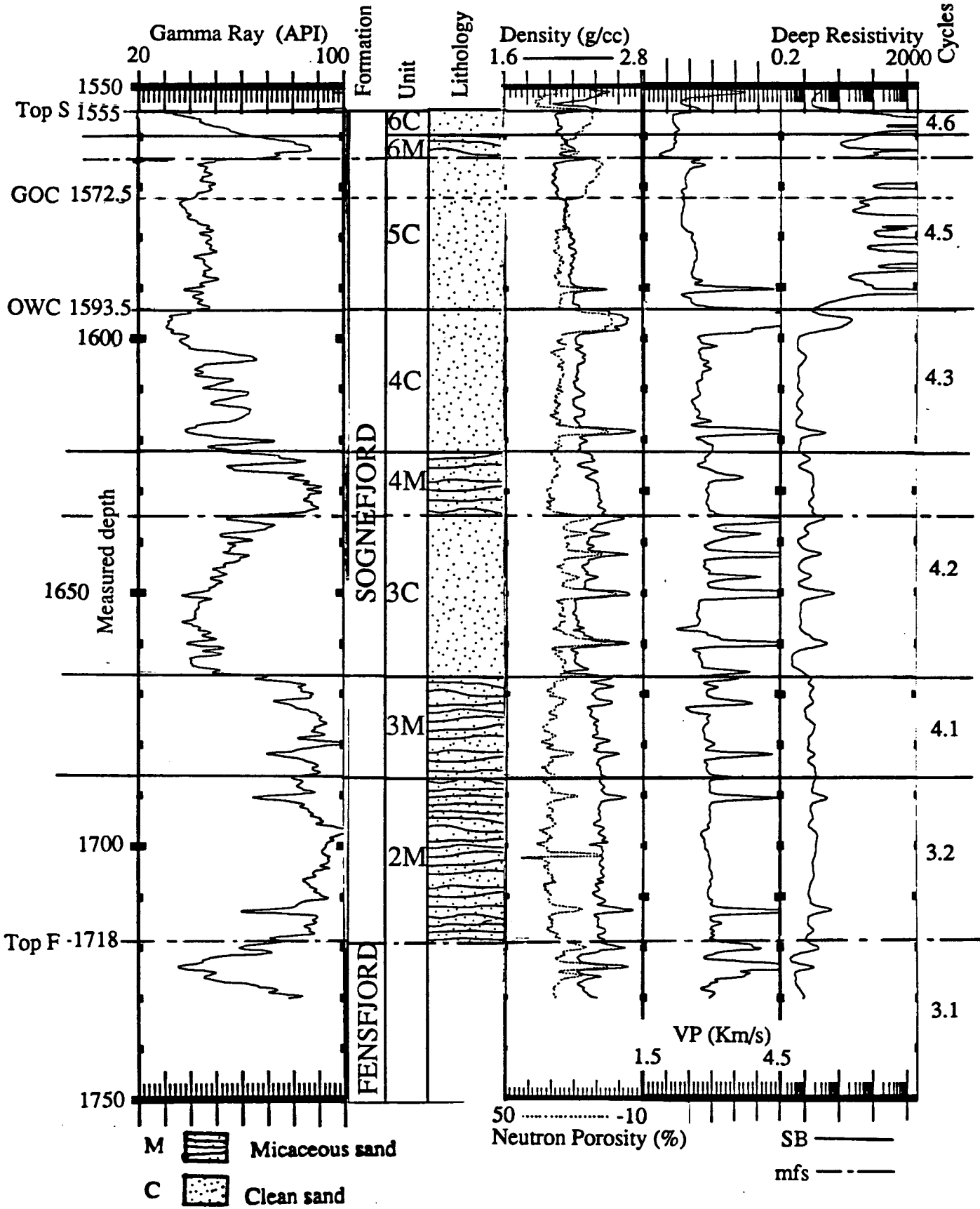
Appendix B.3: Well 31/2-13



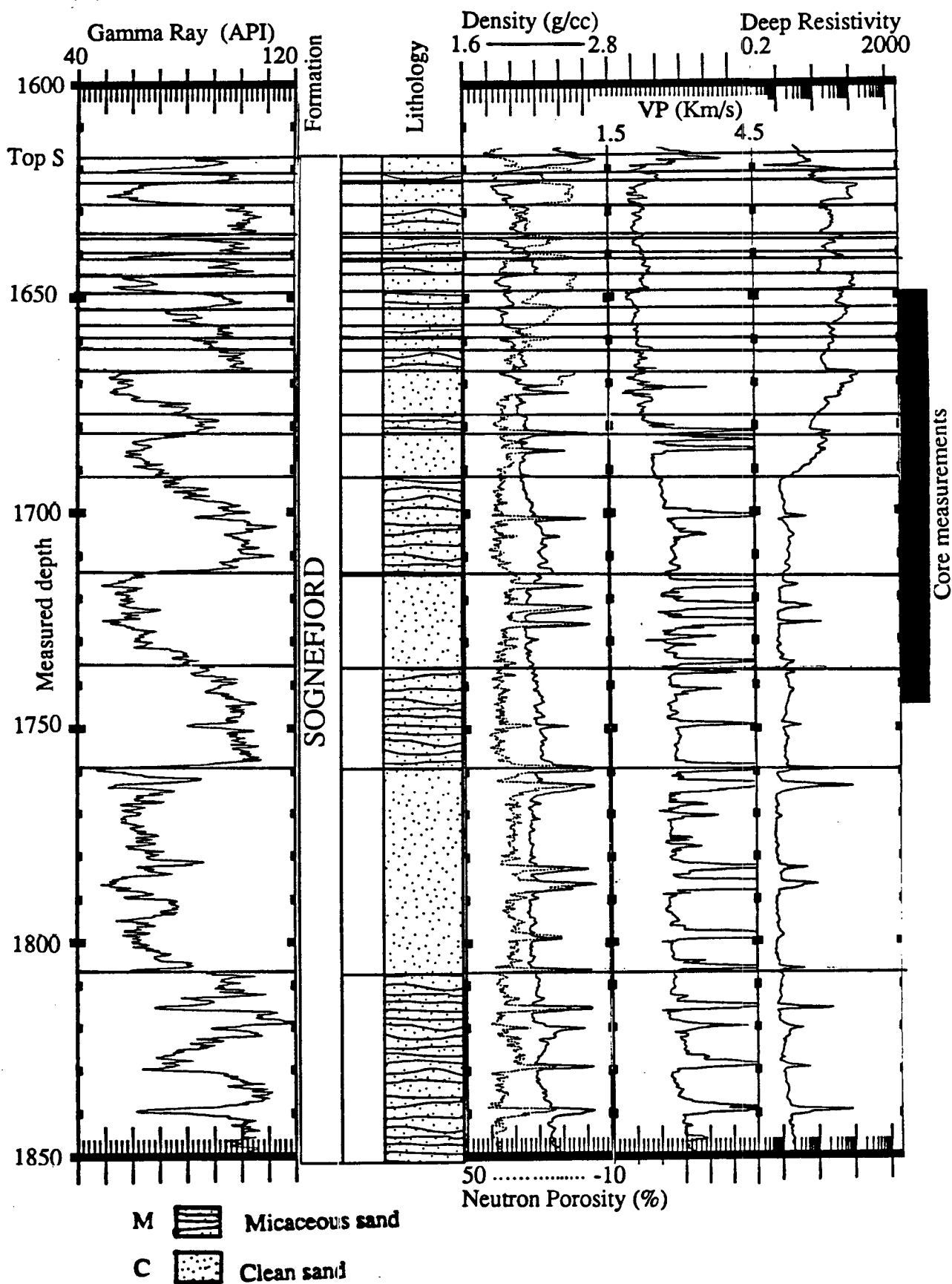
Appendix B.4: Well 31/2-5 (The type well)



Appendix B.5: Well 31/2-16S



Appendix B.6: Well 31/5-3

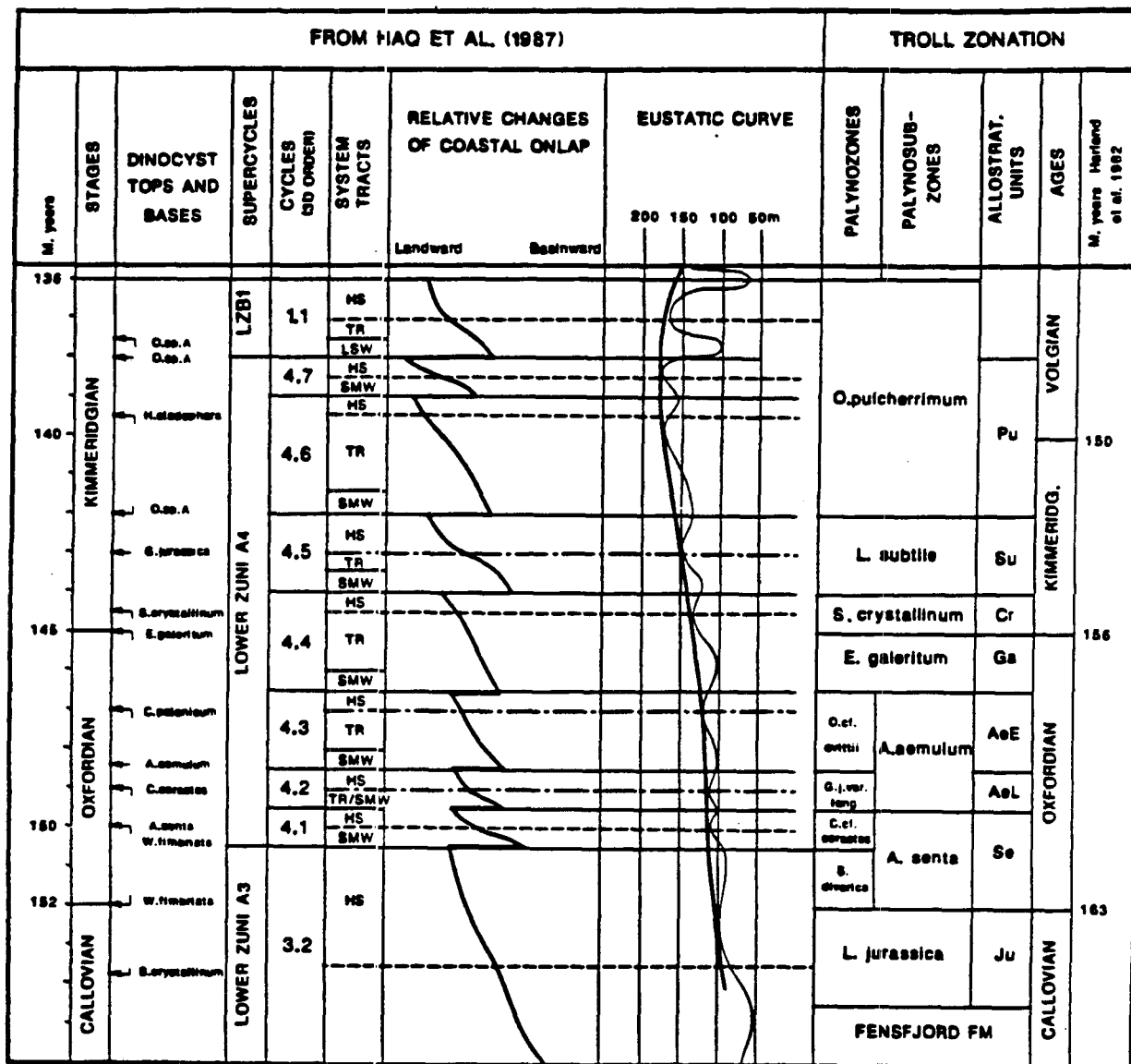


Appendix B.7: Well 31/5-4S (used in the core analysis)

Sequence Boundaries (SB) and Maximum Flooding Surfaces (mfs): in m					
(K.B.) Cycle	(32m) 31/2-5	(25m) 31/2-10	(25m) 31/2-12	(25m) 31/2-13	(26m) 31/5-3
Top Sognefjord	1536.0	1599.5	1565.0	1526.0	1555.0
SB 4.6	-	1600.0	-	-	1555.0
SB 4.5	-	1605.5	-	-	1561.5
SB 4.4	1556.5	1634.0	1388.0	1551.5	1594.5
SB 4.3	1599.0	1636.0	1391.5	1583.0	-
SB 4.2	1614.5	1658.5	1412.0	1602.5	1622.0
SB 4.1	1664.0	1738.0	1487.5	1648.0	1666.0
SB 3.2	1676.5	1749.0	1511.0	1655.0	1686.0
Top Fensfjord	1676.5	1749.0	1511.0	1655.0	1686.0
mfs 4.6	-	1599.5	-	-	1555.0
mfs 4.5	-	-	-	-	-
mfs 4.4	-	1609.0	1375.0	-	1564.5
mfs 4.3	1565.0	1636.0	1391.5	1558.0	-
mfs 4.2	-	1638.5	-	-	-
mfs 4.1	1652.0	1661.0	1416.5	1638.0	1635.0
mfs 3.2	1676.5	1749.0	1511.0	1655.0	1686.0
mfs 3.1	1697.5	1798.0	1541.0	1670.0	1719.0

Transgressive Tract (TR) and High Stand Wedge (HST) thicknesses: in m					
Cycle	31/2-5	31/2-10	31/2-12	31/2-13	31/5-3
TR 4.6	0	0.5	0	0	0
TR 4.5	0	5.5	0	0	6.5
TR 4.4	20.5	25.0	13.0	25.5	20.0
TR 4.3	34.0	0	0	30.0	0
TR 4.2	15.5	20.0	20.5	19.5	27.5
TR 4.1	12.0	77.0	71.0	10.0	31.0
TR 3.2	0	0	0	0	0
HS 4.6	0	0	0	0	0
HS 4.5	0	0	0	0	0
HS 4.4	0	3.5	10.0	0	3.0
HS 4.3	8.5	2.0	3.5	6.5	0
HS 4.2	0	2.5	0	0	0
HS 4.1	37.5	2.5	4.5	35.5	13.0
HS 3.2	12.5	11.0	23.5	7.0	20.0
HS 3.1	21.0	49.0	30.0	16.0	33.0

Appendix B.8: Key bounding surfaces in measured depths (m), and inferred minimum thicknesses of transgressive tracts and high stand wedges. Data from Norsk Hydro (Joint Geological report, 1988).



Appendix B.9: Correlation of Eustatic sea level curves (Haq et al., 1988) to sedimentary cycles observed at Troll. Data from Norsk Hydro, Joint Geological report (1988).

The correlation was established on the basis of the lowest/highest appearance of the following index dinocyst taxa, common to the Troll area and the Haq curves: *Wanaea fimbriata*, *Acanthaulax senta*, *Chytroeisphaeridia cerastes*, *Adnatosphaeridium aemulum*, *Compositosphaeridium polonicum*, *Endoscrinium galeritum*, *Scrinodinium crystallinum*, and *Oligosphaeridium pulcherinum*.

Sequence Boundaries, Sognefjord units, and Eustatic sea level cycles							
Well	ZA3.2	ZA4.1	ZA4.2	ZA4.3	ZA4.4	ZA4.5	ZA4.6 and ZA4.7
31/2-12	2M (3M)	3M	3C/4M	4C	5M	5C	-
31/2-13	2M (3M)	(3M)	3M/4M	4M/4C	4C/5M	(6M?)	-
31/2-10	2M/3M	3M	(3M)/3C/4M	4C	(5C)	5C/6M	6C
31/2-5	2M	3M	3M/4M	4C	4C/5M	5C	-
31/5-3	2M	3M	3C/4M	4C	5C/6M	6C	-
Sognefjord layers	1	2	3	4	5	6	7

Appendix B.10: Possible correlation of Sequence Boundaries, Sognefjord units, and Eustatic sea level cycles (Haq et al., 1988) for the 6 wells in the Southern Troll West oil province.

**APPENDIX C: ULTRASONIC VELOCITY MEASUREMENTS
AT WELL 31/5-4S**

Label	Label	A	B	C	D
Label	sample number	quartz	mica	feldspar	grainsize
1	1650.2	61.8	11	26	0.1
2	1652.15	70.8	2.4	25.8	0.2
3	1654.15	67.6	7.2	23.6	0.2
4	1656.1	67.6	12.8	19.2	0.2
5	1659.16	58.6	24	15.8	0.1
6	1664.91	50	28.2	21	0.1
7	1666.2	48.4	30	21.6	0.1
8	1668.25	73.8	3.2	23	0.3
9	1670.45	78	1	20.6	0.4
10	1672	66	3.8	29.4	0.3
11	1675.06	63.8	8.6	26.6	0.2
12	1677.15	50.4	12.2	37.2	0.2
13	1679.1	52.4	18	28.4	0.2
14	1681.18	72.4	8.6	19	0.2
15	1683.25	69.2	3	23	0.3
16	1685.12	69.8	2	28.2	0.3
17	1689	71.6	2.4	25.8	0.2
18	1691	68	12	19.4	0.2
19	1693.6	67	11	21	0.2
20	1695.05	63.8	7.8	27.6	0.2
21	1697.9	59.8	13	26.4	0.2
22	1699.1	62.8	10.2	26.2	0.2
23	1701.9	57.4	20.2	21.8	0.1
24	1703.1	56	23	20.2	0.1
25	1706.1	53	30.6	16.4	0.1
26	1708.1	60	20	19.2	0.1
27	1717.9	79	1.8	19.2	0.5
28	1719.1	78.4	1.6	18.8	0.4
29	1721.1	75	2.2	22.4	0.4
30	1723.64	75	2	22	0.4
31	1725.1	74.8	1.6	22.6	0.4
32	1729.1	77.2	0.8	22	0.5
33	1731.3	79.2	2.6	17.6	0.3
34	1735.1	68.6	10.8	20.2	0.1
35	1737.1	57.2	24.4	17.4	0.1
36	1739.1	56.8	26.8	14.6	0.1
37	1741.1	50.8	29.6	19	0.1
38	1745.1	58.6	29.6	10.8	0.1

Appendix C.1: Main mineralogy

Label	A	B	C	D	E	F	G	H	I	J
Label	sample number	eff press	corrected poros	vp dry	vs dry	vp/vs dry	vp wet	vs wet	vp/vs wet	grain density
1	1650.200	30.000	0.326	2.301	1.503	1.531	2.513	1.315	1.911	2.648
2	1652.150	30.000	0.364	2.039	1.327	1.537	2.434	1.212	2.007	2.586
3	1654.150	30.000	0.344	2.292	1.457	1.573	2.499			2.630
4	1656.100	30.000	0.331	2.336	1.503	1.554	2.626	1.330	1.974	2.638
5	1659.160	30.000	0.325	2.383	1.535	1.553	2.672	1.317	2.029	2.634
6	1664.910	30.000	0.297	2.448	1.561	1.568	2.903	1.408	2.062	2.624
7	1666.200	30.000	0.319	2.355	1.447	1.627	2.619	1.281	2.045	2.635
8	1668.250	30.000	0.307	2.311	1.527	1.514	2.575	1.280	2.011	2.656
9	1670.450	30.000	0.292	2.297	1.508	1.523	2.541			2.606
10	1672.000	30.000	0.329	2.224	1.394	1.595	2.660	1.270	2.094	2.598
11	1675.060	30.000	0.346	2.213	1.407	1.573	2.519			2.588
12	1677.150	30.000	0.262	2.337	1.478	1.581	2.523	1.266	1.993	2.481
13	1679.100	30.000	0.305	2.515	1.549	1.624	2.702	1.348	2.004	2.526
14	1681.180	30.000	0.355	2.369	1.500	1.575	2.631	1.351	1.947	2.630
15	1683.250	30.000	0.330	2.288	1.439	1.590	2.747	1.392	1.974	2.646
16	1685.120	30.000	0.337	2.380	1.575	1.511	2.774	1.286	2.157	2.616
17	1689.000	30.000	0.337	2.224	1.406	1.582	2.678	1.272	2.105	2.611
18	1691.000	30.000	0.348	2.327	1.407	1.654	2.649	1.230	2.154	2.647
19	1693.600	30.000	0.337	2.192	1.378	1.591	2.668			2.617
20	1695.050	30.000	0.354	2.187	1.377	1.588	2.614	1.257	2.080	2.578
21	1697.900	30.000	0.316	2.280	1.447	1.575	2.490	1.245	1.999	2.608
22	1699.100	30.000	0.243	2.604	1.735	1.500	3.033	1.555	1.951	2.590
23	1701.900	30.000	0.269	2.726	1.727	1.579	2.942	1.494	1.970	2.628
24	1703.100	30.000	0.222	2.675	1.740	1.538	3.010	1.524	1.975	2.539
25	1706.100	30.000	0.250	2.525	1.676	1.507	2.933	1.481	1.994	2.484
26	1708.100	30.000	0.234	2.541	1.659	1.532	2.855	1.454	1.963	2.516
27	1717.900	30.000	0.325	2.267	1.464	1.549	2.606	1.230	2.119	2.627
28	1719.100	30.000	0.304	2.389	1.505	1.588	2.742			2.633
29	1721.100	30.000	0.330	2.202	1.392	1.582	2.564	1.236	2.074	2.639
30	1723.640	30.000	0.348	2.252	1.441	1.563	2.716	1.296	2.096	2.637
31	1725.100	30.000	0.344	2.337	1.541	1.516	2.781	1.308	2.126	2.645
32	1729.100	30.000	0.259	2.699	1.708	1.580	2.984	1.485	2.010	2.611
33	1731.300	30.000	0.315	2.313	1.487	1.555	2.748	1.225	2.243	2.559
34	1735.100	30.000	0.295	2.557	1.707	1.498	2.757	1.464	1.884	2.563
35	1737.100	30.000	0.236	2.674	1.763	1.517	3.011	1.537	1.958	2.565
36	1739.100	30.000	0.290	2.562	1.632	1.570	2.855	1.460	1.956	2.573
37	1741.100	30.000	0.230	2.755	1.834	1.502	3.140	1.661	1.890	2.603
38	1745.100	30.000	0.264	2.775	1.757	1.580	3.016	1.605	1.879	2.594

Appendix C.2: Under 30 MPA effective pressure

Label	A	B	C	D	E	F	G	H	I
	sample number	eff press	corrected poros	vp dry	vs dry	vp/vs dry	vp wet	vs wet	vp/vs wet
1	1659.160	25.000	0.328	2.332	1.522	1.533	2.592	1.281	2.024
2	1656.100	25.000	0.334	2.290	1.493	1.534	2.604	1.298	2.005
3	1693.600	25.000	0.340	2.159	1.362	1.585	2.642		
4	1695.050	25.000	0.357	2.146	1.352	1.587	2.586	1.214	2.130
5	1691.000	25.000	0.351	2.307	1.385	1.665	2.607	1.203	2.168
6	1668.250	25.000	0.310	2.256	1.506	1.498	2.556	1.244	2.056
7	1654.150	25.000	0.347	2.215	1.446	1.532	2.460		
8	1652.150	25.000	0.367	1.993	1.309	1.523	2.410	1.191	2.024
9	1650.200	25.000	0.329	2.262	1.492	1.516	2.507	1.302	1.925
10	1683.250	25.000	0.333	2.089	1.385	1.508	2.663	1.339	1.988
11	1681.180	25.000	0.358	2.364	1.498	1.578	2.597	1.338	1.940
12	1679.100	25.000	0.308	2.459	1.522	1.616	2.674	1.328	2.013
13	1677.150	25.000	0.265	2.306	1.462	1.577	2.498	1.229	2.033
14	1675.060	25.000	0.349	2.154	1.390	1.550	2.477		
15	1664.910	25.000	0.300	2.420	1.555	1.556	2.834	1.366	2.074
16	1708.100	25.000	0.237	2.499	1.646	1.518	2.835	1.426	1.988
17	1737.100	25.000	0.239	2.627	1.738	1.512	2.957	1.483	1.995
18	1739.100	25.000	0.293	2.542	1.610	1.579	2.826	1.438	1.965
19	1699.100	25.000	0.246	2.573	1.718	1.498	2.976	1.494	1.992
20	1706.100	25.000	0.253	2.473	1.652	1.497	2.923	1.471	1.987
21	1735.100	25.000	0.298	2.534	1.682	1.506	2.720	1.457	1.866
22	1701.900	25.000	0.272	2.611	1.704	1.532	2.911	1.482	1.964
23	1741.100	25.000	0.233	2.735	1.826	1.498	3.101	1.641	1.890
24	1703.100	25.000	0.225	2.636	1.724	1.529	2.989	1.501	1.991
25	1745.100	25.000	0.267	2.706	1.724	1.570	2.964	1.587	1.867
26	1717.900	25.000	0.328	2.228	1.453	1.534	2.591	1.226	2.114
27	1697.900	25.000	0.319	2.229	1.421	1.569	2.487	1.224	2.032
28	1666.200	25.000	0.322	2.332	1.431	1.629	2.585	1.248	2.071
29	1721.100	25.000	0.333	2.161	1.373	1.575	2.549	1.213	2.101
30	1719.100	25.000	0.307	2.362	1.488	1.588	2.718		
31	1725.100	25.000	0.347	2.295	1.526	1.504	2.734	1.287	2.125
32	1723.640	25.000	0.351	2.214	1.414	1.565	2.669	1.230	2.270
33	1731.300	25.000	0.318	2.269	1.474	1.540	2.724	1.204	2.262
34	1729.100	25.000	0.262	2.639	1.675	1.575	2.952	1.400	2.108
35	1672.000	25.000	0.332	2.166	1.382	1.568	2.631	1.247	2.110
36	1689.000	25.000	0.340	2.187	1.388	1.576	2.646	1.231	2.148
37	1685.120	25.000	0.340	2.353	1.567	1.502	2.745	1.247	2.202
38	1670.450	25.000	0.295	2.263	1.493	1.515	2.517		

Appendix C.3: Under 25 MPa effective pressure

Label	A	B	C	D	E	F	G	H	I
Label	sample number	eff press	corrected poros	vp dry	vs dry	vp/vs dry	vp wet	vs wet	vp/vs wet
1	1659.160	20.000	0.332	2.265	1.479	1.531	2.562	1.258	2.036
2	1656.100	20.000	0.338	2.223	1.456	1.527	2.576	1.267	2.032
3	1693.600	20.000	0.344	2.095	1.333	1.571	2.578		
4	1695.050	20.000	0.361	2.094	1.326	1.560	2.501	1.147	2.180
5	1691.000	20.000	0.355	2.243	1.352	1.659	2.557	1.155	2.214
6	1668.250	20.000	0.314	2.168	1.479	1.466	2.512	1.204	2.086
7	1654.150	20.000	0.351	2.191	1.417	1.546	2.429		
8	1652.150	20.000	0.371	1.915	1.276	1.501	2.387	1.164	2.051
9	1650.200	20.000	0.333	2.165	1.458	1.485	2.442	1.260	1.939
10	1683.250	20.000	0.337	2.008	1.351	1.486	2.601	1.300	2.001
11	1681.180	20.000	0.362	2.270	1.456	1.559	2.607	1.318	1.978
12	1679.100	20.000	0.312	2.350	1.457	1.614	2.602	1.286	2.023
13	1677.150	20.000	0.269	2.242	1.439	1.558	2.452	1.184	2.071
14	1675.060	20.000	0.353	2.063	1.326	1.556	2.420		
15	1664.910	20.000	0.304	2.365	1.529	1.547	2.778	1.306	2.127
16	1708.100	20.000	0.241	2.432	1.617	1.504	2.782	1.344	2.071
17	1737.100	20.000	0.243	2.582	1.719	1.502	2.900	1.461	1.985
18	1739.100	20.000	0.297	2.377	1.542	1.541	2.792	1.418	1.969
19	1699.100	20.000	0.250	2.510	1.690	1.485	2.905	1.466	1.982
20	1706.100	20.000	0.257	2.403	1.626	1.478	2.899	1.446	2.005
21	1735.100	20.000	0.302	2.439	1.650	1.478	2.595	1.390	1.868
22	1701.900	20.000	0.276	2.548	1.687	1.511	2.857	1.474	1.938
23	1741.100	20.000	0.237	2.627	1.783	1.474	3.061	1.601	1.912
24	1703.100	20.000	0.229	2.552	1.697	1.504	2.943	1.477	1.992
25	1745.100	20.000	0.271	2.681	1.703	1.574	2.954	1.577	1.873
26	1717.900	20.000	0.332	2.179	1.440	1.513	2.548	1.206	2.113
27	1697.900	20.000	0.323	2.159	1.391	1.552	2.449	1.185	2.067
28	1666.200	20.000	0.326	2.274	1.397	1.627	2.558	1.228	2.084
29	1721.100	20.000	0.337	2.102	1.343	1.565	2.504	1.165	2.149
30	1719.100	20.000	0.311	2.290	1.454	1.575	2.556		
31	1725.100	20.000	0.351	2.243	1.492	1.503	2.709	1.244	2.177
32	1723.640	20.000	0.355	2.181	1.393	1.565	2.669	1.176	2.270
33	1731.300	20.000	0.322	2.222	1.455	1.527	2.642	1.175	2.249
34	1729.100	20.000	0.266	2.525	1.662	1.519	2.894	1.374	2.106
35	1672.000	20.000	0.336	2.117	1.366	1.549	2.583	1.182	2.186
36	1689.000	20.000	0.344	2.150	1.374	1.565	2.600	1.208	2.153
37	1685.120	20.000	0.344	2.223	1.487	1.495	2.696	1.180	2.284
38	1670.450	20.000	0.299	2.153	1.450	1.484	2.456		

Appendix C.4: Under 20 MPa effective pressure

Label	A sample number	B leff press	C corrected poros	D vp dry	E vs dry	F vp/vs dry	G vp wet	H vs wet	I vp/vs wet
1	1659.160	15.000	0.335	2.142	1.433	1.495	2.467	1.197	2.061
2	1656.100	15.000	0.341	2.130	1.408	1.513	2.520	1.231	2.047
3	1693.600	15.000	0.347	2.009	1.310	1.534	2.504		
4	1695.050	15.000	0.364	1.996	1.293	1.544	2.449	1.118	2.191
5	1691.000	15.000	0.358	2.185	1.306	1.674	2.494	1.124	2.218
6	1668.250	15.000	0.317	2.023	1.377	1.470	2.392	1.126	2.123
7	1654.150	15.000	0.354	2.111	1.382	1.527	2.393		
8	1652.150	15.000	0.374	1.839	1.208	1.522	2.341	1.119	2.093
9	1650.200	15.000	0.336	1.985	1.378	1.441	2.420	1.225	1.975
10	1683.250	15.000	0.340		1.276		2.552	1.260	2.025
11	1681.180	15.000	0.365	2.179	1.399	1.557	2.518	1.293	1.947
12	1679.100	15.000	0.315	2.232	1.433	1.557	2.561	1.216	2.106
13	1672.150	15.000	0.272	2.149	1.370	1.569	2.414	1.161	2.079
14	1675.060	15.000	0.356	1.965	1.297	1.515	2.351		
15	1664.910	15.000	0.307	2.249	1.465	1.535	2.735		
16	1708.100	15.000	0.244	2.327	1.550	1.502	2.728	1.326	2.057
17	1737.100	15.000	0.246	2.461	1.660	1.483	2.850	1.419	2.009
18	1739.100	15.000	0.300	2.345	1.520	1.542	2.712	1.374	1.975
19	1699.100	15.000	0.253	2.367	1.617	1.464	2.775	1.386	2.003
20	1706.100	15.000	0.260	2.366	1.597	1.481	2.853	1.420	2.010
21	1735.100	15.000	0.305	2.195	1.481	1.482	2.544	1.269	2.004
22	1701.900	15.000	0.279	2.428	1.670	1.454	2.786	1.400	1.990
23	1741.100	15.000	0.240	2.588	1.732	1.494	3.036	1.571	1.933
24	1703.100	15.000	0.232	2.424	1.579	1.535	2.871	1.421	2.020
25	1745.100	15.000	0.274	2.553	1.636	1.561	2.924	1.572	1.860
26	1717.900	15.000	0.335	2.118	1.379	1.537	2.338	1.169	2.000
27	1697.900	15.000	0.329	2.056	1.336	1.539	2.403	1.159	2.074
28	1666.200	15.000	0.329	2.190	1.363	1.607	2.504	1.178	2.125
29	1721.100	15.000	0.340	1.986	1.283	1.548	2.433	1.120	2.172
30	1719.100	15.000	0.314	2.218	1.409	1.575	2.425		
31	1725.100	15.000	0.354	2.179	1.449	1.504	2.666	1.196	2.229
32	1723.640	15.000	0.358	2.114	1.376	1.537	2.563	1.129	2.271
33	1731.300	15.000	0.325	2.142	1.401	1.529	2.572	1.110	2.317
34	1729.100	15.000	0.269	2.363	1.576	1.499	2.862	1.329	2.154
35	1672.000	15.000	0.339	1.999	1.317	1.518	2.551	1.142	2.234
36	1689.000	15.000	0.347	2.018	1.318	1.530	2.555	1.175	2.174
37	1685.120	15.000	0.347	2.130	1.417	1.503	2.647	1.153	2.296
38	1670.450	15.000	0.302	2.021	1.375	1.470	2.412		

Appendix C.5: Under 15 MPa effective pressure

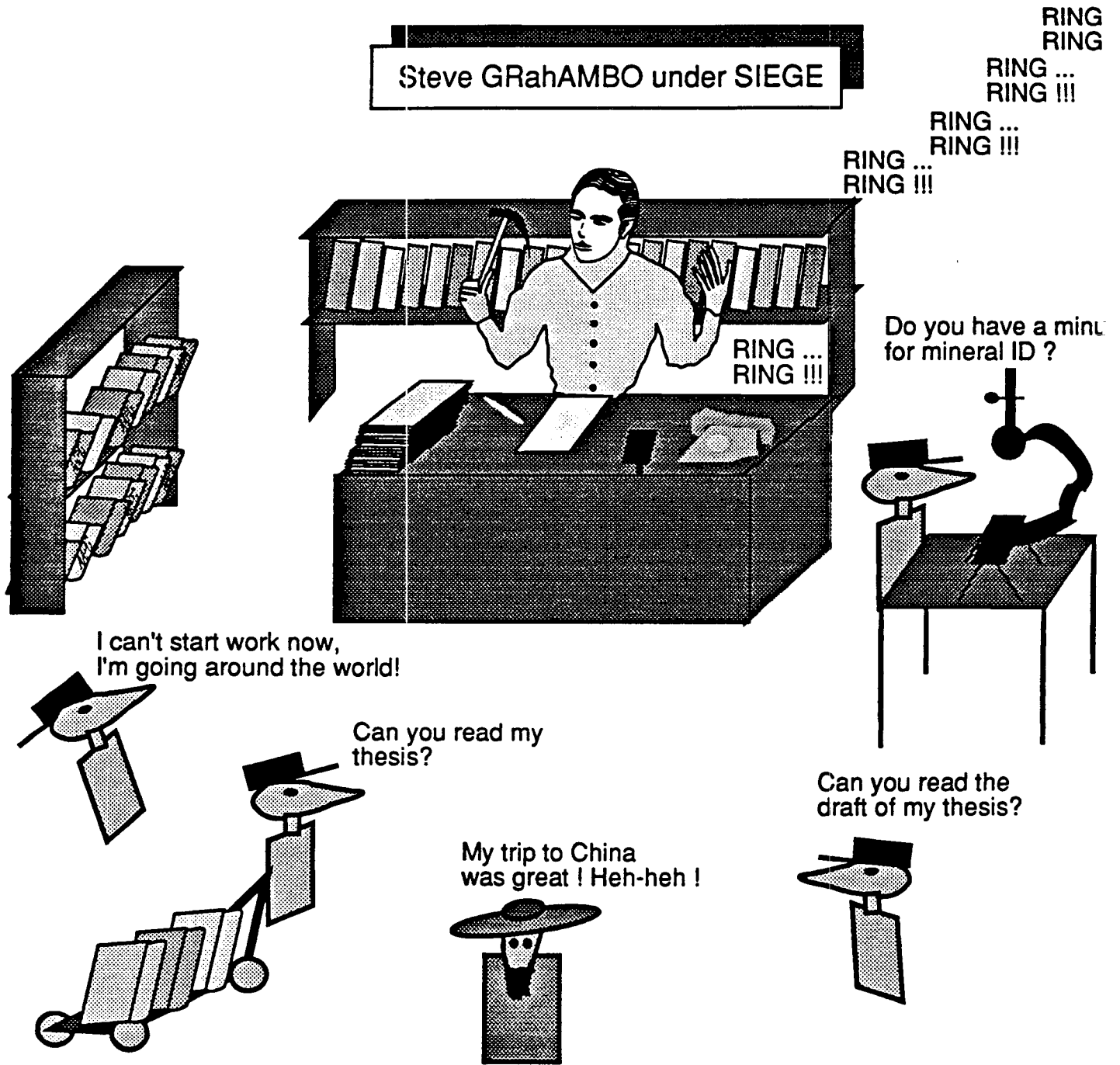
Label	A sample number	B eff. press	C corrected poros	D vp dry	E vs dry	F vp/vs dry	G vp wet	H vs wet	I vp/vs wet
1	1650.200	10.000	0.339	1.849	1.293	1.430	2.372	1.154	2.055
2	1652.150	10.000	0.377	1.719	1.145	1.501	2.267	1.059	2.140
3	1654.150	10.000	0.357	1.924	1.279	1.504	2.329		
4	1656.100	10.000	0.344	1.974	1.316	1.500	2.442	1.171	2.085
5	1659.160	10.000	0.338	1.875	1.307	1.434	2.432	1.137	2.138
6	1664.910	10.000	0.310	2.112	1.394	1.515	2.679		
7	1666.200	10.000	0.332	2.057	1.295	1.588	2.433	1.132	2.148
8	1668.250	10.000	0.320	1.928	1.318	1.462	2.311	1.094	2.112
9	1670.450	10.000	0.305				2.321		
10	1672.000	10.000	0.342	1.840	1.243	1.480	2.427		
11	1675.060	10.000	0.359	1.781	1.236	1.441	2.273		
12	1677.150	10.000	0.275	2.016	1.316	1.532	2.365	1.140	2.074
13	1679.100	10.000	0.318	2.094	1.348	1.554	2.464	1.174	2.099
14	1681.180	10.000	0.368	2.053	1.335	1.537	2.471	1.254	1.971
15	1683.250	10.000	0.343		1.221		2.453	1.202	2.049
16	1685.120	10.000	0.350	1.979	1.329	1.489	2.562	1.104	2.320
17	1689.000	10.000	0.350	1.916	1.258	1.523	2.439	1.112	2.193
18	1691.000	10.000	0.361				2.451	1.091	2.246
19	1693.600	10.000	0.350	1.897	1.258	1.508	2.402		
20	1695.050	10.000	0.367	1.745	1.206	1.447	2.387	1.098	2.175
21	1697.900	10.000	0.329	1.943	1.263	1.539	2.336	1.125	2.077
22	1699.100	10.000	0.256	2.205	1.512	1.458	2.714	1.350	2.011
23	1701.900	10.000	0.282	2.250	1.509	1.491	2.714	1.388	1.955
24	1703.100	10.000	0.235	2.236	1.483	1.507	2.812	1.396	2.015
25	1706.100	10.000	0.263	2.130	1.507	1.413	2.692	1.330	2.024
26	1708.100	10.000	0.247		1.466		2.636	1.251	2.108
27	1717.900	10.000	0.338	2.006	1.317	1.522	2.301	1.131	2.035
28	1719.100	10.000	0.317	2.021	1.314	1.539	2.269		
29	1721.100	10.000	0.343	1.836	1.224	1.500	2.319		
30	1723.640	10.000	0.361	2.016	1.328	1.517	2.490	1.095	2.273
31	1725.100	10.000	0.357	2.065	1.381	1.495	2.571	1.120	2.295
32	1729.100	10.000	0.272	2.260	1.590	1.422	2.783	1.270	2.191
33	1731.300	10.000	0.328	2.052	1.357	1.512	2.526		
34	1735.100	10.000	0.308	2.009	1.393	1.442	2.425	1.135	2.136
35	1737.100	10.000	0.249	2.276	1.532	1.486	2.759	1.345	2.052
36	1739.100	10.000	0.303	2.240	1.458	1.537	2.594	1.342	1.934
37	1741.100	10.000	0.243	2.418	1.655	1.461	2.948	1.539	1.916
38	1745.100	10.000	0.277	2.449	1.583	1.547	2.817	1.555	1.812

Appendix C.6: Under 10 MPa effective pressure

Label	A sample number	B eff press	C corrected poros	D vp dry	E vs dry	F vp/vs dry	G vp wet	H vs wet	I vp/vs wet
1	1659.160	5.000	0.342	1.727	1.217	1.418	2.335	1.079	2.164
2	1656.100	5.000	0.348	1.762	1.219	1.445	2.327	1.105	2.106
3	1693.600	5.000	0.354	1.755	1.204	1.458	2.327		
4	1695.050	5.000	0.371		1.099		2.254		
5	1691.000	5.000	0.365				2.353	1.055	2.231
6	1668.250	5.000	0.324		1.243		0.324		
7	1654.150	5.000	0.361	1.720	1.177	1.462	2.223		
8	1652.150	5.000	0.381	1.650	1.088	1.516	2.139		
9	1650.200	5.000	0.343		1.204		2.225	1.098	2.028
10	1683.250	5.000	0.347		1.148			1.157	
11	1681.180	5.000	0.372		1.264		2.380	1.200	1.984
12	1679.100	5.000	0.322	1.992			2.350	1.122	2.095
13	1677.150	5.000	0.279		1.259	1.385	2.277	1.096	2.078
14	1675.060	5.000	0.363	1.457	1.052		2.146		
15	1664.910	5.000	0.314		1.254		2.597		
16	1708.100	5.000	0.251		1.339		2.530	1.186	2.133
17	1737.100	5.000	0.253		1.401		2.567	1.207	2.127
18	1739.100	5.000	0.307		1.442		2.496		
19	1699.100	5.000	0.260	1.924	1.390	1.384	2.605	1.243	2.096
20	1706.100	5.000	0.267	2.019	1.416	1.425	2.648	1.296	2.044
21	1735.100	5.000	0.312				2.274	1.067	2.131
22	1701.900	5.000	0.286		1.356		2.598	1.244	2.088
23	1741.100	5.000	0.247	2.222	1.511	1.471	2.782	1.462	1.903
24	1703.100	5.000	0.239	2.052	1.403	1.463	2.727	1.273	2.142
25	1745.100	5.000	0.281	2.202	1.566	1.406	2.718		
26	1717.900	5.000	0.342	1.834	1.235	1.486	2.151	1.050	2.050
27	1697.900	5.000	0.333	1.743	1.130	1.542			
28	1666.200	5.000	0.336		1.191		2.335	1.087	2.148
29	1721.100	5.000	0.347	1.727			2.155		
30	1719.100	5.000	0.321		1.110		2.582		
31	1725.100	5.000	0.361	1.920	1.291	1.487	2.488		
32	1723.640	5.000	0.365	1.919	1.292	1.486	2.347		
33	1731.300	5.000	0.332	1.923	1.312	1.466	2.462		
34	1729.100	5.000	0.276	2.046	1.409	1.452	2.678		
35	1672.000	5.000	0.346	1.774	1.213	1.463	2.343		
36	1689.000	5.000	0.354	1.840	1.234	1.491	2.314		
37	1685.120	5.000	0.354	1.785	1.209	1.476	2.447	1.042	2.349
38	1670.450	5.000	0.309				2.246		

Appendix C.7: Under 5 MPa effective pressure

Your thesis committee readers may be under pressure:



Fill-in page

This page was inserted for esthetic purposes only, and does not necessarily reflect the author's opinion or his state of mind. It is NOT an integral part of the thesis at Stanford University, and was obtained from a series of "reliable" sources out there.

APPENDIX D: ELASTIC MODULI OF COMMON MINERALS


compiled from:








- 1) Carmichael, R.S., 1989, Practical handbook of physical properties of Rocks and Minerals, CRC press, Boca Raton, Florida
- 2) Ellis, D., Howard, J., Flaum, C., McKeon, D., Scott, H., Serra, O., and Simmons, G., 1988, Mineral logging parameters: Nuclear and Acoustic, in The technical Review, Schlumberger Ltd., Ridgefield, CT, V. 36, No.1, pages 38-55.
- 3) and the S.R.B. database

Elastic constants of common minerals						
Mineral	Bulk Modulus (Gpa)	Shear modulus (MPa)	Density	Vp(Km/s)	Vs(Km/s)	Poisson Ratio
Olivines						
Forsterite	130	85	3.32	8.58	5.03	.23
"Olivine"	130	80	3.32	8.45	4.91	.24
Garnets						
Almandine	176	95	4.18	8.51	4.77	.27
Zircon	19.8	19.7	4.56	3.18	2.08	.13
Epidotes						
Epidote	106.5	61.1	3.40	7.43	4.24	.26
Dravite	102.1	78.7	3.05	8.24	5.08	.19
Pyroxenes						
Diopside	111.2	63.7	3.31	7.70	4.39	.26
Augite	94.1	57.0	3.29	7.22	4.18	.25
Sheet Silicates						
Muscovite*	52.2	31.6	2.79	5.78	3.33	.25
Phlogopite*	49.4	26.7	2.80	5.50	2.94	.28
Biotite*	50.4	27.4	3.05	5.26	2.87	.28
clays						
Kaolinite	1.5	1.4	1.58	1.46	0.94	.13
"Gulf clays" (Han)	25	9	2.55	3.81	1.88	.34
"Gulf clays" (Tosaya)	21	7	2.6	3.41	1.64	.35
Framework Silicates						
Pertlite	46.7	23.63	2.54	5.55	3.05	.28
Plag. Feldspar (Albite)	75.6	25.6	2.63	6.46	3.12	.35
Quartz	37	44	2.65	6.05	4.09	.08
Qtz w/. clay (Han)	39	33	2.65	5.59	3.52	.17
Oxides						
Corundum	252.9	162.1	3.99	10.84	6.37	.24
Hematite*	127.1	86.3	5.24	6.80	4.06	.22
Rutile	217.1	108.1	4.26	9.21	5.04	.29
Spinel	203.1	116.1	3.63	9.93	5.65	.26
Magnetite*	110.3	55.05	5.00	6.06	3.32	.29

Elastic constants of minerals (continued)						
Mineral	Bulk Modulus (Gpa)	Shear modulus (MPa)	Density	Vp(Km/s)	Vs(Km/s)	Poisson Ratio
Hydroxides						
Limonite	60.1	31.3	3.55	5.36	2.97	.28
Sulfides						
Pyrite*	143	121	4.87	7.91	4.98	.17
Pyrrhotite	53.8	34.7	4.55	4.69	2.76	.23
Sphalerite	75.2	32.3	4.08	5.38	2.81	.31
Sulfates						
Barite*	55.5	23.0	4.48	4.38	2.26	.32
Celestite*	82.2	17.15	3.96	5.15	2.08	.40
Anhydrite	56.1	29.1	2.95	5.67	3.14	.28
Carbonates						
Calcite*	70.2	30.9	2.71	6.53	3.36	.31
Siderite*	123.7	51.0	3.92	7.00	3.61	.32
Dolomite*	82.1	48.3	2.88	7.13	4.09	.25
Aragonite	44.8	38.8	2.92	5.75	3.64	.16
Natronite	52.6	31.6	2.54	6.11	3.53	.25
Phosphates						
Hydroxyapatite	83.9	60.7	3.22	7.15	4.34	.21
Fluorapatite	86.5	46.6	3.21	6.80	3.81	.27
Halides						
Fluorite	86.4	41.8	3.18	6.68	3.62	.29
Halite	24.8	14.9	2.16	4.55	2.63	.25
Organic						
Kerogen	2.9	2.7	1.3	2.25	1.45	.14
Zeolites						
Natrolite*	46.6	28.0	2.25	6.11	3.53	.25

where the minerals marked with a symbol * are anisotropic.



We  not erate Saddam
Hussein for his actions. We will
Mobilize to meet this threat to our
vital interests in the Persian 
until an cable solution is reached. Our
strategy is to prepared. Failing that, we
ming to kick your ass, even if it takes
 years.

Fill-in page

This page was inserted for esthetic purposes only, and does not necessarily reflect the author's opinion or state of mind. It is NOT an integral part of the thesis at Stanford University, and was obtained from a series of "reliable" sources out there.

**APPENDIX E: OTHER RELATED PUBLICATIONS AND REPORTS
COMPLETED BY THE AUTHOR WHILE AT STANFORD**

(1) PAPERS:

Blangy, J.P., and Strandenes, S., 1992, A detailed integrated seismic geophysical reservoir characterization of the Troll West Oil Province: to be submitted to Geophysics or to the AAPG.

Blangy, J.P., Strandenes, S., Moos, D., and Nur, A., 1992, A new look at ultrasonic velocities in sands: submitted to Geophysics.

Samec, P., and Blangy, J.P., 1992, Viscoelastic attenuation, Anisotropy, and AVO: Geophysics, **57**, 441, 450.

(2) ABSTRACTS AND PRESENTATIONS:

Blangy, J.P., Strandenes, S., and Nur, A., 1992, Integrated interpretation of the Troll West area, to be presented at the 1992 Annual AAPG convention, Calgary.

Blangy, J.P., and Nur, A., 1992, A new look at Ultrasonic velocities in sands, to be presented at the 1992 Annual EAEG meeting in Paris.

Strandenes, S., and Blangy, J.P., 1991, Integrated Reservoir Characterization of a field from the North sea, SEG meeting, Houston.

Blangy, J.P., and Strandenes, S., 1991, Integrated Study of an Unconsolidated Reservoir, E.A.E.G., 53rd Meeting and Technical Exhibition, Florence, Italy.

Blangy, J.P., Samec, P., and Nur, A., 1990, Effects of Anelasticity and Anisotropy on Amplitude versus Offset Interpretation, 1990, S.E.G. Convention, San Francisco.

Blangy, J.P., and Samec, P., and Nur, A., 1990, Modeling of Anisotropy and Anelasticity applied to seismic interpretation, International Symposium on Reservoir Characterization, Maracaibo.

(3) REPORTS FOR TROLL PROJECT LICENSE GROUP:

Blangy, J.P., Strandenes, S., 1991, A detailed reservoir geophysical study of the Troll West Oil Province: Part I: Core analysis.

Blangy, J.P., Strandenes, S., 1991, A detailed reservoir geophysical study of the Troll West Oil Province: Part II: A practical approach to combining theory and experiment from microscale to macroscale.

Blangy, J.P., Strandenes, S., 1992, A detailed reservoir geophysical study of the Troll West Oil Province: Part III: Seismic Applications - in preparation.